

## Electron transfer in mesoporous (A1)-MCM-41 hosts

**Author:**

Han, Hongxian

**Publication Date:**

2003

**DOI:**

<https://doi.org/10.26190/unsworks/9082>

**License:**

<https://creativecommons.org/licenses/by-nc-nd/3.0/au/>

Link to license to see what you are allowed to do with this resource.

Downloaded from <http://hdl.handle.net/1959.4/63953> in <https://unsworks.unsw.edu.au> on 2024-04-17

# **Electron Transfer in Mesoporous (Al)-MCM-41 Hosts**

**Hongxian Han**

A thesis submitted in fulfilment of the requirements for the degree of

**Doctor of Philosophy**

**Supervisor: Professor Michael N. Paddon-Row**

**Co-supervisor: Professor Russell F. Howe**



**School of Chemical Sciences  
The University of New South Wales  
Sydney, Australia  
February 2003**



## Certificate of Originality

I hereby declare that this submission is my own work and to the best of my knowledge it contains no materials previously published or written by another person, nor material which to a substantial extent has been accepted for the award of any other degree or diploma at UNSW or any other educational institution, except where due acknowledgement is made in the thesis. Any contribution made to the research by others, with whom I have worked at UNSW or elsewhere, is explicitly acknowledged in the thesis.

I also declare that the intellectual content of this thesis is the product of my own work, except to the extent that assistance from others in the project's design and conception or in style, presentation and linguistic expression is acknowledged.

(Signed) ..

....

### CERTIFICATE OF ORIGINALITY

I hereby declare that this submission is my own work and to the best of my knowledge it contains no materials previously published or written by another person, nor material which to a substantial extent has been accepted for the award of any other degree or diploma at UNSW or any other educational institution, except where due acknowledgement is made in the thesis. Any contribution made to the research by others, with whom I have worked at UNSW or elsewhere, is explicitly acknowledged in the thesis.

I also declare that the intellectual content of this thesis is the product of my own work, except to the extent that assistance from others in the project's design and conception or in style, presentation and linguistic expression is acknowledged.

(Signed) ...

## Acknowledgements

This thesis cannot be completed without many people's help. First and most of all, I would like to express my heartfelt gratitude to my two supervisors, Professor Michael N. Paddon-Row and Professor Russell F. Howe (University of Aberdeen, UK) for supporting and encouraging me, enthusiasm and perseverance throughout my PhD study. Your hardworking and rigorous scientific manner will deeply affect my future work and life.

I am also grateful to the members of Professor Russell F. Howe's group: Paulina Taba, Sorina Popescu, Samitha D. Djajanthi, Sam Zoobi, Dr. M. Azhar Uddin, Dr. Peter Southon, Abdulsallam Eldewik, Dr. Stuart Thomson, Dr. Yannan Yang. Thanks for your assistance in various ways. My thanks also go to the members of Professor Michael N. Paddon-Row's group: Nigel Lokan, Anna Oliver, Peter Bicker and Sandra Hauptli. Thanks for your help in organic synthesis.

Also thanks Dr. Jim Hook for help in running Solid State NMR, Mr. Barry Ward for fixing the vacuum system, Mr. Juan Araya for supplying materials, Mr. John Starling for surface area measurements, Mr. Richard Burgess for the glass blowing work, and Dr. Nagindar Singh for purchasing the graded seal.

Thanks the Department of Education, Science and Training (DEST) for the IPRS scholarship and the school of chemical sciences for the living allowance.

Professor Michael N. Paddon-Row spent lots of valuable time reading throughout each chapter; Professor Russell F. Howe also gave me lots of fruitful discussion in organizing the thesis. Thanks, thanks very much!!!

To you all and the many others.....Thank you!!!

I dedicate this thesis to my faithful wife, Haidan Li, who shared weal and woe with me throughout three and half year PhD study, and my parents, who will be happy at this moment.

*“There must be no barriers for freedom of inquiry. There is no place for dogma in science. The scientist is free, and must be free to ask and question, to doubt any assertion, to see for any evidence, to correct any errors.”*

*----- By Robert Oppenheimer*

---

## Table of Contents

<b>Title page</b>	<b>I</b>
<b>Certificate of originality</b>	<b>II</b>
<b>Acknowledgements</b>	<b>III</b>
<b>Motto</b>	<b>IV</b>
<b>Table of contents</b>	<b>V</b>
<b>Abstract</b>	<b>IX</b>
<b>Chapter 1: Introduction</b>	<b>1</b>
1.1. Electron transfer in heterogeneous materials	1
1.2. Introduction of mesoporous MCM-41 materials	5
1.3. Electron transfer of guest molecules in MCM-41 hosts	14
1.4. Control of energy transfer in mesoporous materials	26
1.5. Application of MCM-41 materials in optical devices	28
1.6. Electron donor and acceptor sites in MCM-41 materials	28
1.7. Aims of the thesis	29
1.8. References for Chapter 1	30
<b>Chapter 2: Experimental</b>	<b>45</b>
2.1. Introduction	45
2.2. Inorganic synthesis	46
2.3. Organic synthesis	53
2.4. Molecular assembly in (Al)-MCM-41	58
2.5. Characterization methods	62

---

2.6 References for Chapter 2	85
2.7. Appendices	87
<b>Chapter 3: Characterization of mesoporous (Al)-MCM-41 hosts</b>	<b>96</b>
3.1. Introduction	96
3.2. Powder XRD patterns	97
3.3. Solid state NMR	114
3.4. Chemical composition of synthesized (Al)-MCM-41 samples	128
3.5. Surface properties	129
3.6. Summary	142
3.7. References for Chapter 3	144
<b>Chapter 4: Template removal by ozone treatments</b>	<b>148</b>
4.1. Introduction	148
4.2. Power XRD patterns	152
4.3. Solid state NMR	163
4.4. Surface properties	178
4.5. Template removal by EtOH/HCl liquid extraction and ozone treatments	192
4.6. Mechanism of ozone on CTAC template removal	206
4.7. Summary	209
4.8. References for Chapter 4	211
<b>Chapter 5: Chemistry of electron acceptor molecules in (Al)-MCM-41 hosts</b>	<b>215</b>
5.1. Introduction	215
5.2. TCNE in (Al)-MCM-41	218
5.3. TCNQ in (Al)-MCM-41	244

---

5.4. 1,4-BQ in (Al)-MCM-41	253
5.5. BQ[2] in (Al)-MCM-41	264
5.6. 1,4-NQ in (Al)-MCM-41	266
5.7. 1,4-AQ in (Al)-MCM-41	270
5.8. Other electron acceptor molecules in (Al)-MCM-41	272
5.9. Electron donating ability of (Al)-MCM-41	275
5.10. Summary	277
5.11. References for Chapter 5	279
 <b>Chapter 6: Chemistry of electron donor molecules in (Al)-MCM-41 hosts</b>	 <b>284</b>
6.1. Introduction	284
6.2. 1,4-DMB in (Al)-MCM-41	286
6.3. 1,4-DMN in (Al)-MCM-41	292
6.4. DMN[2] and DMN[4] in (Al)-MCM-41	296
6.5. 9,10-DMA in (Al)-MCM-41	304
6.6. DMA[2] in (Al)-MCM-41	309
6.7. TTF derivatives in (Al)-MCM-41	311
6.8. Other molecules	316
6.9. Electron accepting ability of Al-MCM-41	317
6.10. Summary	319
6.11. References for Chapter 6	320
 <b>Chapter 7: Chemistry of donor-bridge-acceptor dyads in (Al)-MCM-41 hosts</b>	 <b>323</b>
7.1. Introduction	323
7.2. DMN-6B-DCV in (Al)-MCM-41	325

---

7.3. DMN-8B-BQ in (Al)-MCM-41	332
7.4. Electron transfer mechanism of D-B-A molecules in Al-MCM-41	336
7.5. Summary	339
7.6. References for Chapter 7	340
 <b>Chapter 8: Summary and future work</b>	 <b>343</b>
8.1. Summary	343
8.2. Future work	344

## Abstract

Various kinds of electron donors, acceptors and D-B-A dyads have been assembled into the channels of the mesoporous (Al)-MCM-41 hosts. The chemistry of these organic molecules in the (Al)-MCM-41 hosts and the redox properties of the (Al)-MCM-41 hosts have been extensively studied in this work.

It is found that Al-MCM-41 materials feature both electron donor sites and electron acceptor sites, while Si-MCM-41 has no (or rather weak) redox sites at room temperature. The electron donor and acceptor sites are assigned to the negatively charged oxygen bonded to the extra-framework Al (oxide ions) and the Lewis acid sites, respectively. The oxidation potential of the Al-MCM-41 is determined to be in the range:  $-1.0 \text{ V} \leq E^{\text{Ox}}(\text{Al-MCM-41}) \leq -0.92 \text{ V}$ ; while the reduction potential of the Al-MCM-41 is determined to be in the range:  $1.18 \text{ V} \leq E^{\text{Red}}(\text{Al-MCM-41}) \leq 1.34 \text{ V}$ . Al-MCM-41 materials are ideal heterogeneous hosts for generating and stabilizing radical species. Radical anions and cations generated *via* electron transfer with the Al-MCM-41 framework are long-lived in the Al-MCM-41 hosts.

The DMN-6B-DCV dyad formed long-lived radical cations of the DMN group which were complexed with the Lewis acid sites (extra-framework  $\text{Al}^{3+}$ ) in the Al-MCM-41 hosts after photoirradiation; while the DMN-8B-BQ dyad formed tightly bound “radial anion of the BQ group---Al (extra-framework  $\text{Al}^{3+}$ )” ion pairs which were also long-lived. The extra-framework Al also plays an important role in the formation of long-lived radical cation or anion of the occluded dyads in the Al-MCM-41 hosts.

Electron transfer processes in the Al-MCM-41 hosts largely depend on the molecular assembling conditions, such as the nature of the assembled molecules (e.g., the redox potential, steric effects and adsorption ability), the nature of the hosts (e.g., the Al content in the framework), the pretreatment method (e.g., synthesis procedure, dehydration temperature) and the media (solvent) used for assembling the guest-host systems.



# Chapter 1

## Introduction

### 1.1. Electron Transfer in Heterogeneous Materials

Because solar energy is an inexpensive and renewable energy source, efficient conversion and storage of solar energy into useful chemical or electrical energy based on artificial photoredox systems is an important and active research area.<sup>1-4</sup> The conversion and storage of solar energy requires transformation of abundant and low-cost raw materials like  $\text{H}_2\text{O}$ ,  $\text{CO}_2$  and  $\text{N}_2$  into fuels like  $\text{H}_2$ ,  $\text{CH}_3\text{OH}$ ,  $\text{CH}_4$  and  $\text{NH}_3$ .<sup>1-5</sup> Construction of photoredox systems, which consist of at least one electron donor and one electron acceptor (either of which is photosensitive) to generate a pair of radical ions with long-lived charge separated state, is one of the key methodologies for this purpose. In this system, either donor or acceptor adsorbs a photon of suitable energy and is converted to an electronically excited state which is a better oxidant or reductant than the ground state. Photoinduced electron transfer (PET) between such an excited state and a suitable reaction partner converts a fraction of the absorbed light energy into chemical energy.<sup>6</sup> Then the stored chemical energy of photoproducts may serve as an energy source to drive chemical reactions. Usually the raw material to be converted into a fuel cannot be electronically excited by the visible light. For example, the electronic absorption of water occurs at 167 nm in the far-UV region. In such a case, the process must be mediated by a suitable chemical species called a photosensitiser.<sup>7</sup>

In order to mimic the photosynthesis center, the following two parallel strategies are exploited: on one hand, numerous molecular assemblies of donors (D), chromophores

(S), and acceptors (A) in many variations have been synthesized, forming dyads, triads, tetrads, or even pentads, to achieve charge separation in solution or monolayers.<sup>8,9</sup> On the other hand, the photovoltaic systems combining the intramolecular ET with interfacial light induced charge separation to increase the light-electricity conversion yield is another alternative strategy. One example of the latter is the dye-sensitized nanocrystalline solar cells.<sup>10</sup>

However, in most photoredox systems, the efficiency of the photoinduced ET (photoionization efficiency) is generally limited by the occurrence of deactivating back ET, which competes with the other reactive pathways of the generated ion pairs.<sup>2-4,6,9,11-16</sup> In order to achieve a net production of photoproducts, this undesired back ET must be minimized.<sup>3,17</sup>

Different methodologies are being pursued to minimize the unwanted back ET process aiming to achieve relatively stable and long-lived charge separation between the donor and the acceptor.<sup>2,18-23</sup> One of the promising methodologies is to construct the photoredox systems in heterogeneous hosts such as semiconductor particles,<sup>24-43</sup> organic assemblies of vesicles and micelles<sup>44-54</sup> and porous inorganic solids such as zeolites<sup>42,55-77</sup> and silica gels (or silica)<sup>18,20,78-83</sup>. The back ET rate in such heterogeneous system is dramatically retarded compared to that in homogeneous solutions.<sup>1,3,4,6,11,48-54</sup>

Semiconductors (especially  $\text{TiO}_2$ )<sup>24-43</sup> are one of the most suitable materials with relatively favorable band gap energy, offering the highest light energy conversion efficiency. However, it just responds to the UV lights which correspond to only ca. 5 % of the whole light.

The photoionization efficiency in organic assemblies<sup>44-54</sup> is higher than that in homogeneous solutions, but the photoinduced radicals are not stable at room

temperature. In some cases, the photoyields in organic assemblies are limited by the polarity and the solubility of the photosensitisers in vesicle and micellar solutions.

However, photoionization studies in porous inorganic materials such as zeolites<sup>42,55-77</sup> and silica gels<sup>18,20,78-83</sup> have shown that their cages or pores can provide an appropriate microenvironment to retard back ET and increase the lifetime of the photogenerated radical ions. This is associated with the steric and electrostatic effects in these inorganic materials. A photosensitiser of proper molecular size compared to the pore (or cage) sizes of such inorganic materials can be incorporated into the pores (or cages), and the photoinduced radical ions can even be stable at room temperature.

The surface hydroxyl groups on the silica gel were suggested to serve as the electron acceptor sites to generate trapped hydrogen atoms.<sup>78,80,84</sup> However, the photoyield in silica gel is low.<sup>18,20,78-83</sup> This was explained by the faster decay of the photoinduced radicals due to their greater mobility in the larger pores of the silica gels.<sup>78,80,82,84</sup> Also, fewer silanol groups are adjacent to the photoionizable molecules adsorbed in the pores of the silica gels due to their larger radius of curvature.<sup>82,83</sup> Large pore silica gels provide less confinement effects, which result in greater mobility of the photogenerated radicals and decrease the net photoyield.<sup>78,80,82-84</sup> The irregular pore structure with no long-range order and a wide pore size distribution compared to zeolites are the main disadvantages of the silica gels to be hosts to stabilize the occluded radical species. These structures and surface properties' limitations may also account for the less photoefficiency in micro- and mesopore silica gels.

It is well known that zeolites can stabilize the trapped transient species by markedly retarding back electron transfer. Stabilization effects are usually accounted for by the unique steric, polar and electrostatic microenvironments provided by the zeolites.<sup>63</sup> It was calculated that zeolite internal electric fields could reach  $6.3 \text{ V \AA}^{-1}$  at a distance of a

few angstroms from a cation site in zeolite Y.<sup>65</sup> Electric field of this magnitude can readily polarize molecules in close proximity and alter reactivity.<sup>85</sup> Zeolites may act as electron donors or acceptors and be directly involved in the electron transfer process with the occluded redox species.<sup>63</sup> Following models are considered as the electron acceptor sites or the sites responsible for the corresponding oxidation reaction of the guest molecules: (1) impurities, such as  $\text{Fe}^{3+}$ ,<sup>68,86</sup> (2) Brønsted acid sites,<sup>87,88</sup> (3) Lewis acid sites,<sup>86,89-93</sup> (4) solid defects which are positive holes on oxygen atoms of zeolite framework,<sup>94</sup> (5) strongly chemisorbed molecular oxygen,<sup>68,95,96</sup> (6) coordinatively unsaturated framework Al atoms (three coordinated) generated by loss of framework oxygen during thermal treatment<sup>97</sup> (7) non-framework positively charged aluminum oxide  $\text{Al}(\text{OH})^{2+}$  which is lost from the framework during activation;<sup>98</sup> (8) non-framework aluminum species, especially those which are coordinatively distorted or unsaturated, rather than the framework aluminum sites.<sup>67,68,89,94,99-101</sup> In contrast with the variety of examples that zeolites act as electron acceptors, fewer examples have been reported using zeolites as electron donors.<sup>56,62,63,102-112</sup> The hydroxyl ion was suggested to be the electron donor when zeolites were activated at around 523 K.

Though microporous zeolites provide an appropriate polar microenvironment with strong electrostatic fields inside the pores for retarding the back ET and increasing enormously the lifetime of the photogenerated ion pair,<sup>63,113</sup> impeded diffusion of the reagents and accessibility of the sites are limiting factors of paramount importance. In fact, the relatively small pore size of the micropores (typically  $\leq 1.3$  nm) has been claimed as the main drawback for an intensive use of zeolites as microscopic reactors.<sup>75</sup> Much effort is currently being devoted to explore novel porous materials with larger pore dimensions. It is expected that novel aluminosilicate type materials with larger pore size, which maintain the framework features of zeolites simultaneously, should

overcome most of the adsorption/diffusion limitations of conventional zeolites and constitute a significant breakthrough in the field of inclusion chemistry.<sup>75</sup>

As discussed above, the semiconductors, organic assemblies, microporous zeolites and the silica gels all have their own disadvantages for hosting the photoredox systems. The discovery of the M41S mesoporous materials<sup>114,115</sup> by researchers at Mobil Research and Development Corporation provides a fascinating prospect for constructing photoredox systems in them to achieve long-lived charge separated state. In this work, the mesoporous MCM-41 materials, the most extensively studied member of the M41S family, are used as hosts to assemble various organic donors, acceptors, and donor-bridge-acceptor molecules. The chemistry of these redox molecules in (Al)-MCM-41, the ET between the occluded organic molecules and the MCM-41 framework, the redox properties and the redox sites of the MCM-41 materials have been explored.

## **1.2. Introduction of Mesoporous MCM-41 Materials**

### **1.2.1. Discovery of Mesoporous M41S Family**

According to the IUPAC definition,<sup>116</sup> porous materials are divided into three classes: microporous (< 2 nm), mesoporous (2-50 nm) and macroporous (> 50 nm). Zeolites are one of the most useful catalysts due to their tunable acid strength and well-defined pore diameters.<sup>117,118</sup> However, the usefulness of zeolites in conversion of high-molecular-weight hydrocarbons, which are of increasing importance, is limited by their small pore sizes (usually less than 13 Å). The demand for large-pore catalysts to process heavier chemical feedstocks and the prospect of synthesizing fine chemicals have triggered enormous synthetic efforts which led to the production of larger pore molecular sieves such as VPI-5,<sup>119</sup> cloverite,<sup>120</sup> JDF-20,<sup>121</sup> UTD-1,<sup>122</sup> and pillared clays.<sup>123</sup> However,

the practical application of these materials is still limited because of their poor thermal stability, stacking disorder, difficulty of surfactant removal, and negligible catalytic activity due to electrically neutral framework.

In early 1990s, Mobil scientists<sup>114,115,124</sup> as well as Japanese researchers<sup>125,126</sup> reported the first successful synthesis of novel periodic mesostructured materials. The former employed a new synthesis concept, i.e., self-assembled molecular aggregate or supramolecular assembly of surfactant molecules rather than the conventional single-(amine-) molecules in microporous (zeolites) synthesis. This led to the discovery of the so-called mesoporous M41S family.<sup>114,115,124</sup> Actually, a process for the formation of “low-bulk density silica” had been patented by Chiola et al.<sup>127</sup> in 1971. In this process tetraethyl orthosilicate (TEOS) is hydrolyzed in the presence of cationic surfactants. Although the aforementioned patent does not describe the porosity or the periodicity of the resulting materials, Di Renzo et al.<sup>128</sup> recently showed that the reaction products are similar to the MCM-41. Whatsoever, four different mesostructures,<sup>114,115,129,130</sup> a hexagonal phase (MCM-41), two types of cubic phase with space groups Ia3d (MCM-48) and Pm3n (octamer), respectively, and a lamellar phase (MCM-50) have been reported (Figure 1). The MCM-41 and MCM-48 are thermally stable while the other two are unstable. The most extensively studied members of the M41S family are MCM-41 materials, because of their unusual textural characteristics, such as adjustable uniform pore size, high surface area and long-range ordering of the packing of the pores and potential application for processing large organic molecules.<sup>114,115,129-136</sup>

After the discovery of the M41S, some other mesostructured materials have also been developed, such as FSM-16,<sup>126,137</sup> SBA-*n* (*n*= 1-3, 8, 11, 12, 14-16),<sup>138-144</sup> MSU-*n* (*n* = 1-4),<sup>145,146</sup> KIT-1,<sup>147</sup> CMK-1,<sup>148</sup> SNU-2,<sup>149</sup> HMS,<sup>150,151</sup> MSU-V,<sup>152</sup> MSU-G<sup>153</sup> and APO.<sup>154,155</sup>

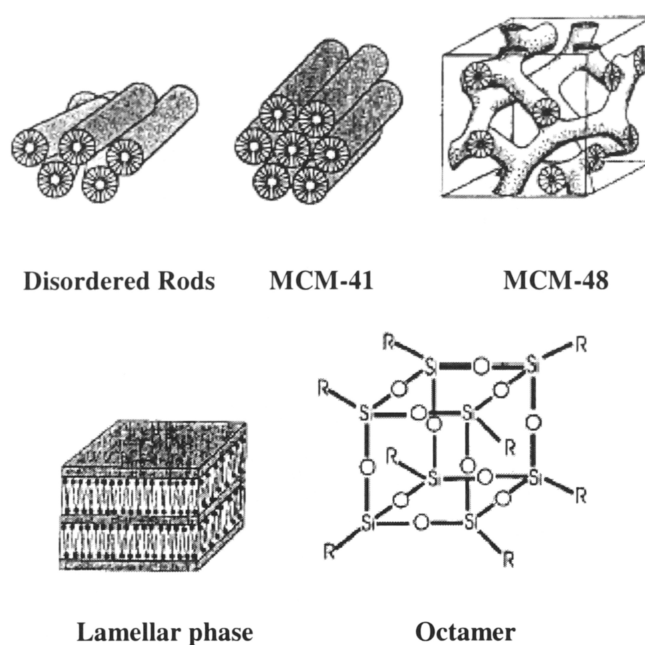


Figure 1: Phase formation of different mesoporous structures.<sup>156</sup>

Here, MCM-41 materials will be introduced in details since they are used as hosts throughout this work. Other microporous and mesoporous materials are beyond the scope of this work and will not be further discussed unless it is necessary.

### 1.2.2. Mechanism of MCM-41 Formation

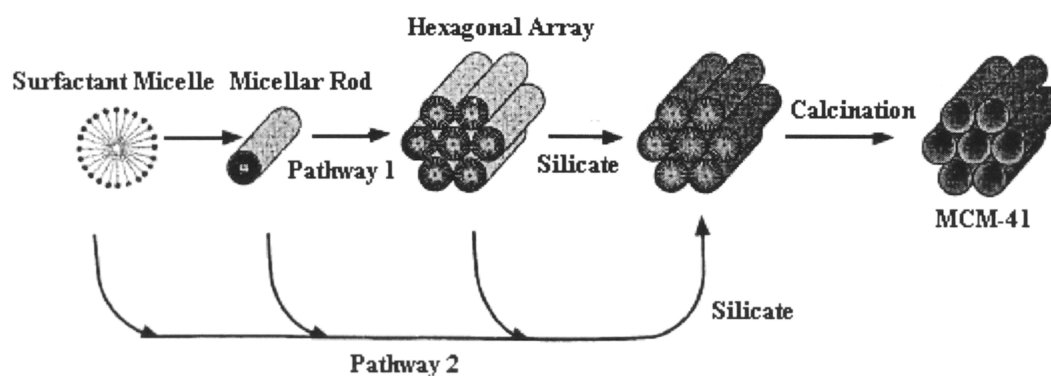
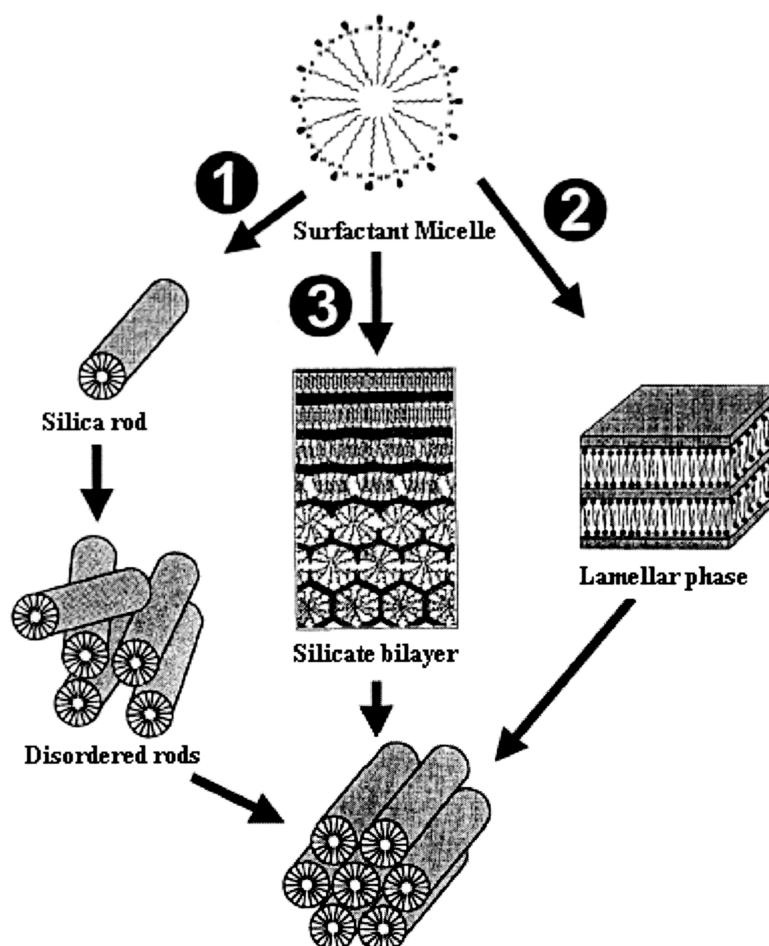


Figure 2: Two possible pathways for the LCT mechanism proposed by Beck et al.<sup>114</sup>



**Figure 3: Proposed formation mechanistic pathways by (1) stacking of silicate surfactant rods, via the formation of an initial (2) lamellar intermediate and (3) silicate bilayer.**<sup>157</sup>

Several mechanisms for the formation of mesoporous MCM-41 have been postulated. Beck and co-workers proposed "liquid crystal templating" (LCT) mechanisms.<sup>114,115</sup> The principle of this mechanism is that the liquid crystalline mesophases or micelles act as templates rather than individual single molecules or ions. Two possible pathways have been established based on the LCT conception: (a) presence of the liquid-crystal mesophase prior to the addition of the reagents, i.e., preexistence of surfactant aggregates (rodlike micelles), followed by the migration and the polymerization of the silicate anions, resulting in the formation of the MCM-41 structure (pathway 1 in Figure



2); (b) self-assembly of the liquid-crystal-like structures as a result of the mutual interactions between the silicate anion and the surfactant cations in the solution, i.e., the silicate species generated in the reaction mixture leads to the ordering of the subsequent silicate surfactant micelles (pathway 2 in Figure 2). Since the amount of surfactants in the synthesis solution was less than the required amount to form liquid crystalline phases in pure water, it was suggested that Pathway 1 in Figure 2 doesn't seem very likely.<sup>157</sup> Formation of hexagonal, cubic, and lamellar structures through variations of the silica concentration at a constant surfactant concentration also supports the mechanism of the pathway 2.<sup>157</sup> Further studies by other researchers also confirmed that pathway 2 is the proper mechanism.<sup>158-165</sup>

Other possible mechanisms have also been documented in the literature. Huo et al.<sup>138,143</sup> and Inagaki et al.<sup>166</sup> observed the transformation of a layered silica-surfactant phase into an MCM-41 structure (pathway 3 in Figure 3). Davis et al.<sup>156</sup> proposed a somewhat similar mechanism (pathway 2 in Figure 3) where, depending on the reaction temperature, the formation of MCM-41 occurs via a disordered or lamellar structure.<sup>167</sup> For the transformation from the lamellar to the hexagonal mesophase, ion exchange and charge matching pathways have been proposed.<sup>168-172</sup>

### 1.2.3. Synthesis of MCM-41 and Template Removal

In a typical MCM-41 synthesis, an aqueous solution of silica source (e.g., fumed silica, sodium silicate, or tetraethyl orthosilicate) is added to a clear aqueous (alkaline) solution of a micelle-forming surfactant (e.g., long-chain quaternary ammonium halides) under constant stirring. Then the silica source coordinates with the surfactant headgroups to assemble into a silica-surfactant phase, i.e. a gel mixture. The gel mixture is then aged at around 343 K for 1-3 days, during which time the pH value of

the gel mixture is adjusted to the range of 8-11. After ageing, the solid product is filtered from the mother liquor, washed with deionized water, and dried.<sup>114,115</sup> This sample is designated as as-synthesized MCM-41.

There are mainly three different kinds of organic molecules used as surfactant templates for MCM-41 synthesis, i.e., the ionic surfactant,<sup>114,115,139,143,165,173-181</sup> neutral surfactant<sup>145,150,182</sup> and non-surfactant organic template.<sup>183-185</sup> The ionic surfactants are the most important and widely used templates. It was suggested that the formation of the mesophase structures through the ionic pathway is based on charge matching between the ionic surfactants and the inorganic silicate precursors through electrostatic interactions. The neutral and the non-surfactant pathway are based on hydrogen bonding between the templates and the precursors.<sup>182,186</sup>

From the catalytic point of view, it is a prerequisite to remove templates occluded inside the as-synthesized samples in order to generate the accessible pores for the guest molecules. Thermal calcination is the most widely used method for template removal. The template removed MCM-41 has a one dimensional hexagonal pore structure with average pore size ca. 30-40 Å, which is large enough to accommodate normal organic molecules.

Although calcination is largely a satisfactory method of template removal, it has some fatal shortcomings. For example, calcination removes large amount of hydroxyl groups (it was shown that about 8-27 % of the silicon atoms present give rise to silanol groups<sup>173</sup>) that are important in catalytic activities, causes undesirable pore wall collapse and structure deterioration, and occasionally leaves carbonaceous residues inside pores which block the pore openings, etc.<sup>187</sup> All of these shortcomings mainly originated from the high temperature treatment of the calcination. In order to obtain high quality products, alternative methods that can remove the template at low temperatures are

needed. Several strategies have been developed for this purpose, including acid treatment,<sup>188</sup> oxygen plasma treatment,<sup>188</sup> liquid extraction,<sup>189-192</sup> supercritical fluid extraction<sup>193</sup> removal of the surfactant templates via simultaneous modification of the pores,<sup>194-197</sup> and ozone treatment.<sup>198-201</sup>

#### 1.2.4. Al-MCM-41

Mesoporous MCM-41, however, is still hindered from practical application due to its low catalytic activity arising from the amorphous nature of its framework.<sup>114,115</sup> In order to improve catalytic activity, similar to microporous zeolites, a key scientific objective is the attainment of tetrahedral Al in the framework of the MCM-41.<sup>202</sup> By direct synthesis<sup>114,115,203-206</sup> or post-synthesis grafting<sup>12,174,207-216</sup> methods, Al can be incorporated into the tetrahedral positions of the MCM-41 framework and generate Brønsted and Lewis acid sites by isomorphous substitution of Al for Si over a large range of framework Si/Al ratios.<sup>131,132,174,217</sup> The level of substitution of silicon by tetrahedral Al depends on the reactants and the preparation method, with the largest amounts of Al being in the region of 9 % mol.<sup>204</sup> Higher levels of Al could be inserted into the MCM-41 framework, approaching the Lowenstein limit (Si/Al = 1),<sup>218,219</sup> which stipulates the avoidance of the Al-O-Al moieties, leading to a maximum Al content (Si/Al = 1) for perfectly alternating silica and alumina tetrahedra. But these materials will readily dealuminate, with conversion of the tetrahedral to the non-framework octahedral Al.<sup>203,220</sup> Aluminium substituted MCM-41 materials have already been proved to be effective catalysts for cracking, hydrocracking, hydrogenation, isomerization and alkylation reactions.<sup>132,202,221-228</sup>

The Al distribution in the Al-MCM-41 largely depends on the incorporated Al content.

<sup>229</sup> At low Al content, Al atoms are located almost exclusively at the channel surface,

while with increasing framework Al content Al atoms are incorporated also inside the channel walls. The Al atoms on the wall surface preferentially form Al-Si<sub>1,2</sub>-Al pairs. The number of single Al atoms increases with framework Al content and overcome 50 % of surface Al atoms for Si/Al = ~11. The Al-Si<sub>1,2</sub>-Al pairs are present in two cationic sites, one is independent of the Al content while the other one significantly increases with increasing the framework Al content. It should also be noted that the distribution of the Al is different in the directly synthesized sample and the post-synthesized sample.<sup>12,174,207-216</sup> In the directly synthesized sample, the Al atoms are not only incorporated in the pore walls, but also are incorporated inside the interior of the pore walls. However, in post-synthesis method Al atoms are incorporated using siliceous MCM-41 as the parent material. In this case, the majority of the Al may be “grafted” on the inner pore wall surface and can be readily accessed by the guest molecules. Furthermore, though most (or all) of the Al can be incorporated into the tetrahedral Al positions in the as-synthesized Al-MCM-41 by the direct synthesized method, evidenced by the <sup>27</sup>Al-MAS-NMR, dealumination usually occurs during template removal. The post-synthesis method can avoid this dealumination to a large extent since the parent MCM-41 materials used are the ones whose templates are removed.

The concentration of the surface hydroxyl groups and the acidic strength of the Al-MCM-41 largely depends on the synthesis conditions, such as the Al source used.<sup>230,231</sup> The acidic properties of the Al-MCM-41 were first studied by Corma et al.<sup>222</sup> as well as Kloestra et al.,<sup>217,232</sup> who reported that the Al-MCM-41 materials only have medium or mild acidic strength. However, Lim et al.<sup>233</sup> reported that the Brønsted acidity and possibly cation exchange sites of Al-MCM-41 arise from ill-defined structural defects and from the silanol groups which are not greatly influenced by the presence of metal cations within the thick-walled honeycomb structure. Inclusion of metal ions such as

Al(III), Ti(IV) cations into the mesoporous MCM-41 structure does not give rise to additional Lewis or Brønsted acidity compared to the Si-MCM-41, though their presence has proved useful in the selective oxidation of alkenes to epoxides.<sup>234</sup> Jentys et al.<sup>235</sup> reported that purely siliceous MCM-41 contains a high concentration of weakly acidic silanol groups, while the Al-MCM-41 materials do have additional Brønsted and strong Lewis acid sites. The concentration of these acidic sites increases with increasing the Al content, while that of the weakly acidic silanol groups decreases. Hunger et al.<sup>236</sup> also showed that weak Brønsted acid sites were present in the Al-MCM-41 samples and proposed a model of Brønsted acid sites in Al-MCM-41 which consists of a silanol groups with 3-4 framework Al atoms in their local structure. Koch et al.<sup>237,238</sup> indicated that protonic form Al-MCM-41 behaves like a solid acid. It was shown that H-Al-MCM-41 possesses a greater number of strong acid sites than H-Y and amorphous aluminosilicates, which could not be bridging OH groups. They suggested that the terminal hydroxyl groups interact with neighboring coordinately unsaturated Al species and that consequently synergistically stronger acid sites are formed. Kosslick et al.<sup>239</sup> examined the acidity and active sites of the Al-MCM-41 at elevated temperatures and found that: (1) at high temperature ( $> 873$  K), only Lewis acid sites are formed; (2) at medium temperature ( $553 - 773$  K), medium to strong Brønsted acid sites are formed. (3) at low temperature (ca.  $490$  K), only weak Brønsted and Lewis sites are formed.

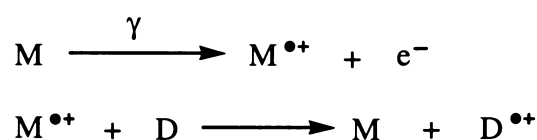
Besides Al, numerous metal elements such as Ni,<sup>240-242</sup> Ti,<sup>43,53</sup> Mn,<sup>243-247</sup> Cu,<sup>245,248</sup> or V,<sup>244</sup> Fe,<sup>249</sup> Cr,<sup>250,251</sup> Ce,<sup>252</sup> Sn<sup>253</sup>, Zr<sup>254,255</sup> and so on, have been incorporated into either framework or extra-framework (ion-exchange) sites of MCM-41. It is noteworthy that Ti(IV)-MCM-41 has already shown its high photoionization efficiency for the incorporated photoionizable molecules.<sup>43,256</sup>

### 1.3. Electron Transfer of Guest Molecules in MCM-41 Hosts

The steric and electrostatic constraint imposed on the guest molecules within the channels or cages of zeolites can alter the photochemical and photophysical properties of the guest molecules and diminish the photodegradation and undesirable back ET reactions.<sup>63</sup> But the pore sizes ( $\sim 13$  Å) of microporous zeolites are too small for encapsulation of bulky photosensitive guests. Therefore, it has been reported that mesoporous MCM-41 materials are successfully used as heterogeneous hosts for the encapsulation of bulky sensitizers.<sup>43,91,257,258</sup> Recent research shows that MCM-41 and Al-MCM-41 are effective catalysts for oxidation reactions<sup>254,259-262</sup> and are promising host systems for photoredox reactions<sup>14,43,93,259</sup> to achieve long-lived photoinduced charge separation.<sup>14,43</sup> Incorporation of reducible transition metal ions into silica and aluminosilica porous materials may further impede back ET.<sup>14,43,263</sup> In the following sections, recent advances using MCM-41 materials as hosts to assembly various photoredox systems are reviewed.

#### 1.3.1. Electron Donor Molecules in MCM-41

Werst et al.<sup>264</sup> reported radical cation reactions on the bare Si-MCM-41 and Si-MCM-41-solvent interfaces. The adsorbed molecules (D) are not ionized directly, but undergo ET reactions with positive holes ( $M^{\bullet+}$ ) created by ionization of the matrix through the following equations:



Observation of radical cations adsorbed on surface depends on the species in question and generally on the adsorbate distribution. It has been shown that the inclusion of solvent hinders bimolecular reactions, such as dimerization and proton transfer. The condensation of solvent into MCM-41 pores was not universally effective at quenching the isomerization reactions of excited radical cations. The geometric effect on molecular packing and mobility also influences the chemical reactivity of occluded species in MCM-41.

Corma et al.<sup>61</sup> used thianthrene (Th) as electron probe molecule to study the electron acceptor properties of several acid zeolites, including MCM-22 and MCM-41. Formation of Th radical cation ( $\text{Th}^+$ ) was confirmed unambiguously by DR-UV-Vis (diffuse reflectance ultraviolet-visible), EPR (electron paramagnetic resonance), and IR (infrared) spectroscopy. Vapour phase incorporation of Th at 473 K under Ar atmosphere was found to be the most clean and convenient adsorption procedure. Ambient moisture ( $\text{H}_2\text{O}$ ) was the major factor responsible for the ageing of the  $\text{Th}^+$  radical cations. On the other hand, formation of  $\text{Th}^+$  was not connected with the existence of oxygen but predominantly with the Brønsted acid sites. This was indirectly proved by the full deactivation of the solids after neutralization of Brønsted acid sites by  $\text{Na}^+$  exchange.

Synthesis of Ti-MCM-41 and monomeric encapsulation of zinc phthalocyanine-dye complexes exhibiting negative, positive or no charges in Si-MCM-41 and Ti-MCM-41 has also been reported.<sup>265,266</sup> The amount of Ti built into the walls of the MCM-41 while maintaining the hexagonal structure was restricted to  $\sim 2$  wt %. Predominantly non-aggregated ZnPc in a monomeric state was obtained by the following two methods: (1) ZnPc was incorporated in the micellar structure of the surfactant molecules by adding it to the synthesis gel of the MCM-41 or (2) ZnPc was adsorbed to Ti-MCM-41

with Ti species in high dispersion in the pores. A tight contact between the donor ZnPc and the acceptor titanium oxide, enabled an ET and a quenching of the fluorescence of the dye.

Toriyama et al.<sup>267</sup> found that the benzene cation radical ( $Bz^+$ ), which was produced by radiolysis of a phenyl-substituted MCM-41 (Ph-MCM-41) with X-rays, showed a unusually stable static Jahn-Teller distortion even at 77 K. The trapped sites of the  $Bz^+$  in the MCM-41 mesoporous silicates were suggested to be the mesopore wall. The cation radical  $C_6H_5^+-Si-R$  which was detected in Ph-MCM-41 was regarded as the precursor of  $Bz^+$  in Ph-MCM-41, while the counter-electron was stabilized as  $-Si-O^\cdot$ .

The photophysical properties of 2,4,6-triphenylpyrylium ( $TP^+$ ), a well known ET photosensitizer,<sup>268</sup> and three tritylium ( $DMT^+$ ,  $TMT^+$  and  $MG^+$ ) ions encapsulated in MCM-41 have been studied by Cano et al.<sup>93</sup> The emission intensity for  $TP^+$  incorporated within MCM-41 was more pronounced than the difference in emission between  $TP^+-HY$  and  $TP^+-LaY$  (where heavy-atom effects dominate). Fornes et al.<sup>77</sup> reported that incorporation of  $TP^+$  and another photosensitizer, dibenzo[a,d]tropylium ( $DT^+$ ) inside the MCM-41 enhanced the reaction efficiency of cyclodimerization of 1,3-cyclohexadiene by a factor of 9, although it remained lower than in the homogeneous system. Corma et al.<sup>259</sup> found that  $TP^+$  incorporated in Al-MCM-41 ( $Si/Al = 95$ ) results in a remarkable increase of the chemical yield (86 %) for the isomerization of the *cis*-stilbene *via* PET. The high efficiency of the MCM-41 host was suggested to arise from the combination of the benefits derived from the restricted microenvironment of zeolites (retardation of back ET) plus a better diffusion of reactants and products through the channels owing to their relative large dimensions. The MCM-41 materials are suitable hosts for PET reactions.



Algarra et al.<sup>269</sup> used MCM-41 as host to condense pyrrole and benzaldehyde (porphyrin precursors) in isooctane or cyclohexane. Formation of tetraphenylporphyrin (TPP) was observed in the organic solution, while formation of porphyrinogen was observed inside the pores.

Holland et al.<sup>270</sup> incorporated *meso*-tetrakis(5-trimethylammoniopentyl)porphyrin (TMAP) in MCM-41 directly during hydrothermal synthesis and by a surfactant-porphyrin ion-exchange reactions with as-synthesized MCM-41. Acid extraction of the surfactant converted the encapsulated free-base porphyrin to the dication TMAP-H<sub>2</sub><sup>2+</sup>, which could be further metalated with Cu<sup>2+</sup>, Ni<sup>2+</sup> and Fe<sup>2+</sup>. TMAP-Cu<sup>2+</sup>, whose porphyrin was directly incorporated in MCM-41 during hydrothermal synthesis, was stabilized and exhibited greater catalytic activity in the oxidative bleaching reaction of the azo dye  $\beta$ -naphthol violet for long periods. It was suggested that the isolation of the porphyrin molecules within MCM-41 channels prevented their mutual oxidation.

Metalloporphyrin and its derivatives have attracted much attention in science and technology due to their promising application in nonlinear optical devices,<sup>271</sup> solar energy conversion<sup>272</sup> and light emitting diodes.<sup>273</sup> Choi et al. encapsulated Zn<sup>II</sup> tetraphenylporphyrin (Zn<sup>II</sup>TPP) into MCM-41 and Cu<sup>II</sup>Al-MCM-41. The Zn<sup>II</sup>TPP in MCM-41 was oxidized to the corresponding radical cation *via* ET to the silicate framework of MCM-41. The Zn<sup>II</sup>TPP radical cation was quite long-lived in MCM-41 and could be investigated by the normal Raman and UV-Vis spectroscopic techniques. Central metal ion exchange of Zn<sup>II</sup>TPP encapsulated into Cu<sup>II</sup>Al-MCM-41 gave Cu<sup>II</sup> tetraphenylporphyrin (Cu<sup>II</sup>TPP) with almost unit transformation efficiency, indicating that metal ion exchanged MCM-41, such as Cu<sup>II</sup>Al-MCM-41, might be used for microreactor-controlled metal-ion exchange reactions of the porphyrin derivatives.

Kim et al.<sup>256</sup> studied PET of 5,10,15,20-tetraphenyl-21H,23H-porphyrin manganese(III) chloride [ $\text{Mn}^{\text{III}}\text{TPP}(\text{Cl})$ ] encapsulated in MCM-41 and Ti-MCM-41 by femtosecond diffuse reflectance photolysis. Two transient species with a lifetime of ca. 10 ps and 80 ps were observed. The short-lived one was attributed to the “trimultiplet” relaxation and the long-lived one to the spin-forbidden relaxation *via* a quintet charge transfer (CT) state. Irradiation generates  $\text{MnTPP}^{\text{Cl}}^+$  cation radicals both in MCM-41 and Al-MCM-41, indicating that mesoporous MCM-41 framework acts as an electron acceptor. Furthermore, the facile formation of  $\text{MnTPP}^{\text{Cl}}^+$  cation radicals in Ti-MCM-41 than in MCM-41 demonstrates that incorporating Ti(IV) into the MCM-41 framework enhances the electron accepting ability of the MCM-41. The MCM-41 molecular sieves are found to be promising hosts for long-lived photoinduced charge separation of the adsorbed  $\text{MnTPP}^{\text{Cl}}^+$ .

Kevan and coworkers<sup>274</sup> also extensively studied photoionization of porphyrin and phenothiazine in MCM-41 materials. In most cases, quite long-lived photoinduced charge separation at room temperature has been achieved. The *meso*-tetraphenylporphyrin ( $\text{H}_2\text{TPP}$ ) was loaded into mesoporous Si-MCM-41, Al-MCM-41 and Ti-MCM-41 at room temperature and 77 K.<sup>43</sup> The formation of porphyrin  $\pi$ -cation radicals ( $\text{H}_2\text{TPP}^+$ ) under visible light ( $\lambda > 350$  nm) excitation was observed by means of electron spin resonance (ESR) and diffuse reflectance UV-Vis (DR-UV-Vis) spectroscopy. It is known that the ionization potential of  $\text{H}_2\text{TPP}^+$  is about 5 eV and the energy of visible light is 1.6-3.1 eV. Apparently, the energy of one photon of visible light is not enough to ionize the porphyrin. However, porphyrin can be excited to a singlet state through  $\pi$ - $\pi^*$  transition by visible light, which may be converted into a long-lived triplet state with high quantum yields ( $\sim 0.8$ ) by intersystem crossing. The lifetime of the porphyrin triplet state is long enough to absorb the second photon, and

this provides sufficient energy for ionization to generate the porphyrin  $\pi$ -cation radical.

<sup>275</sup> The  $\text{H}_2\text{TPP}^+$  radicals were stable in MCM-41 and Ti-MCM-41 at room temperature and decay after 30 min photoirradiation by only ca. 5 % after 48 hr in Ti-MCM-41. The photoionization efficiencies increased in the order Al-MCM-41 < MCM-41 < Ti-MCM-41, indicating that framework modification by incorporating the  $\text{Ti}^{4+}$  into the MCM-41 channels enhances the electron-accepting ability of the MCM-41 framework. The lower  $\text{H}_2\text{TPP}^+$  photoyield in Al-MCM-41 compared to in Si-MCM-41 was attributed to the diprotonation of  $\text{H}_2\text{TPP}$  to  $\text{H}_4\text{TPP}^{2+}$  on acidic Al-MCM-41. The pore size effect on the  $\text{H}_2\text{TPP}^+$  photoyield was also studied using  $\text{C}_n$ -Si-MCM-41 with different pore sizes ( $\text{C}_n$  was the alkyl chain length of the surfactant used in the hydrothermal synthesis) as the hosts. It was found that the  $\text{H}_2\text{TPP}^+$  photoyield increased with increasing alkyl chain length and was greatest in  $\text{C}_{16}$ -MCM-41 with pore size  $\sim 33 \text{ \AA}$ . The  $\text{H}_2\text{TPP}^+$  photoyield was greater at 77 K than at room temperature. This was explained by the decrease of the porphyrin cation mobility at 77 K which reduces the probability of the back ET as analogous to the phenothiazine/silica gel system.<sup>84</sup> According to the authors' conclusion, the mesoporous MCM-41 molecular sieves are effective heterogeneous hosts to accomplish long-lived net PET of bulky porphyrin molecules at room temperature.

Photoionization of  $\text{H}_2\text{TPP}$  in mesoporous Si-MCM-48, Al-MCM-48 and Ti-MCM-48 also generated long-lived  $\text{H}_2\text{TPP}^+$  radicals.<sup>276</sup> The photoyields of  $\text{H}_2\text{TPP}^+$  were in the order MCM-48 < Al-MCM-48 < Ti-MCM-48, indicating that incorporation of Al and Ti into MCM-48 also enhances the electron-accepting ability of the framework. The electron acceptor sites were suggested to be terminal hydroxyl groups in Si-MCM-48, acidic sites in Al-MCM-48 and Ti(IV) sites in Ti-MCM-48. The higher  $\text{H}_2\text{TPP}^+$  photoyield in Al-MCM-48 compared to in Si-MCM-48 was attributed to the negatively

charged Al-MCM-48 framework which enhances the reactivity of  $\text{H}_2\text{TPP}^+$  and acidic sites in Al-MCM-48 which are better electron acceptors than the terminal Si-OH hydroxyl groups in Si-MCM-48.

Kevan and coworkers also studied photoionization yields of N-alkylphenothiazine ( $\text{PC}_n$ ) cation radicals generated by UV irradiation within Si-MCM-41, Al-MCM-41 and Ti-MCM-41 and compared the photoyields in these different mesoporous materials.<sup>14</sup> The photoionization efficiencies to form  $\text{PC}_n^+$  cation radicals increased in the order Si-MCM-41 < Al-MCM-41 < Ti-MCM-41. The electron acceptor sites were suggested to be surface hydroxyl groups in Si-MCM-41 and Ti(IV) in Ti-MCM-41. Increasing the alkyl chain length of the molecules reduces the extent of dark reaction with atmospheric oxygen prior to the photoirradiation. Photoyields of  $\text{PC}_1$  were 2.5 times greater in these Al-MCM-41 hosts at 77 K than those at room temperature. This was explained by the lack of mobility of  $\text{PC}_1^+$  cation radicals at 77 K, which hinders back ET to the  $\text{PC}_1$  molecules and thus increases the photoyield.

Kevan and coworkers further investigated photoinduced charge separation of N-alkylpyrenes ( $\text{PyC}_n$ ) in Si-MCM-41 and transition metal containing Me-MCM-41 [Me = Ti(IV), V(V), Ni(II), Co(II) and Cu(II)].<sup>12</sup> Si-MCM-41 and Me-MCM-41 were shown to be effective heterogeneous hosts for the photoinduced formation and stabilization of  $\text{PyC}_n^+$  cation radicals with a lifetime for several hours at room temperature, indicating that the back ET was dramatically retarded. The photoionization efficiencies were in the order Ti-MCM-41 > Ni-MCM-41 > V-MCM-41 > Si-MCM-41 > Co-MCM-41 > Cu-MCM-41. Interestingly, it was found that the ESR intensities of both V(IV) and  $\text{PyC}_n^+$  cation radicals increased in the same ratio with increasing the irradiation time. Based on this observation, it was concluded that V(V) in V-MCM-41 was the electron acceptor.

Kevan and coworkers also introduced  $PC_n$  into Si-MCM-48, Al-MCM-48 and V-MCM-48 by impregnation.<sup>277</sup> Similar to MCM-41, the photooxidation efficiencies to form  $PC_n^+$  cation radicals increased in the order Si-MCM-48 < Al-MCM-48 < V-MCM-48. A suggestion that  $V^{5+}$  in V-MCM-48 acts as an electron acceptor was made based on the observation of the  $V^{4+}$  by EPR after photoirradiation. The electron acceptor sites were suggested to be the terminal Si-OH hydroxyl groups in Si-MCM-48, acidic sites in Al-MCM-48 and  $V^{5+}$  sites in V-MCM-48. The decrease of the photoyields with increasing the alkyl chain length of  $PC_n$  was also observed. The  $PC_n^+$  cation radicals were stable in these mesoporous hosts at room temperature from several hours to several days.

Kevan and coworkers also used Me-Al-MCM-41 containing transition metal ions [Me = Ni (II), Fe(III) or Cu(II)] as heterogeneous hosts for PET from  $PC_n$  ( $n = 1, 6, 10$  or  $16$  where  $n$  is the number of carbon atoms in the alkyl chain).<sup>278</sup> The formation of the  $PC_n^+$  cation radicals prior to the photoirradiation (dark reaction) was observed. However, 320 nm photoirradiation dramatically increased the photoyield of the  $PC_n^+$  cation radicals to a maximum within one hour. The net photoyields were in the sequences of Ni-Al-MCM-41 > Fe-Al-MCM-41 > Cu-Al-MCM-41 > Al-MCM-41. Long alkyl chains on  $PC_n$  resulted in the decrease of the photoionization efficiency of the N-alkylphenothiazines. Based on the thermogravimetric analysis (TGA), the authors suggested that it was mainly due to the reduction of the diffusion rate of the  $PC_n$  with longer alkyl chains. The following important issues were also addressed: (1) The mobility of the  $PC_n^+$  cation radicals was restricted, which was consistent with the assumption that the  $PC_n$  molecules were loaded inside the channels of Me-Al-MCM-41. (2) The stability of the  $PC_n^+$  in Ni-, Fe- and Cu-Al-MCM-41 are comparable but higher when compared with Al-MCM-41. (3) Incorporation of a metal ion electron acceptor

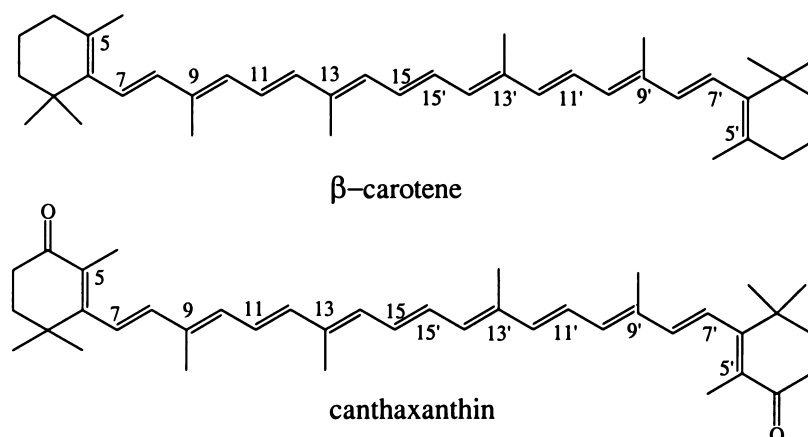
into the ion-exchange sites of the Al-MCM-41 creates a system where light energy can be converted into chemical energy and stored for a period of time.

Only recently, Kevan and coworkers<sup>279</sup> reported their study on photoionization of 10-methylphenothiazine (PC<sub>1</sub>) N, N, N', N'-tetramethylbenzidine (TMB) and pyrene (Py) impregnated into Cr-Al-MCM-41. The Cr ion concentration was varied from Si/Cr = 52 to 121, and the one with intermediate concentration of Si/Cr = 80 exhibited the greatest electron acceptor ability and highest photoionization efficiency. The oxidation state of Cr ions was controlled to be Cr<sup>3+</sup> or Cr<sup>5+</sup>/Cr<sup>6+</sup> by altering the calcination temperature prior to impregnation. Cr-Al-MCM-41 with Cr<sup>5+</sup> gave about 4 times higher photoionization efficiency than with Cr<sup>3+</sup>. The photoionization efficiencies in the Cr-Al-MCM-41 was in the order PC<sub>1</sub> > TMB > Py. The high photoionization efficiency of PC<sub>1</sub> was not explained by the ionization potentials determined by photoelectron spectroscopy, which were PC<sub>1</sub> (7.15 eV), TMB (6.84 eV), and Py (7.45 eV). The low photoyield of TMB<sup>•+</sup> was suggested to be due to formation of some non-paramagnetic (TMB)<sub>2</sub><sup>2+</sup>. The photoyield of PC<sub>1</sub><sup>•+</sup> increased in the order MCM-41 < Al-MCM-41 < Cr-Al-MCM-41. The decrease of the PC<sub>n</sub><sup>•+</sup> photoyield in high Cr containing Cr-MCM-41 sample was explained by the structure degradation of MCM-41 at higher Cr content and/or by the formation of secondary radicals. The author also suggested that the hydroxyl groups of the framework might serve as electron acceptors with production of hydrogen atoms, although they didn't observed the EPR signals of trapped hydrogen atoms. Thus, the photoyield may be controlled by the type of photoionizable molecule, the Cr ion content, and the oxidation state of the Cr ions.

Carotenoids are important components of the light harvesting antenna systems, which are involved in the ET reactions in photosynthetic reaction centers. Konovalova et al.<sup>280</sup> studied photooxidation of  $\beta$ -carotene and canthaxanthin in MCM-41, Ni-MCM-41 and

Al-MCM-41 using 9-220 GHz EPR and 9 GHz (electron nuclear double resonance) ENDOR spectroscopy. Incorporation of metal ions into the MCM-41 framework enhances the efficiency of carotenoid oxidation. Formation of carotenoid radical cations within MCM-41 was due to ET between the incorporated carotenoid molecules and the metal ions, which act as electron acceptor sites. Detected EPR signals of Ni(I) species provided direct evidence for the reduction of Ni(II) ions by carotenoids. The photoyields and stability of the generated carotenoid radical cations increased in the order MCM-41 < Ni-MCM-41 < Al-MCM-41 and depended on the nature and concentration of the incorporated metal ions. The 110 GHz EPR measurements resolved overlapped signals of  $O_2^-$  species ( $g_1 = 2.0115$ ,  $g_2 = 2.0049$ ,  $g_3 = 2.00$ ) and V-centers or so called trapped holes on the framework oxygens ( $g_1 = 2.0154$ ,  $g_2 = 2.0058$ ,  $g_3 = 1.996$ ). The V centers were also observed for metal substituted MCM-41<sup>281</sup> or zeolites<sup>282</sup> after  $\gamma$ -irradiation at 77 K. The ENDOR measurements revealed that the carotenoids are bounded to the MCM-41 pore walls via the ends of the polyene chain in close proximity to the C9,9'-C<sub>3</sub> groups. Incorporation of Al in tetrahedral coordination into the framework of MCM-41 produces Lewis and Brønsted acid sites.<sup>117,204,283</sup> It has been proposed that the Lewis acid sites, i.e., the coordinately unsaturated Al(III) ions, are electron acceptor sites and are responsible for the chemical formation of the Car<sup>+</sup> on silica-alumina supports while the Brønsted acid sites are responsible for their stabilization.<sup>284</sup> Similarly, earlier reports for the paramagnetic complexes of quinones with Al(III) ions in HY zeolites,<sup>285,286</sup> their ENDOR spectrum exhibited a doublet centered about the <sup>27</sup>Al Larmor frequency  $3.6 \pm A/2$  (coupled Al) instead of a matrix <sup>27</sup>Al peak,<sup>280,287</sup> indicating formation of strong complexes between carotenoids and the surface Al(III) sites. These support the authors' suggestion that the Lewis acid sites in

Al-MCM-41 are responsible for the formation of a small amount of the  $\text{Ca}^{+}$  in Al-MCM-41 before irradiation.



Tetrathiafulvalene (TTF), which is a good electron donor used as a structure block for the synthesis of many organic superconductors, has also been encapsulated into zeolite Y and MCM-41.<sup>288</sup> The IR spectra exhibit a broadened and shifted C-H stretch region for TTF after encapsulation, and a band characteristic of dimerized TTF cation radicals after exposure to iodine. A sharp singlet observed by ESR indicates the presence of radical species even prior to iodine treatment. The formation of TTF radical cations is associated with the acidity of the host surface.

### 1.3.2. Electron Acceptor Molecules in MCM-41

Park et al.<sup>289</sup> encapsulated bulky  $[\text{Re}(\text{I})(\text{CO}_3)(\text{bpy})(\text{py})]^+$  (bpy = 2,2'-bipyridine, py = pyridine) into Al-MCM-41. Xe-NMR spectra provided the evidence for the encapsulation of  $[\text{Re}(\text{I})(\text{CO}_3)(\text{bpy})(\text{py})]^+$  into Al-MCM-41. The  $[\text{Re}(\text{I})(\text{CO}_3)(\text{bpy})(\text{py})]$  radical was observed by EPR, DR-UV-Vis and FTIR spectroscopy after photoirradiation of  $[\text{Re}(\text{I})(\text{CO}_3)(\text{bpy})(\text{py})]^+/\text{Al-MCM-41}$  system. The authors further suggested that the aluminosilicate framework of Al-MCM-41 may act as an electron donor for the photoinduced formation of the  $[\text{Re}(\text{I})(\text{CO}_3)(\text{bpy})(\text{py})]$  radical, which is



an active species for activation and reduction of  $\text{CO}_2$  and  $\text{CO}_3^{2-}$  for the purpose of construction of artificial photosynthetic systems.

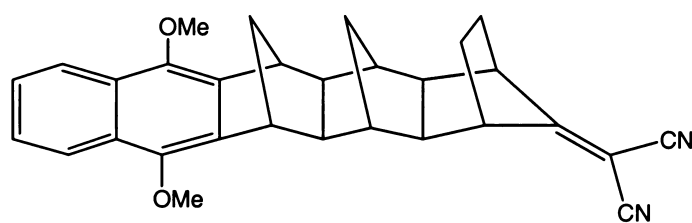
The development of the periodic mesoporous organosilica (PMO), in which the organic component occupies framework positions in the walls rather than in the empty voids of the hexagonal channels,<sup>290-293</sup> paves the way for the preparation of a new type of innovative organic-inorganic hybrid materials with functional properties. Álvaro et al.<sup>294</sup> reported that a PMO solid of the MCM-41 type, which had 4,4'-bipyridinium units covalently inserted in the channel walls during hydrothermal synthesis of MCM-41, implemented the solid with unique electron acceptor ability as well as photo- and thermo-chromic responses characteristic of viologen derivatives. The laser excitation of the powdered samples in a sealed cell gave rise to the formation of the  $\text{BP}^+$  radical cation, which didn't significantly decay even one month after generation. The electron donor was attributed to the silicate framework of MCM-41. The thermal generation of the viologen radical cation upon heating was also observed. It was anticipated that different types of charge transfer complexes (CTC) with viologen imprinted in the walls as the acceptor unit may be assembled in the channels of the MCM-41.

Brunel et al.<sup>295</sup> grafted spin labeling nitroxyl (TEMPO) radicals on the surface of silica gel and MCM-41 through the amide bond on previously grafted amino chains by two different procedures. The TEMPO-immobilized MCM-41 showed electron acceptor ability.

### 1.3.3. Donor-Bridge-Acceptor Molecules in MCM-41

Photoinduced charge separation in covalently linked rigid donor-bridge-acceptor dyads such as DMN-6B-DCV [donor = dimethoxynaphthalene (DMN); bridge = covalently linked 6 bond norbornylogous bridge (6B); acceptor = dicyanovinyl (DCV)]

occurs extremely rapidly, a result of electronic coupling mediated by a through-bond (TB) mechanism.<sup>296,297</sup> However, the lifetimes of the resulting charge-separated state (CS) are usually short in homogeneous solution (usually nanosecond or picosecond scales<sup>298</sup>), which is also the consequence of the back ET due to strong TB electronic coupling. For the first time, Kuchi et al.<sup>299</sup> found that irradiation of the DMN-6B-DCV occluded inside the Al-MCM-41 (Si/Al 15, directly hydrothermally synthesized) led to the formation of a stable radical which was tentatively attributed to the DCV radical anion of the dyad with a lifetime of days. This result is comparable with the report of Mallouk et al.<sup>23,300</sup> that the rates of charge recombination in a series of Ru<sup>II</sup>-viologen dyads adsorbed at the external surface of several microporous zeolites were slowed by a factor of  $10^5$  relative to the same molecules in solution. No radical signals were observed if DMN-6B-DCV was occluded into the purely siliceous MCM-41, indicating that incorporation of Al in the framework of MCM-41 plays an important role. As shown in chapter 7 of this thesis, the signals observed in that work are actually due however, to the radical cations of the DMN group.



DMN-6B-DCV

## 1.4. Control of Energy Transfer in Mesoporous Materials

In the photosynthetic reaction center, the light energy harvested at multiple sites spontaneously flows to the appropriate location in the complex so that ET can take place.<sup>301</sup> Fabrication of systems that allow the flow of energy to be controlled and

directed to the regions useful for the desired purpose, is another challenge to utilize solar energy. Several attempts have been made to mimic this type of behavior, for example, linking chromophores with continually decreasing band gaps along polymer chains<sup>302</sup> or layered chromophores in thin film heterostructures. Although good directional energy transfer can be achieved in these systems, energy is lost because large differences in the emission energy of each successive chromophores are needed.

Tolbert and coworkers<sup>303</sup> first successfully synthesized ordered mesoporous silica with aligned pores using magnetic fields. Then they modified<sup>304</sup> the surface with organic groups to reduce the pore opening and make the silica framework hydrophobic so that semiconducting poly[2-methoxy-5(2-ethoxyhexyloxy)-1,4-phenylenevinylene] (MEH-PPV) could be intercalated into the pores by thermal cycling. Thus, the encapsulated MEH-PPV polymer was well oriented and stable in the mesoporous hosts.

Tolbert and coworkers<sup>305</sup> further reported that energy transfer can be controlled in MEH-PPV polymers embedded in the channels of the oriented, hexagonal nanoporous silica (MCM-41). Polarized femtosecond spectroscopy showed that excitations migrate unidirectionally from aggregated, randomly oriented polymer segments outside the pores to the isolated, aligned polymer chains within the pores. The driving force for the energy transfer arose from the changes in polymer conformation. The short conjugation length segments outside the mesoporous silica have higher energy than the long conjugation length segments inside the pores. It was shown that the intrachain energy transfer is a much slower process than interchain energy transfer, which is in contrast to the carrier transport where intrachain mobility is several orders of magnitude larger than interchain. This study provides a fascinating insight for optimizing nanostructured materials for use in optoelectronic devices, especially in the control of energy flow.

## 1.5. Application of MCM-41 Materials in Optical Devices

Mesoporous and mesostructured materials are promising new optical materials,<sup>306</sup> which may also have potential applications in better constructing photoredox systems.

Low temperature dye doping into sol-gel glasses led to the introduction of optically active sol-gel glasses into the market. All advantages of the sol-gel glasses (high dye dispersion, mechanical robustness, transparency of the matrix in the visible to UV range, high processability, etc.) are also present in mesoporous materials. Moreover, simultaneous silica/block copolymer/dye co-assembly can lead to higher concentration compared to the traditional sol-gel glasses and protective packaging of uniform three-dimensional arrays of optical species. It has already been shown that mesoporous materials are useful in realizing the high dispersion state of dye molecules and are effective in controlling the microenvironment of adsorbed dye molecules.<sup>258</sup> For the construction of the optical devices,<sup>306</sup> mesoporous materials are used as hosts to include various kinds of dye molecules (e.g. rhodamine-B<sup>258</sup>), nanocrystals (e.g. Ge<sup>307</sup>) and quantum dots (e.g. CdSe<sup>308</sup>), luminescent organometallic complexes (e.g. [Ru(bpy)<sub>3</sub>]<sup>2+</sup><sup>309</sup>), polymers (e.g. MEH-PPV<sup>303</sup>), NLO (non-linear optical) materials (e.g. p-nitroaniline (pNA)<sup>310</sup>), laser materials (e.g. rhodamine 6G<sup>311</sup>), photochromic materials (e.g. spirooxazine derivatives<sup>312</sup>) and chemical sensors (e.g. fluoresceinsuccinamide<sup>313</sup>).

## 1.6. Electron Donor and Acceptor Sites in MCM-41 Materials

As shown in the previous sections, hydroxyl groups, Lewis acid sites and metal ions have been suggested to be the electron acceptor sites in MCM-41, Al-MCM-41 and other metal ions incorporated MCM-41 (such as Ti-MCM-41), respectively. No reports

of electron donor sites in MCM-41 or Al-MCM-41 materials have been postulated up to date.

## 1.7. Aims of the Thesis

The main aims of this thesis can be summarized as follows:

1. Synthesize and characterize some simple donor and acceptor molecules, mesoporous silicates and aluminosilicates, and the intercalation compounds derived from them.
2. Better understand electron transfer processes in mesoporous silicate and aluminosilicate materials intercalated with simple organic donor, acceptor and donor-acceptor dyad molecules, explore the mesoporous hosts' ability of extending the life-time of charge-separated states by retarding back electron transfer, thus offering theoretical and experimental foundation toward constructing molecular level photodiodes or optical switches in heterogeneous hosts.

In order to achieve the above aims, this thesis has been developed into the following chapters:

Chapter 1: Introduction.

Chapter 2: Experimental.

Chapter 3: Characterization of mesoporous (Al)-MCM-41 Hosts.

Chapter 4: Template removal by ozone treatments.

Chapter 5: Chemistry of electron acceptor molecules in (Al)-MCM-41 Hosts.

Chapter 6: Chemistry of electron donor molecules in (Al)-MCM-41 Hosts.

Chapter 7: Chemistry of donor-bridge-acceptor dyad molecules in (Al)-MCM-41 Hosts.

Chapter 8: Summary and future work.

## 1.8. References for Chapter 1

- (1) Kalyanasundaram, K. *Photochemistry in Microheterogeneous Systems*; Academic: New York, **1987**.
- (2) Vermeulen, L. A.; Thomas, M. E. *Nature* **1992**, 358, 656.
- (3) Connolly, J. S. *Photochemical Conversion and Storage of Solar Energy*; Academic: New York, **1981**.
- (4) Fox, M. A.; Chanon, M. *Photoinduced Electron Transfer*; Elsevier: Amsterdam, Oxford, New York and Tokyo, **1988**; Vol. Part A-D.
- (5) Bolton, J. R. *Science* **1978**, 202, 705.
- (6) Grätzel, M. *Energy Resources through Photochemistry and Catalysis*; Academic: New York, **1983**.
- (7) Balzani, V.; Moggi, L.; Manfrin, M. F.; Bolletta, F.; Gleria, M. *Science* **1975**, 189, 852.
- (8) Balzani, V.; Scandola, F. *Supramolecular Photochemistry*; Ellis Horwood: New York, **1991**.
- (9) Lehn, J.-M. *Angew. Chem. Int. Ed.* **1990**, 102, 1347.
- (10) Bonhôte, P.; Moser, J.-E.; Humphry-Baker, R.; Vlachopoulos, N.; Zakeeruddin, S. M.; Walder, L.; Grätzel, M. *J. Am. Chem. Soc.* **1999**, 121, 1324. And references therein.
- (11) Grätzel, M. *Heterogeneous Photochemical Electron Transfer*; CRC Press: Boca Raton, FL, **1988**.
- (12) Krishna, R. M.; Kevan, L. *Phys. Chem. Chem. Phys.* **2001**, 3, 5348.
- (13) Krishna, R. M.; Prakash, A. M.; Kurshev, V.; Kevan, L. *Phys. Chem. Chem. Phys.* **1999**, 1, 4119.
- (14) Krishna, R. M.; Prakash, A. M.; Kevan, L. *J. Phys. Chem. B* **2000**, 104, 1796.
- (15) Gener, I.; Buntinx, G.; Brémard, C. *Angew. Chem. Int. Ed.* **1999**, 38, 1819.
- (16) Gener, I.; Moissette, A.; Brémard, C. *Chem. Commun.* **2000**, 1563.
- (17) Lavarnos, G. J.; Turro, N. J. *Chem. Rev.* **1996**, 86, 401.
- (18) Slama-Schwok, A.; Avnir, D.; Ottolenghi, M. *J. Am. Chem. Soc.* **1991**, 113, 3984.
- (19) Slama-Schwok, A.; Avnir, D.; Ottolenghi, M. *Photochem. Photobiol.* **1991**, 54, 525.

- 
- (20) Slama-Schwok, A.; Ottolenghi, M.; Avnir, D. *Nature* **1992**, 355, 240.
- (21) Nakato, T.; Kazuyuki, K.; Koto, C. *Chem. Mater.* **1992**, 4, 128.
- (22) Kang, Y. S.; McManus, H. J. D.; Kevan, L. *J. Phys. Chem.* **1993**, 97, 2027.
- (23) Yonemoto, E. H.; Kim, Y. I.; Schmehl, R. H.; Wallin, J. O.; Shoulders, B. A.; Richardson, B. R.; Haw, J. F.; Mallouk, T. E. *J. Am. Chem. Soc.* **1994**, 116, 10557.
- (24) Bach, U.; Lupo, D.; Comte, P.; Mpser, J. E.; Weissörtel, F.; Salbeck, J.; Spreitzer, H.; Grätzel, M. *Nature* **1998**, 395, 583.
- (25) Cermenati, L.; Pichat, P.; Guillard, C.; Albini, A. *J. Phys. Chem. B* **1997**, 101, 2650.
- (26) Duonghong, D.; Ramsden, J.; Grätzel, M. *J. Am. Chem. Soc.* **1982**, 104, 2977.
- (27) Fan, F. F.; Bard, A. J. *J. Am. Chem. Soc.* **1979**, 101, 6139.
- (28) Giraudeau, A.; Fan, F. F.; Bard, A. J. *J. Am. Chem. Soc.* **1980**, 102, 5138.
- (29) Hagfeldt, A.; Grätzel, M. *Chem. Rev.* **1995**, 95, 49.
- (30) Hidaka, H.; Horikoshi, S.; Ajisaka, K.; Zhao, J.; Serpone, N. *J. Photochem. Photobiol. A: Chem.* **1997**, 108, 197.
- (31) Kalyanasundaram, K.; Vlachopoulos, N.; Krishnan, V.; Monnier, A.; Grätzel, M. *J. Phys. Chem.* **1987**, 91, 2342.
- (32) Mills, A.; Hunte, S. L. *J. Photochem. Photobiol. A: Chem.* **1997**, 108, 1.
- (33) Moser, J.; Grätzel, M. *J. Am. Chem. Soc.* **1983**, 105, 6547.
- (34) Moser, J.; Grätzel, M. *J. Am. Chem. Soc.* **1984**, 106, 6557.
- (35) Muzyka, J. L.; Fox, M. A. *J. Photochem. Photobiol. A: Chem.* **1991**, 57, 27.
- (36) Navio, J. A.; Marchena, F. J. *J. Photochem. Photobiol. A: Chem.* **1991**, 55, 319.
- (37) Pichat, P.; Mozzanega, M.; Courbon, H. *J. Chem. Soc., Faraday Trans. 1* **1987**, 83, 697.
- (38) Tennakone, K.; Tilakaratne, C. T. K.; Kottegoda, I. R. M. *J. Photochem. Photobiol. A: Chem.* **1995**, 87, 177.
- (39) Vlachopoulos, N.; Liska, P.; Augustynski, J.; Grätzel, M. *J. Am. Chem. Soc.* **1988**, 110, 1216.
- (40) Wang, Y.; Wang, C. *J. Photochem. Photobiol. A: Chem.* **1994**, 84, 195.
- (41) Kim, Y.; Yoon, M. *J. Mol. Catal. A: Chem.* **2001**, 168, 257.
- (42) Ledney, M.; Dutta, P. K. *J. Am. Chem. Soc.* **1995**, 117, 7687.
- (43) Sung-Suh, H. M.; Luan, Z.; Kevan, L. *J. Phys. Chem. B* **1997**, 101, 10455.
- (44) Sung-Suh, H. M.; Kevan, L. *J. Phys. Chem. A* **1997**, 101, 1414.
- (45) Pileni, M. P. *Chem. Phys. Lett.* **1980**, 71, 317.

- 
- (46) McManus, H. J. D.; S., K. Y.; Kevan, L. *J. Phys. Chem.* **1992**, *96*, 5622.
- (47) Lanot, M. P.; Kevan, L. *J. Phys. Chem.* **1991**, *95*, 10178.
- (48) Kevan, L. *Radiat. Phys. Chem.* **1991**, *37*, 629.
- (49) Kevan, L. *Int. Rev. Phys. Chem.* **1990**, *9*, 307.
- (50) Kang, Y. S.; Kevan, L. *J. Phys. Chem.* **1994**, *98*, 4389.
- (51) Infelta, P. P.; Grätzel, M.; Fendler, J. H. *J. Am. Chem. Soc.* **1980**, *102*, 1479.
- (52) Hurst, J. K.; Lee, L. Y. C.; Grätzel, M. *J. Am. Chem. Soc.* **1983**, *105*, 7048.
- (53) Fendler, J. H. *Acc. Chem. Res.* **1980**, *13*, 7.
- (54) Dewey, T. G.; Hammes, G. G. *Biophys. J.* **1980**, *32*, 1023.
- (55) Breck, D. W. *Zeolite Molecular Sieves: Structure, Chemistry and Use*; John Wiley & Sons: New York, **1974**.
- (56) Hashimoto, S. *J. Chem. Soc., Faraday Trans.* **1997**, *93*, 4401.
- (57) Dutta, P. K.; Incavo, J. A. *J. Phys. Chem.* **1987**, *91*, 4443.
- (58) Dutta, P. K. *J. Inclusion Phenom. Mol. Recognit. Chem.* **1995**, *21*, 215.
- (59) Bhuiyan, A. A.; Kincaid, J. R. *Inorg. Chem.* **2001**, *40*, 4464.
- (60) Coutant, M. A.; Le, T.; Castagnola, N.; Dutta, P. K. *J. Phys. Chem. B* **2000**, *104*, 10783.
- (61) Corma, A.; Fornés, V.; García, H.; Martí, V.; Miranda, M. A. *Chem. Mater.* **1995**, *7*, 2136.
- (62) Yoon, K. B.; Park, Y. S.; Kochi, J. K. *J. Am. Chem. Soc.* **1996**, *118*, 12710.
- (63) Yoon, K. B. *Chem. Rev.* **1993**, *93*, 321. And reference therein.
- (64) Dutta, P. K.; Turbeville, W. *J. Phys. Chem.* **1992**, *96*, 9410.
- (65) Dutta, P. K.; Ledney, M. "Charge-Transfer Processes in Zeolites: Toward Better Artificial Photosynthetic Models" in *Progress in Inorganic Chemistry (Molecular Level Artificial Photosynthetic Materials, Special Volume edited by Gerald J. Meyer)*; Karlin, K. D., Ed., **1997**; Vol. 44, p 209.
- (66) Stamires, D. N.; Turkevich, J. *J. Am. Chem. Soc.* **1964**, *86*, 749.
- (67) Stamires, D. N.; Turkevich, J. *J. Am. Chem. Soc.* **1964**, *86*, 757.
- (68) Dollish, F. R.; Hall, W. K. *J. Phys. Chem.* **1967**, *71*, 1005.
- (69) Persaud, L.; Bard, A. J.; Campion, A.; Fox, M. A.; Mallouk, T. E.; Webber, S. E.; White, J. M. *J. Am. Chem. Soc.* **1987**, *109*, 7309.
- (70) Kim, Y. I.; Mallouk, T. E. *J. Phys. Chem.* **1992**, *96*, 2879.
- (71) Incavo, J. A.; Dutta, P. K. *J. Phys. Chem.* **1987**, *91*, 4443.
- (72) Borja, M.; Dutta, P. K. *Nature* **1993**, *362*, 43.



- 
- (73) Kurita, Y.; Sonoda, T.; Sato, M. *J. Catal.* **1970**, *19*, 82.
- (74) Slinkin, A. A.; Kucherov, A. V.; Kondrat'ev, D. A.; Bondarenko, T. N.; Rubinshtein, A. M.; Minachev, K. M. *J. Mol. Catal.* **1986**, *35*, 97.
- (75) Davis, M. E. *Acc. Chem. Res.* **1993**, *26*, 111.
- (76) Barrer, R. M. *Zeolites and Clay Minerals as Sorbents and Molecular Sieves*; Academic Press: London, **1978**.
- (77) Fornes, V.; Garcia, H.; Miranda, M. A.; Mojarad, F.; Sabater, M. J.; Suliman, N. N. E. *Tetrahedron* **1996**, *52*, 7755.
- (78) Xiang, B.; Kevan, L. *Colloids Surf. A: Physicochem. Eng. Aspects* **1993**, *72*, 11.
- (79) Scott, R. P. W. *Silica Gel and Bonded Phases*; Wiley: Chichester, **1993**.
- (80) Wilkinson, F.; Worrall, D. R.; Williams, S. L. *J. Phys. Chem.* **1995**, *99*, 6689.
- (81) Marro, M. A. T. *J. Photochem. Photobiol. A: Chem.* **1993**, *72*, 251.
- (82) Bauer, R. K.; Borenstein, R.; De Mayo, P.; Okada, K.; Rafalska, M.; Ware, W. R.; Wu, K. C. *J. Am. Chem. Soc.* **1982**, *104*, 4635.
- (83) Matsuura, K.; Kevan, L. *J. Phys. Chem.* **1996**, *100*, 10652.
- (84) Xiang, B.; Kevan, L. *Langmuir* **1994**, *10*, 2688.
- (85) Rabo, J. A.; Angell, C. L.; Kasai, P. H.; Schoemaker, V. *Discuss. Faraday Soc.* **1966**, *41*, 328.
- (86) Lange, J.-P.; Gutsze, A.; Karge, H. G. *J. Catal.* **1988**, *114*, 136.
- (87) Ozin, G. A.; Godber, J. *J. Phys. Chem.* **1989**, *93*, 878.
- (88) Kasai, P. H.; Bishop, R. J. in *Zeolite Chemistry and Catalysis*; Rabo, J. A., Ed.; ACS: Washington DC, **1974**, p 350.
- (89) Karge, H. G.; Lange, J.-P.; Gutsze, A.; Laniecki, M. *J. Catal.* **1988**, *114*, 144.
- (90) Cano, M. L.; Corma, A.; Fornés, V.; García, H. *J. Phys. Chem.* **1995**, *99*, 4241.
- (91) Cano, M. L.; Corma, A.; Fornés, V.; García, H.; Miranda, M. A.; Baerlocher, C.; Lengauer, C. *J. Am. Chem. Soc.* **1996**, *118*, 11006.
- (92) Cano, M. L.; Cozens, F. L.; Fornes, V.; García, H.; Scaiano, J. C. *J. Phys. Chem.* **1996**, *100*, 18145.
- (93) Cano, M. L.; Cozens, F. L.; Fornes, V.; García, H.; Scaiano, J. C. *J. Phys. Chem.* **1996**, *100*, 18152.
- (94) Chen, F. R.; Fripiat, J. J. *J. Phys. Chem.* **1992**, *96*, 819.
- (95) Sagert, N. H.; Pouteau, R. M. L.; Bailey, M. G.; Sargent, F. P. *Can. J. Chem.* **1972**, *50*, 2041.
- (96) Enzel, P.; Bein, T. *J. Phys. Chem.* **1989**, *93*, 6270.

- 
- (97) Tokunaga, H.; Ono, Y.; Keii, T. *Bull. Chem. Soc. Jpn.* **1973**, *46*, 3569.
- (98) Kerr, G. T. *J. Phys. Chem.* **1967**, *71*, 4155.
- (99) Li, X.; Iu, K. K.; Thomas, J. K.; He, H.; Klinowski, J. *J. Am. Chem. Soc.* **1994**, *116*, 11811.
- (100) Ramamurthy, V.; Caspar, J. V.; Corbin, D. R. *J. Am. Chem. Soc.* **1991**, *113*, 594.
- (101) Alvarez, L. J.; Ramírez-Solís, A.; Giral, P. B. *Zeolites* **1997**, *18*, 54.
- (102) Hui, T.-W.; Baker, M. D. *J. Phys. Chem. B* **2002**, *106*, 827.
- (103) Ranjit, K. T.; Kevan, L. *J. Phys. Chem. B* **2002**, *106*, 1104.
- (104) McManus, H. J. D.; Finel, C.; Kevan, L. *Radiat. Phys. Chem.* **1995**, *45*, 761.
- (105) Szulbinski, W. S. *Inorg. Chim. Acta.* **1998**, *269*, 253.
- (106) Kwon, O.-H.; Yoo, H.; Jang, D.-J. *Eur. Phys. J. D* **2002**, *18*, 69.
- (107) Corma, A.; Fornés, V.; García, H.; Miranda, M. A.; Primo, J.; Sabater, M.-J. *J. Am. Chem. Soc.* **1994**, *116*, 2276.
- (108) Brancaleon, L.; Brousmiche, D.; Rao, V. J.; Johnston, L. J.; Ramamurthy, V. *J. Am. Chem. Soc.* **1998**, *120*, 4926.
- (109) Mercedes, A.; Garcia, H.; Garcia, S.; Marquez, F.; J.C.Scaiano *J. Phys. Chem. B* **1997**, *101*, 3043.
- (110) Alvaro, M.; García, H.; García, S.; Márquez, F.; Scaiano, J. C. *J. Phys. Chem. B* **1997**, *101*, 3043.
- (111) Vaidyalngam, A. S.; Coutant, M. A.; Dutta, P. K. "Electron-Transfer Processes in Zeolites and Related Microheterogeneous Media" in *Electron Transfer in Chemistry*; Balzani, V., Ed.; Wiley-VCH: Weinheim, New York, Chichester, Brisbane, Singapore, Toronto, **2001**; Vol. IV, p 413.
- (112) Park, Y. S.; Um, S. Y.; Yoon, K. B. *J. Am. Chem. Soc.* **1999**, *121*, 3193.
- (113) Ramamurthy, V.; Lakshminarasimhan, P.; Grey, C. P.; Johnston, L. J. *Chem. Commun.* **1998**, 2411.
- (114) Beck, J. S.; Vartuli, J. C.; Roth, W. J.; Leonowicz, M. E.; Kresge, C. T.; Schmitt, K. D.; Chu, C. T.-W.; Olson, D. H.; Sheppard, E. W.; McCullen, S. B.; Higgins, J. B.; Schlenker, J. L. *J. Am. Chem. Soc.* **1992**, *114*, 10834.
- (115) Kresge, C. T.; Leonowicz, M. E.; Roth, W. J.; Vartuli, J. C.; Beck, J. S. *Nature* **1992**, *359*, 710.
- (116) Sing, K. S. W.; Everett, D. H.; Haul, R. A. W.; Moscou, L.; Pierotti, R. A.; Rouquérol, J.; Siemieniewska, T. *Pure Appl. Chem.* **1985**, *57*, 603.
- (117) Biz, S.; Occelli, M. L. *Catal. Rev.-Sci. Eng.* **1998**, *40*, 329.

- (118) Hölderich, W. F.; Van Bekkum, H. *Stud. Surf. Sci. Catal.* **1991**, 58, 631.
- (119) Davis, M. E.; Saldarriaga, C.; Montes, C.; Garces, J. M.; Crowder, J. A. *Nature* **1988**, 331, 698.
- (120) Estermann, M.; McCusker, L. B.; Baerlocher, C.; Merrouche, A.; Kessler, H. *Nature* **1991**, 352, 320.
- (121) Xu, R. R.; Gao, Z.; Xu, Y. In *Progress in Zeolite Science, A China Perspective*; World Scientific: Singapore, **1995**.
- (122) Balkus, K. J.; Gabrielov, A. G.; Zones, S. I.; Chan, I. Y. *Synthesis of Porous Materials: Zeolites, Clays and Nanostructures*; Marcel Dekker, Inc.: New York, **1997**. p77.
- (123) Occelli, M. L.; Takahama, K.; Yokoyama, M.; Hirao, S. in *Expanded Clays and Other Microporous Materials*; Dccelli, M. L., Robson, H., Eds.; Van Nostrand: Van Nostrand and New York, **1992**, p 57.
- (124) Beck, J. S.; U.S. Patent No 5,057,296, **1991**
- (125) Inagaki, S.; Fukushima, Y.; Kuroda, K. *J. Chem. Soc., Chem. Commun.* **1993**, 680.
- (126) Yanagisawa, T.; Shimizu, T.; Kuroda, K.; Kato, C. *Bull. Chem. Soc. Jpn.* **1990**, 63, 988.
- (127) Chiola, V.; Ritsko, J. E.; Vanderpool, C. D.; U. S. Patent No 3,556,725, **1971**
- (128) Di Renzo, F.; Cambon, H.; Dutartre, R. *Microporous Mater.* **1997**, 10, 283.
- (129) Alfredsson, V.; Keung, M.; Monnier, A.; Stucky, G. D.; Unger, K. K.; Schöth, F. *J. Chem. Soc., Chem. Commun.* **1994**, 921.
- (130) Feustion, B. P.; Higgins, J. B. *J. Phys. Chem.* **1994**, 98, 4459.
- (131) Sayari, A. *Chem. Mater.* **1996**, 8, 1840.
- (132) Sayari, A. *Recent Advances and New Horizons in zeolite Science and Technology*; Elsevier: Amsterdam, **1996**. p1.
- (133) Khushalani, D.; Kuperman, A.; Ozin, G. A.; Tanaka, K.; Garces, J.; Olken, M. M.; Coombs, N. *Adv. Mater.* **1995**, 7, 842.
- (134) Cheng, C.-F.; Zhou, W.; Klinowski, J. *Chem. Phys. Lett.* **1996**, 263, 247.
- (135) Corma, A.; Kan, A. Q.; Navarro, M. T.; Perez-Pariente, J.; Rey, F. *Chem. Mater.* **1997**, 9, 2123.
- (136) Ciesla, U.; Schüth, F. *Microporous Mesoporous Mater.* **1999**, 27, 131.
- (137) Inagaki, S.; Fukushima, Y.; Kuroda, K. *J. Colloid Interface Sci.* **1996**, 180, 623.

- (138) Huo, Q.; Margolese, D. I.; Ciesla, U.; Demuth, D. G.; Feng, P.; Gier, T. E.; Sieger, P.; Firouzi, A.; Chmelka, B. F.; Schüth, F.; Stucky, G. D. *Chem. Mater.* **1994**, *6*, 1176.
- (139) Huo, Q.; Leon, R.; Petroff, P. M.; Stucky, G. D. *Science* **1995**, *268*, 1324.
- (140) Lukens, W.; Jr., W.; Schmidt-Winkel, P.; Zhao, D.; Feng, J.; Stucky, G. D. *Langmuir* **1999**, *15*, 5403.
- (141) Zhao, D.; Yang, P.; Melosh, N.; Feng, J.; Chmelka, B. F.; Stucky, G. D. *Adv. Mater.* **1998**, *10*, 1380.
- (142) Feng, P.; Bu, X.; Stucky, G. D.; Pine, D. J. *J. Am. Chem. Soc.* **2000**, *122*, 994.
- (143) Huo, Q.; Margolese, D. I.; Ciesla, U.; Feng, P.; Gier, T. E.; Sieger, P.; Leon, R.; Petroff, P. M.; Schüth, F.; Stucky, G. D. *Nature* **1994**, *368*, 317.
- (144) Zhao, D.; Huo, Q.; Feng, J.; Kim, J.; Han, Y.; Stucky, G. D. *Chem. Mater.* **1999**, *11*, 2668.
- (145) Bagshaw, S. A.; Prouzet, E.; Pinnavaia, T. J. *Science* **1995**, *269*, 1242.
- (146) Prouzet, E.; Cot, F.; Nabias, G.; Larbot, A.; Kooyman, P.; Pinnavaia, T. J. *Chem. Mater.* **1999**, *11*, 1498.
- (147) Ryoo, R.; Kim, J. M.; Ko, C. H.; Shin, C. H. *J. Phys. Chem.* **1996**, *100*, 17718.
- (148) Ryoo, R.; Ko, C. H.; Park, I. S. *Chem. Commun.* **1999**, 1413.
- (149) J. Lee; Yoon, S.; Hyeon, T.; Oh, S. M.; Kim, K. B. *Chem. Commun.* **1999**, 2177.
- (150) Tanev, P. T.; Pinnavaia, T. J. *Science* **1995**, *267*, 865.
- (151) Tanev, P. T.; Pinnavaia, T. J. *Chem. Mater.* **1997**, *9*, 2491.
- (152) Tanev, P. T.; Liang, Y.; Pinnavaia, T. J. *J. Am. Chem. Soc.* **1997**, *119*, 8616.
- (153) Kim, S. S.; Zhang, W.; Pinnavaia, T. J. *Science* **1998**, *282*, 1302.
- (154) Kimura, T.; Sugahara, Y.; Kuroda, K. *Chem. Commun.* **1998**, 559.
- (155) Kimura, T.; Sugahara, Y.; Kuroda, K. *Microporous Mesoporous Mater.* **1998**, *22*, 115.
- (156) Davis, M. E.; Burkett, S. L. *Zeolites* **1995**, *12*, 33.
- (157) Vartuli, J. C.; Roth, W. J.; Beck, J. S.; McCullen, S. B.; Kresge, C. T. "The Synthesis and Properties of M41S and Related Mesoporous Materials" in *Molecular Sieves*; Springer-Verlag: Berlin, **1998**; Vol. 1, p 97.
- (158) Steel, A.; Carr, S. W.; Anderson, M. W. *J. Chem. Soc., Chem. Commun.* **1994**, 1571.
- (159) Cheng, C. F.; He, H.; Zhou, W.; Klinowski, J. *Chem. Phys. Lett.* **1995**, *244*, 117.
- (160) Cheng, C. F.; Luan, Z.; Klinowski, J. *Langmuir* **1995**, *11*, 2815.

- (161) Kolodziejski, W.; Corma, A.; Navarro, M. T.; Pérez-Pariente, J. *Solid State Nucl. Magn. Reson.* **1993**, 2, 253.
- (162) Vartuli, J. C.; Schmitt, K. D.; Kresge, C. T.; Roth, W. J.; Leonowicz, M. E.; McCullen, S. B.; Hellring, S. D.; Beck, J. S.; Schlenker, J. L.; Olson, D. H.; Sheppard, E. W. "Development of a formation mechanism for M41S materials" in *Zeolites and Related Microporous Materials: State of the Art 1994*, Stud. Surf. Sci. Catal.; Weitkamp, J., Karge, H. G., Pfeifer, H., Hölderich, W., Eds.; Elsevier Science B. V.: Amsterdam, **1994**; Vol. 84, p 53.
- (163) Vartuli, J. C.; Schmitt, K. D.; Kresge, C. T.; Roth, W. J.; Leonowicz, M. E.; McCullen, S. B.; Hellring, S. D.; Beck, J. S.; Schlenker, J. L.; Olson, D. H.; Sheppard, E. W. *Chem. Mater.* **1994**, 6, 2317.
- (164) Beck, J. S.; Kennedy, J. C. V. J.; Kresge, C. T.; Roth, W. H.; Schramm, S. E. *Chem. Mater.* **1994**, 6, 1816.
- (165) Vartuli, J. C.; Kresge, C. T.; Leonowicz, M. E.; Chu, A. S.; McCullen, S. B.; Johnson, I. D.; Sheppard, E. W. *Chem. Mater.* **1994**, 6, 2070.
- (166) Inagaki, S.; Sakamoto, Y.; Fukushima, Y.; Terasaki, O. *Chem. Mater.* **1996**, 8, 2089.
- (167) Luan, Z.; He, H.; Zhou, W.; Klinowski, J. *J. Chem. Soc., Faraday Trans.* **1998**, 94, 979.
- (168) Ren, F. Y.; Waite, S. W.; Harris, J. M. *Anal. Chem.* **1995**, 67, 3441.
- (169) Ryoo, R.; Ko, C. H.; Howe, R. F. *Chem. Mater.* **1997**, 9, 1607.
- (170) Chorro, M.; Vhorro, C.; Dolladille, O.; Partyka, S.; Zana, R. *Colloid Interface. Sci.* **1999**, 210, 134.
- (171) Kruk, M.; Jaroniec, M.; Ryoo, R.; Joo, S. H. *Chem. Mater.* **1999**, 11, 2568.
- (172) Kruk, M.; Jaroniec, M.; Ryoo, R.; Joo, S. H. *J. Phys. Chem. B* **2000**, 104, 7960.
- (173) Chen, C. Y.; Bruckett, S. L.; Li, H. X.; Davis, M. E. *Microporous Mater.* **1993**, 2, 27.
- (174) Raman, N. K.; Anderson, M. T.; Brinker, C. J. *Chem. Mater.* **1996**, 8, 1682.
- (175) Tanev, P. T.; Pinnavaia, T. J. *Chem. Mater.* **1996**, 8, 2068.
- (176) Yang, H.; Kuperman, A.; Coombs, N.; Mamiche-Afara, S.; Ozin, G. A. *Nature* **1996**, 379, 703.
- (177) Firouzi, A.; Kumar, D.; Bull, L. M.; Besier, T.; Sieger, P.; Huo, Q.; A. Walker, S.; Zasadzinski, J. A.; Glinka, C.; Nicol, J.; Margolese, D.; Stucky, G. D.; Chmelka, B. *F. Science* **1995**, 267, 1138.

- (178) Monnier, A.; Schüth, F.; Huo, Q.; Kumar, D.; Margolese, D.; Maxwell, R. S.; Stucky, G. D.; Krishnamurty, M.; Petroff, P. M.; Firouzi, A.; Janicke, M.; Chmelka, B. *F. Science* **1993**, *261*, 1299.
- (179) Huo, Q.; Margolese, D. I.; Stucky, G. D. *Chem. Mater.* **1996**, *8*, 1147.
- (180) Petrovic, I.; Navrotsky, A.; Chen, C.-Y.; Davis, M. E. *Stud. Surf. Sci. Catal.* **1994**, *84*, 677.
- (181) Kim, J. M.; Kwak, J. H.; Jun, S.; Ryoo, R. *J. Phys. Chem.* **1995**, *99*, 16742.
- (182) Attard, G. S.; Glyde, J. C.; Göltner, C. G. *Nature* **1995**, *378*, 317.
- (183) Wei, Y.; Jin, D.; Ding, T.; Shih, W.-H.; Liu, X.; Cheng, S. Z. D.; Fu, Q. *Adv. Mater.* **1998**, *3*, 313.
- (184) Feng, Q.; Xu, J.; Dong, H.; Wei, Y. *Polym. Prepr.* **2000**, *41*, 515.
- (185) Feng, Q.; Xu, J.; Dong, H.; Li, S.; Wei, Y. *J. Mater. Chem.* **2000**, *10*, 2490.
- (186) Ying, J. Y.; Mehnert, C. P.; Wong, M. S. *Angew. Chem. Int. Ed.* **1999**, *38*, 56.
- (187) Luan, Z.; He, H.; Zhou, W.; Cheng, C.-F.; Klinowski, J. *J. Chem. Soc., Faraday Trans.* **1995**, *91*, 2955.
- (188) Schüth, F. *Chem. Mater.* **2001**, *13*, 3184.
- (189) Schmidt, R.; Akporiaye, D.; Stöcker, M.; Ellestad, O. H. *Stud. Surf. Sci. Catal.* **1994**, *84*, 61.
- (190) Hitz, S.; Prins, R. *J. Catal.* **1997**, *168*, 194.
- (191) Montes, A.; Cosenza, E.; Giannetto, G.; Urquieta, E.; Melo, R. A.; Gnep, N. S.; Guisnet, M. *Stud. Surf. Sci. Catal.* **1998**, *117*, 237.
- (192) Malla, P. B.; Komarneni, S. *Zeolites* **1995**, *15*, 324.
- (193) Kawi, S.; Lai, M. N. *J. Chem. Soc., Chem. Commun* **1998**, 1407.
- (194) Danumah, C.; Zaidi, S. M. J.; Voyer, N.; Giasson, S.; Kaliaguine, S. *Stud. Surf. Sci. Catal.* **1998**, *117*, 281.
- (195) Antochshuk, V.; Jaroniec, M. *J. Chem. Soc., Chem. Commun.* **1999**, 2373.
- (196) Antochshuk, V.; Jaroniec, M. *Stud. Surf. Sci. Catal.* **2000**, *129*, 265.
- (197) Antochshuk, V.; Jaroniec, M. *Chem. Mater.* **2000**, *12*, 2496.
- (198) Keene, M. T. J.; Denoyel, R.; Llewellyn, P. L. *Chem. Commun.* **1998**, 2203.
- (199) Büchel, G.; Denoyel, R.; Llewellyn, P. L.; Rouquaurol, J. *J. Mater. Chem.* **2001**, *11*, 589.
- (200) Clark, T.; Jr.; Ruiz, J. D.; Fan, H.; Brinker, C. J.; Swanson, B. I.; Parikh, A. N. *Chem. Mater.* **2000**, *12*, 3879.

- 
- (201) Moon, D. W.; Kurokawa, A.; Ichimura, S.; Lee, H. W.; Jeon, I. C. *J. Vac. Sci. Technol. A* **1999**, *17*, 150.
- (202) Corma, A.; Kumar, D. *Stud. Surf. Sci. Catal.* **1998**, *117*, 201.
- (203) Fu, G.; Fyfe, C. A.; Schwieger, W.; Kokotailo, G. T. *Angew. Chem. Int. Ed.* **1995**, *34*, 1499.
- (204) Luan, Z.; Cheng, C.-F.; Zhou, W.; Klinowski, J. *J. Phys. Chem.* **1995**, *99*, 1018.
- (205) Borarde, R. B.; Clearfield, A. *Catal. Lett.* **1995**, *31*, 267.
- (206) Hamdan, H.; Endud, S.; He, H.; Muhid, M. N. M.; Klinowski, J. *J. Chem. Soc., Faraday Trans.* **1996**, *92*, 2311.
- (207) Mokaya, R. *Chem. Commun.* **2000**, 1891.
- (208) Mokaya, R. *Chem. Commun.* **2000**, 1541.
- (209) Mokaya, R.; Jones, W. *Chem. Commun.* **1997**, 2185.
- (210) Mokaya, R.; Jones, W. *J. Mater. Chem.* **1999**, *9*, 555.
- (211) Mokaya, R.; Jones, W. *Phys. Chem. Chem. Phys.* **1999**, *1*, 207.
- (212) Mokaya, R.; Jones, W.; Luan, Z.; Alba, M. D.; Klinowski, J. *Catal. Lett.* **1996**, *37*, 113.
- (213) Mokaya, R.; Zhou, W.; Jones, W. *Chem. Commun.* **1999**, 51.
- (214) Mokaya, R.; Jones, W. *Chem. Commun.* **1998**, 1839.
- (215) Ryoo, R.; Jun, S.; Kim, J. M.; Kim, M. J. *Chem. Commun.* **1997**, 2225.
- (216) Janicke, M. T.; Landry, C. C.; Christiansen, S. C.; Kumar, D.; Stucky, G. D.; Chmelka, B. F. *J. Am. Chem. Soc.* **1998**, *120*, 6940.
- (217) Kloestra, K. R.; Zandbergen, H. W.; Bekkum, H. v. *Catal. Lett.* **1995**, *33*, 157.
- (218) Engelhardt, G.; Michael, D. *High-Resolution Solid State NMR of Silicates and Zeolites*; John Wiley & Sons: New York, **1987**.
- (219) Cabrera, S.; Haskouri, J. E.; Mendioroz, S.; Guillem, C.; Latorre, J.; -Porter, A. B.; -Porter, D. B.; Marcos, M. D.; Amorós, P. *J. Chem. Soc., Chem. Commun.* **1999**, 1679.
- (220) Cabrera, S.; Haskouri, J. E.; Mendioroz, S.; Guillem, C.; Latorre, J.; Beltrán-Porter, A.; Beltrán-Porter, D.; Marcos, M. D.; Amorós, P. *Chem. Commun.* **1999**, 1679.
- (221) Reddy, K. M.; Song, C. *Catal. Today* **1996**, *31*, 137.
- (222) Corma, A.; V., F. s.; Navarro, M. T.; Pe´rez-Pariente, J. *J. Catal.* **1994**, *148*, 569.
- (223) Corma, A.; Grande, M. S.; Gonzalez-Alfaro, V.; Orchilles, A. V. *J. Catal.* **1996**, *159*, 375.

- (224) Corma, A.; Martinez, A.; Martinez-Soria, V.; Monton, J. B. *J. Catal.* **1995**, *153*, 25.
- (225) Luan, Z. H.; Cheng, C. F.; H.Y. He; Klinowski, J. *J. Phys. Chem.* **1995**, *99*, 10590.
- (226) Roos, K.; Liepold, A.; Reschetilowski, W.; Schmidt, R.; Karlsson, A.; Stöcker, M. *Stud. Surf. Sci. Catal.* **1995**, *94*, 389.
- (227) Morin, S.; Ayrault, P.; Mouahid, S. E.; Gnep, N. S.; Guisnet, M. *Appl. Catal. A: General* **1997**, *159*, 317.
- (228) Armengol, A.; Cano, M. L.; Corma, A.; Garcia, H.; M.L., N. *J. Chem. Soc., Chem Commun.* **1995**, 519.
- (229) Dedecek, J.; Zilkova, N.; Cejka, J. *Microporous Mesoporous Mater.* **2001**, *44-45*, 259.
- (230) Reddy, K. M.; Song, C. *Stud. Surf. Sci. Catal.* **1998**, *117*, 291.
- (231) Occelli, M. L.; VBiz, S.; Auroux, A.; Ray, G. J. *Microporous Mesoporous Mater.* **1998**, *26*, 193.
- (232) Kloestra, K. R.; Van Bekkum, H. *J. Chem. Res. Synop.* **1995**, 26.
- (233) Lim, Y.-Y.; MacLachlan, D. J.; Smith, T. D.; Jamis, J.; Pilbrow, J. R.; Song, R. *Aust. J. Chem.* **1997**, *50*, 53.
- (234) Corma, A.; Navavro, M. T.; Pérez Pariente, J. *J. Chem. Soc., Chem. Commun.* **1994**, 147.
- (235) Jentys, A.; Kleestorfer, K.; Vinek, H. *Microporous Mesoporous Mater.* **1999**, *27*, 321.
- (236) Hunger, M.; Schenk, U.; Breuninger, M.; Gläser, R.; Weitkamp, J. *Microporous Mesoporous Mater.* **1999**, *27*, 261.
- (237) Koch, H.; Böhmer, U.; Klemm, A.; Reschetilowski, E.; Stöcker, M. *J. Chem. Soc., Faraday Trans.* **1998**, *94*, 817.
- (238) Koch, H.; Liepold, A.; Roos, K.; Stöcker, M.; Reschetilowski, W. *Chem. Eng. Technol.* **1999**, *27*, 807.
- (239) Kosslick, H.; Lischke, G.; Parlitz, B.; Storek, W.; Fricke, R. *Appl. Catal. A: General* **1999**, *184*, 49.
- (240) Hartmann, M.; Püppl, A.; Kevan, L. *J. Phys. Chem.* **1995**, *99*, 17494.
- (241) Prakash, A. M.; Kevan, L. *J. Phys. Chem.* **1996**, *100*, 19587.
- (242) Chang, Z.; Zhu, Z.; Kevan, L. *J. Phys. Chem. B* **1999**, *103*, 9442.
- (243) Kim, S.-S.; Zhang, W.; Pinnavaia, T. J. *Catal. Lett.* **1997**, *43*, 149.



- (244) Luan, Z.; Xu, J.; He, H.; Klinowski, J.; Kevan, L. *J. Phys. Chem. B* **1996**, *100*, 19595.
- (245) Luan, Z.; Xu, J.; Kevan, L. *Nukleonika* **1997**, *42*, 493.
- (246) Xu, J.; Luan, Z.; Wasowicz, T.; Kevan, L. *Microporous Mesoporous Mater.* **1998**, *22*, 179.
- (247) Zhang, J.; Goldfarb, D. *J. Am. Chem. Soc.* **2000**, *122*, 7034.
- (248) Püppl, A.; Newhouse, M.; Kevan, L. *J. Phys. Chem.* **1995**, *99*, 10019.
- (249) Yuan, Z. Y.; Liu, S. Q.; Chen, T. H.; Wang, J. Z.; Li, H. X. *J. Chem. Soc., Chem. Commun.* **1995**, 973.
- (250) Zhang, W.; Pinnavaia, T. J. *J. Catal.* **1996**, *38*, 261.
- (251) Zhu, Z.; Hartmann, M.; Maes, E. M.; Czernuszewicz, R. C.; Kevan, L. *J. Phys. Chem. B* **2000**, *104*, 4690.
- (252) Antochshuk, V.; Araujo, A. S.; Jaronies, M. *J. Phys. Chem. B* **2000**, *104*, 9713.
- (253) Das, T. K.; Chaudhari, K.; Chandwadkar, A. J.; Sivasanker, S. *J. Chem. Soc., Chem. Commun.* **1995**, 2495.
- (254) Chaudhari, K.; Bal, R.; Das, T. K.; Chandwadkar, A.; Srinivas, D.; Sivasanker, S. *J. Phys. Chem. B* **2000**, *104*, 11066.
- (255) Occelli, M. L.; Biz, S.; Auroux, A. *Appl. Catal. A: General* **1999**, *183*, 231.
- (256) Kim, Y.; Choi, J. R.; Yoon, M.; Furube, A.; Asahi, T.; Masuhara, H. *J. Phys. Chem. B* **2001**, *105*, 8513.
- (257) Honma, I.; Zhou, H. S. *Chem. Mater.* **1998**, *10*, 103.
- (258) Yamashita, H.; Tanaka, A.; Nishimura, M.; Koyano, K.; Tatsumi, T.; Anpo, M. *Stud. Surf. Sci. Catal.* **1998**, *117*, 551.
- (259) Corma, A.; Fornés, V.; García, H.; Miranda, M. A.; Sabater, M. J. *J. Am. Chem. Soc.* **1994**, *116*, 9767.
- (260) Long, R. Q.; Yang, R. T. *Ind. Eng. Chem. Res.* **1999**, *38*, 873.
- (261) Climent, M. J.; Corma, A.; Iborra, S.; S., M.; Primo, J.; Rey, F. *J. Catal.* **1999**, *183*, 76.
- (262) Kageyama, K.; Ogino, S.; Aida, T.; Tatsumi, T. *Macromolecules* **1998**, *31*, 4069.
- (263) Ranjit, K. T.; Chang, Z.; Krishna, R. M.; Prakash, A. M.; Kevan, L. *J. Phys. Chem. B* **2000**, *104*, 7981.
- (264) Werst, D. W.; Choure, S. C.; Vinokur, E. I.; Xu, L.; Trifunac, A. D. *Radiat. Phys. Chem.* **2000**, *58*, 223.

- (265) Wark, M.; Ortlam, A.; Ganschow, M.; Schulz-Ekloff, G.; Wöhrle, D. *Ber. Bunsenges. Phys. Chem.* **1998**, *102*, 1548.
- (266) Hoppe, R.; Ortlam, A.; Rathouský, J.; Schulz-Ekloff, G.; Zukal, A. *Microporous Mater.* **1997**, *8*, 267.
- (267) Toriyama, K.; Okazaki, M. *Phys. Chem. Chem. Phys.* **1999**, *1*, 2607.
- (268) Miranda, M. A.; Garcia, H. *Chem. Rev.* **1994**, *94*, 1063. And reference therein.
- (269) Algarra, F.; Esteves, M. A.; Fornés, V.; García, H.; Primo, J. *New. J. Chem.* **1998**, 333.
- (270) Holland, B. T.; Walkup, C.; Stein, A. *J. Phys. Chem. B* **1998**, *102*, 4301.
- (271) Priyadarshy, S.; Therien, M. J.; Beratan, D. N. *J. Am. Chem. Soc.* **1996**, *118*, 1504.
- (272) Tanimura, K.; Kawal, T.; Sakata, T. *J. Phys. Chem.* **1980**, *84*, 751.
- (273) Khairutdinov, R. F.; Serpone, N. *J. Phys. Chem. B* **1999**, *103*, 761.
- (274) Kevan, L. "Photoionization of Porphyrins and Phenothiazines in Microporous Oxide Materials" in *Books of Abstracts, 217th ACS National Meeting*; ACS, Washington D. C.: Anaheim, Calif, **1999**.
- (275) Counterman, M.; Holten, D. *Photochem. Photobiol.* **1982**, *19*, 209.
- (276) Chang, Z.; Kevan, L. *Langmuir* **2002**, *18*, 911.
- (277) Chang, Z.; Krishna, R. M.; Xu, J.; Koodali, R.; Kevan, L. *Phys. Chem. Chem. Phys.* **2001**, *3*, 1699.
- (278) Sinlapadech, S.; Krishna, R. M.; Luan, Z.; Kevan, L. *J. Phys. Chem. B* **2001**, *105*, 4350.
- (279) Sinlapadech, S.; Koodali, R.; Krishna, R. M.; Kevan, L. *J. Phys. Chem. B* **2002**, *106*, 6251.
- (280) Konovalova, T. A.; Gao, Y.; Schad, R.; Kispert, L. D. *J. Phys. Chem. B* **2001**, *105*, 7459.
- (281) Prakash, A. M.; Sung-Suh, H. M.; Kevan, L. *J. Phys. Chem. B* **1998**, *102*, 857.
- (282) Abou-Kais, A.; Vendrine, J. C.; Masardier, J. *J. Chem. Soc., Faraday Trans.* **1975**, *71*, 1697.
- (283) Biz, S.; White, M. G. *J. Phys. Chem. B* **1999**, *103*, 8432.
- (284) Jeevarajan, A. S.; Kispert, L. D.; Piekara-Sady, L. *Chem. Phys. Lett.* **1993**, *209*, 269.
- (285) Samoilova, R. I.; Shubin, A. A.; Bowman, M. K.; Hüttermann, J.; Dikanov, S. *A. Chem. Phys. Lett.* **2000**, *316*, 404.

- (286) Samoilova, R. I.; Astashkin, A. V.; Dikanov, S. A.; Goldfarb, D.; Lunina, E. V. *Colloids Surf. A: Physicochem. Eng. Aspects* **1993**, 72, 29.
- (287) Konovalova, T. A.; Kispert, L. D. *J. Chem. Soc., Faraday Trans.* **1998**, 94, 1465.
- (288) Hoekstra, K.; Bein, T. "Encapsulation of Tetrathiafulvalene in Zeolites and Mesoporous Hosts" in *Book of Abstracts, 213th ACS National Meeting*; American Chemical Society: Washington, D. C, **1997**.
- (289) Park, S. E.; Sung-Suh, H. M.; Kim, D. S.; Ko, J. *Stud. Surf. Sci. Catal.* **2000**, 129, 807. reference therein.
- (290) MacLachlan, M. J.; Asefa, T.; Ozin, G. A. *Chem. Eur. J.* **2000**, 6, 2507.
- (291) Inagaki, S.; Guan, S.; Fukushima, Y.; Oshuna, T.; Terasaki, O. *J. Am. Chem. Soc.* **1999**, 121, 9611.
- (292) Melde, B. J.; Holland, B. T.; Blandford, C. F.; Stein, A. *Chem. Mater.* **1999**, 11, 3302.
- (293) Yoshina-Ishii, C.; Asefa, T.; Coombs, N.; MacLachlan, M. J.; Ozin, G. A. *Chem. Commun.* **1999**, 2539.
- (294) Alvaro, M.; Ferrer, B.; Fornés, V.; García, H. *Chem. Commun.* **2001**, 2546.
- (295) Brunel, D.; Lentz, P.; Sutra, P.; Deroide, B.; Fajula, F.; Nagy, J. B. *Stud. Surf. Sci. Catal.* **1999**, 125, 237.
- (296) Paddon-Row, M. N. *Acc. Chem. Res.* **1994**, 27, 18.
- (297) Oevering, H.; Paddon-Row, M. N.; Heppener, H.; Oliver, A. M.; Cotsaris, E.; Verhoeven, J. W.; Hush, N. S. *J. Am. Chem. Soc.* **1987**, 1987, 3258.
- (298) Paddon-Row, M. N.; Oliver, A. M.; Warman, J. M.; Smit, K. J.; deHass, M. P.; Oevering, H.; Verhoeven, J. W. *J. Phys. Chem.* **1988**, 92, 6958.
- (299) Kuchi, V.; Oliver, A. M.; Paddon-Row, M. N.; Howe, R. F. *Chem. Commun.* **1999**, 1149.
- (300) Brigham, E. S.; Snowden, P. T.; Kim, Y. I.; Mallouk, T. E. *J. Phys. Chem.* **1993**, 97, 8650.
- (301) Orritt, M. *Science* **1999**, 285, 349. And references therein.
- (302) Fox, M. A. *Acc. Chem. Res.* **1999**, 32, 201. And references therein.
- (303) Tolbert, S. H.; Firouzi, A.; Stucky, G. D.; Chmelka, B. F. *Science* **1997**, 278, 264.
- (304) Wu, J.; Gross, A. F.; Tolbert, S. H. *J. Phys. Chem. B* **1999**, 103, 2374.

- 
- (305) Nguyen, T.-Q.; Wu, J.; Doan, V.; Schwartz, B. J.; Tolbert, S. H. *Science* **2000**, 288, 652. And references therein.
- (306) Scott, B. J.; Wirnsberger, G.; Stucky, G. D. *Chem. Mater.* **2001**, 13, 3140. And references therein.
- (307) Leon, R.; Margolese, D.; Stucky, G. D.; Petroff, P. M. *Phys. Rev. B: Condens. Mater. Mater. Phys.* **1995**, 52, R2285.
- (308) Parala, H.; Winkler, H.; Kolbe, M.; Wohlfart, A.; Fischer, R. A.; Schmechel, R.; Seggern, H. v. *Adv. Mater.* **2000**, 12, 1050.
- (309) Ogawa, M.; Nakamura, T.; Mort, J.; Kuroda, K. *J. Phys. Chem. B* **2000**, 104, 8554.
- (310) Kinski, I.; Gies, H.; Marlow, F. *Zeolites* **1997**, 19, 375.
- (311) Marlow, F.; McGehee, M. D.; Zhao, D. Y.; Chmelka, B. F.; Stucky, G. D. *Adv. Mater.* **1999**, 11, 632.
- (312) Wirnsberger, G.; Scott, B. J.; Chmelka, B. F.; Stucky, G. D. *Adv. Mater.* **2000**, 12, 1450.
- (313) Fan, H. Y.; Lu, Y. F.; Stump, A.; Reed, S. T.; Baer, T.; Schunk, R.; Perez-Luna, V.; Lopez, G. P.; Brinker, C. J. *Nature* **2000**, 405, 56.

## Chapter 2

### Experimental

#### 2.1. Introduction

This experimental chapter comprises the following four sections:

- (1) The inorganic synthesis section mainly describes hydrothermal synthesis of purely siliceous mesoporous MCM-41 and three Al-MCM-41 samples with Si/Al ratio of 39, 15, and 7 respectively. Ozone generation and methods to remove the CTAC surfactant templates from the as-synthesized samples, i.e., conventional thermal calcination and ozone treatment are included. Post-grafting synthesis of an Al-MCM-41 with Si/Al ratio of 14 is also described.
- (2) The organic synthesis section describes the synthesis of some electron donor and acceptor molecules which are not commercially available.
- (3) The molecular assembly in MCM-41 section describes the experimental methods of assembling the organic donor, acceptor, and donor-bridge-acceptor molecules into mesoporous MCM-41 materials.
- (4) The characterization section describes various spectroscopic and other analytical techniques used for the characterization of mesoporous MCM-41 materials and the study of electron transfer processes in MCM-41 mesoporous hosts.
- (5) Appendix 2.1 lists the commercially available chemicals and reagents together with their sources, physical properties and purification methods. Appendix 2.2 lists some special compounds which were commercially unavailable.

## 2.2. Inorganic Synthesis

### 2.2.1. Hydrothermal Synthesis of Mesoporous MCM-41 and Al-MCM-41

Purely siliceous MCM-41 and three Al-MCM-41 ( $\text{Si/Al} = \infty, 39, 15, 7$  respectively) samples were hydrothermally synthesized by following Ryoo's procedures.<sup>1,2</sup> The silicate source was freshly prepared sodium silicate solution [NaOH with colloidal silica, Ludox HS40] with a Na/Si ratio of 0.5. The alumina source was freshly prepared sodium aluminate solution. In order to facilitate the study of the surfactant template removal by various methods, only one surfactant, namely, cetyltrimethylammonium chloride (CTAC) was used as template without auxiliary surfactant such as tetrapropylammonium (TPA). Typical synthesis procedures are described in the following sections.

#### 2.2.1.1. Synthesis of Purely Siliceous MCM-41

To an aqueous NaOH solution (46.9 g, 1M) was added colloidal silica (14.3 g, Ludox HS40, 39.5 wt %  $\text{SiO}_2$ , 0.4 wt %  $\text{Na}_2\text{O}$ , and 60.1 wt %  $\text{H}_2\text{O}$ ), and the mixture was heated for 2 hrs at 353 K with vigorous magnetic stirring. This freshly prepared sodium silicate solution has a Na/Si ratio of 0.5 and was used as the silicate source in the following procedure. An aqueous  $\text{NH}_3$  (0.29 g, 28 wt %) and CTAC (20 g, 25 wt%) solutions were added into a 250 mL polypropylene bottle, respectively. To this mixture, the above clear sodium silicate solution was added dropwise at room temperature under vigorous magnetic stirring. The molar composition of the resulting gel mixture was 6  $\text{SiO}_2$  : 1 CTAC : 1.5  $\text{Na}_2\text{O}$  : 0.15  $(\text{NH}_4)_2\text{O}$  : 250  $\text{H}_2\text{O}$ . The mixture was stirred for a further one hour, after which time it was sealed and heated (aged) in an oven at 370 K

for 3 days. At each 24 hrs interval, the polypropylene bottle was taken out from the oven, cooled to the room temperature, and the pH value of the mixture was adjusted to 10.2 with 30 wt % acetic acid. On the fourth day, the gel mixture was cooled to room temperature, repeatedly washed with large amount of deionized water and filtered. The gel mixture was then dried again at 370 K in the oven to give dried white powder (7.8 g). The dried sample (designated as “as-synthesized” sample) was kept in a sealed glass sample container and stored in a desiccator.

#### **2.2.1.2. Synthesis of Al-MCM-41 with Si/Al = 39, 15, and 7**

The gel mixture with a molar ratio of 6 SiO<sub>2</sub> : 1 CTAC : 1.5 Na<sub>2</sub>O : 0.15 (NH<sub>4</sub>)<sub>2</sub>O : 250 H<sub>2</sub>O was freshly prepared as described in the synthesis of purely siliceous MCM-41. After this gel mixture was magnetically stirred for one hour, sodium aluminate solution (0.43 g, dissolved in 5 mL deionized water) was added dropwise. The resulting gel mixture, possessing the molar composition as 6 SiO<sub>2</sub> : 0.1 Al<sub>2</sub>O<sub>3</sub> : 1 CTAC : 0.15 (NH<sub>4</sub>)<sub>2</sub>O : 1.5 Na<sub>2</sub>O : 300 H<sub>2</sub>O, was stirred for a further 30 min. The following three days' ageing and pH adjustment procedures were exactly the same as those in the synthesis of purely siliceous MCM-41. On the fourth day, the gel mixture was cooled to room temperature, repeatedly washed with large amount of deionized water and filtered. The gel mixture was then dried again at 370 K in the oven to give dried white powder (8.25 g). The dried sample (designated as “as-synthesized” sample) was kept in a sealed glass sample container and stored in a desiccator.

The procedures for the preparation of the other two samples with Si/Al = 15 and 7 were identical to that described above for the preparation of sample with Si/Al = 39, except that 1.118 g and 2.396 g of sodium aluminate solution were used for the

preparation of the samples with Si/Al = 15 and 7, respectively. The yields of these two as-synthesized white products were 8.97 g and 9.70 g, respectively.

### 2.2.1.3. Ozone Generation

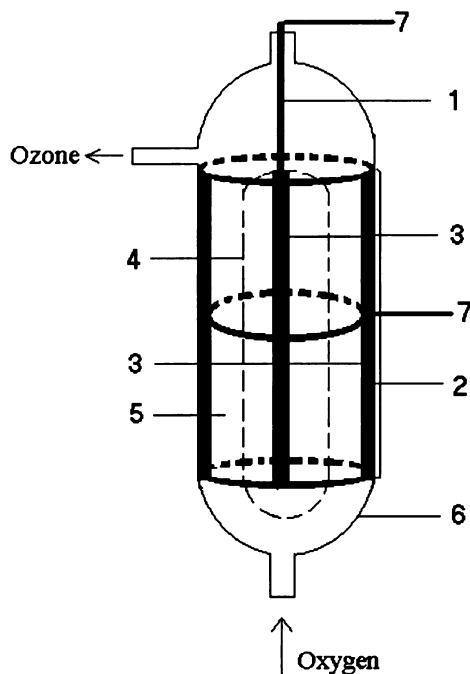


**Figure 2.1:** A Schematic drawing of the ozone generator. 1-steel high-potential electrode; 2-steel low-potential electrode; 3-ceramic dielectric coatings; 4-glass separator; 5-discharge space; 6-glass reactor; 7- electric wires connected to the electric transformer.

Of the various methods by which ozone can be generated, the barrier discharge method is the most often used.<sup>3</sup> The schematic drawing of the ozone generator used in the following experimental sections is shown in Figure 2.1. It consists of two steel electrodes that are coated with ceramic dielectric barriers, glass separators that separate two electrodes, and a transformer for Neon tubes (Type T 1524, from Standard Electric Works, Hong Kong). The oxygen (>98%) was blown along the electrodes through the opening space between them. A high potential alternating current voltage (15 kV) was



applied to the electrodes. The ozone flow-rate was controlled and kept constant by setting the pressure of the oxygen cylinder at 4 pounds/inch<sup>2</sup>.

#### **2.2.1.4. CTAC Template Removal**

##### **(1) Extraction of CTAC Templates from As-synthesized Samples by Ethanol / HCl Treatment**

It has been reported that quaternary ammonium surfactant template has different kinds of interaction forces with silanol groups and Al species in the framework of MCM-41.<sup>4</sup> The template in purely siliceous MCM-41, which is mainly associated with the silanol groups, can be readily removed by conventional calcination method. However, the template in Al-MCM-41, which is also additionally associated with the Al species through much stronger electrostatic interaction forces, cannot be completely removed simply by the use of the standard thermal calcination procedure.<sup>5-7</sup> In order to completely remove the surfactant template in the Al-MCM-41 sample, the following ethanol / HCl extraction procedures were employed to the three Al-MCM-41 samples (Si/Al=39, 15, and 7 respectively) prior to the further treatment. The ethanol / HCl extracted Al-MCM-41 samples are referred to as “pre-washed” Al-MCM-41 samples in the following sections. The ethanol / HCl extraction procedures are as follows:

After three times pH adjustment of the gel mixture, the dried Al-MCM-41 sample was added into a 250 mL flask containing HCl / ethanol solution (0.1 M, 150 mL), and refluxed for 1 hr with magnetic stirring. The mixture was then filtered while it was hot, washed with plenty of ethanol, and dried at 370 K in the oven for 2 days. Yields of

products: 7.00 g of Al-MCM-41 (Si/Al=39), 7.76 g of Al-MCM-41 (Si/Al=15), and 8.80 g of Al-MCM-41 (Si/Al=7).

For comparison, one batch of as-synthesized MCM-41 was also treated with ethanol/HCl as described above (designated as “pre-washed MCM-41”), and the yield was 6.10 g.

### **(2) Removal of the CTAC Template Using Conventional Calcination Method**

The as-synthesized MCM-41 and pre-washed Al-MCM-41 samples were calcined in a muffle furnace at 813 K as described by Ryoo et al.<sup>1,2</sup> The sample was placed evenly onto a crucible, and calcined in a programmed muffle furnace in airflow. The temperature was set to increase slowly from room temperature to 813 K over 10 hrs and then maintained at this temperature for 18 hrs. The yield of products were: 5.70 g of MCM-41 (theoretical yield is 5.65 g); 6.14 g of Al-MCM-41 (Si/Al=39, theoretical yield is 5.96 g); 6.82 g of Al-MCM-41 (Si/Al=15, theoretical yield is 6.77 g); and 7.44 g of Al-MCM-41 (Si/Al=7, theoretical yield is 7.38 g). Here, the real product yields are larger than the theoretical yields. This is due to the adsorption of water from the atmosphere by the void MCM-41 after calcination. The calcined samples were kept in a sealed glass sample container and stored in a desiccator.

### **(3) Removal of CTAC Template with Ozone at Room Temperature and at 423 K**

The CTAC templates in as-synthesized MCM-41 and pre-washed Al-MCM-41 samples were removed with ozone at room temperature (partially) and 423 K (completely), respectively. The reactor was a U-shape quartz glass tube with a porous screen plate inside one branch for holding the sample (Figure 2.2, the diameters labeled in the figure are inside diameters). About 200 mg of as-synthesized sample was loaded

onto the porous screen plate of the sample tube, into which ozone was introduced at a constant flow rate by setting the pressure of the oxygen cylinder at 4 pounds/inch<sup>3</sup>.

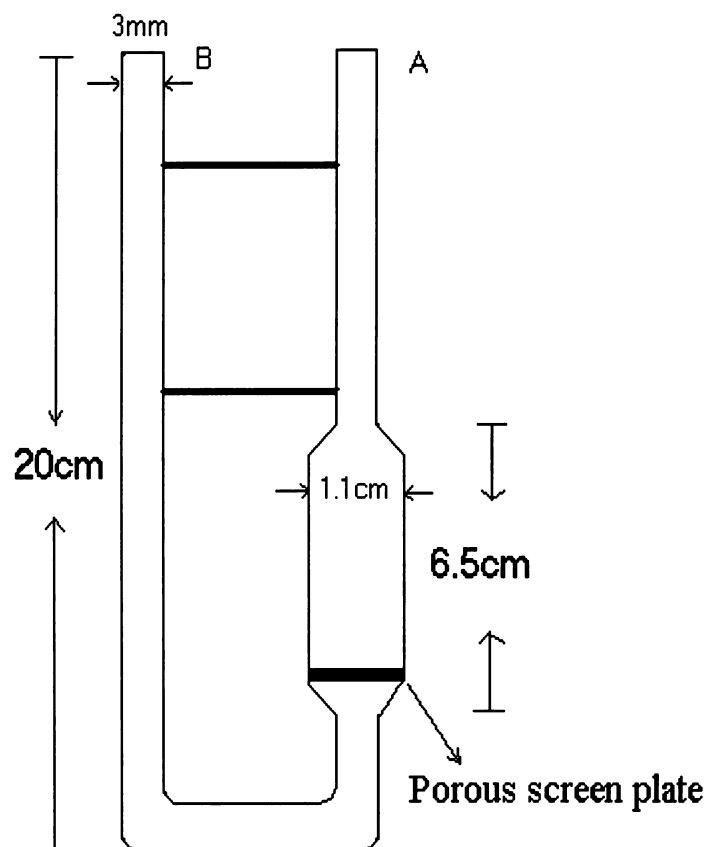


**Figure 2.2: A schematic drawing of the sample tube that was used to remove CTAC templates in the as-synthesized MCM-41 and Al-MCM41 samples by ozone treatment.**

The sample was reacted with ozone either at room temperature for 2 days or at 423 K by heating with electric furnace for one day. In the latter case, in order to avoid explosion, the temperature was slowly increased from room temperature to 423 K. The template removed samples were kept in a sealed glass sample container and stored in a desiccator.

#### **(4) Removal of CTAC Template by Combination of Ozone Treatment at Room Temperature and Thermal Calcination**

The CTAC templates in as-synthesized MCM-41 and pre-washed Al-MCM-41 samples were also removed by ozone treatment at room temperature first, and then calcined at 813 K in muffle furnace as described above.

##### **2.2.2. Post-Synthesis of Al-MCM-41 with Si/Al = 14**

Al can be introduced into MCM-41 framework by direct hydrothermal synthesis as described above, or by post-synthesis grafting methods. Al-MCM-41 with Si/Al as 14 was synthesized following Mokaya's procedures:<sup>8</sup>

The purely siliceous MCM-41, which was hydrothermally synthesized and thermally calcined at 813 K in muffle furnace as described above, was used as the starting material. Typically, purely siliceous MCM-41 (3.21 g) were dispersed in dry hexane (50 mL) and added into another dry hexane (150 mL) containing aluminium isopropoxide (0.770 g). Thus prepared Al grafting gel has a Si/Al ratio of 14. The mixture was sealed and stirred at room temperature for 2 days, after which time, the resulting mixture was filtered off, washed with dry hexane, and dried at room temperature in the dry box. The dried sample was then calcined in muffle furnace. The temperature of the muffle furnace was set to increase from room temperature to 813 K in 10 hrs, and then maintained at this temperature for 10 hrs. After calcination, white powder material (3.2 g) was obtained. The calcined material is just a pre Al-grafted sample and designated as PB-NH<sub>3</sub>. In order to increase the amount of grafted Al by transferring the octahedral Al into tetrahedral Al, this pre Al grafted sample was added into 320 mL 1M NH<sub>4</sub>OH at a

solution to solid ratio of 100 mL / g and stirred for 2 hrs at room temperature. The resulting solid material was filtered off, thoroughly washed with plenty of deionized water, and dried at 423 K in the oven over night. This “stir-wash-dry” cycle was repeated for four times in total. The yield of the product (designated as PA-NH<sub>3</sub>) was 3.16 g.

### 2.3. Organic Synthesis

Melting points were determined with a Melt-Temp (II) apparatus.

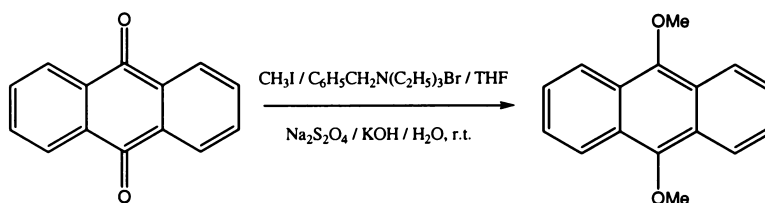
Solution <sup>1</sup>H-NMR spectra were measured on a Bruker AC300F (300MHz) spectrometer. <sup>1</sup>H-NMR data are reported as follows: Chemical shift (δ) measured in parts per million (PPM) down field from TMS, multiplicity, proton count and observed coupling constant (J) in Hertz (Hz). Multiplicity is reported as singlet (s), doublet (d), triplet (t), and multiplet (m).

Chromatography was performed using gravity columns packed with Merck silica gel 7724 60 (70-230 mesh). Thin layer preparative chromatography was performed on 1mm silica glass plates using Merck silica gel 7747 60PF<sub>254</sub>. Celite filter aid R70 was obtained from AJAX Chemicals, NSW, Australia. Light petroleum relates to the fraction of boiling point in the range of 333-353 K.

For a list of the commercially available reagents and chemicals that were used during the entire experiments and their purification, please see appendix 2. 1. All the other commercially available chemicals and reagents were used directly without further purification if there was no special notification. Appendix.2.2 lists the sources of chemicals that are commercially unavailable.

### 2.3.1. Synthesis of Some Electron Donor and Acceptor Molecules

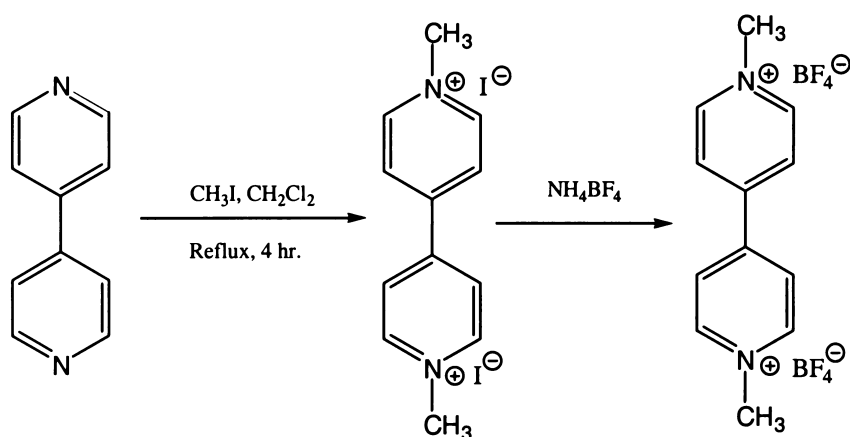
#### 2.3.1.1. Synthesis of 9,10-Dimethoxyanthracene<sup>9,10</sup>



To a solution of 9,10-anthraquinone (2g, 9.610 mmol) in anhydrous THF (40 mL) was added benzyltriethylammonium bromide phase transfer catalyst (350 mg, 1.286 mmol) in milli-Q water (2 mL). The solution was deoxygenated with argon for 20 min. and stirred for another 20 min. after which time a solution of sodium dithionite (9.2 g) in water (10 mL) was added. The mixture was stirred for 30 min and then a solution of potassium hydroxide (5.6 g, 0.1 mol) in water (5 mL) was added dropwise to the above mixture under an argon atmosphere. The color of the mixture turned dark red brown. After stirring for 20 min, iodomethane (10 mL, 0.161 mol) was added dropwise in an ice bath. The mixture was stirred for 20 min. and allowed to further react at room temperature for 16 hrs. The resulting mixture was then poured into iced water and extracted with diethyl ether (3 times). The combined ether extracts were dried over  $\text{MgSO}_4$  and filtered. The solvent of the filtrate was removed under reduced pressure to afford a yellow product which was recrystallized from ethanol twice to give light yellow needle-like crystals of 9,10-dimethoxyanthracene (1.43 g, 6.00 mmol, 62.30 %).

Melting point: 201-203 °C (lit.<sup>9</sup> 201-203 °C).

<sup>1</sup>H-NMR ( $\text{CDCl}_3$ ):  $\delta$  4.13 (s, 6H), 7.48-7.52 (m, 4H), 8.29-8.32 (m, 4H).

**2.3.1.2. Synthesis of Dimethyl Viologen Ditetrafluoroborate**<sup>11,12</sup>

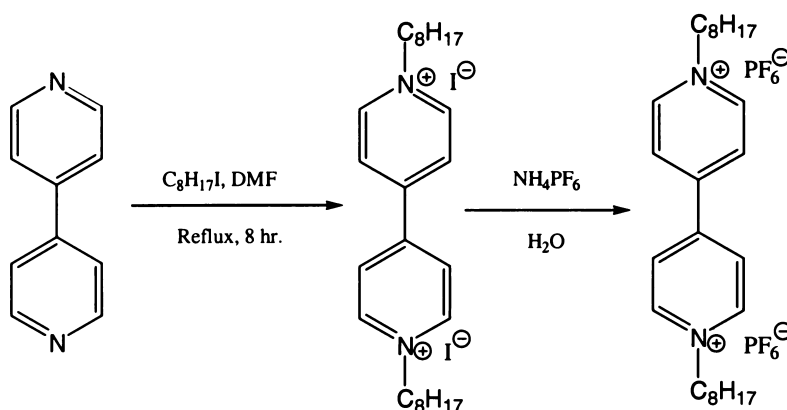
To a solution of 4,4-dipyridyl (0.78 g, 0.005 mol) in dry  $\text{CH}_2\text{Cl}_2$  (10 mL) in a 50 mL glass reactor was added iodomethane (2.84 g, 0.02 mol, excess amount). The reactor was sealed tightly and refluxed while magnetic stirring for 4 hrs. The resulting mixture was cooled to room temperature, filtered, and washed with acetone to give crude residues (3.5 g, 97 %). This crude product was dissolved in DMSO (20 mL) and added dropwise excess amount of  $\text{NH}_4\text{BF}_4$  (3.15 g, 0.03 mol) dissolved in water (10 mL). The mixture was stirred for 30min, filtered, washed with water and ethanol, and dried at room temperature under reduced pressure to afford white needle-like crystals (1.52 g, 84.44 %).

Melting point: 260-264 °C.

$^1\text{H}$ -NMR (acetone- $\text{d}_6$ ):  $\delta$  4.76-4.80 (s, 6H), 8.72-8.79 (m, 4H), 9.32-9.37 (m, 4H).

### 2.3.1.3. Synthesis of 1,1'-Dioctyl-4,4'-Bipyridinium Dihexafluorophosphate (DOV)

13,14



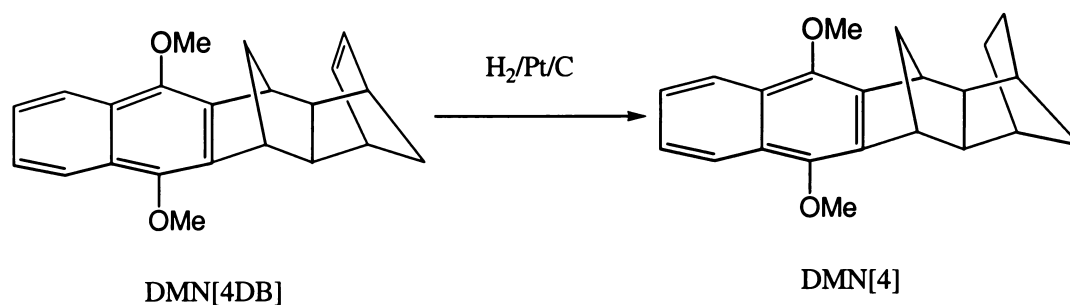
4,4'-dipyridyl (1.56 g, 0.01 mol) was dissolved in freshly distilled DMF (10 mL) in a 50 mL glass reactor and stirred for 10 min. To the mixture was added 1-iodooctane (7.2 g, 0.03 mol, excess amount). The reactor was sealed tightly and refluxed while magnetic stirring for 8 hrs. The resulting mixture was cooled to room temperature, filtered, and washed with acetone. Thus red crystals of 1,1'-dioctyl-4,4'-bipyridinium diiodide (3.64 g) were obtained. The iodide product is not stable at the ambient atmosphere and needs to be further transformed into the stable forms. The product was dissolved in DMSO (20mL) and an excess amount of  $NH_4PF_6$  (4.9 g, 0.03 mol) in water was added dropwise. The colour of the solution gradually turned yellow. The mixture was stirred for 30min., filtered, washed with water and ethanol, and dried at room temperature under reduced pressure to give the final yellow powder product of 1,1'-dioctyl-4,4'-bipyridinium dihexafluorophosphate (5.6 g, 83.26 %).

Melting point: > 300 °C.

$^1H$ -NMR (acetone- $d_6$ ):  $\delta$  0.96 (t, 6H), 1.36-1.42 (m, 24H), 4.76-4.80 (t, 4H), 8.85-8.87 (d, 4H), 9.46-9.48 (d, 4H). These data are comparable with the literature spectrum.<sup>14</sup>



#### 2.3.1.4. Synthesis of 6,11-dimethoxy-1,2,3,4,5,12-hexahydro-1,4-methano-5,12-methano-tetracene(DMN[4])<sup>15,16</sup>



The starting material DMN[4DB] (provided by Dr. Nigel Lokan, School of Chemistry, UNSW, Sydney, Australia) was hydrogenated to the DMN[4] according to the following procedures:

To a solution of DMN[4DB] (1.59 g, 5.03 mmol) in ethyl acetate (50mL) in 100 mL flask was added palladium on activated carbon (catalyst, 0.3 g, 10 %) and hydrogenated at atmosphere pressure for 3 days. The resulting product was filtered through Celite and evaporated the solvent off under reduced pressure to afford a light yellow solid residue which was recrystallized from ethanol to give DMN[4] product in good yield (1.44 g, 90 %).

Melting point: 136-139 °C (lit.: 139-140 °C).<sup>15</sup>

<sup>1</sup>H-NMR (CDCl<sub>3</sub>) of DMN[4]:  $\delta$  1.35-1.69 (br m, 7H), 2.01 (s, 2H), 2.18 (d, J = 10.4 Hz, 1H), 2.41 (br s, 2H), 3.58 (br s, 2H), 3.98 (s, 6H), 7.40-7.44 (m, 2H), 8.03-8.07 (m, 2H). This is in good agreement with the literature data:<sup>15</sup>  $\delta$  1.37-1.70 (br m, 7H), 2.01 (s, 2H), 2.18 (d, J = 10.4 Hz, 1H), 2.41 (br s, 2H), 3.58 (br s, 2H), 3.98 (s, 6H, 2  $\times$  OCH<sub>3</sub>), 7.41-7.44 (m, 2H), 8.03-8.07 (m, 2H).

### 2.3.2. Generation of Radical Cations in Solution

In order to compare and identify the radical cation species formed in the mesoporous Al-MCM-41 materials, the corresponding radical cations of the electron donor molecules were also generated in solution. A variety of methods<sup>17</sup> are available to generate radical cations in solutions. The most widely used methods for generation of radical cations are: (1) with protic acids; (2) with Lewis acids; (3) with oxidizing metal ions; (4) with  $\pi$ -conjugated electron acceptors; (5) with aminium radical cations; (6) protonation of a neutral radical; (7) Electrolysis. Here, the radical cations of electron donor compounds were generated with either the  $\text{AlCl}_3/\text{CH}_3\text{NO}_2$  Lewis acid method (suitable for the substrates with ionization energies less than 8 eV)<sup>18</sup> or  $\text{CF}_3\text{COOH}/\text{CH}_2\text{Cl}_2/\text{DDQ}$   $\pi$ -conjugated electron acceptor method.<sup>19,20</sup>

For the  $\text{CF}_3\text{COOH}/\text{CH}_2\text{Cl}_2/\text{DDQ}$  method, the sample was dissolved in a 9:1 (volume ratio) solution of dry  $\text{CH}_2\text{Cl}_2$  and  $\text{CF}_3\text{COOH}$ . Then 1 to 1.5 equivalent of 2,3-dichloro-5,6-dicyano-benzoquinone (DDQ) was added. The color of the solution immediately became dark, indicating the formation of radical cations. The radical cations generated in this way are usually long-lived and relatively easy to observe by routine EPR technique, since the protonation of the DDQ radical anion to give the neutral radical overcomes the reversibility of the electron transfer.

## 2.4. Molecular Assembly in (Al)-MCM-41

Molecular assembly of the guest molecules (the electron donor, acceptor, or donor-bridge-acceptor molecules) into (Al)-MCM-41 (purely siliceous MCM-41 and Al-MCM-41) mesoporous hosts were carried out in the dry box atmosphere and vacuum atmosphere, respectively.

#### **2.4.1. Molecular Assembly of Guest Molecules into (Al)-MCM-41 Hosts in a Dry Box Atmosphere (Method A1 and Method A2)**

The templateless (Al)-MCM-41 sample was loaded into a vacuum cell and degassed at certain temperature under a pressure of  $\sim 10^{-7}$  Mbar for overnight. In order to avoid the sample flushing into the vacuum line and damaging the diffusion pump, quartz glass wool was filled at the neck of the vacuum cell (diameter is 4 cm and length is 25 cm) that was jointed to the vacuum line. If the required dehydrating temperature was over 373 K, the heating temperature was controlled to increase slowly. Then the degassed vacuum cell was detached from the vacuum line and quickly transferred into a nitrogen purged dry box. In order to drive off the air which entered when opening the dry box, the vacuum cell containing the sample was left in the dry box without opening at least for 1 hr, after which time a given amount of the dehydrated (Al)-MCM-41 sample was weighed quickly in a sample container using the balance inside the dry box and sealed immediately. In the meantime, a certain amount of guest compound (donor, acceptor, or D-B-A molecules) was exactly weighed and dissolved in an appropriate solvent, which was outgassed by passing argon. The solution thus prepared was added into the (Al)-MCM-41 sample container and mixed well by shaking. The resulting mixture was either directly transferred into a normal quartz EPR cell to measure the EPR spectrum (**method A1**), or left inside the dry box to evaporate the solvent off, followed by transferring into a normal quartz EPR cell (**method A2**) for EPR measurement. In Method A1, the EPR tube contains both solid and liquid phases. The solid phase is the (Al)-MCM-41 immersed in a solution of the probing molecules (donor, acceptor, or donor-bridge-acceptor dyad), while the liquid phase is the solution of the probing molecules. EPR measurements were done for these two phases separately by adjusting

the corresponding phase in the center of the EPR cavity ( $\sim 3$  cm height). **Method A2** was also applied to the sample preparations for IR and DR-UV-Vis measurements.

#### 2.4.2. Molecular Assembly of Guest Molecules into (Al)-MCM-41 in a Rigorously Oxygen Free Atmosphere (Method B1 and Method B2)

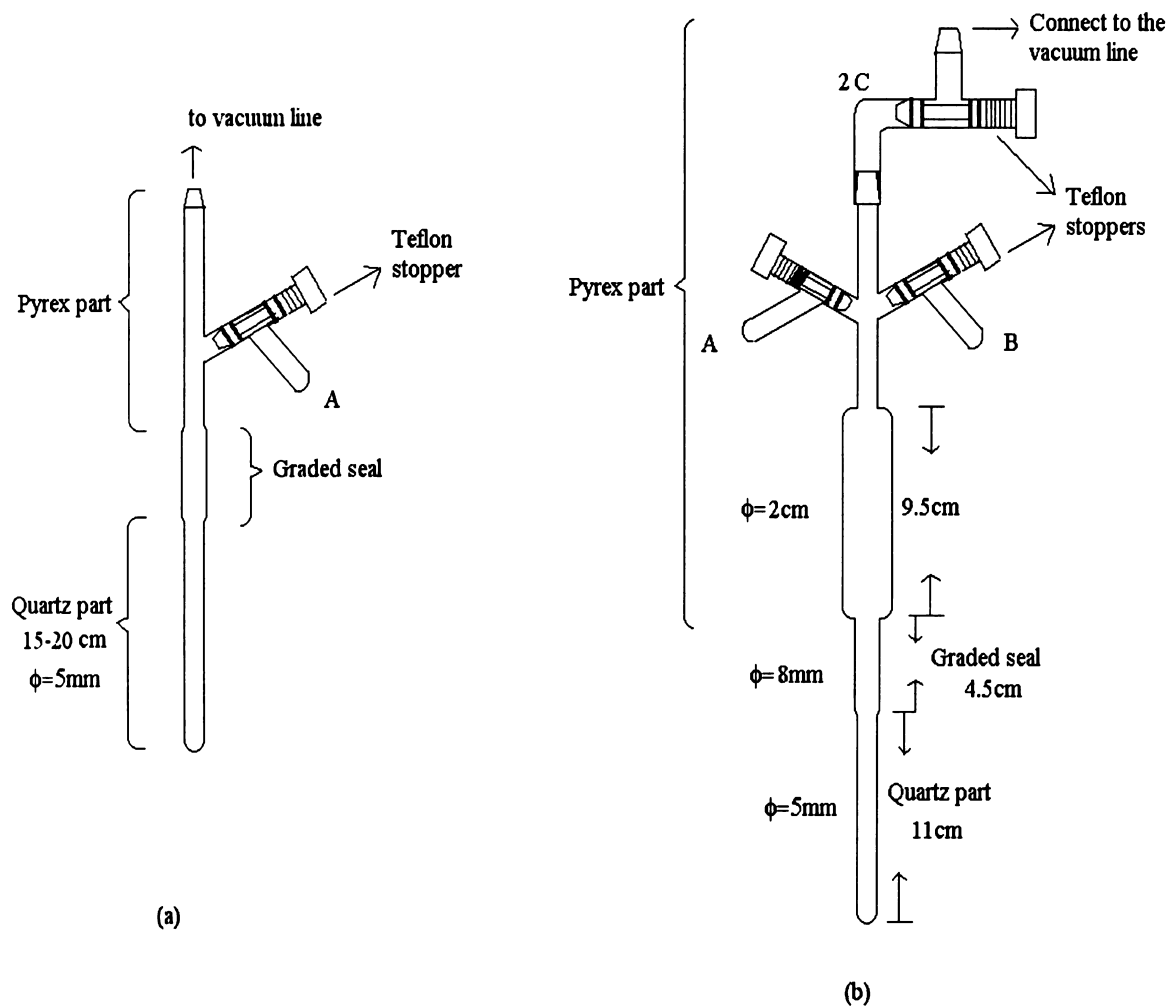


**Figure 2.3: Schematic drawings of the EPR cells. Figure (a) shows the EPR cell used in method B1 and Figure (b) shows the EPR cell used in method B2. Tube A and tube B are for the guest compounds; 2C- two vacuum joints (only one is shown).**

In the dry box atmosphere, although the flowing nitrogen can drive off the air inside the dry box, there is no guarantee that it is an absolutely oxygen-free atmosphere. To

exclude the affect of oxygen, instead of handling samples in the dry box, two kinds of alternative methods were employed to load samples into (Al)-MCM-41 hosts under vacuum conditions, i.e., “sealing” (**method B1**) and “double stoppering” methods (**method B2**).

The “Sealing method” was mainly used for TCNE that can be sublimated at relatively low temperature under a reduced pressure during EPR experiments. Solid TCNE and (Al)-MCM-41 samples were loaded into part A and the quartz part of the EPR cell, respectively (Figure 2.3 (a)). Both TCNE and (Al)-MCM-41 were degassed for 1 hr at room temperature first, then only the (Al)-MCM-41 sample was further degassed at 423 K overnight. The cell was cooled to room temperature, detached from the vacuum line, and the TCNE was transferred into the quartz part. The mixture of TCNE and (Al)-MCM-41 was then degassed for 1 hr in the vacuum line and sealed off from the vacuum line at the quartz part. The sealed off quartz part was heated at 383 K which caused the sublimation of TCNE into the MCM-41 mesopores.

“Double stoppering” method was used for all of the samples. Typically, the “guest compound” (dissolved in an argon degassed solution) and (Al)-MCM-41 sample were loaded into the tube A (or B) and the quartz tube of the EPR cell (**b**) (Figure 2.3), respectively. The sample-loaded EPR cell was attached to the vacuum line, and only the (Al)-MCM-41 sample was degassed for at least 1 hr. The solution of the guest compound was frozen using liquid nitrogen cold trap and degassed for ca. 30 min, after which time it was stoppered from the vacuum line and thawed. This “freeze-pump-thaw” procedure was repeated three times in order to remove the oxygen. The (Al)-MCM-41 sample was connected to the vacuum line and dehydrated at a certain temperature overnight. The EPR cell was then cooled to the room temperature,

stoppered tightly and detached from the vacuum line. Finally, the solution of the guest compound was poured into quartz part and mixed with the (Al)-MCM-41 sample.

## 2.5. Characterization Methods

### 2.5.1. Powder X-ray Diffraction (XRD)

**Table 2.1: Information contained in a powder X-ray diffraction pattern.**

Feature	Information
Peak positions ( $2\theta$ values)	Unit cell dimensions
Non-indexable lines	Presence of a crystalline impurity (or incorrect indexing)
Systematically absent reflections	Symmetry
Background	Presence (or absence) of amorphous material
Width of peaks	Crystalline (domain) size Stress/strain Stacking faults
Peak intensities	Crystal structure

Power X-ray diffraction was applied to determine the textural uniformity of hexagonal mesoporous MCM-41 materials.

The powder X-ray diffraction was performed on a Siemens D-500 X-ray powder diffractometer equipped with Ni-filtered Cu-K $\alpha$  radiation source (8978 eV or  $\lambda = 1.5418 \text{ \AA}$ ). The diffractometer was interfaced to a PC computer, and manipulated using Sietronic SIE 122D operating software. An accelerating voltage of 40 kV and a current of 30 mA were used for the X-ray set-up. The sample preparation for the XRD analysis involved gently grinding the solid sample into a fine powder with the aid of a mortar and a pestle, and packing of approximately 100-200 mg of sample into an Al sample holder with light compression to produce a flat sample surface. The high-resolution

XRD patterns were recorded for  $2\theta$  value over the range of  $0.8^\circ$  to  $10^\circ$  with a step size of  $0.02^\circ$  and a scanning rate of  $1^\circ$  / minute for all samples.

Powder X-ray Diffraction data are commonly used as a structure “fingerprint” in the identification of an unknown material.<sup>21</sup> The possible information contained in a powder X-ray diffraction pattern is summarized in Table 2.1. Among these features, the peak positions, peak intensities, and peak width are most important characteristics for identification and characterization of porous materials.

(1) Peak positions: If the pattern is to be indexed (i.e., Miller indices  $hkl$  are assigned to each of the peaks and thereby the unit cell dimensions extracted from the pattern), it is essential that the peak positions be determined accurately. The sharper a peak, the better its  $2\theta$  value can be determined. Usually, the instrument’s  $2\theta$  scale is calibrated using standard material such as the NIST silicon standard 640b, and the diffractometer is also adjusted to give a full width at half maximum (FWHM) for the Si (111) reflection ( $28.44^\circ$   $2\theta$  with Cu-K $\alpha$  radiation) of  $0.10^\circ$   $2\theta$  or less. The peak position information is often given in terms of  $d$ -space rather than  $2\theta$  values, because  $d$ -space values are independent to the X-ray wavelength ( $\lambda$ ) used. The relationship between  $d$ -space and  $2\theta$  values is expressed by the Bragg equation:

$$d = \lambda / 2 \sin \theta$$

To identify an unknown material or monitor the effects of a synthesis treatment, it is necessary to compare the measured pattern with an existing one, whether it is a pattern in the “Collection of simulated XRD powder patterns for zeolites”,<sup>22</sup> the powder diffraction file (PDF) of the ICDD,<sup>23</sup> or an in-house data file.

(2) Peak intensities: The peak intensities are irrelevant for indexing purposes. But for identification or structure analysis, accurate relative intensities are essential. The low-angle lines are most strongly affected by non-framework species and are more intense

in the calcined material than in as-synthesized form, and similar materials containing different cations or different organic species may have quite different relative intensities at low angles. However, the intensities of the higher angle reflections are generally dominated by the positions of the framework atoms. Three commonly ignored factors can severely affect the relative peak intensities, i.e., sample thickness, preferred orientation, and the divergence slits.

In order to keep the volume of effectively irradiated sample remains constant as  $2\theta$  changes, Bragg-Brentano reflection geometries require an “infinitely thick sample”. That is, it is assumed that the sample is thick enough that all of the X-rays interact with the sample (by absorption or diffraction) before they reach the sample holder. If this “infinite thickness” criterion is not met, the relative intensities of the low-angle reflections will be too large.

Powder diffraction data analyses assume that the sample consists of millions of randomly orientated crystallites. If this is not the case, relative intensities will be distorted.

At low angles, the X-ray beam is spread over a larger surface of the sample than it is at high angles. To ensure that the X-rays interact only with the sample (and not the edges of the sample holder), a slit is insert between the X-ray source and the sample to confine the beam to the sample (divergence slit). As the  $2\theta$  angle increases, this slit can be opened wider to allow more X-rays through and thereby increase the counting rate.

(3) Peak widths: Peak widths are usually influenced by instrument resolution, lattice strain/ stress, particle domain size, and stacking faults.



### 2.5.2. Infrared (IR) Spectroscopy

Infrared (IR) spectroscopy is one of the most useful techniques to study adsorbed species in porous materials.<sup>24,25</sup> The routine KBr pellet technique is used for investigations on the vibrations of the framework, the template removal, and the assembled organic compounds in (Al)-MCM-41 hosts, while *in-situ* IR measurements were used to determine the thermal stability of the (Al)-MCM-41 samples against dehydration (or dehydroxylation).

#### 2.5.2.1. Routine Fourier Transform Infrared (FT-IR) Spectroscopy

Routine FT-IR spectroscopic analyses were carried out on an ATI MATTSON Genesis Series Fourier Transform Infrared spectrometer. The samples for FT-IR analysis were prepared by mixing the sample with dried KBr (spectroscopic grade) powder in the ratio of around 1:10 and grinding into fine powder in a mortar. The resulting ground powder was compressed in a stainless steel mould into a thin disk at a pressure of 1.5 Kpa. The background was run first with an empty mould. The absorption spectra of the background and the samples were recorded directly in the ambient atmosphere in the scanning range of 500-4000  $\text{cm}^{-1}$  with the parameter settings as follows: 4  $\text{cm}^{-1}$  of resolution, 20 scans of the background and 100 scans of the samples. All of the data were recorded with a WIN-FIRST software and manipulated with Grams software (distributed by Galactic Industries Corp.).

### 2.5.2.2. *In-situ* Infrared (IR) Spectroscopy

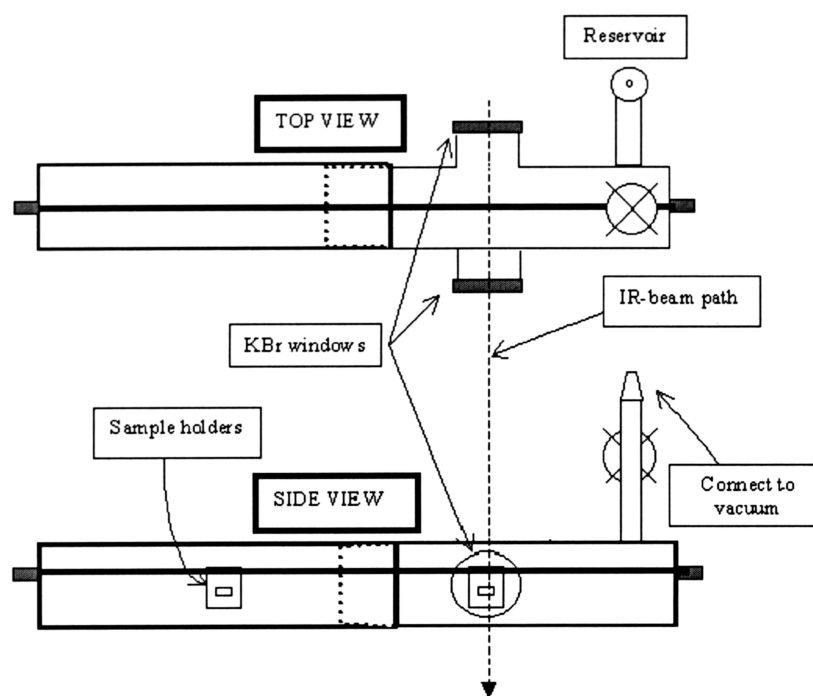


Figure 2.4. Schematic diagram of the *in-situ* cell from top view and side view.

The *in-situ* IR measurements were carried on a BOMEM MB-100 Series IR spectrometer equipped with a mercury cadmium telluride (MCT) detector. At certain intervals, liquid nitrogen was filled up to keep the instrument at constant 77 K. The IR spectra were recorded in the range of  $500\text{--}4000\text{ cm}^{-1}$  with a resolution of  $4\text{ cm}^{-1}$ . To obtain a better signal to noise ratio, 1000 scans were employed. A thin wafer of the sample with a size of around  $0.8 \times 1.2\text{ cm}$  and weight of about 8–15 mg was prepared by compressing the powder sample in a stainless steel die with a diameter of 4 cm at a pressure of 1.5 Kpa. The resulting continuous wafer was placed in a stainless steel sample holder, which was then introduced into the *in-situ* cell. The special *in-situ* cell was equipped with two NaBr windows exactly face-to-face as shown in Figure 2.4. The reference background was run first without sample in the beam line position. The *in-situ* cell containing the sample wafer was evacuated to  $10^{-6}$  Mbar for one hour at various

temperature stages (room temperature, 373 K, 473 K, 573 K and 673 K, 773 K) and then the IR spectra were measured.

### **2.5.3. Solid State Nuclear Magnetic Resonance (NMR) Spectroscopy**

During recent years, the solid-state NMR technique has been dramatically improved to be one of powerful tools for studies on solid materials with respect to structure elucidation, catalytic behavior and mobility properties.<sup>26</sup> Solid-state NMR can be regarded as a complementary technique to XRD, since both crystalline and amorphous powdered materials can be investigated. While XRD provides information about the long-range ordering and periodicities, solid state NMR allows investigations on the short-range ordering (local environment) and structure geometries.<sup>27</sup>

Solid state NMR is more complicated than liquid NMR. Distinct nuclear spin interactions such as chemical shift anisotropy, dipolar and quadrupolar interactions, which lead to excessive line broadening, are averaged in liquids owing to fast thermal and molecular motions of molecules, but are operative in the rigid lattice of solids (the molecules are less mobile). As a consequence, the fine structure is lost since broad lines are obtained, hiding the essential information of analytical character. In addition, long spin-lattice relaxation times, due to the lack of translation and rotation motions in solids, control the entire NMR experiment recording times. Several techniques have been developed to average these interactions and phenomena to zero, or reduce them to the isotropic values, allowing the recording of high-resolution NMR spectra of solids. These techniques and their relations to the mentioned interactions and phenomena are shown in Table 2.2.

During magic angle spinning (MAS), the sample is placed in a rotor, and spin at high speed at an angle of  $\theta = 54^\circ 44'$  to the axis of the external applied magnetic field. Chemical shift anisotropy, dipolar and first order quadrupolar interactions have a dependence on the second-order Legendre polynomial,  $3 \cos^2 \theta - 1$ , where  $\theta$  describes the orientation with respect to the magnetic field. This expression becomes equal to zero if  $\theta$  is chosen to be  $54^\circ 44'$  (the “magic angle”), which means that the above three interactions are averaged to zero or reduced to the isotropic values, resulting in dramatically increased resolutions.

**Table 2.2: Techniques used to improve the resolution of solid state NMR**

Techniques	Interactions or phenomena involved
Dipolar decoupling (DD)	Heteronuclear dipolar interactions
Multiple pulse sequences (MPS)	Homonuclear dipolar interactions
Magic angle spinning (MAS)	Chemical shift anisotropy, dipolar and First order quadrupolar interactions
Dynamic angle spinning (DAS) or Double orientation rotation (DOR)	Second order quadrupolar interactions
Cross-polarization (CP)	Long spin-lattice relaxation times

Cross-polarization (CP) is used to improve the signal to noise ratios by transferring a magnetization (or polarization) from an abundant species (usually  $^1\text{H}$ ) to a dilute species (such as  $^{13}\text{C}$ ,  $^{29}\text{Si}$ , and  $^{31}\text{P}$ ), which is under observation. The benefits of the CP are primarily an intensity enhancement of the dilute spin signal and a reduction in the recycling time between experiments, since the rate-determining relaxation time is now that of the abundant species, whose relaxation time is usually much faster. The spinning speed of a rotor during MAS experiments should be at least in the range of the linewidth of the signal recorded under static conditions, otherwise the main resonance line will be accompanied by a series of spinning side.

In order to obtain optimum line narrowing and improved sensitivity in a solid state NMR spectrum, in practice, these experimental techniques are sometimes used in combination, for example, CP-MAS.

**$^{29}\text{Si}$ -MAS-NMR** was used to study the condensation of Si-O in (Al)-MCM-41 materials. The most important application of  $^{29}\text{Si}$ -MAS-NMR is due to the relationship between its chemical shift sensitivity and the degree of condensation of the Si-O tetrahedra, i.e.,  $^{29}\text{Si}$  ( $n\text{Al}$ ) with  $n = 0, 1, 2, 3$ , or 4 (chemical shift range: -80 to -115 ppm, with the high field signal for Si (0Al), where  $n$  indicates the number of Al atoms sharing oxygen with the  $\text{SiO}_4$  tetrahedron (differences in chemical shifts between Si ( $n\text{Al}$ ) and Si ( $n + 1 \text{ Al}$ ) are ~5-6 ppm). The Si/Al ratio may be calculated from the peak areas of the five peaks in the  $^{29}\text{Si}$ -MAS-NMR spectrum according to the following equation: <sup>28</sup>

$$\frac{\text{Si}}{\text{Al}} = \frac{\sum_{n=0}^4 I_{\text{Si}(n\text{Al})}}{\sum_{n=0}^4 0.25 n [I_{\text{Si}(n\text{Al})}]}$$

where  $I$  is the corresponding peak areas.

The different coordination species in purely siliceous MCM-41, i.e.,  $\text{Q}^4$  [ $\text{Si}-(\text{OSi})_4$ , -110 ppm],  $\text{Q}^3$  [ $(\text{HO})\text{Si}-(\text{OSi})_3$ , -100 ppm],  $\text{Q}^2$  [ $(\text{HO})_2\text{Si}-(\text{OSi})_2$ , -90 ppm] were also distinguished with  $^{29}\text{Si}$ -MAS-NMR.

**$^{27}\text{Al}$ -MAS-NMR** was used to study the Al coordination (tetrahedrally coordinated Al at ~40-65 ppm and octahedrally coordinated Al at ~ 0 ppm) in the synthesized Al-MCM-41 framework. The extra-framework Al content (%) in the Al-MCM-41 sample was determined by comparing the integrated octahedral Al peak area and the sum of the integrated octahedral and tetrahedral Al peak areas in the  $^{27}\text{Al}$ -MAS-NMR:

$$\text{Extra-framework Al content (\%)} = \frac{\text{Octahedral Al peak area}}{\text{Tetrahedral Al peak area} + \text{Octahedral Al peak area}}$$

**<sup>13</sup>C-CP/MAS-NMR** was used to study the template removal in (Al)-MCM-41 samples and to prove the evidence whether the guest molecules are inside the (Al)-MCM-41 samples.

All of <sup>29</sup>Si, <sup>27</sup>Al and <sup>13</sup>C-MAS-NMR spectra were recorded on a Bruker MSL-300 NMR spectrometer operating at a magnetic field strength of 7.2 Tesla, and the corresponding operating parameters used for recording the high-power proton decoupling (HPDEC) <sup>29</sup>Si MAS-NMR, <sup>27</sup>Al-MAS-NMR and <sup>13</sup>C-CP/MAS-NMR spectra are summarized in Table 2.3.

**Table 2.3: Operating parameters used for recording <sup>29</sup>Si, <sup>27</sup>Al and <sup>13</sup>C-MAS-NMR spectra.**

Operating parameters	<sup>29</sup> Si-NMR	<sup>27</sup> Al-NMR	<sup>13</sup> C-NMR
Nuclei resonance frequency (MHz)	59.61	78.19	75.47
MAS frequency (KHz)	2.5	10	3.0
Reference standard (ppm)	Kaolin (-91.5 )	Kaolin (-2.5 )	Adamantane (38.7)
Rotor diameter (mm)	7	4	4
Spinning rate (kHz)	4.0	10	4.0
Pulse delay time (μsec)	5	2	5
Pulse width (μsec)	1.500	0.600	1.000

**\* The chemical shift reference was set with Kaolin as a secondary reference with respect to aluminum trichloride hexahydrate.**

#### **2.5.4. Inductively Coupled Plasma Atomic Emission Spectroscopy (ICP-AES)**

Elemental compositions of the Al-MCM-41 samples were determined using inductively coupled plasma atomic emission spectroscopy (ICP-AES), which was

performed on a GBC Integral XMP ICP-AES instrument. The samples were prepared according to the following procedures:

Zeolite acid reagent (Z-A) was prepared by mixing together 50 mL of 32% hydrochloric acid and 200 mL of 50% hydrofluoric acid. The spectrasol silicate dissolution HF neutralizing reagent (Z-B) was purchased from spectrasol, INC. McAfee, N.J. USA and used without further purification. An Exact amount of MCM-41 sample (around 50 mg) was weighed in a polypropylene bottle and then 0.5 mL of deionized-distilled water together with 0.25 mL of concentrated nitric acid was added. 3.75 mL of Z-A was measured in a plastic graduated cylinder and added into the above mixture. The polypropylene bottle was closed tightly and heated in the oven at 368 K for at least 1/2 hr. The resulting mixture was then transferred into a pre-tared 250 mL polyethylene bottle. 18.5 mL of Z-B was measured in a graduated plastic cylinder and added dropwise to the above mixture. The weight of the final solution was brought to 25 g by adding deionized-distilled water. The resulting clear solution was injected into the ICP spectrometer for the elemental composition analysis.

### **Notes**

- 1) The standard used to correct parameters was ZSM-5 ( $\text{SiO}_2/\text{Al}_2\text{O}_3=56$ ). The blank sample was also prepared and measured for subtraction.
- 2) All blanks and standards were prepared with the same volumes of Z-A and Z-B as used for the samples to matrix match standards and samples.
- 3) During ICP analysis, glass concentric neutralizers, glass spray chambers and glass torches can be used.
- 4) Heat of neutralization is generated when Z-B is added to the acid digested sample. So it was operated under a fume hood.

- 5) Upon shaking, air bubbles were entrained in the solution. It was shaken vigorously for a few seconds to remove the entrained air.

The Si/Al ratios of the Al-MCM-41 (39, 15, and 7) samples were calculated from the following equations using the ICP experimental results.

$$K = 28 / [(Si_S - Si_B) / (Al_S - Al_B)]$$

$$N_i = K \times [(Si_{Sa} - Si_B) / (Al_{Sa} - Al_B)]$$

Where K is the ratio factor obtained from the standard sample; 28 is the real Si/Al ratio of the standard ZSM-5 sample;  $Si_S$  is the Si content in the standard;  $Si_B$  is the Si content in the blank sample;  $Al_S$  is the Al content in the standard sample;  $Al_B$  is the Al content in the blank sample;  $Si_{Sa}$  is the Si content in the Al-MCM-41 sample;  $Al_{Sa}$  is the Al content in the sample;  $N_i$  is the calculated Si/Al ratio of the Al-MCM-41 sample. Due to the variations of the Si and Al contents in the blank samples, the direct result of Si/Al ratio of sample  $[(Si_{Sa} - Si_B) / (Al_{Sa} - Al_B)]$  is not equal to the real Si/Al ratio ( $N_i$ ). The known Si/Al ratio standard ZSM-5 was used to normalize this difference.

### 2.5.5. Surface Area Measurements

Surface area is one of the most important parameters for evaluating the catalytic activities of molecular sieves. From surface area measurement, lots of useful information can be obtained, including not only surface area, but also pore volume, average pore size and pore size distribution.

All of the surface area data were determined by nitrogen adsorption-desorption measurement on a Micromeritics ASAP 2000 V2.02 instrument. The sample (ca. 100 mg) was degassed in a pre-weighed glass flask on the manifold at 473 K under a pressure of  $<10^{-5}$  Mbar over-night, after which time the sample was cooled to 77 K with liquid nitrogen. Then the sample was exposed to a known amount of nitrogen gas. At



this stage, the pressure drop was observed, indicating that the nitrogen gas was being adsorbed by the sample. After the system reached a constant higher pressure, another known amount of nitrogen gas was introduced. This procedure, i.e., adsorption of the nitrogen gas by the sample followed by increasing the pressure, was performed several times until the relative pressure ( $P/P_0$ ) reached ca. 0.99. The nitrogen adsorption isotherm can be obtained by plotting the adsorbed nitrogen volume (Y-axis) against the corresponding relative pressure (X-axis). The reverse experiment, i.e., evacuating the sample to a relative lower pressure for nitrogen desorption from the sample, was carried out which enabled a plot of the nitrogen desorption isotherm to be determined. Finally, the sample was detached from the manifold, and the dead spaces of the sample flask were determined using helium.

**Calculation of surface area:** The specific surface area was determined by the Brunauer-Emmet-Teller (BET) method.<sup>29</sup> The BET equation is usually used in the multilayer-adsorption region of the adsorption isotherm:

$$\frac{P}{V_a(P_0 - P)} = \frac{1}{V_m C} + \frac{(C-1)P}{V_m C P_0}$$

where  $V_a$  is the number of moles adsorbed per gram adsorbent at gas pressure  $P$ ,  $V_m$  is the monolayer capacity of the surface (the number of moles of gas per gram of adsorbent, required to form a monolayer),  $P_0$  is the saturation pressure, and  $C$  is the BET constant, which is a function of the heat of adsorption.

Mathematical treatment of the nitrogen adsorption points in the  $P/P_0$  region 0.05-0.35 with the BET equation can give the two unknowns  $C$  and  $V_m$ . Then the specific surface area ( $S_{\text{BET}}$ ) of the sample can be easily calculated according to the following equation:

$$S_{\text{BET}} = V_m \cdot a_m \cdot N_A \cdot 10^{-20} \text{ (m}^2 \text{ / g)}$$

where  $N_A$  is the Avogadro number ( $6.02 \times 10^{23}$  molecules / mol),  $a_m$  is the molecular cross sectional area of the gas molecule, which is commonly assumed to be about  $0.162 \text{ nm}^2$  for nitrogen on an oxide surface,<sup>30</sup> and  $S_{\text{BET}}$  is the calculated surface area.

**Calculation of average pore diameter:** Assuming that the external surface of the sample is negligible, and that the pores are cylindrically shaped, the average pore diameter of a substrate can be calculated by the Wheeler formula:<sup>31</sup>

$$d_p = 4 \times 10^3 (V_p / S_{\text{BET}}) \text{ (nm)}$$

where  $V_p$  is the volume (mL / g) of adsorbate, which can be calculated from the volume of adsorbed nitrogen ( $V_a$ ) by means of the Gurvitsch rule:<sup>32</sup>

$$V_p = 1.54 \times 10^{-3} V_a \text{ (mL / g)}$$

**Calculation of pore size distribution:** The relationship between the core radius of the liquid adsorbate ( $r_k$ ) and the relative pressure is:

$$\ln \frac{P}{P_0} = \frac{-2 \gamma V_l \cos(\theta)}{RT} \cdot \frac{1}{r_k}$$

where  $\gamma$  is the surface tension of liquid nitrogen at 77 K ( $8.85 \times 10^{-3} \text{ N/m}$ );  $\theta$  is the contact angle, which is assumed to be 0;  $V_l$  is the molar volume of liquid nitrogen at 77 K ( $34.65 \times 10^{-3} \text{ L / mol}$ ); and  $r_k$  is the Kelvin radius (nm).

Thus, for liquid nitrogen at 77 K, this equation becomes:

$$r_k = \frac{-0.415}{\log \frac{P}{P_0}}$$

Here, the Kelvin radius ( $r_k$ ) is not equal to the actual pore radius ( $r_p$ ) due to the pore narrowing caused by the multilayer adsorption prior to the capillary condensation. The real  $r_p$  should also include the thickness of the adsorbed layers ( $t$ ), i.e.:  $r_p = r_k + t$ . The  $t$  value can be calculated using the following Halsey equation:<sup>33</sup>

$$t = m \left[ \frac{n}{\ln (P/P_0)} \right]^x$$

where  $x$  is the Halsey exponent (1/3 for nitrogen at 77 K);  $m$  is the monolayer thickness (0.354 for nitrogen at 77 K); and  $n$  is the Halsey constant ( -5.0 for nitrogen at 77 K).

The pore size distributions of (Al)-MCM-41 materials have been calculated by computational method based on Barrett-Joyner-Halenda model (BJH model) <sup>34</sup> using desorption branches of the isotherms. BJH model depends on two fundamental assumptions: (1) the pores are cylindrical, and (2) the amount of adsorbate in equilibrium with the gas phase is retained by the adsorbent by two mechanisms, i.e., physical adsorption on the pore walls and capillary condensation in the inner capillary volume. Both phenomena are related to the relative pressure, by means of the Kelvin and the Halsey equations. Under these two assumptions, the following practical basic equations for the computation of pore volume distributions from desorption isotherms with respect to pore radii can be obtained:

$$V_{pn} = R_n \Delta V_n - R_n \Delta t_n \sum_{j=1}^{n-1} c_j A_{pj}$$

where  $c$  is a constant, which is equal to  $(r_p - t_r)/r_p$  ( $t_r$  is the thickness of the physically adsorbed layer at the corresponding relative pressure value of  $P/P_0$ ,  $r_p$  is the average pore radius); at each steps of the relative pressure of  $P/P_0$  lowered to a smaller value,  $cA_p$  represents the average area from which the physically adsorbed nitrogen gas is desorbed,  $\Delta V$  represents the observed volume of gas desorbed,  $\Delta t_n$  is the amount of thickness reduction of the physically adsorbed gas layer, and  $R = r_p^2 / (r_k + \Delta t)^2$  ( $r_k$  is the radius of the inner capillary);  $V_p$  is the pore volume.

According to the above equation, the plot of  $[dV/d \log(D)/\text{\AA}]/\text{cm}^3\text{g}^{-1}$  against pore diameter can be obtained. For detailed computation methods, please see reference <sup>34</sup>.

### 2.5.6. Gas Chromatography-Mass Spectroscopy (GC-MS)

GC-MS analysis was carried out using a Hewlett-Packard 5890 Series II Gas chromatograph with LAB-BASE software for data acquisition and analysis. A VG Quattro mass spectrometer with  $EI = 70$  eV was used for the detection and identification of the reaction products. Product separation was achieved using either a DB-WAX or a DB-5 GC column subject to a temperature program from room temperature to 473 K at a rate of 5 K/min.

The as-synthesized MCM-41 sample was used as a typical example of ozone treatment for GC-MS analysis. The possible gaseous products arising from the removal of template by ozone treatment were collected using a self-made U-shape glass tube in an acetone-dry ice trap (195 K), which is shown in Figure 2.5. The inside diameter of the tube is 1.0 cm, and the height of the tube is 18 cm. The gaseous products were injected into the GC column immediately after collection.

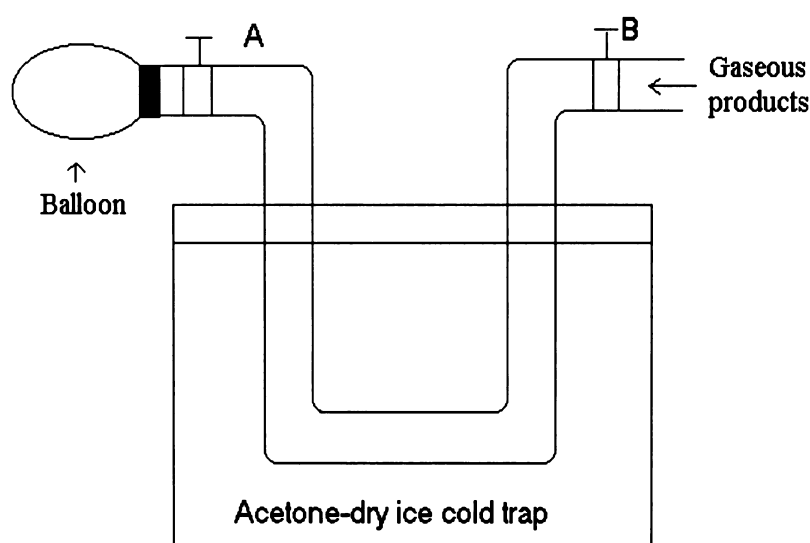


**Figure 2.5:** The Schematic drawing of the self-made U-shape glass tube used for collecting gaseous products in ozone treatment of MCM-41 with an acetone-dry ice trap.

### 2.5.7. Electrochemical Measurements of the Redox Potentials

All of the electrochemical measurements of oxidation and reduction potentials of the electron donor and acceptor molecules were performed using the cyclic voltammetry method with a BAS 100B electrochemical analyser (provided by Bioanalytical System Inc., USA). A conventional three electrode system, which comprises a glassy carbon working electrode, a Ag/AgCl | 3 mol / KCl (from BAS) reference electrode, and a Cu counter electrode was employed. The measured potentials were reported versus this reference at room temperature.

In general, the concentrations of the samples were ca.  $2 \times 10^{-4}$  M in HPLC grade acetonitrile solution with 0.02 M tetrabutylammonium tetrafluoroborate  $[(C_4H_9)_4NBF_4]$  as electrolyte. Unfortunately, some compounds could not be completely dissolved in the above electrolyte solution, and so, the saturated solutions were used instead. The  $(C_4H_9)_4NBF_4$  electrolyte was recrystallized from ethanol / ether and dried before use.

In order to avoid the previous redox deposits on the surface of the electrode contaminate the following measurement, before each measurement, the glassy carbon working electrode was pretreated by polishing with 1.0  $\mu\text{m}$ , 0.3  $\mu\text{m}$ , and 0.5  $\mu\text{m}$  alumina slurries on microcloth pads (Buehler, Lake Bluff, IL, USA) for 20 min, respectively. The electrode was rinsed with deionized water to remove the trace alumina on the electrode surface, and further cleaned in an ultrasonic bath for 20 min. Before the first measurement, the electrode was also cleaned by electrochemical etching in a 0.1 M  $H_2SO_4$  by cycling the electrode potential between  $-0.3$  to  $+1.5$  V until a reproducible cyclic voltammogram was obtained. The reference and counter electrodes were rinsed and dried in the air before each measurement, and used directly without further treatment.

The cyclic voltammetry was carried out with a scan rate of 100 mV / s in the positive direction and sensitivity of 10  $\mu$ A / V in the range of -1.8 — +1.5 V.

### 2.5.8. Ultraviolet-Visible (UV-Vis) Spectroscopy

UV-Vis spectroscopy measurements were performed on a Varian Cary 50 UV-VIS-NIR spectrometer.

Solution state UV-Vis spectra of the guest molecules were recorded for comparison with those assembled in (Al)-MCM-41 hosts. The substrates were dissolved in either  $\text{CH}_2\text{Cl}_2$  or  $\text{CH}_3\text{CN}$  ( $\sim 10^{-6}$  M), and transferred to a quartz cuvette for measurement. The absorption spectra were recorded in the range of 200-800 nm.

Solid state DR-UV-Vis spectra of the assembled (Al)-MCM-41 materials were recorded using a Cary 50 diffuse reflectance accessory (DRA, shown in Figure 2.6) at room temperature. The Cary 50 DRA features a 110 mm diameter integrating sphere with a port to sphere area ratio of 3 %. The sphere is coated with polytetrafluoroethylene (PTFE) with a density of approximately 1 g / cm<sup>3</sup>, a coating material which exhibits superior NIR performance compared to traditional coatings. It also consists of a built-in high performance photomultiplier (PMT) and a Lead Sulphide (PbS) detector. The powder cell is made of Teflon or stainless steel with 10 mm diameter and 3 mm depth, and equipped with a quartz window. 20-30 mg powder sample was filled evenly into the powder cell and covered tightly with a Teflon cork for analysis. The baseline was run first with the provided white Barium Sulphate ( $\text{BaSO}_4$ ) as a reference material in the same wavelength range applied for the samples (1500nm-200nm or 800nm-200nm depending on the samples). The spectra were analysed using Grams software distributed by Galactic Industries Corp.. To obtain the relative

absorption spectra, the original spectra were performed Kubelka-Munk conversion (Kubelka-Munk remission function  $F(R) = [(1-R)^2/2R] \approx k/s$ , where  $R$  is absolute reflectance,  $k$  is absorption coefficient, and  $s$  is scattering coefficient).

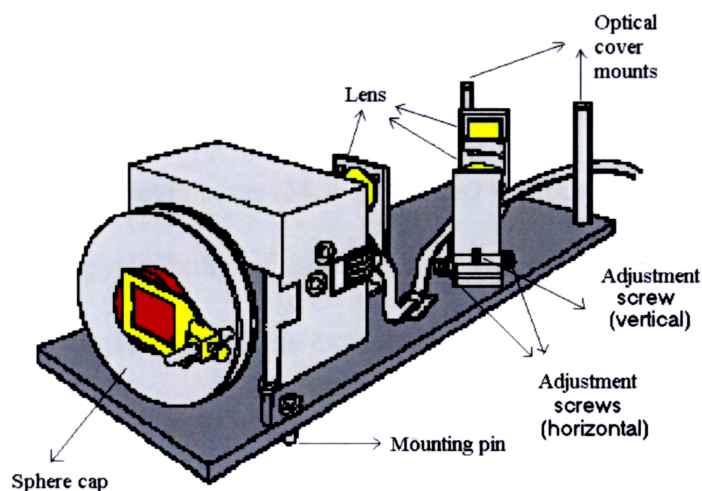


Figure 2.6: A Schematic diagram of the Cary 5 Diffuse Reflectance Accessory

### 2.5.9. Electron Paramagnetic Resonance (EPR) Spectroscopy

Electron spin resonance (ESR), or, more generally, electron paramagnetic resonance (EPR), is a powerful tool to study electronic structures of materials possessing unpaired electrons,<sup>35-38</sup> for example: (1) atoms with odd number of electrons, such as H; (2) ions with unpaired electrons in incomplete inner orbitals, such as transition-metal ions; (3) molecules with odd number of electrons, such as NO; (4) some molecules do not have odd number of electrons, but contain two electrons with parallel spins and the net magnetic moment is not zero, such as O<sub>2</sub>; (5) radical cations and anions; (6) the F or V center in the solid defects, semi-conductors and metals, etc..

EPR technique is used to study the generated radical cations and anions throughout the entire electron transfer processes in (Al)-MCM-41 materials, which comprises of the main parts of this project.

(1) **Generation of EPR signal:** The unpaired electron is a spin  $\frac{1}{2}$  particle with a magnetic moment ( $\mu$ ). When it is placed into an external magnetic field ( $B_0$ ), the unpaired electron will interact with the magnetic field, which causes the energy of the electron to be further split into two extremely opposite energy level states: a lowest energy state ( $M_s = -1/2$  state) when the moment of electron is aligned with the magnetic field, and a highest energy level state ( $M_s = 1/2$  state) when it is against the magnetic field. This kind of energy splitting of electron in a magnetic field is called Zeeman effect. The energy difference ( $\Delta E$ ) can be expressed by the following equation:  $\Delta E = h\nu = g\mu_B B_0$ , where  $g$  is the  $g$  value, which is a dimensionless constant approximately equal to 2 for most samples (2.0023193 for a free electron), but varies for different samples;  $\mu_B$  is the Bohr magneton, which is equal to  $9.2740514 \times 10^{-24}$  J / T; and  $B_0$  is the external magnetic field.

**Table 2.4: Relationship of fields for resonance with microwave frequencies**

Microwave band	Frequency (GHz)	$B_{\text{res}}$ (G)
L	1.1	392
S	3.0	1070
X	9.75	3480
Q	34.0	12000
W	94.0	34000

There are two ways to measure this energy difference: apply a constant magnetic field and scan the frequency of the electromagnetic radiation (conventional method), or keep the electromagnetic radiation constant and scan the magnetic field (Bruker method). In the latter case, the magnetic field, which “tunes” the two spin states so that their energy difference matches the energy of the radiation (therefore, the peak in the absorption



spectrum occur), is called “field for resonance”. Table 2.4 lists the fields for resonance ( $B_{\text{res}}$ ) for a  $g = 2$  signal at corresponding microwave bands and frequencies.

The EPR spectra analyses involve the determination of the spectrum center and hence the  $g$  value, the intensity (or spin concentration), the linewidths (and line positions), the line shapes, and the most importantly, the hyperfine interactions (the interaction between the unpaired electron and the nuclei).

**(2) EPR spectrometer:** All of the EPR spectra were recorded on a Bruker EMX 10 EPR spectrometer, which consists of a microwave bridge (electromagnetic radiation source and the detector are inside), a microwave cavity for samples (a metal box that helps the amplify weak signals from the sample, a magnet (to “tune” the electronic energy levels), a console (contains signal processing and control electronics), and a computer (for analyzing data as well as coordinating all the units for acquiring a spectrum).

**Microwave bridge:** Figure 2.7 shows the block diagram of a microwave bridge. Point A is the microwave source. Point B is a variable attenuator, which blocks the flow of microwave radiation. With the help of attenuator, the microwave power can be controlled precisely and accurately. Circulator C restricts microwaves coming in port 1 only go to the cavity through port 2 first, and then the reflected microwaves from the sample are directed only to the detector through port 3. The detector at point E is a Schottky barrier diode, which converts microwave power to an electrical current. At low power levels ( $< 1 \mu\text{W}$ ), the diode current is proportional to the microwave power and the detector is called a square law detector; at higher power levels ( $> 1 \text{ mW}$ ) the diode current is proportional to the square root of the microwave power and the detector is called a linear detector. Point F is a reference arm, which supplies the detector with

some extra microwave power or “bias” to insure the diode of the detector works in the linear region.

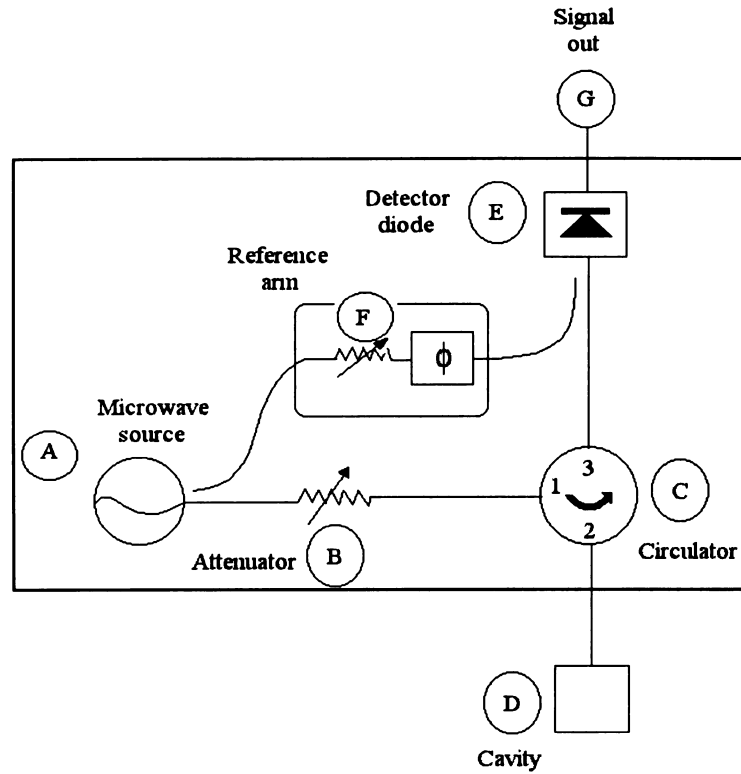


Figure 2.7: The block diagram of a microwave bridge.

**Microwave cavity:** The function of a microwave cavity is to amplify weak signals from the sample. The cavity is simply a rectangular metal box, which stores the microwave energy by resonating with microwaves. The efficiency of the cavity on storing the microwave energy are usually characterized by Q (quality) factor:

$$Q = \frac{2\pi (\text{energy stored})}{\text{energy dissipated per cycle}} = \frac{\nu_{\text{res}}}{\Delta\nu}$$

where the energy dissipated per cycle is the amount of energy lost during one microwave period,  $\nu_{\text{res}}$  is the resonant frequency of the cavity, and  $\Delta\nu$  is the width at half height of the resonance. The microwaves are coupled to the cavity via a hole called an “iris”, the size of which controls the amount of microwaves that reflect back from the cavity and that enter the cavity.

**Signal channel:** The signal channel (also known as “lock-in amplifier” or “phase sensitive detector”), which fits in the console, contains electronics for the phase sensitive detection. The EPR sensitivity can be increased by phase sensitive detection with magnetic field modulation; however, one must be careful in choosing the appropriate modulation amplitude, frequency and time constant. Time constant filters out noise by slowing down the response time of the spectrometer. To get better signal to noise ratio, the scan time usually should be at least ten times greater than that of the time constant.

**Magnetic field controller:** The magnetic field controller allows one to sweep the magnetic field in a controlled and precise manner. It consists of two parts: one is to set the field value and the timing of the field sweep, and the other one is to regulate the current in the windings of the magnet to attain the requested magnetic field value.

**(3) EPR measurements:** EPR measurements (for the samples' preparations subjected to the EPR measurements, please see Section 2.4). An X band microwave with a frequency of 9.80 GHz and a field for resonance of 3480 G, a modulation frequency of 100 kHz, and resolution of 1024 points were applied to all measurements. The time constant was set to twice the conversion time. All the other parameters were varied according to the sample. The obtained spectra were analyzed using the WIN-EPR software, and if necessary, simulated with WINEPR SimFonia software (both softwares are distributed by Bruker). The second derivative EPR spectra were obtained by differentiating the first derivative EPR spectra once with WIN-EPR software.

Two standards were used for spin concentration estimates, a 0.01M DPPH ( $\alpha, \alpha'$ -diphenyl- $\beta$ -picryl hydrazyl) in THF (or  $\text{CH}_2\text{Cl}_2$ ) solution ( $6 \times 10^{-6}$  moles of spins in the cavity) and a strong pitch ( $1.8 \times 10^{-8}$  moles of spins in the cavity). The spin concentrations of the samples were estimated by comparing double integrated

intensities with those of the standards. For the solid samples, the amount of the solid estimated to be in 3-cm effective height (Figure 2.8) of the cavity was 30 mg. For the liquid samples, the volume of liquid was taken as  $0.6 \text{ cm}^3$ .

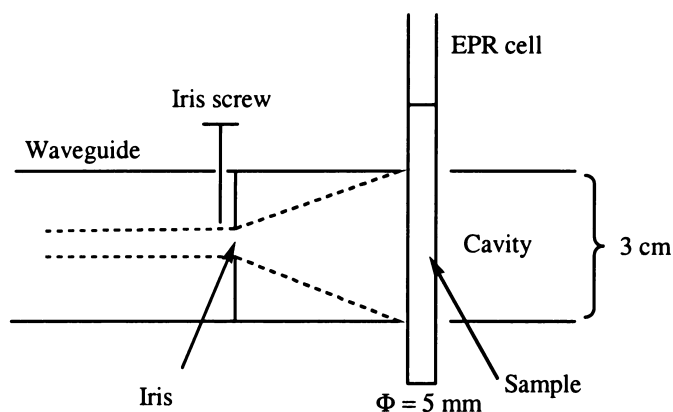


Figure 2.8: Schematic show of the effective height of the EPR tube in the EPR cavity.

#### 2.5.10. Irradiation of Samples with UV Lamps

Before the samples were subject to the EPR and DR-UV-Vis measurements, if necessary, they were irradiated with UV lamps. Two kinds of UV lamps were used for the irradiation purposes. One was 100W Hg Arc lamp (6281) equipped with Oriel Q-series housing and Oriel 68806 basic power supply (50-200 Watts), which generates intense spectral irradiance peaks in the range of 200-500 nm ( $>1.0 \mu\text{W cm}^{-2} \text{ nm}^{-1}$ ) and becomes flat after 500 nm ( $0.5 \mu\text{W cm}^{-2} \text{ nm}^{-1}$ ) at 50 cm distance. The other lamp used was a powerful Philips Mercury lamp choke (125W) with a light intensity measured with a powermeter to be  $7.98 \text{ mW/m}^2$ .

## 2.6. References for Chapter 2

- (1) Ryoo, R.; J.M., K. *J. Phys. Chem.* **1995**, *99*, 16742.
- (2) Ryoo, R.; J.M., K. *J. Chem. Soc., Chem. Commun.* **1995**, 711.
- (3) Razumovskii, S. D.; Zaikov, G. E. "Ozone and its reactions with organic compounds"; New York: Amsterdam, 1984.
- (4) Schmidt, R.; Akporiaye, D.; Stöcker, M.; Ellestad, O. H. *Stud. Surf. Sci. Catal.* **1994**, *84*, 61.
- (5) Beck, J. S.: US, Patent No. 5057296, 1991.
- (6) Beck, J. S.; Chu, C. T.-U.; Johnson, I. D.; Kresge, C. T.; Leonowicz, M. E.; Rorth, W. J.; Vartuli, J. C. US, Patent No. 5108725, 1992.
- (7) Kresge, C. T.; Leonowicz, M. E.; Rorth, W. J.; Vartuli, J. C. US, Patent No. 5098684, 1992.
- (8) Mokaya, R. *Chem. Commun.* **2000**, 1891.
- (9) Seitz, U.; Daub, J. *Synthesis* **1986**, 686.
- (10) Pollart, D. J.; Rickborn, B. *J. Org. Chem.* **1987**, *52*, 792.
- (11) Fischer, H.; Summers, L. A. *J. Heterocyclic Chem.* **1980**, *17*, 333.
- (12) Stehle, P.; Fürst, P.; Ratz, R.; Rau, H. *J. Chromatogr.* **1988**, *449*, 299.
- (13) Mandler, D.; Degani, Y.; Willner, I. *J. Phys. Chem.* **1984**, *88*, 4366.
- (14) Arduini, A.; Ferdani, R.; Pochini, A.; Secchi, A.; Ugozzoli, F. *Angew. Chem. Int. Ed.* **2000**, *39*, 3453.
- (15) Oevering, H.; Paddon-Row, M. N.; Heppener, M.; Oliver, A. M.; Cotsaris, E.; Verhoeven, J. W.; Hush, N. S. *J. Am. Chem. Soc.* **1987**, *109*, 3258.
- (16) Paquette, L. A.; Bellamy, F.; Böhm, M. C.; Gleiter, R. *J. Org. Chem.* **1980**, *45*, 4913.
- (17) Davies, A. G.; Courtneidge, J. *Acc. Chem. Res.* **1987**, *20*, 90.
- (18) Roduner, E.; Wu, L. M.; Crockett, R.; Rhodes, C. J. *Catal. Lett.* **1992**, *14*, 373.
- (19) Venkataraman, B.; Fraenkel, G. K. *J. Am. Chem. Soc.* **1955**, *77*, 2707.
- (20) Venkataraman, B.; Fraenkel, G. K. *J. Chem. Phys.* **1955**, *23*, 588.
- (21) Baerlocher, C.; McCusker, L. B. *Stud. Surf. Sci. Catal.* **1994**, *85*, 391.
- (22) Treacy, M. M. J.; Higgins, J. B.; Ballmoos, R. v. *zeolites* **1996**, *16*.
- (23) PDF Database (Sets 1-44), International Centre for Diffraction Data, 12 Campouns, Blvd, Newtown square, PA 19073-3273, USA, 1994.

- 
- (24) Bauer, F.; Geudel, E.; Ch.Peuker; Pitz, W. *zeolites* **1996**, 17, 278.
- (25) Geidel, E.; Böhlig, H.; Peuker, C.; Pilz, W. *Stud. Surf. Sci. Catal.* **1991**, 65, 511.
- (26) Engelhardt, G.; Michael, D.; John Wiley and Sons: London, 1987.
- (27) Fyfe, C. A.; Feng, Y.; Grondey, H.; Kokotailo, G. T.; Gies, H. *Chem. Rev.* **1991**, 91, 1525.
- (28) Klinowski, J.; Ramdas, S.; Thomas, J. M.; Fyfe, C. A.; Hartmann, J. S. *J. Chem. Soc. Faraday Trans.* **1983**, 78, 1025.
- (29) Gregg, S. J.; Sing, K. S. W. "*Adsorption, Surface Area and Porosity*"; 2nd ed.; Academic Press: London, 1982.
- (30) McClellan, A. L.; Harnsberger, H. F. *J. Colloid. Interface. Sci.* **1967**, 23, 577.
- (31) Wheeler, A. *Adv. Catal.* **1951**, 3, 250.
- (32) Gurvitsch, L. *J. Phys. Chem. Soc. Russ.* **1915**, 47, 805.
- (33) Halsey, G. *J. Chem. Phys.* **1948**, 16, 931.
- (34) Barrett, E. P.; Joyner, L. G.; Halenda, P. H. *J. Am. Chem. Soc.* **1951**, 73, 373.
- (35) Ayscough, P. B. "*Electron Spin Resonance in Chemistry*"; METHUEN & CO LTD: London, 1967.
- (36) Wertz, J. E.; Bolton, J. R. "*ELECTRON SPIN RESONANCE Elementary Theory and Practical Applications*"; Chapman and Hall: New York, London, 1986.
- (37) Weil, J. A.; Bolton, J. R.; Wertz, J. E., Eds. "*Electron Paramagnetic Resonance*"; Wiley: New York, 1994.
- (38) Charles P. Poole, J.; Farach, H. A. "*Handbook of ELECTRON SPIN RESONANCE (Data Sourcecs, Computer Technology, Relaxation, and ENDOR)*"; American Institute of Physics: New York, 1994.

## 2.7. Appendices

### Appendix 2.1: Commercially Available Chemicals and Reagents

#### (Alphabetical Order)

Acetic acid,  $\text{CH}_3\text{COOH}$ , 99.7 %, F.W. 60.05, freezing point  $16\text{ }^\circ\text{C}$ ,  $d\ 1.048\text{--}1.050 \times 10^3\text{ kg / m}^3$ . AJAX Chemicals, NSW, Australia.

Acetone- $d_6$ ,  $\text{CD}_3\text{CCD}_3$ , 99.9 atom % D, F.W. 64.13, b.p.  $55.5\text{ }^\circ\text{C}$ , m.p.  $-93.8\text{ }^\circ\text{C}$ ,  $n_D^{293\text{ K}}\ 1.3554$ ,  $d\ 0.872 \times 10^3\text{ kg / m}^3$ , Aldrich Chem. Co. Inc..

Acetonitrile,  $\text{CH}_3\text{CN}$ , 99.9 %, HPLC grade, F.W. 41.05, b.p.  $81\text{--}82\text{ }^\circ\text{C}$ ,  $n_D^{293\text{ K}}\ 1.3440$ ,  $d\ 0.786 \times 10^3\text{ kg / m}^3$ , Aldrich Chem. Co. Inc..

Aluminium chloride,  $\text{AlCl}_3$ , 98 %, F.W. 133.34,  $d\ 2.440 \times 10^3\text{ kg / m}^3$ , Aldrich Chem. Co. Inc..

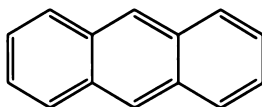
Aluminium isopropoxide,  $\text{Al}(\text{OC}_3\text{H}_7)_3$ , 98+ %, F.W. 204.25, m.p.  $138\text{--}142\text{ }^\circ\text{C}$ ,  $d\ 1.035 \times 10^3\text{ kg / m}^3$ , Aldrich Chem. Co. Inc..

Ammonium,  $\text{NH}_3$ , 28 wt % solution in water, AR, F.W. 17, Histo • Labs Pty, Ltd. A.C.N., distributed by Fronine Pty. Ltd..

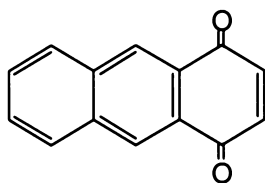
Ammonium hexafluorophosphate,  $\text{NH}_4\text{PF}_6$ , 95+ %, F.W. 163.00,  $d\ 2.180 \times 10^3\text{ kg / m}^3$ , Aldrich Chem. Co. Inc..

Aniline,  $\text{C}_6\text{H}_5\text{NH}_2$ , 99+ %, F.W. 93.3, b.p.  $95\text{ }^\circ\text{C}$ , AJAX Chemicals, NSW, Australia.

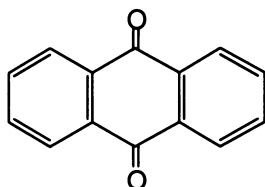
Anthracene, F.W. 178.23, m.p.  $214\text{--}217\text{ }^\circ\text{C}$ , AJAX Chemicals, NSW, Australia.



1,4-Anthraquinone (1,4-AQ), F.W. 208.22, purified by column chromatography (silica,  $\text{CH}_2\text{Cl}_2$ ) and recrystallization from  $\text{CH}_2\text{Cl}_2$ , Aldrich Chem. Co. Inc..



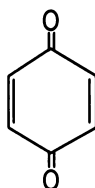
9,10-Anthraquinone (9,10-AQ), F.W. 208.22, recrystallized from benzene, light yellow crystal, BDH Chemicals Ltd., Poole, England.



Benzene,  $C_6H_6$ , 99+%, F.W. 78.11, b.p. 80-80.2 °C, m.p. 5.5 °C,  $n_D^{293\text{ K}}$  1.5010,  $d$   $0.874 \times 10^3 \text{ kg / m}^3$ , Aldrich Chem. Co. Inc..

Benzophenone,  $(C_6H_5)_2CO$ , F.W. 182.2, b.p. 305 °C, m.p. 48-50.5 °C, Aldrich Chem. Co. Inc..

Benzoquinone (BQ), F.W. 108, purified by sublimation at 333 K under vacuum with a pressure of 0.05 Mbar, Aldrich Chem. Co. Inc..



Benzyltriethylammonium bromide,  $C_6H_5CH_2N(C_2H_5)_3Br$ , 99 %, F.W.272.24, m.p. 194 °C (dec.), Aldrich Chem. Co. Inc..

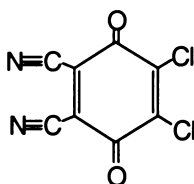
Cesium ammonium nitrate  $Cs(NH_4)_2(NO_3)_6$ , F.W. 541, Aldrich Chem. Co. Inc..

Cetyltrimethylammonium chloride (Hexadecyltrimethylammonium chloride, CTAC),  $C_{16}H_{33}N(CH_3)_3Cl$ , 25 wt % solution in water, F.W. 320.01,  $n_D^{293\text{ K}}$  1.3778,  $d$   $0.968 \times 10^3 \text{ kg / m}^3$ , Aldrich Chem. Co. Inc..

Chloroform-d, 99.8 atom % D,  $CDCl_3$ , F.W. 120.39, b.p. 60.9 °C, m.p. -64 °C,  $n_D^{293\text{ K}}$  1.440,  $d$   $1.500 \times 10^3 \text{ kg / m}^3$ , Aldrich Chem. Co. Inc..



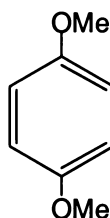
2,3-Dichloro-5,6-dicyano-1,4-benzoquinone (DDQ), 98 %, F.W. 227.01, m.p. 213-216 °C, Aldrich Chem. Co. Inc..



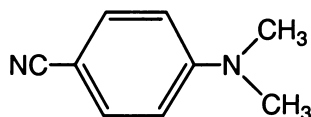
Dichloromethane,  $\text{CH}_2\text{Cl}_2$ , A.R., F.W. 84.93, b.p. 40 °C, m.p. -97 °C,  $n_D^{293\text{ K}}$  1.4240, d  $1.325 \times 10^3 \text{ kg / m}^3$ , distilled over  $\text{CaH}_2$  twice before use, APS Chemicals Ltd..

Diethyl Ether,  $\text{CH}_3\text{COOCH}_2\text{CH}_3$ , 99 %, F.W. 74.12, stabilized with 0.5-1.5mg/L of BHT, d  $0.7079 \times 10^3 \text{ kg / m}^3$ , APS Chemicals Ltd..

1,4-Dimethoxybenzene (1,4-DMB), 99 %, F.W. 138.17, b.p. 213 °C, m.p. 56.6 °C, d  $1.053 \times 10^3 \text{ kg / m}^3$ , Aldrich Chem. Co. Inc..



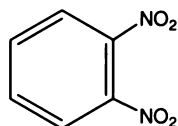
4-(Dimethylamino)-benzonitrile (4-DMABN), 98 %, F.W. 146.19, b.p. 318 °C, Aldrich Chem. Co. Inc..



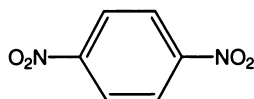
N,N-Dimethylformamide (DMF),  $\text{HCON}(\text{CH}_3)_2$ , F.W. 73.10, b.p. 153 °C, m.p. -61 °C,  $n_D^{293\text{ K}}$  1.4310, d  $0.944 \times 10^3 \text{ kg / m}^3$ , distilled over  $\text{CaH}_2$  before use, Aldrich Chem. Co. Inc..

Dimethyl sulphoxide (DMSO),  $\text{CH}_3\text{SOCH}_3$ , 99 %, F.W. 78.13, b.p. 189 °C, freezing point 18.4 °C, d  $1.10 \times 10^3 \text{ kg / m}^3$ , AJAX Chemicals, NSW, Australia.

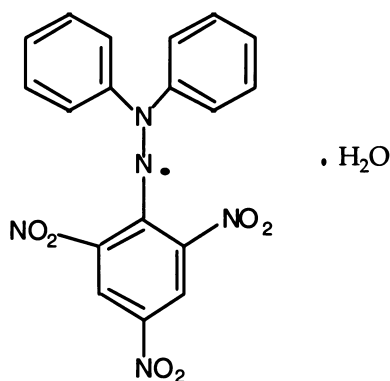
1,2-Dinitrobenzene (1,2-DNB), 99 %, F.W. 168.11, Aldrich Chem. Co. Inc..



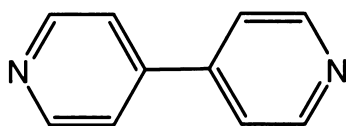
1,4-Dinitrobenzene (1,4-DNB), 98 %, F.W. 168.11, b.p. 183.4 °C / 34 mm, m.p. 172-174 °C, d  $1.625 \times 10^3 \text{ kg / m}^3$ , Aldrich Chem. Co. Inc..



2,2-Diphenyl-1-picrylhydrazyl ( $\alpha, \alpha'$ -diphenyl- $\beta$ -picryl hydrazyl, DPPH), 95 %, free radical, F.W. 394.32, m.p. 130 °C, Aldrich Chem. Co. Inc..



4,4'-Dipyridyl, 98 %, F.W. 156.19, b.p. 305 °C, m.p. 111-114 °C, Aldrich Chem. Co. Inc..



Ethanol (absolute),  $\text{CH}_3\text{CH}_2\text{OH}$ , F.W. 46.1, APS Chemicals Ltd.

Fullerene,  $\text{C}_{60}$ , F.W. 720, Aldrich Chem. Co. Inc..

Hexane,  $\text{C}_6\text{H}_{12}$ , 99.5 %, spectrosoL, F.W. 86.2, APS Chemicals Ltd..

Hydrochloric acid,  $\text{HCl}$ , 32 %, F.W. 36.5, AR, APS Chemicals Ltd..

Hydrofluoric acid,  $\text{HF}$ , 50 %, F.W. 20, AR, AJAX Chemicals, NSW, Australia.

Iodomethane,  $\text{CH}_3\text{I}$ , 99 %, F.W. 141.94, b.p. 41-43 °C,  $n_D^{293 \text{ K}}$  1.5310, d  $2.280 \times 10^3 \text{ kg / m}^3$ , Aldrich Chem. Co. Inc..

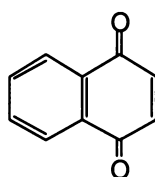
1-Iodooctane,  $C_8H_{17}I$ , 98 %, F.W. 240.13, b.p. 225-226 °C, m.p. -46 — -45 °C,  $n_D^{293\text{ K}}$  1.4878, Aldrich Chem. Co. Inc..

Ludox HS40 (39.5 wt %  $SiO_2$ , 0.4 wt %  $Na_2O$ , and 60.1 wt %  $H_2O$ ), Du Pont, Australia.

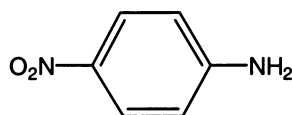
Magnesium Sulphate,  $MgSO_4 \cdot 3H_2O$ , F.W. 174.40, AJAX Chemicals, NSW, Australia.

Naphthalene (Crystals),  $C_{10}H_8$ , F.W. 128.17, AJAX Chemicals, NSW, Australia.

1,4-Naphthaquinone (1,4-NQ), 97 %, F.W. 158.16, m.p. 121-122 °C, recrystallized from ethanol, Aldrich Chem. Co. Inc..



4-Nitroaniline, F.W. 138.12, m.p. 147-149 °C, BDH Chemicals Ltd., Poole, England.



Nitromethane,  $CH_3NO_2$ , 99+%, spectroquality reagent, F.W. 61.04, b.p. 101.2 °C, m.p. -29 °C,  $n_D^{293\text{ K}}$  1.382, d  $1.127 \times 10^3\text{ kg / m}^3$ , Matheson Coleman & Bell.

Potassium hydroxide, KOH, F.W. 56.1, Merck Pty. Ltd..

Palladium on activated carbon (catalyst), Aldrich Chem. Co. Inc..

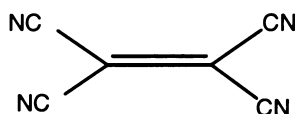
Sodium aluminate,  $NaAlO_2$ , F.W. 81.9, m.p. 1800 °C, AJAX Chemicals, NSW, Australia.

Sodium dithionite,  $Na_2S_2O_4$ , F.W. 174.1, APS AJAX Fine Chem..

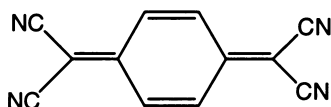
Sodium hydroxide, NaOH, 97 %, F.W. 40, APS AJAX Fine Chem..

Tetrabutylammonium tetrafluoroborate,  $(C_4H_9)_4NBF_4$ , 99%, F.W. 329.28, Recrystallized from Ethanol / Ether, Aldrich Chem. Co. Inc..

Tetracyanoethylene (TCNE), 98 %, F.W. 128.1, recrystallized twice from dried chlorobenzene, and then sublimated at 120 °C under vacuum with a pressure of 0.05 Mbar, Aldrich Chem. Co. Inc..

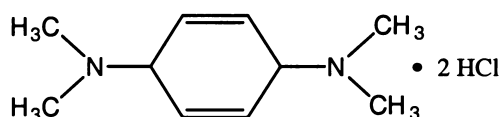


7,7,8,8-Tetracyano-quinodimethane (TCNQ), 98 %, F.W. 204.19, m.p. 287 °C (dec.), recrystallized from acetonitrile twice, and then sublimated at 120 °C under vacuum with a pressure of 0.05 Mbar, Aldrich Chem. Co. Inc..



Tetrahydrofuran (THF), C<sub>4</sub>H<sub>8</sub>O, 99+ %, F.W. 72.11, m.p. -108 °C, b.p. 65 °C, d 0.889 × 10<sup>3</sup> kg / m<sup>3</sup>, dried and distilled over sodium with benzophenone (blue means no water) as indicator, Aldrich Chem. Co. Inc..

N,N,N',N'-Tetramethyl-1,4-phenylenediamine (TMPDA) dihydrochloride, 98 %, F.W. 237.17, m.p. 222-224 °C, Aldrich Chem. Co. Inc..



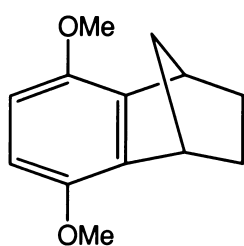
Trifluoroacetic acid, CF<sub>3</sub>COOH, 99 %, F.W. 114.02, b.p. 72 °C, m.p. -15.3 — -15 °C, n<sub>D</sub><sup>293 K</sup> 1.3000, d 1.48 × 10<sup>3</sup> kg / m<sup>3</sup>, Aldrich Chem. Co. Inc..

Water, a milli-Q water purification system was used to supply deionized water.

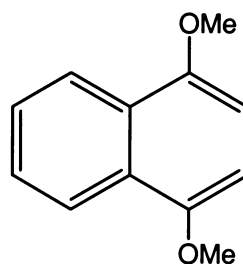
## Appendix 2.2: Commercially Unavailable Compounds:

I express my sincere thanks to Professor Michael N. Paddon-Row's group, UNSW, who provided me the following donor, acceptor and donor-bridge-acceptor molecules. These compounds were all passed NMR test and I give my full credit to them.

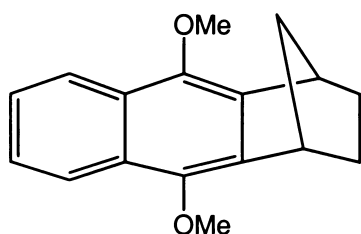
### Electron Donor Molecules:



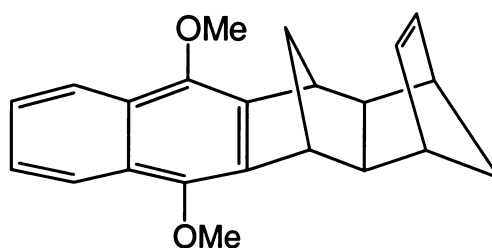
DMB[2]



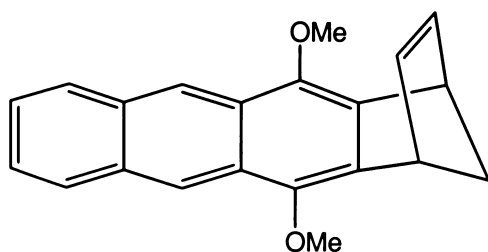
DMN



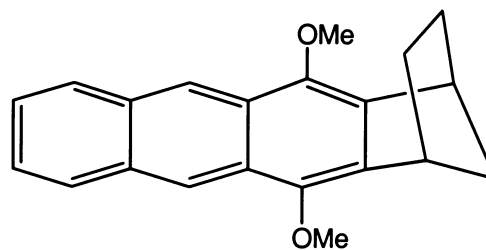
DMN[2]



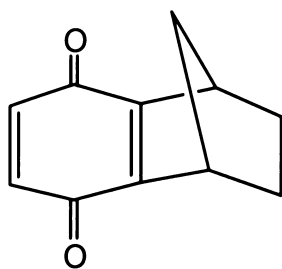
DMN[4DB]



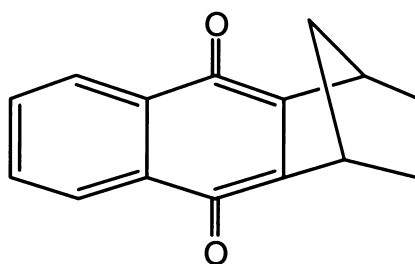
DMA[2DB]



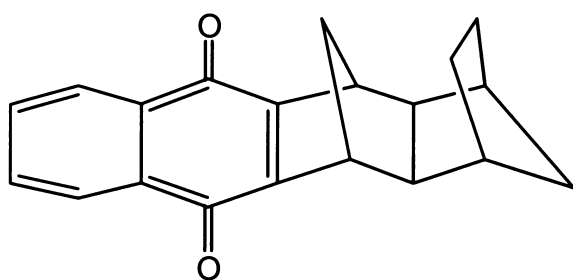
DMA[2]

**Electron Acceptor Molecules:**

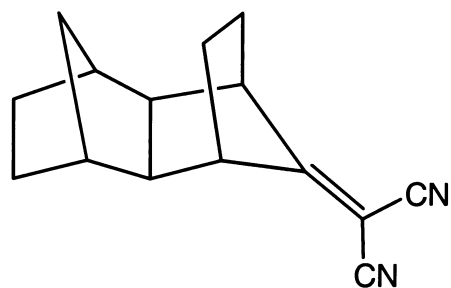
BQ[2]



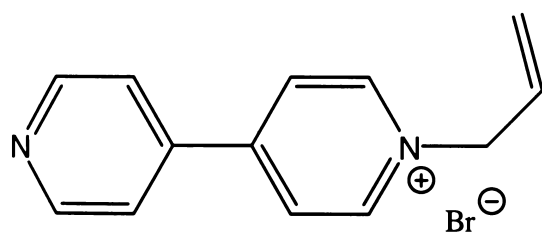
NQ[2]

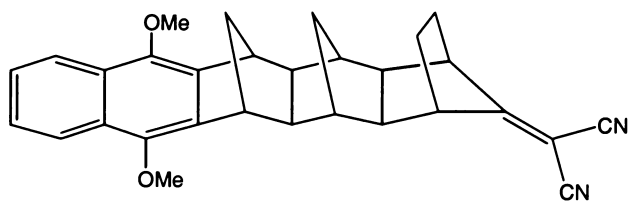


NQ[4]

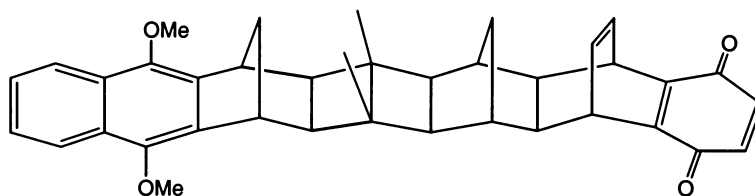


DCV[4]

1-VMV<sup>+</sup>Br<sup>-</sup>

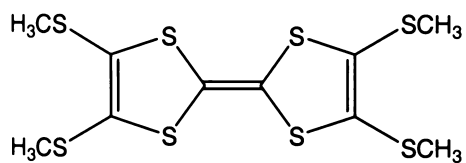
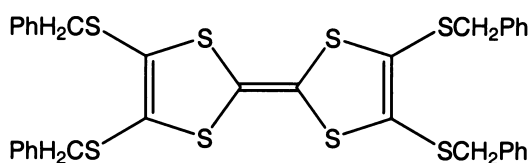
**Donor –Bridge-Acceptor Molecules:**

DMN-6B-DCV

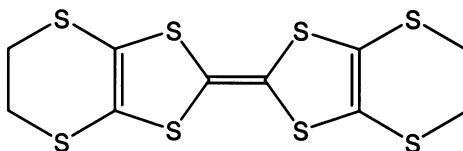


DMN-8B-BQ

I am also grateful to Professor Yulan Zhu, Yanbian University, Jilin Province, P. R. China, for providing me the following three TTF derivatives. These compounds passed NMR test and I give my full credit to them.

TTC<sub>1</sub>-TTF

TBT-TTF



BEDT-TTF

## Chapter 3

### Characterization of Mesoporous (Al)-MCM-41 Hosts

#### 3.1. Introduction

This chapter mainly describes the characterization of various kinds of synthesized mesoporous (Al)-MCM-41 materials using specific characterization methods, such as XRD patterns, solid state  $^{29}\text{Si}$ -MAS-NMR and  $^{27}\text{Al}$ -MAS-NMR, and routine FTIR and *in-situ* IR. The surface properties of the de-templated samples were determined with nitrogen adsorption-desorption isotherms (for the corresponding detailed synthetic and spectroscopic experiments, please refer to Chapter 2). The characterized mesoporous (Al)-MCM-41 materials include the following samples, which are synthesized from different synthetic methods or are in different porous states:

- (1) As-synthesized (Al)-MCM-41 samples ( $\text{Si}/\text{Al} = \infty, 39, 15$  and  $7$ ) which were directly hydrothermally synthesized.
- (2) Pre-washed (Al)-MCM-41 samples ( $\text{Si}/\text{Al} = \infty, 39, 15$  and  $7$ ). Here “pre-washed” means that the surfactant in the above as-synthesized samples were partially “washed out” by treating with EtOH/HCl).
- (3) Thermally calcined (Al)-MCM-41 samples (the as-synthesized purely siliceous MCM-41 and the pre-washed Al-MCM-41 samples with  $\text{Si}/\text{Al} = 39, 15$ , and  $7$ , respectively, were calcined at  $813\text{ K}$  in muffle furnace to remove surfactant template).
- (4) Post Al-grafted Al-MCM-41 ( $\text{Si}/\text{Al} = 14$ ) sample

This chapter is comprised of the following sections:



Section 3.1. Introduction. Section 3.2. Powder XRD patterns. Section 3.3. Solid state NMR ( $^{29}\text{Si}$ -MAS-NMR,  $^{27}\text{Al}$ -MAS-NMR). Section 3.4. Chemical composition of synthesized (Al)-MCM-41 samples. Section 3.5. Surface properties. Section 3.6. *in-situ* IR of Al-MCM-41. Section 3.7. Effectiveness of the acidic ethanol extraction on template removal.

### 3.2. Powder XRD Patterns

Power X-ray diffraction is a major tool for the investigation of MCM-41 structure. It is well known that one of the characteristic structural features of MCM-41 is its one-dimensional hexagonal array packing of the pores.<sup>1</sup> In X-ray diffraction patterns, MCM-41 can show up to seven Bragg peaks ( $hkl$ ), which can be indexed in P6 hexagonal symmetry as (100), (110), (200), (210), (300), (220), and (310),<sup>2-6</sup> indicating a high sample quality with long-range ordering of the framework. There are no peaks with  $l \neq 0$ , which is generally attributed to the lack of order along the wall axis. Since the experimental error of a diffraction instrument is considerably high for very low angle peaks, one must bear in mind that only those well enough resolved reflections in the powder patterns can be used for the determination of MCM-41 structures. As shown in the following sections, due to the fact that the MCM-41 materials are not crystalline at the atomic level,<sup>7</sup> in practice, usually only three to five distinct ( $hk0$ ) reflections between  $2\theta = 1.5^\circ$  and  $8^\circ$  can be observed, i.e., a very strong peak at a low angle, and two to four relatively weaker peaks at higher angles, which can be ascribed to (100), (110), (200), (210) and (300) reflection lines.<sup>8,9</sup>

### 3.2.1. XRD Patterns of Purely Siliceous MCM-41 Samples

The XRD patterns of various synthesized MCM-41 samples are shown from Figure 3.1 to Figure 3.3, and only those clearly distinguishable XRD pattern parameters are reported and summarized in Table 3.1. Since the observed reflection lines can be indexed on a hexagonal unit cell, the repeating distance ( $a_0$ ) between two pore centers (the average distance between the adjacent pore centers) are calculated by the equation  $a_0 (\text{\AA}) = (2 / 3^{1/2}) d_{100}$ .<sup>10-12</sup>

#### 3.2.1.1. As-synthesized and Thermally Calcined MCM-41 Samples

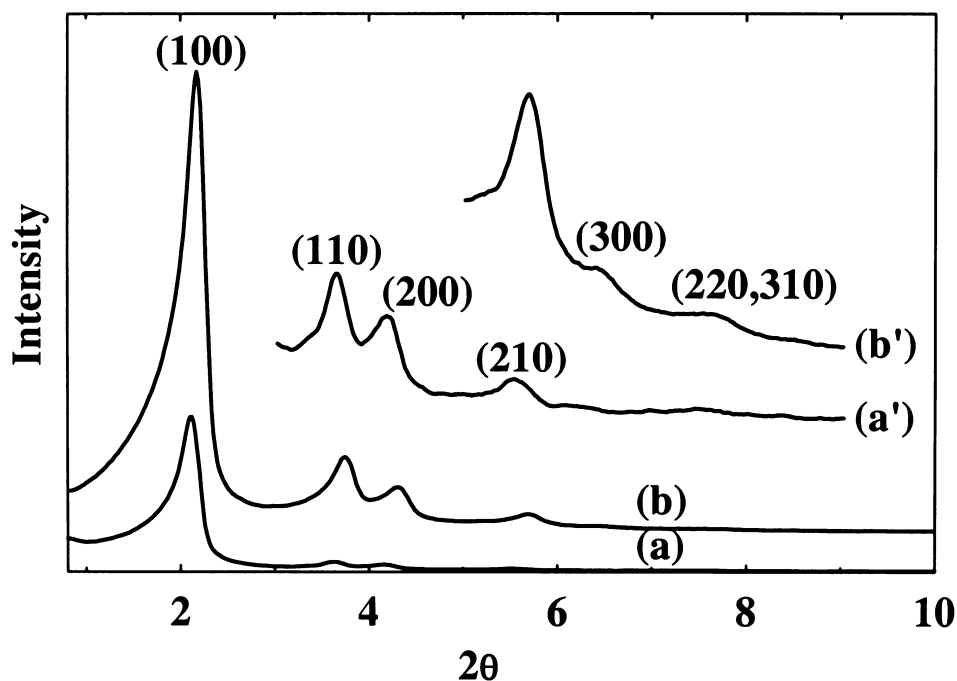


Figure 3.1: XRD patterns of MCM-41: (a) as-synthesized MCM-41; (b) thermally calcined MCM-41 (as-synthesized sample was calcined at 813 K in air-flow). Curve (a') and (b') are parts of the original pattern (a) and (b), respectively, which are magnified 16 times.

Figure 3.1 shows the powder XRD patterns of the as-synthesized (a) and the thermally calcined MCM-41 samples (b).

The as-synthesized siliceous MCM-41 exhibits an intense reflection at  $2\theta = 2.12^\circ$ , corresponding to (100) reflection line with  $d_{100} = 41.6 \text{ \AA}$ . The calculated distance between the adjacent pore centers ( $a_0$ ) is  $48.0 \text{ \AA}$ .<sup>13</sup> Besides this strong (100) Bragg peak, three relatively weak ones can also be observed at  $2\theta = 3.66^\circ$  ( $d = 24.1 \text{ \AA}$ ),  $4.24^\circ$  ( $d = 20.9 \text{ \AA}$ ), and  $5.56^\circ$  ( $d = 16.1 \text{ \AA}$ ). These reflections are due to the ordered hexagonal array of parallel silica tubes and can be indexed as (110), (200) and (210), respectively. The presence of these high order peaks indicates that the as-synthesized MCM-41 has a high degree of long-range ordering.<sup>1</sup>

**Table 3.1: XRD data of MCM-41 samples**

Sample	<i>hkl</i>	Angle	Counts	$d_{\text{space}} (\text{\AA})$	FWHM <sup>a</sup>	$a_0 (\text{\AA})$ <sup>b</sup>
As-synthesized MCM-41	(100)	$2.12^\circ$	18826	41.6	$0.27^\circ$	48.0
	(110)	$3.66^\circ$	1087	24.1		
	(200)	$4.22^\circ$	817	20.9		
	(210)	$5.46^\circ$	407	16.1		
Thermally calcined MCM-41	(100)	$2.18^\circ$	52520	40.5	$0.30^\circ$	46.8
	(110)	$3.74^\circ$	8904	23.6		
	(200)	$4.30^\circ$	5184	20.5		
	(210)	$5.68^\circ$	2123	15.5		
	(300)	$6.38^\circ$	813	13.8		
	(220), (310)	$7.58^\circ$	499	11.7		
Pre-washed MCM-41	(100)	$2.18^\circ$	40481	40.5	$0.21^\circ$	46.8
	(110)	$3.74^\circ$	5027	23.6		
	(200)	$4.28^\circ$	2938	20.6		
	(210)	$5.64^\circ$	734	15.7		
	(300)	$6.40^\circ$	357	13.8		
Calcined pre- washed MCM-41	(100)	$2.20^\circ$	39046	40.1	$0.18^\circ$	46.3
	(110)	$3.80^\circ$	4942	23.2		
	(200)	$4.36^\circ$	873	20.3		
	(210)	$5.76^\circ$	807	15.3		
	(300)	$6.54^\circ$	350	13.5		

**Notes:** (a) FWHM = full width at half maximum. (b) The distance between the adjacent pore centers ( $a_0$ ) is calculated by the equation of  $a_0 = 2 d_{100} / 3^{1/2}$ .

After removal of the CTAC template by thermal calcination at 813 K in air-flow, the calcined MCM-41 shows (100) reflection line at  $2\theta = 2.18^\circ$  with  $d_{100} = 40.5 \text{ \AA}$ . The corresponding calculated  $a_0$  is  $46.8 \text{ \AA}$ . The reduction of  $d_{100}$  space as well as the shifts of (100), (110), (200), and (210) Bragg peaks to the higher  $2\theta$  values (smaller  $2\theta$  value of (100) peak indicates a larger unit cell size) are also observed. These are probably due to the lattice contractions (2.6 %, based on  $d_{100}$  space, compared with the as-synthesized MCM-41) upon high temperature thermal calcination. Ryoo et al.<sup>11,12</sup> reported that repeating pH adjustment to 10.2 during hydrothermal synthesis can improve the thermal stability and textural uniformity of MCM-41, which is reflected by less lattice contraction of the pH adjusted samples (< 5 %) than those without pH adjustment (lattice contraction is between 10 - 25 %<sup>14-16</sup>). This effect was attributed to increasing degrees of silanol groups condensation in MCM-41 due to equilibrium shifts for the silicate polymerization after pH adjustment. Similar lattice contraction has also been reported by other researchers.<sup>1,13,14</sup> Interestingly, additional clear reflections at  $2\theta = 6.38^\circ$  ( $d = 13.8 \text{ \AA}$ ) and  $2\theta = 7.58^\circ$  can also be observed (Figure 3.1 (b')), which can be ascribed to (300) and diffuse (220, 310) peaks.<sup>1-5</sup> The presence of these higher order peaks indicates that the calcined MCM-41 material possesses a better-defined pore structure with long-range ordering. Generally, the full width at half maximum (FWHM) represents the scattering domain (or crystal) size and the order of the solid. The narrower the FWHM, the more ordered the sample. The negligible difference ( $0.03^\circ$ ) of FWHM of (100) peak between the calcined and as-synthesized MCM-41 indicates that the long-range ordering of the thermally calcined sample is almost unchanged. This result is in good agreement with the previous report of Luan et al.<sup>17</sup> Another distinct feature of the calcined sample is the dramatic increases of the (100), (110), (200) and (210) Bragg peaks intensities (approximately by a factor of 3, 8, 6 and 5, respectively),

which enhance the resolution of the XRD pattern. Anderson et al.<sup>18</sup> also found that removal of surfactant by calcination was accompanied by an increase in intensity of the (100) peak. The reverse experimental evidence<sup>18-21</sup> for a decrease in X-ray Bragg intensities upon filling the pores of MCM-41 was also reported. Hammond et al.<sup>22</sup> studied the effect of surfactant removal on the Bragg intensity of MCM-41 silicas using a periodic wall model and suggested that the differences in the Bragg intensities of the as-synthesized and the calcined forms of MCM-41 arise from the scattering contrast between the framework walls and pores of MCM-41. Since the long-range order in the direction perpendicular to the channel axis is preserved in hexagonal MCM-41 systems, template removal by calcination should increase the intensities of the Bragg peaks (the scattering intensity is affected only weakly by short-range disorder within the framework walls).

#### **3.2.1.2. Pre-washed MCM-41 and Calcined Pre-washed MCM-41 Samples**

To compare the effect of EtOH/HCl liquid extraction of CTAC surfactant on the porous structure of pure silica MCM-41 and Al-MCM-41, the as-synthesized MCM-41 sample was also washed with EtOH/HCl to partially remove CTAC surfactant (the product is designated as “pre-washed MCM-41”) and then was subject to calcination under the same experimental conditions as those of the thermally calcined sample (the calcined product is designated as “calcined pre-washed MCM-41”). Figure 3.2 shows the related XRD patterns. For comparison purposes, the XRD patterns of the as-synthesized MCM-41 and the thermally calcined MCM-41 are also plotted together.

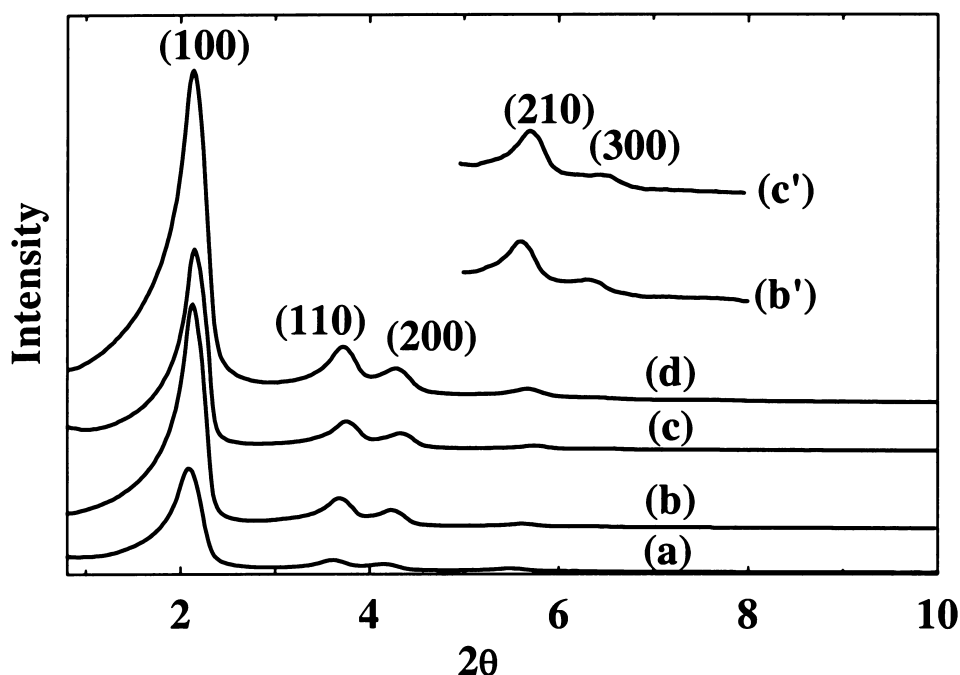


**Figure 3.2: XRD patterns of MCM-41: (a) as-synthesized MCM-41; (b) pre-washed MCM-41 (as-synthesized sample treated with EtOH/HCl to partially remove the CTAC surfactant); (c) calcined pre-washed MCM-41; (d) thermally calcined MCM-41. Curve (b') and (c') are parts of the original pattern (b) and (c), respectively, which are magnified 15 times.**

The XRD pattern of pre-washed MCM-41 (Figure 3.2 (b) and (b')) shows a strong dominant (100) peak at  $2\theta = 2.18^\circ$  with  $d_{100} = 40.5 \text{ \AA}$ . As shown in Table 3.1, the calculated  $a_0$  is  $46.8 \text{ \AA}$ , which is the same as that of thermally calcined sample. This indicates that template extraction with liquid EtOH/HCl leads to around 2.6 % lattice contraction (based on  $d_{100}$  space, compared with the as-synthesized sample), which is comparable to 3.6 % caused by EtOH/H<sub>2</sub>SO<sub>4</sub> extraction reported by Hitz et al.<sup>23</sup> Four higher ordered peaks can also be observed at  $2\theta = 3.74^\circ$  ( $d = 23.6 \text{ \AA}$ ),  $4.28^\circ$  ( $d = 20.6 \text{ \AA}$ ),  $5.64^\circ$  ( $d = 15.7 \text{ \AA}$ ) and  $6.40^\circ$  ( $d = 15.7 \text{ \AA}$ ) which can be ascribed to (110), (200), (210), and (300), respectively. The presence of these higher ordered peaks, as well as

the narrower FWHM of (100) peak ( $0.21^\circ$ ), indicates that the pre-washed MCM-41 still possesses a well defined ordered pore structure.

The XRD pattern of calcined pre-washed MCM-41 (Figure 3.2 (c) and (c')) shows a (100) peak at  $2\theta = 2.20^\circ$  with  $d_{100} = 40.1 \text{ \AA}$ . As shown in Table 3.1, the calculated  $a_0$  is  $46.3 \text{ \AA}$ . The lattice contraction caused by thermal calcination is around 1 % compared with pre-washed MCM-41 and 3.6 % if compared with the as-synthesized sample. Less lattice contraction from pre-washed MCM-41 to calcined pre-washed MCM-41 may be due to: 1) unlike the severe thermal calcination, template removal by acidic ethanol extraction is carried out under mild experimental conditions; 2) as suggested by Hitz et al.,<sup>23</sup> removal of template ions from siloxy groups by acidic ethanol solution extraction method is followed by a precondensation of silanol groups, which stabilizes the lattice before calcination. Notably, the observed FWHM of (100) peak is  $0.18^\circ$  for the calcined pre-washed MCM-41, which is the narrowest value among all of the synthesized MCM-41 samples. The FWHM value of (100) peak of MCM-41 is generally reported in the range of  $0.2\text{-}0.4^\circ$ .<sup>1,13,19,24-29</sup> Under optimum experimental conditions, high quality MCM-41 with FWHM of (100) peak as low as  $0.11\text{-}0.17^\circ$  can be obtained.<sup>6,8,25</sup> The lowest of FWHM value of the calcined pre-washed MCM-41 indicates that it has the largest scattering domain size.<sup>30</sup> Compared with the direct calcination, it seems that two step treatment (liquid extraction plus thermal calcination) doesn't significantly change the crystalline structure of pure MCM-41.

### 3.2.2. XRD Patterns of Directly Hydrothermally Synthesized Al-MCM-41

For the purpose of clarity, the following abbreviations are used in the following sections: "as-synthesized ( $\chi$ )" for the as-synthesized sample; "pre-washed ( $\chi$ )" for the

sample obtained by washing the as-synthesized sample with EtOH/HCl) prior to thermal calcination; “calcined ( $\chi$ )” for the sample obtained by calcining pre-washed sample (not as-synthesized sample as in purely siliceous MCM-41) at 813 K in air-flow. The “ $\chi$ ” here stands for the Si/Al ratio of the corresponding Al-MCM-41 sample in the gel mixture.

### 3.2.2.1. Al-MCM-41 (Si/Al = 39)

Figure 3.3 shows the XRD patterns of the as-synthesized (39) (Figure 3.3 (a)), pre-washed (39) (Figure 3.3 (b)) and calcined (39) (Figure 3.3 (c)). The as-synthesized (39) exhibits the dominant (100) peak at  $2\theta = 2.20^\circ$  with  $d_{100} = 41.1 \text{ \AA}$ . The calculated distance between the adjacent pore centers ( $a_0$ ) is  $46.3 \text{ \AA}$ . Compared with the as-synthesized MCM-41, the  $d_{100}$  space of the as-synthesized (39) is decreased, demonstrating that the substitution of the framework silicon by the larger Al atoms, which might be expected to increase the unit cell parameter due to the longer bond length of Al-O than that of Si-O, <sup>31,32</sup> in fact leads to a contraction of the unit cell.<sup>33</sup> Besides this strong (100) Bragg reflection, three relatively weak reflections (see inset of Figure 3.3) can also be observed at  $2\theta = 3.80^\circ$  ( $d = 23.2 \text{ \AA}$ ),  $4.10^\circ$  ( $d = 2021.5 \text{ \AA}$ ) and  $5.66^\circ$  ( $d = 15.6 \text{ \AA}$ ), which can be ascribed to (110), (200) and (210) peaks, respectively ((110) and (200) peaks overlapped to some degree but are still clearly distinguishable). The presence of these high order peaks indicates that the as-synthesized Al-MCM-41 (Si/Al = 39) has well maintained long-range ordering. Compared with the as-synthesized MCM-41 sample, the intensity of the (100) peak in the as-synthesized (39) sample is much lower, indicating some reduced mesoscopic order in the as-synthesized (39).<sup>34</sup> The other high order peaks, such as (110), (200) peaks, still show the similar



intensities as the as-synthesized MCM-41, indicating that the incorporation of Al during hydrothermal synthesis decreases the order of the crystalline structure.<sup>32,34-36</sup> Luan et al.<sup>37</sup> suggested that this is due to the reduction of the crystal size along the *a* and *b* axes after incorporation of Al, while Reddy et al.<sup>32</sup> attributed this intensity decrease to the incorporation of Al in the feed hinders the crystallization processes. The FWHM of (100) peak is  $0.52^\circ$ , which is larger than that of the as-synthesized MCM-41 ( $0.27^\circ$ ), further confirms the structure disorder of Al-MCM-41 (Si/Al = 39) sample.

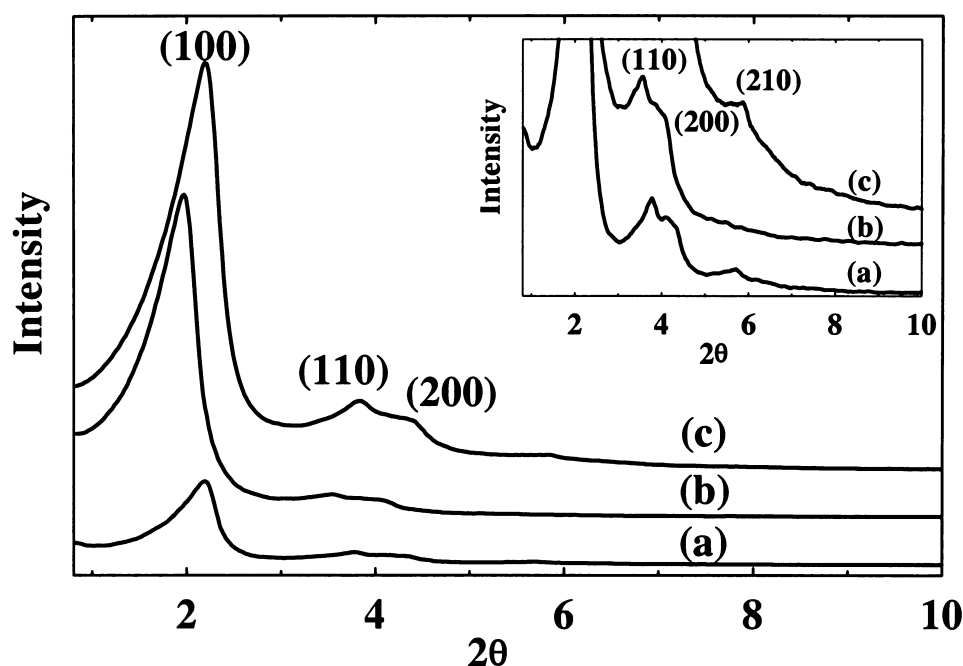


**Figure 3.3: XRD patterns of Al-MCM-41 (Si/Al = 39): (a) as-synthesized (39); (b) pre-washed (39); (c) calcined (39). The inset shows the relevant fine structures of the high order peaks.**

After washing with EtOH/HCl to partially remove the CTAC surfactant (Figure 3.3 (b)), the significant increase in the intensity of the (100) peak is expected due to the template removal, which enhances the scattering contrast between the framework and the pores.<sup>22</sup> The shift of the (100) peak position toward a lower  $2\theta$  value, as well as the increase of the  $d_{100}$  spacing, indicates the expansion of lattice parameters (9.5 % based

on  $d_{100}$  space). Unlike purely siliceous MCM-41, washing Al-MCM-41 (Si/Al = 39) sample with acidic ethanol further decreases the domain size, indicated by the increase of the FWHM of (100) peaks. The absence of the (210) peak as well as the further overlap of (110) and (200) peaks demonstrates that the acidic ethanol treatment leads to the decrease of the structure order.<sup>36-39</sup>

Figure 3.3 (c) shows the XRD pattern of calcined (39) which was obtained by calcining the acidic ethanol pre-washed sample. It can be seen that calcination leads to the shift of (100) peak toward the higher  $2\theta$  position and a lattice contraction about 10 % compared with the pre-washed sample.<sup>34</sup> As observed in purely siliceous MCM-41, due to the pH adjustment, the synthesized MCM-41 is stable toward thermal calcination, which is reflected by less lattice contraction (2.6 % from the as-synthesized MCM-41 to the calcined MCM-41, 1 % from the pre-washed MCM-41 to the calcined pre-washed MCM-41). Larger lattice contraction of Al-MCM-41 (Si/Al = 39) upon calcination confirms that incorporation of even a small amount of Al into the MCM-41 framework will result in less thermal stability and less structural order than siliceous MCM-41. This observation could also result from Al segregation from the MCM-41 matrix at high temperatures. Calcination also leads to increases of the Bragg peaks intensities<sup>35</sup> and reappearance of the (210) Bragg peak, indicating the restoration of the long range ordering of the original as-synthesized sample. The overlap of (110) and (200) Bragg peaks is still maintained although their intensities are increased after calcination. The increase of the FWHM of (100) peak value is due to the decrease of the domain size.

The detailed XRD parameters for the above Al-MCM-41 (Si/Al = 39) samples are summarized in Table 3.2.

**Table 3.2: XRD data of Al-MCM-41 samples with Si/Al = 39**

Sample	<i>Hkl</i>	Angle	Counts	$d_{\text{space}}$ (Å)	FWHM <sup>a</sup>	$a_0$ (Å) <sup>b</sup>
As-synthesized (39)	(100)	2.20°	6512	41.1	0.52°	46.3
	(110)	3.80°	1037	23.2		
	(200)	4.10°	818	21.5		
	(210)	5.66°	303	15.6		
Pre-washed (39)	(100)	1.96°	24336	45.0	0.60°	52.0
	(110)	3.50°	1758	25.2		
	(200)	4.04°	1319	21.9		
Calcined (39)	(100)	2.18°	30845	40.5	0.69°	46.8
	(110)	3.80°	5339	23.2		
	(200)	4.32°	3902	20.4		
	(210)	5.86°	1241	15.1		

\* The notes for a, and b are the same as those in Table 3.1.

### 3.2.2.2. Al-MCM-41 (Si/Al = 15)

The XRD pattern of as-synthesized (15) (Figure 3.4 (a)) exhibits the dominant (100) peak at  $2\theta = 2.24^\circ$  with  $d_{100} = 39.4$  Å. Compared with the as-synthesized (39), the (100) peak position is further shifted to the higher  $2\theta$  value and the corresponding  $d_{100}$  space is further decreased. Three high order peaks can also be observed at  $2\theta = 3.76^\circ$ ,  $4.28^\circ$  and  $5.66^\circ$ , which can be ascribed to (110), (200) and (210) peaks, respectively. The (110) and (200) peaks are overlapped but are still clearly distinguishable, indicating that the as-synthesized (15) still possesses long range ordering but less order than the as-synthesized MCM-41. The intensity of (100) peak in the as-synthesized (15) is much lower than that in the as-synthesized MCM-41, nevertheless, the high order (110) and (200) peaks still show similar intensities as do those in the as-synthesized MCM-41. This is consistent with the previous observation for the as-synthesized (39). The FWHM of (100) peak is  $0.41^\circ$ , which is larger than that observed in the as-synthesized MCM-41 ( $0.27^\circ$ ), indicating that as-synthesized (15) has smaller domain size.

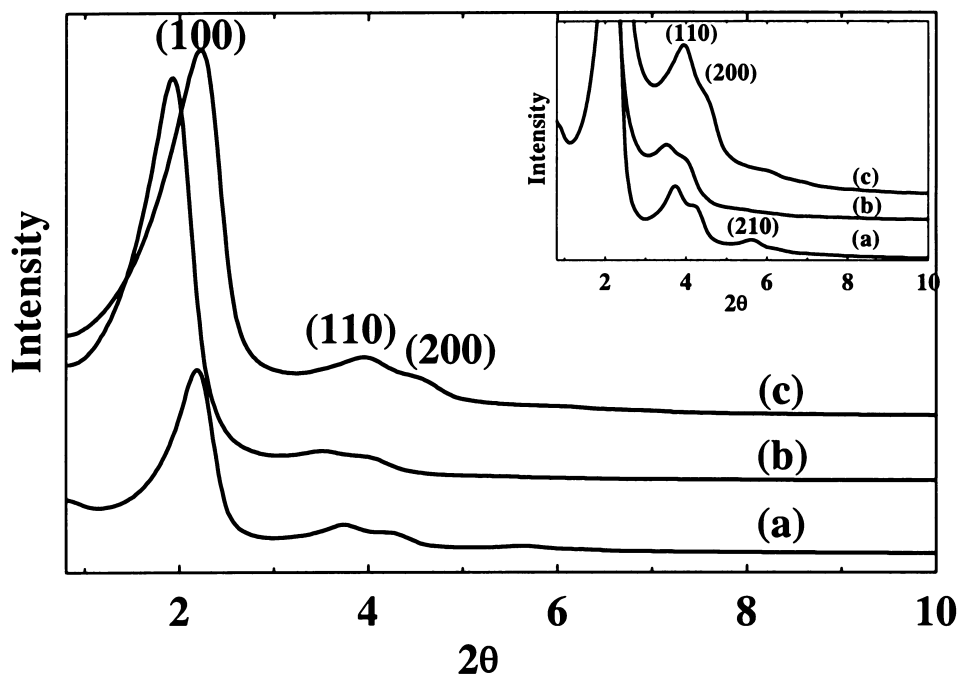


**Figure 3.4:** XRD patterns of Al-MCM-41 (Si/Al = 15): (a) as-synthesized (15); (b) pre-washed (15); (c) calcined (15). The inset shows the relevant fine structures of the high order peaks.

After washing with EtOH/HCl to partially remove the CTAC surfactant (Figure 3.4 (b)), the pre-washed (15) shows a shift of (100) peak position toward lower  $2\theta$  value accompanied by significant increase of the intensity. The increase of the  $d_{100}$  space and the FWHM of (100) peak, as well as further overlapping of (110) and (200) peaks is observed. The (210) peak is not observed. After acidic ethanol extraction to partially remove the CTAC surfactant, the lattice expansion is about 6.6 % compared with the as-synthesized (15). These results are similar to those obtained in pre-washed (39).

The XRD pattern of the calcined (15) shows the dominant (100) peak at  $2\theta = 2.28^\circ$  ( $d_{100} = 38.7 \text{ \AA}$ ) and two higher order peaks at  $2\theta = 3.98^\circ$  and  $4.60^\circ$  corresponding to (110) and (200) reflections, respectively. It can be seen that calcination of the pre-washed (15) sample results in 7.9 % lattice contraction. In contrast to the calcined (39), the calcined (15) shows a slight decrease of the (100) peak intensity and increases of the

higher order peaks ((110) and (200)) intensities. In addition, the reemergence of the (210) peak is not observed. It is also observed that the (110) and (200) peaks are further overlapped and thus the (200) peak can only be assigned approximately. Similar like the calcined (39), the increase of the FWHM value of (100) peak from  $0.64^\circ$  in the pre-washed (15) to  $0.73^\circ$  in the calcined (15) sample is also observed. All of these XRD parameters indicate that increasing the amount of incorporated Al will decrease long range ordering.

**Table 3.3: XRD data of Al-MCM-41 samples with Si/Al = 15**

Sample	<i>Hkl</i>	Angle	Counts	$d_{\text{space}}$ (Å)	FWHM <sup>a</sup>	$a_0$ (Å) <sup>b</sup>
As-synthesized (15)	(100)	$2.24^\circ$	6209	39.4	$0.41^\circ$	45.5
	(110)	$3.76^\circ$	924	23.5		
	(200)	$4.28^\circ$	645	20.6		
	(210)	$5.66^\circ$	282	15.6		
Pre-washed (15)	(100)	$2.10^\circ$	29856	42.0	$0.64^\circ$	48.5
	(110)	$3.66^\circ$	2602	24.1		
	(200)	$4.18^\circ$	2163	21.1		
Calcined (15)	(100)	$2.28^\circ$	21407	38.7	$0.73^\circ$	44.7
	(110)	$3.98^\circ$	3440	22.2		
	(200)	$4.60^\circ$	2107	19.2		

- The notes for a and b are the same as those in Table 3.1.

The detailed XRD parameters for the above Al-MCM-41 (Si/Al = 15) samples are summarized in Table 3.3.

### 3.2.2.3 Al-MCM-41 (Si/Al = 7)

The as-synthesized (7) (Figure 3.5 (a)) shows the dominant (100) peak at  $2\theta = 1.88^\circ$  with  $d_{100}$  space of 47.0 Å. The calculated  $a_0$  is 54.3 Å. Compared with the as-synthesized MCM-41 and the other two low Al containing Al-MCM-41 (Si/Al = 39 and 15) samples, as-synthesized (7) has the largest unit cell parameters. This may be ascribed to the formation of some macropores as shown in the pore size distribution analysis (see surface properties section). It is also noticed that the intensity of the (100)

Bragg peak is greatly decreased. Furthermore, the overall XRD pattern of as-synthesized (7) is poorly resolved. The calculation of FWHM value is inexecutable due to the high background intensity. Besides, the high order peaks are seriously overlapped and the (110) peak can only be approximately indexed. Tanev et al.<sup>40</sup> attributed this kind of higher order peak overlapping to the broadening effects of higher reflection lines due to small particle size. The above XRD pattern analyses indicate that the as-synthesized (7) has the least ordered structure among all of the as-synthesized samples in this study.

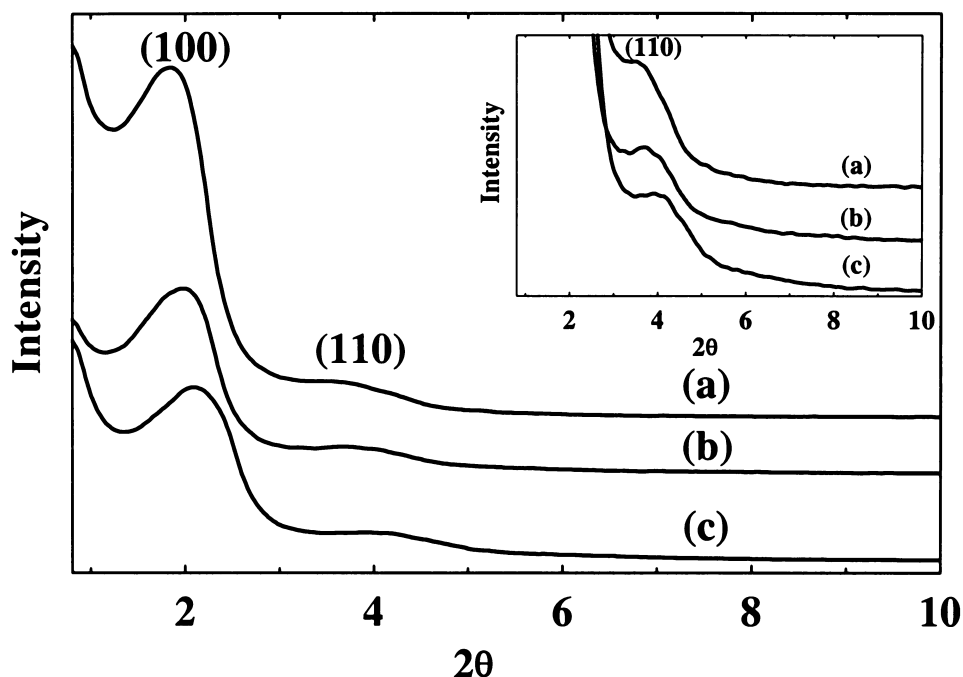


**Figure 3.5: XRD patterns of Al-MCM-41 (Si/Al = 7): (a) as-synthesized (7); (b) pre-washed (7); (c) calcined (7). The inset shows the relevant fine structures of the high order peaks.**

The XRD pattern of the pre-washed (7) (Figure 3. 5 (b)) shows the dominant (100) peak at  $2\theta = 1.98^\circ$  with  $d_{100}$  space of 44.6 Å. The calculated  $a_0$  is 51.5 Å. Washing as-synthesized (7) with acidic ethanol, which might be expected to expand the unit cell

parameters due to the incorporation of a greater amount more amount of Al, actually leads to 5.1 % lattice contraction. This may be due to the ready collapse of the macropores on acidic ethanol treatment. The intensity of the (100) Bragg peak is greatly decreased (ca. 46 %) after acidic ethanol washing, indicating the pre-washed (7) has less ordered structure.

**Table 3.4: XRD data of Al-MCM-41 samples with Si/Al = 7**

Sample	<i>Hkl</i>	Angle	Counts	$d_{\text{space}}$ (Å)	FWHM <sup>a</sup>	$a_0$ (Å) <sup>b</sup>
As-synthesized (7)	(100)	1.88°	9596	47.0	— <sup>c</sup>	54.3
	(110)	3.62°	1064	24.4		
Pre-washed (7)	(100)	1.98°	5201	44.6	—	51.5
	(110)	3.74°	833	23.6		
Calcined (7)	(100)	2.20°	4777	42.9	—	49.5
	(110)	3.96°	837	22.4		

**\* The notes for a and b are the same as those in Table 3.1. (c) The FWHM calculation for peak (100) is not available due to the high background noise.**

After thermal calcination (Figure 3.5 (c)), the (100) peak position is further shifted to the higher  $2\theta$  value (2.20°), and the corresponding  $d_{100}$  space is 42.9 Å. The intensity of the (100) peak is further decreased, and the higher order peaks are still ill-defined and cannot be distinguished. These results indicate that, although the calcined (7) sample poorly maintained the hexagonal structure, the structural order is largely destroyed. It seems that it is difficult to obtain highly ordered high Al content Al-MCM-41 by direct hydrothermal synthesis.

The detailed XRD parameters for the above Al-MCM-41 (Si/Al = 7) samples are summarized in Table 3.4.

### 3.2.3. XRD Patterns of Post-synthesized Al-MCM-41 (Si/Al = 14)

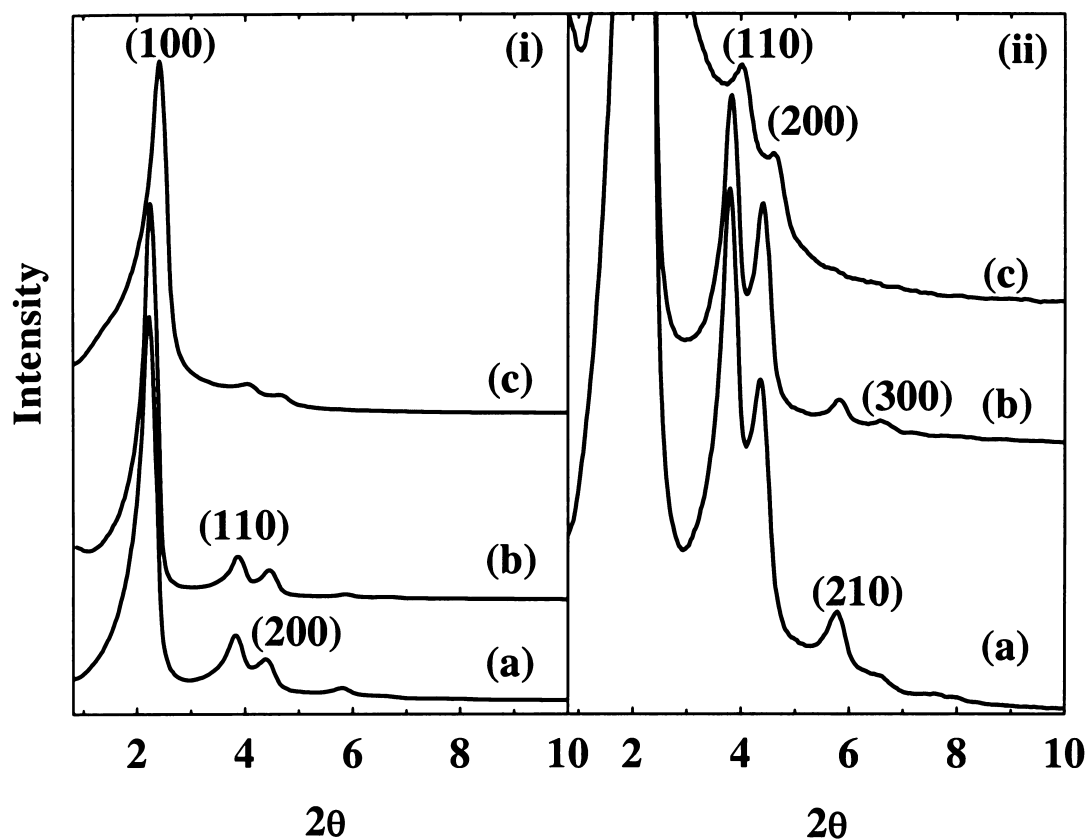


Figure 3.6: XRD patterns of post-synthesized Al-MCM-41 (Si/Al = 14): (a) parent MCM-41; (b) Al-MCM-41 (PB-NH<sub>3</sub>); (c) Al-MCM-41 (PA-NH<sub>3</sub>). Figure (ii) is focused on the low intensity area to show the fine structures of the high order peaks.

Clear observation of high order peaks, especially the (300) peak in the XRD pattern of the parent MCM-41 (Figure 3.6 (a)) demonstrates that this sample has a highly ordered hexagonal structure. After an initial attempt to incorporate Al into the Al-MCM-41 framework, the (PB-NH<sub>3</sub>) sample, which is not treated with ammonia solution, shows slightly decreased Bragg peak intensities. On the other hand, the high order peaks (including (300) peak) are well retained. These observations indicate that the structural order is still well maintained after Al insertion.<sup>41</sup> The  $d_{100}$  space of the Al-MCM-41



(PB-NH<sub>3</sub>) sample is also slightly decreased compared with that of the parent siliceous MCM-41.

**Table 3.5: XRD data of post-synthesized Al-MCM-41 samples with Si/Al = 14**

Sample	<i>Hkl</i>	Angle	Counts	$d_{\text{space}}$ (Å)	FWHM <sup>a</sup>	$a_0$ (Å) <sup>b</sup>
Parent MCM-41 <sup>c</sup>	(100)	2.20°	39046	40.1	0.18°	46.3
	(110)	3.80°	4942	23.2		
	(200)	4.36°	873	20.3		
	(210)	5.76°	807	15.3		
	(300)	6.54°	350	13.5		
Al-MCM-41 (PB-NH <sub>3</sub> )	(100)	2.24°	32005	39.4	0.19°	45.5
	(110)	3.84°	3136	23.0		
	(200)	4.42°	2116	20.0		
	(210)	5.84°	445	15.1		
	(300)	6.62°	225	13.3		
Al-MCM-41 (PA-NH <sub>3</sub> )	(100)	2.42°	12232	36.5	0.36°	42.1
	(110)	4.06°	946	21.7		
	(200)	4.64°	610	19.0		

\* The notes for a and b are the same as those in Table 3.1. (c) The same sample as “Calcined pre-washed MCM-41” sample shown in Table 3.1.

Figure 3.6 (c) shows the XRD pattern of Al-MCM-41 (PA-NH<sub>3</sub>), which was obtained after repeating four cycles of “stir-wash-dry” NH<sub>3</sub> treatment. It also can be seen that repeating NH<sub>3</sub> treatment decreases the Bragg peaks intensities almost at the same level. At the same time, (210) and (300) high order reflections are undetectable. These results indicate that after post-grafting Al into the MCM-41 framework, the pore structure becomes less uniform, lacking the long range ordering compared with the parent MCM-41 sample. Comparison of the XRD patterns of the parent MCM-41, the Al-MCM-41 (PB-NH<sub>3</sub>) and the Al-MCM-41 (PA-NH<sub>3</sub>) sample demonstrates that the structure randomness increases with the increasing amount of tetrahedrally coordinated Al on the framework of MCM-41. Since the post-synthesis procedure used here is the same as that reported by Mokaya et al.,<sup>42</sup> it was expected that post-grafting of Al on the framework would result in a shift of (100) peak to the lower 2θ value and a larger  $d_{100}$  space value in the XRD pattern due to the longer Al-O bond length compared to the Si-

O bond.<sup>31,41,43</sup> However, decrease of the  $d_{100}$  space is observed in this work. This contradictory result may arise from the different parent MCM-41 samples, which were synthesized using different materials and methods. Probably most of the Al atoms are anchored on the inner wall surface of the Al-MCM-41 (PA-NH<sub>3</sub>) sample due to the rigid framework of the parent MCM-41 caused by repeating pH adjustment during hydrothermal synthesis.

The detailed XRD parameters are summarized and tabulated in Table 3.5.

### 3.3. Solid State NMR

#### 3.3.1. <sup>29</sup>Si-MAS-NMR Spectra

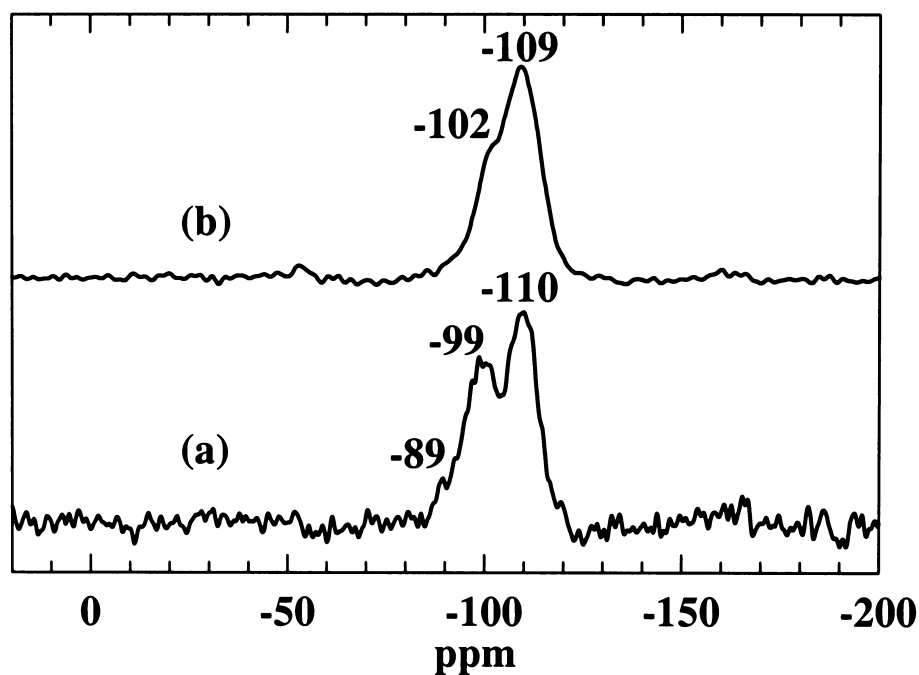
In <sup>29</sup>Si-MAS-NMR Spectra, the peak at ca. -90 ppm is due to Q<sup>2</sup> [(OH)<sub>2</sub>Si(OSi)<sub>2</sub>], that at ca. -100 ppm is due to Q<sup>3</sup> [(OH)Si(OSi)<sub>3</sub>], and that at ca. -110 ppm is due to Q<sup>4</sup> [Si(OSi)<sub>4</sub>].<sup>14,44</sup> These peaks were also observed for the amorphous SiO<sub>2</sub>, suggesting that the pore wall structure of MCM-41 is amorphous.<sup>45,46</sup> Q<sup>3</sup> is the most important framework species, which carries single hydroxyl groups and is also referred to as the isolated or vicinal silanols. Q<sup>2</sup> carries geminal hydroxyl groups and is also referred to as geminal silanols. At certain temperatures, for example, during calcination, Q<sup>2</sup> and Q<sup>3</sup> tend to condense and form Q<sup>4</sup> by loss of water.<sup>1,7,9</sup> For the Al containing samples, considering different kinds of Al coordination with Si atoms in the framework, the contribution of these Al connected species, such as Si(OSi)<sub>3</sub>OAl, Si(OSi)<sub>2</sub>(OAl)<sub>2</sub>, Si-OSi(OAl)<sub>3</sub> to the chemical shifts in the <sup>29</sup>Si-MAS-NMR spectra has to be expected.<sup>33,34,44,47,48</sup> So, for the Al containing samples, especially for the high Al containing samples, these Al coordinated species overlap with Q<sup>2</sup>, Q<sup>3</sup> and Q<sup>4</sup>, resulting in difficulties in identification of the coordination states of the silicon atoms directly from

its chemical shifts in the  $^{29}\text{Si}$ -MAS-NMR spectra. The chemical shift ranges of each type of Si and Al coordinated siloxanes are summarized in Table 3.6.

**Table 3.6: The chemical shift ranges of each type of Si and Al coordinated siloxanes.**

Species	Chemical shifts (ppm)	Species	Chemical shifts (ppm)
Q <sub>4</sub> : Si(OSi) <sub>4</sub>	-(100-116)	Si(1Al): Si-(OSi) <sub>3</sub> OAl	-(96--106)
Q <sub>3</sub> : Si(OSi) <sub>3</sub> OH	-(85-100)	Si(2Al): Si(OSi) <sub>2</sub> (OAl) <sub>2</sub>	-(92-102)
Q <sub>2</sub> : Si(OSi) <sub>2</sub> (OH) <sub>2</sub>	-(80-105)	Si(3Al): SiOSi(OAl) <sub>3</sub>	(-88-96)
Q <sub>1</sub> : SiOSi(OH) <sub>3</sub>	(-70-85)	Si(4Al): Si (AlO) <sub>4</sub>	-(80-90)

### 3.3.1.1. Purely Siliceous MCM-41



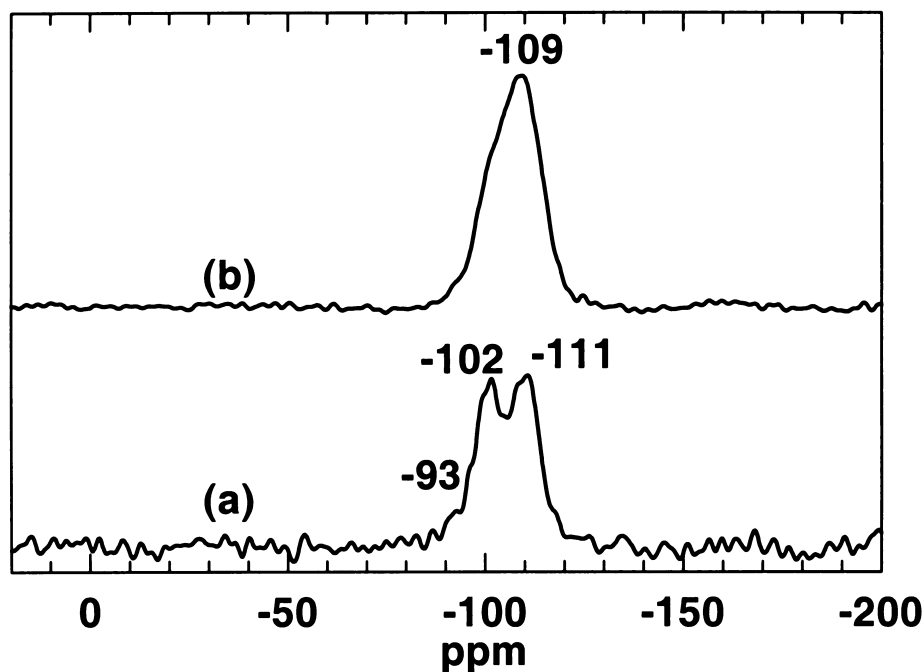
**Figure 3.7:  $^{29}\text{Si}$ -MAS-NMR spectra of purely siliceous MCM-41: (a) as-synthesized MCM-41; (b) calcined MCM-41.**

Figure 3.7 shows the  $^{29}\text{Si}$ -MAS-NMR spectra of as-synthesized (Figure 3.7 (a)) and thermally calcined (Figure 3.7 (b)) purely siliceous MCM-41. The as-synthesized MCM-41 shows signals at ca.  $-89$ ,  $-99$  and  $-110$  ppm, which can be assigned to  $\text{Q}^2$ ,  $\text{Q}^3$  and  $\text{Q}^4$  respectively. Presence of  $\text{Q}^2$  and  $\text{Q}^3$  demonstrates that the as-synthesized MCM-41 sample is not completely condensed. However, the predomination of  $\text{Q}^4$  in the as-synthesized MCM-41 sample is seldom seen in the literature. So far, most of the as-synthesized MCM-41 prepared without pH adjustment showed that the noncondensed  $\text{Q}^3$  species are dominant in the  $^{29}\text{Si}$ -MAS-NMR spectra.<sup>1,9,47,49</sup> Again, the predomination of  $\text{Q}^4$  in the as-synthesized MCM-41 sample further supports that the pH adjustment facilitates the condensation of silanol groups during hydrothermal synthesis.<sup>11,12,16</sup>

The calcined MCM-41 exhibits a dominant peak at  $-109$  ppm due to  $\text{Q}^4$  species and a shoulder at  $-102$  ppm, which can be assigned to  $\text{Q}^3$  species. It also can be seen that the  $\text{Q}^2$  signal disappears and the relative intensity of  $\text{Q}^4$  is increased significantly in the calcined sample. Meanwhile, the relative intensity of  $\text{Q}^4$  is increased at the expense of  $\text{Q}^3$ , indicating that the hydroxyl groups were further condensed *via* loss of water. Chen et al.<sup>14,50</sup> suggested that 100 % fully condensed  $\text{Q}^4$  of the electrostatically templated MCM-41 framework cannot be reached because uncondensed  $\text{SiO}^-$  groups are needed for charge compensation of the cationic quaternary ammonium template. It is also noteworthy that the  $^{29}\text{Si}$ -MAS-NMR spectrum of calcined MCM-41 is narrower than that of the as-synthesized MCM-41, suggesting that calcination results in a more uniform silicate framework.

### 3.3.1.2 Directly Hydrothermally Synthesized Al-MCM-41

#### 3.3.1.2.1. Al-MCM-41 (Si/Al = 39)



**Figure 3.8:**  $^{29}\text{Si}$ -MAS-NMR spectra of Al-MCM-41 (Si/Al = 39): (a) Pre-washed (39); (b) calcined (39).

Figure 3.8 shows the  $^{29}\text{Si}$ -MAS-NMR spectra of acidic ethanol pre-washed (Figure 3.8 (a)) and thermally calcined (Figure 3.8 (b)) Al-MCM-41 with Si/Al = 39. To facilitate the elucidation, these two samples are designated as pre-washed (39) and calcined (39), respectively. The pre-washed (39) sample shows three peaks at ca. -93, -102 and -111 ppm, which are approximately in line with the chemical shifts of  $\text{Q}^2$ ,  $\text{Q}^3$  and  $\text{Q}^4$  coordinated species, respectively. Compared with the  $^{29}\text{Si}$ -MAS-NMR spectrum of the as-synthesized MCM-41 sample, the relative intensity of  $\text{Q}^3$  compared to  $\text{Q}^4$  is higher in pre-washed (39), indicating that substitution of Si atoms with even small amount of Al hinders the precondensation of the silanol groups during hydrothermal synthesis. In

other words, existence of the Al atoms in the silicate framework reduces the degree of cross-linking of the silicate framework. This is in good agreement with the report by Reddy et al.<sup>32</sup> The increase in the amount of the uncondensed  $Q^2$  and  $Q^3$  species in the Al-MCM-41 sample is unlikely to be due to either pH adjustment during hydrothermal synthesis with acetic acid or the removal of the template by acidic ethanol (EtOH/HCl) extraction, since increases of  $Q^4$  species were observed in both cases.<sup>23</sup>

The calcined (39) shows a dominant peak at  $-109$  ppm, which is assigned to  $Q^4$  coordinated Si atom species. This peak is unlikely due to the Si(1Al) resonance which does not occur as high as  $-109$  ppm in MCM materials (see Table 3.6). The spectrum looks asymmetric and the protruded shoulder at the left side is due to the  $Q^3$  coordinated Si atom species. After calcination,  $Q^4$  became the dominant peak at the expense of  $Q^3$ , indicating that calcination results in further condensation of the aluminosilicate MCM-41 framework and a more uniform pore wall structure has been created. This result is consistent with that of calcined MCM-41. Compared with the as-synthesized sample, narrowing of the  $^{29}\text{Si}$ -MAS-NMR spectrum of the calcined (39) indicates that calcination leads to a more uniform aluminosilicate framework, which is consistent with the result of MCM-41 samples.

#### 3.3.1.2.2. Al-MCM-41 (Si/Al = 15)

Figure 3.9 shows the  $^{29}\text{Si}$ -MAS-NMR spectra of acidic ethanol pre-washed (Figure 3.9 (a)) and thermally calcined (Figure 3.9 (b)) Al-MCM-41 (Si/Al = 15). In the following interpretation, these two samples are designated as pre-washed (15) and calcined (15), respectively. The pre-washed (15) sample also shows three peaks at ca.  $-91$ ,  $-101$  and  $-107$  ppm in the  $^{29}\text{Si}$ -MAS-NMR spectrum, which can be assigned to  $Q^2$ ,  $Q^3$  and  $Q^4$

coordination of Si atoms, respectively. In the as-synthesized MCM-41 and the pre-washed (39), the dominant peak is  $Q^4$ . However, the  $^{29}\text{Si}$ -MAS-NMR spectrum of pre-washed (15) shows that the dominant peak is  $Q^3$ , indicating that substitution of Si atoms with a larger amount of Al further hinders the precondensation of the silanol groups during hydrothermal synthesis.

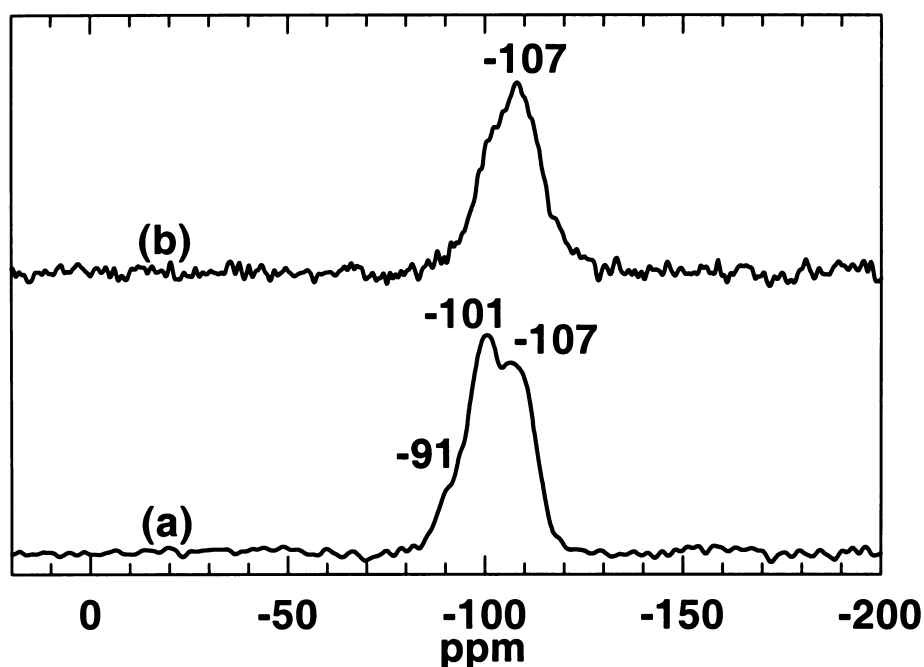


**Figure 3.9:**  $^{29}\text{Si}$ -MAS-NMR spectra of Al-MCM-41 (Si/Al = 15): (a) Pre-washed (15); (b) calcined (15).

In similar fashion to the calcined (39) sample, the calcined (15) shows a dominant peak at  $-107$  ppm due to the  $Q^4$  coordinated Si atom species. The spectrum also looks asymmetric and the protruding shoulder to the larger frequency may be due to the  $Q^3$  coordinated Si atom species. The increase of the relative intensity of  $Q^4$ , together with the absence of the  $Q^2$  species, indicates that calcination results in further condensation of the aluminosilicate MCM-41 framework. This is the same trend as observed in the calcined MCM-41 and calcined (39) samples. It is also noteworthy that the chemical

shift of  $Q^4$  is slightly shifted downfield about 2 ppm compared to the calcined MCM-41. This may be due to the contribution of the Al coordinated species in this higher Al content sample, which may generate some Si-O and Al-O bonds with different bond lengths and angles. After calcination, the  $^{29}\text{Si}$ -MAS-NMR spectrum of the calcined (15) also became narrower than that of the as-synthesized sample.

### 3.3.1.2.3. Al-MCM-41 (Si/Al = 7)

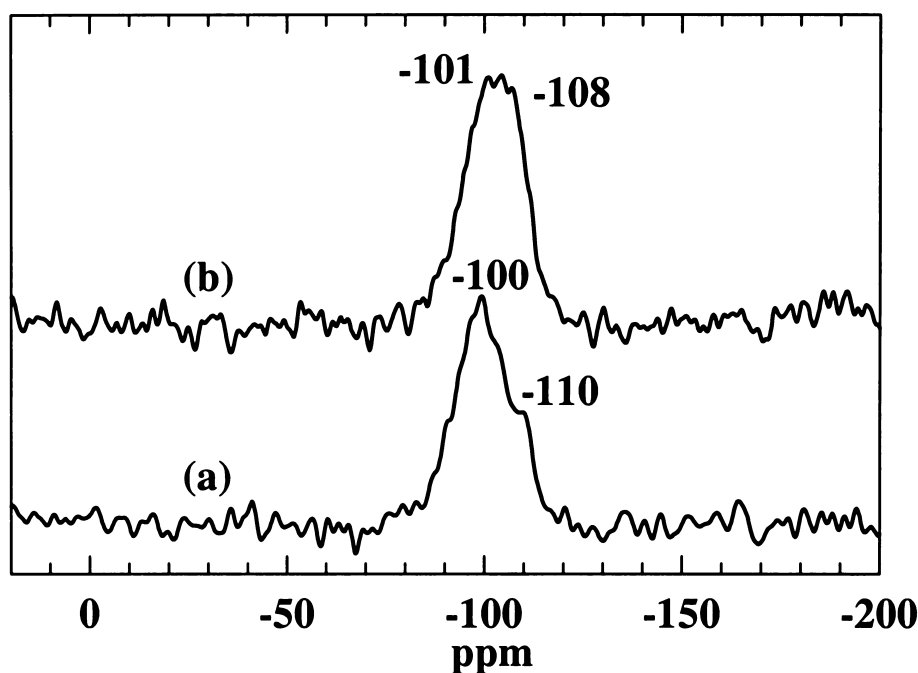


**Figure 3.10:**  $^{29}\text{Si}$ -MAS-NMR spectra of Al-MCM-41 (Si/Al = 7): (a) pre-washed (7); (b) calcined (7).

Figure 3.10 (a) shows the  $^{29}\text{Si}$ -MAS-NMR spectrum of acidic ethanol pre-washed Al-MCM-41 with Si/Al = 7 (designated as pre-washed (7)). The pre-washed (7) sample shows three peaks at ca. -100 and -110 ppm, which can be assigned to  $Q^3$  and  $Q^4$  coordination of Si atoms, respectively. The predominance of the  $Q^3$  in the  $^{29}\text{Si}$ -MAS-NMR spectrum of pre-washed (7) indicates that a larger amount of Al in the starting



synthesis gel mixture further decreases the precondensation of the silanol groups during hydrothermal synthesis. Also, the possibility of the Al segregation from the matrix of the high Al content Al-MCM-41 sample at high temperature cannot be ruled out.

Figure 3.10 (b) shows the  $^{29}\text{Si}$ -MAS-NMR spectrum of calcined Al-MCM-41 (Si/Al = 7) sample (designated as calcined (7)). After calcination, the calcined (7) shows chemical shift at  $-108$  ppm ( $\text{Q}^4$ ) and  $-101$  ppm ( $\text{Q}^3$ ). The spectrum again looks narrower than the pre-washed sample, indicating that the sample became more uniform after complete template removal. The  $\text{Q}^2$  species is not present in the calcined sample. The intensity of  $\text{Q}^3$  is close to that of  $\text{Q}^4$ , which is in line with the other Al-MCM-41 samples. The increases of  $\text{Q}^3$  with increasing Al content in the starting synthesis gel mixture indicate the relative number of Si-O-Al linkages increases at the expense of Si-O-Si moieties.<sup>34</sup>

### 3.3.1.3. Post-synthesized Al-MCM-41 (Si/Al = 14)

Figure 3.11 shows the  $^{29}\text{Si}$ -MAS-NMR spectra of the post-synthesized Al-MCM-41 (Si/Al = 14) before (Figure 3.11 (a)) and after (Figure 3.11 (b))  $\text{NH}_3$  treatment. Before  $\text{NH}_3$  treatment, the  $^{29}\text{Si}$ -MAS-NMR spectrum of Al-MCM-41 (PB- $\text{NH}_3$ ) exhibits a broad band with chemical shifts at ca.  $-100$ ,  $-107$  and  $-111$  ppm, which can be approximately assigned to  $\text{Q}^3$ ,  $\text{Si}(\text{OSi})_3(\text{OAl})$  and  $\text{Q}^4$  species respectively.

After  $\text{NH}_3$  treatment, the spectrum (Figure 3.11 (b)) shows three peaks at ca.  $-101$ ,  $-104$  and  $-107$  ppm, respectively, which can be assigned to  $\text{Q}^3$ ,  $\text{Si}(\text{OSi})_3(\text{OAl})$  and  $\text{Q}^4$  species respectively. The narrowness of the spectrum compared to that before  $\text{NH}_3$  treatment is also observed, indicating a more uniform framework structure for the Al-MCM-41 (PA- $\text{NH}_3$ ) sample.

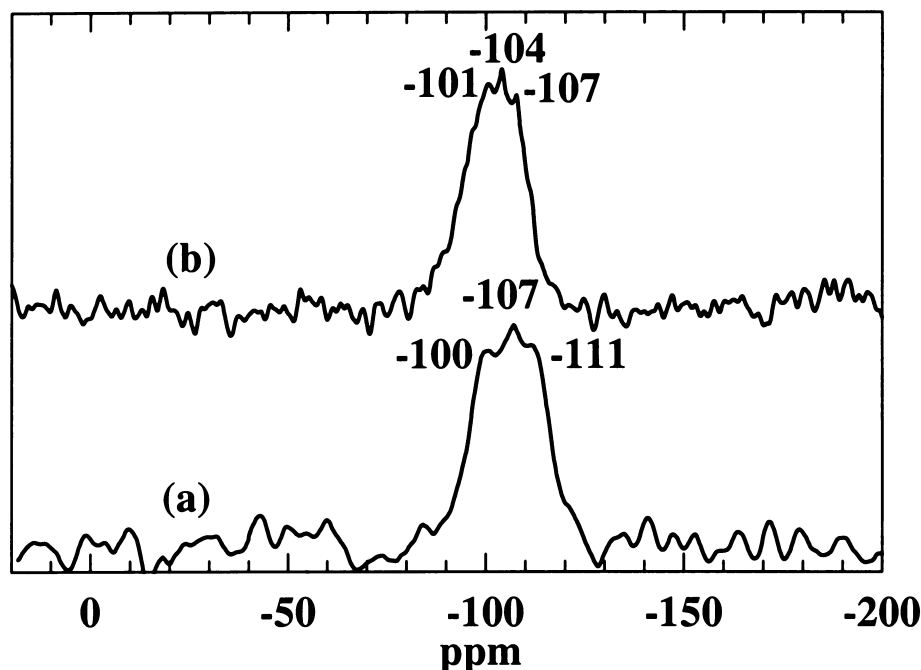


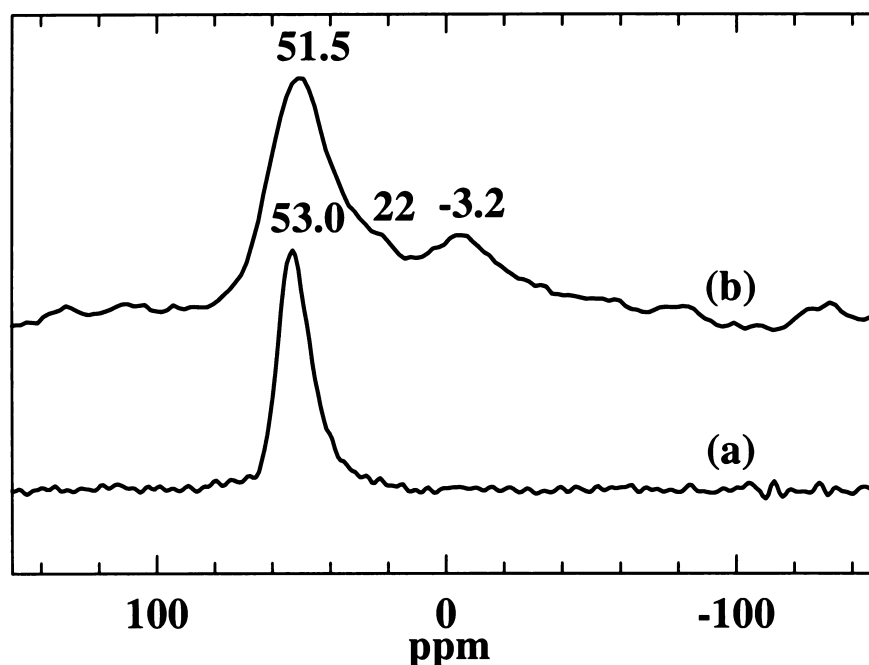
Figure 3.11.  $^{29}\text{Si}$ -MAS-NMR spectra of post-synthesized Al-MCM-41 (Si/Al = 14): (a) before  $\text{NH}_3$  treatment (Al-MCM-41 (PB- $\text{NH}_3$ )); (b) after  $\text{NH}_3$  treatment (Al-MCM-41 (PA- $\text{NH}_3$ )).

### 3.3.2. $^{27}\text{Al}$ -MAS-NMR Spectra

Usually in solid state  $^{27}\text{Al}$ -MAS-NMR spectra, the signals at ca. 52-55 ppm are due to tetrahedrally coordinated framework aluminium (tetrahedral Al), and those at ca. 0 ppm are assigned to distorted or octahedrally coordinated aluminium at extra-framework positions (extra-framework Al, or octahedral Al) or by the aluminium in a separated phase.<sup>14</sup> Tetrahedrally coordinated Al is of special interest and desirable species, because it is incorporated into the framework and therefore is responsible for the formation of the acid sites, while the octahedral Al species are occluded in the pores or exist as an amorphous by-product.<sup>7</sup> In  $^{27}\text{Al}$ -MAS-NMR spectra, five (25 ~ 42 ppm) and six-coordinated non-framework Al (-10 ~ 15 ppm) can also be observed if Al is in a distorted environment or in a low symmetry.<sup>51</sup>

### 3.3.2.1. Directly Hydrothermally Synthesized Al-MCM-41

#### 3.3.2.1.1. Al-MCM-41 (Si/Al = 39)



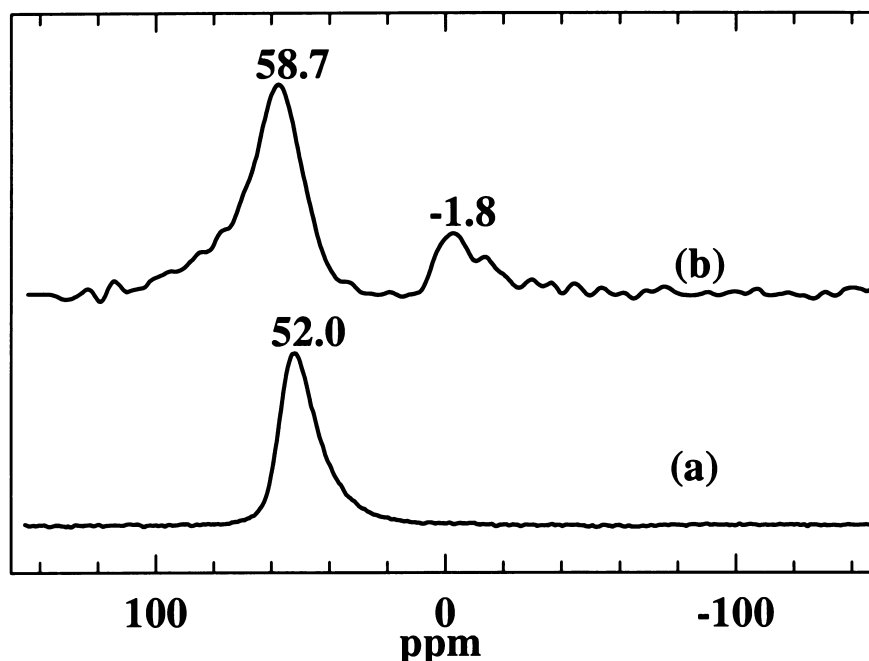
**Figure 3.12:**  $^{27}\text{Al}$ -MAS-NMR spectra of Al-MCM-41 (Si/Al = 39): (a) pre-washed (39); (b) calcined (39).

Figure 3.12 shows the  $^{27}\text{Al}$ -MAS-NMR spectra of pre-washed (39) (Figure 3.12 (a)) and calcined (39) (Figure 3.12 (b)). The pre-washed (39) sample exhibits only one peak with a chemical shift at ca. 53.0 ppm, which can be typically assigned to tetrahedrally coordinated Al species, indicating that Al is completely incorporated into the inorganic framework. After thermal calcination in the air-flow at 813 K, as generally observed, the peak is shifted to 51.5 ppm, accompanied by peak broadening and emergence of a new peak at ca. -3.2 ppm. This new peak is usually assigned to octahedrally coordinated Al.<sup>36,39</sup> The presence of the octahedral Al species indicates that calcination results in the extraction of the Al species from the framework. It is also noted that the

peak at ca. 51.5 ppm is not symmetrical, which is probably due to the formation of some five-coordinated Al species whose chemical shift is at ca. 30 ppm. The peak broadening after calcination may be an indication of the presence of Al in a more distorted environment or in a low symmetry due to the larger range of T-O-T bond angles (where T represents an individual  $\text{SiO}_4$  or  $\text{AlO}_4$  tetrahedron). The peak at ca. 22 ppm is tentatively assigned to the non-framework five coordinated Al.<sup>14,52-55</sup> The ratio between tetrahedral Al and octahedral Al can be calculated by comparing the integrated peak areas, which is ca. 3.5 for the calcined (39), i.e., about 22 % Al atoms are in the extra framework position.

#### 3.3.2.1.2. Al-MCM-41 (Si/Al = 15)

Figure 3.13 shows the  $^{27}\text{Al}$ -MAS-NMR spectra of pre-washed (15) (Figure 3.12 (a)) and calcined (15) (Figure 3.12 (b)). Like the pre-washed (39) sample, the pre-washed (15) exhibits only one peak with a chemical shift at ca. 52.0 ppm due to tetrahedrally coordinated Al species, indicating that most of the Al atoms are incorporated into the inorganic framework. After thermal calcination in the air-flow at 813 K, the peak for tetrahedral Al is shifted to 58.7 ppm, accompanied by peak broadening and emergence of a new peak at ca. -1.8 ppm due to octahedrally coordinated Al,<sup>36,39</sup> indicating that calcination results in the extraction of the Al species from the framework. No peak at ca. 25 ppm for five-coordinated Al is observed. The calculated peak area ratio between the tetrahedral Al and the octahedral Al is ca. 5 for the calcined (15), which means that about 17 % Al atoms are in the extra framework positions.



**Figure 3.13:**  $^{27}\text{Al}$ -MAS-NMR spectra of Al-MCM-41 (Si/Al = 15): (a) pre-washed (15); (b) calcined (15).

#### 3.3.2.1.3. Al-MCM-41 (Si/Al = 7)

Figure 3.14 shows the  $^{27}\text{Al}$ -MAS-NMR spectra of pre-washed (7) (Figure 3.14 (a)) and calcined (7) (Figure 3.14 (b)). The pre-washed (7) exhibits a peak with a chemical shift at ca. 53.9 ppm due to tetrahedrally coordinated Al species, and a tiny peak at ca. 3.0 ppm due to the octahedrally coordinated Al species, indicating that most of the Al atoms are incorporated into the inorganic framework. After thermal calcination in the air-flow at 813 K, the peak for tetrahedral Al is shifted to 50.6 ppm, accompanied by peak broadening. It is plausible to draw a conclusion from observation of only one broad peak that all of the Al atoms are incorporated into the framework. Since calcination expels Al out of the framework even at low Al content samples (Si/Al = 39 and 15), extraction of Al from higher Al content sample after calcination is inevitable. Assuming that the chemical shift of the octahedral Al is at 0 ppm, deconvolution of the

spectrum of the calcined (7) indicates that ca. 25 % Al atoms are in the extra framework position.

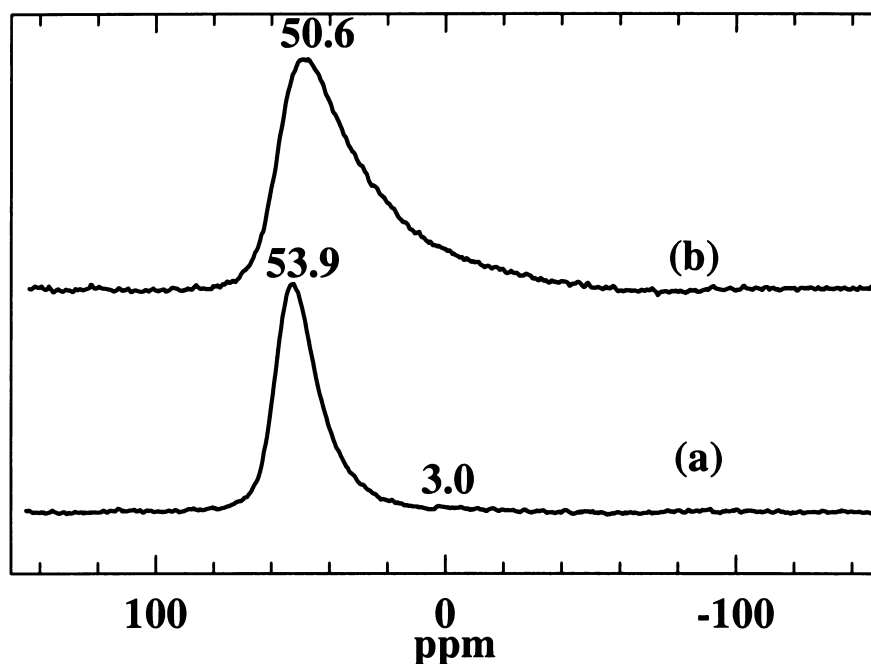
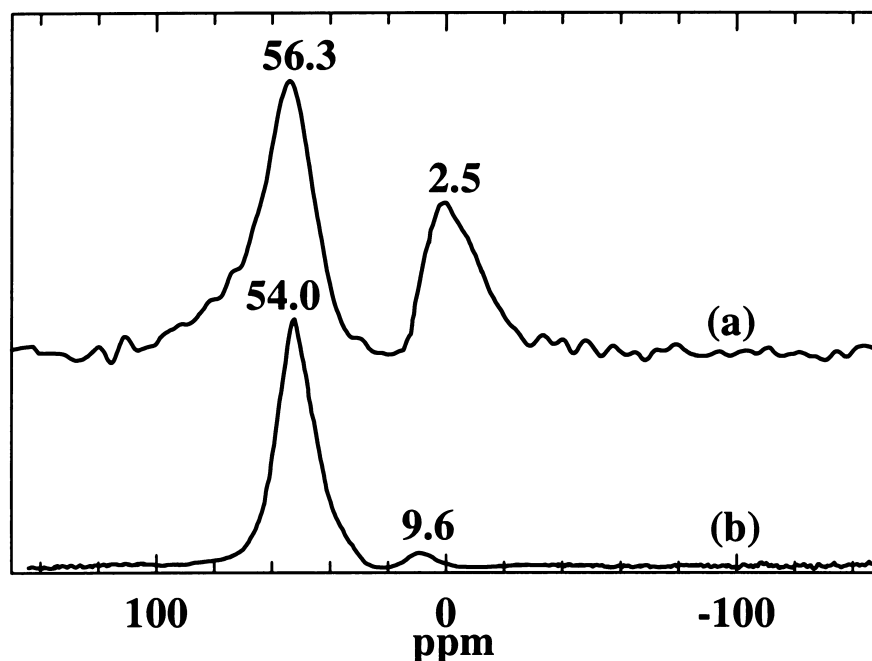


Figure 3.14:  $^{27}\text{Al}$ -MAS-NMR spectra of Al-MCM-41 (Si/Al = 7): (a) pre-washed (7); (b) calcined (7).

### 3.3.2.2. Post-synthesized Al-MCM-41 (Si/Al = 14)

Figure 3.15 shows the  $^{27}\text{Al}$ -MAS-NMR spectra of Al-MCM-41 (PB-NH<sub>3</sub>) (Figure 3.15 (a)) and Al-MCM-41 (PA-NH<sub>3</sub>) (Figure 3.15 (b)). Before NH<sub>3</sub> treatment, the Al-MCM-41 (PB-NH<sub>3</sub>) sample exhibits a peak at ca. 56.3 ppm due to tetrahedrally coordinated framework Al and another peak at ca. 2.5 ppm due to non-framework Al. The ratio between the tetrahedral framework Al and the non-framework Al, calculated by comparing the integrated peak areas, is about 2.5.



**Figure 3.15:**  $^{27}\text{Al}$ -MAS-NMR spectra of post-synthesized Al-MCM-41 (Si/Al = 14): (a) before  $\text{NH}_3$  treatment (Al-MCM-41 (PB- $\text{NH}_3$ )); (b) after  $\text{NH}_3$  treatment (Al-MCM-41 (PA- $\text{NH}_3$ )).

After further  $\text{NH}_3$  treatment, the product Al-MCM-41 (PB- $\text{NH}_3$ ) shows a dominant peak at ca. 54.0 ppm due to the tetrahedral framework Al and a small peak at ca. 9.6 ppm due to the non-framework Al. The increase of the tetrahedral Al is at the expense of the non-framework Al, i.e., most of the extra-framework Al is converted into the tetrahedral framework Al.<sup>56</sup> The peak area ratio between these two peaks is ca. 35, which means that there are only ca. 2.7 % Al atoms still in the extra framework position. Compared with the 17 % of the non-framework Al atoms in the calcined (15) sample, which was directly hydrothermally synthesized and has the similar Si/Al ratio as 15 in the initial gel mixture, it is obvious that the post-synthesis method is superior to the direct hydrothermal synthesis method in incorporating Al into the MCM-41 framework. The narrowness of the tetrahedral Al peak demonstrates that post-synthesis Al grafting method not only successfully incorporates Al into the MCM-41 framework,

but also provides a much more uniform aluminosilicate framework. This is consistent with the result of the XRD pattern study. The estimated extra-framework Al contents in Al-MCM-41 samples are summarized in Table 3.7.

**Table 3.7: The estimated extra-framework Al contents in Al-MCM-41 samples**

Sample	Al-MCM-41 (Si/Al=39)	Al-MCM-41 (Si/Al = 15)	Al-MCM-41 (Si/Al = 7)	Post-synthesized Al-MCM-41 (Si/Al =14)
<b>Extra-framework Al content %</b>	<b>22</b>	<b>17</b>	<b>25</b>	<b>2.7</b>

### 3.4. Chemical Composition of Synthesized (Al)-MCM-41 Samples

**Table 3.8: Chemical analysis results of Al-MCM-41 samples with different Si/Al ratios**

Sample	Molar Si/Al ratios	
	Gel mixture	ICP-AES result
Calcined (39)	39	45
Calcined (15)	15	17
Calcined (7)	7	10

The Si/Al ratios of three calcined Al-MCM-41 samples have been determined by inductively coupled plasma atomic emission spectroscopy (ICP-AES) analyses and the results are summarized in Table 3.8. The Si/Al ratios calculated based on the ICP-AES results are larger than those in the gel mixtures.<sup>57,58</sup> This may be due to the loss of Al during hydrothermal synthesis or template removal by combining EtOH/HCl extraction and thermal calcination. It can be seen from the ICP-AES analyses that most of the Al



present in the starting gel mixture is retained in the MCM-41 as tetrahedral or octahedral Al species, as evidenced by the  $^{27}\text{Al}$ -MAS-NMR spectra.

### 3.5. Surface Properties

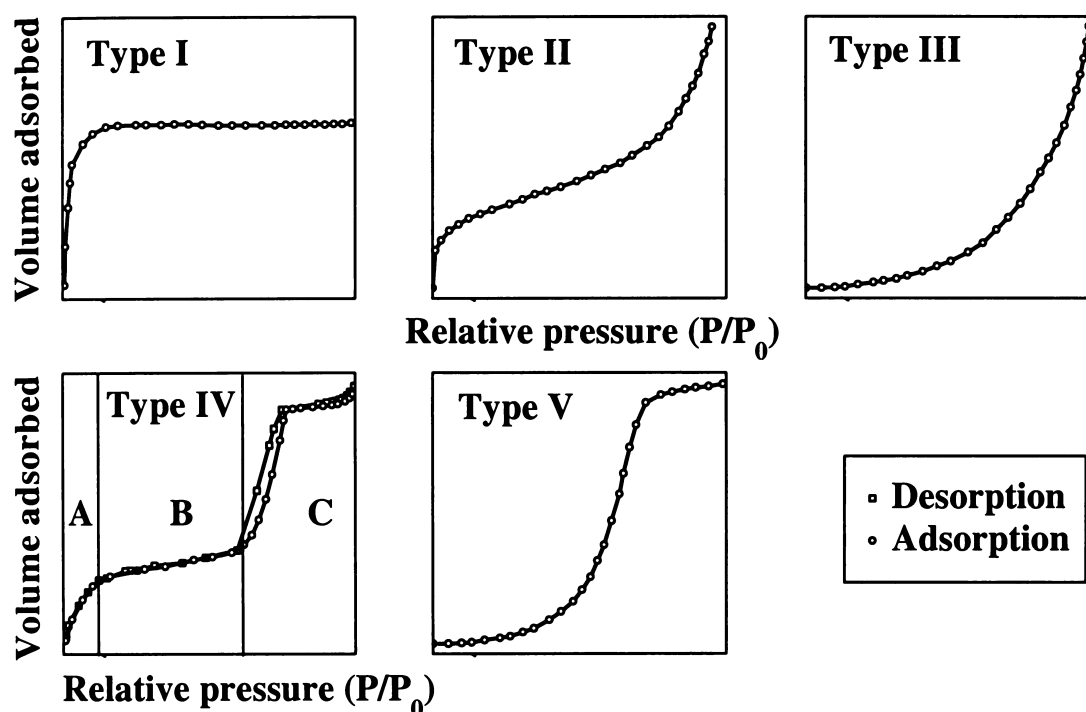


Figure 3.16: Five types of sorption isotherms according to the classification of Brunauer et al. In Type IV isotherm, region A, B and C correspond to the stage of forming monolayer, multilayer and capillary condensation, respectively.

There are various methods to characterize the surface properties. Usually, the most frequently used three parameters *specific surface area*, *pore size distribution* and *particle size* are sufficient to fully characterize the surface properties of the mesoporous MCM-41 matrix. The specific surface area gives a microscopical image of the surface loading, while the pore size distribution gives a deeper insight into the availability of the reactive surface silanols and sorption characteristics. The particle size is an

underlying parameter for the surface area and pore size. Information on surface area and porosity can be obtained by direct measurement of the particle size and *vice versa*.

These surface properties can be obtained by analyzing the gas (usually N<sub>2</sub>) sorption isotherm at temperature (77 K for nitrogen) at which the gas at atmospheric pressure is in the liquid state. The sorption isotherms can be grouped into five types (see Figure 3.16), according to the classification of Brunauer, Emmet and Teller (BET classification).<sup>59,60</sup> According to the IUPAC classification, the pores can be also classified into four types, which is given in Table 3.9. Type I isotherms are characteristic for microporous adsorbents, such as zeolites and carbons, Type IV isotherms are typical for the mesoporous adsorbents, such as MCM-41. At low relative pressure, a monolayer of the adsorbate forms on the surface (region A in type IV). Further increasing the relative pressure, a multilayer of the adsorbate (region B in type IV) will be formed. Then depending on the pore diameter, capillary condensation occurs (region C in type IV), resulting in a further increase of the adsorbed volumes of the adsorbate. The horizontal branch goes up nearly to the saturation pressure ( $P/P_0 = 1$ ), indicating that all mesopores are filled with liquid adsorbate. The desorption branch does not follow the adsorption branch, but gives a distinct hysteresis loop: the amount adsorbed is always greater along the desorption branch compared to the adsorption branch. This kind of hysteresis is due to the capillary condensation of the adsorbate in the pores, causing an increase of the amount of the adsorbate during the adsorption run, and a consequent retardation during the desorption. The increasing adsorption volume at relative pressure near the saturation pressure corresponds in all cases to the capillary condensation between the mesophase particles. This region, together with the monolayer region will not be considered in this study due to lack of significant information about the surface properties. The shift of the inflection point toward the low

relative pressure indicates some particles with smaller pore sizes are formed. Tanev et al.<sup>61</sup> showed that the desorption branch usually carries more information about the degree of pore blocking than the adsorption branch and BJH computation procedure can be satisfactorily applied in practice. The pore size distributions of the (Al)-MCM-41 samples are analyzed using BJH method.<sup>62</sup> based on the nitrogen desorption isotherm (For the BJH pore size distribution method and its assumptions, please refer to Section 2.5.5 in Chapter 2).

**Table 3.9: IUPAC classification of pores.**

Type of pores	Pore diameters (nm)
Micropores	0-2
Mesopores	2-50
Macropores	50-7500
Megapores	>7500

### 3.5.1. Thermally Calcined Purely Siliceous MCM-41

Figure 3.17 shows the nitrogen adsorption-desorption isotherms of calcined MCM-41, which are typical type IV isotherms according to the BET classification.<sup>59,60</sup> At the adsorption branch, the amount of adsorbed N<sub>2</sub> increases gradually with an increase of the relative pressure  $P/P_0$  by multilayer adsorption. Over a narrow range of relative pressure  $P/P_0$  between ca. 0.35 and 0.45, a distinct sudden uptake of the adsorbed amount is observed, which is due to the capillary condensation of N<sub>2</sub> in the mesopores. The horizontal branch from relative pressure  $P/P_0 = 0.45$  to the near saturation pressure  $P/P_0 = 0.97$  indicates that all mesopores are filled with liquid N<sub>2</sub>. The desorption branch of the isotherm basically coincides with the adsorption branch except that a slight hysteresis due to capillary condensation is observed.

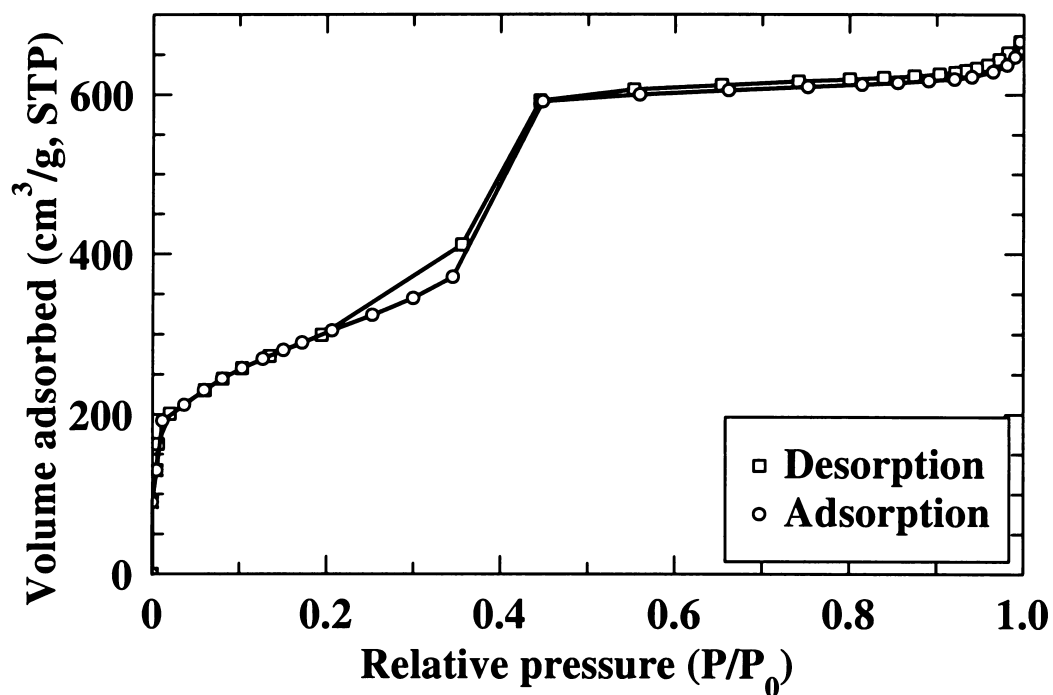


Figure 3.17: Nitrogen adsorption-desorption (77 K) isotherms of calcined MCM-41.

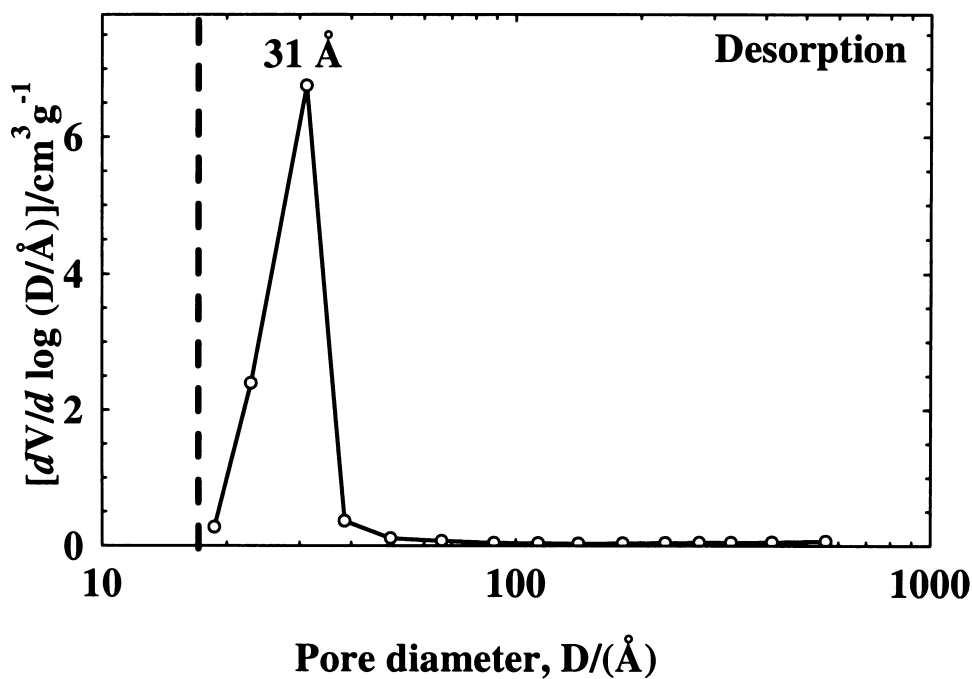
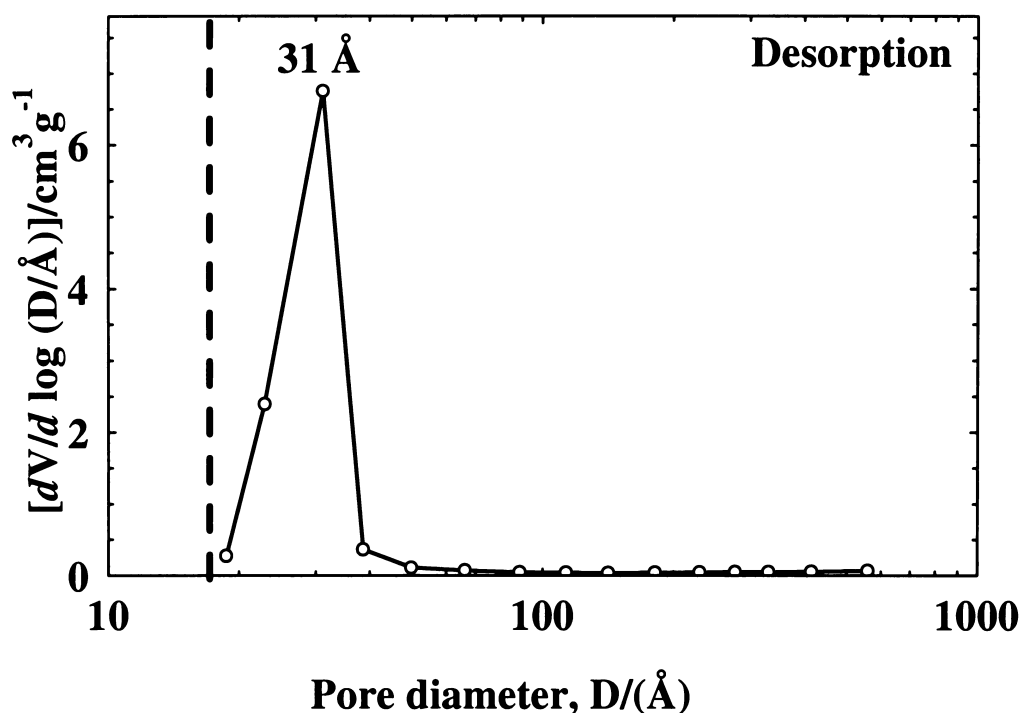


Figure 3.18: BJH pore size distributions of calcined MCM-41 based on the nitrogen desorption isotherm.

According to the  $N_2$  adsorption-desorption isotherm, the calculated BET surface area is about  $1094 \text{ m}^2/\text{g}$ . The BJH average pore volume is about  $1.1 \text{ m}^3/\text{g}$  and the BJH

average pore diameter is about 31 Å, which is in the mesopore size range. The high surface area and the large pore volume are typical surface properties of MCM-41.<sup>1</sup> Using the adjacent pore center distance obtained from the corresponding XRD pattern, the calculated pore wall thickness is ca. 17 Å, which is comparable with the assumed value in the XRD pattern study.



**Figure 3.18: BJH pore size distributions of calcined MCM-41 based on the nitrogen desorption isotherm.**

Figure 3.18 shows the BJH pore size distribution plot based on the N<sub>2</sub> desorption isotherm. It can be seen that the pore size is centered at ca. 31 Å. The sharp and narrow pore size distribution indicates that the calcined MCM-41 has uniform pore structure with large domain size, which is consistent with the XRD result.

### 3.5.2. Directly Hydrothermally Synthesized Al-MCM-41 Samples

#### 3.5.2.1. Thermally Calcined (39)

Figure 3.19 shows the nitrogen adsorption-desorption isotherms of calcined (39). At the adsorption branch, a steep increase of the adsorbed volume at relative pressure  $P/P_0$  between ca. 0.30 and 0.45 is observed, which is due to the capillary condensation. This range is wider than that observed for purely siliceous MCM-41. The near flat branch after relative pressure  $P/P_0 = 0.45$  indicates all mesopores are filled with liquid  $N_2$ . The desorption branch of the isotherm is basically coincident with the adsorption branch except that a distinct hysteresis takes place. The hysteresis in the range 0.5 to 0.8 is not due to incomplete outgassing but to the presence of larger mesopores. The entire isotherm shows the characteristic of type IV mesopore isotherm.

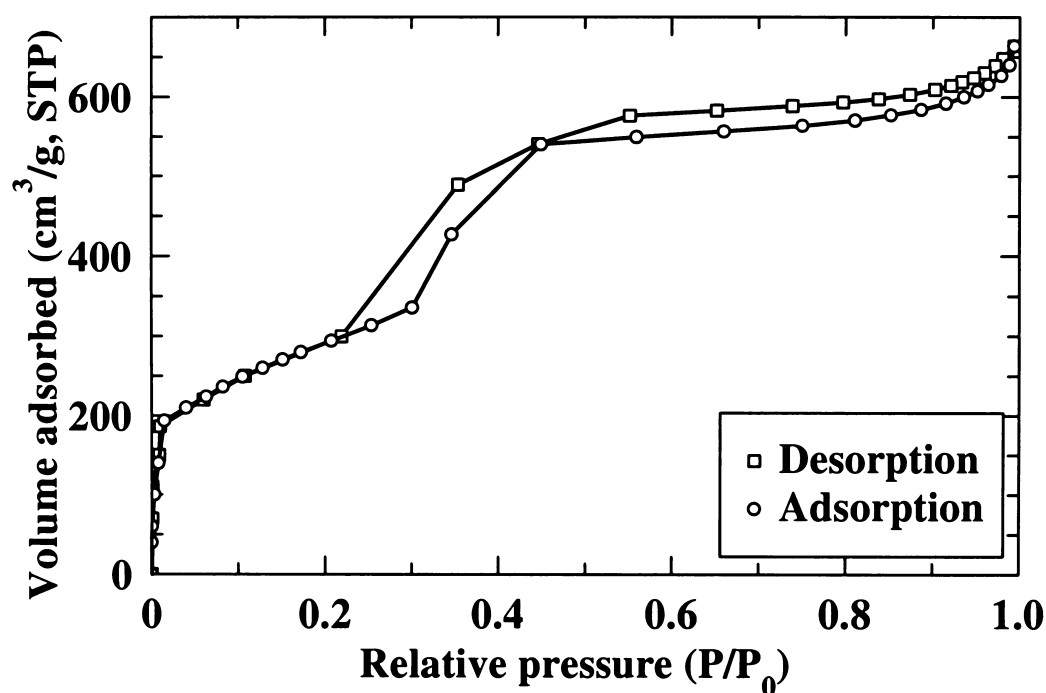


Figure 3.19: Nitrogen adsorption-desorption (77 K) isotherms of calcined (39).

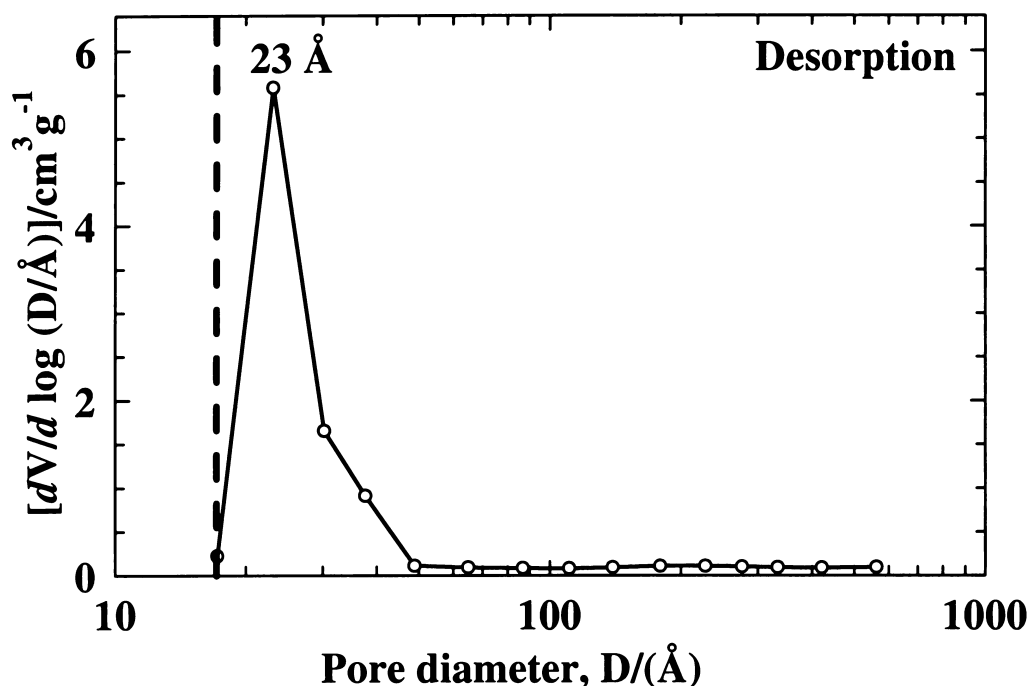


Figure 3.20: BJH pore size distributions of calcined (39) based on the nitrogen desorption isotherm.

The calculated BET surface area is about 1057 m<sup>2</sup>/g, smaller than that of the pure MCM-41. Based on the desorption isotherm, the BJH average pore volume is about 1.1 m<sup>3</sup>/g and the BJH average pore diameter is about 28 Å. Using the adjacent pore center distance obtained from the corresponding XRD pattern, the calculated pore wall thickness is ca. 19 Å, comparable with the largest pore wall thickness reported in the literature.<sup>8</sup>

Figure 3.20 shows the BJH pore size distribution plot based on the N<sub>2</sub> desorption isotherm. It can be seen that the pore size is centered at ca. 23 Å. Compared with the pure siliceous MCM-41, the pore size of the calcined (39) sample is smaller, indicating that Al incorporation really reduces the average pore size. Furthermore, observation of an expansion of the low adsorbed volume part in the pore size distribution plot indicates that some slightly larger mesopores coexist.<sup>63</sup> This may be explained as follows: given enough time for the AlO<sub>2</sub><sup>-</sup> ions to diffuse into the initially formed silicate mesophase,

the stronger electrostatic interaction between the  $\text{AlO}_2^-$  and the positively charged quaternary ammonium head groups of CTAC micelle in the initial gel mixture will bind the  $\text{AlO}_2^-$  tightly close to the surfactant. This kind of “binding” effect will result in uneven dispersion of the  $\text{NaAlO}_2$  aluminum source during hydrothermal synthesis. Furthermore, low Al loading level will also leave some mesophases unaluminated due to the Al distribution may not be homogeneous at low Al levels. Thus it is inevitable that some aluminated mesophases with different pore sizes will be formed and coexist with unaluminated siliceous mesophases. Careful analysis of the nitrogen adsorption-desorption isotherms also shows that the capillary condensation (pore filling) step actually consists of two stages: first stage is at lower relative pressure  $P/P_0$  region in the range of 0.30 to 0.35, which can be ascribed to the filling of the aluminated pores (smaller pore size); and the second stage is at a successive higher relative pressure region in the range of 0.35 to 0.45, which can be ascribed to non-aluminated pores. Although there is no evidence of splittings in the XRD patterns, the Al segregation effect cannot be completely ruled out in the Al-MCM-41 samples (including the other Al-MCM-41 samples studied in this work), which needs to be further examined.

#### 3.5.2.2. Thermally calcined (15)

Figure 3.21 shows the nitrogen adsorption-desorption isotherms of calcined (15). At the adsorption branch, a rapid increase of the adsorbed volume at relative pressure  $P/P_0$  between ca. 0.26 and 0.46 is observed, which is due to the capillary condensation. This range is wider than that observed for the calcined (39), indicating that increasing the amount of incorporated Al further decreases the uniformity of the pore structure. The desorption branch basically coincides with the adsorption branch. A hysteresis loop due



to the capillary condensation is also observed. However, the entire curve still maintains well the characteristic of type IV mesopore isotherm.

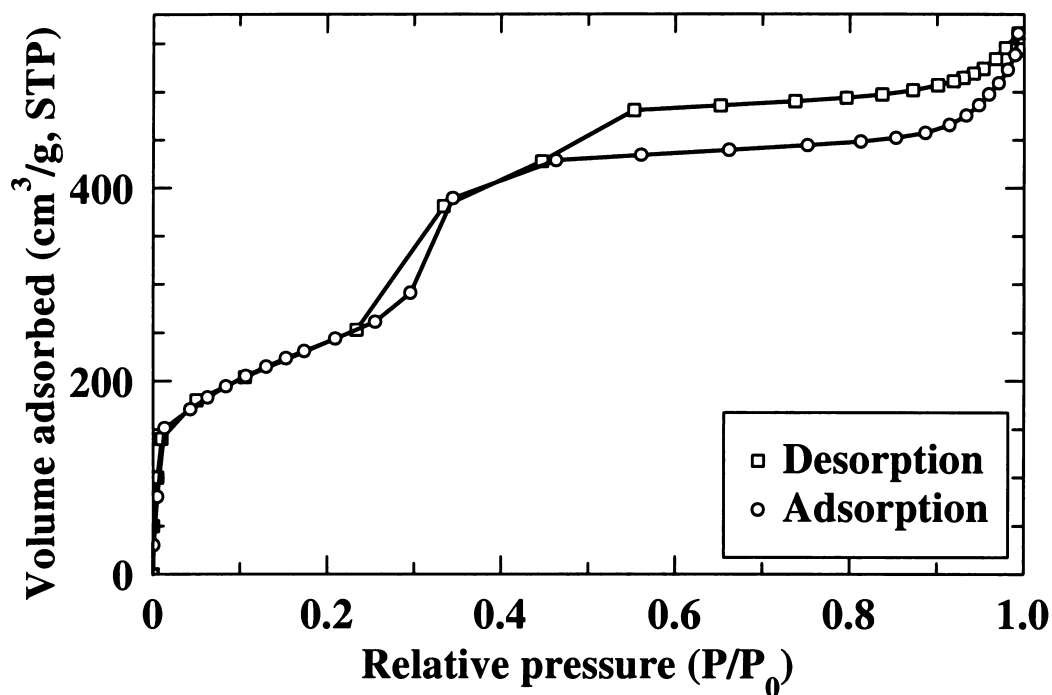


Figure 3.21: Nitrogen adsorption-desorption (77 K) isotherms of calcined (15).

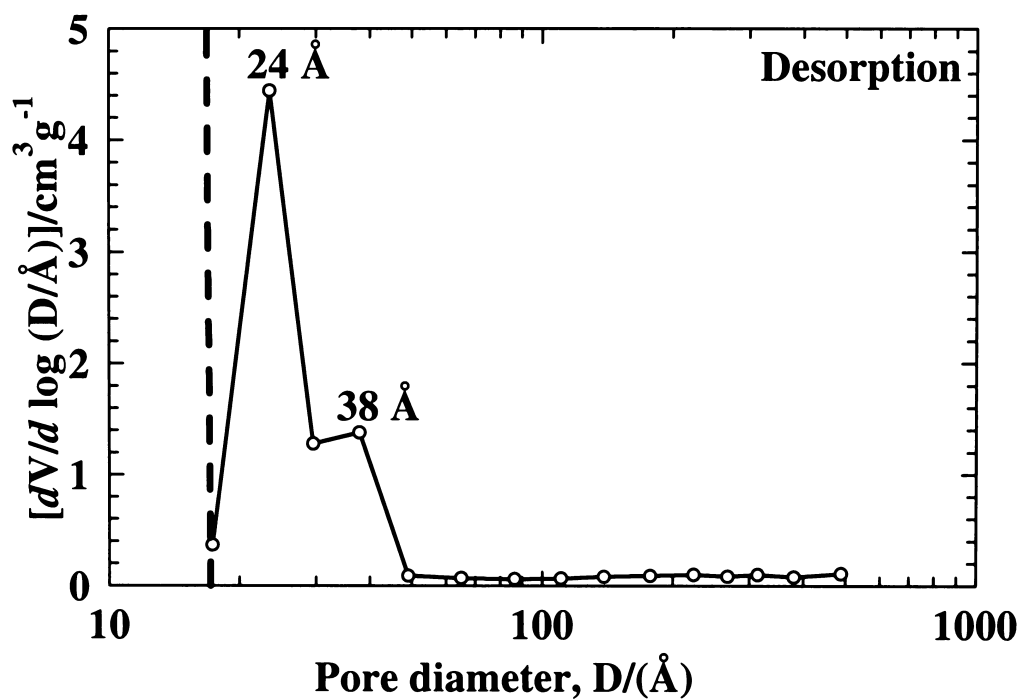


Figure 3.22: BJH pore size distributions of calcined (15) based on the nitrogen desorption isotherm.

The calculated BET surface area is about  $876 \text{ m}^2/\text{g}$ , smaller than that of the calcined (39) sample, indicating that the surface area decreases as the incorporated Al content increases. Based on the desorption isotherm, the BJH average pore volume is about  $0.9 \text{ m}^3/\text{g}$  and the BJH average pore diameter is about  $29 \text{ \AA}$ . Using the adjacent pore center distance obtained from the corresponding XRD pattern, the calculated pore wall thickness is ca.  $16 \text{ \AA}$ .

Figure 3.22 shows the BJH pore size distribution plot based on the  $\text{N}_2$  desorption branch. It can be seen that the pore size is centered at ca.  $23.5 \text{ \AA}$ , accompanied by a shoulder peak at  $38 \text{ \AA}$ , again indicating the coexistence of mesoporous particles with different pore sizes. As suggested before, this kind of bimodal pore size distribution was due to the existence of some unaluminated mesopores.

### 3.5.2.3. Thermally calcined (7)

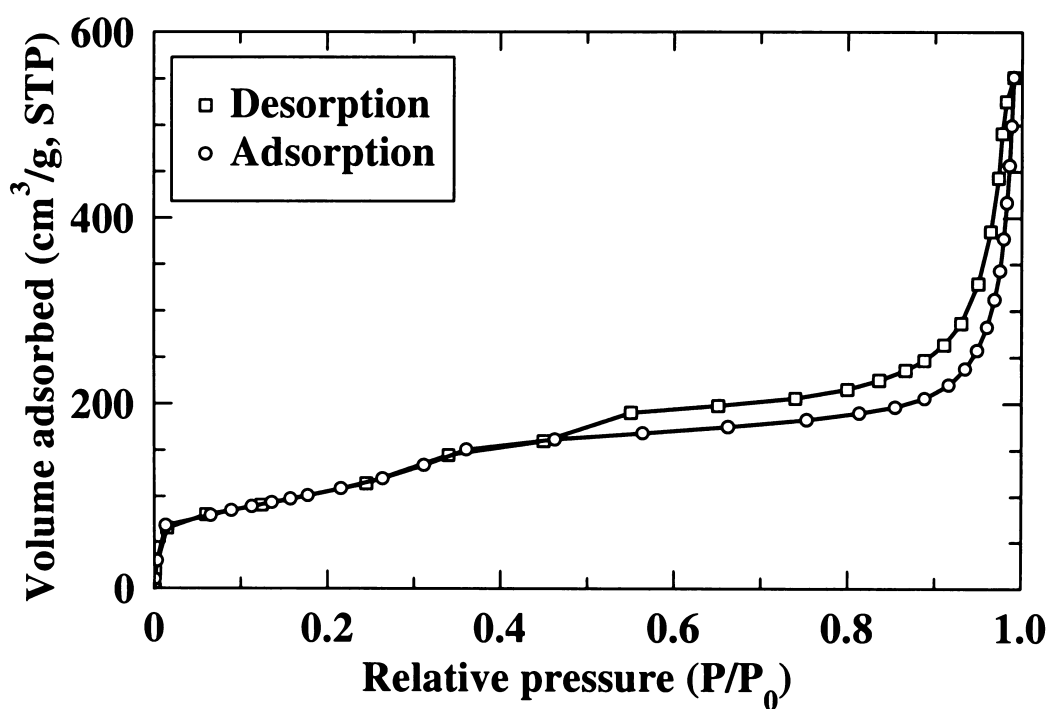


Figure 3.23: Nitrogen adsorption-desorption (77 K) isotherms of calcined (7).

Figure 3.23 shows the nitrogen adsorption-desorption isotherms of calcined (7). The adsorption branch looks like a typical type II isotherm, which corresponds to macroporous adsorbents. A sudden uptake of the adsorbed volume in the mesoporous region was not observed. However, in the desorption branch, a step at relative pressure  $P/P_0$  between ca. 0.34 and 0.55 was observed, indicating that the mesoporous hexagonal structure of the calcined (7) sample has been poorly developed. This remark is consistent with the observation in XRD study. The shift of the inflection point toward the higher relative pressure indicates that some particles with larger pores are formed. The observed hysteresis at high  $P/P_0$  is due to inter-particle porosity. The calculated BET surface area is about  $389 \text{ m}^2/\text{g}$ . Low surface area and loss of the capillary condensation step in the mesoporous region indicate that the mesoporosity has gone.

### 3.5.3. Post-synthesized Al-MCM-41 (Si/Al = 14)

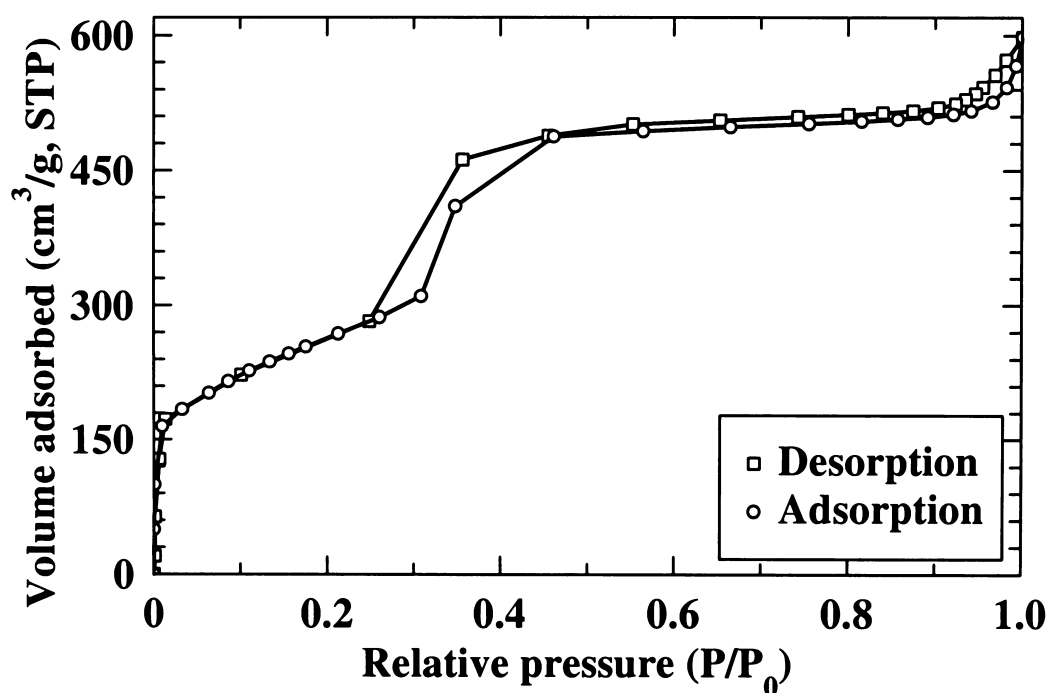
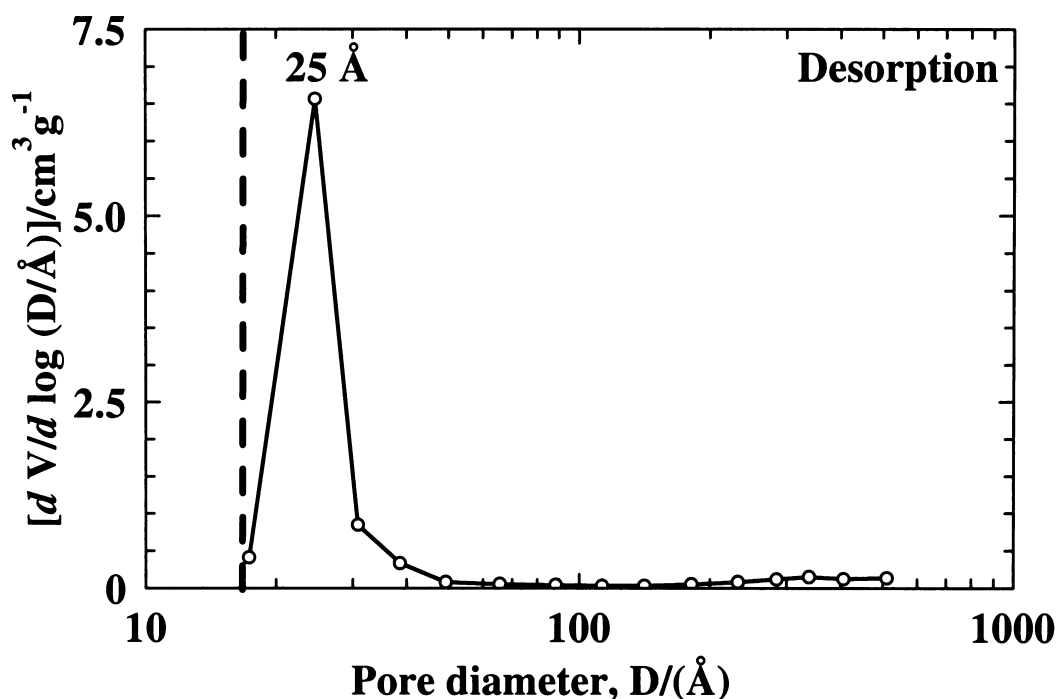


Figure 3.25: Nitrogen adsorption-desorption (77 K) isotherms of post-synthesized Al-MCM-41 (Si/Al=14) after  $\text{NH}_3$  treatment.

Figure 3.25 shows the nitrogen adsorption-desorption isotherms of post-synthesized Al-MCM-41 with Si/Al = 14 in the grafting gel mixture. At the adsorption branch, a sudden uptake of the adsorbed volume at relative pressure  $P/P_0$  between ca. 0.26 and 0.46 was observed, which is due to the capillary condensation. This range is the same as that of the calcined (15). Though the adsorption branch shows two-step capillary condensation due to the pore filling, the desorption branch doesn't. Since the desorption branch is more reliable and carries more accurate information about the surface properties,<sup>61</sup> it seems that post-synthesized Al-MCM-41 (Si/Al =14) generates more uniform pore structure. A hysteresis loop due to the capillary condensation is also observed. The entire curve is the characteristic of type IV mesopore isotherm.



**Figure 3.26: BJH pore size distributions of post-synthesized Al-MCM-41 (Si/Al=14) (after  $\text{NH}_3$  treatment) based on the nitrogen desorption isotherm.**

The calculated BET surface area is about  $958 \text{ m}^2/\text{g}$ , smaller than purely siliceous MCM-41, but larger than that of the calcined (15) sample. Based on the nitrogen

desorption isotherm, the BJH average pore volume is about  $1.0 \text{ m}^3/\text{g}$  and the BJH average pore diameter is about  $29.6 \text{ \AA}$ . Using the adjacent pore center distance obtained from the corresponding XRD pattern, the calculated pore wall thickness is ca.  $14 \text{ \AA}$ .

Figure 3.26 shows the BJH pore size distribution plot based on the  $\text{N}_2$  desorption isotherm. It can be seen that the pore size is centered at ca.  $24.6 \text{ \AA}$ . Unlike the directly hydrothermally synthesized calcined (15), no coexistence of other pores is observed, indicating grafting Al using post-synthesized method provides more uniform pore structure. This is consistent with the result of the isotherm analyses.

The data of the surface properties of the (Al)-MCM-41 samples discussed above are summarized in Table 3.10. The value of the pore wall thickness is comparable with the reports in the literature.<sup>8,64,65</sup>

**Table 3.10: Surface properties of the (Al)-MCM-41 samples synthesized in this work**

Sample	Calcined MCM-41	Calcined (39)	Calcined (15)	Calcined (7)	Post- synthesized (14)
BET surface area ( $\text{m}^2/\text{g}$ )	1094	1057	876	389	958
BJH pore volume ( $\text{cm}^3/\text{g}$ )	1.1	1.1	0.9	-	1.0
BJH average pore diameter ( $\text{\AA}$ )	31	28	29	-	28
Adjacent pore center distance (XRD) ( $\text{\AA}$ )	47	47	45	-	42
Pore wall thickness ( $\text{\AA}$ )	17	19	16	-	14

**Notes:** (a) the number in the parenthesis is from the BJH adsorption pore size distribution plot; (b) the number in the parenthesis is an average pore size from the BJH desorption pore size distribution plots; (c) the number in the parenthesis is the average of number of (a) and (b).

### 3.6. Summary

In summary, purely siliceous MCM-41 and three Al-MCM-41 samples with Si/Al =  $\infty$ , 39, 15 and 7 have been successfully synthesized by hydrothermally directly synthesis method. Also an Al-MCM-41 with Si/Al ratio of 14 has been synthesized using post-synthesized method. The structure and surface properties of the samples were characterized with XRD patterns, solid state  $^{29}\text{Si}$ -MAS-NMR and  $^{27}\text{Al}$ -MAS-NMR, ICP-AES elemental analyses and nitrogen adsorption-desorption isotherms.

XRD patterns show that, after removal of the CTAC template by thermal calcination, the purely siliceous MCM-41 has well ordered pore structure with long range ordering. However, calcination of the directly hydrothermally synthesized Al-MCM-41 samples results in less uniform pore structures and loss of long range ordering, especially in higher Al content samples. Interestingly, the post-synthesized Al-MCM-41 sample shows better long range ordering compared with the directly hydrothermally synthesized samples.

The  $^{29}\text{Si}$ -MAS -NMR study shows that all of the calcined samples have more Si atoms in  $\text{Q}^4$  coordination than in other coordination states, which is a result of the condensation of the silanol groups during high temperature calcination. In all samples,  $\text{Q}^3$  can not be completely converted into  $\text{Q}^4$ , because they are needed to compensate the charge balancing in the matrix. During direct hydrothermal synthesis of Al-MCM-41, the  $\text{AlO}_2^-$  ions are incorporated into the tetrahedral Al position, which is evidenced by the  $^{27}\text{Al}$ -MAS-NMR spectra of the pre-washed Al-MCM-41 samples. The strong interaction between the charge balancing CTAC surfactant molecules and the framework Al sites causes the lattice contraction, which is reflected by the reduction of the  $d_{100}$  space in the XRD patterns with increasing the incorporated Al content.

The  $^{27}\text{Al}$ -MAS-NMR investigation indicates that all (or most) of the Al in the gel mixture are incorporated into the MCM-41 framework as tetrahedral Al. Unfortunately, removal of the CTAC template by thermal calcination results in the formation of certain amount of undesired extra-framework Al. The post-synthesis method indicates that proper  $\text{NH}_3$  treatment after initial Al incorporation in the MCM-41 can convert the extra-framework Al into tetrahedrally coordinated framework Al.

The nitrogen adsorption-desorption isotherms study demonstrates that the purely siliceous MCM-41 has an average pore diameter around 31 Å as well as high surface area, large pore volume, narrow pore size distribution and thick pore wall thickness. For the Al-MCM-41, with increase of the Al content in the gel mixture, the surface area and the pore volume decrease. Coexistence of the mesophases with different pore sizes is also observed for the Al-MCM-41 samples, suggesting that alumination leads to less uniformity of the pore structure.

The template removed (Al)-MCM-41 has one dimensional hexagonal pore structure with average pore size ca. 30-40 Å, which is large enough for the normal organic molecules to diffuse in. Provided its catalysis activity is improved, it would be a good host for processing large feeding stocks.

Formation of tetrahedral Al in the MCM-41 framework requires charge balancing cations, like sodium ions beside the cationic head groups of the surfactant, which can contribute in compensating the additional anionic charge introduced by the aluminum. After template removal, the additional negative charge in the framework has to be compensated. If this negative charge cannot be compensated by the non-framework cationic species, the framework itself has to create some positively charged sites to meet the charge balancing requirement. Thus positively and negatively charged local sites on the framework are formed, which may act as redox active sites. Positively charged sites

perform as electron acceptor sites, while negatively charged sites as electron donor sites. This kind of redox sites, together with the electrostatic fields and the polar microenvironment, will provide fascinating potential applications in many research fields.

### 3.7. References for Chapter 3

- (1) Beck, J. S.; Vartuli, J. C.; Roth, W. J.; Leonowicz, M. E.; Kresge, C. T.; Schmitt, K. D.; Chu, C. T.-W.; Olson, D. H.; Sheppard, E. W.; McCullen, S. B.; Higgins, J. B.; Schlenker, J. L. *J. Am. Chem. Soc.* **1992**, *114*, 10834.
- (2) Edler, K. J.; White, J. W. *Chem. Mater.* **1997**, *9*, 1226.
- (3) Mokaya, R.; Zhou, W.; Jones, W. *Chem. Commun.* **1999**, 51.
- (4) Khushalani, D.; Kuperman, A.; Coobs, N.; Ozin, G. A. *Chem. Mater.* **1996**, *8*, 2188.
- (5) Schacht, S.; Janicke, M.; Schüth, F. *Microporous and Mesoporous Mater.* **1998**, *22*, 485.
- (6) Cai, Q.; Lin, W.-Y.; Xiao, F.-S.; Pang, W.-Q.; Chen, X.-H.; Zou, B.-S. *Microporous and Mesoporous Mater.* **1999**, *32*, 1.
- (7) Ciesla, U.; Schüth, F. *Microporous and Mesoporous Mater.* **1999**, *27*, 131.
- (8) Cheng, C.-F.; Park, D. H.; Klinowski, J. *J. Chem. Soc., Faraday Trans.* **1997**, *93*, 193.
- (9) Zhao, X. S.; Lu, G. Q.; Millar, G. J.; Li, X. S. *Catal. Lett.* **1996**, *38*, 33.
- (10) Biz, S.; Occelli, M. L. *Catal. Rev.-SCI. ENG.* **1998**, *40*, 329.
- (11) Kim, J. M.; Kwak, J. H.; Jun, S.; Ryoo, R. *J. Phys. Chem.* **1995**, *99*, 16742.
- (12) Ryoo, R.; Jun, S.; Kim, J. M.; Kim, M. J. *Chem. Commun.* **1997**, 2225.
- (13) Kresge, C. T.; Leonowicz, M. E.; Roth, W. J.; Vartuli, J. C.; Beck, J. S. *Nature* **1992**, *359*, 710.
- (14) Chen, C. Y.; Burkett, S. L.; Li, H. X.; Davis, M. E. *Microporous Mater.* **1993**, *2*, 17.
- (15) Janicke, M.; Kumar, D.; Stucky, G. D.; Chmelka, B. F. *Stud. Surf. Sci. Catal.* **1994**, *84*, 243.



- 
- (16) Ryoo, R.; Kim, J. M. *J. Chem. Soc., Chem. Commun.* **1995**, 711.
- (17) Luan, Z.; He, H.; Zhou, W.; Klinowski, J. *J. Chem. Soc., Faraday Trans.* **1998**, *94*, 979.
- (18) Anderson, M. T.; Martin, J. E.; Odinek, J.; Newcomer, P. In *"Access in Nanoporous materials"*; Pinnavaia, T. J., Thorpe, M. F., Eds.; Plenum Press: New York, 1995, p 29.
- (19) Marler, B.; Oberhagemann, U.; Vortmann, S.; Gies, H. *Microporous Mater.* **1996**, *6*, 375.
- (20) Glinka, C. J.; Nicol, J. M.; Stucky, G. D.; Ramli, E.; Margolese, D.; Huo, Q.; Higgins, J. B.; Leonowicz, M. E. *J. Porous Mater.* **1996**, *3*, 93.
- (21) Edler, K. J.; White, J. W. *J. Chem. Soc., Chem. Commun.* **1995**, 155.
- (22) Hammond, W.; Prouzet, E.; Mahanti, S. D.; Pinnavaia, T. J. *Microporous and Mesoporous Mater.* **1999**, *27*, 19.
- (23) Hitz, S.; Prins, R. *J. Catal.* **1997**, *168*, 194.
- (24) Firouzi, A.; Kumar, D.; Bull, L. M.; Besier, T.; Sieger, P.; Huo, Q. S.; Walker, S. A.; Zasadzinski, J. A.; Glinka, C.; Nicol, J.; Margolese, D.; Stucky, G. D.; Chmelka, B. *F. Science* **1995**, *267*, 1138.
- (25) Huo, Q.; Margolese, D. I.; Stucky, G. D. *Chem. Mater.* **1996**, *8*, 1147.
- (26) Sayari, A.; Liu, P.; Kruk, M.; Jaroniec, M. *Chem. Mater.* **1997**, *9*, 2499.
- (27) Yang, H.; Coombs, N.; Sokolov, I.; Ozin, G. A. *Nature* **1995**, *381*, 589.
- (28) Yang, H.; Kuperman, A.; Coombs, N.; Mamiche-Afara, S.; Ozin, G. A. *Nature* **1996**, *379*, 703.
- (29) Huo, Q.; Margolese, D. I.; Ciesla, U.; Feng, P.; Gier, T. E.; Sieger, P.; Leon, R.; Petroff, P. M.; Schüth, F.; Stucky, G. D. *Nature* **1994**, *368*, 317.
- (30) Tanev, P. T.; Chibwe, M.; Pinnavaia, T. J. *Nature* **1994**, *368*, 321.
- (31) Mokaya, R.; Jones, W. *Chem. Commun.* **1998**, 1839.
- (32) Reddy, K. M.; Song, C. *Stud. Surf. Sci. Catal.* **1998**, *117*, 291.
- (33) Hamdan, H.; Endud, S.; He, H.; Muhih, M. N. M.; Klinowski, J. *J. Chem. Soc., Faraday Trans.* **1996**, *92*, 2311.
- (34) Janicke, M. T.; Landry, C. C.; Christiansen, S. C.; Birtalan, S.; Stucky, G. D.; Chmelka, B. F. *Chem. Mater.* **1999**, *11*, 1342.
- (35) Luan, Z.; Cheng, C.-F.; Zhou, W.; Klinowski, J. *J. Phys. Chem.* **1995**, *99*, 1018.
- (36) Kosslick, H.; Landmesser, H.; Fricke, R.; Storek, W. *Stud. Surf. Sci. Catal.* **2000**, *129*, 243.

- (37) Luan, Z.; He, H.; Zhou, W.; Cheng, C.-F.; Klinowski, J. *J. Chem. Soc., Faraday Trans.* **1995**, *91*, 2955.
- (38) Cabrera, S.; Haskouri, J. E.; Mendioroz, S.; Guillem, C.; Latorre, J.; -Porter, A. B.; -Porter, D. B.; Marcos, M. D.; Amorós, P. *Chem. Commun.* **1999**, 1679.
- (39) Kosslick, H.; Lischke, G.; Walther, G.; Storek, W.; Martin, A.; Fricke, R. *Microporous Mater.* **1997**, *9*, 13.
- (40) Tanev, P. T.; Pinnavaia, T. J. *Science* **1995**, *267*, 865.
- (41) Mokaya, R.; Jones, W. *Phys. Chem. Chem. Phys.* **1999**, *1*, 207.
- (42) Mokaya, R. *Chem. Commun.* **2000**, 1891.
- (43) Mokaya, R.; Jones, W. *J. Mater. Chem.* **1999**, *9*, 555.
- (44) Kolodziejewski, W.; Corma, A.; Navarro, M.-T.; Perez-Pariente, J. *Solid State Nucl. Magn. Reson.* **1993**, *2*, 253.
- (45) Feustion, B. P.; Higgins, J. B. *J. Phys. Chem.* **1994**, *98*, 4459.
- (46) Behrens, G.; Stucky, G. D. *Science* **1993**, *32*, 696.
- (47) Schmidt, R.; Akporiaye, D.; Stöcker, M.; Ellestad, O. H. *Stud. Surf. Sci. Catal.* **1994**, *84*, 61.
- (48) Engelhardt, G.; Michael, D. *"High-Resolution Solid State NMR of Silicates and Zeolites"*; John Wiley & Sons: New York, 1987.
- (49) Monnier, A.; Schüth, F.; Huo, Q.; Kumar, D.; D.Margolese; Maxwell, R. S.; Stucky, G. D.; Krishnamurty, M.; Petroff, P.; Firouzi, A.; Janicke, M.; Chemelka, B. F. *Science* **1993**, *261*, 1299.
- (50) Chen, C. Y.; Bruckett, S. L.; Li, H. X.; Davis, M. E. *Microporous Mater.* **1993**, *2*, 27.
- (51) Stebbins, J. F. In *"Handbook of Physical constants"*; American Geophysical Union: Washington DC, 1995, p 303.
- (52) Kloetstra, K. R.; Zandbergen, H. W.; Bekkum, H. v. *Catal. Lett.* **1995**, *33*, 157.
- (53) Schmidt, R.; Akporiaye, D.; Stöcker, M.; Ellestad, O. H. *Stud. Surf. Sci. Catal.* **1994**, *84*, 58.
- (54) Janicke, M.; Kumar, D.; Stucky, G. D.; Chmelka, B. F. *Stud. Surf. Sci. Catal.* **1994**, *84*, 61.
- (55) Oldfield, E.; Haasse, J.; Schmitt, K. D.; Schramm, S. E. *Zeolites* **1994**, *14*, 101.
- (56) Janicke, M. T.; Landry, C. C.; Christiansen, S. C.; Kumar, D.; Stucky, G. D.; Chmelka, B. F. *J. Am. Chem. Soc.* **1998**, *120*, 6940.
- (57) Reddy, K. M.; Song, C. *Catal. Lett.* **1996**, *36*, 103.

- 
- (58) Matthae, F. P.; Genske, D.; Minchev, C.; Lechert, H. *Stud. Surf. Sci. Catal.* **1998**, *117*, 223.
- (59) Brunauer, S.; Deming, L. S.; Deming, W. S.; Teller, E. *J. Am. Chem. Soc.* **1940**, *62*, 1723.
- (60) Brunauer, S.; Emmet, P. H.; Teller, E. *J. Am. Chem. Soc.* **1938**, *60*, 309.
- (61) Tanev, P. T.; Vlaev, L. T. *J. Colloid Interface Sci.* **1993**, *160*, 110.
- (62) Barrett, E. P.; Joyner, L. G.; Halenda, P. P. *J. Am. Chem. Soc.* **1951**, *73*, 373.
- (63) Mokaya, R. *Chem. Commun.* **2000**, 1541.
- (64) Grün, M.; Unger, K. K.; Matsumoto, A.; Tsutsumi, K. *Microporous and Mesoporous Mater.* **1999**, *27*, 207.
- (65) Coustel, N.; Renzo, F. D.; Fajula, F. *J. Chem. Soc., Chem. Commun.* **1994**, 967.

## Chapter 4

### Template Removal by Ozone Treatments

#### 4.1. Introduction

Usually, three kinds of organic compounds are used for preparing mesoporous MCM-41 materials: (1) ionic surfactant;<sup>1-9</sup> (2) neutral surfactant;<sup>10-12</sup> (3) non-surfactant organic template.<sup>13-15</sup> It was suggested that the ionic pathway is based on charge matching between the ionic surfactants and inorganic precursors through electrostatic interactions, and the neutral and the non-surfactant pathways are based on hydrogen bonding between the templates and the inorganic precursors.<sup>11,16</sup>

From the catalytic point of view, it is a prerequisite to remove occluded templates to provide porous channels for guest molecules to diffuse into the channels. The most convenient and widely used method for template removal is conventional thermal calcination. Although calcination is largely satisfactory, it has some disadvantages. Firstly, calcination occasionally leaves carbonaceous residues (cokes) inside channels, which block the pores. Secondly, it removes large amount of hydroxyl groups that are important in catalytic activities. Thirdly, undesirable pore wall collapse and structural deterioration<sup>17</sup> may occur. Fourthly, calcination tends to result in the undesired production of a significant proportion of extra-framework (octahedrally coordinated) Al<sup>18,19</sup> for the Al containing samples. Finally, higher temperatures are generally required to completely remove the templates associated with the Al-species, due to much stronger interactions of the template with the Al species than that with silanol groups.<sup>20,21</sup> This also leads to a more severe structure deterioration problem for Al-MCM-41.

An alternative method to solve these problems is to remove surfactant templates at a low temperature.

To date, various kinds of methods have been developed to remove templates in molecular sieves at low temperature, such as liquid phase extraction,<sup>20,22-24</sup> supercritical fluid extraction,<sup>25</sup> removal of the surfactant templates via simultaneous modification of the pores,<sup>26-29</sup> low temperature plasma calcination and nitrous oxide calcination.<sup>30-35</sup> All of these methods, however, have their own disadvantages, for example, liquid extraction cannot completely remove templates.<sup>20,22-24</sup>

Ozone is a strong oxidizing reagent.<sup>32</sup> It can react with olefinic and aromatic hydrocarbons.<sup>36</sup> Saturated hydrocarbons are resistant to ozone<sup>31</sup> in aqueous solutions at low temperature. At temperatures as high as 473 K, ozone is extremely explosive and dangerous when mixed with organic compounds.<sup>32</sup> Since template molecules in the as-synthesized molecular sieves are usually aliphatic hydrocarbons, it was once thought that ozone would not be effective in template removal<sup>32</sup> because of its inert reactive activities toward the aliphatic hydrocarbons.<sup>35-40</sup> Corless et al.<sup>40</sup> studied aqueous ozonation of saturated and unsaturated cationic quaternary ammonium chloride surfactants and found that the saturated quaternary ammonium surfactants do not react with ozone under the aqueous conditions employed. In contrast, unsaturated analogues readily react with ozone under identical conditions to form aldehydes, carboxylic acids and quaternary ammonium carboxylic acids. Copperthwaite et al.<sup>33,38,39</sup> compared oxygen and ozone/oxygen reactivation of pentasil zeolite ZSM-5 and H-zeolite-Y and concluded that, although ozone/oxygen treatment can remove alkene and aromatic hydrocarbons from the above two zeolites, it cannot lead to extensive oxidation of aliphatic, ether or ketonic carbon at low temperatures. On the other hand, van der Waal et al.<sup>37</sup> synthesized pure zeolite boron beta using dibenzyltrimethylammonium

hydroxide as a template which was completely removed by calcination in 1 % of ozone in oxygen at 383 K, followed by a hot acetone wash. Kiricsi et al.<sup>41</sup> removed template material carbon nanotubes for the inorganic silica and alumino-silica tubes by ozone oxidation at 473 K instead of burning off at 1023 K. Low temperature treatment helped to protect the wall structure of the nanotubes during carbon removal. Carlton et al.<sup>35</sup> suggested that the carbonaceous residues formed during ozone/oxygen treatment may anchor to the zeolite framework *via* Al-O or Si-O linkages, which leads to difficulties in further removal. Recently, a patent<sup>42</sup> has appeared which describes activation of a synthetic titanium substituted zeolite containing an organic template, such as a quaternary ammonium salt (tetrapropylammonium hydroxide), which was at least *partially* removed (reacted) by treating with ozone at moderate temperature (298-573 K). Jones et al.<sup>43</sup> successfully synthesized ultrathin aluminosilicate films from Langmuir-Blodgett multilayers which were subsequently decomposed by exposure to the ultraviolet ozone (UVO). In this way, the film melting and coalescing into droplets, which usually happen during thermal decomposition, was avoided. Gilbert et al.<sup>44</sup> also reported that starting decomposition temperature of the tetrapropylammonium bromide (TPABr) template in silicalite-1 under ozone/air atmosphere was approximately 100 K lower than in air. These arguments indicate that: (1) the organic surfactant templates (saturated and unsaturated) can be at least partially eliminated (reacted) from zeolites by proper ozone treatments. (2) the efficiency of ozone on template removal not only depends on the nature of the surfactant template itself, but also largely depends on the microenvironments where the surfactant template resides. Especially, the pore sizes and the interactions between the surfactant template and the zeolite framework play crucial roles in template removal by ozone treatments.

For microporous materials such as zeolites, the elimination of the organic template by ozone treatment may be hindered by the steric hindrance of the micropores themselves. However, this is not the case for the mesoporous materials, such as MCM-41. Surprisingly, limited work has been done using ozone to remove the surfactant template in MCM-41. Recently, Keene et al.<sup>45</sup> reported that the organic surfactant template (cetyltrimethylammonium, CTABr) in the as-synthesized purely siliceous MCM-41 can be removed successfully using UVO at room temperature. Interestingly, MCM-41 thus obtained had higher surface area, larger sized pores, and narrower pore size distribution than those calcined at 823 K. Clark et al.<sup>46</sup> used UV-ozone treatment to completely remove the non-ionic surfactant template  $C_{16}H_{33}(OCH_2CH_2)_{10}OH$  in the preparation of mesoporous thin films. Büchel et al.<sup>47</sup> studied *in-situ* surfactant (CTABr) removal from MCM-41 by ozone treatment (no UV light) under uncontrolled exothermic reaction temperature (estimated temperature was 1073 K from the bright red colour of the reaction mixture) and suggested that water plays a key role in the degradation of the mesostructure by ozone treatment.

Though it is unambiguous that UVO treatment is efficient in template removal from mesoporous materials, the argument on the efficiency of ozone itself on template removal in the absence of UV light still exists. For example, Keene et al.<sup>45</sup> and Büchel et al.<sup>47</sup> suggested that gaseous ozone in the absence of UV light is as effective in the surfactant template removal from MCM-41 type materials as UV-generated ozone. In contrast, Moon et al.<sup>48</sup> showed that ozone alone is ineffective in removing saturated contaminants from silicate surfaces, but presence of UV light significantly enhances the process. Clark et al.<sup>46</sup> also showed that the presence of UV light improves the effect of ozone both in template removal and in fostering silicate condensation. Furthermore, the mechanisms of ozone reactions with organic surfactant templates at different

temperatures are still not clear. No attempt has been made using ozone to eliminate the organic surfactant template from Al-MCM-41 samples, which is more important than siliceous MCM-41 in the catalytic point of view. The effect of ozone on the porous structure and surface properties of (Al)-MCM-41 is still far less understood. In this work, attempts are made to give better understanding of these issues.

The CTAC template in directly hydrothermally synthesized as-synthesized MCM-41 and three pre-washed Al-MCM-41 samples (Si/Al ratio =  $\infty$ , 39, 15 and 7, respectively) were partially or completely removed by ozone treatments at room temperature and 423 K, respectively in the absence of UV light. Detailed sample preparations and ozone treatments have been already described in Chapter 2. All of the ozone treated samples were characterized by XRD patterns, solid state  $^{29}\text{Si}$ -MAS-NMR,  $^{27}\text{Al}$ -MAS-NMR and, in situ TIR and FTIR spectra, and  $\text{N}_2$  adsorption-desorption isotherms. The preliminary mechanism study was carried out by analyzing the gaseous products collected using an acetone - dry ice cold trap with GC-MS, while the residues remained inside the pores with FTIR and CP- $^{13}\text{C}$ -MAS-NMR spectra.

## 4.2. Powder XRD Patterns

For convenience the following abbreviations are used: “as-synthesized ( $\chi$ )” for the as-synthesized sample; “pre-washed ( $\chi$ )” for the sample obtained by washing the as-synthesized sample with EtOH/HCl prior to thermal calcination; “calcined ( $\chi$ )” for the sample obtained by calcining pre-washed sample (not as-synthesized sample as in purely siliceous MCM-41) at 813 K in air-flow; “ $\chi$  (o-rt)” for the sample obtained by treating the pre-washed sample with ozone at room temperature (rt = room temperature); “ $\chi$  (o-rt-813K)” for the sample obtained by further calcining the  $\chi$  (o-rt) sample at 813 K in air-flow; and “ $\chi$  (o-423K)” for the sample obtained by treating pre-



washed sample with ozone at 423 K. The “ $\chi$ ” here stands for the Si/Al ratio of the corresponding Al-MCM-41 sample in the gel mixture.

#### 4.2.1. MCM-41 Samples that were Treated with Ozone

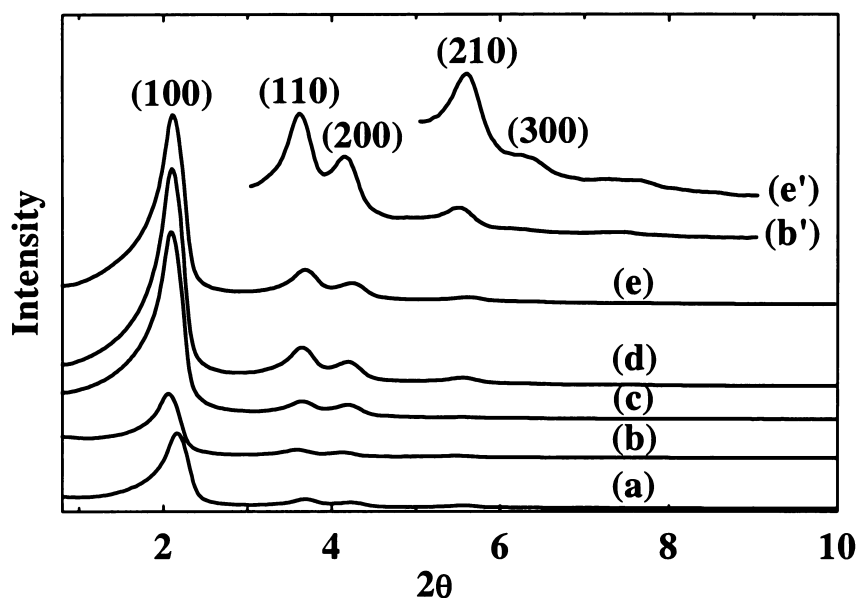


**Figure 4.1:** XRD patterns of MCM-41: (a) as-synthesized MCM-41; (b) MCM-41 (o-rt) (as-synthesized MCM-41 was treated with ozone at room temperature); (c) MCM-41 (o-rt-423K) (MCM-41 (o-rt) was heated at 423 K); (d) MCM-41 (o-rt-423K-813K) (MCM-41 (o-rt-423K) was calcined at 813 K in air-flow); (e) MCM-41 (o-423K) (as-synthesized MCM-41 was treated with ozone at 423 K). Curve (b') and (e') are parts of the original pattern (b) and (d), which are magnified 10 times and 5 times respectively.

Figure 4.1 shows the XRD patterns of MCM-41 (o-rt), MCM-41 (o-rt-423K), MCM-41 (o-423K) and MCM-41 (o-rt-423K-813K). For comparison, the XRD pattern of the as-synthesized MCM-41 is also plotted together.

The XRD pattern of MCM-41 (o-rt) sample (Figure 4.1 (b) and (b')) exhibits (100) peak at  $2\theta = 2.12^\circ$ , which is the same as that of the as-synthesized MCM-41 sample. Using the corresponding  $d_{100}$  space of 41.6 Å, the distance between the adjacent pore

centers ( $a_0$ ) is 48.0 Å. Keene et al.<sup>45</sup> also studied template removal by ozone treatment at 298 K and obtained similar XRD patterns. The fact that the  $d$ -space of (100) peak does not decrease indicates that the pore structure remains almost as intact as the original as-synthesized MCM-41 sample. It seems that less shrinkage of the pore structure of MCM-41 is a common feature upon template removal by ozone treatment at room temperature.<sup>45,47,49</sup> Well-resolved (110), (200) and (210) peaks are also observed at  $2\theta = 3.64^\circ$  ( $d = 24.2$  Å),  $4.16^\circ$  ( $d = 21.2$  Å) and  $5.52^\circ$  ( $d = 16.0$  Å), respectively, indicating that the long range ordering of the hexagonal unit cell is well preserved without significant change. This result is in agreement with the reports by Keene et al.<sup>45</sup> and Thakulsukanant et al.<sup>49</sup>, but is contrary to that by Büchel et al.<sup>47</sup> who observed loss of long range ordering after ozone treatment of dried MCM-41 resuspended in water or mother liquor for up to 26 hours. The stability of the sample upon ozone treatment in this study may be attributed to the following factors. Firstly, the as-synthesized MCM-41 is more stable than that used by Büchel et al. due to the repeated pH adjustment to 10.2 during the hydrothermal synthesis.<sup>50</sup> Secondly, powdered as-synthesized MCM-41 was used instead of a suspension of MCM-41. In the latter case, due to rehydration, hydrolysis of siloxane bridges and therefore structure collapses may be accompanied by the template removal,<sup>51</sup> as evidenced by the poorly resolved XRD patterns.<sup>47</sup> The observed FWHM value of (100) peak is  $0.33^\circ$ , which is larger than that of the as-synthesized sample ( $0.27^\circ$ ). This is probably due to the partial removal of the template. After ozone treatment at room temperature, although the majority of the mesostructure is kept intact as in the as-synthesized sample, as indicated by the unchanging of the  $d_{100}$  space, small numbers of void (or half void) mesostructures with different pore sizes may be generated and coexist with the mesostructures that filled up with the CTAC surfactant. Apparently, coexistence of these different mesostructures

will lead to a slight decrease in the dominant pore size, manifested by an increase of the FWHM value of the (100) peak in the XRD pattern. The lattice strain in the channel walls caused by the high density of the silanol groups after room temperature ozone treatment <sup>47</sup> may also contribute to the increase of the FWHM value and cannot be excluded.

The XRD pattern of MCM-41 (o-rt-423K) (Figure 4.1 (c)) shows a strong dominant (100) peak at  $2\theta = 2.16^\circ$  with  $d_{100} = 40.9 \text{ \AA}$ . The corresponding calculated  $a_0$  is  $47.2 \text{ \AA}$ . The (110), (200) and (210) peaks are also observed at  $2\theta = 3.68^\circ$  ( $d = 24.0 \text{ \AA}$ ),  $4.24^\circ$  ( $d = 20.8 \text{ \AA}$ ) and  $5.62^\circ$  ( $d = 15.7 \text{ \AA}$ ), respectively. The shift of these Bragg peaks positions to the higher  $2\theta$  value indicates a decrease of the unit cell size and the decrease of the  $d_{100}$  space of (100) peak indicates that the lattice contraction of about 1.7% occurred compared with the MCM-41 (o-rt) sample (or the as-synthesized MCM-41). Distinct increase of the Bragg peaks intensities is also observed. Especially, the intensity of the (100) peak almost reaches that of thermally calcined MCM-41 (o-rt-423K-813K) sample, indicating that heating the sample at 423 K has greatly improved the “crystallinity” of the sample. As evidenced by the infrared study (Section 4.5), heating at 423 K may further remove some organic residues formed during ozone treatment at room temperature <sup>52</sup>. Further removal of the occluded species may enhance the scattering contrast between the framework walls and pores of MCM-41. <sup>53</sup> The decrease of FWHM of (100) peak from  $0.33^\circ$  for MCM-41 (o-rt) sample to  $0.27^\circ$  for MCM-41 (o-rt-423K) sample demonstrates that heating at 423 K may either increase the scattering domain size or decrease the lattice strain. Actually, these two effects may take place simultaneously through further condensation of silanol groups on the channel walls.

**Table 4.1: XRD data of the MCM-41 samples that were treated with ozone**

Sample	<i>hkl</i>	Angle	Counts	$d_{\text{space}}$ (Å)	FWHM <sup>a</sup>	$a_0$ (Å) <sup>b</sup>
MCM-41 (o-rt) <sup>c</sup>	(100)	2.12°	14578	41.6	0.33°	48.0
	(110)	3.64°	1868	24.2		
	(200)	4.16°	1248	21.2		
	(210)	5.52°	546	16.0		
MCM-41 (o-rt-423K)	(100)	2.16°	43796	40.9	0.27°	47.2
	(110)	3.68°	3908	24.0		
	(200)	4.24°	2967	20.8		
	(210)	5.62°	497	15.7		
MCM-41 (o-rt-423K-813K)	(100)	2.18°	43726	40.5	0.27°	46.8
	(110)	3.72°	7428	23.7		
	(200)	4.28°	4442	20.6		
	(210)	5.64°	1533	15.7		
	(300)	6.44°	646	13.7		
MCM-41 (o-423K)	(100)	2.14°	50298	41.2	0.27°	47.6
	(110)	3.66°	8330	24.1		
	(200)	4.24°	5104	20.8		
	(210)	5.58°	1834	15.8		
	(300)	6.26°	702	14.1		

**Notes:** (a) FWHM = full width at half maximum. (b) The distance between the adjacent pore centers ( $a_0$ ) is calculated by the equation of  $a_0 = 2 d_{100} / 3^{1/2}$ . (c) rt = room temperature.

Figure 4.1 (d) shows the XRD pattern of MCM-41 (o-rt-423K-813K) sample. Compared with the MCM-41 (o-rt-423K) sample, the (100) peak shows only slightly changes in intensity (in the same order),  $2\theta$  position ( $\Delta 2\theta = 0.02^\circ$ ) and  $d_{100}$  space ( $\Delta d_{100}$  space =  $0.02^\circ$ ). Keene et al.<sup>52</sup> also reported that the  $d_{100}$  space of calcined sample diminishes as the material is heated up to 423 K, and then remains constant up to 823 K. The lattice contraction is 2.6 % compared with the as-synthesized MCM-41, which is the same as that of the directly thermally calcined MCM-41. The FWHM of (100) peak is also not changed. The noticeable appearance of the (300) high order peak suggests that the MCM-41 (o-rt-423K-813K) sample possesses a well-defined hexagonal pore structure with long range ordering. All of these unit cell parameters are quite close to those of directly thermally calcined MCM-41 sample.

Figure 4.1 (e) and (e') represents the XRD pattern of the MCM-41 (o-423K) sample. The (100) peak locates at  $2\theta = 2.14^\circ$  with  $d_{100} = 41.2$  Å. The relevant adjacent pore

center distance  $a_0$  is 47.6 Å. Based on the  $d_{100}$  space, the calculated lattice contraction is about 1 % compared with the as-synthesized MCM-41, which is the smallest one among all of the completely template-removed MCM-41 samples (for the evidence of complete template removal, please refer to Section 4.5) synthesized in our experiments. Some distinguishable high order reflections can also be observed at  $2\theta = 3.66^\circ$  ( $d = 24.1$  Å),  $4.24^\circ$  ( $d = 20.8$  Å),  $5.58^\circ$  ( $d = 15.8$  Å), and  $6.26^\circ$  ( $d = 14.1$  Å), which can be ascribed to the (110), (200), (210) and (300) peaks, respectively. The presence of these high order peaks<sup>54-58</sup> indicates that ozone treatment of MCM-41 silicate at 423 K may develop well-defined hexagonal arrayed MCM-41 porous structure with long range ordering. The observed FWHM of (100) peak is the same as that of the as-synthesized MCM-41 ( $0.27^\circ$ ). From the comparison of the XRD patterns among the completely template-removed MCM-41 samples, it is noteworthy that template removal by ozone treatment at 423 K gives the largest unit cell parameters due to the low temperature treatment as expected.

The detailed XRD parameters for the above MCM-41 samples that were treated with ozone are summarized in Table 4.1.

#### **4.2.2. XRD Patterns of Directly Hydrothermally Synthesized Al-MCM-41 Samples that were Treated with Ozone**

##### **4.2.2.1. Al-MCM-41 (Si/Al = 39) Samples that were Treated with Ozone**

XRD pattern of 39 (o-rt) (Figure 4.2 (b)) shows (100) peak at  $2\theta = 2.18^\circ$  with  $d_{100}$  space of 40.5 Å. Compared with the pre-washed sample (Figure 4.2 (a)), the lattice contraction is 10 %. The shift of (100) peak position to the higher  $2\theta$  value is also observed. The high order (110) and (210) peaks are still overlapped to a certain degree

but distinguishable. The FWHM value of the (100) peak, which is an indication of the domain size, is almost unchanged. It was shown in Chapter 3 that most of the CTAC surfactant may be washed out by acidic ethanol extraction (60-80%, refer to Section 3.7 in Chapter 3). Further reaction of ozone with the residual surfactant, which was expected to further increase the lattice parameters, actually leads to structure shrinkage. This may be due to the further condensation of silanol groups during ozone treatment. The structure collapse may not occur since it is treated at room temperature.

Figure 4.2 (d) shows the XRD pattern of 39 (o-rt-813K). Like MCM-41, complete removal of the template from 39 (o-rt) by thermal calcination results in a slight shift of the (100) peak position to higher  $2\theta$  value together with a lattice contraction of 1 %. It can be seen that calcination also leads to an increase of the Bragg peaks intensities. The appearance of noticeable (210) peak indicates that the calcined 39 (o-rt-813K) has a better ordered structure. The FWHM of the (100) peak is also increased after calcination, indicating a decrease of the domain size. Comparison of the XRD patterns of 39 (o-rt-813K) with calcined (39) (Figure 4.2 (e)) shows that complete template removal by two-step treatment (ozone treatment at room temperature followed by thermal calcination) results in no significant changes on the crystalline structure.

Figure 4.2 (c) shows the XRD pattern of 39 (o-423K). The (100) peak position ( $2\theta = 1.96^\circ$ ) and the corresponding  $d_{100}$  space (45.0 Å) are unchanged compared with the original pre-washed (39). This kind of less lattice contraction is also observed in the MCM-41 (o-423K) sample. But it is plausible that the 39 (o-423K) has better defined hexagonal pore structure than the pre-washed (39) since the (100) peak intensity of the former is decreased (31 %) compared with the latter. However, the higher order peak intensities remain at the same level. It also can be seen that the FWHM of the (100) peak ( $0.73^\circ$ ) of the former is the largest of any these Al-MCM-41 (Si/Al = 39) samples.

This may be due to more lattice defects generated during template removal from the pre-washed (39) by ozone (which is a strong oxidant) treatment at 423 K or incomplete condensation of silanol groups. Two higher order Bragg peaks corresponding to (110) and (200) reflections are also observed. Compared with the calcined (39), the absence of the (210) peak indicates that ozone treatment at 412K does not improve the long range ordering of the sample as does thermal calcination.

The detailed XRD parameters for the above Al-MCM-41 (Si/Al = 39) samples that were treated with ozone are summarized in Table 4.2.

**Table 4.2: XRD data of Al-MCM-41 (Si/Al = 39) samples that were treated with ozone**

Sample	<i>Hkl</i>	Angle	Counts	$d_{\text{space}}$ (Å)	FWHM <sup>a</sup>	$a_0$ (Å) <sup>b</sup>
39 (o-rt) <sup>c</sup>	(100)	2.18°	20989	40.5	0.59°	46.8
	(110)	3.74°	2352	23.6		
	(200)	4.22°	1910	20.9		
39 (o-rt-813K)	(100)	2.20°	35833	40.1	0.67°	46.3
	(110)	3.84°	4720	23.0		
	(200)	4.28°	3398	20.6		
	(210)	5.82°	1043	15.2		
39 (o-423K)	(100)	1.96°	16755	45.0	0.73°	52.0
	(110)	3.48°	1656	25.4		
	(200)	4.04°	1124	21.9		

\* The notes for a, b and c are the same as those in Table 4.1.

#### 4.2.2.2. Al-MCM-41 (Si/Al = 15) Samples that were Treated with Ozone

The XRD pattern of 15 (o-rt) (Figure 4.3 (b)) shows the (100) peak at  $2\theta = 2.16^\circ$  with  $d_{100}$  space of 40.9 Å. Compared with the pre-washed sample (Figure 4.3(a)), the (100) peak position is shifted to the higher  $2\theta$  value, and the lattice contraction is 2.6 %. The high order (110) and (210) peaks are not well resolved. The FWHM value of the (100) peak, which is an indication of the domain size, is almost unchanged. These results are also observed in 39 (o-rt).

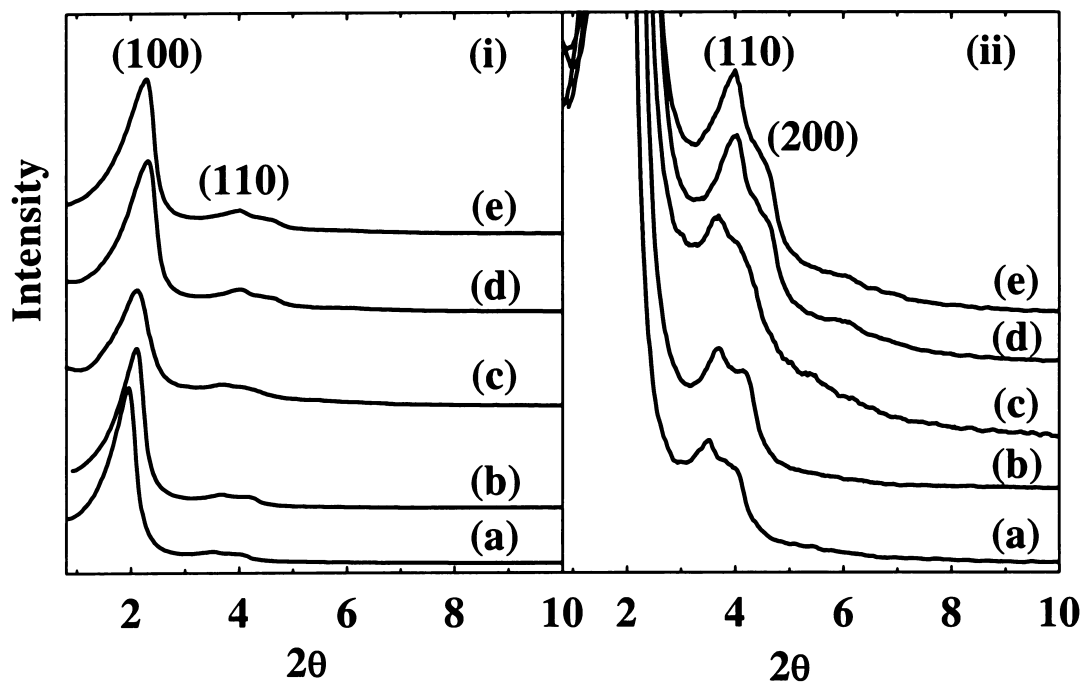


**Figure 4.3:** XRD patterns of Al-MCM-41 (Si/Al = 15): (a) pre-washed (15); (b) 15 (o-rt); (c) 15 (o-423K); (d) 15 (o-rt-813K); (e) calcined (15). Spectra (a) to (e) in Figure (i) and those in Figure (ii) are the same spectra. Figure (ii) is focused on the low intensity area to show the fine structures of the high order peaks.

**Table 4.3:** XRD data of Al-MCM-41 samples (Si/Al = 15) that were treated with ozone

Sample	<i>hkl</i>	Angle	Counts	$d_{\text{space}}$ (Å)	FWHM <sup>a</sup>	$a_0$ (Å) <sup>b</sup>
15 (o-rt) <sup>d</sup>	(100)	2.16°	22530	40.9	0.62°	47.2
	(110)	3.70°	2102	23.9		
	(200)	4.18°	1776	21.1		
15 (o-rt-813K)	(100)	2.30°	20660	38.4	0.71°	44.3
	(110)	4.02°	3223	22.0		
	(200)	4.56°	2121	19.4		
15 (o-423K)	(100)	2.16°	16193	40.9	0.88°	47.2
	(110)	3.68°	1266	24.0		
	(200)	4.28°	1038	20.6		

\* The notes for a, b, c and d are the same as those in Table 4.1.

The XRD pattern of 15 (o-rt-813K) (Figure 4.3 (d)) shows the (100) peak at  $2\theta = 2.30^\circ$ , which has shifted to the higher  $2\theta$  value compared with that of the 15 (o-rt) sample. The corresponding  $d_{100}$  space is 38.4 Å and the lattice contraction is about 6.1 %. It is noteworthy that the intensity of the (100) peak is slightly decreased, while the



intensities of the other Bragg peaks are increased. Also there is no reemergence of the higher order peaks is observed. These results are consistent with those observed in calcined (15). The increase of the FWHM value of the (100) peak after calcination also indicates decrease of the domain size. Similar XRD lattice parameters of 15 (o-rt-813K) with calcined (15) (Figure 4.3 (e)) demonstrates that complete template removal by two-step treatment (ozone treatment at room temperature followed by thermal calcination) results in no significant changes in the crystalline structure.

The XRD pattern of 15 (o-423K) is shown in Figure 4.3 (c). The (100) peak is located at  $2\theta = 2.16^\circ$  with  $d_{100}$  space of 40.9 Å. Compared with the pre-washed sample, the lattice contraction is about 2.6%, which is much smaller than the calcined sample. After removal of the template with ozone at 423 K, the (100) peak intensity decreased nearly 47 %. The other higher order peaks intensities also decreased to the same level. The FWHM of the (100) peak of 15 (o-423K) is  $0.88^\circ$ , which is the largest one among all of the Al-MCM-41 (Si/Al = 15) samples studied here.

The detailed XRD parameters for the above Al-MCM-41 (Si/Al = 15) samples that were treated with ozone are summarized in Table 4.3.

#### 4.2.2.3. Al-MCM-41 (Si/Al = 7) Samples that were Treated with Ozone

The XRD pattern of 7 (o-rt) (Figure 4.4 (b)) shows the (100) peak at  $2\theta = 2.04^\circ$  with  $d_{100}$  space of 43.7 Å. Compared with the pre-washed sample (Figure 4.4 (a)), the (100) peak position is slightly shifted to the higher  $2\theta$  value, and the corresponding lattice contraction is ca. 2.0 %. These results are consistent with the previous low Al content samples.

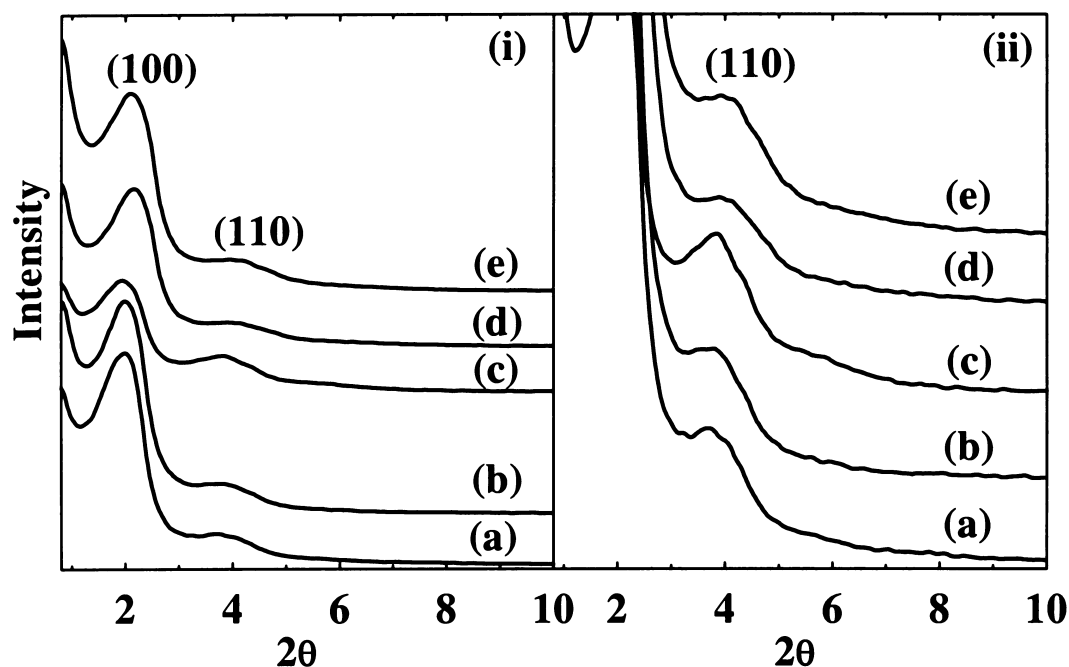


**Figure 4.4:** XRD patterns of Al-MCM-41 (Si/Al = 7): (a) pre-washed (7); (b) 7 (o-rt); (c) 7 (o-423K); (d) 7 (o-rt-813K); (e) calcined (7). Spectra (a) to (e) in Figure (i) and those in Figure (ii) are the same spectra. Figure (ii) is focused on the low intensity area to show the fine structures of the high order peaks.

**Table 4.4:** XRD data of Al-MCM-41 samples (Si/Al = 7) that were treated with ozone

Sample	<i>Hkl</i>	Angle	Counts	$d_{\text{space}}$ (Å)	FWHM <sup>a</sup>	$a_0$ (Å) <sup>b</sup>
7 (o-rt) <sup>c</sup>	(100)	2.04°	5138	43.7	— <sup>d</sup>	50.5
	(110)	3.84°	800	23.2		
7 (o-rt-813K)	(100)	2.22°	3817	40.9	—	47.2
	(110)	4.16°	625	21.4		
7 (o-423K)	(100)	2.12°	2654	41.6	—	48.0
	(110)	3.92°	988	22.5		

\* The notes of a, b and c are the same as those in Table 4.1. (d) The FWHM calculation for peak (100) is not available due to the high background.

Further thermal calcination of the 7 (o-rt) sample results in a further shift of the (100) peak position toward a higher  $2\theta$  value (Figure 4.4 (d)). The corresponding lattice contraction of 7 (o-rt-813K) is ca. 6.4 % compared with the 7 (o-rt). In addition, calcination also results in the reduction of the (100) peak intensity, which is in sharp

contrast to the increase of the (100) peak intensity in MCM-41 and low Al content (Si/Al = 39) samples.

The XRD pattern of 7 (o-423K) (Figure 4.4 (c)) presents the (100) peak at  $2\theta = 2.12^\circ$  with  $d_{100}$  space of 41.6 Å. Compared with the pre-washed sample, the lattice contraction is about 6.7 %. Besides, the (100) peak intensity is also dramatically decreased (49 %).

The detailed XRD parameters for the above Al-MCM-41 (Si/Al = 7) samples that were treated with ozone are summarized in Table 3.4.

### 4.3. Solid State NMR

#### 4.3.1. $^{29}\text{Si}$ -MAS-NMR Spectra

##### 4.3.1.1. MCM-41 Samples that were Treated with Ozone

Figure 4.5 shows the  $^{29}\text{Si}$ -MAS-NMR spectra of purely siliceous MCM-41 samples that were treated with ozone. The MCM-41 (o-rt) (Figure 4.5 (b)) shows signals at ca. -91, -101 and -111 ppm, which can be assigned to  $\text{Q}^2$ ,  $\text{Q}^3$  and  $\text{Q}^4$  respectively. It is obvious that the distribution of the Si atom environments in MCM-41 (o-rt) has barely changed compared with the as-synthesized MCM-41 sample (Figure 4.5 (a)). The preservation of the  $\text{Q}^2$  and  $\text{Q}^3$  in MCM-41 (o-rt) is no doubt due to the mild room temperature reaction conditions. It is also noted that the  $\text{Q}^4$  species is the dominant peak. As suggested in chapter 3, this may be due to the pH adjustment during hydrothermal synthesis, which enhances the polymerization of silanol groups.<sup>1,50,59</sup>

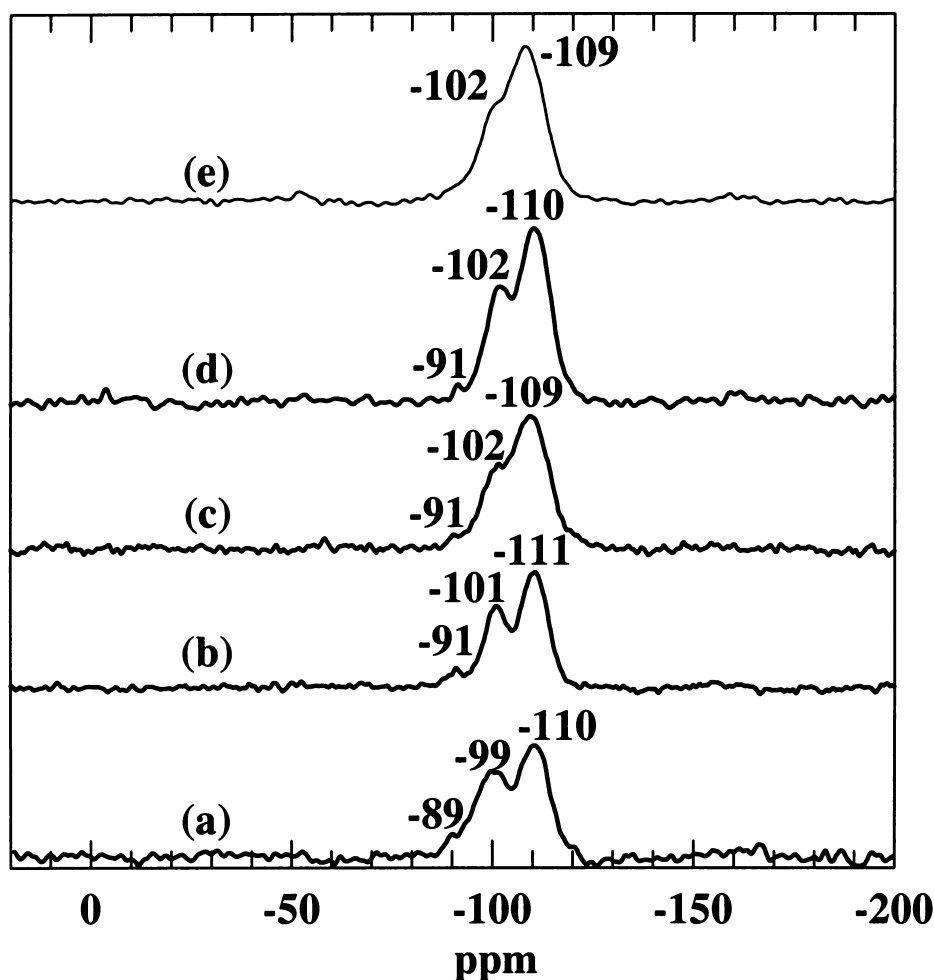


**Figure 4.5:**  $^{29}\text{Si}$ -MAS-NMR spectra of purely siliceous MCM-41: (a) as-synthesized MCM-41; (b) MCM-41 (o-rt); (c) MCM-41 (o-rt-813K); (d) MCM-41 (o-423K); (e) directly calcined MCM-41.

After further calcination to completely remove the CTAC template, the  $^{29}\text{Si}$ -MAS-NMR spectrum of MCM-41 (o-rt-813K) (Figure 4.5 (c)) exhibits a dominant peak at ca. -109 ppm due to the  $\text{Q}^4$  species and a shoulder at ca. -102 ppm, which can be assigned to  $\text{Q}^3$  species. The entire spectrum of MCM-41(o-rt-823K) looks quite similar to that of the directly calcined MCM-41 (Figure 4.5 (e)) except the observation of  $\text{Q}^2$  at ca. -91 ppm, indicating that two-step template removal (ozone treatment at room temperature followed by thermal calcination) may maintain more silanol groups in the MCM-41 sample than direct thermal calcination.

The  $^{29}\text{Si}$ -MAS-NMR spectrum of MCM-41 (o-423K) (Figure 4.5 (d)) shows three distinguishable peaks at  $-91$ ,  $-102$  and  $-110$  ppm, which can be ascribed to  $\text{Q}^2$ ,  $\text{Q}^3$  and  $\text{Q}^4$ , respectively. It can be seen the intensity of  $\text{Q}^4$  has been increased at the expense of  $\text{Q}^3$  and  $\text{Q}^2$ . However, the relative intensity of  $\text{Q}^3$  in MCM-41(o-423K) is higher than that in the directly calcined sample. This indicates that the sample that was treated with ozone at 423 K has maintained more isolated silanol groups than the directly calcined one.

#### 4.3.1.2 Al-MCM-41 (Si/Al = 39) Samples that were Treated with Ozone

The  $^{29}\text{Si}$ -MAS-NMR spectrum of 39 (o-rt) (Figure 4.6 (b)) shows three peaks at ca.  $-91$ ,  $-101$  and  $-110$  ppm, which can be assigned to  $\text{Q}^2$ ,  $\text{Q}^3$  and  $\text{Q}^4$  respectively. As shown in Section 3.3.1. in Chapter 3, due to low Al content, the contribution from the Al coordinated species is not considered in interpreting  $^{29}\text{Si}$ -MAS-NMR spectra of the Al containing MCM-41 samples. A slight increase in the relative intensity of  $\text{Q}^4$  indicates that the condensation degree of 39 (o-rt) has been maintained at the same level as that of pre-washed (39) (Figure 4.6 (a)). As suggested before, this may be due to the mild room temperature reaction conditions.

After complete template removal by further calcination, the  $^{29}\text{Si}$ -MAS-NMR spectrum of the 39 (o-rt-813K) sample (Figure 4.6 (c)) exhibits a dominant peak at ca.  $-109$  ppm due to the  $\text{Q}^4$  species and a shoulder at ca.  $-101$  ppm due to the  $\text{Q}^3$  species. No  $\text{Q}^2$  peak is observed as in MCM-41 (o-rt-813K). However, compared with the calcined (39) (Figure 4.6 (e)), the 39 (o-rt-813K) shows a more distinguishable  $\text{Q}^3$  species, indicating that the two-step template removal (ozone treatment at room temperature followed by thermal calcination) may result in the preservation of more isolated silanol groups.

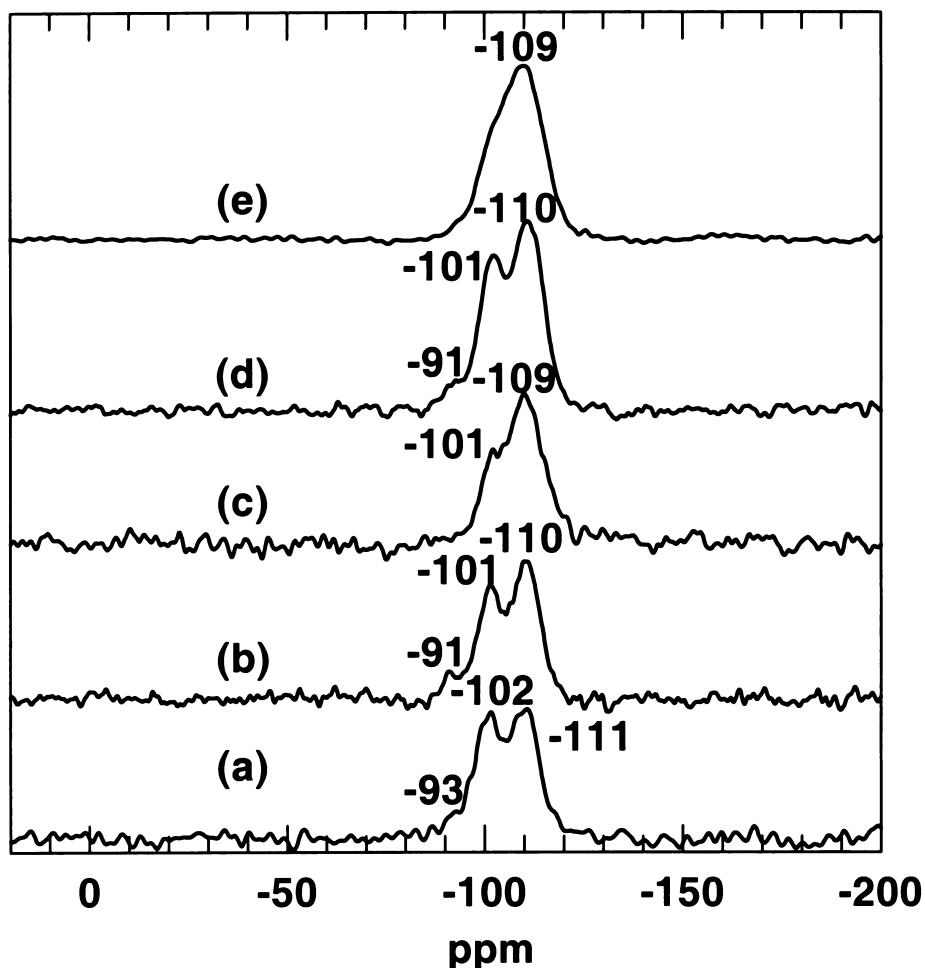


Figure 4.6:  $^{29}\text{Si}$ -MAS-NMR spectra of Al-MCM-41 (Si/Al = 39): (a) pre-washed (39); (b) 39 (o-rt); (c) 39 (o-rt-813K); (d) 39 (o-423K); (e) calcined (39).

The  $^{29}\text{Si}$ -MAS-NMR spectrum of 39 (o-423K) (Figure 4.6 (d)) shows three distinguishable peaks at -91, -101 and -110 ppm, which can be ascribed to  $\text{Q}^2$ ,  $\text{Q}^3$  and  $\text{Q}^4$ , respectively. It can be seen that the relative intensity ratio of  $\text{Q}^4$  and  $\text{Q}^3$  in the 39 (o-423K) is comparable with that in 39 (o-rt). The high relative intensity of  $\text{Q}^3$  in the 39 (o-423K) sample demonstrates that it contains more isolated silanol groups. The presence of  $\text{Q}^2$  may be due to either (or both) of the following two reasons: (1) the 423 K reaction temperature is not necessarily adequate to condense the vicinal silanol groups, i.e., a higher temperature is required to remove vicinal hydroxyls in Al-MCM-41. Reddy et al.<sup>60</sup> also suggested that Al incorporation hinders the silanol condensation process; (2) or

the rehydration process readily occurs in the Al-MCM-41 sample due to stronger interaction of the incorporated Al species with ambient water.

#### 4.3.1.3. Al-MCM-41 (Si/Al = 15) Samples that were Treated with Ozone

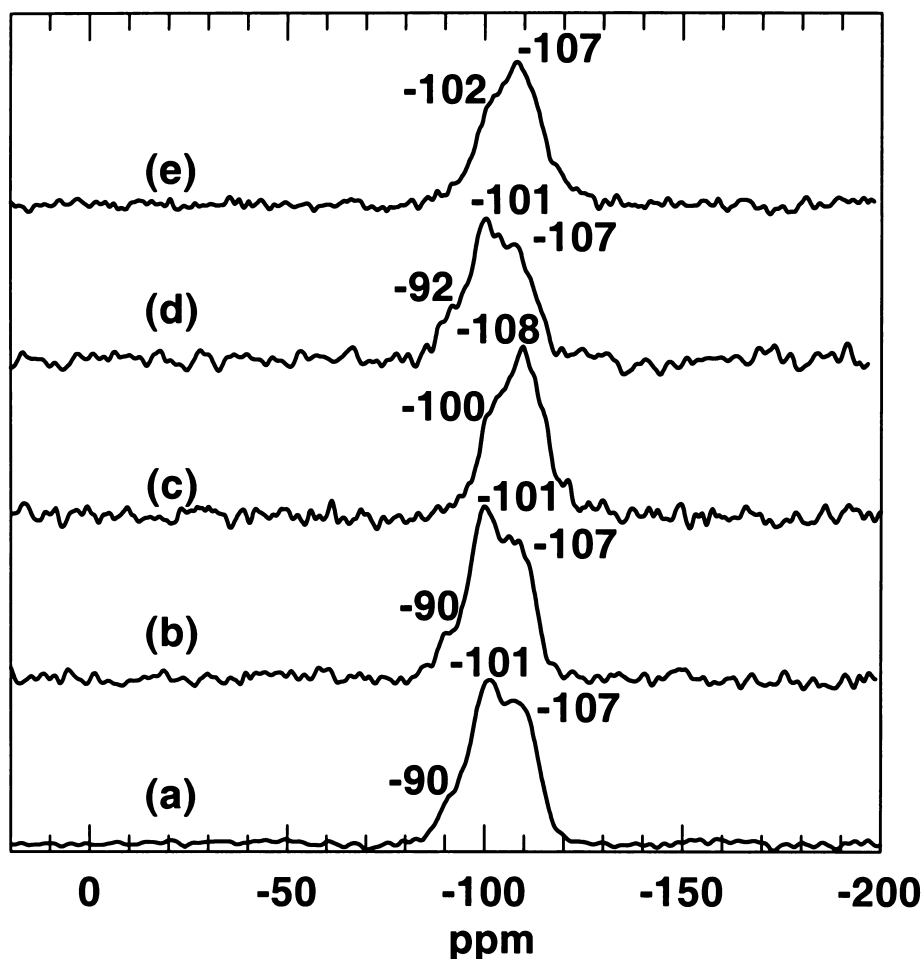


Figure 4.7:  $^{29}\text{Si}$ -MAS-NMR spectra of Al-MCM-41 (Si/Al = 15): (a) pre-washed 15; (b) 15 (o-rt); (c) 15 (o-rt-813K); (d) 15 (o-423K); (e) calcined (15).

The  $^{29}\text{Si}$ -MAS-NMR spectrum of 15 (o-rt) (Figure 4.7 (b)) shows three peaks at ca. -90, -101 and -107 ppm, which can be assigned to  $\text{Q}^2$ ,  $\text{Q}^3$  and  $\text{Q}^4$  respectively. The dominant peak is still  $\text{Q}^3$  as is the case in pre-washed (15) after ozone treatment at room temperature. This result is consistent with the notion that Al incorporation hinders the condensation of silanol groups.<sup>60</sup>

After complete template removal by further thermal calcination, the  $^{29}\text{Si}$ -MAS-NMR spectrum of the 15 (o-rt-813K) sample (Figure 4.7 (c)) exhibits a dominant peak at ca.  $-108$  ppm due to the  $\text{Q}^4$  species and a shoulder peak at ca.  $-100$  ppm due to the  $\text{Q}^3$  species. A  $\text{Q}^2$  peak is not observed. Similar results were also observed in directly calcined (15) (Figure 4.7 (e)).

The  $^{29}\text{Si}$ -MAS-NMR spectrum of the 15 (o-423K) (Figure 4.7 (d)) shows three distinguishable peaks at  $-92$ ,  $-101$  and  $-107$  ppm, which can be ascribed to  $\text{Q}^2$ ,  $\text{Q}^3$  and  $\text{Q}^4$ , respectively. It can be seen that  $\text{Q}^3$  is still the dominant peak in 15 (o-423K), suggesting that the (o-423K) sample has undergone a lesser degree of condensation, i.e., it possess more isolated silanol groups.

#### 4.3.1.4. Al-MCM-41 (Si/Al = 7) Samples that were Treated with Ozone

The  $^{29}\text{Si}$ -MAS-NMR spectrum of 7 (o-rt) (Figure 4.8 (b)) shows three peaks at ca.  $-90$ ,  $-101$  and  $-108$  ppm, which can be assigned to  $\text{Q}^2$ ,  $\text{Q}^3$  and  $\text{Q}^4$  respectively. After ozone treatment at room temperature, the dominant peak is still  $\text{Q}^3$  as is the case in the pre-washed (7) (Figure 4.8 (a)), demonstrating that the 7 (o-rt) sample has maintained the same degree of cross-linking as the pre-washed (7) sample after ozone treatment at room temperature.

After complete template removal by further calcination, the  $^{29}\text{Si}$ -MAS-NMR spectrum of the 7 (o-rt-813K) sample (Figure 4.8 (c)) exhibits peaks at ca.  $-108$  ppm due to the  $\text{Q}^4$  species and ca.  $-98$  ppm due to the  $\text{Q}^3$  species. A  $\text{Q}^2$  peak is not observed. The dominant peak is  $\text{Q}^4$ , which is the same in the calcined (7) (Figure 4.8 (e)).



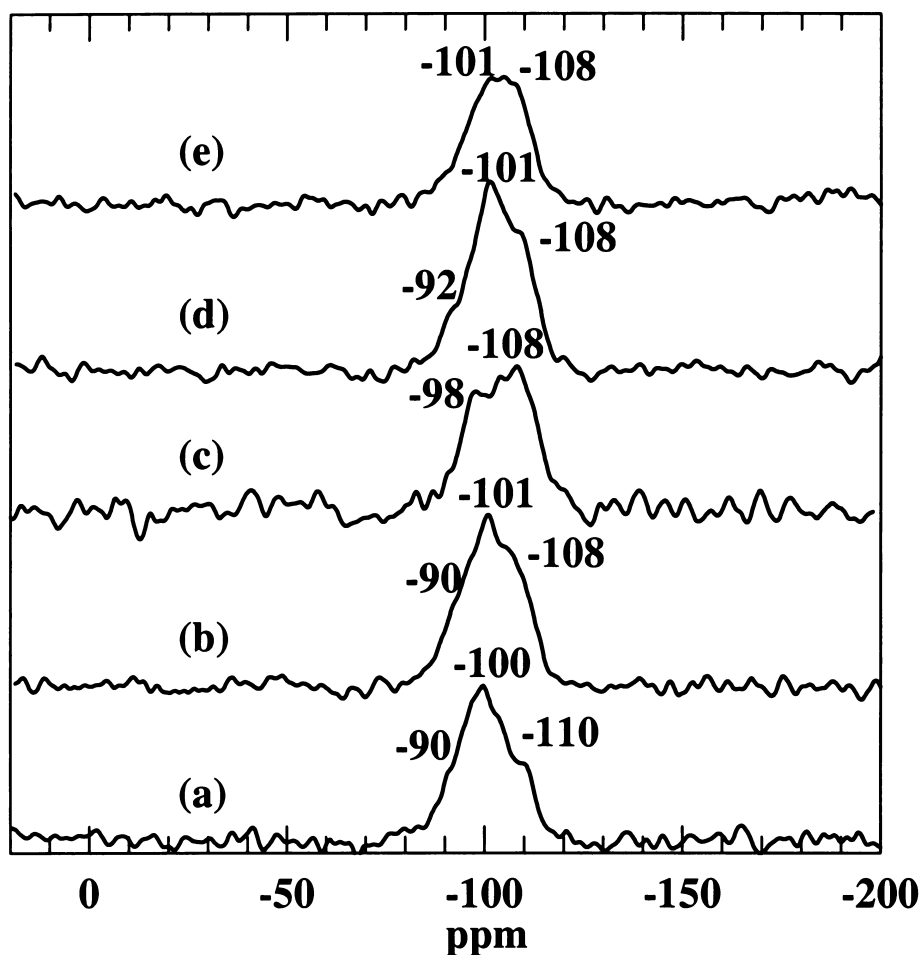


**Figure 4.8:**  $^{29}\text{Si}$ -MAS-NMR spectra of Al-MCM-41 (Si/Al = 7): (a) pre-washed (7); (b) 7 (o-rt); (c) 7 (o-rt-813K); (d) 7 (o-423K); (e) calcined (7).

The  $^{29}\text{Si}$ -MAS-NMR spectrum of 7 (o-423K) (Figure 4.8 (d)) shows three distinguishable peaks at  $-92$ ,  $-101$  and  $-108$  ppm, which can be ascribed to  $\text{Q}^2$ ,  $\text{Q}^3$  and  $\text{Q}^4$  silicon coordination species, respectively. The dominant peak in 7 (o-423K) is still  $\text{Q}^3$ , which is also observed in the previous samples that were treated with ozone at 423 K. As suggested before, the domination of  $\text{Q}^4$  in the 7 (o-423K) sample indicates that it has more isolated silanol groups.

### 4.3.2. $^{27}\text{Al}$ -MAS-NMR Spectra

#### 4.3.2.1. Al-MCM-41 (Si/Al = 39) Samples that were Treated with Ozone

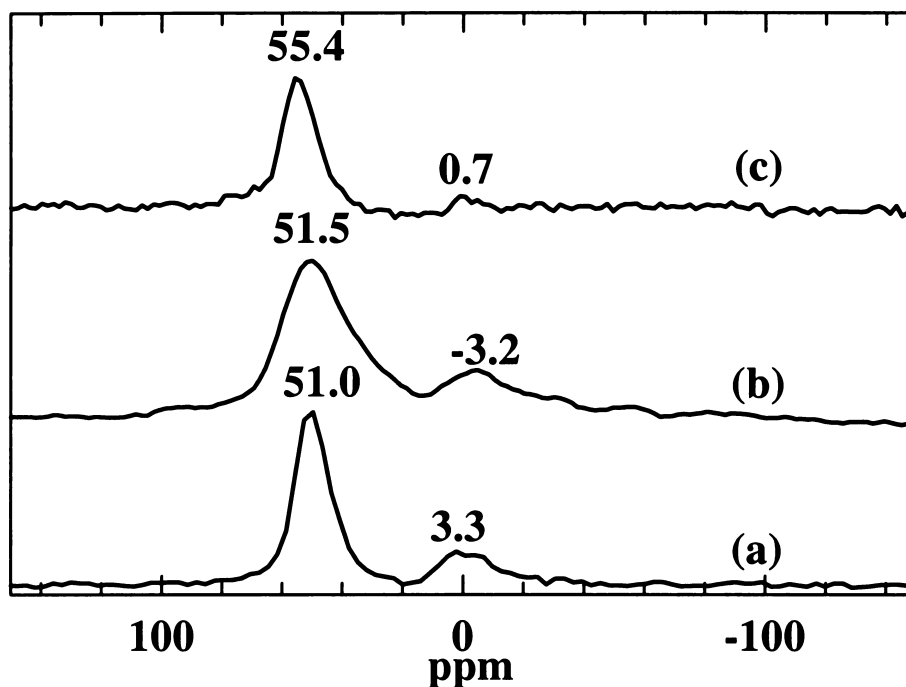


Figure 4.9:  $^{27}\text{Al}$ -MAS-NMR spectra of Al-MCM-41 (Si/Al = 39): (a) 39 (o-rt); (b) 39 (o-rt-813K); (c) 39 (o-423K).

The  $^{27}\text{Al}$ -MAS-NMR spectrum of the 39 (o-rt) (Figure 4.9 (a)) shows two peaks with chemical shifts of ca. 51.0 and 3.3 ppm, which can be assigned to tetrahedrally and octahedrally coordinated Al species, respectively. The presence of octahedral Al indicates that ozone treatment at room temperature causes conversion of some framework Al into undesired non-framework Al. The relative peak area ratio between octahedral Al and octahedral Al is 4.5, i.e., about 18 % of Al atoms are in the extra-framework positions.

After further thermal calcination to completely remove the CTAC template, the  $^{27}\text{Al}$ -MAS-NMR spectrum of 39 (o-rt-813K) (Figure 4.9 (b)) shows peaks at ca. 51.5 ppm (tetrahedral Al) and ca. -3.2 ppm (octahedral Al), respectively. The relative peak area ratio between tetrahedral Al and octahedral Al is 6.3, i.e., about 14 % of Al atoms are at the extra-framework positions, which is lower than that of 22 % in directly calcined sample (see Section 3.3.2.1.1. in Chapter 3). This demonstrates that two step complete template removal (ozone treatment at room temperature plus further calcination) reserves more tetrahedral Al in the framework than direct calcination method. It is also noted that the tetrahedral Al peak is not symmetrical, which is probably due to the formation of some other coordinated Al. The peak broadening after further calcination indicates the presence of some Al in a more distorted environment or in a low symmetry due to the larger range of T-O-T bond angles (where T represents an individual  $\text{SiO}_4$  or  $\text{AlO}_4$  tetrahedron).<sup>61-65</sup>

The  $^{27}\text{Al}$ -MAS-NMR spectrum of 39 (o-423K) (Figure 4.9 (c)) shows two peaks at 55.4 and 0.7 ppm, which correspond to tetrahedral and octahedral Al, respectively. Interestingly, the relative peak area between these two coordinations is 12.4, i.e., there are only ca. 3 % of Al atoms in undesired non-framework positions, which is much lower than that after direct calcination. As suggested above, this may be due to relatively low temperature template removal. It is also noteworthy that ozone treatment at 423 K generates less non-framework Al than during room temperature ozone treatment (14 %), indicating that choosing the proper temperature may also enhance the insertion of Al into the framework. Compared with the directly calcined (39), the spectrum of 39 (o-423K) looks narrower and more symmetrical, indicating that a smaller amount of Al atoms are in distorted environments.

#### 4.3.2.2. Al-MCM-41 (Si/Al = 15) Samples that were Treated with Ozone

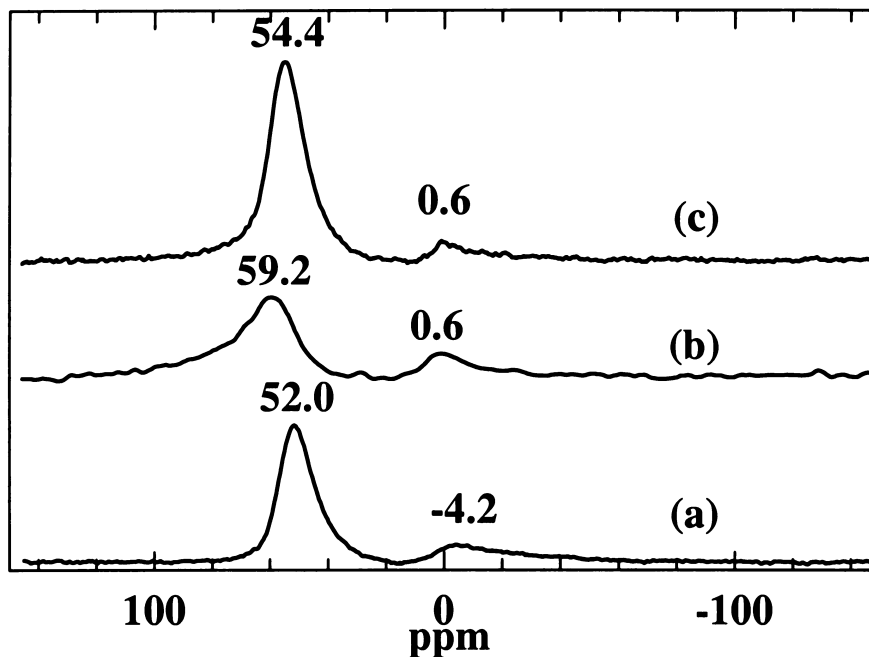


**Figure 4.10:**  $^{27}\text{Al}$ -MAS-NMR spectra of Al-MCM-41 (Si/Al = 15): (a) 15 (o-rt); (b) 15 (o-rt-813K); (c) 15 (o-423K).

The  $^{27}\text{Al}$ -MAS-NMR spectrum of 15 (o-rt) (Figure 4.10 (a)) shows two peaks with chemical shifts of ca. 52.0 and  $-4.2$  ppm, which can be assigned to tetrahedrally and octahedrally coordinated Al species, respectively. The relative peak area ratio between tetrahedral Al and octahedral Al is 6.7, i.e., about 13 % of Al atoms are in the extra-framework positions.

After further thermal calcination to completely remove the CTAC template, the  $^{27}\text{Al}$ -MAS-NMR spectrum of 15 (o-rt-813K) (Figure 4.10 (b)) shows peaks at ca. 59.2 ppm (tetrahedral Al) and ca. 0.6 ppm (octahedral Al), respectively. The relative peak area ratio between tetrahedral Al and octahedral Al is 5.7, i.e., about 17.5 % of Al atoms are in the extra-framework positions, which is close to the 17 % if it were directly calcined (see Section 3.3.2.1.2. in Chapter 3). It is also noted that the tetrahedral Al peak is not symmetrical. As suggested before, this is probably due to the formation of some other

coordinated Al species. The tetrahedral Al peak is broadened and further shifted to higher chemical shifts after further calcination, indicating that the Al species are in more distorted environments.

#### 4.3.2.3. Al-MCM-41 (Si/Al = 7) Samples that were Treated with Ozone

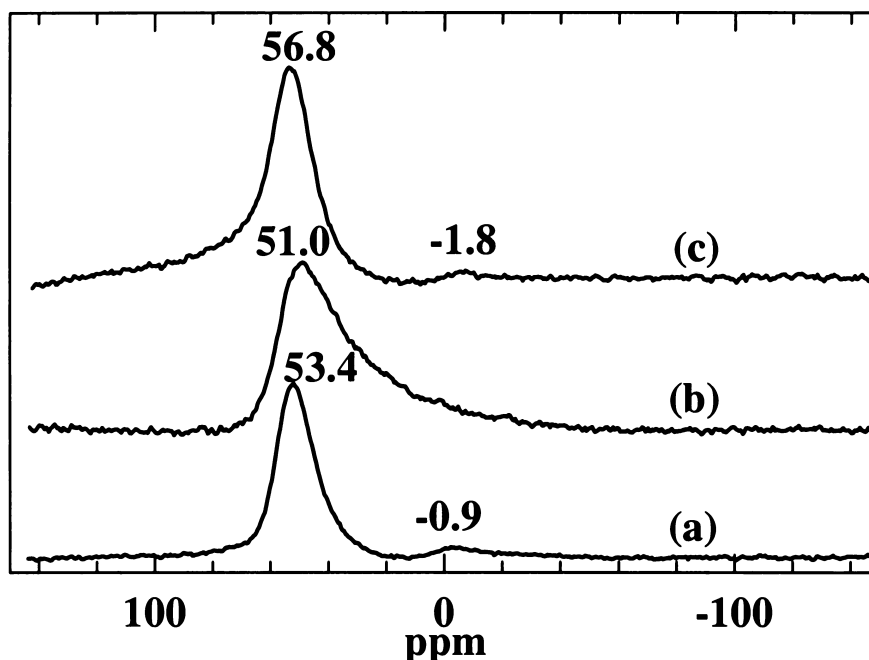


Figure 4.11:  $^{27}\text{Al}$ -MAS-NMR spectra of Al-MCM-41 (Si/Al = 7): (a) 7 (o-rt); (b) 7 (o-rt-813K); (c) 7 (o-423K).

The  $^{27}\text{Al}$ -MAS-NMR spectrum of 7 (o-rt) (Figure 4.11 (a)) shows two peaks with chemical shifts of ca. 53.4 (tetrahedral Al) and  $-0.9$  (octahedral Al) ppm, respectively. The relative peak area ratio between tetrahedral Al and octahedral Al is 20, i.e., about 5 % of Al atoms are in the extra-framework positions.

The  $^{27}\text{Al}$ -MAS-NMR spectrum of 15 (o-423K) (Figure 4.10 (c)) shows two peaks at ca. 54.4 and 0.7 ppm, which can be ascribed to tetrahedral and octahedral Al, respectively. Interestingly, the relative peak area between these two coordinations is 37.5, i.e., there are only ca. 3 % of Al atoms in undesired non-framework positions,

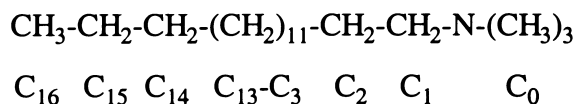
which is much lower than that after direct calcination. As suggested before, this may be due to relatively low temperature template removal. Compared with the directly calcined (15), the tetrahedral Al peak in the spectrum of 15 (o-423K) looks narrower and more symmetrical, indicating that more uniform Al coordination state in 15 (o-423K).

The  $^{27}\text{Al}$ -MAS-NMR spectrum of 7 (o-rt-813K) (Figure 4.11 (b)) shows only one peak at ca. 51.0 ppm due to tetrahedral Al, which is broader and unsymmetric compared to the spectrum of 7 (o-rt) sample, indicating that some other coordinated Al species (including octahedral Al) are formed during high temperature calcination. Assuming that the octahedral Al is at a chemical shift of 0 ppm, the peak area ratio between the tetrahedral Al and the octahedral Al is 9.8, i.e., ca. 9.3 % Al atoms are in the non-framework positions, much lower than that for the directly calcined (7) sample (25 %, see Section 3.3.2.1.3. in Chapter 3).

The  $^{27}\text{Al}$ -MAS-NMR spectrum of 7 (o-423K) (Figure 4.11 (c)) shows two peaks at ca. 56.8 and -1.8 ppm, which can be ascribed to tetrahedral and octahedral Al, respectively. Interestingly, the relative peak area between these two coordinations is 37.5, i.e., only ca. 2.7 % of Al atoms are in undesired non-framework positions, which is much lower than that after direct calcination. Compared with the calcined (7), the spectrum of 7 (o-423K) looks narrower and more symmetrical, indicating that the Al coordination in 7 (o-423K) is more uniform than that in calcined (7).

### 4.3.3. CP- $^{13}\text{C}$ -MAS-NMR Spectra

Figure 4.12 (a) shows the CP- $^{13}\text{C}$ -MAS-NMR spectrum of as-synthesized MCM-41, which contains the CTAC surfactant template. The carbon positions in the CTAC molecule are numbered as follows:



Then based on the data in the literature<sup>52,66</sup>, the peaks are assigned as follows: 53.3 ppm ( $\text{C}_0$  carbon), 30.1 ppm ( $\text{C}_3\text{-C}_{13}$  carbon), 22.9 ppm ( $\text{C}_{15}$  carbon), 26.3 ppm ( $\text{C}_2$  carbon), and 66.4 ppm ( $\text{C}_1$ ). The weak peak at 13.4 ppm, which is still above the noise level, can be assigned to  $\text{C}_{16}$ . The peak for  $\text{C}_{14}$  (33 ppm) cannot be directly observed due to the signal overlay. Figure 4.12 also shows the CP- $^{13}\text{C}$ -MAS-NMR spectra of three pre-washed Al-MCM-41 samples with Si/Al = 39 (Figure 4.12 (b)), 15 (Figure 4.12 (c)) and 7 (Figure 4.12 (d)), respectively. It can be seen that the chemical shift of the carbon atoms in the CTAC template are not significantly changed after Al incorporation and acidic ethanol washing. Simple calculation shows that in all samples the relative peak intensity ratio between the  $\text{-N(CH}_3\text{)}_3$  (53.3 ppm) and the  $\text{CH}_3\text{-CH}_2\text{-CH}_2\text{-(CH}_2\text{)}_n\text{-}$  (29 ppm) is ca. 0.2.

For comparison, the CP- $^{13}\text{C}$ -MAS-NMR spectrum of as-synthesized MCM-41 is also plotted together in Figure 4.13. Figure 4.13 (b) shows the CP- $^{13}\text{C}$ -MAS-NMR spectrum of MCM-41 (o-rt). The peaks can be assigned as follows:<sup>67</sup> 178.2 ppm (**new**,  $\text{C=O}$ ), 66.5 ppm ( $\text{-CH}_2\text{-N(CH}_3\text{)}_3$ ), 63 ppm (**new**,  $\text{CH}_3\text{-NO}_2$ ), 57.9 ppm (**new**,  $\text{-CH}_2\text{-COOH}$ ), 53.3 ppm ( $\text{-N(CH}_3\text{)}_3$ ), 41.3 ppm (**new**,  $\text{-CH}_2\text{-CH}_2\text{-COOH}$ ), 33.1 ppm (**new**,  $\text{CH}_3\text{-CH}_2\text{-CH}_2\text{-(CH}_2\text{)}_n\text{-}$ ), 29 ppm ( $\text{CH}_3\text{-CH}_2\text{-CH}_2\text{-(CH}_2\text{)}_n\text{-}$ ), 24 ppm ( $\text{-CH}_2\text{-CH}_2\text{-N(CH}_3\text{)}_3$ ), 22.5 ppm ( $\text{CH}_3\text{-CH}_2\text{-CH}_2\text{-}$ ) and 12.3 ppm ( $\text{CH}_3\text{-CH}_2\text{-}$ ). The relative peak intensity ratio between the  $\text{-N(CH}_3\text{)}_3$  (53.3 ppm) and the  $\text{CH}_3\text{-CH}_2\text{-CH}_2\text{-(CH}_2\text{)}_n\text{-}$  (29 ppm) is about 1, indicating that the amount  $\text{CH}_2$  in the system is dramatically decreased. These results demonstrate that part of CTAC molecules long alkyl chains were cleaved by ozone at room temperature and thus some new organic residues were produced. The emergence of a new peak at 33.1 ppm, which is assigned to  $\text{CH}_3\text{-CH}_2\text{-CH}_2\text{-(CH}_2\text{)}_n\text{-}$ , also can be

attributed to the cleavage of the alkyl chains of CTAC molecules, which will decrease the amount of the  $-(\text{CH}_2)_n$  and thus enhance the relative intensity of  $\text{CH}_3\text{-CH}_2\text{-CH}_2\text{-(CH}_2)_n\text{-}$ .

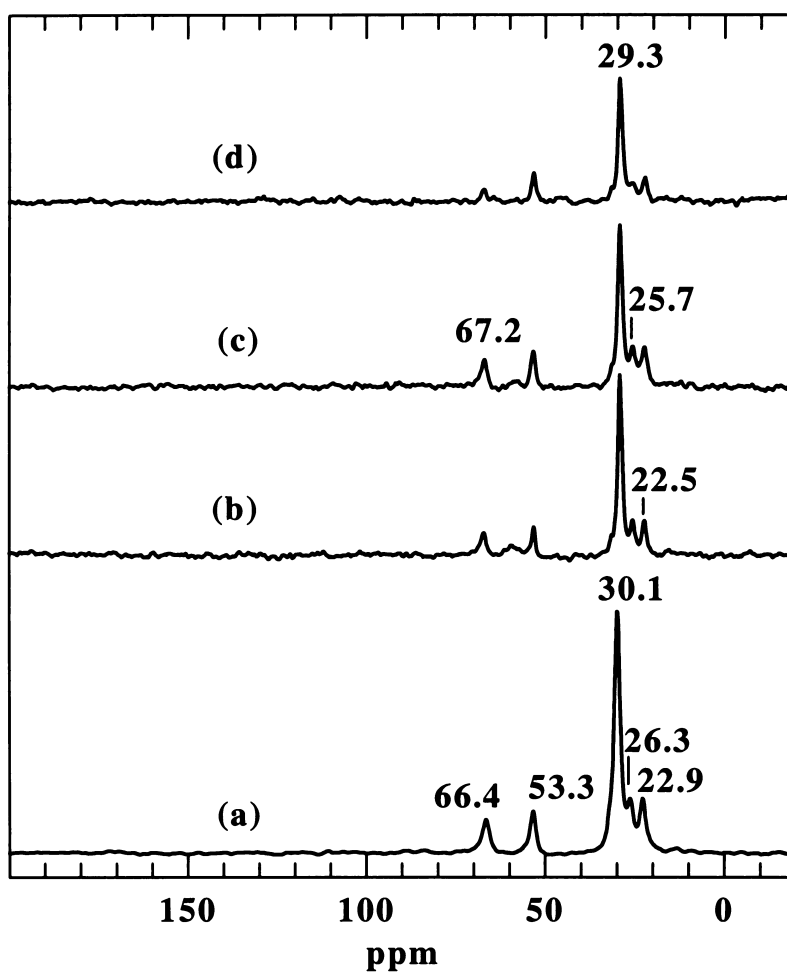


**Figure 4.12:** CP-<sup>13</sup>C-MAS-NMR spectra of: (a) as-synthesized MCM-41; (b) pre-washed (39); (c) pre-washed (15); (d) pre-washed (7).

After heating overnight at 423 K (Figure 4.13 (c)), the new peaks at 57.9 and 41.3 ppm disappeared, accompanied by decreases of the other peak intensities in certain levels compared to the peak at 53.3 ppm ( $-\text{N}(\text{CH}_3)_3$ ), indicating that some of those organic residues formed during ozone treatment at room temperature can be further removed by simple heating.



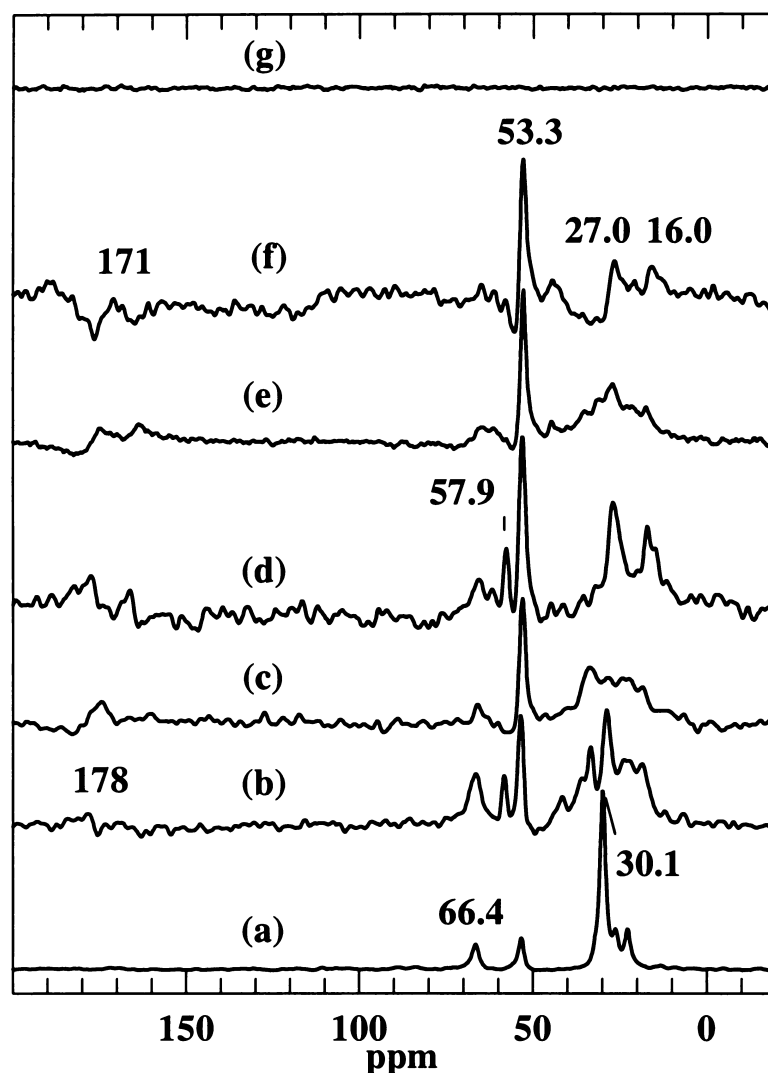


**Figure 4.13:** CP- $^{13}\text{C}$ -MAS-NMR spectra of: a) as-synthesized MCM41; (b) MCM-41 (o-rt); c) MCM41 (o-rt-423K); d) 39 (o-rt); e) 15 (o+rt); (f) 7(o- rt); g) MCM41, 39, 15, and 7 (o-423K).

Figures from 4.13 (d) to 4.13 (f) show the CP  $^{13}\text{C}$ -MAS-NMR spectra of the pre-washed Al-MCM-41 samples after ozone treatment at room temperature. Most of the peaks shown in Figure 4.13 (b) can also be seen in these spectra, except that the relative peak intensities are varied depending on the sample. This demonstrates that the ozonization degree of CTAC molecules largely depends on the sample conditions, but the final products are the same.

Interestingly, no organic residues were detected with solid state CP  $^{13}\text{C}$ -MAS-NMR for the samples whose templates were removed by ozone treatment at 423 K (see Figure 3.13 (g)).

## 4.4. Surface Properties

### 4.4.1. MCM-41 (o-rt-813K)

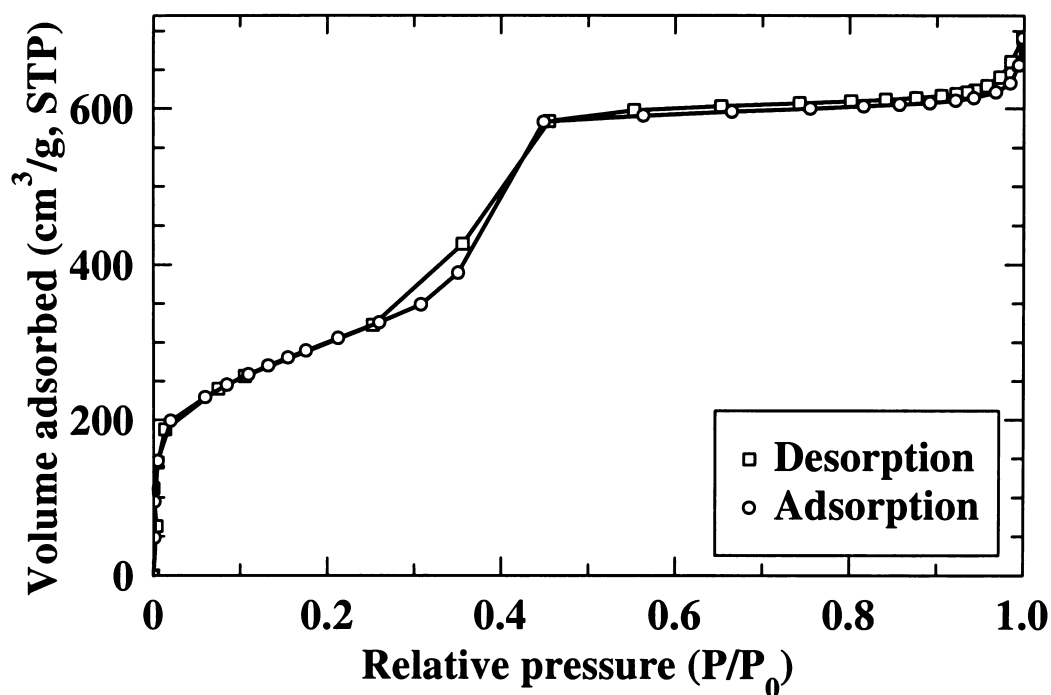
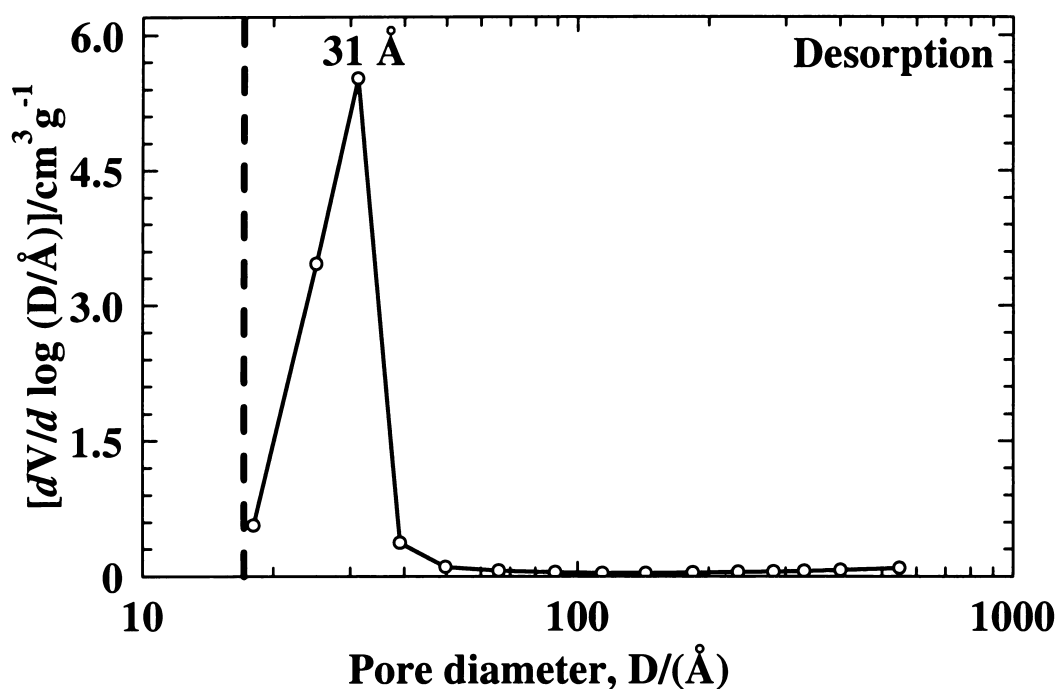


Figure 4.14: Nitrogen adsorption-desorption (77 K) isotherms of MCM-41 (o-rt-813K).

Figure 4.14 shows the nitrogen adsorption-desorption isotherms of MCM-41 (o-rt-813K). At the adsorption branch, the inflection at relative pressure  $P/P_0$  between ca. 0.31 and 0.45 is due to the capillary condensation. The desorption branch of the isotherm basically matches the adsorption branch except a small hysteresis loop due to capillary condensation was observed.



**Figure 4.15: BJH pore size distributions of MCM-41 (o-rt-813K) based on the nitrogen desorption isotherm.**

According to the  $N_2$  adsorption-desorption isotherm, the computed BET surface area is about  $1087 \text{ m}^2/\text{g}$ . The BJH cumulative desorption pore volume is about  $1.1 \text{ m}^3/\text{g}$  and the BJH desorption average pore diameter is about  $30 \text{ Å}$ . Using the adjacent pore center distance obtained from the corresponding XRD pattern, the calculated pore wall thickness is ca.  $17 \text{ Å}$ . These data are close to those for the direct calcined MCM-41 (see Section 3.5 in Chapter 3), indicating that the two step template removal (ozone treatment at room temperature followed by thermal calcination) has no significant change on the surface properties of MCM-41 compared to the direct calcination.

Figure 4.15 shows the BJH pore size distribution plot based on the  $N_2$  desorption isotherm. It can be seen that the pore size is centered at ca.  $31 \text{ Å}$ . Detailed surface properties are summarized in Table 4.5.

#### 4.4.2. MCM-41 (o-423K)

Figure 4.16 shows the nitrogen adsorption-desorption isotherms of MCM-41 (o-423K). The adsorption and desorption branches match well, indicating that the template was completely removed thus there is no pore blockage. The inflection at relative pressure  $P/P_0$  between ca. 0.35 and 0.45 is due to the capillary condensation, which is in the same range as that observed in the directly calcined sample.

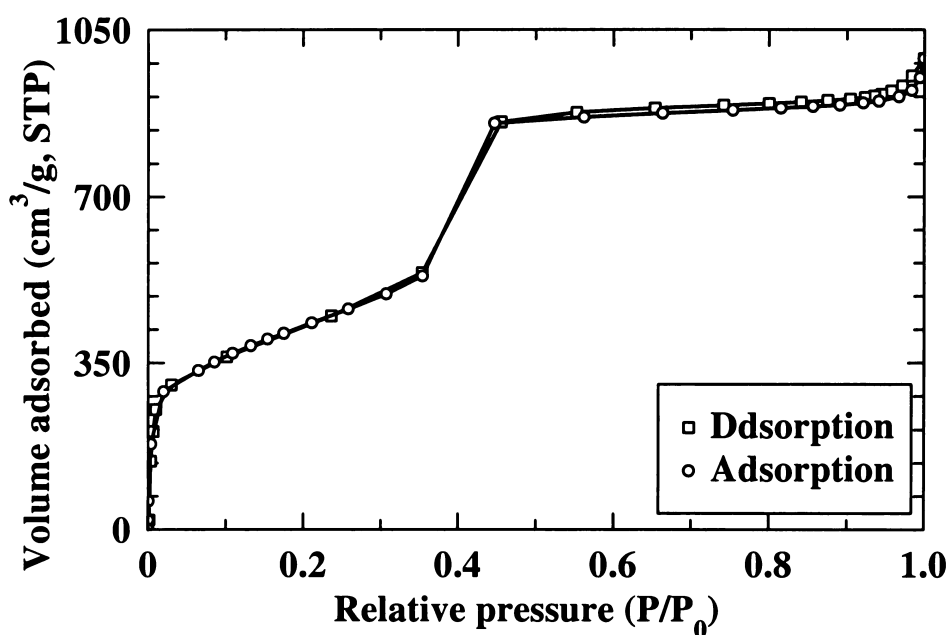


Figure 4.16: Nitrogen adsorption-desorption (77 K) isotherms of MCM-41 (o-423K).

The computed BET surface area is about  $1545 \text{ m}^2/\text{g}$ . The BJH average pore volume is about  $1.6 \text{ m}^3/\text{g}$ . These surface parameters are much larger than those for directly calcined MCM-41. However, the BJH desorption average pore diameter is about  $31 \text{ \AA}$ . Using the adjacent pore center distance obtained from the corresponding XRD pattern, the calculated pore wall thickness is ca.  $17 \text{ \AA}$ , close to that of the directly calcined MCM-41 (see Section 3.5 in Chapter 3). High surface area, large pore volume and a

thick pore wall given by MCM-41 (o-423K) indicate the superiority of the template removal by ozone treatment at 423 K over conventional thermal calcination.

Figure 4.17 shows the BJH pore size distribution plot based on the N<sub>2</sub> desorption isotherm. It can be seen that the pore size distribution is centered at ca. 32 Å. The narrow pore sized distribution indicates the structural uniformity of the MCM-41 (o-423K). Detailed surface properties are summarized in Table 4.6.

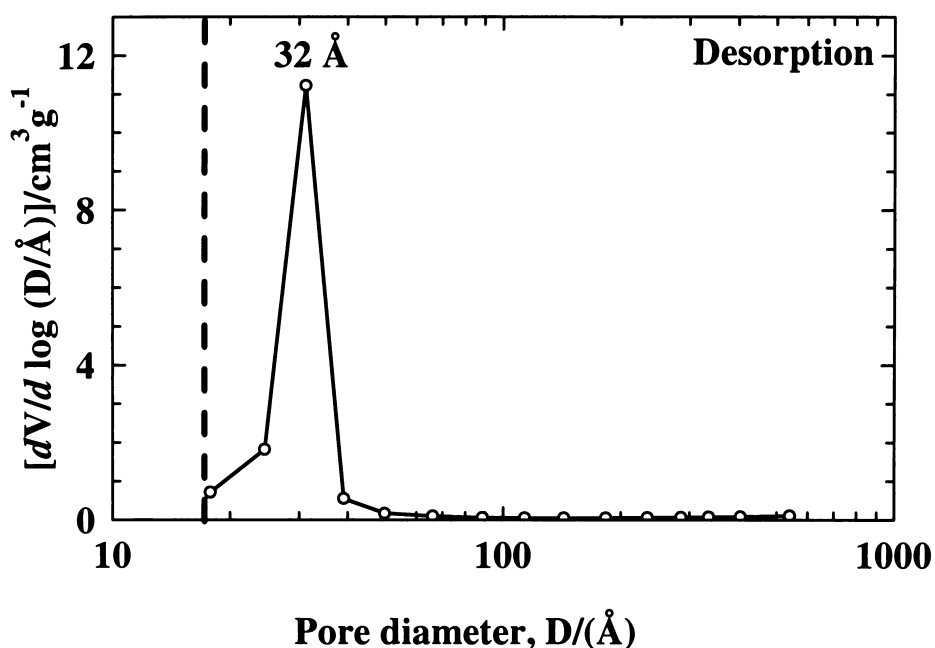


Figure 4.17: BJH pore size distributions of MCM-41 (o-423K) based on nitrogen desorption isotherm.

#### 4.4.3. 39 (o-rt-813K)

Figure 4.18 shows the nitrogen adsorption-desorption isotherms of 39 (o-rt-813K). At the adsorption branch, the inflection at relative pressure  $P/P_0$  between ca. 0.35 and 0.45 is due to the capillary condensation. Compared with the isotherms of the calcined (39) (see Section 3.5 in Chapter 3), the isotherms of the 39 (o-rt-813K) sample shows less hysteresis, indicating that the porous structure is better developed.

The BET surface area is about  $1170 \text{ m}^2/\text{g}$ . The BJH cumulative desorption pore volume is about  $1.3 \text{ m}^3/\text{g}$  and the BJH desorption average pore diameter is about  $33 \text{ \AA}$ . Using the adjacent pore center distance obtained from the corresponding XRD pattern, the calculated pore wall thickness is ca.  $13 \text{ \AA}$ .

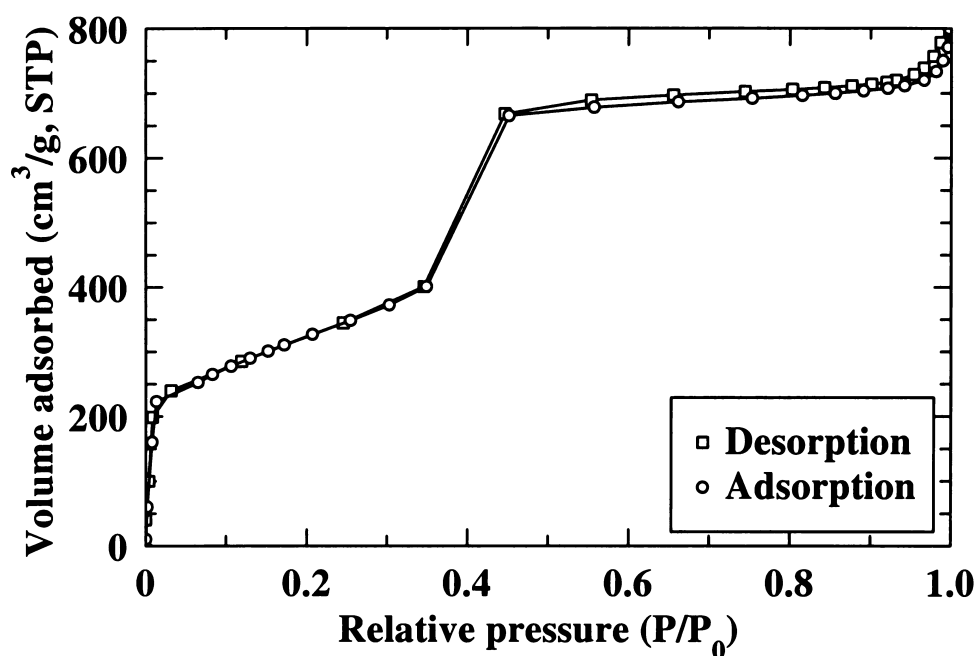


Figure 4.18: Nitrogen adsorption-desorption (77 K) isotherms of 39 (o-rt-813K).

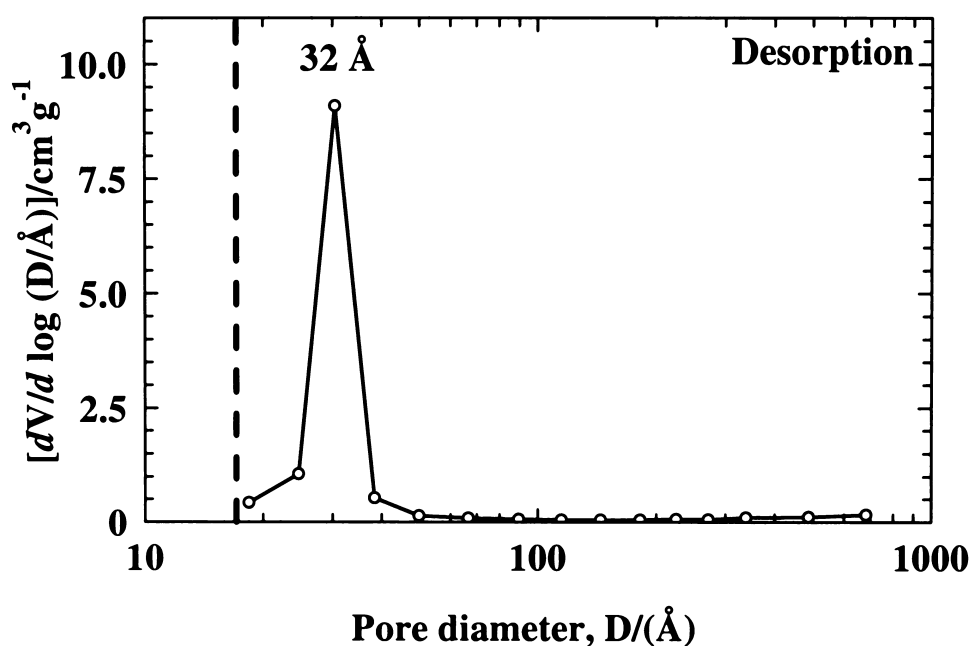


Figure 4.19: BJH pore size distributions of 39 (o-rt-813K) based on the nitrogen desorption isotherm.

Figure 4.19 shows the BJH pore size distribution plot based on the N<sub>2</sub> adsorption-desorption isotherm. It can be seen that the pore size distribution is centered at ca. 32 Å. Narrow pore sized distribution indicates that 39 (o-rt-813K) has a uniform pore structure. Unlike the directly calcined sample, coexistence of different mesopores is not observed. Detailed surface properties are summarized in Table 4.5.

#### 4.4.4. 39 (o-423K)

Figure 4.20 shows the nitrogen adsorption-desorption isotherms of 39 (o-423K). Compared with the directly calcined (39) (see Section 3.5 in Chapter 3), the isotherms of 39 (o-423K) shows less hysteresis, indicating that template removal by ozone treatment at 423 K generates a more open pore structure. The inflection at relative pressure  $P/P_0$  between ca. 0.31 and 0.45 is due to the capillary condensation, which is slightly narrower than that observed in the directly calcined sample.

The BET surface area is about 1183 m<sup>2</sup>/g. The BJH cumulative desorption pore volume is about 1.2 m<sup>3</sup>/g, both of which are larger than those for directly calcined (39). However, the BJH desorption average pore diameter (ca. 30 Å) shows significant change. Using the adjacent pore center distance obtained from the corresponding XRD pattern, the calculated pore wall thickness is ca. 17 Å, close to that of the directly calcined (39) (see Section 3.5 in Chapter 3).

Figure 4.21 shows the BJH pore size distribution plot based on the N<sub>2</sub> desorption isotherm. It can be seen that the pore size is centered at ca. 31 Å. The narrow pore size distribution indicates the structural uniformity of the 39 (o-423K). In addition, no distinct coexistence of different pore size is observed, which is a common feature in directly calcined Al-MCM-41 samples. Detailed surface properties are summarized in Table 4.6.

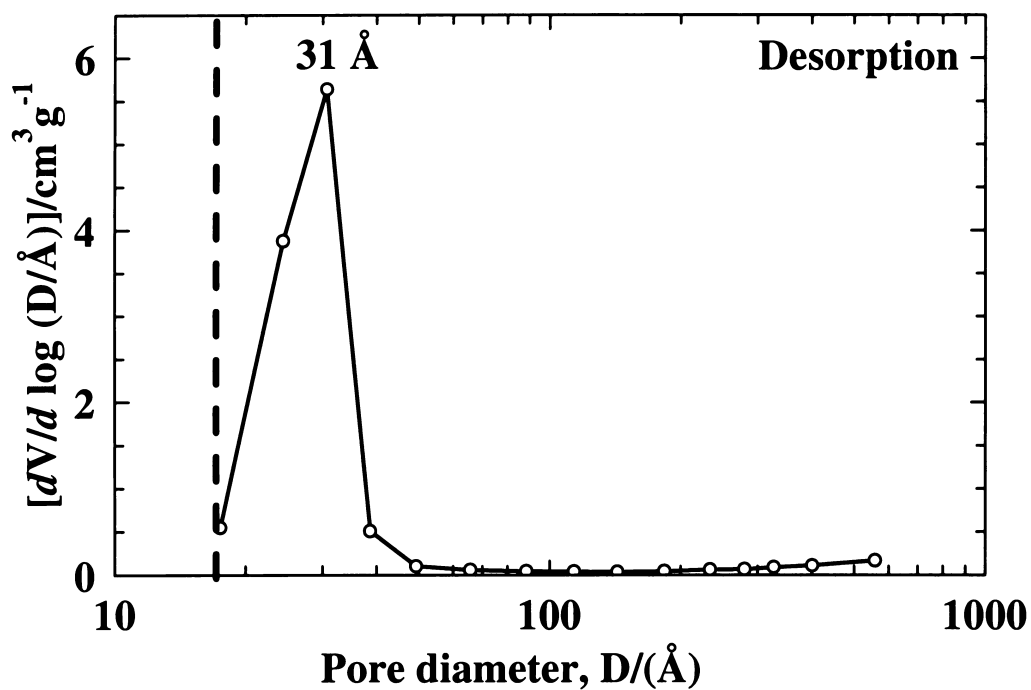


Figure 4.21: BJH pore size distributions of 39 (o-423K): (A) from nitrogen adsorption isotherm; (B) from nitrogen desorption isotherm.

#### 4.4.5. 15 (o-rt-813K)

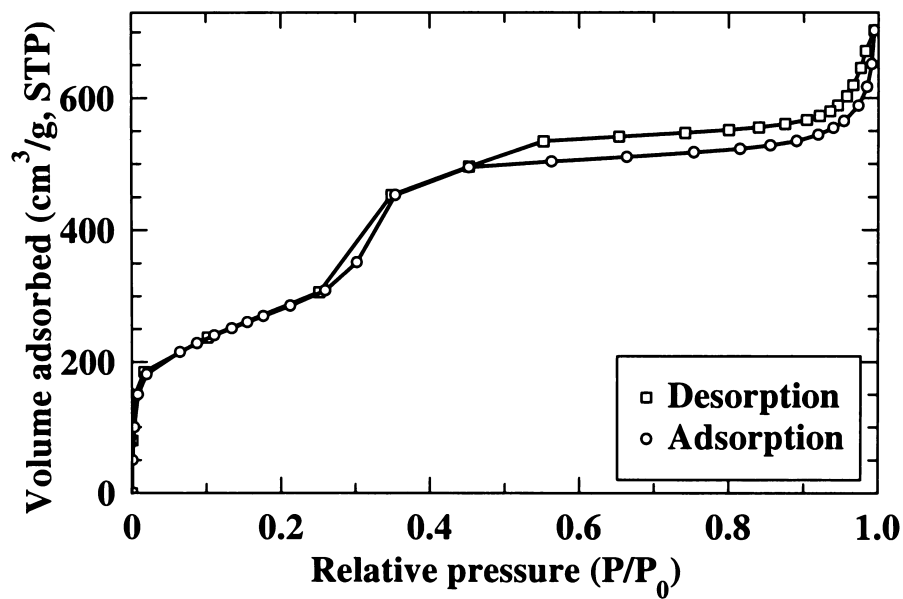


Figure 4.22: Nitrogen adsorption-desorption (77 K) isotherms of 15 (o-rt-813K).



Figure 4.22 shows the nitrogen adsorption-desorption isotherms of 15 (o-rt-813K). Two step capillary condensation can be observed: that at  $P/P_0 = 0.25-0.35$  is due to smaller pore size and that at  $P/P_0 = 0.35-0.45$  is due to larger pore size. Compared with the isotherms of the calcined (15) (see Section 3.5 in Chapter 3), the isotherms of the 39 (o-rt-813K) sample shows less hysteresis, indicating that the porous structure is better developed. This may be due to the fact that ozone treatment at room temperature removes or/and degrades part of the CTAC templates, which will lessen the exothermic heating effect in the following calcination process and thus reduce the pore wall collapse at high temperatures.

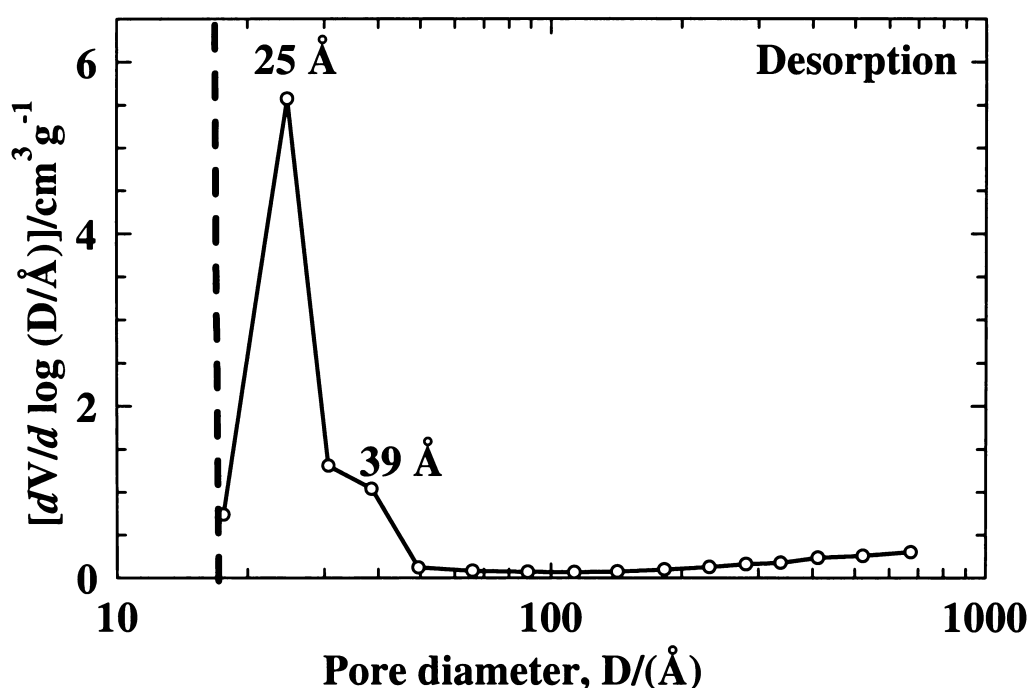


Figure 4.23: BJH pore size distributions of 15 (o-rt-813K) based on the nitrogen desorption isotherm.

The BET surface area is about 1022 m<sup>2</sup>/g. The BJH cumulative desorption pore volume is about 1.1 m<sup>3</sup>/g and the BJH desorption average pore diameter is about 31 Å. Using the adjacent pore center distance obtained from the corresponding XRD pattern, the calculated pore wall thickness is ca. 13 Å.

Figure 4. 24 shows the BJH pore size distribution plot based on the N<sub>2</sub> desorption isotherm. It can be seen that the pore size is centered at ca. 25 Å accompanied by some larger pore sizes centered at 39 Å. This result is consistent with the result of the isotherm analyses. Detailed surface properties are summarized in Table 4.5.

#### 4.4.6. 15 (o-423K)

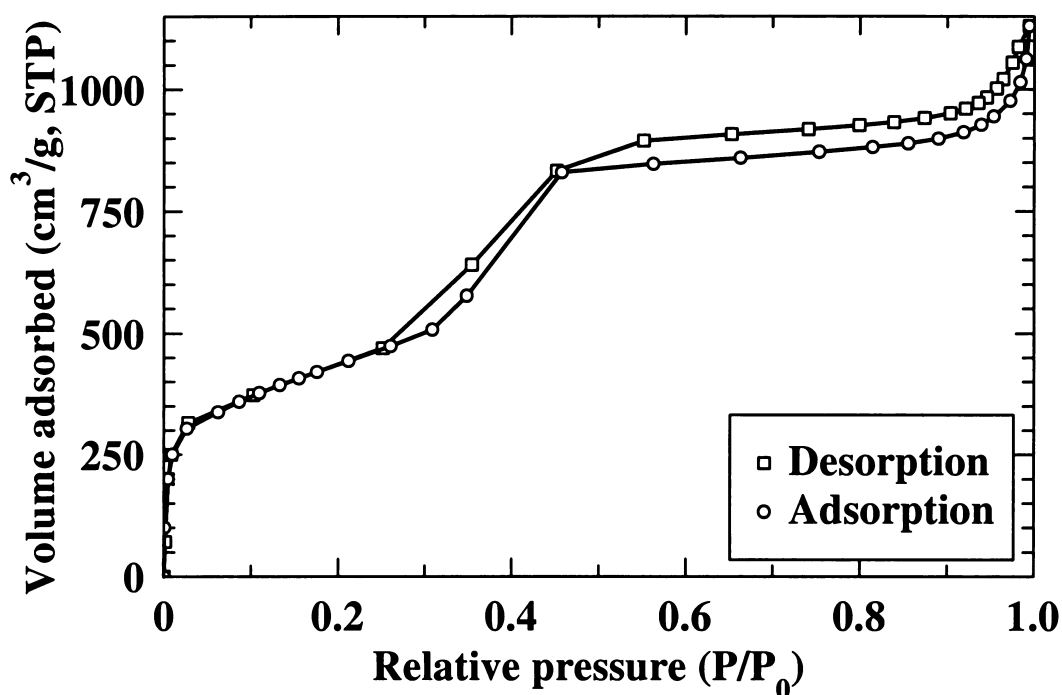


Figure 4.24: Nitrogen adsorption-desorption (77 K) isotherms of 15 (o-423K).

Figure 4.24 shows the nitrogen adsorption-desorption isotherms of 15 (o-423K). Compared with the directly calcined (15) (see Section 3.5 in Chapter 3), the isotherms of 15 (o-423K) shows less hysteresis, indicating that template removal by ozone treatment at 423 K generates a more open pore structure. The step at relative pressure  $P/P_0$  between ca. 0.25 and 0.46 is due to capillary condensation. Though this is a straight inflection line, the shift of the inflection to a low relative pressure indicates that some particles with smaller pore size coexist.

The BET surface area is about  $1073 \text{ m}^2/\text{g}$ , larger than the thermally calcined sample (See Section 3.5 in Chapter 3). The BJH cumulative desorption pore volume is about  $1.8 \text{ m}^3/\text{g}$  and the BJH desorption average pore diameter is ca.  $33 \text{ \AA}$ . Using the adjacent pore center distance obtained from the corresponding XRD pattern, the calculated pore wall thickness is ca.  $14 \text{ \AA}$ .

Figure 4.25 shows the BJH pore size distribution plot based on the  $\text{N}_2$  desorption isotherm. It can be seen that the pore size is centered at ca.  $31 \text{ \AA}$  with a shoulder at  $25 \text{ \AA}$ , indicating coexistence of two different pores. Detailed surface properties are summarized in Table 4.6.

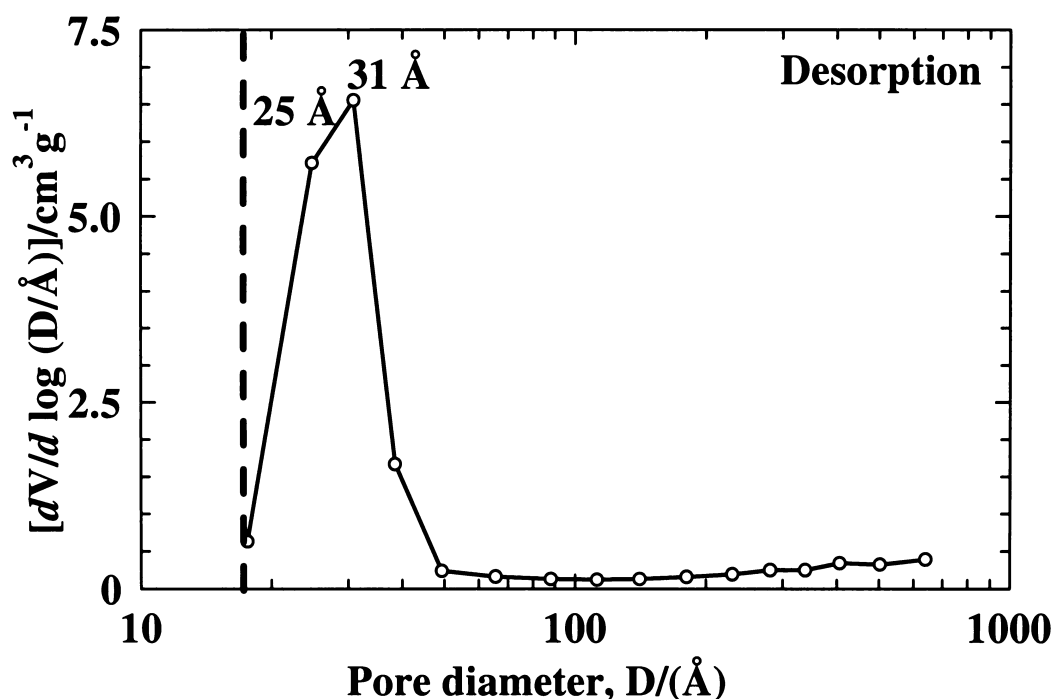


Figure 4.25: BJH pore size distributions of 15 (o-423K) based on the nitrogen desorption isotherm.

#### 4.4.7. 7 (o-rt-813K)

Figure 4.26 shows the nitrogen adsorption-desorption isotherms of 7 (o-rt-813K), which are type IV. The capillary condensation clearly presents at  $P/P_0 = 0.32\text{--}0.45$

which is in the mesopores region, and the sudden uptake at  $P/P_0 = 0.89-0.99$  is due to the pore filling of the macropores. Compared with the isotherms of the calcined (7) (see Section 3.5 in Chapter 3), the isotherms of the 7 (o-rt-813K) sample show less hysteresis, indicating that the porous structure is better developed. As suggested before, this may be due to part of the CTAC molecules have been degraded by room temperature ozone treatment and thus reduced the exothermic heat effect in the following thermal calcination.

The BET surface area is about  $472 \text{ m}^2/\text{g}$ . The BJH cumulative desorption pore volume is about  $1.0 \text{ m}^3/\text{g}$  and the BJH desorption average pore diameter is about  $66 \text{ \AA}$ . Large BJH average pore diameter is due to the formation of the larger mesopores and macropores.

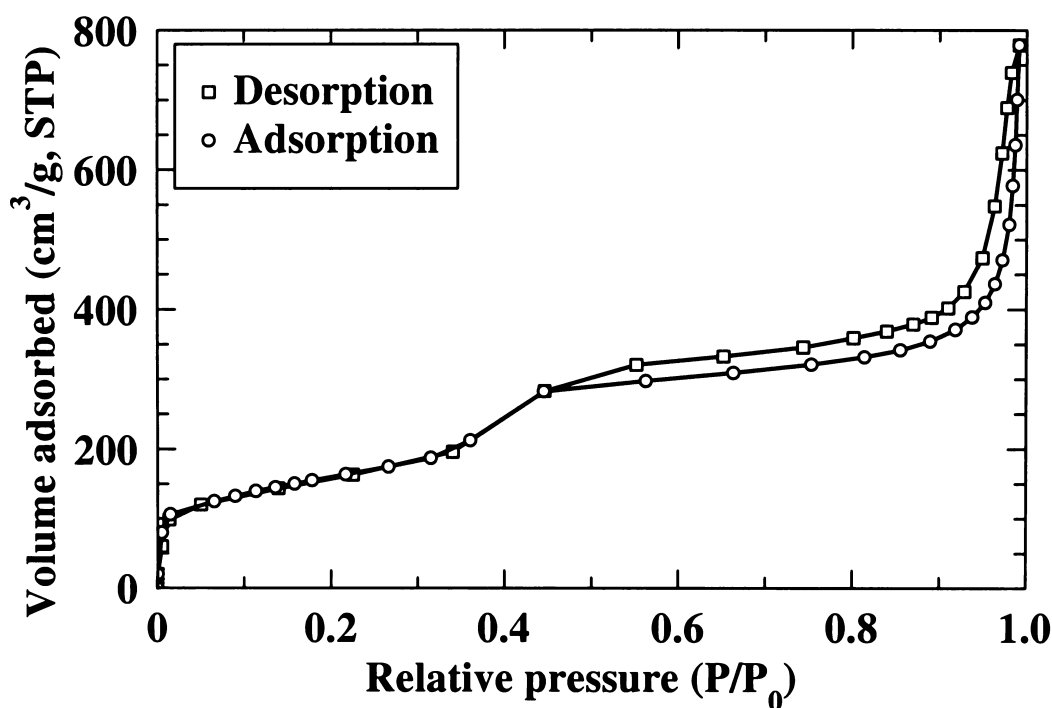


Figure 4.26: Nitrogen adsorption-desorption (77 K) isotherms of 7 (o-rt-813K).

Figure 4. 27 shows the BJH pore size distribution plot based on the  $\text{N}_2$  desorption isotherm. It can be seen that the pore size distributions are mainly centered at ca.  $25 \text{ \AA}$ ,

38 Å and 598 Å, respectively. The relative intensity ( $dV/d \log D / (\text{Å}) / \text{cm}^3 \text{g}^{-1}$ ) of the macropores region for the 7 (o-rt-813 K) is much less than that for the directly calcined (7) (See Section 3.5 in Chapter 3). This comparison further confirms that partial removal of the surfactant template with ozone at room temperature before calcination may lessen the pore wall collapse. Using the adjacent pore center distance obtained from the corresponding XRD pattern, and the centered mesopore diameter of (25 Å), shown in the pore size distribution plot based on the desorption branch, the calculated pore wall thickness is ca. 24 Å. Detailed surface properties are summarized in Table 4.5.

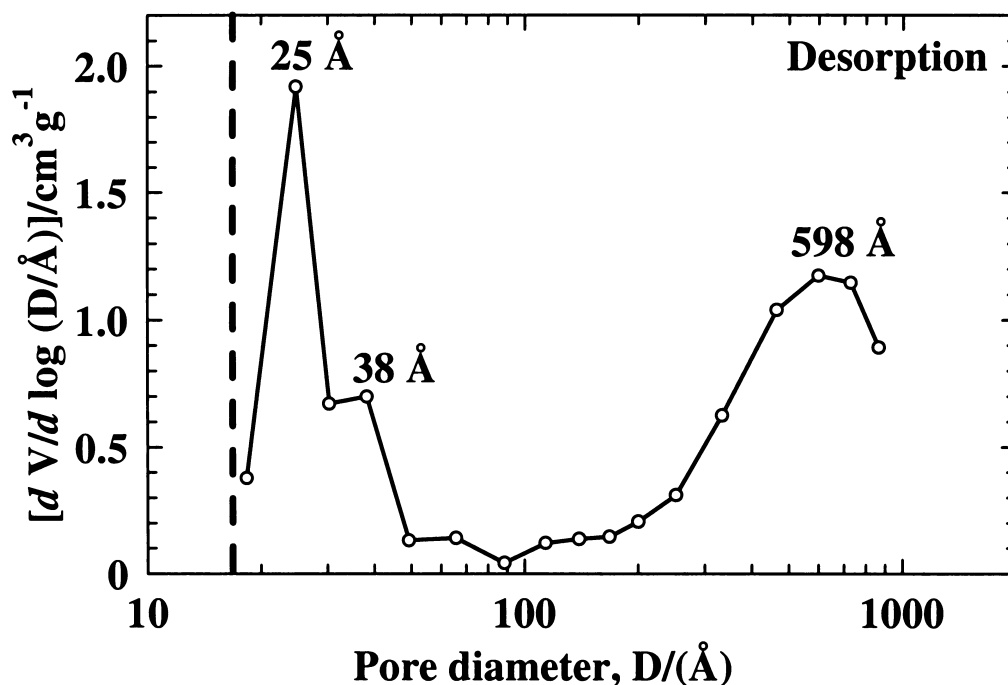


Figure 4.27: BJH pore size distributions of 7 (o-rt-813K) based on the nitrogen desorption isotherm.

#### 4.4.8. 7 (o-423K)

Figure 4.28 shows the nitrogen adsorption-desorption isotherms of 7 (o-423K). The inflection point due to capillary condensation at  $P/P_0 = 0.32$ -0.45 is in the mesopores region, and the sudden uptake at  $P/P_0 = 0.89$ -0.99 is due to the pore filling of the macropores. Compared with the isotherms of the calcined (7) (see Section 3.5 in Chapter 3), the isotherms of the 7 (o-rt-813K) sample shows less hysteresis, indicating that the porous structure is better developed. This may be attributed to the template removal at a relatively low temperature (423K) causes less pore wall collapse.

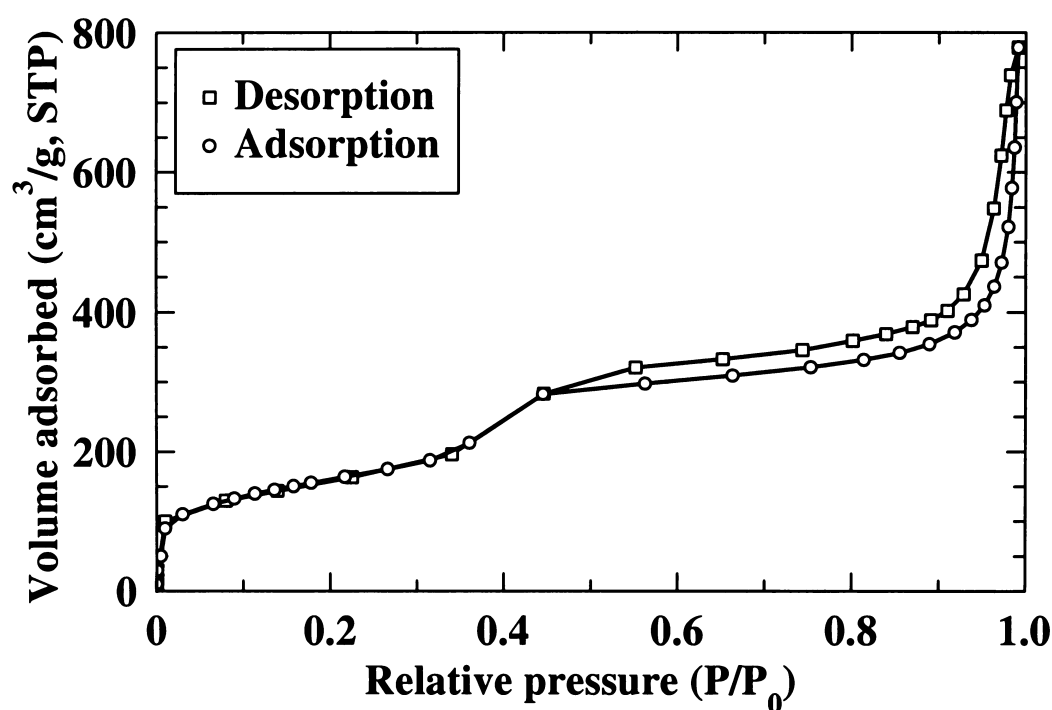


Figure 4.28: Nitrogen adsorption-desorption (77 K) isotherms of 7 (o-423K).

The BET surface area is about 579 m<sup>2</sup>/g. The BJH cumulative desorption pore volume is about 1.2 m<sup>3</sup>/g and the average pore diameter is about 66 Å. Large average pore diameter is due to coexistence of some larger mesopores and macropores (see BJH pore size distribution analyses below).

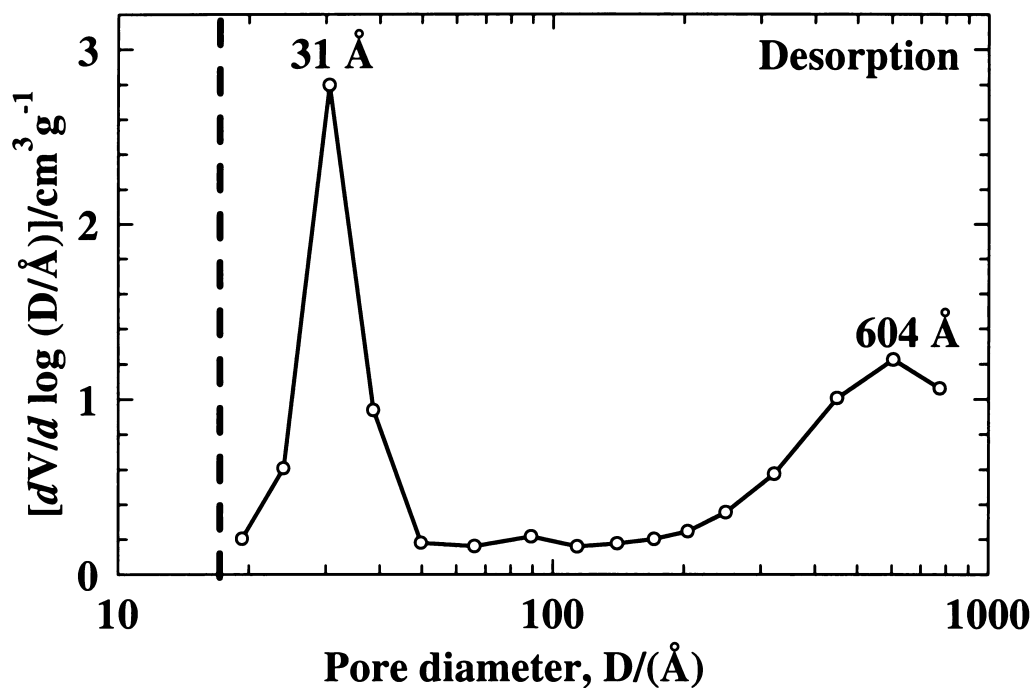


Figure 4.29: BJH pore size distributions of 7 (o-423K): (A) from nitrogen adsorption isotherm; (B) from nitrogen desorption isotherm.

Table 4.5: Surface properties of (Al)-MCM-41 samples that were treated with ozone at room temperature, followed by thermal calcination at 813K

Sample	MCM-41(o-rt-813K)	39 (o-rt-813K)	15(o-rt-813K)	7(o-rt-813K)
BET surface area (m <sup>2</sup> /g)	1087	1170	1022	472
BJH cumulative desorption pore volume (cm <sup>3</sup> /g)	1.1	1.3	1.1	1.0
BJH desorption average pore diameter (Å)	30	33	31	66 (25) <sup>a</sup>
Adjacent pore center distance (XRD) (Å)	47	46	44	47
Pore wall thickness (Å)	17	13	13	24

Notes: (a) the number in parenthesis is from the pore size distribution plot based on the desorption isotherm.

Figure 4. 29 shows the BJH pore size distribution plot based on the N<sub>2</sub> desorption branch. It can be seen that the pore size is centered mainly at ca. 31 Å. However,

distribution of some macropores centered at ca. 604 Å can also be observed. The relative intensity of the macropores region for the 7 (o-423K) is much less than that for the directly calcined (7) (See Section 3.5 in Chapter 3), indicating that the porous structure in 7 (o-423K) is more uniform. Using the adjacent pore center distance obtained from the corresponding XRD pattern and the centered mesopore diameter (31 Å) shown in the desorption pore size distribution plot, the calculated pore wall thickness is ca. 17 Å.

**Table 4.6: Surface properties of (Al)-MCM-41 samples that were treated with ozone at 423 K**

Sample	MCM-41(o-423K)	39(o-423K)	15(o-423K)	7(o-423K)
BET surface area (m <sup>2</sup> /g)	1545	1183	1073	579
BJH cumulative desorption pore volume (cm <sup>3</sup> /g)	1.6	1.2	1.8	1.2
BJH desorption average pore diameter (Å)	31	30	33	66 (31) <sup>a</sup>
Adjacent pore center distance (XRD) (Å)	48	47	47	48
Pore wall thickness (Å)	17	17	14	17

**Notes: (a) the number in parenthesis is from the pore size distribution plot based on the desorption isotherm.**

#### **4.5. Template Removal by EtOH/HCl Liquid Extraction and Ozone Treatments**

The infrared band assignments for the MCM-41 and the CTAC surfactant molecule are summarized in Table 4.7 and Table 4.8, respectively.



**Table 4.7: Infrared band assignments<sup>68</sup> of MCM-41 in the frequency range of 500-4000 cm<sup>-1</sup>**

Stretching O-H vibrations		Other infrared vibrations	
Species	Frequency (cm <sup>-1</sup> )	Species	Frequency (cm <sup>-1</sup> )
Free OH	3746	Bending OH (molecular water)	1625
Geminal OH	3742	Asymmetrical Si-O-Si stretching	1250-1020
Hydrogen perturbed OH	3730-3720	Si-O-(H....H <sub>2</sub> O) bending	970
Intraglobular OH	3650	Bending O-H (silanol)	870
Oxygen perturbed OH	3520	In-plane bending (geminol)	800
Molecular adsorbed H <sub>2</sub> O	3400-3500	In-plane bending (geminol)	600

**Table 4.8: CTAC surfactant template IR modes<sup>69</sup>**

Band / cm <sup>-1</sup>	assignment
3017	$\nu_{as} \text{CH}_3-(\text{N}^+)$
2944	$\nu_s \text{CH}_3-(\text{N}^+)$
2958	$\nu_{as} \text{CH}_3$
2924	$\nu_{as} \text{CH}_2$
2872	$\nu_s \text{CH}_3$
2853	$\nu_s \text{CH}_2$
1490	$\delta_{as} \text{CH}_3-(\text{N}^+)$
1480	$\delta_{as} \text{CH}_3-(\text{N}^+)$
1468	$\delta \text{CH}_2$ scissor

**Note:** These band assignments are based on the published data for CTABr in reference 70.

#### 4.5.1. Efficiency of EtOH/HCl Liquid Extraction on Template Removal

The efficiency of acidic ethanol extraction of the CTAC template from the as-synthesized (Al)-MCM-41 materials was studied using FTIR. Figure 4.30 shows the FTIR spectra of as-synthesized MCM-41 and acidic ethanol pre-washed Al-MCM-41 samples (the spectrum of pre-washed MCM-41 is not shown). For purposes of comparison, all of the spectra were normalized to the same intensity of the framework bands between 1400-850 cm<sup>-1</sup>. Percentages of the removed (or degraded) CTAC

template were calculated using the alkyl stretching bands between 2990-2820  $\text{cm}^{-1}$  (designated as “bands T”) as internal standards for the CTAC molecules, while the MCM-41 framework bands between 1400-850  $\text{cm}^{-1}$  (designated as “bands S”) as internal standards for the MCM-41 silicate framework. During calculation, the following assumptions are made: (1) The as-synthesized MCM-41 and Al-MCM-41 (Si/Al = 39, 15, 7) possessed the same amount of the CTAC templates. (2) The loss of the (alumino)silicate framework due to dissolution during acidic ethanol treatment was the same for the four samples.

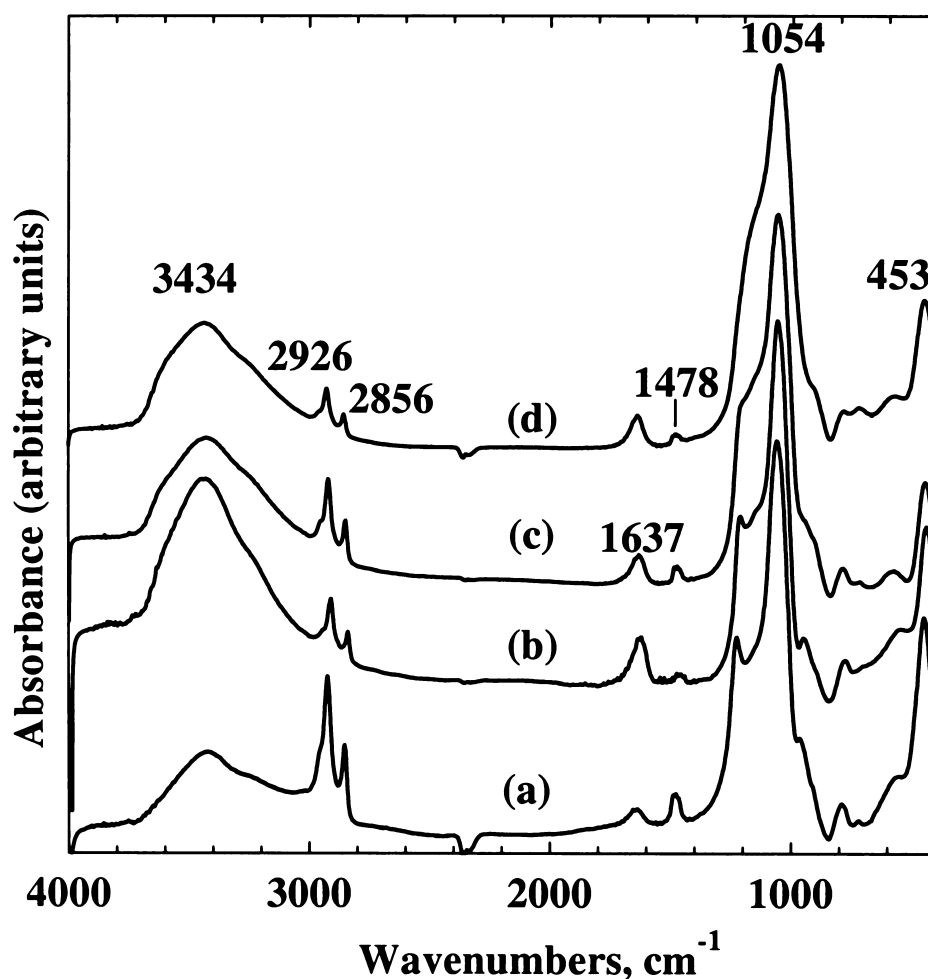


Figure 4.30: FTIR (KBr) absorption spectra for: (a) as-synthesized MCM-41; (b) pre-washed Al-MCM-41 (Si/Al = 39); (c) pre-washed Al-MCM-41 (Si/Al = 15); and (d) pre-washed Al-MCM-41 (Si/Al = 7).

It was found that ca. 82 %, 62 %, 58 % and 78 % of CTCA surfactant template were removed from as-synthesized MCM-41, Al-MCM-41 (Si/Al =39), Al-MCM-41 (Si/Al = 15) and Al-MCM-41 (Si/Al =7), respectively. In experimental error, it can be roughly figured out that the acidic ethanol washing can extract up to 60-80 % of CTAC surfactant from (Al)-MCM-41 samples. This result is in good agreement with the report of Hitz et. al,<sup>22</sup> who suggested an ion-exchange mechanism for liquid extraction of the template and pointed out that the pore size and therefore the mobility of the cation in the close packed micellar aggregates is one of the factors determining the amount of template that can be removed by extraction with ethanol.

#### **4.5.2. Efficiency of Ozone Treatments on Template Removal**

##### **4.5.2.1. Purely Siliceous MCM-41**

The FTIR spectra shown in Figure 4.31 are normalized to the same intensity as the framework bands located between 1400-850  $\text{cm}^{-1}$ . The FTIR spectrum of as-synthesized MCM-41 (Figure 4.31 (a)) shows absorption bands at 2925 ( $\nu_{\text{as}} \text{CH}_3$ ), 2854 ( $\nu_{\text{as}} \text{CH}_2$ ) and 1483  $\text{cm}^{-1}$  ( $\delta_{\text{as}} \text{CH}_3\text{-(N}^+)$ ). The broad absorption band at 3000-3750  $\text{cm}^{-1}$ , which is centered at around 3337  $\text{cm}^{-1}$ , is mainly due to the hydrogen bonded silanol groups and physically adsorbed water. The peak at 1635  $\text{cm}^{-1}$  is due to the -OH bending mode of water. The bands between 1400-500  $\text{cm}^{-1}$  are characteristic of absorption of the silicate skeleton framework.

The FTIR spectra were measured at various time intervals in order to determine a suitable reaction time. It was found that ozone reacts with CTAC surfactant template slowly at room temperature, which was reflected by the slow rate of decrease of the intensity of the 2925 and 2854  $\text{cm}^{-1}$  C-H stretching bands in the FTIR spectra. After 2

days, the intensity of these stretching bands reached the minimum and did not change in the next 2 days, indicating that ozone could not react further with CTAC. In this case, 2 days reaction time was adopted during ozone treatment at room temperature.

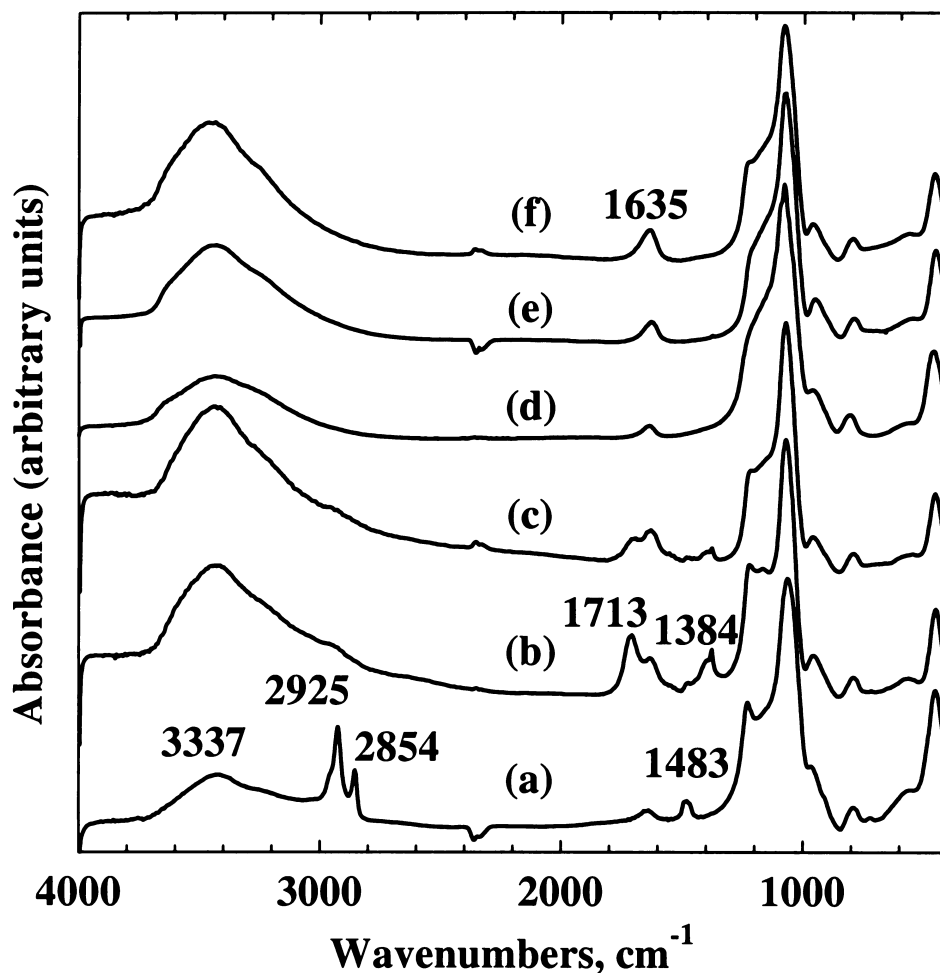


Figure 4.31: FTIR (KBr) absorption spectra for: (a) as-synthesized MCM-41; (b) MCM-41 (o-rt); (c) MCM-41 (o-rt-423K); (d) MCM-41 (o-rt-423K-813K); (e) MCM-41 (o-423K); (f) calcined MCM-41.

After ozone treatment at room temperature, most of the CTAC template molecules were degraded (or removed), indicated by the dramatic reduction of the  $\nu_{\text{as}} \text{CH}_3$  (2925  $\text{cm}^{-1}$ ) and  $\nu_{\text{as}} \text{CH}_2$  (2854  $\text{cm}^{-1}$ ) bands into barely detectable peaks (Figure 4.31 (b)). Besides, two new bands at 1713 ( $\nu \text{C=O}$ ) and 1384  $\text{cm}^{-1}$  ( $\delta \text{-OCOCH}_3$  or  $\text{-COCH}_3$ ) indicate that some residues with carbonyl groups were formed and remained inside the

pores and cannot be removed by simple heating at 423 K (Figure 4.31 (c)). However, these residues can be removed completely by thermal calcination (Figure 4.31 (d)).

Since ozone can at least partially remove (or degrade) the CTAC in MCM-41 at room temperature, it is hoped that under proper experimental conditions, ozone can completely remove CTAC surfactant. Interestingly, this is the case when the as-synthesized four samples were treated with ozone at 423 K for one day (Figure 4.31 (e)). The bands associated with C-H stretching modes of the alkyl group at around  $2900\text{--}2800\text{ cm}^{-1}$  were absent and no new peaks were observed. The spectrum looked no different from the one for the directly calcined sample (Figure 4.31 (f)).

#### 4.5.2.2. Al-MCM-41

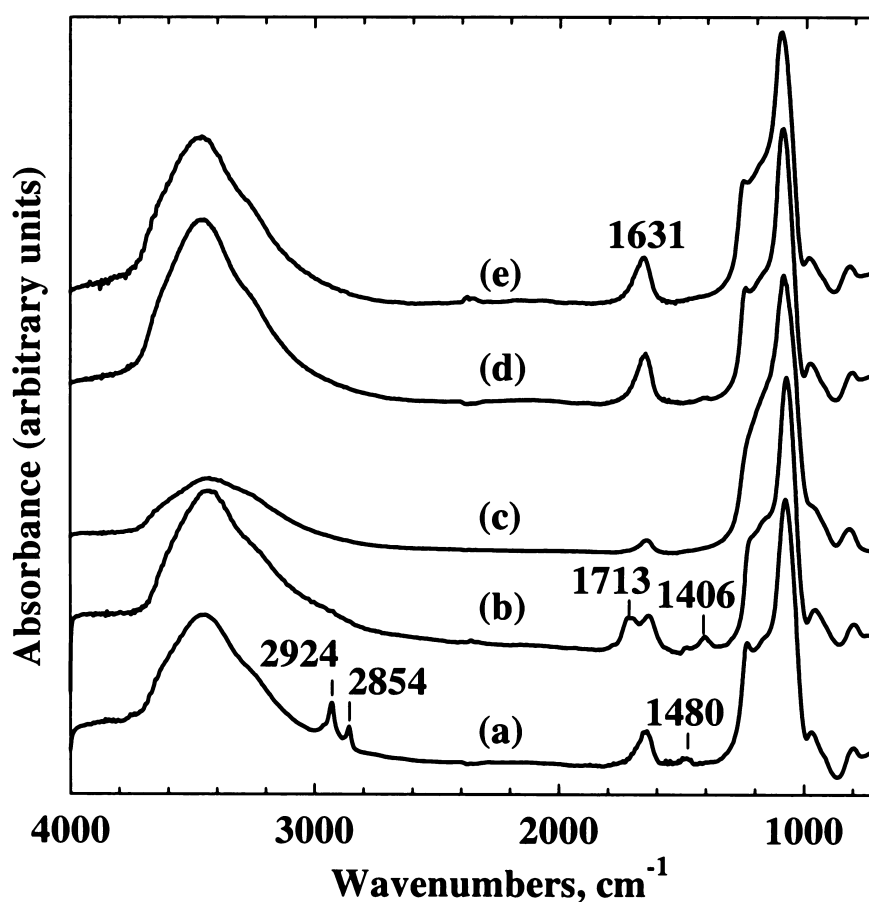
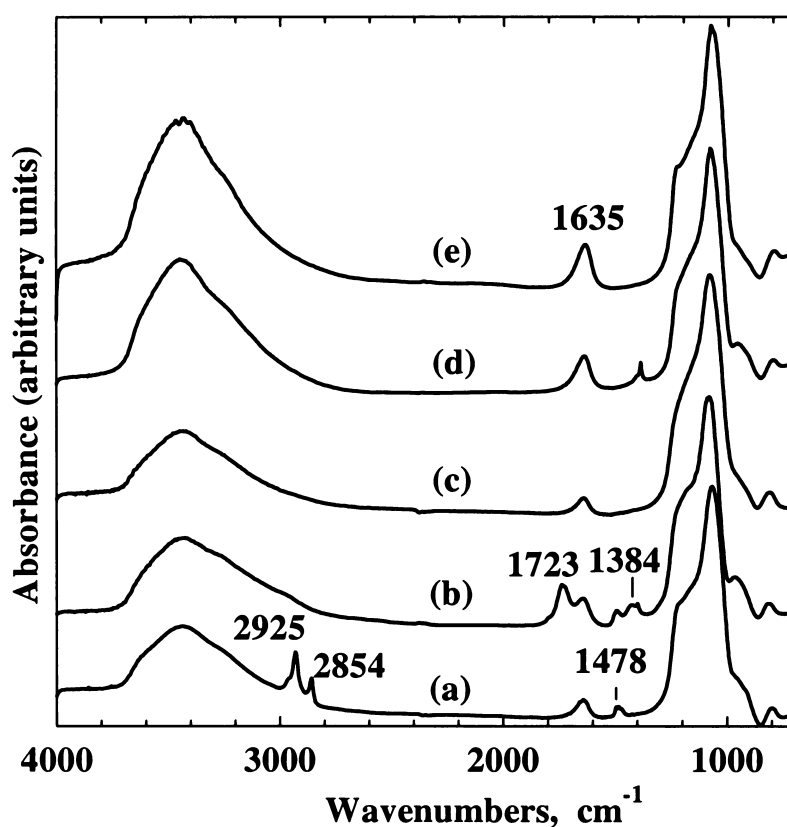


Figure 4.32: FTIR (KBr) absorption spectra for: (a) pre-washed (39); (b) 39 (o-rt); (c) 39 (o-rt-813K); (d) 39 (o-423K); (e) calcined (39).

The FTIR spectra shown in Figure 4.32 are normalized to the same intensity as the framework bands located between 1400-850  $\text{cm}^{-1}$ . The FTIR spectra of ozone treated Al-MCM-41 (Si/Al = 39) (Figure 4.32) demonstrate that CTAC template molecules were degraded (or removed) by ozone treatment at room temperature and some organic residues were formed. However, the CTAC template molecules were completely removed by ozone treatment at 423K. The FTIR spectra and corresponding analyses results for the ozone treated Al-MCM-41 (Si/Al = 39) are similar to those for the ozone treated MCM-41. Hence, only the spectra are present here and the analyses are omitted.



**Figure 4.33:** FTIR (KBr) absorption spectra for: (a) pre-washed (15); (b) 15 (o-rt); (c) 15 (o-rt-813K); (d) 15 (o-423K); (e) calcined (15).

The FTIR spectra shown in Figure 4.33 and Figure 4.44 are normalized to the same intensity as the framework bands located between 1400-850  $\text{cm}^{-1}$ . Figure 4.33 and 4.44 show the FTIR spectra for ozone treated Al-MCM-41 (Si/Al = 15) and Al-MCM-41

(Si/Al =7), respectively. It can be seen that ozone treatment at room temperature degrades (or removes) the CTAC template molecules, indicated by the diminution of the  $\nu_{\text{as}} \text{CH}_3$  ( $2925 \text{ cm}^{-1}$ ) and  $\nu_{\text{as}} \text{CH}_2$  ( $2854 \text{ cm}^{-1}$ ) bands. At the same time, the absorption bands due to  $\nu \text{C=O}$  ( $1723$  and  $1710 \text{ cm}^{-1}$ , respectively, in Figure 4.33 and 4.34) and  $\delta \text{-OCOCH}_3$  or  $\text{-COCH}_3$  ( $1384$  and  $1385 \text{ cm}^{-1}$ , respectively, in Figure 4.33 and 4.34) are present. These bands cannot be removed simply by lengthening the reaction time, but can be removed completely by further thermal calcination. This is consistent with the previous observation for the MCM-41 (o-rt) and 39 (o-rt). However, unlike the MCM-41 and the Al-MCM-41 (Si/Al =39), the ozone treatment at  $423 \text{ K}$  cannot remove the band at  $1384$  (or  $1385 \text{ cm}^{-1}$ ), which was assigned to the absorption of  $\delta \text{-OCOCH}_3$  or  $\text{-COCH}_3$  groups. This may be explained by the stronger interactions of the Al species with these organic residues.

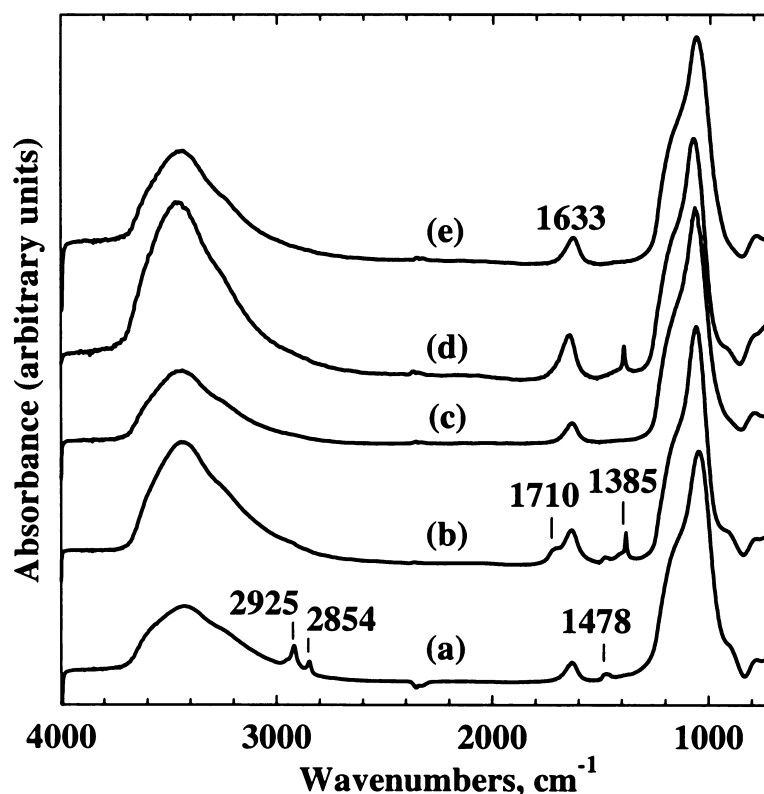


Figure 4.34: FTIR (KBr) absorption spectra for: (a) pre-washed (7); (b) 15 (o-rt); (c) 7(o-rt-813K); (d) 7 (o-423K); (e) calcined (7).

### 4.5.3. *In-situ* IR Spectra of Al-MCM-41

It is expected that the MCM-41 samples whose templates are removed with ozone at 423 K should possess more silanol groups than those directly calcined ones. The following *in-situ* IR studies provide preliminary evidence for the above comments. For comparison purposes, all of the *in-situ* IR spectra presented here are normalized to the overtone bands at ca.  $1850\text{ cm}^{-1}$  with equal intensity.

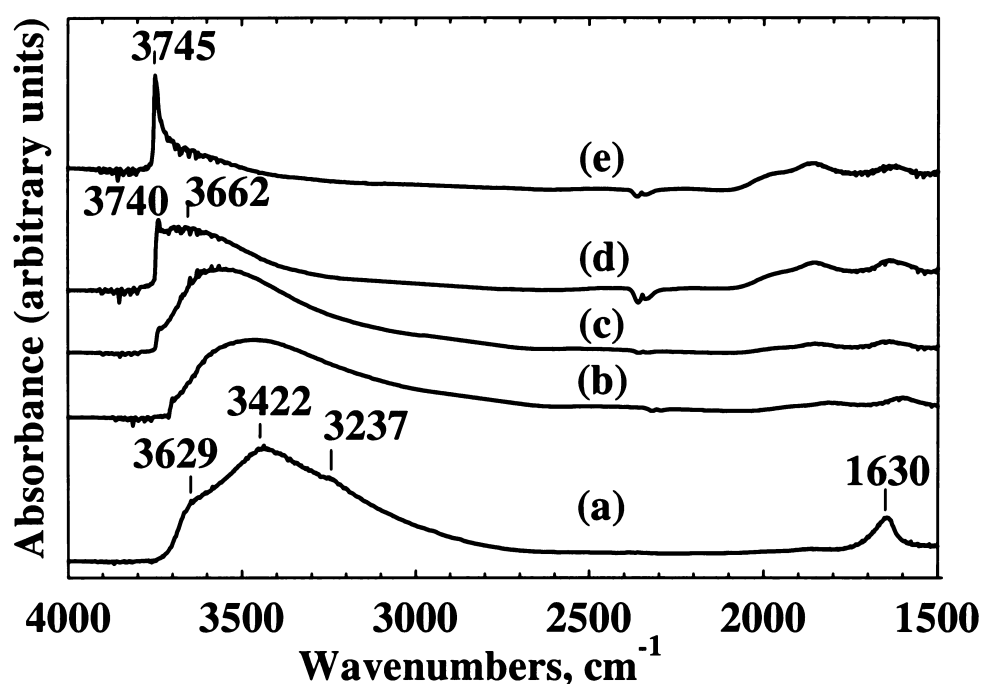


Figure 4.35: *In-situ* IR absorption spectra for calcined (15). The sample was evacuated for 1 hr. at: (a) room temperature; (b) 373 K; (c) 473 K; (d) 573 K; and (e) 673 K.

Figure 4.35 shows the *in-situ* IR spectra of Al-MCM-41 ( $\text{Si}/\text{Al} = 15$ ) whose template was removed by thermal calcination. After evacuation at room temperature for 1 hour (Figure 4.35 (a)), the IR spectrum shows a broad absorption band between  $3800\text{ cm}^{-1}$  and  $2800\text{ cm}^{-1}$ , due to the overlay of the stretching bands of Si-OH and physically adsorbed water. The absorption at  $1635\text{ cm}^{-1}$  is due to the bending mode of the



physically adsorbed water. At 373 K, the band due to the physically adsorbed water disappeared, and a new peak at  $3740\text{ cm}^{-1}$  associated with the vicinal (or geminal) silanol groups<sup>70</sup> could be clearly observed. Further increasing the evacuation temperature from 373 K to 673 K, the maxima of the broad band shifts to the higher frequency, which is caused by the condensation of the silanol groups. At 573 K (Figure 4.35 (d)), the broad band centered at  $3662\text{ cm}^{-1}$  may be assigned to the contributions from the intraglobular Si-OH groups and the hydroxyl groups on octahedrally coordinated Al atoms.<sup>71</sup> At 673 K (Figure 4.35 (e)), the sharp peak at  $3745\text{ cm}^{-1}$  is due to the isolated silanol groups. It was reported that at an evacuation temperature as high as 673 K, only the peak at  $3745\text{ cm}^{-1}$  due to the isolated silanol groups remains in siliceous MCM-41.<sup>72</sup> So, the peak centered at  $3662\text{ cm}^{-1}$  in Figure 4.35 (e) can only be assigned to the hydroxyl groups on octahedrally coordinated Al. The peak at  $3607\text{ cm}^{-1}$ , which was assigned to Brönsted acid bridging hydroxyl groups (Si-O(H)-Al) by Holmes et.al,<sup>69</sup> was not observed, probably due to broad band overlay.

Figure 4.36 shows the *In-situ* IR absorption spectra for 15 (o-423K) that evacuated at various temperatures. With increasing evacuation temperature, the maxima of the broad absorption band centered at  $3475\text{ cm}^{-1}$  at 373 K (Figure 4.36 (a)) gradually shifted to the higher frequency. At 773 K, the peak at  $3744\text{ cm}^{-1}$  is due to the isolated silanol groups. The peak centered at ca.  $3660\text{ cm}^{-1}$  may be assigned to the hydroxyl groups associated with the octahedrally coordinated Al species.<sup>71</sup> This demonstrates that template removal at 423 K by ozone treatment can maintain more silanol groups than thermal calcination. The excess amount of silanol groups cannot be easily removed by evacuation at 773 K for 1 hour.<sup>20</sup> The following scheme shows the definitions of the different silanol groups used in this chapter.

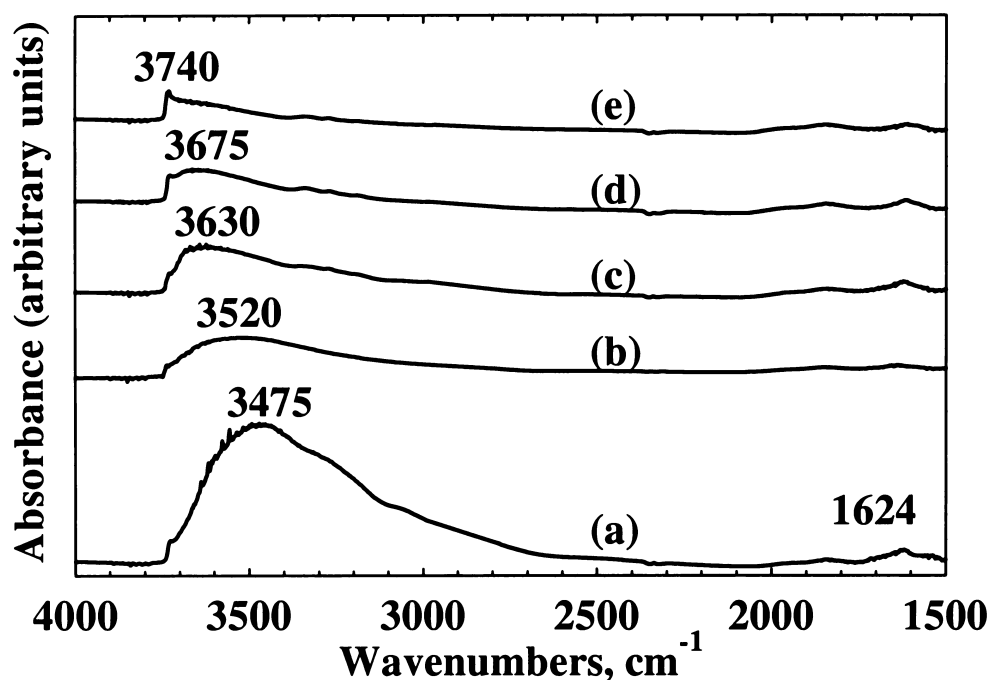
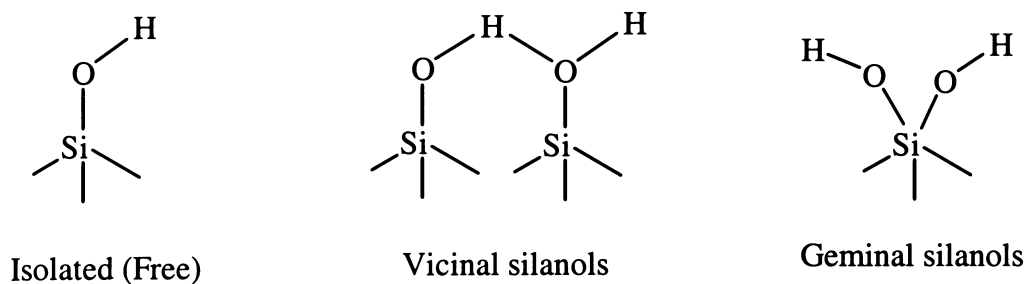


Figure 4.36: *In-situ* IR absorption spectra for 15 (o-423K). The sample was evacuated for 1 hr. at: (a) room temperature; (b) 373 K; (c) 473 K; (d) 573 K; and (e) 673 K.

Figure 4.37 shows the *in-situ* IR spectra of calcined (15) evacuated at 673 K for 1 hr (Figure 4.37 (a)), 15 (o-423K) evacuated at 673 K for 1 hr (Figure 4.37 (b)) and 15 (o-4213K) evacuated at 773 K for 1 hr (Figure 4.37 (c)). After evacuation at 673 K, the calcined (15) exhibits a dominant peak at  $3744\text{ cm}^{-1}$ , which is due to the isolated silanol groups, as well as a broad band at  $3624\text{ cm}^{-1}$ ; however, the 15 (o-423K) shows not only the isolated silanol groups at  $3744\text{ cm}^{-1}$  with higher intensity, but also a much broader band centered at  $3675\text{ cm}^{-1}$ , which provides strong evidence that the sample that were treated with ozone at 423 K possesses more silanol groups. Further increasing the

evacuation temperature of 15 (o-423K) to 773 K, the peak at  $3744\text{ cm}^{-1}$  became the dominant peak as was observed in the calcined (15); nevertheless, the intensity of the shoulder band centered at  $3650\text{ cm}^{-1}$  due to hydrogen bonded silanol groups is still much higher than that in calcined (15), which further confirms the conclusion that the sample that were treated with ozone at 423 K has more silanol groups.

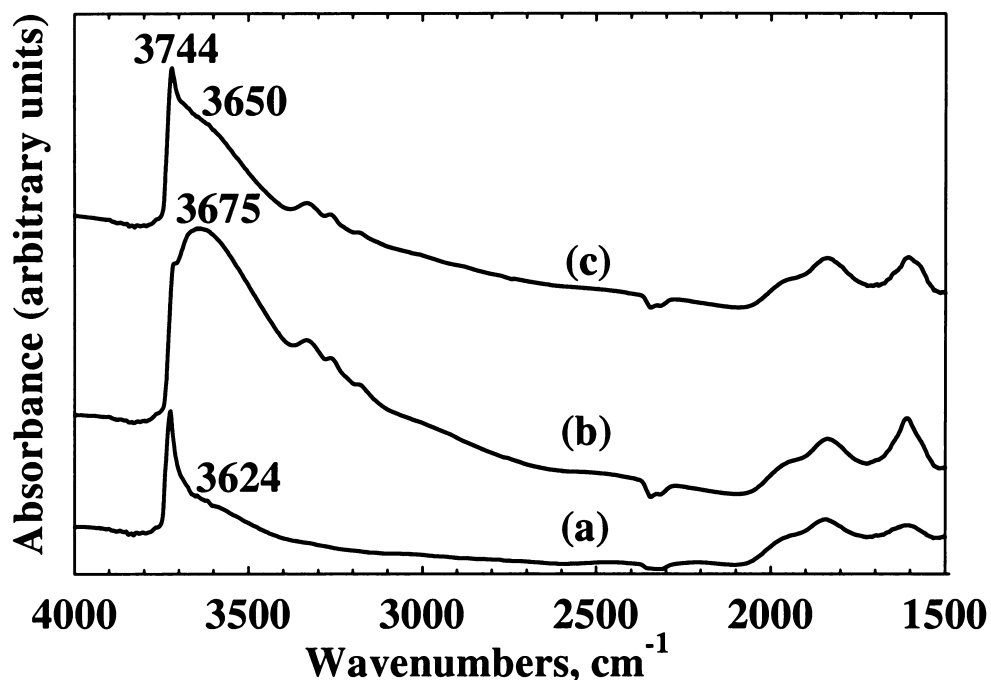
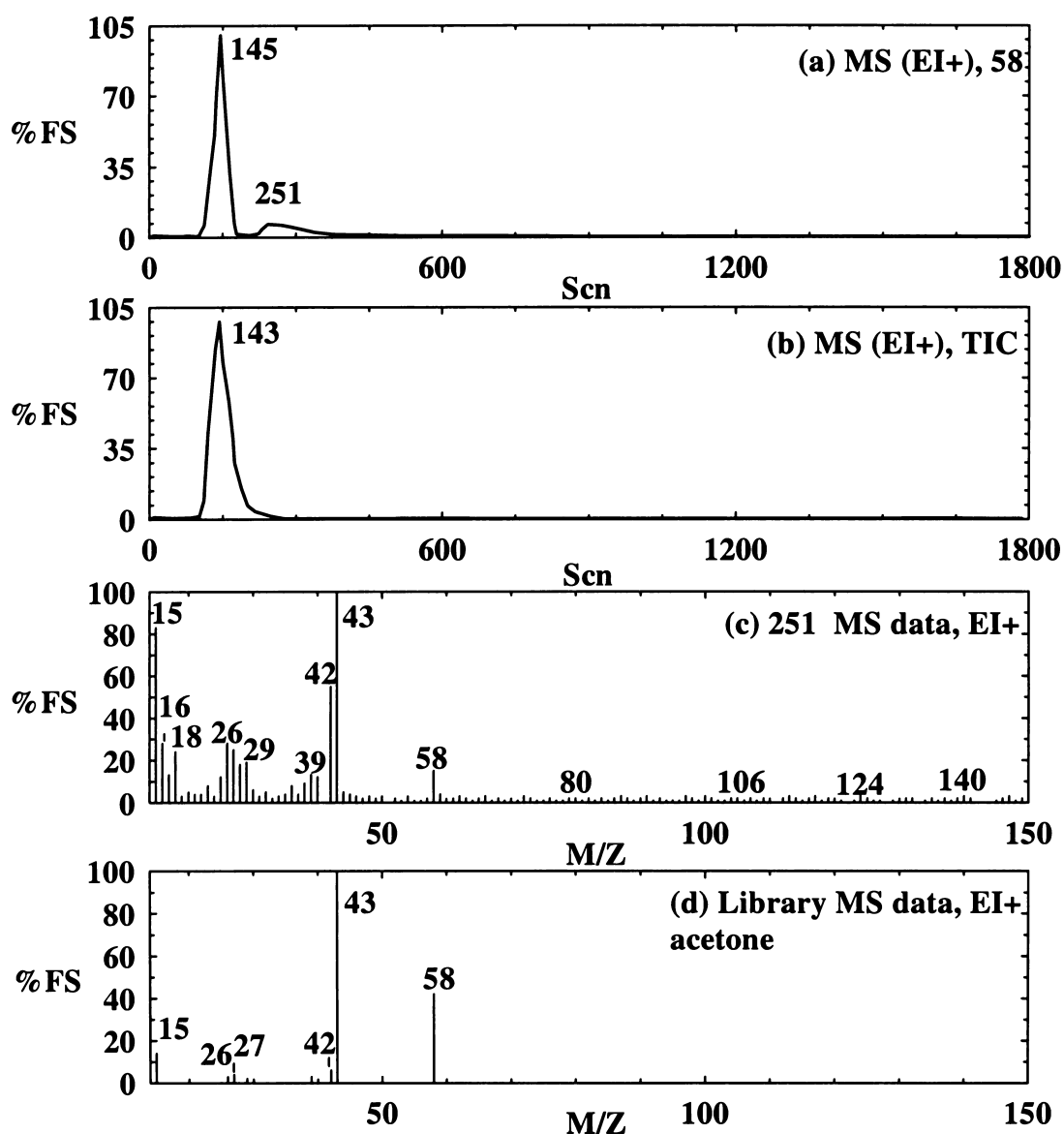


Figure 4.37: *in-situ* IR spectra of (a) calcined (15) evacuated at 673 K for 1 hr.; (b) 15 (o-423K) evacuated at 673 K for 1 hr.; (c) 15 (o-423K) evacuated at 773 K for 1 hr.

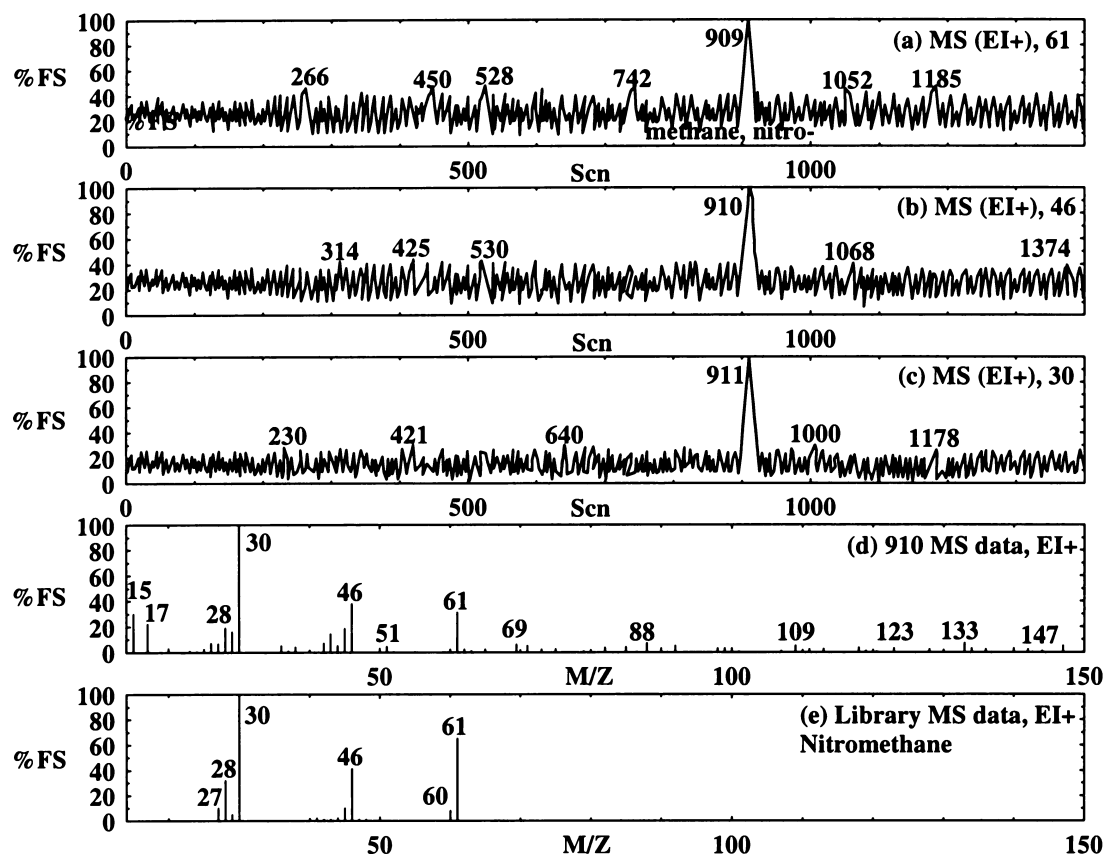
#### 4.5.4. GC-MS Study on Template Removal by Ozone Treatments

Figure 4.38 shows the typical GC-MS spectra of the gaseous products generated by ozone treatment of as-synthesized MCM-41 at room temperature. Figure 4.38 (a) shows the GC trace of the  $m/z = 58$  fragment, which is centered at 145 seconds and 251 seconds, while Figure 4.38 (b) shows the GC trace of fragment with  $m/z$  other than 58, which mainly centered at 143 seconds, MS analysis (not shown here) shows that these

other fractions are mainly H<sub>2</sub>O and CO<sub>2</sub>, while the fraction centered at 251 seconds (Figure 4.38 (c)) approximately matches the library MS data.<sup>73</sup>



**Figure 4.38:** GC-MS spectra of the cold trapped gaseous products generated in ozone treatment of MCM-41 at room temperature: (a) GC spectrum of the fraction with MS (EI+) 58; (b) GC spectrum of the fraction with MS (EI+) other than 58; (c) MS spectrum of the fraction detected at 251 second in GC spectrum (a); (d) MS spectrum of the acetone drawn based on the data in the literature.



**Figure 4.39:** GC-MS spectra of the cold trapped gaseous products generated in ozone treatment of MCM-41 at room temperature: (a) GC spectrum of the fraction with MS (EI+) 61; (b) GC spectrum of the fraction with MS (EI+) 46; (c) GC spectrum of the fraction with MS (EI+) 30; (d) MS spectrum of the fraction detected at around 910 second in GC spectrum; (e) library MS data for nitromethane.

The trapped gaseous products were heated at ca. 383 K for a few minutes and injected into the chromatograph again for analysis. After around 910 seconds, three fractions with  $m/z = 61$ , 46 and 30, respectively, were detected (see Figure 4.39 (a), (b) and (c)). The mass fragmentation pattern of the fraction shown at 910 seconds (Figure 4.39 (d)) is approximately consistent with the standard MS library data for nitromethane.

GC-MS analyses of the gaseous products generated from the MCM-41 sample that were treated with ozone at 423 K showed nothing but  $H_2O$  and  $CO_2$  (not shown here). No acetone was detected, indicating that the acetone detected in the previous MCM-

41(o-rt) sample was not from the atmosphere because both these experiments were performed under the same conditions except for the temperature.

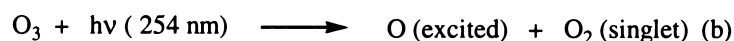
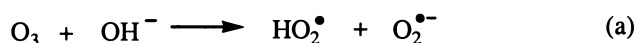
#### 4.6. Mechanism of Ozone on CTAC Template Removal

For the samples ((MCM-41 and the other three Al-MCM-41) that were treated with ozone at room temperature, FTIR spectra detected some organic residues with the C=O and  $-\text{OCOCH}_3$  or  $-\text{COCH}_3$  groups; CP- $^{13}\text{C}$ -MAS-NMR spectra detected some carboxylic acid compounds and nitromethane. Both of these spectroscopy analyses show that the long alkyl chains of the CTAC molecules were cleaved by ozone at room temperature. Furthermore, the GC-MS analyses revealed the existence of acetone and nitromethane in the gaseous products of MCM-41 (o-rt).

For the samples (MCM-41 and the other three Al-MCM-41) that were treated with ozone at 423 K, CP- $^{13}\text{C}$ -MAS-NMR spectra detected nothing. GC-MS analyses of MCM-41 (o-423K) gaseous products also showed nothing but carbon dioxide and water. Furthermore, FTIR spectra further confirmed that no organic residues were left in MCM-41 (o-423K) and 39 (o-423K) samples, however, some organic residues with  $\text{OCOCH}_3$  or  $-\text{COCH}_3$  groups were detected in high Al content samples, which could not be removed by lengthening the reaction time.

In the literature, several different mechanisms were postulated. Moon et al.<sup>74</sup> showed that ozone alone is ineffective in removing saturated contaminants on silicon surfaces, but the presence of UV light significantly enhances the process. In contrast, Keene et al.<sup>45</sup> suggested that gaseous ozone in the absence of UV-light is as effective in the surfactant removal from MCM-41 as UV/ozone treatment. Clark et al.<sup>46</sup> also showed that UV/ozone treatment of mesoporous thin films (occluded with  $\text{C}_{16}\text{H}_{33}(\text{OCH}_2\text{CH}_2)_{10}\text{OH}$  nonionic surfactant) at room temperature provides an efficient

means for the removal of the surfactant template while simultaneously stabilizing the inorganic silica skeleton. The suggested mechanism by which UV/ozone destroys the organics is as follows: First, UV light with a wavelength below 245.4 nm (optimally at  $\lambda = 184$  nm) facilitates the dissociation of oxygen to produce ozone and atomic oxygen. Simultaneously, the 253.7 nm line emitted by the same lamp excites and/or dissociates the organic matrix in the mesostructure, thereby producing activated species, such as ions, free radicals, and excited molecules. Finally, the activated organic species are readily attacked by atomic oxygen and ozone synergistically to form simpler volatile molecules, such as  $\text{CO}_2$ ,  $\text{H}_2\text{O}$ ,  $\text{N}_2$ , etc. Büchel et al.<sup>47</sup> studied removal of cetyltrimethylammonium bromide (CTABr) surfactant template from MCM-41 mesostructure with an ozone generator instead of a UV lamp. They concluded that water seems to play an important role in template removal. A “radical mechanism” was also put forward to explain the ozonization. The radicals can be formed either by the reaction of ozone with hydroxyl ions present inside the channels of mesostructure according to the equation (a), or by the help of UV irradiation, according to the equations (b-c):



These radicals may further attack the hydrocarbon chain of the template and gradually degrade it into small fragments.

Gilbert et al.<sup>44</sup> also reported that the decomposition of tetrapropylammonium bromide (TPABr) template in silicalite-1 under ozone/air atmosphere started gradually at a temperature that was approximately 100 K lower than in air. In agreement with our results, their on-line mass spectrometry study indicated that the final products were also

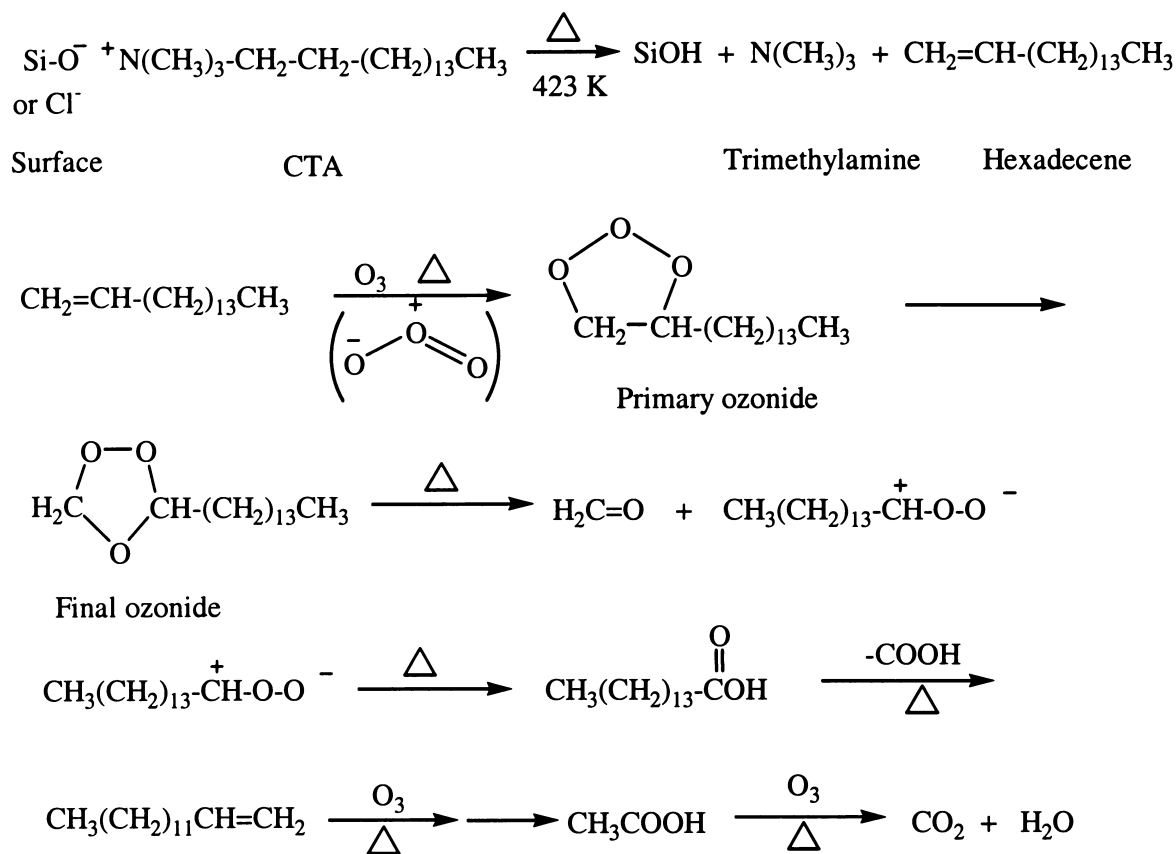
carbon dioxide and water. They suggested that this exothermic reaction is the combination of pyrolysis and oxidation, which may be catalyzed by zeolite. Keene et al.<sup>52</sup> also studied the mechanism of CTABr thermal decomposition in MCM-41. Their results indicate that the majority of the surfactant breaks down in the region from 373 K-473 K.

Based on the above experimental results and literature investigations, the following ozonization mechanisms are suggested.

During ozone treatment at room temperature, some active species, such as hydroxyl radical ions  $\text{OH}^\bullet$  may be formed, which are responsible for the initial ozonization stage. These active species may directly attack the hydrocarbon chain. It is unlikely that ozone will attack the “head” of the quaternary ammonium cation since it is saturated. As with the reaction of ozone with a saturated hydrocarbon,<sup>75,76</sup> the ozonization of the CTAC molecule is assumed to be detachment of a hydrogen atom from the saturated molecule. Then the further oxidation reactions occur, which finally cleave the entire CTAC molecule into small fragments, such as nitromethane, acetone, aldehydes and carboxylic acids. However, it is still difficult to explain how the acetone was formed during ozone treatment at room temperature within the usual framework of the mechanism of chain oxidation.

During ozone treatment at 423 K, though it is not clear about the initial ozonization of the CTAC molecule and the following detailed reaction processes, the final products of  $\text{CO}_2$  and  $\text{H}_2\text{O}$  strongly confirm that the CTAC molecule was “broken down” by ozone, and further “burned off” in the form of water and carbon dioxide at 423 K:





## 4.7. Summary

Though thermal calcination can completely remove the surfactant template from the as-synthesized sample, it is always accompanied by undesired structure deterioration and dealumination. Ozone treatment of (Al)-MCM-41 samples at 423 K minimizes these unwanted effects, which result from the high energy released during decomposition accompanying calcination.

The XRD pattern analyses show that the structural order of (Al)-MCM-41 samples can be better maintained by ozone treatment either at room temperature or at 423 K. Two-step treatment (combination of ozone treatment at room temperature and thermal calcination) shows that no significant improvement on structural order of (Al)-MCM-41 materials.  $^{29}\text{Si}$ -NMR shows that the ozone treated Al-MCM-41 samples contain more  $\text{Q}^3$  than the directly calcined sample;  $^{27}\text{Al}$ -MAS-NMR shows that ozone treated samples

generally retain more Al in the tetrahedral framework than the directly calcined samples. The *in situ* IR studies demonstrate that the samples treated with ozone at 423 K possess more silanol groups. The nitrogen adsorption-desorption isotherm analyses indicate that the sample that was treated with ozone at 423 K has higher surface area and larger pore volume without significant loss of structure uniformity. Combining the FTIR, CP-<sup>13</sup>C-MAS-NMR, and GC-MS spectroscopy techniques, it was found that although ozone treatment at room temperature can largely cleave the long hydrocarbon chain of the CTAC molecule, it cannot remove some organic residues derived from the ozonization reaction. However, ozone treatment at 423 K completely removes CTAC template molecules from MCM-41 and low Al content Al-MCM-41 (Si/Al = 39), but is unable to completely remove residues in higher Al content samples (Si/Al = 15, 7). Based on the experimental results and the arguments in the literature, preliminary mechanisms for CTAC template removal by ozone treatment at room temperature and 423 K have been postulated.

## 4.8. References for Chapter 4

- (1) Kim, J. M.; Kwak, J. H.; Jun, S.; Ryoo, R. *J. Phys. Chem.* **1995**, *99*, 16742.
- (2) Firouzi, A.; Kumar, D.; Bull, L. M.; Besier, T.; Sieger, P.; Huo, Q. S.; Walker, S. A.; Zasadzinski, J. A.; Glinka, C.; Nicol, J.; Margolese, D.; Stucky, G. D.; Chmelka, B. F. *Science* **1995**, *267*, 1138.
- (3) Huo, Q. S.; Margolese, D. I.; Stucky, G. D. *Chem. Mater.* **1996**, *8*, 1147.
- (4) Yang, H.; Kuperman, A.; Coombs, N.; Mamiche-Afara, S.; Ozin, G. A. *Nature (London)* **1996**, *379*, 703.
- (5) Huo, Q.; Margolese, D. I.; Ciesla, U.; Feng, P.; Gier, T. E.; Sieger, P.; Leon, R.; Petroff, P. M.; Schüth, F.; Stucky, G. D. *Nature (London)* **1994**, *368*, 317.
- (6) Tanev, P. T.; Pinnavaia, T. J. *Chem. Mater.* **1996**, *8*, 2068.
- (7) Vartuli, J. C.; Kresge, C. T.; Leonowicz, M. E.; Chu, A. S.; McCullen, S. B.; Johnson, I. D.; Sheppard, E. W. *Chem. Mater.* **1994**, *6*, 2070.
- (8) Petrovic, I.; Navrotsky, A.; Chen, C.-Y.; Davis, M. E. *Stud. Surf. Sci. Catal.* **1994**, *84*, 677.
- (9) Huo, Q.; Leon, R.; Petroff, P. M.; Stucky, G. D. *Science* **1995**, *268*, 1324.
- (10) Tanev, P. T.; Pinnavaia, T. J. *Science* **1995**, *267*, 865.
- (11) Attard, G. S.; Glyde, J. C.; Göltner, C. G. *Nature* **1995**, *378*, 317.
- (12) Bagshaw, S. A.; Prouzet, E.; Pinnavaia, T. J. *Science* **1995**, *269*, 1242.
- (13) Feng, Q.; Xu, J.; Dong, H.; Li, S.; Wei, Y. *J. Mater. Chem.* **2000**, *10*, 2490.
- (14) Feng, Q.; Xu, J.; Dong, H.; Wei, Y. *Polym. Prepr.* **2000**, *41*, 515.
- (15) Wei, Y.; Jin, D. L.; Ding, T. Z.; Shih, W. H.; Liu, X. H.; Cheng, S. Z. D.; Fu, Q. *Adv. Mater.* **1998**, *3*, 313.
- (16) Behrens, P. *Angew. Chem. Int. Ed. Engl.* **1996**, *35*, 515.
- (17) Luan, Z.; He, H.; Zhou, W.; Cheng, C.-F.; Klinowski, J. *J. Chem. Soc., Faraday Trans.* **1995**, *91*, 2955.
- (18) Mokaya, R.; Jones, W.; Luan, Z.; Alba, M. D.; Klinowski, J. *Catal. Lett.* **1996**, *37*, 113.
- (19) Mokaya, R.; Jones, W. *J. Chem. Soc., Chem. Commun.* **1997**, 2185.
- (20) Schmidt, R.; Akporiaye, D.; Stöcker, M.; Ellestad, O. H. *Stud. Surf. Sci. Catal.* **1994**, *84*, 61.

- 
- (21) Sauerland, C.; Llewellyn, P.; Grillet, Y.; Patarin, J.; Rouquerol, F. In *Proc. Int. Zeolite Conf., 12th.*; Treacy, M. M. J., Ed., 1999; Vol. 3, pp 1707.
- (22) Hitz, S.; Prins, R. *J. Catal.* **1997**, *168*, 194.
- (23) Montes, A.; Cosenza, E.; Giannetto, G.; Urquieta, E.; Melo, R. A.; Gnep, N. S.; Guisnet, M. *Stud. Surf. Sci. Catal.* **1998**, *117*, 237.
- (24) Malla, P. B.; Komarneni, S. *Zeolites* **1995**, *15*, 324.
- (25) Kawi, S.; Lai, M. N. *J. Chem. Soc., Chem. Commun* **1998**, 1407.
- (26) Danumah, C.; Zaidi, S. M. J.; Voyer, N.; Giasson, S.; Kaliaguine, S. *Stud. Surf. Sci. Catal.* **1998**, *117*, 281.
- (27) Antochshuk, V.; Jaroniec, M. *J. Chem. Soc., Chem. Commun.* **1999**, 2373.
- (28) Antochshuk, V.; Jaroniec, M. *Stud. Surf. Sci. Catal.* **2000**, *129*, 265.
- (29) Antochshuk, V.; Jaroniec, M. *Chem. Mater.* **2000**, *12*, 2496.
- (30) Bibby, D. M.; Milestone, N. B.; Patterson, J. E.; Aldridge, L. P. *J. Catal.* **1986**, *97*, 493.
- (31) Maesen, T. L. M.; Bruinsma, D. S. L.; Kouwenhoven, H. W.; Van Bekkum, H. *J. Chem. Soc., Chem. Commun.* **1987**, 1284.
- (32) Maesen, T. L. M.; Kouwenhoven, H. W.; Van Bekkum, H. *J. Chem., Faraday Trans.* **1990**, *86*, 3967.
- (33) Copperthwaite, R. G.; Foulds, G.; Themistocleous, T.; Hutchings, G. J. *J. Chem. Soc., Chem. Commun.* **1987**, 748.
- (34) Hutchings, G. J.; Comninos, H.; Copperthwaite, R. G.; Rensburg, L. J. v.; Hunter, R.; Themistocleous, T. *J. Chem. Soc. Faraday Trans. I* **1989**, *85*, 633.
- (35) Carlton, L.; Copperthwaite, R. G.; Hutchings, G. J.; Reynhardt, E. C. *J. Chem. Soc., Chem. Commun.* **1986**, 1008.
- (36) Hutchings, G. J.; Copperthwaite, R. G.; Themistocleous, T.; Foulds, G. A.; Bielovitch, A. S.; Loots, B. J.; Nowitz, G.; Van Eck, P. *Appl. Catal.* **1987**, *34*, 153.
- (37) Van der Waal, J. C.; Rigutto, M. S.; Van Bekkum, H. *J. Chem. Soc., Chem. Commun.* **1994**, 1241.
- (38) Copperthwaite, R. G.; Hutchings, G. J.; Johnston, P.; Orchard, S. W. *J. Chem. Soc., Faraday Trans.* **1986**, *82*, 1007.
- (39) Copperthwaite, R. G.; Hutchings, G. J.; Johnston, P.; Orchard, S. W. *J. Chem. Soc., Chem. Commun.* **1985**, 644.
- (40) Corless, C.; Reynolds, G.; Graham, N.; Perry, R.; Gibson, T. M.; Haley, J. *Water. Res.* **1989**, *23*, 1367.

- 
- (41) Kiricsi, I.; Kukovecz, Á.; Fudala, Á.; Kónya, Z.; Willems, I.; Nagy, J. B. *Stud. Surf. Sci. Catal.* **2000**, *130B*, 1115.
- (42) Saxton, R. J.; Crocco, G. L.; Zajacek, J. G.: U.S., 1997, p 6.
- (43) Jones, C. M.; Kalaji, M.; Rees, J. A.; Taylor, D. M. *Langmuir* **1998**, *14*, 379.
- (44) Gilbert, K. H.; Baldwin, R. M.; Way, J. D. *Ind. Eng. Chem. Res.* **2001**, *40*, 4844.
- (45) Keene, M. T. J.; Denoyel, R.; Llewellyn, P. L. *Chem. Commun.* **1998**, 2203.
- (46) Clark, T.; Jr.; Ruiz, J. D.; Fan, H.; Brinker, C. J.; Swanson, B. I.; Parikh, A. N. *Chem. Mater.* **2000**, *12*, 3879.
- (47) Büchel, G.; Denoyel, R.; Llewellyn, P. L.; Rouquaurol, J. *J. Mater. Chem.* **2001**, *11*, 589.
- (48) Moon, D. W.; Kurokawa, A.; Ichimura, S.; Lee, H. W.; Jeon, I. C. *J. Vac. Sci. Technol. A* **1999**, *17*, 150.
- (49) Thakulsukanant, C.; Lobban, L. L.; Osuwan, S.; Waritswat, A. *Langmuir* **1997**, *13*, 4595.
- (50) Ryoo, R.; Jun, S.; Kim, J. M.; Kim, M. J. *Chem. Commun.* **1997**, 2225.
- (51) Zhao, X. S.; Audsley, F.; Lu, G. Q. *J. Phys. Chem. B* **1998**, *102*, 4143.
- (52) Keene, M. T. J.; Gougeon, R. D. M.; Denoyel, R.; Harris, R. K.; Rouquero, J.; Llewellyn, P. L. *J. Mater. Chem.* **1999**, *9*, 2843.
- (53) Hammond, W.; Prouzet, E.; Mahanti, S. D.; Pinnavaia, T. J. *Microporous and Mesoporous Mater.* **1999**, *27*, 19.
- (54) Beck, J. S.; Vartuli, J. C.; Roth, W. J.; Leonowicz, M. E.; Kresge, C. T.; Schmitt, K. D.; Chu, C. T.-W.; Olson, D. H.; Sheppard, E. W.; McCullen, S. B.; Higgins, J. B.; Schlenker, J. L. *J. Am. Chem. Soc.* **1992**, *114*, 10834.
- (55) Edler, K. J.; White, J. W. *Chem. Mater.* **1997**, *9*, 1226.
- (56) Mokaya, R.; Zhou, W.; Jones, W. *Chem. Commun.* **1999**, 51.
- (57) Khushalani, D.; Kuperman, A.; Coobs, N.; Ozin, G. A. *Chem. Mater.* **1996**, *8*, 2188.
- (58) Schacht, S.; Janicke, M.; Schüth, F. *Microporous and Mesoporous Mater.* **1998**, *22*, 485.
- (59) Ryoo, R.; Kim, J. M. *J. Chem. Soc., Chem. Commun.* **1995**, 711.
- (60) Reddy, K. M.; Song, C. *Stud. Surf. Sci. Catal.* **1998**, *117*, 291.
- (61) Chen, C. Y.; Burkett, S. L.; Li, H. X.; Davis, M. E. *Microporous Mater.* **1993**, *2*, 17.
- (62) Kloetstra, K. R.; Zandbergen, H. W.; Bekkum, H. v. *Catal. Lett.* **1995**, *33*, 157.

- (63) Schmidt, R.; Akporiaye, D.; Stöcker, M.; Ellestad, O. H. *Stud. Surf. Sci. Catal.* **1994**, *84*, 58.
- (64) Janicke, M.; Kumar, D.; Stucky, G. D.; Chmelka, B. F. *Stud. Surf. Sci. Catal.* **1994**, *84*, 61.
- (65) Oldfield, E.; Haasse, J.; Schmitt, K. D.; Schramm, S. E. *Zeolites* **1994**, *14*, 101.
- (66) Wang, L.-Q.; Liu, J. L.; Exarhos, G. J.; Bunker, B. C. *Langmuir* **1996**, *12*, 2663.
- (67) Breitmaier, E.; Haas, G.; Voelter, W. *Atlas of Carbon-13 NMR Data*; Heyden & Son Limited: London-Philadelphia-Rheine, 1979.
- (68) Vansant, E. F.; Voort, P. V. D.; Vrancken, K. C. *Stud. Surf. Sci. Catal.* **1995**, *93*, 59.
- (69) Holmes, S. M.; Zholobenko, V. L.; Thursfield, A.; Plaisted, R. J.; Cundy, C. S.; Dwyer, J. J. *J. Chem., Faraday Trans.* **1998**, *94*, 2025.
- (70) Bronnimann, C. E.; Zeigler, R. G.; Maciel, G. E. *J. Am. Chem. Soc.* **1988**, *110*, 2023.
- (71) Jentys, A.; Phan, N. H.; Vinek, H. *J. Chem. Soc., Faraday Trans.* **1996**, *93*, 3287.
- (72) Chen, J.; Li, Q.; Xu, R.; Xiao, F. *Angew. Chem. Int. Ed. Engl.* **1995**, *34*, 2694.
- (73) Grasselli, J. G.; Ritchey, W. M. *Atlas of Spectral Data and Physical Constants for Organic Compounds*; CRC press: Ohio, 1984; Vol. 2.
- (74) Mokaya, R.; Jones, W. *Phys. Chem. Chem. Phys.* **1999**, *1*, 207.
- (75) Varkony, T. H.; Pass, S.; Mazur, Y. *J. Chem. Soc., Chem. Commun.* **1975**, 709.
- (76) Razumovskii, S. D.; Zaikov, G. E. *Ozone and Its Reactions with Organic Compounds*; Elsevier: Amsterdam-Oxford-New York-Tokyo, 1984.

## Chapter 5

### Chemistry of Electron Acceptor Molecules in (Al)-MCM-41 Hosts

#### 5.1. Introduction

This chapter deals with the assembly of various electron acceptor molecules within mesoporous (Al)-MCM-41 hosts (unless stated otherwise, the term “(Al)-MCM-41” hereafter refers to either purely siliceous Si-MCM-41 or Al-MCM-41 samples whose templates were removed by thermal calcination). The (Al)-MCM-41 hosts used include Si-MCM-41, three directly synthesized Al-MCM-41 with Si/Al ratio of 39, 15 and 7 (designated as Al-MCM(39), Al-MCM(15) and Al-MCM(7) respectively), and a post-synthesized Al-MCM-41 with Si/Al as 14. The assembled electron acceptor molecules, which act as electron transfer probe molecules for exploring the nature and the location of the electron donor sites in (Al)-MCM-41 hosts, are tetracyanoethylene (TCNE), 7,7,8,8-tetracyanoquinodimethane (TCNQ), 1,4-benzoquinone (1,4-BQ), 1,2,3,4-tetrahydro-1,4-methano-5,8-naphthoquinone (BQ[2]), 1,4-naphthoquinone (1,4-NQ) and 1,4-anthraquinone (1,4-AQ). The structures of these molecules as well as their half-wave reduction potentials ( $E_{1/2}^{\text{Red}}$  (V) vs Ag/AgCl, CH<sub>3</sub>CN) are shown in Scheme 5.1. The formation of radical anions of these electron acceptors in (Al)-MCM-41 hosts was monitored by EPR, FTIR and DR-UV-Vis spectroscopy.

TCNE, the simplest of the percyano olefins,<sup>1</sup> is a good  $\pi$  electron acceptor. It can be easily reduced to radical anion and dianion, or form charge transfer (CT) complexes with even fairly weak electron donor molecules. TCNE is also a strong  $\pi$  acid relative to

the small  $\pi$ -base system represented by durene and hexamethylbenzene.<sup>2,3</sup> TCNQ is also a strong  $\pi$  electron acceptor.<sup>3-8</sup> Compared with TCNE, the TCNQ radical anion may be more stable due to the delocalization of the accepted electrons throughout the entire molecule *via* the conjugated aromatic ring. Dimerization of the TCNQ and its radical anion to form corresponding TCNQ dimer or dianion is well documented.<sup>3,4,7,9-17</sup> It is expected that strong electron acceptors, such as TCNE and TCNQ, can act as powerful electron transfer probe molecules for exploring even relatively weak electron donor sites in (Al)-MCM-41.

Quinones (BQ, NQ and AQ) may undergo oxidation or reduction reactions depending on the reaction conditions.<sup>18</sup> The intermediates are usually referred to as “semiquinones” (designated as “SQ” in the following sections), which include the neutral and charged forms (SQ radicals).<sup>19</sup> The SQ radical anions are usually stable in alkaline and organic solvents and are readily observed using EPR and other optical spectroscopy. However, SQ radical cations are stable only in a strong acidic media.<sup>19,20</sup>

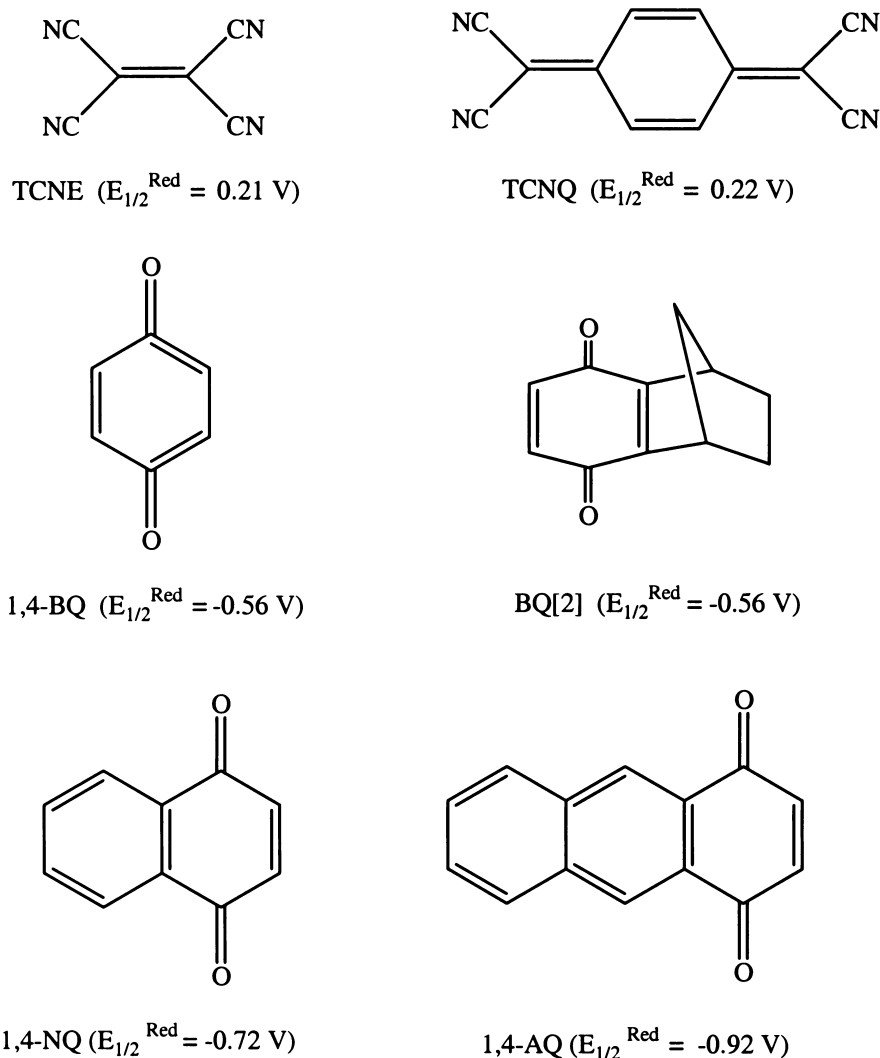
Three different assembling methods (for detailed methods please refer to Section 2.4 in Chapter 2) are used to make radical anions in (Al)-MCM-41: (1) method A1, where the solvent coexists with the solid (Al)-MCM-41; (2) method A2, where the solvent is evaporated off naturally in the dry box; and (3) method B1, where the molecule is sublimated into the (Al)-MCM-41 without presence of the solvent. Method B1 is applied only to TCNE and other methods are applied to all molecules.

The blank EPR experiments showed no paramagnetic species in directly synthesized and post-synthesized (Al)-MCM-41 samples treated with the four assembling methods (method A1, A2 and method B1 and B2, see Section 2.4 in Chapter 2) without occluding the probe molecules before and after irradiation. In the DR-UV-Vis experiments on blank samples, some rather weak absorption bands were observed in the



region between 200-1500 nm. However, the influence of these backgrounds derived from the (Al)-MCM-41 themselves on the DR-UV-Vis spectra of the assembled organic redox molecules can be ignored, because they become just a straight line due to relatively much higher absorption intensities of the redox molecules.

For the method of spin concentration estimation, please refer to Section 2.5.9.



**Scheme 5.1: The electron acceptors used as electron transfer probe molecules in this work, together with their reduction potentials, in parentheses. Reduction potentials are with respect to the Ag/AgCl reference electrode in CH<sub>3</sub>CN.**

## 5.2. TCNE in (Al)-MCM-41

### 5.2.1. FTIR Spectra of TCNE in (Al)-MCM-41

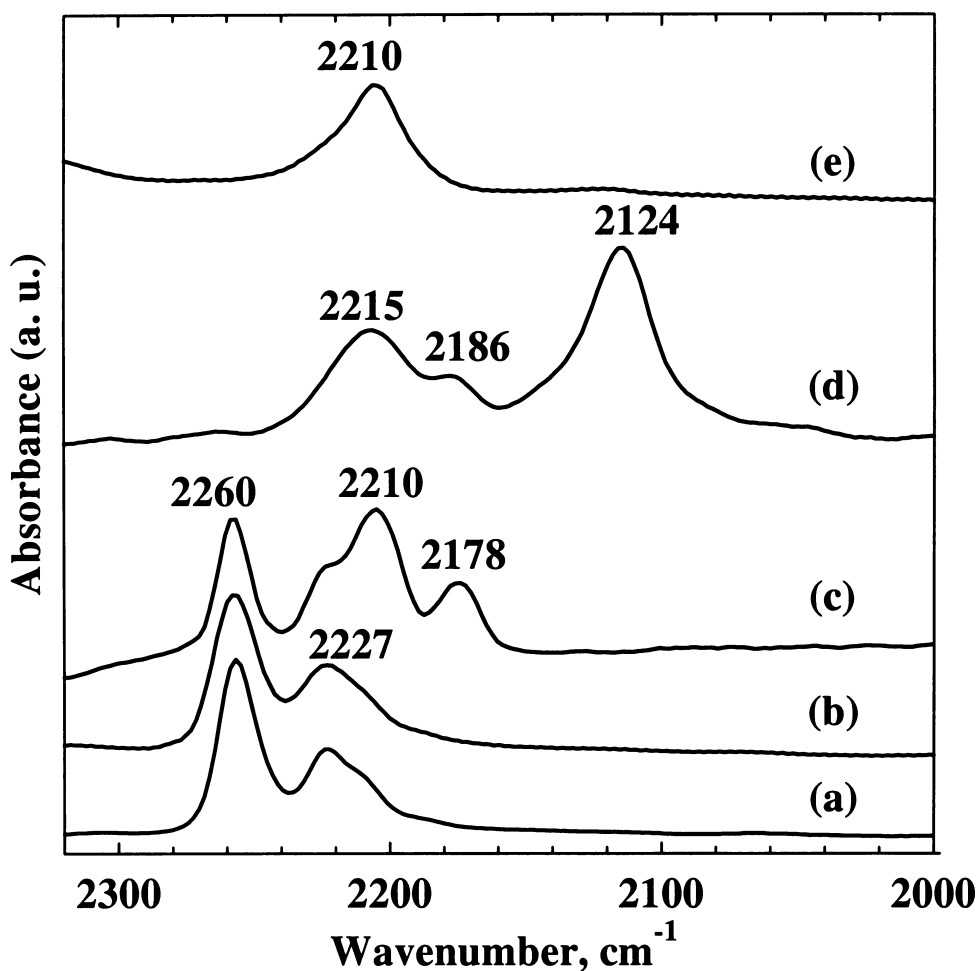


**Figure 5.1:** FTIR spectra of (a) pure TCNE; (b) TCNE and THF mixture; (c) TCNE in Si-MCM-41; (d) TCNE in Al-MCM(15); (e) TCNE in Al-MCM(7).

Information on the location of the electron transfer probe molecules in (Al)-MCM-41 may give an insight into the location of the redox sites in the porous materials. Attempts to use the solid state  $^{13}\text{C}$ -MAS-NMR to identify the chemical environment of the TCNE molecules in (Al)-MCM-41 failed, because only extremely broad and poorly resolved spectra were obtained. However, the following FTIR spectra (Figure 5.1) provide

preliminary evidence that TCNE molecules were assembled into the channels of the (Al)-MCM-41.

TCNE molecules may show two IR-detectable vibrational bands due to the CN stretching ( $b_{1u}$ ,  $b_{2u}$ ) modes in the region between 2000 and 2300  $\text{cm}^{-1}$ .<sup>7,14,21-28</sup> In the FTIR spectrum, the pure TCNE (Figure 5.1 (a)) displays the CN stretching modes at ca. 2260 and 2227  $\text{cm}^{-1}$ . The frequency of these two bands showed no significant change after mixing with THF (Figure 5.1 (b)). However, when TCNE was loaded into the Si-MCM-41 with THF as solvent, using method A2, two new absorption bands at 2210 and 2178  $\text{cm}^{-1}$  appeared (Figure 5.1 (c)). These two new bands may be assigned to the CN stretching modes of the TCNE molecules adsorbed on the surface of the Si-MCM-41 framework.

The appearance of these two new CN stretching modes may be explained by the strong interactions between the TCNE molecules and the active species on the Si-MCM-41 framework (such as hydroxyl groups), which diminishes the  $\pi$  bond order of the CN groups and results in a low energy shift of the corresponding CN stretching modes compared to those of the free TCNE molecules in the IR spectra.<sup>14</sup> The observation of the CN stretching modes for the adsorbed TCNE molecules provides strong evidence that the TCNE molecules were assembled into the channels of the MCM-41. In Figure 5.1 (c), the bands at 2260 and 2227  $\text{cm}^{-1}$  are due to the CN stretching modes of free TCNE molecules. The above IR investigation indicates that TCNE molecules are in two different states in Si-MCM-41: some molecules are in a free state and others are in an adsorbed (or strongly perturbed) state. In the FTIR spectrum of TCNE assembled into the Al-MCM(15) (Figure 5.1 (d)), however, the CN stretching modes due to the free TCNE molecules were not clearly observed. The absorption bands at 2215 and 2186  $\text{cm}^{-1}$ , which are assigned to the perturbed CN stretching modes, were further shifted

about  $5\text{ cm}^{-1}$  to the higher wavenumbers compared to the perturbed CN stretching modes in Si-MCM-41. In addition, a new absorption band at  $2124\text{ cm}^{-1}$  was observed.

The CN vibrations of the free TCNE radical anion are reported to occur at 2183 and  $2144\text{ cm}^{-1}$ .<sup>29</sup> The new band at  $2124\text{ cm}^{-1}$  in the Al-MCM(15) sample is most probably due to the TCNE radical anion perturbed by interaction with the surface, given the relatively high concentration of the TCNE radical anion detected by EPR in this sample (see below). Apart from the CN stretching bands, other features characteristic of TCNE IR bands are not discernible in (Al)-MCM-41. Similar results were reported when TCNE was adsorbed on the zeolites.<sup>25</sup>

In calcined (7) sample, only one peak due to CN stretching was observed at  $2210\text{ cm}^{-1}$ . As already shown in Chapter 3, the high Al content calcined (7) sample has low surface area and low structural order. Therefore, the radicals formed in the calcined (7) sample may be unstable, reflected by the absence of the absorption band at ca.  $2120\text{ cm}^{-1}$  due to the CN vibrations of the TCNE radical anions (note that the FTIR spectra here were all recorded under the ambient conditions).

It was expected that the observation of the perturbed CN stretching vibrations is due to the interaction of the CN groups of TCNE with the hydroxyl groups of the (Al)-MCM-41 framework. In this case, the OH stretching region of the (Al)-MCM-41 framework could be also perturbed mutually and shown in the FTIR spectra. However, due to the adsorption of water by the samples, it is difficult to determine if hydroxyl groups are influenced by the TCNE molecules from the OH stretching region in FTIR spectra. Comparison of the (Al)-MCM-41 samples without TCNE with those containing TCNE showed no distinct difference in the OH stretching region in the FTIR spectra.

### 5.2.2. DR-UV-Vis Spectra of TCNE in (Al)-MCM-41

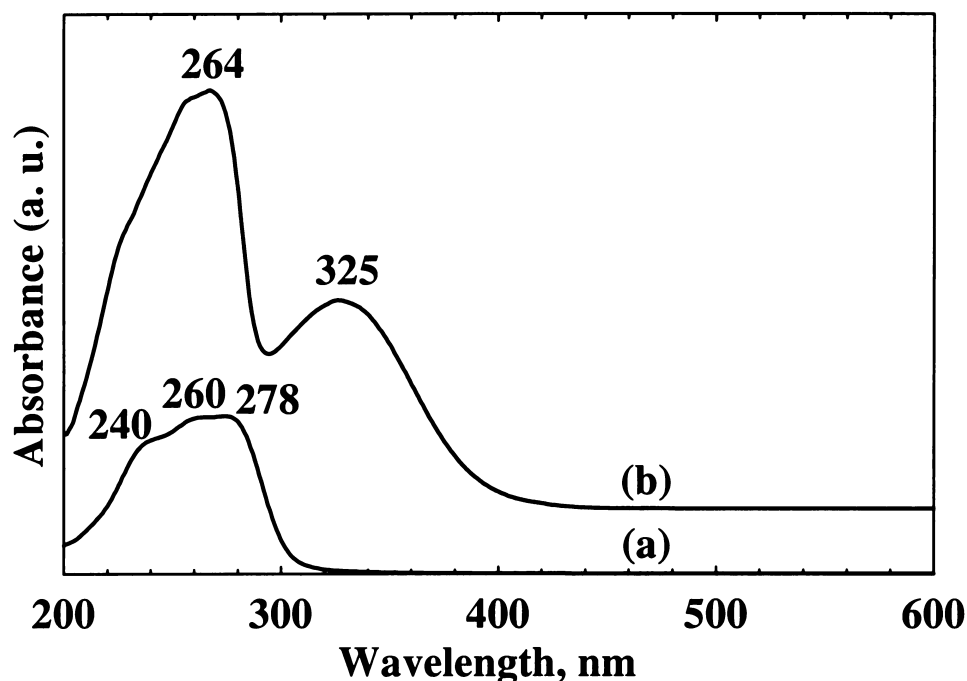


**Figure 5.2:** (a) UV-Vis spectrum of TCNE ( $\sim 2 \times 10^{-5}$  M) in  $\text{CH}_2\text{Cl}_2$ ; (b) DR-UV-Vis spectrum of TCNE in Si-MCM-41 (dehydrated at 473 K). TCNE was assembled into the Si-MCM-41 with THF as solvent, using method A2.

The UV-Vis spectrum of the free TCNE molecule in  $\text{CH}_2\text{Cl}_2$  solution is shown in Figure 5.2 (a). The absorption bands at 240, 260 and 278 nm are due to the  $\pi \rightarrow \pi^*$  transition of the free TCNE molecules.<sup>29-32</sup>

Figure 5.2 (b) shows the DR-UV-Vis spectrum of TCNE in Si-MCM-41 (dehydrated at 473 K). The spectrum exhibits absorption bands with  $\lambda_{\text{max}}$  at 264 and 325 nm, respectively. The absorption with  $\lambda_{\text{max}}$  at 264 nm is due to the  $\pi \rightarrow \pi^*$  transition.<sup>29-32</sup> The new absorption band with  $\lambda_{\text{max}}$  at 325 nm may be assigned to the CT band<sup>2,24,33,34</sup> of the TCNE/THF CT complex (Literature value of the  $\lambda_{\text{max}}$  for the CT band of TCNE/THF is at 310-318 nm<sup>28-30,32</sup>).

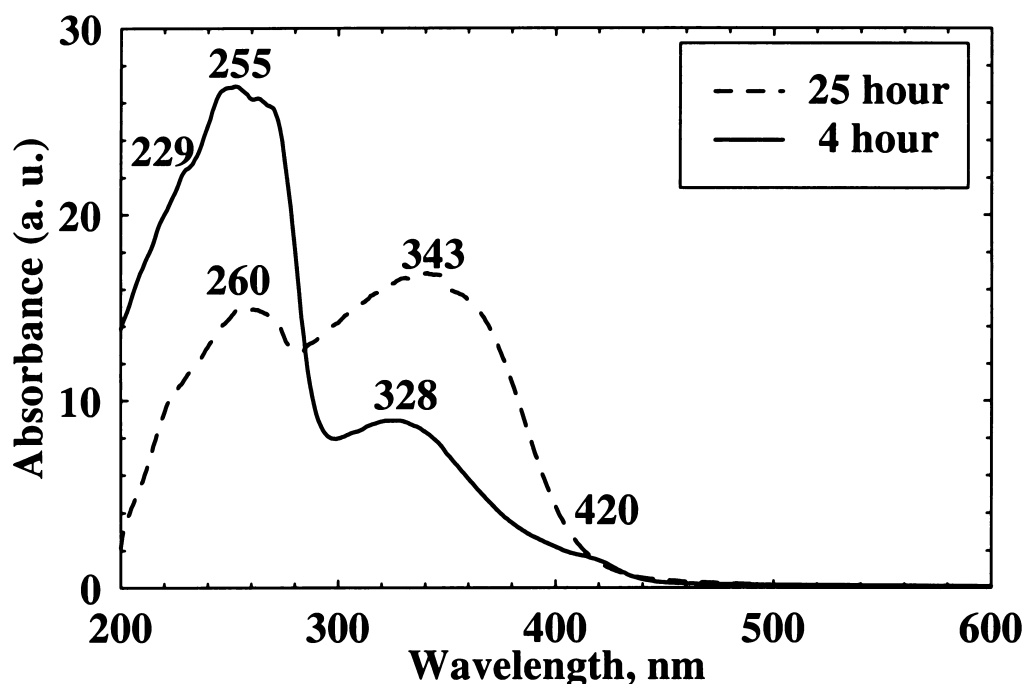


**Figure 5.3: DR-UV-Vis spectra of TCNE assembled into the Al-MCM(39) with THF as solvent, using method A2. Solid line: evaporated the THF solvent off after 4 hours contact time; dotted line: evaporated the THF solvent off after 25 hours contact time.**

From the above UV-Vis study, the following important information is obtained: TCNE exists as a free molecule in  $\text{CH}_2\text{Cl}_2$  without forming a CT complex. In THF solution, however, it does form a CT complex with THF; furthermore, the TCNE/THF CT complex exists inside the channels of the Si-MCM-41 after drying. The absorption due to the TCNE radical anion was not observed. This may be due to the fact that the amount of the TCNE radical anions formed in Si-MCM-41 is too low to detect by the normal UV-Vis spectroscopy.

Figure 5.3 shows the DR-UV-Vis spectra of TCNE assembled into the Al-MCM(39) with THF as solvent, using method A2. It can be seen that the absorption band at 260 nm at 4 hours contact time was blue shifted to 255 nm after long contact time (25 hours). Meanwhile, extending the contact time also results in the red shift of TCNE/THF CT band from 328 nm to 343 nm, accompanied by dramatic increase in

relative intensity. Apparently, extending the contact time will generate more TCNE/THF CT complexes. The characteristic absorption band of the TCNE radical anion is at  $\lambda_{\max} = \sim 420 \text{ nm}$ <sup>28-30,32</sup> and that of the TCNE dimer radical anion is at  $\lambda_{\max} = \sim 520 \text{ nm}$ .<sup>28,32</sup> Thus the absorption band at  $\lambda_{\max} = \sim 420 \text{ nm}$  in Figure 5.3 is assigned to the TCNE radical anion. The low intensity of this band indicates that only small amounts of TCNE radical anions were formed in the Al-MCM(39).

### 5.2.3. EPR Spectra of TCNE Radical Anion in THF Solution and Computer Simulation

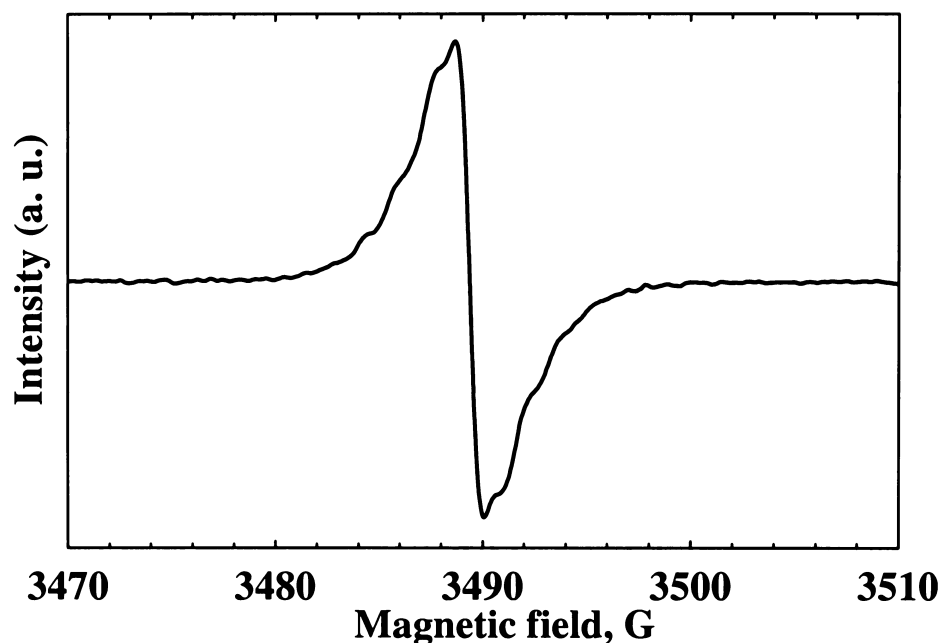


**Figure 5.4:** First derivative EPR spectrum (room temperature) of TCNE radical anion generated by dissolving TCNE in THF solution ( $\sim 0.1\text{M}$ ) in the dry box.

Theoretically, the number of the hyperfine splitting lines in an isotropic EPR spectrum is given by the equation  $2nI+1$ , where  $I$  is the nuclear spin angular momentum,  $n$  is the number of the equivalent atoms with the same nucleon in the investigating molecules.

The nuclear spin angular momentum ( $I$ ) of nitrogen atom is 1. For the TCNE radical anion, four isotopic nitrogen atoms ( $^{14}\text{N}$ ) on the four CN groups will give a 9 line hyperfine spectrum with intensity ratio of 1:4:10:16:19:16:10:4:1.<sup>35</sup>

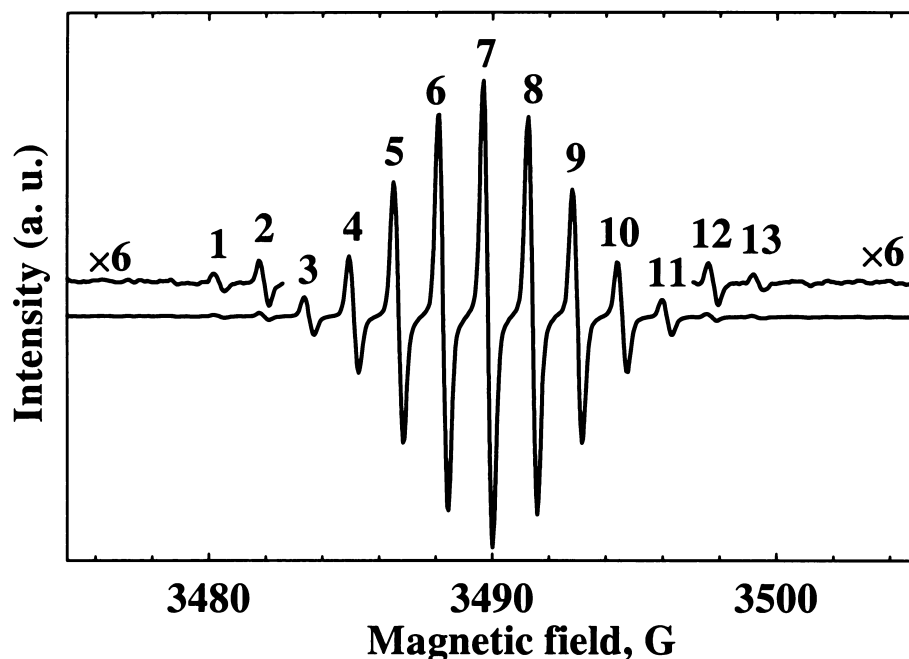


**Figure 5.5:** First derivative EPR spectrum (room temperature) of TCNE radical anion generated by dissolving TCNE in THF solution ( $\sim 0.01\text{M}$ ) in dry box.

When TCNE was merely dissolved in a THF solution in the dry box, the TCNE radical anion was formed spontaneously. Two EPR spectra (Figure 5.4 and Figure 5.5) with different shapes were obtained at high and low TCNE concentration, respectively. At high TCNE concentration ( $\sim 0.1\text{ M}$ ), the EPR spectrum is poorly resolved, having a signal with  $g$  value = 2.0040, linewidth = 1.4 G, and number of spins =  $1.8 \times 10^8$  mole in the cavity. This EPR signal was stable at least for several hours in THF solution.



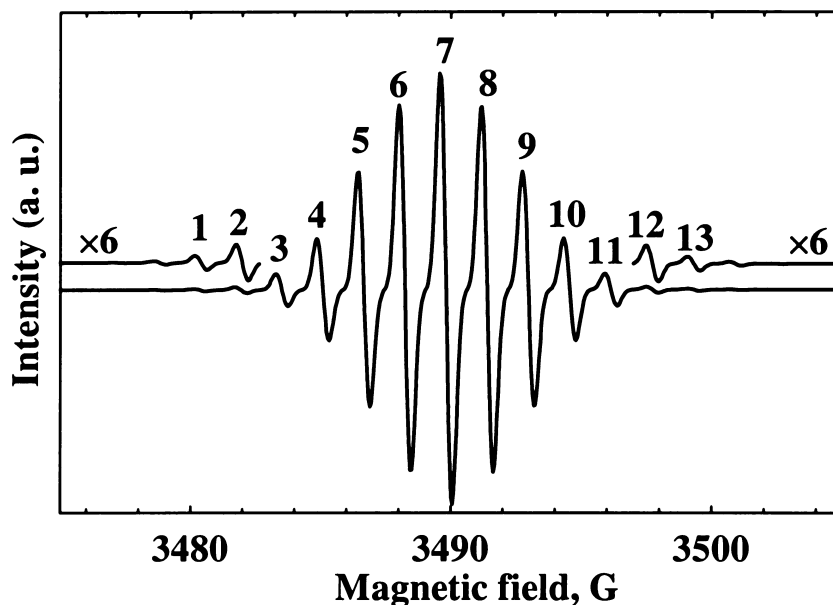


**Figure 5.6:** Simulated first derivative EPR spectrum of TCNE radical anion in solution using the following parameters: splitting constant  $a(^{14}\text{N}) = 1.58$  G,  $a(^{13}\text{C}=\text{C}) = 9.51$  G, and  $a(^{13}\text{C}\equiv\text{N}) = 6.16$  G; linewidth = 0.35 G; and  $g$  value = 2.0040.

However, diluting the above sample to a concentration of ca. 0.01 M gave a well-resolved EPR spectrum (Figure 5.5). The spectrum consists of isotropic 13 lines with  $g$  value = 2.0040,  $a(^{14}\text{N}) = 1.58$  G, and linewidth = 0.35 G. The central 9 lines (line 3-11), which are due to the four equivalent  $^{14}\text{N}$  nuclei, show approximately an intensity ratio of 1:4:10:16:19:16:10:4:1. This well-resolved spectrum can be well simulated using the following EPR parameters: splitting constants  $a(^{14}\text{N}) = 1.58$  G,  $a(^{13}\text{C}=\text{C}) = 9.51$  G,  $a(^{13}\text{C}\equiv\text{N}) = 6.16$  G; linewidth = 0.35 G; and  $g$  value = 2.0040. The simulated first derivative EPR spectrum is shown in Figure 5.6. The EPR splitting constants used for simulation are comparable to those for the TCNE radical anion reported in the literature.<sup>6,34,36-40</sup> The additional outside lines (line 1, 2, 12, 13) in Figure 5.5 and Figure 5.6 are due to the  $^{13}\text{C}$  satellite splittings.<sup>6,34,36,38-40</sup>

The formation of the TCNE radical anion in THF solution may be attributed to the dissociation of trace amount of the TCNE/THF CT complexes. It is well known that

TCNE readily dissolves in many organic solvents to produce intensively colored solutions<sup>2</sup> due to the formation of intermolecular CT complexes between the TCNE acceptor molecules and the solvent donor molecules, such as DMF<sup>40</sup> and THF.<sup>37</sup> The TCNE/THF CT complexes may be dissociated and generate TCNE radical anions after photo-irradiation.<sup>31,37,40</sup> It is also noteworthy that the EPR signals may also be observed from the TCNE THF solution which has been subjected only to the “room light”.<sup>37</sup> As indicated by Ward et al.,<sup>37</sup> in THF solution, both  $\alpha$ -hydrogen abstraction and electron transfer from the oxygen’s nonbonding electrons can take place and are responsible for the formation of the TCNE radical anion. To maintain the charge balance in solution, charge compensating radical cations are needed. Although not observed, the THF positive ion may be formed and act in this role. Inability to observe the THF positive ion may be due to: (1) the THF positive ion being unstable and rapidly dimerizing or disproportionating to a diamagnetic product,<sup>37</sup> which cannot be observed by EPR technique. (2) or a large excess of the THF neutral molecules over the THF positive ions makes the hole migration from  $\text{THF}^+$  to THF neutral species freely throughout the solution, which would be expected to result in broadening of the EPR signal so that it is undetectable.<sup>31</sup>

The shape of the EPR spectrum largely depends on the linewidth, which can be seen from the simulated EPR spectra of the TCNE radical anion at various linewidth settings shown in Figure 5.7. With increasing the linewidth, the spectrum gradually loses the hyperfine structure. At linewidth  $\geq 2.5$  G, the spectrum becomes just a single paramagnetic signal. The linewidth broadening effect may explain the observed poorly resolved EPR spectra at high TCNE concentration in THF solution.

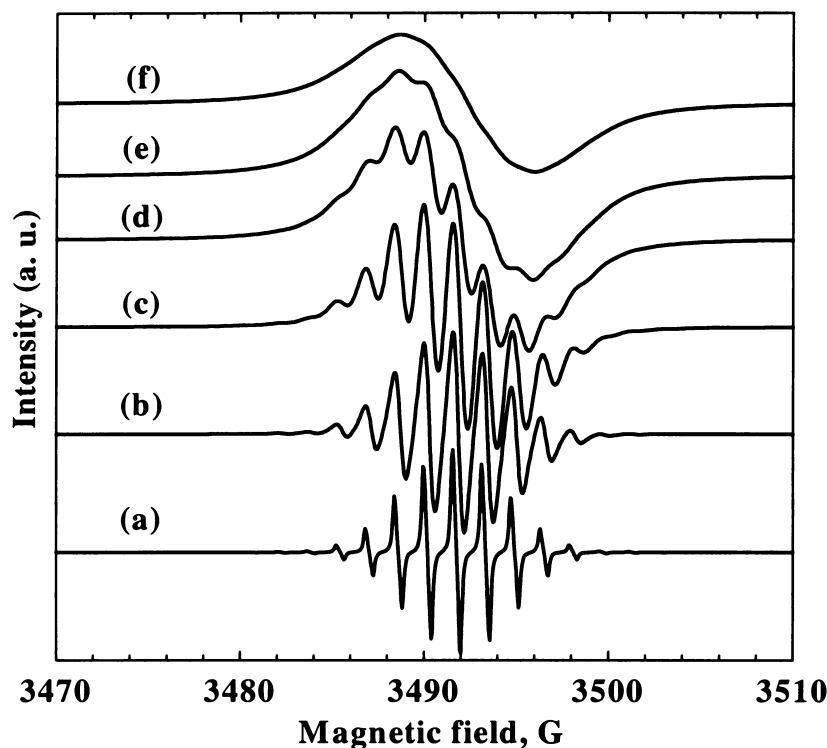


**Figure 5.7:** Computer simulation showing the relationship between the shape of the EPR spectra and the linewidths. The linewidths for each curve are: (a) 0.1 G; (b) 0.5 G; (c) 1 G; (d) 1.5 G; (e) 2 G; (f) 2.5 G.

#### 5.2.4. TCNE Assembled into (Al)-MCM-41 Using Method A1

##### 5.2.4.1. EPR Spectra of TCNE Assembled into Si-MCM-41 Using Method A1

Figure 5.8 shows the EPR spectra of the TCNE radical anion formed spontaneously in the Si-MCM-41 (dehydrated at 473 K). TCNE (~0.1 M in THF) was assembled into the Si-MCM-41 using method A1. The color of the sample was light yellow. The EPR spectrum of the solid Si-MCM-41 phase exhibits approximately 9 lines with  $g$  value = 2.0040,  $a(^{14}\text{N}) = 1.57$  G, and linewidth = 0.55 G. The EPR spectrum of the liquid THF phase consists of 13 lines with  $g$  value = 2.0040,  $a(^{14}\text{N}) = 1.52$  G, and linewidth = 0.66 G. These EPR parameters confirm that the observed EPR spectra are due to the formation of TCNE radical anion in Si-MCM-41.

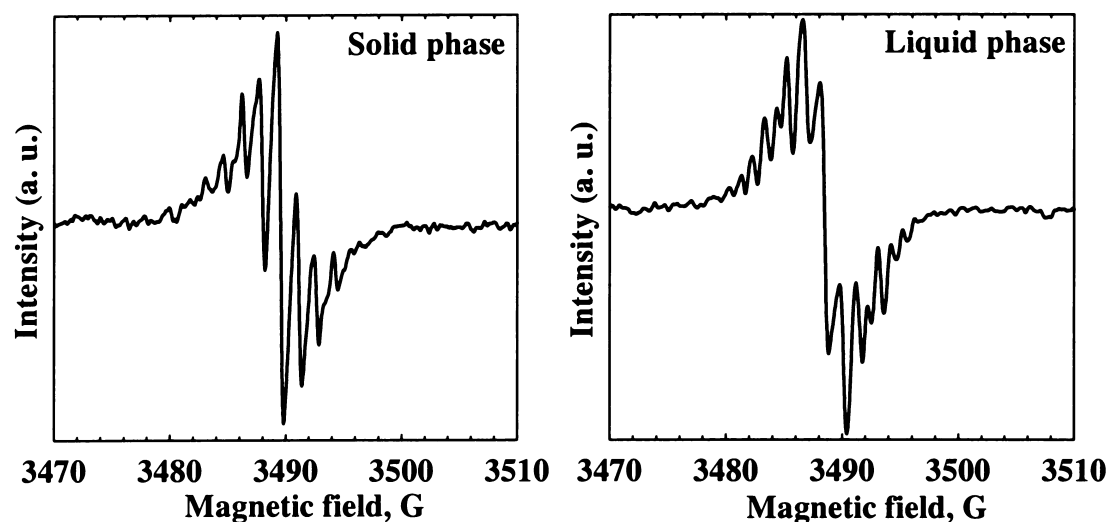


**Figure 5.8:** First derivative EPR spectra (room temperature) of TCNE radical anion in Si-MCM-41. TCNE was assembled into Si-MCM-41 with THF as solvent, using method A1.

Formation of the TCNE radical anion in Si-MCM-41 may be attributed to the dissociation of trace amounts of TCNE/THF CT complexes rather than electron transfer (ET) from the Si-MCM-41 framework to the TCNE molecules. This assumption was supported by the observation that, with increasing contact time, the spin concentration of the TCNE radical anion in the liquid phase increases while that in the solid phase remains approximately constant. Furthermore, the number of spins of the TCNE radical anion formed in the Si-MCM-41 ( $1.5 \times 10^{-8}$  moles in the cavity) is approximately the same as that found in the THF solution ( $1.8 \times 10^{-8}$  moles in the cavity) at the same TCNE concentration ( $\sim 0.1$  M) and contact time, confirming that the formation of the TCNE radical anion in Si-MCM-41 is surely due to the dissociation of TCNE/THF CT complex. The Si-MCM-41 has no electron donor sites which can reduce TCNE, a strong electron acceptor, at room temperature.

#### 5.2.4.2. EPR Spectra of TCNE Assembled into Al-MCM-41 Using Method A1

For Al-MCM-41, the optimum dehydration temperature was determined by varying the dehydration temperature of the Al-MCM-41 samples from room temperature to 973 K. Unlike the zeolite HY, silica-aluminas and alumina,<sup>25,41,42</sup> the dehydration temperature was found not to be critical for the Al-MCM-41 samples provided temperatures in the samples of 400 K are used (i.e. sufficient to remove adsorbed water). In the following experiments, a temperature of 473 K was chosen to dehydrate (Al)-MCM-41 samples.

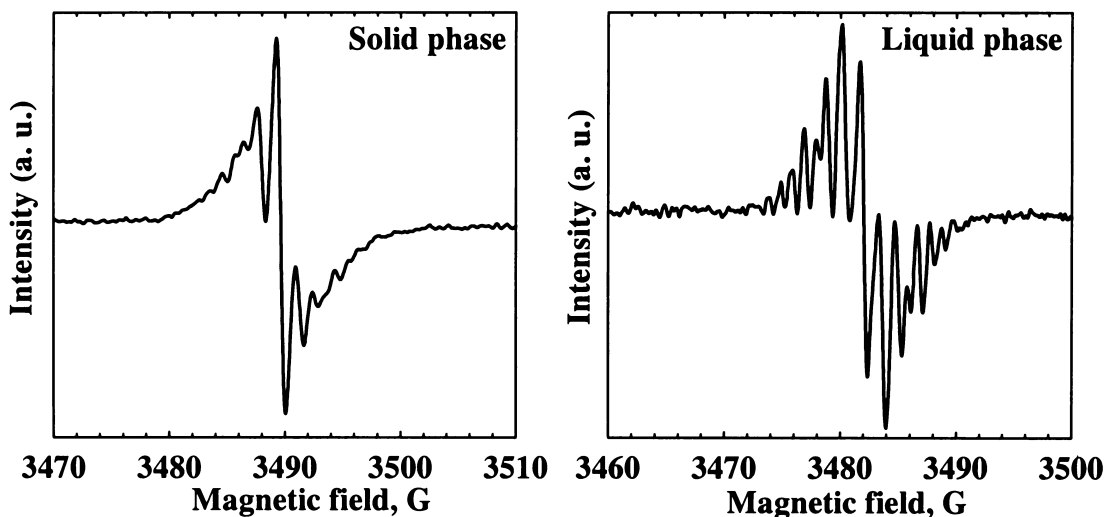


**Figure 5.9:** First derivative EPR spectra (room temperature) of TCNE radical anion in Al-MCM(39). TCNE was assembled into the Al-MCM(39) with THF as solvent, using method A1.

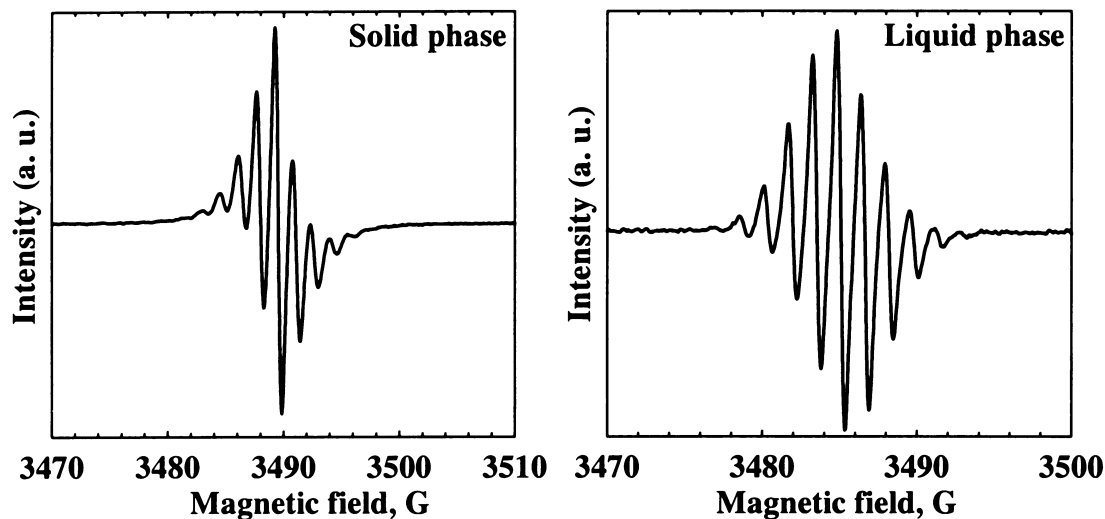


**Figure 5.10:** First derivative EPR spectra (room temperature) of TCNE radical anion in Al-MCM(15). TCNE was assembled into Al-MCM(15) with THF as solvent, using method A1.

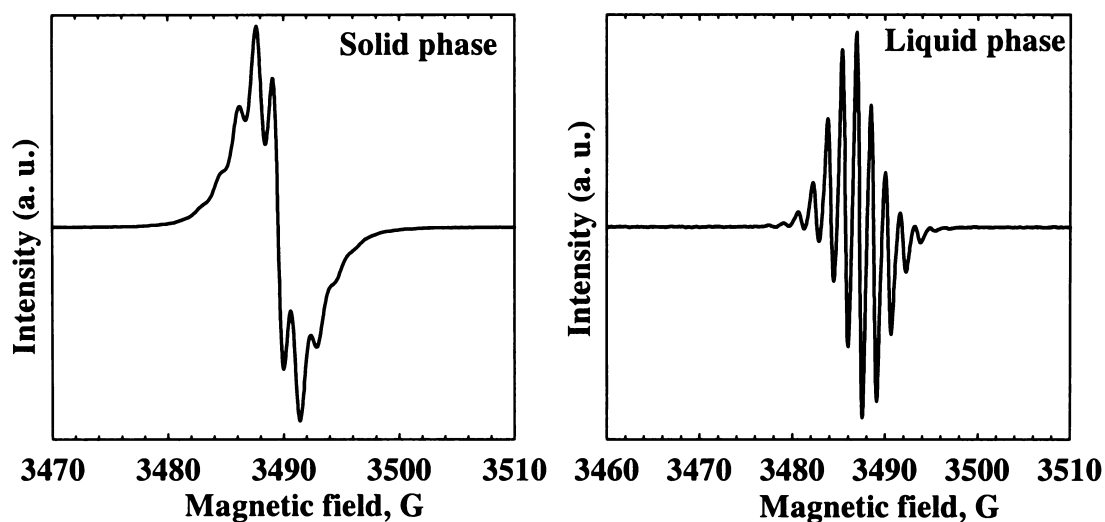


**Figure 5.11:** First derivative EPR spectra (room temperature) of TCNE radical anion in Al-MCM(7). TCNE was assembled into Al-MCM(7) with THF as solvent, using method A1.

Figures 5.9-5.11 show the EPR spectra of the TCNE radical anion spontaneously formed in Al-MCM(39), Al-MCM(15) and Al-MCM(7). TCNE was assembled into these hosts with THF as solvent, using method A1. The time taken for the TCNE to reach the maximum EPR intensities in these three Al-MCM-41 hosts were ca. 72, 24

and 24 hrs, respectively. The colors of the samples were light yellow to yellow. The EPR spectra of the solid phases exhibit 5 to 9 lines with splitting constants  $a(^{14}\text{N})$  of about 1.58 G. The EPR spectra of the liquid THF phases consist of 11-15 lines with splitting constants  $a(^{14}\text{N})$  of 1.58 G. There is no doubt that the observed EPR spectra are due to the formation of the TCNE radical anion in these Al-MCM-41 hosts.

#### **5.2.4.3. Spin Concentration Results for TCNE Assembled into (Al)-MCM-41 Using Method A1**

The spin concentration results are summarized in Table 5.1. All of the spin concentrations (mol/g) listed in Table 5.1 are taken as the maximum values measured after two weeks. The proportion of extra-framework Al in Al-MCM-41 was determined by integrating the peak areas of the tetrahedral Al and the octahedral Al in the corresponding  $^{27}\text{Al}$ -MAS-NMR. The calculated results show the following facts.

- (1) The spin concentration of the TCNE radical anion in the Si-MCM-41 is 10-100 times less than that in the Al-MCM-41 and can be ignored.
- (2) In Al-MCM-41 samples, the spin concentration of the TCNE radical anion increases with increasing Al content in the Al-MCM-41 samples. This demonstrates that the electron donor sites in the Al-MCM-41 correlate with the Al content in the Al-MCM-41.
- (3) Although the TCNE loading level is at least equal to the total Al content in the Al-MCM-41 samples, the spin concentration of the TCNE radical anion formed in Al-MCM-41 is no more than 1 % of the total Al content in Al MCM-41, and also at least 10 times less than the extra-framework Al content. No quantitative relationship between the spin concentration of the TCNE radical anion (i.e., the amount of the electron donor sites in Al-MCM-41 probed by TCNE) and the Al

content in the Al-MCM-41 samples has been established using the present assembly method A1.<sup>43-47</sup>

- (4) Most of the TCNE radical anions reside in the Al-MCM-41 solid phase rather than in the liquid phase. It is also noted that the EPR spectra of the TCNE radical anion in the Al-MCM-41 solid phases are broader than those in the liquid phases, indicating that TCNE radical anions are adsorbed (or perturbed) by the surface of the Al-MCM-41. This implies that the Al atoms in Al-MCM-41 must be responsible for the formation of the TCNE radical anion, i.e., the electron donor sites are associated with the Al in the Al-MCM-41.

**Table 5.1: Spin concentration results for TCNE assembled into the (Al)-MCM-41**

**Using method A1**

	Si-MCM-41	Al-MCM(39)	Al-MCM(15)	Al-MCM(7)
Number of spins in the solid phase (moles in the cavity)	$6 \times 10^{-9}$	$33 \times 10^{-9}$	$72 \times 10^{-9}$	$510 \times 10^{-9}$
<b>Spin concentration in solid phase (mol/g)</b>	<b><math>2 \times 10^{-7}</math></b>	<b><math>1.1 \times 10^{-6}</math></b>	<b><math>2.4 \times 10^{-6}</math></b>	<b><math>1.7 \times 10^{-5}</math></b>
Number of spins in the liquid phase (moles in the cavity)	$9 \times 10^{-9}$	$2.4 \times 10^{-8}$	$5.4 \times 10^{-8}$	$1.5 \times 10^{-9}$
Spin concentration in liquid phase (mol/cm <sup>3</sup> )	$1.5 \times 10^{-8}$	$4 \times 10^{-8}$	$9 \times 10^{-8}$	$0.25 \times 10^{-8}$
<b>Total Al content (mol /g)</b>	<b>0</b>	<b><math>4.2 \times 10^{-4}</math></b>	<b><math>1 \times 10^{-3}</math></b>	<b><math>2.1 \times 10^{-3}</math></b>
<b>Extra-framework Al (mol/g)</b>	<b>0</b>	<b><math>9.2 \times 10^{-5}</math></b>	<b><math>1.8 \times 10^{-4}</math></b>	<b><math>5.0 \times 10^{-4}</math></b>

\* Note: The uncertainty of the spin concentration measurement is estimated to be ca.  $\pm(5-30)$  %.

Simple calculation shows that the formation of smaller amounts of the TCNE radical anion than the Al content in Al-MCM-41 is not due to surface area, pore volume or diffusion problems. In a typical experiment, 16 mg of TCNE was loaded into 60 mg Al-MCM-41 samples. This amount of TCNE occupies less than 1 % of the available pore volume or surface area of the host material. Also, the pore size of the Al-MCM-41 is ca. 30 Å, which is large enough for the TCNE molecules to diffuse in and out freely.



The solvent effect then may be considered as the main drawback for exploiting the electron donor sites in Al-MCM-41 using method A1. Druon et al. suggested<sup>48</sup> in their EPR study of TCNE adsorbed on type-X and Y zeolites that the presence of solvent benzene restricts the number of paramagnetic centers formed on the zeolite surface and the interactions between them, resulting in better resolved EPR spectra. THF may also act in a similar way in Al-MCM-41. The existence of the THF solvent may lessen the accessibility of the TCNE molecules to the electron donor sites in Al-MCM-41, reduce the interaction between the TCNE molecules and the electron donor sites in Al-MCM-41, or prevent the formation of the TCNE radical anion by forming TCNE/THF CT complexes. These factors may account for the reduced concentration of the TCNE radical anion formed in Al-MCM-41 using assembly method A1.

#### **5.2.4.4. Life-Time and Stability of TCNE Radical Anion in Al-MCM-41**

The EPR signal of the TCNE radical anion could still be observed in the solid phase of the Al-MCM-41 even after one month. This indicates that the dehydrated Al-MCM-41 samples not only provide electron donor sites to reduce the TCNE molecules into the radical anions, but also dramatically stabilize the formed TCNE radical anions. Generally, the polar and electrostatic microenvironment of the Al-MCM-41 is considered to play an important role in stabilization of the occluded radical species.

43,49,50

When Al-MCM-41 samples assembled with TCNE using method A1 were exposed to the air, the EPR intensity of the TCNE radical anion was sharply decreased within ca. 5 hours and diminished gradually in the next few hours. This indicates that the TCNE radical anion formed in Al-MCM-41 are not quite stable in air.

### 5.2.5. EPR Study of TCNE Assembled into (Al)-MCM-41 Using Method A2

#### 5.2.5.1. Solvent Effects

Formation of the TCNE radical anion in (Al)-MCM-41 largely depends on the solvent applied. The following are the EPR measurement results of TCNE assembled into the (Al)-MCM-41 with different solvents, using method A2:

**Acetone:** No EPR radical signal was observed both in Si-MCM-41 and Al-MCM-41.

**Benzene:** No EPR radical signal was observed in Si-MCM-41. However, a poorly resolved EPR signal without hyperfine structure was detected in Al-MCM-41.

**Dichloromethane:** No EPR radical signal was observed in Si-MCM-41. However, a relatively weak EPR radical signal without hyperfine structure was detected in Al-MCM-41.

**THF:** No EPR radical signal was observed in Si-MCM-41. However, relatively intense radical signals were detected in Al-MCM-41 samples. Washing these paramagnetic samples with THF in the dry box gave well-resolved EPR spectra with certain hyperfine lines, which are the typical EPR signal of the TCNE radical anion.

It can be seen that the formation of the TCNE radical anion in (Al)-MCM-41 depends not only on the framework nature of the (Al)-MCM-41 hosts, but also on the solvents used. Choosing a proper solvent is critical in determining the redox properties of the porous materials.

Similar solvent effects were observed when TCNQ was assembled into the Al-MCM-41.

#### 5.2.5.2. EPR Study of TCNE Assembled into (Al)-MCM-41 Using Method A2.

Figures 5.12-5.14 show the EPR spectra of the TCNE radical anion formed in Al-MCM(39), Al-MCM(15) and Al-MCM(7), respectively. TCNE was assembled into these Al-MCM-41 hosts with THF as solvent, using method A2. All of the dried samples (Spectra (a) in Figure 5.12-5.14) exhibit narrow singular paramagnetic signals with  $g$  value = 2.0040. The corresponding linewidths are 1.0 G in Al-MCM(39), 1.2 G in Al-MCM(15) and 1.5 G in Al-MCM(7), respectively. The increase of the linewidth is due to the dipolar interactions between the adjacent spins, just as in the more concentrated TCNE in THF solution. The increase in linewidth with increasing Al content is due to increased concentration of the TCNE radical anion, which leads to an initial broadening of the linewidth.<sup>35</sup> Further evaporating off the THF solvent may leave a high concentration of the TCNE radical anion in the channels of the Al-MCM-41. The exchange narrowing then occurs, reflected in the EPR spectra (spectra (a) in Figure 5.12-5.14) as the narrow sharp signals.

Washing the dried samples with THF gave better-resolved EPR spectra (spectra (b) in Figure 5.12-5.14), which feature 9-11 hyperfine lines with splitting constants ( $a(^{14}\text{N})$ ) = ~1.60 G and  $g$  value = ~2.004. Better resolved EPR spectra are due to the washing effects: (1) washing the dried sample with THF will dilute (and wash off large amount of TCNE and TCNE radicals) the TCNE radical anions (2) meanwhile, the THF solvent may also restrict the interaction between TCNE radical anions.

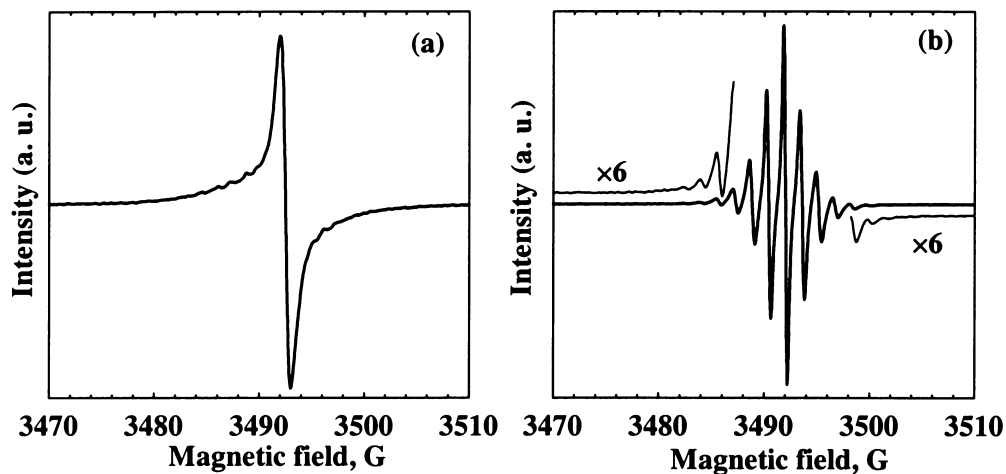


**Figure 5.12:** First derivative EPR spectra (room temperature) of TCNE radical anion in Al-MCM(39). TCNE was assembled into the Al-MCM(39) with THF as solvent, using method A2. (a) Dried sample; (b) washed with THF.

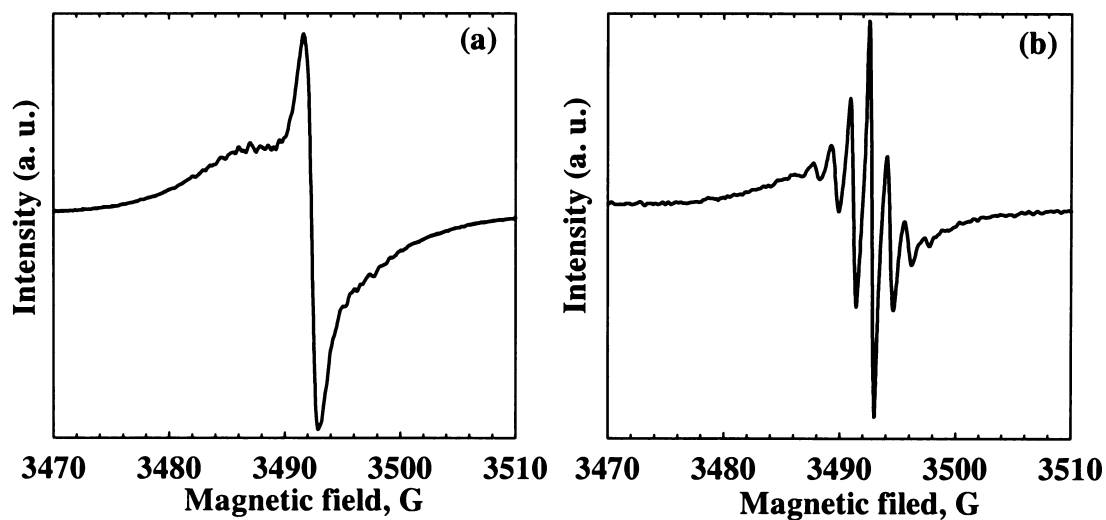


**Figure 5.13:** First derivative EPR spectra (room temperature) of TCNE radical anion in Al-MCM(15). TCNE was assembled into the Al-MCM(15) with THF as solvent, using method A2. (a) Dried sample; (b) washed with THF.

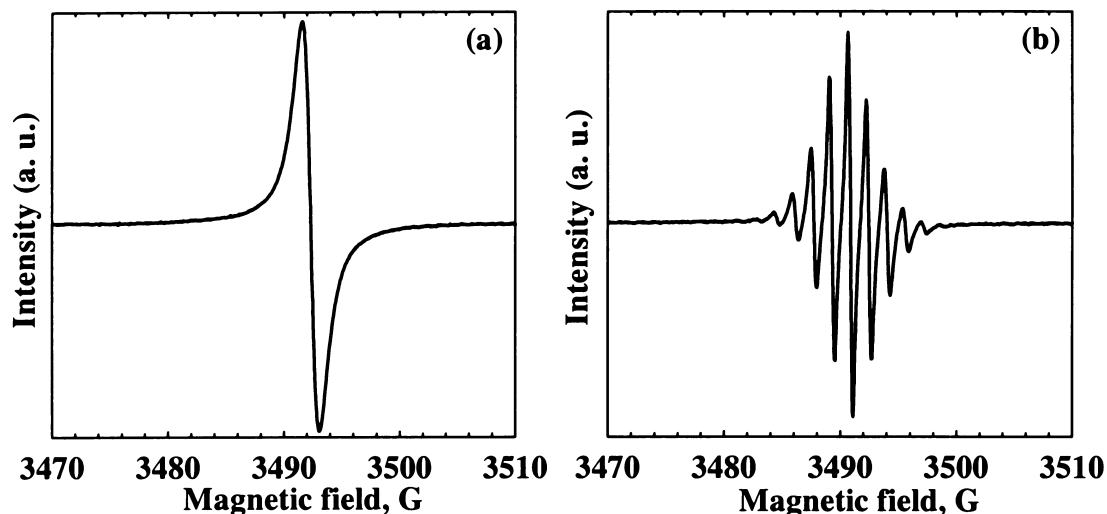


Figure 5.14: First derivative EPR spectra (room temperature) of TCNE radical anion in Al-MCM(7). TCNE was assembled into Al-MCM(7) with THF as solvent, using method A2. (a) Dried sample; (b) washed with THF.

#### 5.2.5.3. TCNE Assembled into Post-Synthesized Al-MCM-41 Using Method A2

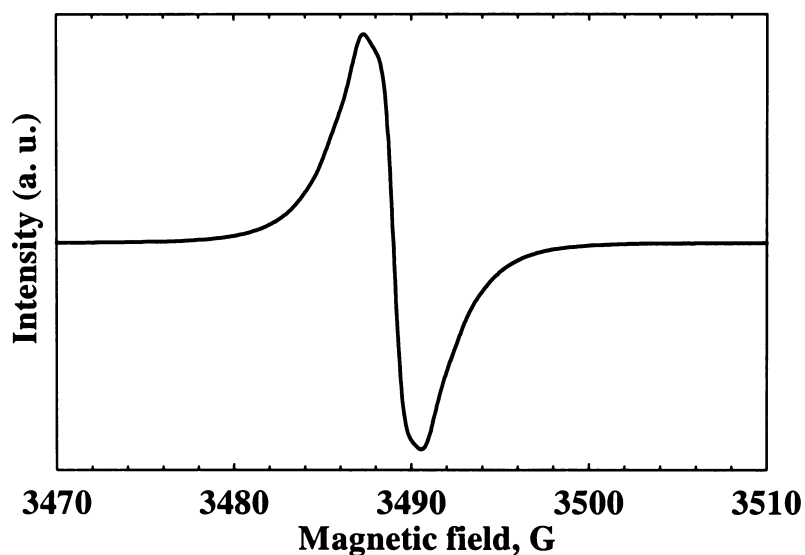


Figure 5.15: First derivative EPR spectrum (room temperature) of TCNE radical anions in post-synthesized Al-MCM-41 (Si/Al =14). TCNE was assembled into post-synthesized Al-MCM-41 with THF as solvent, using method A2.

The post-synthesized Al-MCM-41 is different from the directly synthesized Al-MCM-41. In directly synthesized Al-MCM-41, a certain amount of Al might be incorporated

into the inner wall structures of the framework, which are not accessible by the probe molecules. However, in the post-synthesized Al-MCM-41,<sup>51-58</sup> the Al atoms are mainly “grafted” on the surface of the parent MCM-41 framework, which (both tetrahedral Al and extra-framework Al) are readily accessible by the probe molecules.

When TCNE was assembled into the post-synthesized Al-MCM-41 (Si/Al = 14) (dehydrated at 473 K), the sample gradually turned into orange. The EPR spectrum (Figure 5.15) gave only a single paramagnetic signal with high intensity. The DR-UV-Vis spectrum confirms that this EPR signal is due to the formation of the TCNE radical anion (see below).

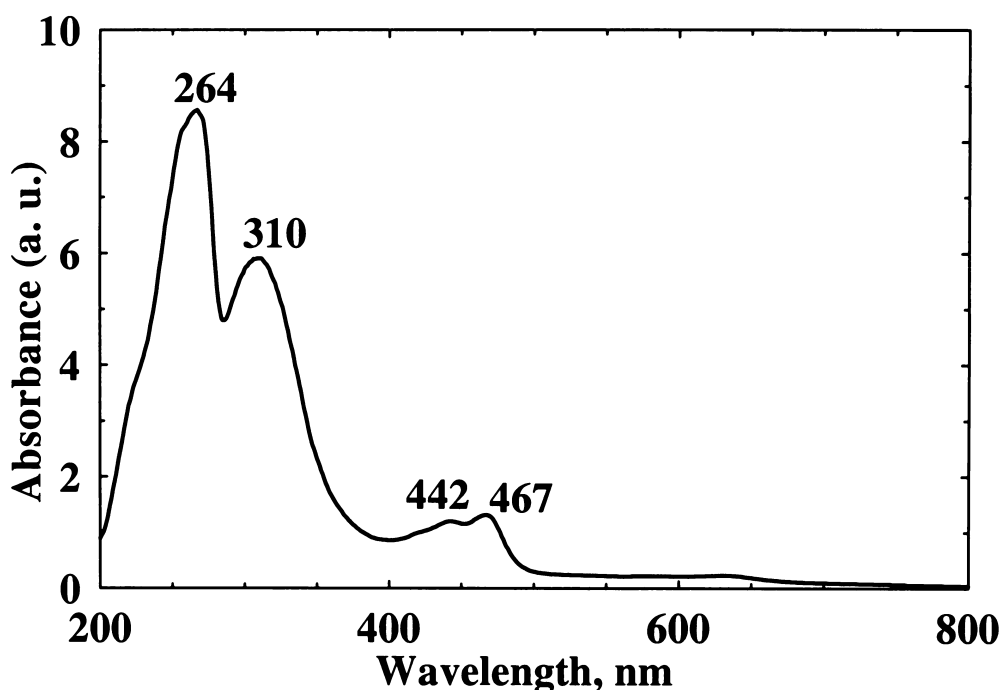


Figure 5.16: DR-UV-Vis spectrum of TCNE radical anion in post-synthesized Al-MCM-41 (Si/Al=14).

Figure 5.16 shows the DR-UV-Vis spectrum of the TCNE radical anions generated in the post-synthesized Al-MCM-41. According to the discussion in the previous sections, the absorption at 264 nm is due to the  $\pi \rightarrow \pi^*$  transition of the free TCNE molecules,

the absorption band at 310 nm is the CT band of the TCNE/THF CT complex, and the bands at 442 and 467 nm are assigned to the TCNE radical anions. DR-UV-Vis spectrum confirms that the unresolved EPR spectra shown in Figure 5.15 is the paramagnetic signal of the TCNE radical anion.

#### 5.2.5.4. Spin Concentration Results for TCNE Loaded into (Al)-MCM-41 Using Method A2

**Table 5.2: Spin concentration results for TCNE assembled into (Al)-MCM-41 with method A2**

	Si-MCM-41	Al-MCM(39)	Al-MCM(15)	Al-MCM(7)	Post-synthesized Al-MCM-41 (Si/Al = 14)
Number of spins before washing with THF (moles in the cavity)	0	$4 \times 10^{-7}$	$5.7 \times 10^{-7}$	$6.3 \times 10^{-7}$	$9 \times 10^{-7}$
<b>Spin concentration before washing with THF (mol/g)</b>	<b>0</b>	<b><math>1.3 \times 10^{-5}</math></b>	<b><math>1.9 \times 10^{-5}</math></b>	<b><math>2.1 \times 10^{-5}</math></b>	<b><math>3.0 \times 10^{-5}</math></b>
Number of spins after washing with THF (moles in the cavity)	0	$1.7 \times 10^{-7}$	$2.9 \times 10^{-7}$	$1.7 \times 10^{-7}$	–
Spin concentration after washing with THF (mol/g)	0	$5.7 \times 10^{-6}$	$1.0 \times 10^{-5}$	$5.7 \times 10^{-6}$	–
<b>Total Al content (mol /g)</b>	<b>0</b>	<b><math>4.2 \times 10^{-4}</math></b>	<b><math>1 \times 10^{-3}</math></b>	<b><math>2.1 \times 10^{-3}</math></b>	<b><math>1.1 \times 10^{-3}</math></b>
<b>Extra-framework Al (mol/g)</b>	<b>0</b>	<b><math>9.2 \times 10^{-5}</math></b>	<b><math>1.8 \times 10^{-4}</math></b>	<b><math>5.0 \times 10^{-4}</math></b>	<b><math>3.0 \times 10^{-5}</math></b>

**\* Note: The uncertainty of the spin concentration measurement is estimated to be ca.  $\pm(5-30)$  %.**

The spin concentration results are listed in Table 5.2. All of the spin concentrations (mol/g) listed in Table 5.2 are the maximum values taken after two weeks. The calculated results show the following facts:

(1) The spin concentration of the TCNE radical anion generated using method A2 are approximately an order of magnitude higher than those generated using method A1 except for the high Al content Al-MCM(7) sample. This may be due to the

enhancement of the interactions between the TCNE molecules and the electron donor sites in Al-MCM-41 after the THF solvent was evaporated off. The exception in Al-MCM(7) may be associated with its low surface area and poor pore wall ordering.

(2) With increasing Al content, the spin concentration of TCNE radical anion also increases. However, these values are still about one to two order of magnitude lower than the total Al content in the corresponding Al-MCM-41 samples. No quantitative relationship between the spin concentration of the TCNE radical anion (i.e., the amount of the electron donor sites probed by TCNE using method A2) and the Al content in Al-MCM-41 samples has been established.

(3) Lack of observation of the EPR radical signal in Si-MCM-41 proves that the TCNE radical anions generated in Si-MCM-41 using method A1 are due to the dissociation of the TCNE/THF CT complexes rather than the electron transfer from Si-MCM-41 to TCNE. The Si-MCM-41 has no electron donor sites that are strong enough to reduce TCNE, a strong electron acceptor, into corresponding radical anion at room temperature.

(4) Washing the samples with THF may also wash out large amounts of TCNE radical anions, indicating that not all of the TCNE radical anions are bonded strongly on the surface of the Al-MCM-41.

For the post-synthesized Al-MCM-41 sample, the calculation results indicate that the spin concentration of the TCNE radical anion is still much less than the Al content. No quantitative relationship has been established between the probed electron donor sites and the total Al content. However, interestingly, the spin concentration of the TCNE radical anion ( $\sim 3.0 \times 10^{-5}$  mol/g) matches well with the amount ( $\sim 3.0 \times 10^{-5}$  mol/g) of the extra-framework Al content in the post-synthesized Al-MCM-41 (2.7 % of extra-framework Al, please kindly refer to Section 3.3.2.2 in Chapter 3). **The electron donor**



sites probed by TCNE correlate quantitatively (or at least semi-quantitatively) with the extra-framework Al content (rather than the tetrahedral Al) in the post-synthesized Al-MCM-41 sample. Unfortunately, the exact electron donor sites cannot be determined only from the current experimental data.

#### 5.2.6. TCNE Loaded into (Al)-MCM-41 Using Method B1

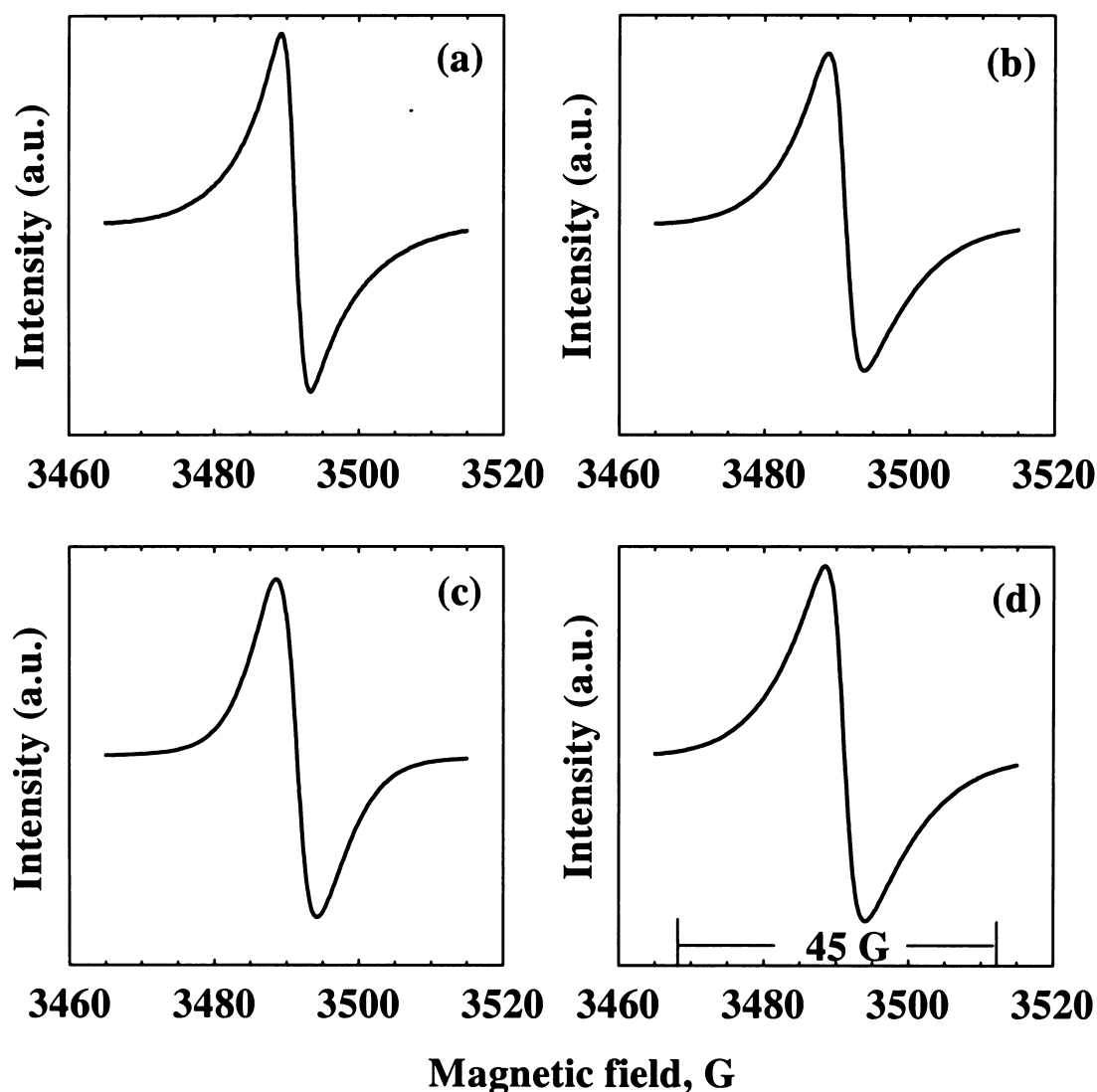


Figure 5.17: First derivative EPR spectra (room temperature) of TCNE radical anion in (a) Si-MCM-41; (b) Al-MCM(39); (c) Al-MCM(15); (d) Al-MCM(7). TCNE was assembled into (Al)-MCM-41 samples using method B1.

TCNE sublimates easily at temperatures above 393 K at atmosphere pressure and melts at 471-473 K.<sup>1</sup> High thermal stability of TCNE is shown by its ability to sublime unchanged even at 873 K at a pressure of 2.7 mmHg.<sup>1</sup> However, sublimation at atmosphere pressure by heating at 1273 K can result in about 50 % conversion of TCNE to cyanogens.<sup>1</sup> Method B1 (see Section 2.4.2 in Chapter 2) utilizes the ease of sublimation and the high thermal stability properties of TCNE to introduce TCNE molecules into (Al)-MCM-41 hosts instead of using organic solvent as transferring media. Thus the solvent affects on electron transfer was avoided in Method B1. Method B1 can be regarded as the cleanest assembling method.

After heating the sealed EPR tubes containing TCNE and (Al)-MCM-41 samples (Si/Al =  $\infty$ , 39, 15 and 7) at 383 K, immediately the sample became dark brown. First derivative EPR spectra (room temperature) recorded for these samples are shown in Figure 5.17. Only broad paramagnetic signals with overall width of ~ 45 G were obtained. A similar broad resonance with overall width of ~ 50 G for the TCNE radical anion was reported by Flockhart et al.<sup>25</sup> when TCNE was adsorbed on dehydrated gibbsite. TCNE radical anions generated using method B1 are quite stable and long-lived, as evidenced by the lack of significant change of the EPR signal intensities even after months.

With the decrease of the Si/Al ratio in Al-MCM-41, the linewidth increases in the order of 4.1 (Si/Al =  $\infty$ ), 4.8 (Si/Al = 39), 5.5 (Si/Al = 15) and 6.0 (Si/Al = 7), respectively. The broadening may be attributed to: (1) the stronger adsorption of the TCNE radical anions on the surface of the higher Al content Al-MCM-41 samples, (2) or/and formation of more TCNE radical anions in high Al content samples enhancing the spin-spin or dipolar interactions between the TCNE radical anions and the neutral molecules.<sup>35</sup>

The spin concentration results are shown in Table 5.3. All of the spin concentrations (mol/g) listed in Table 5.3 are the maximum values taken after two weeks. The calculation results indicate the follow facts:

- (1) Only up to ca. 5 % of TCNE molecules were reduced to the radical anions. This is not due to the loading level of TCNE, because the amounts of TCNE loaded into the Al-MCM-41 are at least equal to the Al content in the Al-MCM-41 sample.
- (2) The spin concentration of the TCNE radical anion (i.e. the amount of the electron donor sites probed by TCNE using method B1) has no quantitative relationship with the total Al content in the Al-MCM-41 samples.
- (3) In the low Al content sample, the spin concentration of the TCNE radical anion is of the same order of the magnitude as the extra-framework Al. However, in the high Al content sample, the difference between these two values is greater. This may be due to part of Al being incorporated into the interior pore wall which cannot be accessed by the TCNE probe molecules.
- (4) Si-MCM-41 also gives an EPR signal, indicating that Si-MCM-41 may also act as electron donor at elevated temperatures, although the signal intensity is less than those achieved with Al-MCM-41 samples.

**Table 5.3: Spin concentration results for TCNE assembled into (Al)-MCM-41 using method B1**

	Si-MCM-41	Al-MCM(39)	Al-MCM(15)	Al-MCM(7)
Number of spins (moles in the cavity)	$6 \times 10^{-7}$	$20 \times 10^{-7}$	$26 \times 10^{-7}$	$29 \times 10^{-7}$
<b>Spin concentration (mol/g)</b>	<b><math>2.0 \times 10^{-5}</math></b>	<b><math>6.7 \times 10^{-5}</math></b>	<b><math>8.7 \times 10^{-5}</math></b>	<b><math>9.7 \times 10^{-5}</math></b>
Total Al content (mol /g)	0	$4.2 \times 10^{-4}$	$1 \times 10^{-3}$	$2.1 \times 10^{-3}$
Extra-framework Al (mol/g)	0	$9.2 \times 10^{-5}$	$1.8 \times 10^{-4}$	$5.0 \times 10^{-4}$

\* Note: The uncertainty of the spin concentration measurement is estimated to be ca.  $\pm(5-30)$  %.

### 5.3. TCNQ in (Al)-MCM-41

#### 5.3.1. FTIR Spectra of TCNQ in (Al)-MCM-41

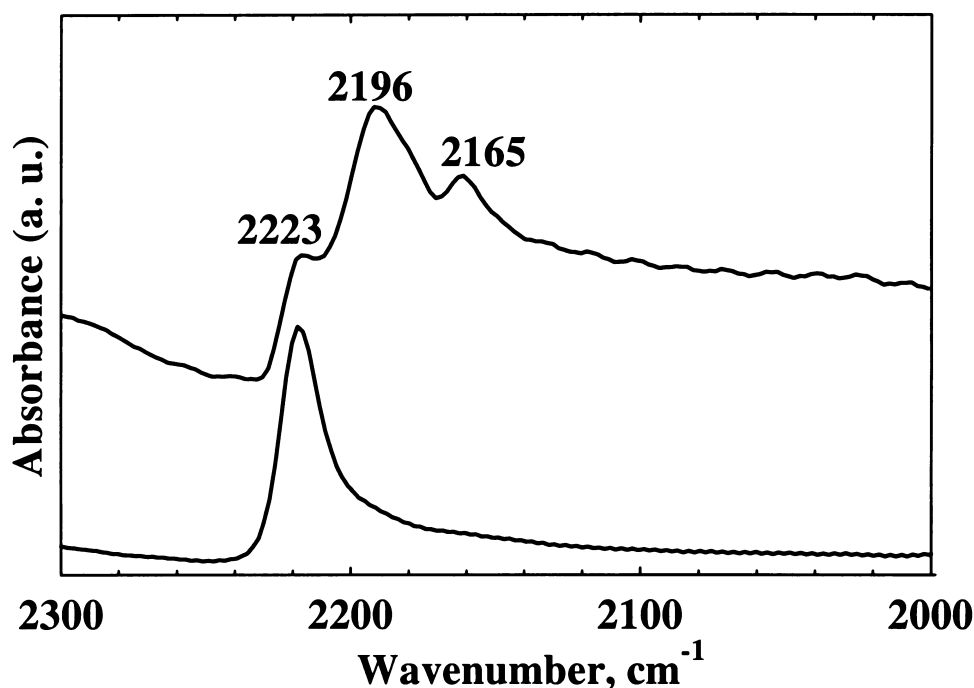


Figure 5.18: FTIR spectra of TCNQ in Si-MCM-41 (bottom) and in Al-MCM(39) (top) in the range between 2000-2300 cm<sup>-1</sup>. TCNQ was assembled into these hosts with THF as solvent, using method A2.

Figure 5.18 shows the FTIR spectra of TCNQ in Si-MCM-41 (bottom) and in Al-MCM-41 (top). Both spectra display an absorption band at 2223 cm<sup>-1</sup>, which is notably shifted to the lower frequency compared to the  $\nu_{\text{CN}}$  at 2230 cm<sup>-1</sup> reported for the free TCNQ molecules.<sup>14</sup> The band at 2223 cm<sup>-1</sup> is assigned to the perturbed CN stretching mode. According to the literature, the  $\nu_{\text{CN}}$  of TCNQ<sup>•-</sup> are at 2197 and 2166 cm<sup>-1</sup>, and the  $\nu_{\text{CN}}$  of TCNQ<sup>2-</sup> are at 2164 and 2096 cm<sup>-1</sup>.<sup>14</sup> Thus, the absorption bands at 2196 and 2165 cm<sup>-1</sup> in Figure 5.18 are assigned to the CN stretching modes of the TCNQ radical anion generated in Al-MCM(39). The absorption at 2165 cm<sup>-1</sup> is unlikely to be due to

the  $\nu_{\text{CN}}$  mode of  $\text{TCNQ}^{2-}$  since another characteristic absorption of  $\text{TCNQ}^{2-}$  at ca. 2096  $\text{cm}^{-1}$  was not observed. This assignment is in good agreement with the reports<sup>7,10,14,59-61</sup> in the literature.

### 5.3.2. DR-UV-Vis Spectra of TCNQ in (Al)-MCM-41

The UV-Vis spectrum of TCNQ in  $\text{CH}_3\text{CN}$  (dashed line in Figure 5.19) displays a dominant absorption band at  $\lambda_{\text{max}} = 390$  nm, which is a characteristic absorption band of free TCNQ molecules.<sup>12</sup> As a typical example, Figure 5.19 also shows the DR-UV-Vis spectra of TCNQ assembled into the Si-MCM-41 (dotted line) and Al-MCM-41 (solid line) with THF as solvent, using method A2. The absorption band at 403 nm for the TCNQ in Si-MCM-41 and Al-MCM-41 is shifted ca. 13 nm to the higher wavenumbers compared to the absorption band at 390 nm for the neutral TCNQ in  $\text{CH}_3\text{CN}$  solution, indicating that the TCNQ molecules are perturbed in (Al)-MCM-41, probably through hydrogen-bonding. This is consistent with the result of the FTIR study. The DR-UV-Vis spectrum of TCNQ in Al-MCM-41 also shows additional absorption bands with maxima at 750 and 851 nm in the red-band system. These are characteristic absorption bands of the TCNQ radical anion.<sup>11,14,59,62-65</sup> It was suggested<sup>62</sup> that the bands in the red-system might represent separate electronic transitions to the first two doublet excited states of the TCNQ radical anions. Jeanmaire et al.<sup>65</sup> assigned these bands to a  ${}^2\text{B}_{3g} \rightarrow {}^2\text{B}_{1u}$  transition (long axis polarized) with fine structure representing partially resolved vibronic transitions and the blue-band which extends from 350 to 480 nm to arise from both the  ${}^2\text{B}_{3g} \rightarrow {}^2\text{B}_{1u}^{(2)}$  (long axis polarized) and the  ${}^2\text{B}_{3g} \rightarrow {}^2\text{A}_u$  (short-axis polarized) transitions.

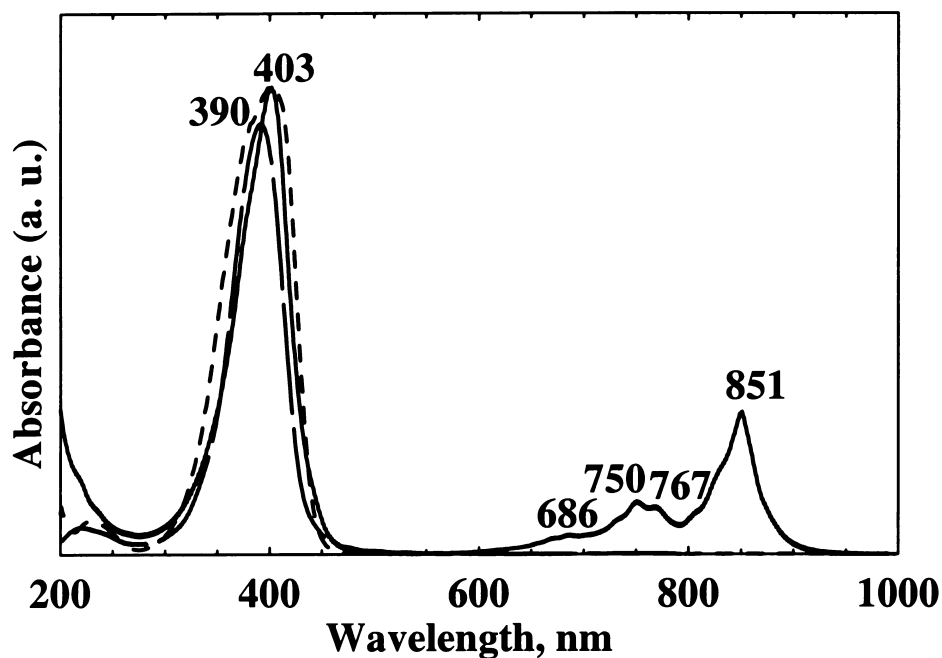


Figure 5.19: UV-Vis spectrum of TCNQ in CH<sub>3</sub>CN ( $\sim 2 \times 10^{-5}$  M) (dashed line) and DR-UV-Vis spectrum of TCNQ in Al-MCM(39) (solid line) and Si-MCM-41 (dotted line).

### 5.3.3. EPR Spectra of TCNQ Radical Anion in THF Solution and Computer Simulation

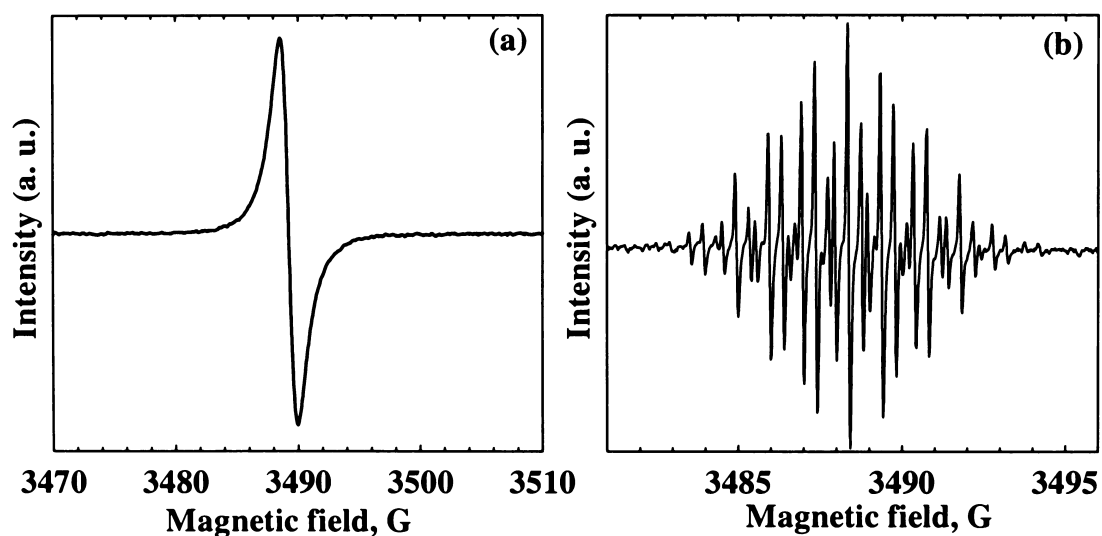
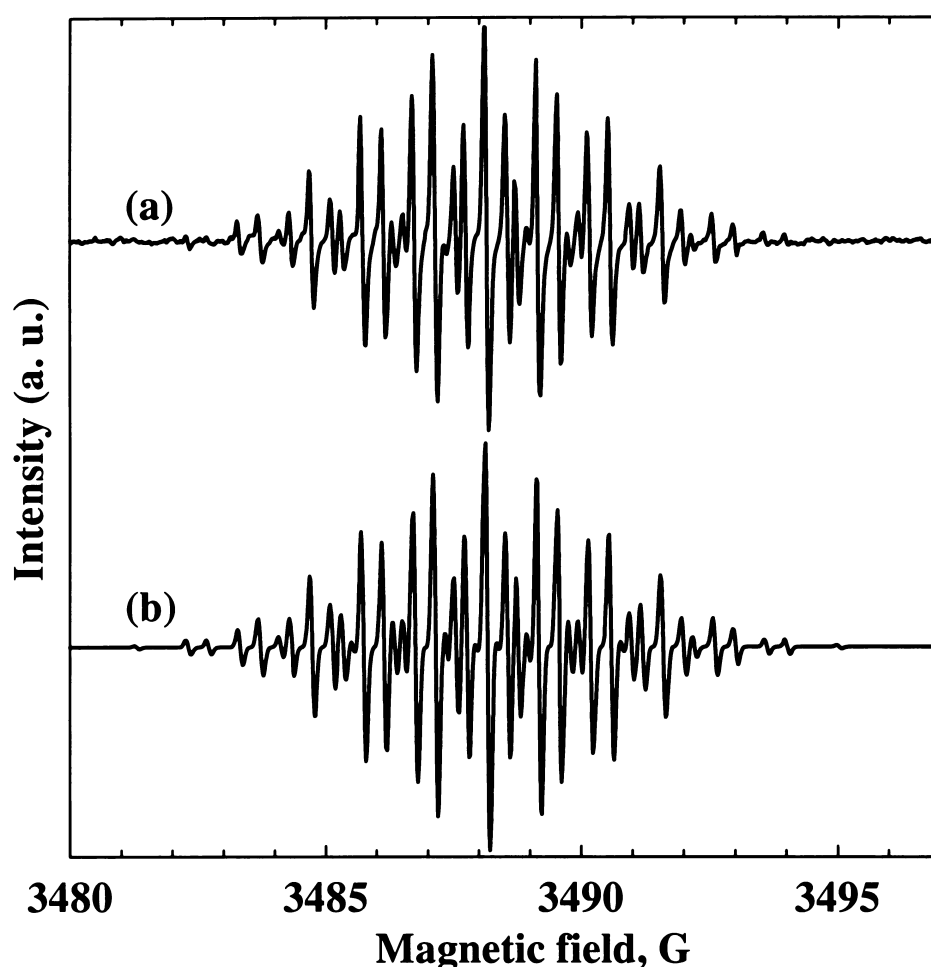


Figure 5.20: First-derivative EPR spectra (room temperature) of TCNQ radical anion generated by dissolving TCNQ in THF solution in the dry box. The concentration of TCNQ was (a)  $\sim 0.1$  M and (b)  $\sim 0.01$  M.



**Figure 5.21: Comparison of the experimental (a) and the simulated (b) first-derivative EPR spectra (room temperature) of TCNQ radical anion in solution.**

The EPR signal of the TCNQ radical anion was also observed in THF solution. Figure 5.20 shows the EPR spectrum of the TCNQ radical anion generated by merely dissolving TCNQ in a THF solution in the dry box. At higher TCNQ concentrations ( $\sim 0.1$  M), the spectrum (Figure 5.20 (a)) exhibits a single paramagnetic signal with a spin population of  $5.1 \times 10^{-7}$  moles in the cavity. At low concentration ( $\sim 0.01$  M), a well-resolved EPR spectrum (Figure 5.20 (b)) was obtained. Analysis of this more than 36 line spectrum gave the following EPR parameters:  $g$  value = 2.0040,  $a(^{14}\text{N}) = 1.01$  G,  $a(\text{H}) = 1.42$  G, linewidth = 0.1 G, and number of spins =  $4.8 \times 10^{-8}$  moles in the cavity. In theory, four equivalent  $^{14}\text{N}$  in TCNQ should give 9 lines in EPR spectrum.

These lines will be further split by four equivalent hydrogens to give a 36 line pattern. The observed well-resolved EPR spectrum is in good agreement with this predication. TCNQ radical anions are stable in THF solution for at least 10 hours. The formation of TCNQ radical anions in THF solution may also be explained by the formation and dissociation of TCNQ/THF CT complexes.

The well-resolved EPR spectrum of TCNQ radical anion shown in Figure 5.20 (b) can be well simulated. Figure 5.21 shows the computer simulation results. The experimental spectrum (Figure 5.21 (a)) was simulated using the following EPR parameters according to the data in the literature:<sup>4,6,8,15,17,38,66-68</sup>  $g \text{ value} = 2.0040$ ,  $a(^{14}\text{N}) = 1.01 \text{ G}$ ,  $a(\text{H}) = 1.41 \text{ G}$ , linewidth =  $0.1 \text{ G}$ . The simulated spectrum is shown in Figure 5.21 (b). The two spectra match perfectly, indicating that the observed spectra were due to the formation of TCNQ radical anion in solution.

#### 5.3.4. EPR Study of TCNQ in (Al)-MCM-41

When TCNQ was assembled into (Al)-MCM-41 (dehydrated at 473 K) with THF as solvent, using method A1, the color of the sample gradually changed from orange to light green. The numbers of spins shown below are maximum values measured after two weeks.

Only a very weak radical signal with poorly resolved resolution was detected in Si-MCM-41. The number of spins were about  $1.7 \times 10^{-8}$  moles in the cavity for the liquid phase and  $2.4 \times 10^{-8}$  moles in the cavity for the solid phase. The sum of the number of spins was  $4.1 \times 10^{-8}$  moles in the cavity, which is comparable with the value of  $4.8 \times 10^{-8}$  moles in the cavity for the TCNQ radical anion generated by directly dissolving TCNQ ( $\sim 0.01\text{M}$ ) in THF solution.



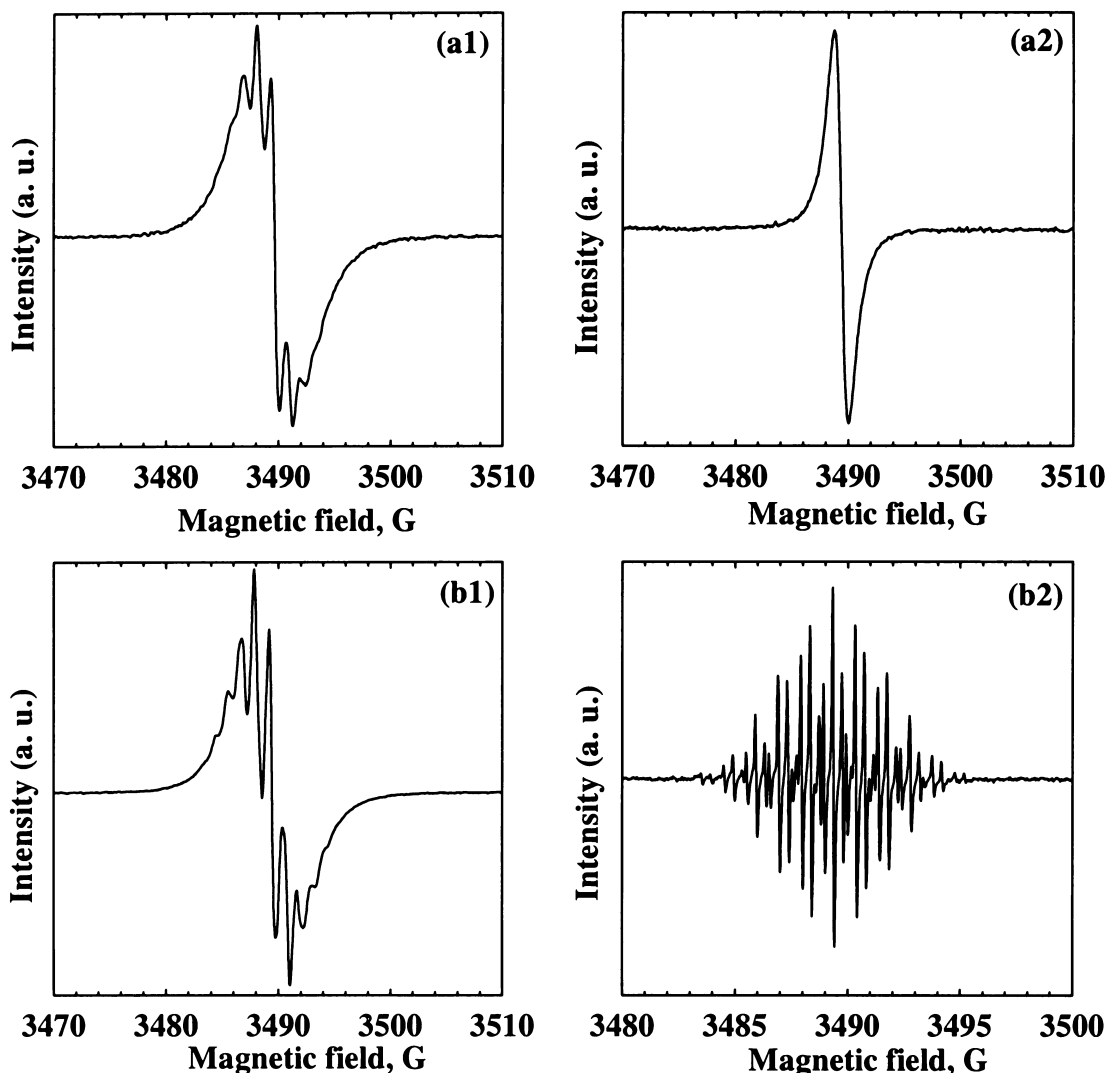


**Figure 5.22: First-derivative EPR spectra (room temperature) of TCNQ radical anions in Al-MCM(15). TCNQ was loaded with THF as solvent, using method A1. Figure (a1) and (a2) are the solid and liquid phase spectra measured after 4 hours contact time; Figure (b1) and (b2) are the solid and liquid phase spectra measured after 48 hours contact time.**

However, relatively strong EPR signals were detected in Al-MCM-41. Figure 5.22 shows the first derivative EPR spectra of the TCNQ radical anion spontaneously generated in Al-MCM(15) with THF as solvent, using method A1 as a typical example. The color of the samples was green. After four hours of contact, the spectrum for the solid phase (Figure 5.22 (a1)) showed some hyperfine structure (5 lines pattern) while

that for the liquid phase (Figure 5.22 (a2)) only showed a sharp narrow single paramagnetic signal. After contact time of 48 hours, the spectrum for the solid phase was transferred into a nine line pattern (Figure 5.22 (b1)) and that for liquid phase (Figure (b2)) evolved into a well resolved 36 line pattern (Figure (b2)), which is a typical isotropic EPR spectrum of the TCNQ radical anion.

TCNQ was also assembled into the (Al)-MCM-41 with THF as solvent, using method A2. Like TCNE, no radical signals were observed when TCNQ was loaded into Si-MCM-41. However, EPR spectra similar to those in Figure 5.22 (a1 and b1) were obtained in Al-MCM-41.

### 5.3.5. TCNQ in Post-Synthesized Al-MCM-41 (Si/Al = 14)

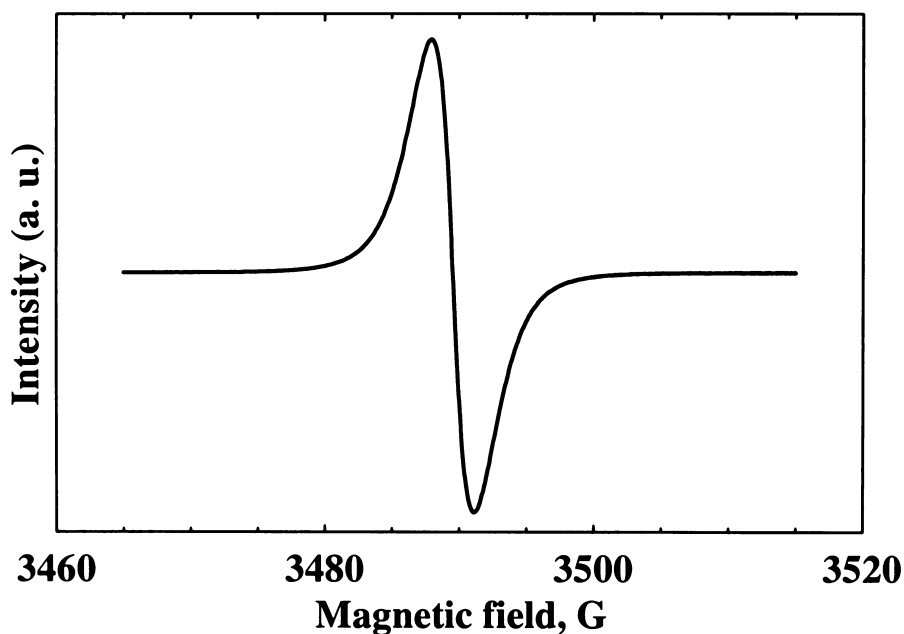


**Figure 5.23: First-derivative EPR spectra (room temperature) of TCNQ radical anion in post-synthesized Al-MCM-41. TCNQ was assembled into the post-synthesized Al-MCM-41 with THF as solvent, using method A2.**

TCNQ was also assembled into post-synthesized Al-MCM-41 (Si/Al = 14) (dehydrated at 473 K) with THF as solvent, using method A2. The color of the sample

was dark green. The spectrum is shown in Figure 5.23. Analysis of the spectrum gives  $g$  value = 2.005 and linewidth = 3.0 G.

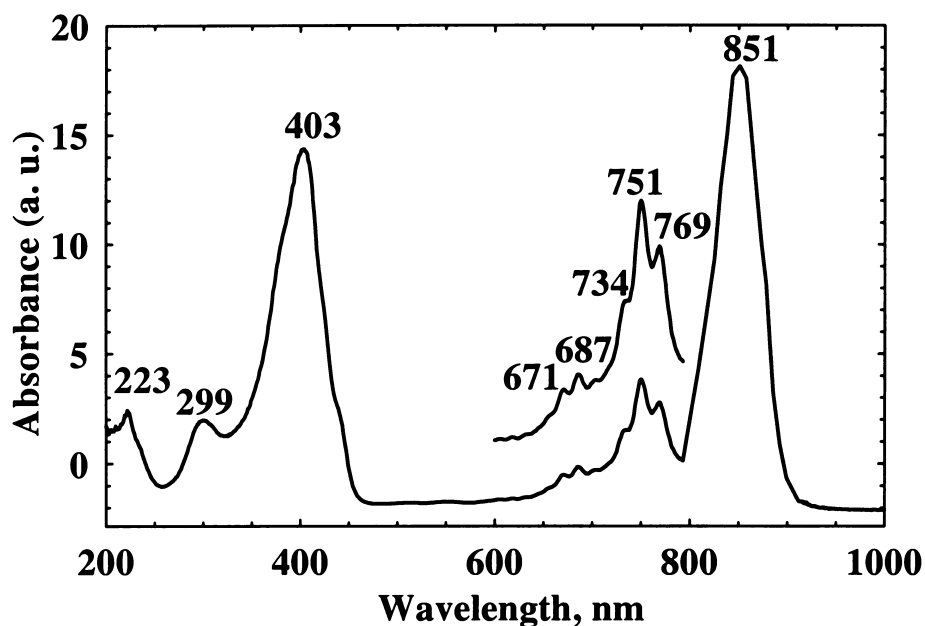


**Figure 5.24:** DR-UV-Vis spectrum of TCNQ in post-synthesized Al-MCM-41 (Si/Al =14).

TCNQ radical anion is readily dimerized<sup>9,15-17,69</sup> at high radical concentration. Figure 5.24 shows the DR-UV-Vis spectrum of TCNQ in post-synthesized Al-MCM-41. The relative intensities of the bands in the range 650-900 nm (the notable absorption bands are at 671, 687, 734, 751 and 769 nm), which are characteristic absorption of the TCNQ radical anion,<sup>11,14,59,62-65</sup> are higher in the post-synthesized Al-MCM-41 than those in the directly synthesized Al-MCM(15) (Figure 5.19). This demonstrates that more TCNQ radical anions were formed in the post-synthesized Al-MCM-41. It was reported that the TCNQ<sup>2-</sup> has characteristic absorption bands at 210, 240, 330 and 477 nm.<sup>5,64</sup> Matsubayashi et al.<sup>63</sup> further studied the assignment of these bands and suggested that the visible band at 477 nm was due to the presence of oxygen. The actual longest wavelength absorption band of TCNQ<sup>2-</sup> is 330 nm. Based on these arguments, two new

bands at 223 and 299 nm in Figure 5.24 are assigned to the dimerized TCNQ<sup>2-</sup>. DR-UV-Vis study reveals that part of the TCNQ radical anions are further dimerized in the post-synthesized Al-MCM-41.

### 5.3.6. Spin Concentration Results for TCNQ Assembled into (Al)-MCM-41 Using Method A1 and A2

**Table 5.4: Spin concentration results for TCNQ assembled into (Al)-MCM-41 using method A1 and A2**

	Si-MCM-41	Al-MCM(39)	Al-MCM(15)	Al-MCM(7)	Post synthesized Al-MCM-41 (Si/Al = 14)
Number of spins in method A1 (mole in the cavity)	$1.2 \times 10^{-9}$	$3.4 \times 10^{-8}$	$9.4 \times 10^{-8}$	$8.6 \times 10^{-7}$	-
Spin concentration in method A1 (mol/g)	$4 \times 10^{-8}$	$1.1 \times 10^{-6}$	$3.1 \times 10^{-6}$	$2.9 \times 10^{-5}$	-
Number of spins in method A2 (moles in the cavity)	0	$8.7 \times 10^{-9}$	$5.7 \times 10^{-8}$	$2.9 \times 10^{-7}$	$5 \times 10^{-7}$
Spin concentration in method A2 (mol/g)	0	$2.9 \times 10^{-7}$	$1.9 \times 10^{-6}$	$9.5 \times 10^{-6}$	$1.7 \times 10^{-5}$
Total Al content (mol /g)	0	$4.2 \times 10^{-4}$	$1 \times 10^{-3}$	$2.1 \times 10^{-3}$	$1.1 \times 10^{-3}$
Extra-framework Al (mol/g)	0	$9.2 \times 10^{-5}$	$1.8 \times 10^{-4}$	$5.0 \times 10^{-4}$	$3.0 \times 10^{-5}$

\* Note: The uncertainty of the spin concentration measurement is estimated to be ca.  $\pm(5-30)$  %.

The spin concentration results are listed in Table 5.4. The extra-framework Al was determined by integrating the tetrahedral and the octahedral Al peak areas in the <sup>27</sup>Al-NMR spectra. For method A1, the spin concentration of the solid phase were taken as the spin concentration of the sample, because the concentration of TCNQ radical anion in the solution phase was much lower than that in the solid phase, and could be ignored. Calculation results indicate the following facts:

- (1) The spin concentration of the TCNQ radical anion (i.e., the amount of the electron donor sites probed by TCNQ) increases with increasing the Al content in Al-MCM-41. The electron donor sites in Al-MCM-41 appear to have correlation with

the incorporated Al in the Al-MCM-41 samples. However, the Al content is 2-3 orders of magnitude higher than the spin concentration of the TCNQ radical anions. No quantitative relationship has been established between the electron donor sites probed by TCNQ using assembly method A1 and A2 and the total Al content in the directly synthesized Al-MCM-41.

- (2) The extra-framework Al content in the directly synthesized Al-MCM-41 is still at least an order of magnitude higher than the amount of the electron donor sites probed by TCNQ. However, the spin concentration of the TCNQ radical anion is of the same order of magnitude as the extra-framework Al content in the post-synthesized Al-MCM-41, indicating that the extra-framework Al correlates with the electron donor sites in the post-synthesized Al-MCM-41.
- (3) Using method A2, no observation of the TCNQ radical anion in Si-MCM-41 demonstrates that Si-MCM-41 has no electron donor sites to reduce a strong electron acceptor such as TCNQ at room temperature.

## 5.4. 1,4-BQ in (Al)-MCM-41

### 5.4.1. FTIR Spectra of 1,4-BQ in (Al)-MCM-41

Figure 5.25 shows the FTIR spectra of the pure 1,4-BQ and the 1,4-BQ in the Al-MCM(39). For pure 1,4-BQ, the absorption band at  $1591\text{ cm}^{-1}$  is due to the  $\nu_{\text{s}}\text{ C}=\text{C}$  mode, and the absorption at  $1648$  (with a shoulder at  $\text{ca. } 1664\text{ cm}^{-1}$ ) and  $1714\text{ cm}^{-1}$  are assigned to the  $\nu\text{ C}=\text{O}$  mode which was split into a triplet. These band assignments are in agreement with the reports in the literature.<sup>70-77</sup> For 1,4-BQ in Si-MCM-41, the absorption band due to the  $\nu\text{ C}=\text{O}$  mode was broadened and split into two components with absorption maxima at  $1656$  and  $1634\text{ cm}^{-1}$ , respectively. The peak due to  $\text{C}=\text{C}$

stretching mode at  $1591\text{ cm}^{-1}$  in spectrum (a) was reduced to a shoulder in spectrum (b). The new peak at  $1512\text{ cm}^{-1}$  can be assigned to the perturbed C-C stretching mode of the 1,4-BQ aromatic ring, indicating that the 1,4-BQ molecules were assembled inside the channels of the Si-MCM-41.

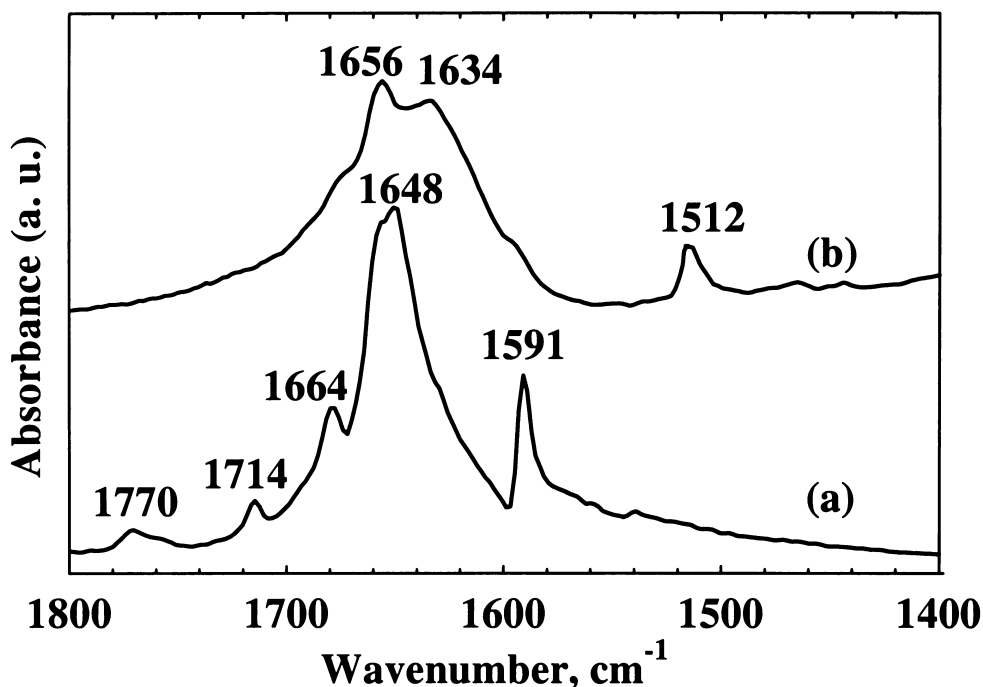


Figure 5.25: FTIR spectra of (a) pure 1,4-BQ and (b) 1,4-BQ in Si-MCM-41.

#### 5.4.2. DR-UV-Vis Spectra of 1,4-BQ in (Al)-MCM-41

The UV-Vis absorption band assignments for the various 1,4-BQ species are summarized in Table 5.5 according to the literature data.

Figure 5.26 shows the UV-Vis spectrum of 1,4-BQ and DR-UV-Vis spectra of 1,4-Bq in (Al)-MCM-41 hosts. In solution (dotted line), 1,4-BQ shows only one peak at 238 nm (lit.:  $\lambda_{\text{max}} = 240\text{ nm}$  for the neutral 1,4-BQ in ethanol <sup>78</sup>). The dashed line in Figure 5.25 represents the DR-UV-Vis spectrum of 1,4-BQ in the Si-MCM-41, and curves (a) and (b) are shown as typical examples for 1,4-BQ in the directly synthesized and post-synthesized (Al)-MCM-41 samples, respectively. In Si-MCM-41, 1,4-BQ shows

absorption bands at  $\lambda_{\max}$  of 221, 263 and 296 nm, respectively. Since no EPR paramagnetic signal was detected when 1,4-BQ was assembled into the Si-MCM-41, the formation of the paramagnetic species listed in Table 5.5 are not considered in interpreting the spectrum. In this case, the peaks at 221 and 296 nm are assigned to the absorption band of 1,4-BQH<sub>2</sub>.<sup>78-80</sup> and the most intense peak at 263 nm is assigned to the absorbed neutral 1,4-BQ. The dramatic red-shift of the 1,4-BQ absorption band (from 237 in solution to 263 nm in Si-MCM-41) may be explained by the hydrogen bonding between the C=O of the 1,4-BQ and the hydroxyl groups on the surface of the Si-MCM-41. The DR-UV-Vis spectrum of 1,4-BQ in Si-MCM-41 demonstrates that part of 1,4-BQ protonated to form 1,4-BQH<sub>2</sub> and others are hydrogen bonded, probably with the hydroxyl groups on the surface of the MCM-41.

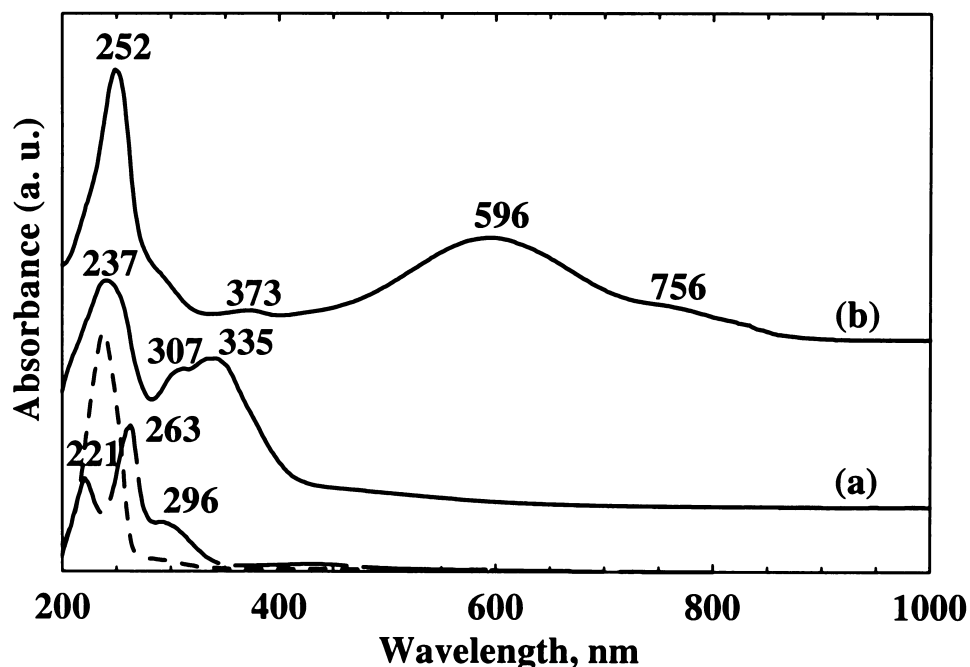


**Figure 5.26:** UV-Vis spectrum of 1,4-BQ ( $\sim 2 \times 10^{-5}$  M) in CH<sub>3</sub>CN solution (dotted line) and DR-UV-Vis spectra of 1,4-BQ in Si-MCM-41 (dashed line), Al-MCM(39) (curve (a)), and post-synthesized Al-MCM-41 (curve (b)).

The DR-UV-Vis spectrum of 1,4-BQ in Al-MCM(39) displays absorption maxima at 237 and 335 nm as well as a shoulder peak at 307 nm. The peak at 237 nm is no doubt the characteristic absorption band of the neutral 1,4-BQ. The peak at 307 nm is tentatively assigned to 1,4-BQH<sup>-</sup>,<sup>80</sup> and the peak at 335 nm is assigned to the 1,4-BQ<sup>2-</sup>.<sup>79,80,83</sup> These two species are both EPR silent, and may be regarded as the products of further electron addition to the 1,4-BSQ radical anion, i.e., 1,4-BQH<sup>-</sup> is the protonated 1,4-BQ dianion and the 1,4-BQ<sup>2-</sup> is the 1,4-BQ dianion. The DR-UV-Vis spectrum thus indirectly confirms the formation of 1,4-BSQ radical anion when 1,4-BQ was loaded into Al-MCM-41.

**Table 5.5: UV-Vis absorption band assignments of various 1,4-BQ species in literature**

Species	$\lambda_{\text{max}}$ (nm)	Remarks
1,4-BQ	240	Ref. <sup>78</sup>
1,4-BQ <sup>•-</sup>	450-550 ( $n \rightarrow \pi^*$ ) 430, 406, 370 ( $\pi \rightarrow \pi^*$ )	Ref. <sup>79,81,82</sup>
	First band (432, 407) Second band (385) Third band (316, 308, 301, 295)	Ref. <sup>79</sup>
	325, 451	Ref. <sup>83</sup>
	432, 408	Ref. <sup>82</sup>
	428, 404	Ref. <sup>84</sup>
	315, 370, 405, 428	Ref. <sup>85</sup>
1,4-BQH <sup>-</sup>	305 (H <sub>2</sub> O) 302 (CH <sub>2</sub> Cl <sub>2</sub> )	Ref. <sup>80</sup>
1,4-BQH <sub>2</sub>	295	Ref. <sup>79</sup>
	220, 280	Ref. <sup>78</sup>
	287 (H <sub>2</sub> O) 292 (CH <sub>2</sub> Cl <sub>2</sub> )	Ref. <sup>80</sup>
1,4-BQH <sup>•</sup>	First band (415, 406, 399, 391) Second band (349, 357, 342) Third band (292, 282)	Ref. <sup>79</sup>
1,4-BQ <sup>2-</sup>	323	Ref. <sup>79</sup>
	350-370	Ref. <sup>83</sup>
	320 (H <sub>2</sub> O) 324 (CH <sub>2</sub> Cl <sub>2</sub> )	Ref. <sup>80</sup>



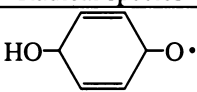
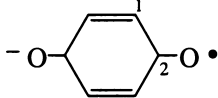


In post-synthesized Al-MCM-41, the absorption band at 252 nm is assigned to the hydrogen bonded 1,4-BQ and that at 373 nm to the 1,4-BSQ radical anions. The broad absorption bands at 596 and 756 nm haven't been reported for any of the simple 1,4-BQ species before and are most probably due to the highly polymerized 1,4-BQ species.

18,70,71,74-77,82,83,86-92

### 5.4.3. EPR Study of 1,4-BQ in (Al)-MCM-41

The proton hyperfine splitting constants of the 1,4-BQ radical species are summarized in Table 5.6 according to the data in the literature.

**Table 5.6: Hyperfine splitting constants of 1,4-BQ radical species**

Radical species	Splitting constants	Remarks
	$a(\text{H, ortho}) = 5.11 \text{ G}$ $a(\text{H, meta}) = 0.28 \text{ G}$ $a(\text{OH}) = 1.79 \text{ G}$	Ref. <sup>93</sup>
	$a(\text{H}) = 2.31 \text{ G}$	Ref. <sup>94</sup>
	$a(\text{H}) = 2.3 \text{ G}$ $a(^{13}\text{C} (1)) = 0.6 \text{ G}$ $a(^{13}\text{C} (2)) = 0 \text{ G}$	Ref. <sup>95</sup>
	$a(\text{H}) = 2.33 \text{ G}$	Ref. <sup>93,96,97</sup>
	$a(\text{H}) = 2.37 \text{ G}$	Ref. <sup>98-101</sup>
	$a(\text{H}) = 2.22 \text{ G}$	Ref. <sup>93</sup>
	$a(\text{H}) = 2.24 \text{ G}$ $a(\text{OH}) = 5.08 \text{ G}$	Ref. <sup>93</sup>
	$a(\text{H}) = 2.36 \text{ G}$ $a(\text{OH}) = 3.44 \text{ G}$	Ref. <sup>20</sup>

#### 5.4.3.1. Solvent Effects

No EPR paramagnetic signal was detected when 1,4-BQ was assembled into the Al-MCM-41 (dehydrated at 473 K) with THF as solvent, using method A1 or A2. However, single paramagnetic EPR signals were observed when  $\text{CH}_2\text{Cl}_2$  was used as solvent using the same experimental conditions. This result is opposite to the solvent

effects of TCNE and TCNQ. The electron transfer processes in Al-MCM-41 hosts depends not only on the nature of the guest molecules, but also on the media (solvent) used to transport the guest molecules into the hosts. Similar solvent effects were also observed for the other quinones used in this study.

Based on the above investigations, dichloromethane was chosen as the solvent for assembling the quinones into the (Al)-MCM-41.

#### 5.4.3.2. EPR Study of 1,4-BQ Assembled into (Al)-MCM-41 Using Method A2.

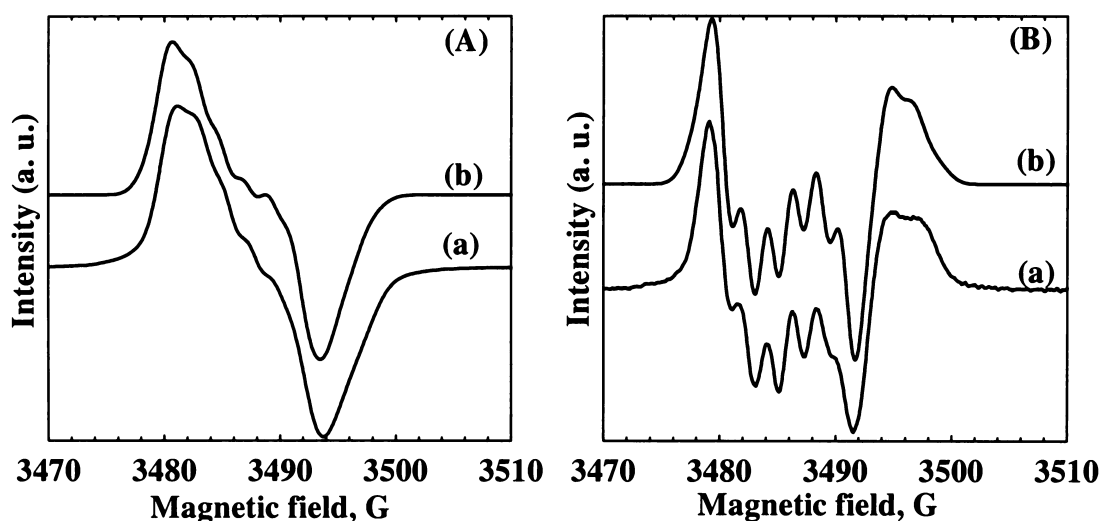


**Figure 5.27: First (A) and second (B) derivative EPR spectra (room temperature) of 1,4-BQ in Al-MCM(39). In each set: (a) experimental spectra; (b) computer simulated spectra.**

No EPR paramagnetic signal was detected when 1,4-BQ was assembled into the Si-MCM-41 (dehydrated at 473 K) with  $\text{CH}_2\text{Cl}_2$  as solvent, using method A1 or A2.

However, a dark brown color evolved within 5 minutes when 1,4-BQ was assembled into the Al-MCM-41 samples in the same experimental conditions. As a typical example of 1,4-BQ in Al-MCM41 samples, Figure 5.27 shows the EPR spectra of 1,4-BQ assembled into the Al-MCM(39) with  $\text{CH}_2\text{Cl}_2$  as solvent, using method A2. The signal

intensity continued to increase in two weeks. Unlike TCNE and TCNQ, the observed EPR signal was quite stable, even in air, as evidenced by the observation of the EPR signal even after the sample was exposed to the air for one week.

It is difficult to assign the source of the EPR pattern from the first derivative spectrum (Figure 5.27 (A-a)) which is just a single paramagnetic pattern with some rather poorly resolved fine structure near the center of the spectrum. The second derivative spectrum (Figure 5.27 (B-a)) gave an unsymmetrical 6 line pattern with a splitting constant of 2.1 G and *g* value of 2.0063 (*g* value of 1,4-BSQ radical anion<sup>93,95-101</sup> was reported to be around 2.004 in various solutions). In solution, 1,4-BSQ will give an isotropic five line EPR pattern with relative line intensity ratio of 1:4:6:4:1 due to the four equivalent proton (*I* = 1/2) splittings.<sup>93-101</sup> Apparently, the observed EPR spectra are not due only to the 1,4-BSQ radical anion. Attempts to computer simulate the spectra using only the splitting constants of the various 1,4-BSQ radical species listed in Table 5.9 failed, suggesting that the observed spectra are not due only to the formation of the 1,4-BQ radical species.

The possibility of an ion pair effect<sup>99</sup> involving  $\text{Al}^{3+}$  was then considered. Indeed, by introducing  $^{27}\text{Al}$  into the Hamiltonian parameters of the simulation, both the first and the second derivative experimental EPR spectra were successfully simulated using the following parameters:  $A(x,x) = A(y,y) = 2.00$  G,  $A(z,z) = 2.15$  G for one  $^{27}\text{Al}$  (*I* = 5/2);  $A(x,x) = A(y,y) = 2.0$  G for the four protons (*I* = 1/2) on the BQ ring;  $g(x) = g(y) = 2.0060$ ,  $g(z) = 2.0072$  for the electrons (*I*=1/2); and *x* direction = *y* direction = 2.48 G, *z* direction = 1.8 G for the linewidths. The simulated first and second derivative EPR spectra are shown in Figure 5.27(A-b) and Figure 5.27 (B-b), respectively. It can be seen that the simulated spectra match quite well with the experimental ones. The  $^{27}\text{Al}$  hyperfine splitting constant  $A(z,z) = 2.15$  G used for the simulation is comparable with

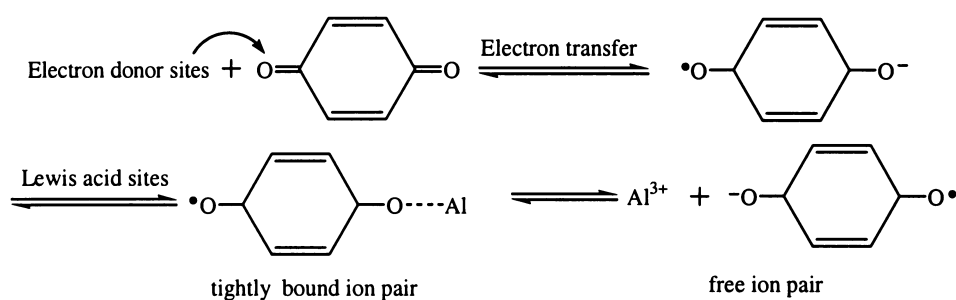
the  $^{27}\text{Al}$  isotropic hyperfine splitting constants of 2.37 G and 2.7 G reported for the complex of “ $\text{Al}^{3+}$  and *o*-BSQ”<sup>102</sup> and “ $\text{AlCl}_3$  and *o*-chloranil (tetrachloro-1,2-benzoquinone)”,<sup>103</sup> respectively.

It should be emphasized that the experimental spectra cannot be simulated well without including either Al or protons in the Hamiltonian parameter settings. Successful simulation of the experimental spectra needs to assume that the hyperfine couplings arise from both the  $^{27}\text{Al}$  and the 1,4-BSQ radical species.

Actually, the above experimental spectra can also be closely simulated by varying the proton  $A(x,x) = A(y,y)$  parameters between 1.8 to 2.3 G. Beyond this range, the simulated spectra do not match with the experimental ones. In this case, the assignments to the diprotonated 1,4-BSQ radical cation and the neutral 1,4-BSQ radical are ruled out, because both of these two radical species have a large splitting constant ( $>5$  G). However, it is still difficult to determine whether the observed EPR signals are due to formation of the 1,4-BSQ radical cations or 1,4-BSQ radical anions in this system.

Al-MCM-41 is different from zeolites. In Al-MCM-41, there are several kinds of Al species:<sup>104</sup> one is tetrahedral Al, which is responsible for the formation of the Brönsted acid sites ( $\text{Al-O(H)-Si}$ ); the other one is octahedral Al, which is occluded in the pores, or exists as amorphous by-product. Besides, five- and six-coordinated Al species might also be present in the framework of Al-MCM-41. However, Al-MCM-41 has only weak Brönsted and/or Lewis acid sites at 473 K.<sup>105</sup> The BSQ radical cations are only stable in a strong acidic environment ( $\text{pH} \leq 2$ ),<sup>20,93,106</sup> such as in  $\text{H}_2\text{SO}_4$  and  $\text{CF}_3\text{SO}_3\text{H}$ . The cationic mechanism, i.e., proton (or hole) transfer from the Brönsted sites (or Lewis sites) to the 1,4-BQ to form 1,4-BSQ radical cation, may be ruled out. In this case, the observed EPR spectra are mostly likely to be due to the **1,4-BSQ radical anion**.

It is possible that “tightly bound ion pairs” may explain the superposition of the  $^{27}\text{Al}$  and the BSQ radical anion signals in the EPR spectra.<sup>90,91,107</sup> Electron transfer from the electron donor sites to the adsorbed 1,4-BQ molecules generates 1,4-BSQ radical anions, which further interact with the Lewis acid sites and form tightly bound “ $\text{Al}^{3+}/1,4\text{-BSQ}$  radical anion” ion pairs. “Tightly bound ion pairs” may reach equilibrium with the corresponding dissociated  $\text{Al}^{3+}$  and free (or adsorbed) 1,4-BSQ radical anion (Scheme 5.2). By analogy with aluminum oxide,<sup>25,41</sup> the electron donor sites in Al-MCM-41 may be assigned to the basic oxide ions bonded to the Al.



**Scheme 5.2:** Supposed mechanism for the formation of “tightly bound ion pairs”.

#### 5.4.3.3. Loading Level Study of 1,4-BQ in Al-MCM-41

1,4-BQ was assembled into the Al-MCM(39) (dehydrated at 473 K) using method A2. The spin concentration was the maximum value taken after 2 weeks. The plot in Figure 5.28 shows the relationship between the spin concentration of the 1,4-BSQ radical anion generated in Al-MCM(39) *versus* the moles of BQ/moles of Al content in Al-MCM-41 (Si/Al = 39). It can be seen that the spin concentration increases sharply with increasing the 1,4-BQ loading level when the molar ratio between 1,4-BQ and the Al content is less than 1. Further increasing the loading level of 1,4-BQ doesn't increase the spin concentration much. At the inflection point of moles of 1,4-BQ/moles of Al = 1, the spin concentration is ca.  $3.0 \times 10^{-5}$  mol/g. As shown in previous spin related

calculations for TCNE and TCNQ, the total Al and the extra-framework Al contents are ca.  $4.2 \times 10^{-4}$  mol/g and  $9.2 \times 10^{-5}$  mol/g (about 22 % Al are in the extra-framework position, see Section 3.3.2.1.1 in Chapter 3), respectively, for the Al-MCM(39). It can be seen that the spin concentration of the 1,4-BSQ radical anion formed in Al-MCM(39) is approximately of the same order of magnitude as the amount of the extra-framework Al. Loading level study of 1,4-BQ also supports that the electron donor sites in Al-MCM-41 are associated with the extra-framework Al.

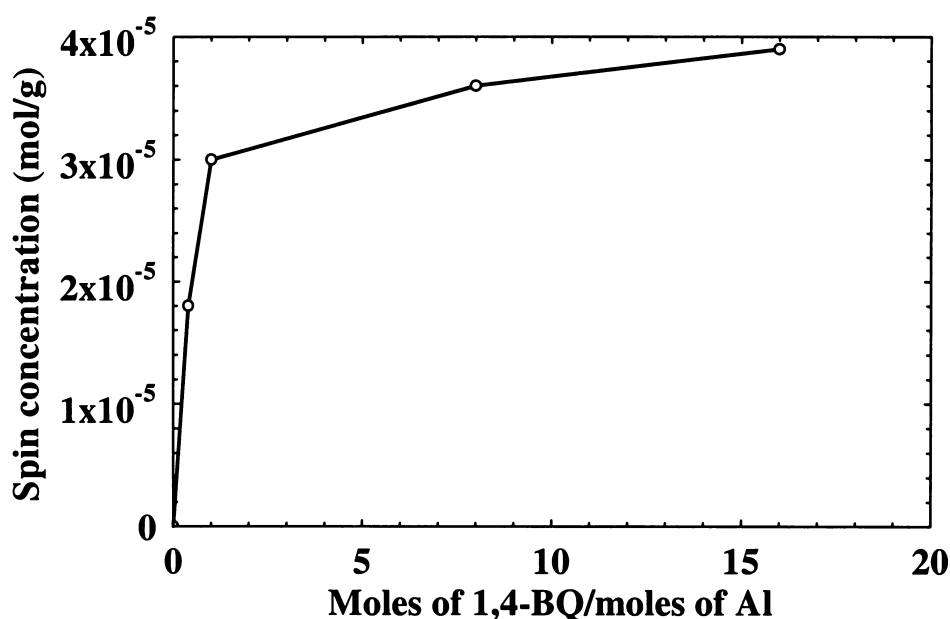


**Figure 5.28:** The loading level plot of spin concentration (mol/g) of 1,4-BSQ radical anion vs moles of 1,4-BQ/moles of Al content in Al-MCM(39).

#### 5.4.3.4. 1,4-BQ Assembled into Post-Synthesized Al-MCM-41 Using Method A2

When 1,4-BQ was assembled into the post-synthesized Al-MCM-41 ( $\text{Si}/\text{Al} = 14$ ) (dehydrated at 473 K) with  $\text{CH}_2\text{Cl}_2$  as solvent, using method A2, the color of the sample gradually turned into brown, dark-brown, and finally pale blue. Figure 5.29 shows the EPR spectra of 1,4-BQ in the post-synthesized Al-MCM-41. Attempts to simulate the

spectra (both first and second derivative) by assuming the paramagnetic signal arose from the 1,4-BQ paramagnetic monomer species failed. However, the central regions of the spectra (both first and second derivatives) can be approximately simulated by assuming that 1,4-BQ was **dimerized**. The simulation was carried out using the following EPR parameter settings:  $A(x,x) = A(y,y) = 3.2$  G,  $A(z,z) = 0.75$  G for one  $^{27}\text{Al}$  ( $I = 2/5$ );  $A(x,x) = A(y,y) = 2.35$  G,  $A(z,z) = 1.13$  G for six protons; ( $I=1/2$ );  $g(x) = g(y) = 2.005700$ ;  $g(z) = 2.00700$  for electrons ( $I=1/2$ ); and  $x$  direction =  $y$  direction =  $z$  direction = 3.20 G for the linewidths. The simulated results are shown in Figure 5.29. The outer regions of the spectra could not be simulated well, probably due to the formation of highly polymerized 1,4-BQ paramagnetic products<sup>108</sup> which were seen in the DR-UV-Vis study.

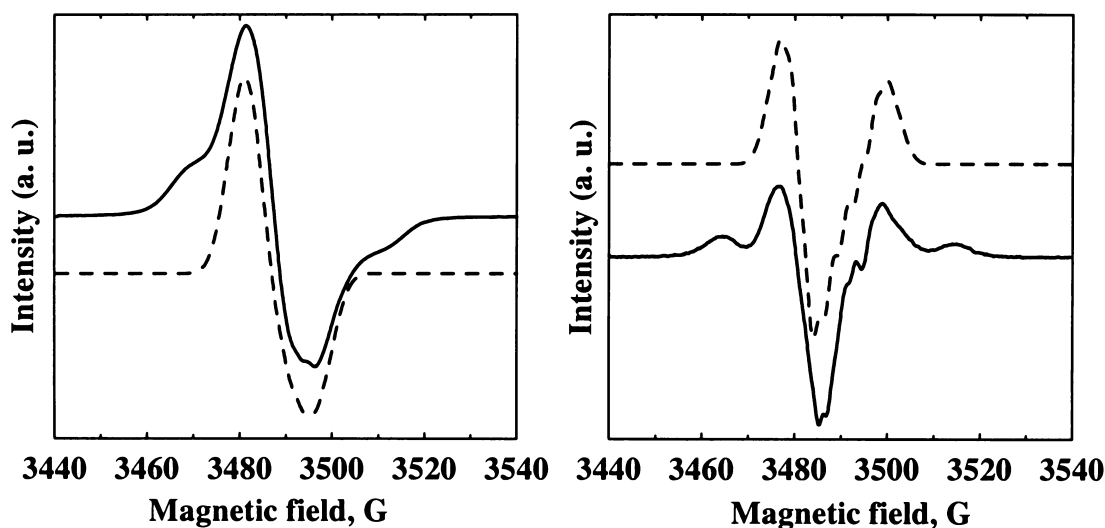


**Figure 5.29:** EPR spectra (room temperature) of 1,4-BQ in post-synthesized Al-MCM-41. Solid line — experimental spectra; dotted line — computer simulated spectra. Left-side spectra — first derivative; right-side spectra — second derivative.

The spin concentration results for 1,4-BQ in post-synthesized Al-MCM-41 (Si/Al = 14) are listed in Table 5.7. The spin concentration of the 1,4-BQ radical anion in post-

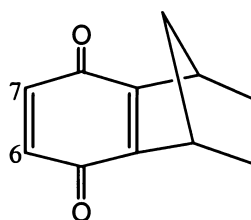
synthesized Al-MCM-41 is less than the estimated concentration of the extra-framework Al, but this may in part be due to the polymerization of 1,4-BQ.

**Table 5.7: Spin concentration results of 1,4-BQ assembled into post-synthesized Al-MCM-41 (Si/Al = 14) using method A2**

	Post-synthesized Al-MCM-41 (Si/Al = 14)
Spin concentration of 1,4-BQ (mol/g)	$5 \times 10^{-6}$
Total Al content (mol/g)	$1.1 \times 10^{-3}$
Extra-framework Al (mol/g)	$3.0 \times 10^{-5}$

\* Note: The uncertainty of the spin concentration measurement is estimated to be ca.  $\pm(5-30)$  %.

## 5.5. BQ[2] in (Al)-MCM-41



BQ[2]

When BQ[2] was assembled into the Al-MCM-41 with  $\text{CH}_2\text{Cl}_2$  as solvent, using method A1 and A2, a dark brown color evolved gradually in several minutes. Figure 5.30 shows the first (Figure 5.30 (A-a)) and second derivative (Figure 5.30 (B-a)) EPR spectra of BQ[2] in Al-MCM(39) as a typical example. The spectra can be approximately simulated using the following EPR parameters:  $A(x,x) = A(y,y) = 2.00$  G for one  $^{27}\text{Al}$ ;  $A(x,x) = A(y,y) = 2.0$  G,  $A(z,z) = 3.25$  G for two protons at position 6 and 7;  $g(x) = g(y) = 2.00600$ ,  $g(z) = 2.0052$  for the electrons ( $I = 1/2$ ); and x direction = y direction = z direction = 2.50 G for the linewidths. The simulated first and second derivative spectra are shown in Figure 5.30 (A-b) and Figure 5.30 (B-b), respectively. The paramagnetic species responsible for the observed EPR spectra are assigned to the



BQ[2] radical anion based on the previous discussion for 1,4-BQ. The experimental spectra shown in Figure 5.30 can be simulated well only if considering the spin coupling contribution from both the  $^{27}\text{Al}$  and the BQ[2] radical anion. The spin concentration is ca.  $6 \times 10^{-6}$  mol/g, which is less than the estimated extra-framework Al content. This may be due to the steric hindrance of the norbornane ring.

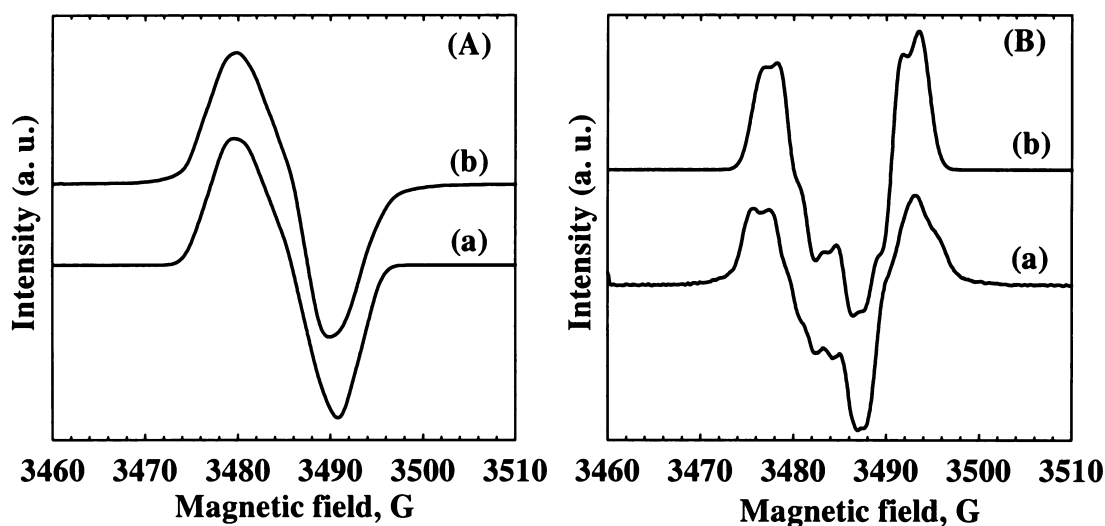
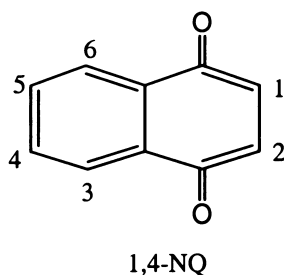


**Figure 5.30: First (A) and second (B) derivative EPR spectra (room temperature) of BQ[2] in Al-MCM(39). In each set: (a) experimental spectra; (b) computer simulated spectra.**

No EPR paramagnetic signal was detected when BQ[2] was assembled into the (Al)-MCM-41 with THF as solvent, using method A1 and A2. When BQ[2] was assembled into the Si-MCM-41 with  $\text{CH}_2\text{Cl}_2$  as solvent, using method A1 and A2, still no EPR paramagnetic signal was detected, indicating no electron transfer occurred between BQ[2] and the Si-MCM-41. Si-MCM-41 has no electron donor sites that are strong enough to reduce BQ[2] at room temperature.

## 5.6. 1,4-NQ in (Al)-MCM-41



### 5.6.1. FTIR spectra of 1,4-NQ in Si-MCM-41

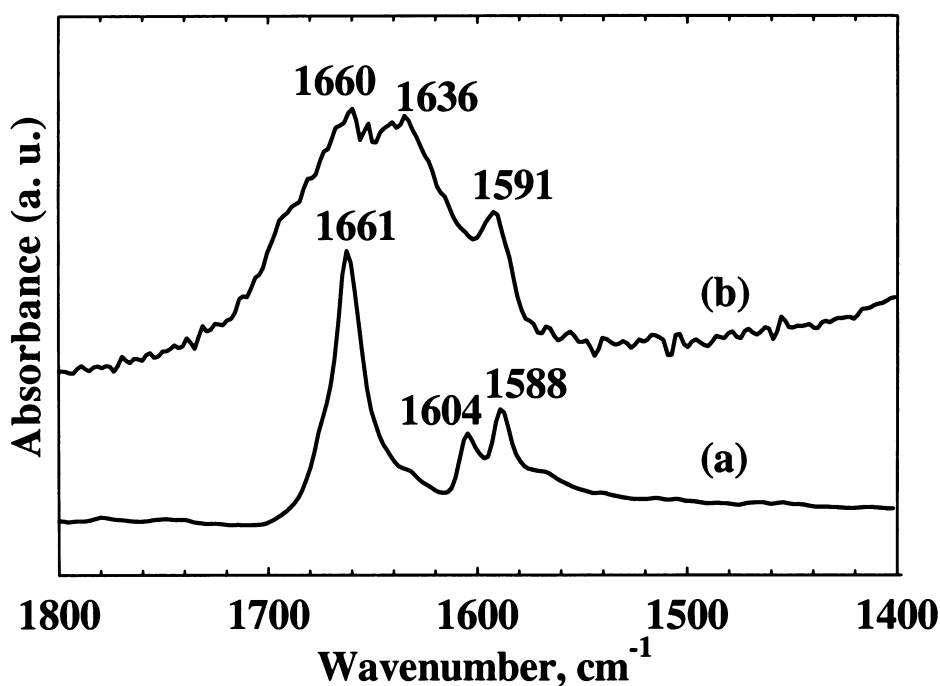
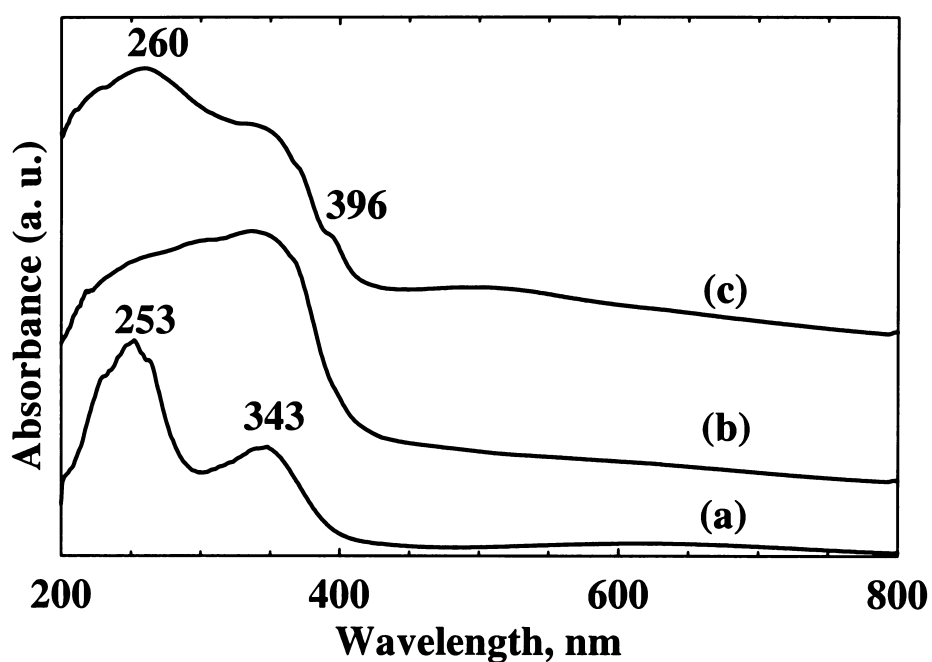


Figure 5.31: FTIR spectra of (a) pure 1,4-NQ and (b) 1,4-NQ in Si-MCM-41.

Figure 5.31 shows the FTIR spectra of 1,4-NQ (Figure 5.31 (a)) and 1,4-NQ in Si-MCM-41 (Figure 5.31 (b)). In spectrum (a), the peak at  $1661\text{ cm}^{-1}$  is due to the  $\nu\text{ C=O}$   $a_1$  mode, and the other two absorption bands may be assigned to the ring stretching modes of 1,4-NQ. According to the literature,<sup>86,87,89</sup> the absorption band at  $1604\text{ cm}^{-1}$  is attributed to a  $\nu\text{ C=O}$   $a_1$  mode and the absorption band at  $1588\text{ cm}^{-1}$  to the  $\nu\text{ C=O}$   $b_2$  mode. 1,4-NQ in Si-MCM-41 shows broad and overlapping absorption bands in the same region which are similar to the free 1,4-NQ. In Figure 5.31 (b), the absorption

band at  $1660\text{ cm}^{-1}$  is assigned to the  $\nu\text{ C=O } a_1$  mode, and those at  $1636$  and  $1591\text{ cm}^{-1}$  are assigned to the  $\nu\text{ C=O } b_2$  modes. The broadening of the spectrum implies that the carbonyl group and aromatic ring in 1,4-NQ are perturbed in Si-MCM-41, probably by the hydroxyl groups in MCM-41, indicating that 1,4-NQ molecules are assembled inside the channels of the MCM-41.

### 5.6.2. DR-UV-Vis Spectra of 1,4-NQ in (Al)-MCM-41



**Figure 5.32:** DR-UV-Vis spectra of 1,4-NQ in (a) Si-MCM-41, (b) in Al-MCM(15) and (c) in Al-MCM(15) after irradiation.

Figure 5.32 shows the DR-UV-Vis spectra of 1,4-NQ assembled into the Si-MCM-41 (Figure 5.32 (a)), Al-MCM(15) (Figure 5.32 (b)), and Al-MCM(15) (Figure 5.32 (c)) which was irradiated with a UV-lamp. 1,4-NQ was assembled into these hosts with  $\text{CH}_2\text{Cl}_2$  as solvent, using method A2. The DR-UV-Vis spectrum of 1,4-NQ in Si-MCM-41 (Figure 5.32 (a)) exhibits absorption maxima at 253 and 343 nm, respectively. These two bands are assigned to the neutral 1,4-NQ according to the report that the

characteristic absorption bands of the neutral 1,4-NQ are at ~230 and ~270 nm.<sup>109</sup> The DR-UV-Vis spectrum of 1,4-NQ in Al-MCM(15) (Figure 5.32 (b)) displays absorption maxima at 343 and 250 nm which are due to the absorption of the neutral 1,4-NQ. However, the relative intensity ratio between these two bands is reversed, i.e., the intensity of the higher wavelength band is increased at the expense of the lower wavelength band and the entire spectrum becomes broad and unresolved. This may be due to the formation of 1,4-NQ radical anion whose characteristic absorption bands are at 370-390 nm.<sup>88,109,110</sup> Further irradiation of the sample using the UV lamp brought a new distinguishable band at 396 nm (Figure 5.32 (c)), which may be assigned to the 1,4-NSQ radical anions. Due to the spectra broadening, it is difficult to rule out formation of other 1,4-NQ species, such as protonated 1,4-NSQ radicals which has an absorption maxima at 370 nm with a bandwidth of 35 nm.<sup>111</sup>

### 5.6.3. EPR Study of 1,4-NQ in (Al)-MCM-41

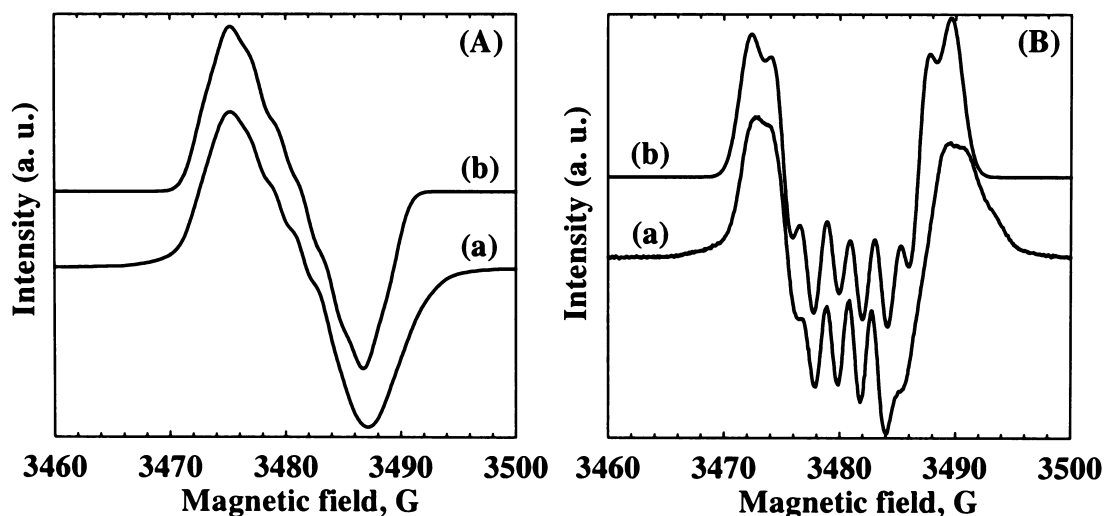
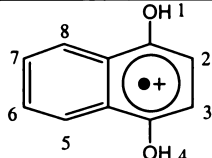
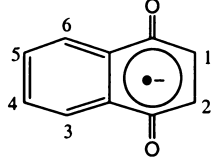
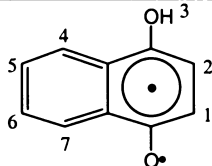


Figure 5.33: First (A) and second (B) derivative EPR spectra (room temperature) of 1,4-NQ in Al-MCM(39). In each set: (a) experimental spectra (b) simulated spectra.

To facilitate the comparison and the interpretation of the observed EPR spectra, the hyperfine splitting constants for various 1,4-NQ radical species are listed in Table 5.8 according to the literature.

No EPR paramagnetic signal was detected when 1,4-NQ was assembled into the (Al)-MCM-41 with THF as solvent, using method A1 or A2.

**Table 5.8: Proton hyperfine splitting constants of 1,4-NQ radical species**

Radical species	Splitting constants (G)	Remarks
	$a_2 = a_3 = 2.42$ , $a_5 = a_6 = a_7 = a_8 = 1.80$ ; or $a_2 = a_3 = 3.20$ , $a_5 = a_6 = a_7 = a_8 = 0.86$	51 lines in $H_2SO_4$ . Ref. <sup>19</sup>
	$a_1 = a_2 = 3.23$ , $a_3 = a_6 = 0.513$ $a_4 = a_5 = 0.655$	Ref. <sup>19,112</sup>
	$a_1 = a_2 = 3.22 \pm 0.03$ , $a_3 = a_4 = a_5 = a_6 = 0.57 \pm 0.03$	3 sets of 5. Ref. <sup>101</sup>
	$a_1 = a_2 = 3.19 \pm 0.04$ , $a_3 = a_4 = a_5 = a_6 = 0.58 \pm 0.04$	Three quintuplets Ref. <sup>100</sup>
	$a_1 = a_2 = 3.20$ , $a_3 = a_4 = a_5 = a_6 = 0.66$	Ref. <sup>109,113</sup>
	In isopropanol: $a_1 = 6.92$ , $a_2 = 0.35$ , $a_3 = a_5 = a_7 = 1.70$ , $a_4 = a_6 = 0.18$ In dioxane: $a_1 = 7.67$ , $a_2 = 0.80$ , $a_3 = 1.25$ , $a_4 = 0.40$ , $a_6 = 0.52$ , $a_5 = a_7 = 1.85$	Ref. <sup>92</sup>

Like 1,4-BQ and BQ[2], no EPR paramagnetic signal was detected when 1,4-NQ was assembled into the Si-MCM-41 with  $CH_2Cl_2$  as solvent, using method A1 and A2. However, a dark grey-green color evolved gradually in several minutes when 1,4-NQ was assembled into the Al-MCM-41 under the same experimental conditions. As a typical example, Figure 5.33 shows the first (Figure 5.33 (A-a)) and second (Figure 5.33 (B-a)) derivative EPR spectra of the 1,4-NQ assembled into the Al-MCM(39) with  $CH_2Cl_2$  as solvent, using method A2. The observed spectra can be well simulated using the following EPR parameters:  $A(x,x) = A(y,y) = 2.15$  G,  $A(z,z) = 0.25$  G for one  $^{27}Al$ ;  $A(x,x) = 1.8$  G,  $A(y,y) = 0.3$  G,  $A(z,z) = 3.5$  G for two protons ( $I = 1/2$ );  $g(x) = g(y) =$

2.00670,  $g(z) = 2.0064$  for electrons ( $I = 1/2$ ); and linewidth = 2.35 G for all x, y and z directions. Based on the discussion of the results for the 1,4-BQ, this paramagnetic species is assigned to the naphthosemiquinone (1,4-NSQ) radical anion. It is noteworthy that the experimental spectra cannot be simulated well without considering either the  $^{27}\text{Al}$  or the NSQ radical anion. The observed spectra are due to the contribution of both  $^{27}\text{Al}$  and the NSQ radical anion, indicating that tightly bound “ $\text{Al}^{3+}/1,4\text{-NSQ}$  radical anion” ion pairs are also formed in the case of 1,4-NQ.

Irradiation of the Si-MCM-41 sample that was assembled with 1,4-NQ with  $\text{CH}_2\text{Cl}_2$  as solvent, using method A1 and A2, doesn't give any EPR radical signal. Also, irradiation of the Al-MCM-41 sample that was assembled with 1,4-NQ using the same method doesn't increase the EPR signal intensity, but results in the loss of the hyperfine structure in the second derivative spectra.

### 5.7. 1,4-AQ in (Al)-MCM-41

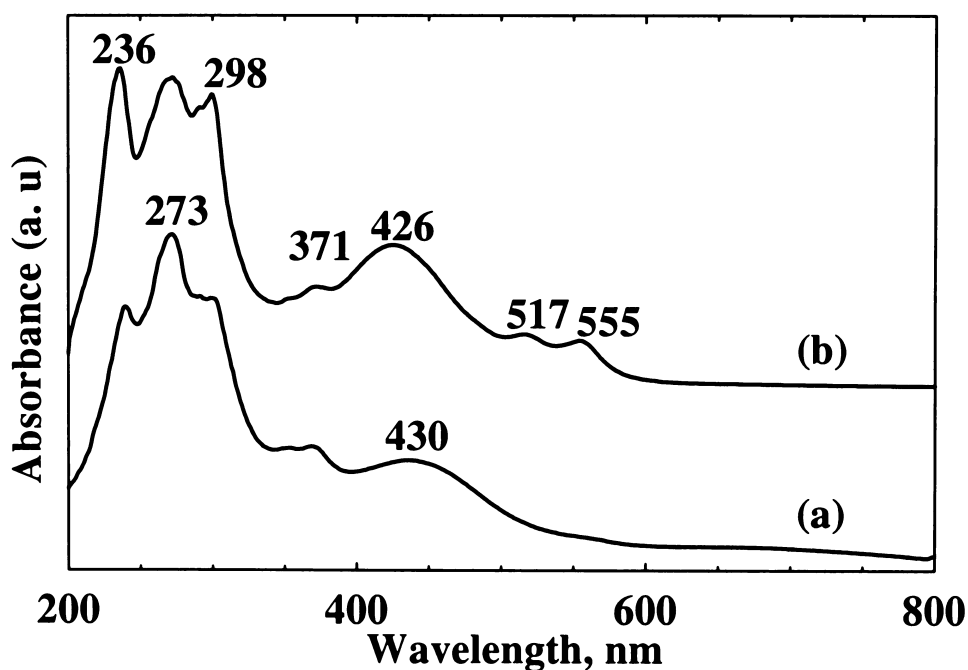
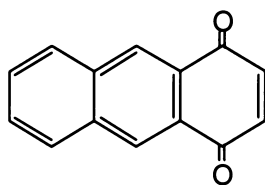
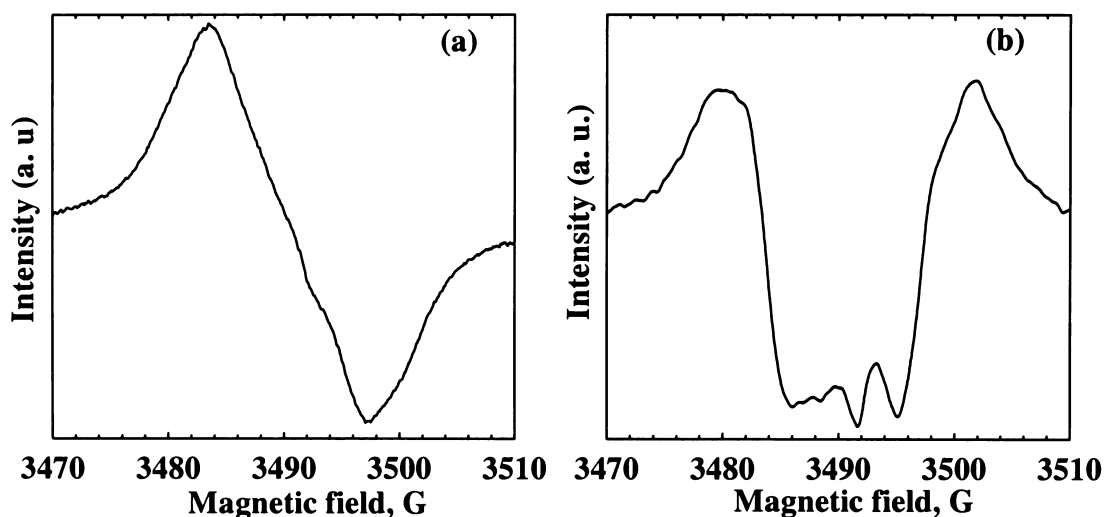


Figure 5.34: DR-UV-Vis spectra of 1,4-AQ in (a) Si-MCM-41 and (b) in Al-MCM(39).



1,4-AQ

Figure 5.34 shows the DR-UV-Vis spectra of 1,4-AQ in the Si-MCM-41 (curve (a)) and in the Al-MCM(39) (curve (b)). Comparison of the two curves indicates that those absorption bands with  $\lambda_{\max}$  at ca. 236, 273, 298, 371, 430 nm are due to the absorption of the neutral 1,4-AQ molecules. Two new absorption bands at 517 and 555 nm in Al-MCM(39) may be assigned to the 1,4-AQ radical species. Based on the discussion for the assignment of the 1,4-BSQ radical anion, these two new bands are tentatively assigned to the 1,4-ASQ radical anion.



**Figure 5.35:** EPR spectrum of 1,4-AQ in Al-MCM(15). 1,4-AQ was assembled with  $\text{CH}_2\text{Cl}_2$  as solvent, using method A2. Spectrum (a) is the first derivative and (b) is the second derivative.

1,4-AQ gave no EPR paramagnetic signal when it was assembled into the MCM-41 with THF or  $\text{CH}_2\text{Cl}_2$  as solvent, using method A1 or A2. However, when 1,4-AQ was assembled into the Al-MCM-41 with  $\text{CH}_2\text{Cl}_2$  as solvent, using method A1 and A2, a

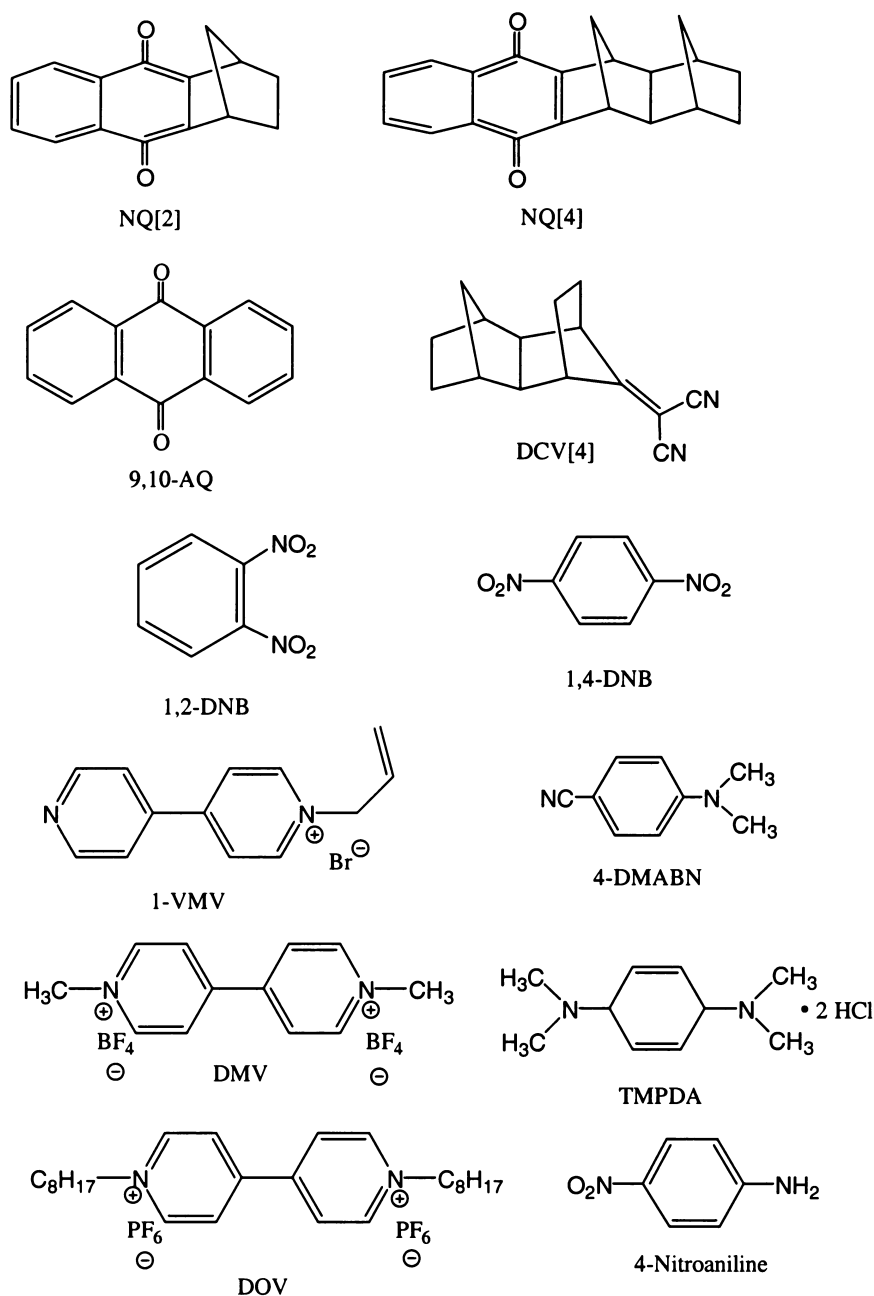
relatively weak EPR signal was detected. The intensity of this signal doesn't increase after irradiation. Figure 5.35 shows the EPR spectra of 1,4-AQ assembled into the Al-MCM(15) sample. First derivative EPR spectrum is just a single paramagnetic pattern whereas the second derivative spectrum shows some hyperfine structure. Unfortunately, an attempt to simulate the second derivative spectrum was not successful at the present. However, the similarity of the second derivative spectrum to those of the 1,4-BSQ radical anion described above suggests strongly that this is also due to a radical anion/aluminum (III) ion pair.

### 5.8. Other Electron Acceptor Molecules in (Al)-MCM-41

Other electron acceptor molecules listed in Scheme 5.3 were also used as electron transfer probe molecules and assembled into the (Al)-MCM-41 hosts. However, these molecules do not spontaneously form corresponding radical anions in (Al)-MCM-41. In solution, the driving force for the electron transfer is usually determined by the redox potentials of the donors and acceptors. The half-wave reduction potentials of the electron acceptor molecules studied in this work were measured by cyclic voltammetry under the same experimental conditions and are summarised in Table 5.9, because the reported values under different experimental conditions showed discrepancies.

Apparently, using only the reduction potentials cannot explain why those molecules having high reduction potentials were not reduced to the corresponding radical anions. Considering the specific porous solid state microenvironment in Al-MCM-41 host, failure to observe the radical anions of those molecules listed in Scheme 5.3 may be explained as follows:





**Scheme 5.3: The molecular structures of other electron acceptor molecules studied in this work.**

**4-DMABN (-1.0 V), 9,10-AQ (-1.1 V), DCV (-1.72 V) and 4-nitroaniline (-1.3 V):**

These molecules have lower **reduction potential** than those reduced by Al-MCM-41.

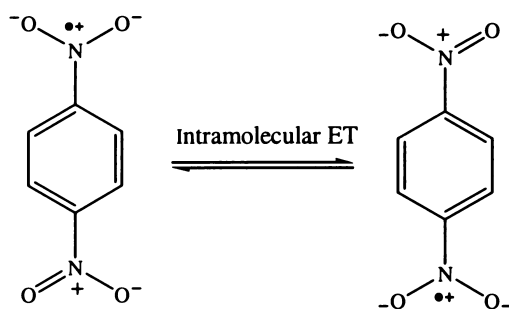
Low reduction potential may explain no observation of radical anions of these molecules.

**NQ[2] and NQ[4]:** These two molecules have the same reduction potentials as 1,4-NQ (-0.72 V), but do not give the corresponding radical anions in (Al)-MCM-41 spontaneously or even after irradiation. This may be explained by reduced accessibility of these two molecules due to the steric hindrance caused by the additional norbornane ring(s) and the aromatic ring. Steric hindrance prevents these two molecules from approaching the electron donor sites in Al-MCM-41.

Steric hindrance effects may also explain failure to observe the **TMPDA** radical anion.

**DMV (-0.47 V), DOV (-0.43 V) and 1-VMV (-0.43 V):** The viologen compounds are usually good electron acceptors. These three viologen molecules have higher reduction potentials than 1,4-BQ. However, no corresponding radicals were observed spontaneously as is the case with 1,4-BQ. This may be due to the **polar solvents** (water and CH<sub>3</sub>CN) used to assemble them into Al-MCM-41. These polar solvents may poison the electron donor sites before electron transfer to these viologen molecules occurs. It is well known that viologen molecules can easily form corresponding radicals in zeolites when irradiated.<sup>44,45,49,114,115</sup> However, the lifetime of MV<sup>•+</sup> generated by photoirradiation in Al-MCM-41 is reported to be short.<sup>44</sup> The likely rationalization is that the basic strength of Al-MCM-41 is not strong enough to stabilize MV<sup>•+</sup> which will then decay *via* reaction with water or back electron transfer. Short lifetime may also explain failure to observe MV<sup>•+</sup> radical signals by routine EPR technique.

**1,2-DNB (-0.84V) and 1,4-DNB (-0.65 V):** The reduction potentials of these two molecules are higher than 1,4-AQ, but do not spontaneously form corresponding radical anions in Al-MCM-41. It is known that dinitrobenzene may undergo intramolecular electron transfer to form corresponding radical anions after photoirradiation. 1,4-DNB may serve as a typical example:<sup>116</sup>



Photoirradiation of these two molecules in Al-MCM-41 should be further studied.

### 5.9. Electron Donating Ability of (Al)-MCM-41

Knowing the oxidation and reduction potentials of the porous materials can provide criteria for choosing proper donor and acceptor molecules to assemble redox systems in these confined heterogeneous media. However, zeolites, including mesoporous materials are not soluble in organic or inorganic solvents without losing their porous structures. Unlike other organic or inorganic redox compounds, the redox properties of these porous materials cannot be explored using routine electroanalytical methods. One of the possible ways to determine the redox properties of the porous materials is to use electron transfer probe molecules, such as electron donors or acceptors, to give an indication of the redox strengths of these porous materials. In this way, the electron acceptor or donor sites may also be explored.

At present, the theory for quantitative treatment of electron transfer in porous materials is unavailable. Hence, the electron transfer theory developed in solution phase is used to determine the oxidation potential of the Al-MCM-41. The following well-known equation in solution is used for calculation:

**Table 5.9: Reduction potentials of the electron acceptors used as electron transfer probe molecules in this work**

Compound	Literature	Reference	This work	No IR <sup>a</sup>	IR <sup>b</sup>
	E <sub>1/2</sub> <sup>Red</sup> (V) (solvent, ref. electrode)		E <sub>1/2</sub> <sup>Red</sup> (V) (CH <sub>3</sub> CN, Ag/AgCl)		
TMPDA	-0.10 (CH <sub>3</sub> CN, Ag/AgCl) 0.16 (C <sub>6</sub> H <sub>5</sub> CN, Ag/AgCl)	117	0.23	No <sup>c</sup>	— <sup>d</sup>
TCNQ	0.18 (CH <sub>3</sub> CN, SCE)	6	0.22	Yes <sup>e</sup>	—
TCNE	0.24 (CH <sub>3</sub> CN, SCE) 0.16 (DMF, SCE)	117	0.21	Yes	—
DOV	-	-	-0.43	No	—
1-VMV	-	-	-0.43	No	—
DMV	-0.46 (CH <sub>3</sub> CN, SCE)	118	-0.47	No	—
	-0.44 (CH <sub>3</sub> CN, NHE)	50			
	-0.78 (CH <sub>3</sub> CN, SCE)	43			
1,4-BQ	-0.45 (DMF, SCE)	119	-0.56	Yes	—
	-0.51 (CH <sub>3</sub> CN, SCE)	120			
	-0.56 (CH <sub>3</sub> CN, SCE)	121			
	-0.52 (CH <sub>3</sub> CN, SCE)	122			
	-0.62 (CH <sub>3</sub> CN, Pt)	107			
	-0.60 (C <sub>6</sub> H <sub>5</sub> CN, Ag/AgCl)	117			
	-0.54 (radical anion), -1.33 (dianion), -0.54 (hydroquinone), (CH <sub>3</sub> CN, Pt)	123			
BQ[2]	-	-	-0.56	Yes	—
1,4-DNB	-0.69 (CH <sub>3</sub> CN, SCE)	119	-0.65	No	—
	-0.70 (CH <sub>3</sub> CN, SCE)	123			
1,4-NQ	-0.63 (DMF, SCE)	119	-0.72	Yes	—
	-0.69 (Acetone, SCE)	117			
	-0.72 (C <sub>6</sub> H <sub>5</sub> CN, Ag/AgCl)				
	-0.70 (CH <sub>3</sub> CN, SCE)				
NQ[2]	-	-	-0.72	No	No
NQ[4]	-	-	-0.72	No	No
1,2-DNB	-0.83 (CH <sub>3</sub> CN, SCE)	117	-0.84	No	—
1,4-AQ	-0.75 (CH <sub>3</sub> CN, Pt)	123	-0.92	Yes	—
4-DMABN	-	-	-1.0	No	—
9,10-AQ	-0.96 (radical anion), -1.67 (dianion) (CH <sub>3</sub> CN, Pt)	123	-1.1	No	No
	-0.86 (DMF, SCE)	119			
	-0.94 (CH <sub>3</sub> CN, SCE)	118			
4-nitroaniline	-1.36 (CH <sub>3</sub> CN, SCE)	117	-1.3	No	—
	-1.39 (CH <sub>3</sub> CN, SCE)	123			
	-1.37 (DMF, SCE)				
DCV[4]	-1.73 (CH <sub>3</sub> CN, SCE)	124	-1.72	No	—
	-1.7 to -1.8 (CH <sub>3</sub> CN, SCE)	125			

Notes: (a) The sample was not irradiated. (b) The sample was irradiated. (c) No radical anion was formed. (d) Not available. (e) Radical anion was formed.

$$\Delta G = E_{1/2}^{\text{Ox}} - E_{1/2}^{\text{Red}} - \Delta E_{00}^*$$

where  $\Delta G$  is the Gibbs energy change;  $E_{1/2}^{\text{Ox}}$  Al-MCM-41 is the oxidation potential of the Al-MCM-41, which is regarded as the electron donor here;  $E_{1/2}^{\text{Red}}$  is the reduction potential of the electron acceptor molecule; and  $\Delta E_{00}^*$  is the energy level of the excited states (singlet and triplet excited states). For the spontaneous electron transfer (without irradiation), the value of  $\Delta E_{00}^*$  is zero.

It can be seen from Table 5.9 that Al-MCM-41 can reduce 1,4-AQ (−0.92 V) ( $\Delta G \leq 0$ ) but can not reduce 4-DMABN (−1.0 V) ( $\Delta G \geq 0$ ). Thus the oxidation potential of the Al-MCM-41 is estimated to be in the following narrow range:

$$-0.92 \text{ V} \geq E^{\text{ox}}(\text{Al-MCM-41}) \geq -1.0 \text{ V}.$$

Approximately, a value of −0.95 V may be taken as the oxidation potential of Al-MCM-41. This value is much smaller than that of 3.1 V estimated for  $\text{MV}^{2+}$  systems<sup>44</sup> and 2.1 V for the CsNaY zeolites,<sup>43</sup> indicating that Al-MCM-41 materials are strong electron donors.

## 5.10. Summary

In summary, various kinds of electron acceptor molecules were used as electron transfer probe molecules to explore the electron donor sites in Al-MCM-41 by means of EPR, DR-UV-Vis and FTIR spectroscopy. The following results and findings should be addressed:

- (1) Several methods (A1, A2 and B1) for assembling the organic molecules into (Al)-MCM-41 have been examined. Choosing the proper assembling method is critical in exploring the redox nature and the redox sites in (Al)-MCM-41. This result may also extended to the other porous materials.

- 
- (2) Pure MCM-41 has no electron donating ability at room temperature under the experimental conditions studied in this work.
  - (3) Incorporated Al plays an important role in generating electron donor sites in Al-MCM-41.
  - (4) Semi-quantitatively, the numbers of the electron donor sites in Al-MCM-41 is associated with the numbers of the extra-framework Al in Al-MCM-41.
  - (5) The electron transfer process from Al-MCM-41 to the electron acceptor molecules is largely influenced by several factors: (1) nature of the assembled molecules, such as the reduction potential, steric effects and the adsorption ability of the probe molecules; (2) nature of the hosts, such as the Al content in the framework; (3) the pretreatment method, such as synthesis procedure (direct or post synthesis), dehydration temperature, etc. (4) the solvent used for assembling the guest-host systems.
  - (6) The oxidation potential of the Al-MCM-41 is determined to be about  $-0.95$  V.

## 5.11. References for Chapter 5

- (1) Cairns, T. L.; Carboni, R. A.; Coffman, D. D.; Engelhardt, V. A.; Heckert, R. E.; Little, E. L.; McGeer, E. G.; McKusick, B. C.; Middleton, W. J.; Scribner, R. M.; Theobald, C. W.; Winberg, H. E. *J. Am. Chem. Soc.* **1958**, *80*, 2775.
- (2) Merrifield, R. E.; Phillips, W. D. *J. Am. Chem. Soc.* **1958**, *80*, 2778.
- (3) Melby, L. R.; Harder, R. J.; Hertler, W. R.; Mahler, W.; Benson, R. E.; Mochel, W. E. *J. Am. Chem. Soc.* **1962**, *84*, 3374.
- (4) Gerson, F.; Heckendorn, R.; Cowan, D. O.; Kini, A. M.; Maxfield, M. *J. Am. Chem. Soc.* **1983**, *105*, 7017.
- (5) Jonkman, H. T.; Velde, G. A. V. D.; Nieuwpoort, W. C. *Chem. Phys. Lett.* **1974**, *25*, 62.
- (6) Kaplan, M. L.; Haddon, R. C.; Bramwell, F. B.; Wudl, F.; Marshall, J. H.; Cowan, D. O.; Gronowitz, S. *J. Phys. Chem.* **1980**, *84*, 427.
- (7) Acker, D. S.; Hertler, W. R. *J. Am. Chem. Soc.* **1962**, *84*, 3370.
- (8) Johansen, H. *Int. J. Quantum. Chem.* **1975**, *IX*, 459.
- (9) Sakata, T.; Nakane, A.; Tsubomura, H. *Bull. Chem. Soc. Jpn.* **1975**, *48*, 3391.
- (10) Yumoto, Y.; Kato, F.; Tanaka, T. *Bull. Chem. Soc. Jpn.* **1979**, *52*, 1072.
- (11) Khatkale, M. S.; Devlin, J. P. *J. Chem. Phys.* **1979**, *70*, 1851.
- (12) Jonkman, H. T.; Kommandeur, J. *Chem. Phys. Lett.* **1972**, *15*, 496.
- (13) Grossel, M. C.; Evans, F. A.; Hriljac, J. A.; Prout, K.; Weston, S. C. *J. Chem. Soc., Chem. Commun.* **1990**, 1494.
- (14) Moscherosch, M.; Waldhör, E.; Binder, H.; Kaim, W.; Fiedler, J. *Inorg. Chem.* **1995**, *34*, 4326.
- (15) Hoffmann, S. K.; Corvan, P. J.; Singh, P.; Sethulekshmi, C. N.; Metzger, R. M.; Hatfield, W. E. *J. Am. Chem. Soc.* **1983**, *105*, 4605.
- (16) Morosin, B.; Plastas, H. J.; Coleman, L. B.; Stewart, J. M. *Acta Cryst.* **1978**, *B34*, 540.
- (17) Dong, V.; Endres, H.; Keller, H. J.; Moroni, W.; Nöthe, D. *Acta Cryst.* **1977**, *B33*, 2428.
- (18) Morton, R. A. *Biochemistry of Quinones*; Academic Press: New York, **1965**.
- (19) Bolton, J. R.; Carrington, A.; Santos-Veiga, J. D. *Mol. Phys.* **1962**, *5*, 465.
- (20) Bolton, J. R.; Carrington, A. *Proc. Chem. Soc.* **1961**, 385.

- (21) Beck, W.; Schlodder, R.; Lechler, K. H. *J. Organomet. Chem.* **1973**, *54*, 303.
- (22) Khatkale, M. S.; Delvin, J. P. *J. Chem. Phys.* **1979**, *70*, 1581.
- (23) Campana, C.; Dunbar, K. R.; Xiang, O. *Chem. Commun.* **1996**, 2427.
- (24) Novoa, J. J.; Lafuente, P.; Sesto, R. E. D.; Miller, J. S. *Angew. Chem. Int. Ed.* **2001**, *40*, 2540.
- (25) Flockhart, B. D.; Leith, I. R.; Pink, R. C. *Trans. Faraday Soc.* **1969**, *65*, 542.
- (26) Miller, F. A.; Sala, O.; Devlin, P.; Overend, J.; Lippert, E.; Lüder, W.; Moser, H.; Varchmin, J. *Spectrochim. Acta* **1964**, *20*, 1233.
- (27) Hinkel, J. J.; Devlin, J. P. *J. Chem. Phys.* **1973**, *58*, 4750.
- (28) Matsuzaki, S.; Mitsuishi, T.; Toyoda, K. *Chem. Phys. Lett.* **1982**, *91*, 296.
- (29) Bell, S. E.; Field, J. S.; Haines, R. J.; Moscherosch, M.; Matheis, W.; Kaim, W. *Inorg. Chem.* **1992**, *31*, 3269.
- (30) Bock, H.; Kleine, M. *Helv. Chim. Acta* **1997**, *80*, 516.
- (31) Ilten, D. F.; Calvin, M. *J. Am. Chem. Soc.* **1965**, *42*, 3760.
- (32) Dixon, D. A.; Miller, J. S. *J. Am. Chem. Soc.* **1987**, *109*, 3656.
- (33) Webster, O. W.; Mahler, W.; Benson, R. E. *J. Am. Chem. Soc.* **1962**, *84*, 3678.
- (34) Šeršen, F.; Banacký, P.; Krasnec, L. *Collection Czech. Chem. Commun.* **1974**, *39*, 3224.
- (35) Ayscough, P. B. *Electron Spin Resonance in Chemistry*; METHUEN & CO LTD: London, **1967**.
- (36) Phillips, W. D.; Rowell, J. C.; Weissman, S. I. *J. Chem. Phys.* **1960**, *33*, 626.
- (37) Ward, R. L. *J. Chem. Phys.* **1963**, *39*, 852.
- (38) Rieger, P. H.; Fraenkel, G. K. *J. Chem. Phys.* **1962**, *37*, 2795.
- (39) Stamires, D. N.; Turkevich, J. *J. Am. Chem. Soc.* **1963**, *85*, 2557.
- (40) Rieger, P. H.; Bernal, I.; Fraenkel, G. K. *J. Am. Chem. Soc.* **1961**, *83*, 3918.
- (41) Flockhart, B. D.; Uppal, S. S.; Leith, I. R.; Pink, R. C. In *Proceedings of the Fourth International Congress on Catalysts*: Moscow, U.S.S.R., **1968**.
- (42) Flockhart, B. D.; McLoughlin, L.; Pink, R. C. *J. Catal.* **1972**, *25*, 305.
- (43) Hashimoto, S. *J. Chem., Faraday Trans.* **1997**, *93*, 4401.
- (44) Alvaro, M.; García, H.; García, S.; Márquez, F.; Scaiano, J. C. *J. Phys. Chem. B* **1997**, *101*, 3043.
- (45) Yoon, K. B.; Park, Y. S.; Kochi, J. K. *J. Am. Chem. Soc.* **1996**, *118*, 12710.
- (46) Hashimoto, S. *Chem. Phys. Lett.* **1996**, *252*, 236.
- (47) McManus, H. J. D.; Finel, C.; Kevan, L. *Radiat. Phys. Chem.* **1995**, *45*, 761.



- (48) Druon, C.; Pasquet, D.; Tabourier, P.; Wacrenier, J.-M. *J. Chem. Soc., Faraday Trans. 1* **1978**, 74, 530.
- (49) Park, Y. S.; Um, S. Y.; Yoon, K. B. *J. Am. Chem. Soc.* **1999**, 121, 3193.
- (50) Vitale, M.; Castagnola, N. B.; Ortins, N. J.; Brooke, J. A.; Vaidyalingam, A.; Dutta, P. K. *J. Phys. Chem. B* **1999**, 103, 2408.
- (51) Mokaya, R. *Chem. Commun.* **2000**, 1891.
- (52) Mokaya, R.; Zhou, W.; Jones, W. *Chem. Commun.* **1999**, 51.
- (53) Mokaya, R.; Jones, W.; Luan, Z.; Alba, M. D.; Klinowski, J. *Catal. Lett.* **1996**, 37, 113.
- (54) Mokaya, R.; Jones, W. *J. Mater. Chem.* **1999**, 9, 555.
- (55) Mokaya, R.; Jones, W. *Phys. Chem. Chem. Phys.* **1999**, 1, 207.
- (56) Mokaya, R.; Jones, W. *Chem. Commun.* **1998**, 1839.
- (57) Mokaya, R.; Jones, W. *Chem. Commun.* **1997**, 2185.
- (58) Mokaya, R. *Chem. Commun.* **2000**, 1541.
- (59) Cea, P.; Artigas, H.; Urieta, J. S.; Lopez, M. C.; Royo, F. M. *J. Colloid Interface. Sci.* **2001**, 243, 156.
- (60) Truong, K. D.; Bandrauk, A. D.; Ishii, K.; Carlone, C.; Jandl, S. *Mol. Cryst. Liq. Cryst.* **1985**, 120, 105.
- (61) Futamata, M.; Morioka, Y.; Nakagawa, I. *Spectrochim. Acta* **1983**, 39A, 515.
- (62) Lowitz, D. A. *J. Chem. Phys.* **1967**, 46, 4698.
- (63) Matsubayashi, G.-E.; Kondo, K.; Tanaka, T. *Inorg. Chim. Acta* **1983**, 69, 167.
- (64) Suchanski, M. R.; Duyne, R. P. V. *J. Am. Chem. Soc.* **1976**, 98, 250.
- (65) Jeanmaire, D. L.; Duyne, R. P. V. *J. Am. Chem. Soc.* **1976**, 98, 4029.
- (66) Fischer, P. H. H.; McDowell, C. A. *J. Am. Chem. Soc.* **1963**, 85, 2694.
- (67) Gendell, J.; Freed, J. H.; Fraenkel, G. K. *J. Chem. Phys.* **1964**, 41, 949.
- (68) Maniero, A. L.; Priolisi, O.; Corvaja, C. *J. Chem. Soc., Faraday Trans. 1* **1987**, 83, 57.
- (69) Martin, N.; Segura, J. L.; Seoane, C. *J. Mater. Chem.* **1997**, 7, 1661.
- (70) Davis, M.; Prichard, F. E. *Trans. Faraday Soc.* **1963**, 59, 1248.
- (71) Becker, E. D.; Ziffer, H.; Charney, E. *Spectrochim. Acta* **1963**, 19, 1871.
- (72) Prichard, F. E. *Spectrochim. Acta* **1964**, 20, 1283.
- (73) Hartmann, H.; Eisenbraun, E.; Heidberg, J. *Z. Phys. Chem.* **1969**, 67, S., 51.
- (74) Charney, E.; Becker, E. D. *J. Chem. Phys.* **1965**, 42, 910.
- (75) Becker, E. D.; Charney, E.; Anno, T. *J. Chem. Phys.* **1965**, 42, 942.

- (76) Stammreich, H.; Sans, T. T. *J. Chem. Phys.* **1965**, *42*, 920.
- (77) Chipman, D. M.; Prebenda, M. F. *J. Phys. Chem.* **1986**, *90*, 5557.
- (78) Park, S.-E.; Huang, L.; Lee, C. W.; Chang, J.-S. *Catal. Today* **2000**, *61*, 117.
- (79) Kimura, K.; Yoshinaga, K.; Tsubomura, H. *J. Phys. Chem.* **1967**, *71*, 4485.
- (80) Babaei, A.; McQuillan, A. J. *J. Electroanal. Chem.* **1999**, *462*, 266.
- (81) Hester, R. E.; Williams, K. P. J. *J. Chem. Soc. Faraday Trans. 2* **1982**, *78*, 573.
- (82) Harada, Y.; Inokuchi, H. *Mol. Phys.* **1964**, *8*, 265.
- (83) Gamage, R. S. K. A.; Umapathy, S.; McQuillan, A. J. *J. Electroanal. Chem.* **1990**, *284*, 229.
- (84) Tripathi, G. N. R. *J. Chem. Phys.* **1981**, *74*, 6044.
- (85) Tripathi, G. N. R.; Sun, Q.; Schuler, R. H. *Chem. Phys. Lett.* **1989**, *156*, 51.
- (86) Girlando, A.; Ragazzon, D.; Pecile, C. *Spectrochim. Acta* **1980**, *36A*, 1053.
- (87) Stenman, F.; Räsänen, J. *Spectrochim. Acta* **1973**, *29A*, 405.
- (88) Patel, K. B.; Wilson, R. L. *J. Chem. Soc., Faraday Trans. 1* **1973**, *69*, 814.
- (89) Pecile, C.; Lunelli, B.; Busetti, V. *J. Chem. Soc. (A)* **1970**, 690.
- (90) Astashkin, A. V.; Samoilova, R. I. *Zeolites* **1991**, *11*, 282.
- (91) Samoilova, R. I.; Astashkin, A. V.; Dikanov, S. A.; Goldfarb, D.; Lunina, E. V. *Colloids Surf. A: Physicochem. Eng. Aspects* **1993**, *72*, 29.
- (92) Wong, S. K.; Sytnyk, W.; Wan, J. K. S. *Can. J. Chem.* **1972**, *50*, 3052.
- (93) Craw, M. T.; Depew, M. C.; Wan, J. K. S. *Can. J. Chem.* **1986**, *64*, 1414.
- (94) Kubozono, Y.; Ata, M.; Aoyagi, M.; Gondo, Y. *Chem. Phys. Lett.* **1987**, *137*, 467.
- (95) Reitz, D. C.; Dravnieks, F.; Wertz, J. E. *J. Chem. Phys.* **1960**, *33*, 1880.
- (96) Venkataraman, B.; Fraenkel, G. K. *J. Am. Chem. Soc.* **1955**, *77*, 2707.
- (97) Venkataraman, B.; Fraenkel, G. K. *J. Chem. Phys.* **1955**, *23*, 588.
- (98) Bersohn, R. *J. Chem. Phys.* **1956**, *24*, 1066.
- (99) Lucken, E. A. C. *J. Chem. Soc.* **1964**, 4234.
- (100) Brandon, R. W.; Lucken, E. A. C. *J. Chem. Phys.* **1961**, 4273.
- (101) Adams, M.; Blois, M. S.; Jr.; Sands, R. H. *J. Chem. Phys.* **1958**, *28*, 774.
- (102) Felix, C. C.; Sealy, R. C. *J. Am. Chem. Soc.* **1982**, *104*, 1555.
- (103) Abakumov, G. A.; Klimov, E. S. *Izv. Akad. Nauk SSSR, Ser. Khim.* **1972**, 1199.
- (104) Ciesla, U.; Schüth, F. *Microporous and Mesoporous Mater.* **1999**, *27*, 131.
- (105) Kosslick, H.; Lischke, G.; Parlitz, B.; Storek, W.; Fricke, R. *Appl. Catal. A: General* **1999**, *184*, 49.

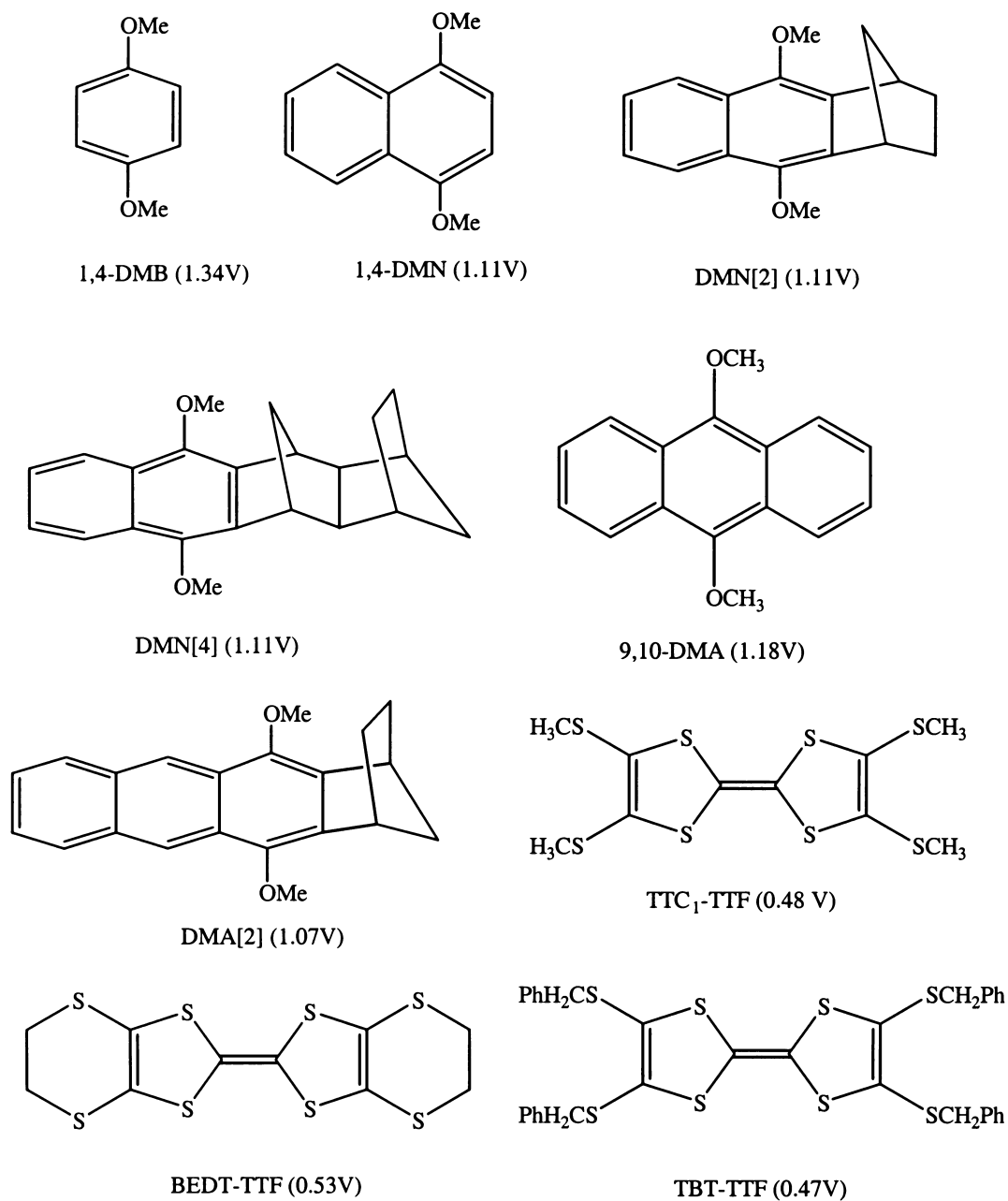
- (106) Pyun, C.-H.; Park, S.-M. *J. Electrochem. Soc.* **1985**, *132*, 2426.
- (107) Hoshino, T.; Oyama, M.; Okazaki, S. *Electroanal.* **2000**, *12*, 1373.
- (108) Lygin, V. L. *Adv. Chem. Ser.* **1971**, *102*, 86.
- (109) Takamori, D.; Aoki, T.; Yashiro, H.; Murai, H. *J. Phys. Chem. A* **2001**, *105*, 6001.
- (110) Balakrishnan, G.; Mohandas, P.; Umapathy, S. *J. Phys. Chem.* **1996**, *100*, 16472.
- (111) Hayon, E.; Simic, M. *J. Am. Chem. Soc.* **1973**, *95*, 1029.
- (112) Vincow, G.; Fraenkel, G. K. *J. Chem. Phys.* **1961**, *34*, 1333.
- (113) Holton, D. M.; Murphy, D. *J. Chem. Soc., Faraday. Tans.1* **1982**, *78*, 1223.
- (114) Alvaro, M.; García, H.; García, S.; Fernández, L. *Tetrahedron Lett.* **1996**, *37*, 2873.
- (115) Dutta, P. K.; Turbeville, W. *J. Phys. Chem.* **1992**, *96*, 9410.
- (116) Telo, J. P.; Grampp, G.; Schohoji, M. C. B. L. *Phys. Chem. Chem. Phys.* **1999**, *1*, 99.
- (117) Meites, L.; Zuman, P.; Scott, W. J.; Campbell, B. H.; Kardos, A. M.; Dubinsky, A.; Lampugnani, L.; Zuman, R. *Electrochemical Data (Part 1, Organic, Organometallic, and Biochemical Substances)*; John Wiley & Sons: New York, London, Sydney and Toronto, **1974**; Vol. A.
- (118) Keita, B.; Kawenoki, I.; Kossanyi, J. *J. Electroanal. Chem.* **1983**, *145*, 293.
- (119) Murov, S. L.; Carmichael, I.; Hug, G. L. *Handbook of Photochemistry*; Marcel Dekker, Inc.: New York, Basel and Hong Kong, **1993**. p261.
- (120) Peover, M. E.; Davies, J. D. *Trans. Faraday Soc.* **1964**, *60*, 476.
- (121) Eggins, B. R.; Chambers, J. Q. *J. Chem. Soc., Chem. Commun.* **1969**, 232.
- (122) Peover, M. E. *Nature* **1961**, *191*, 702.
- (123) Bard, A. J.; Lund, H. *Encyclopedia of Electrochemistry of the Elements (Organic Section)*; Marcel Dekker, Inc.: New York and Basel, **1984**.
- (124) Koeberg, M.; Groot, M. d.; Verhoeven, J. W.; Lokan, N. R.; Shephard, M. J.; Paddon-Row, M. N. *J. Phys. Chem. A* **2001**, *105*, 3417.
- (125) Oevering, H.; Paddon-Row, M. N.; Heppener, M.; Oliver, A. M.; Cotsaris, E.; Verhoeven, J. W.; Hush, N. S. *J. Am. Chem. Soc.* **1987**, *109*, 3258.

## Chapter 6

### Chemistry of Electron Donor Molecules in (Al)-MCM-41 hosts

#### 6.1. Introduction

This chapter deals with the assembly of various electron donor molecules in mesoporous (Al)-MCM-41 hosts. The host (Al)-MCM-41 materials are the same as those described in Chapter 5. The blank EPR and DR-UV-Vis results of these (Al)-MCM-41 hosts have already been shown in the introduction of Chapter 5. The assembled electron donors, which act as electron probe molecules for exploring the electron acceptor sites in (Al)-MCM-41 hosts, include dimethoxy compounds: 1,4-dimethoxybenzene (**1,4-DMB**), 1,4-dimethoxynaphthalene (**1,4-DMN**), 5,10-dimethoxy-1,4-methano-1,2,3,4-tetrahydro-anthracene (**DMN[2]**), 6,11-dimethoxy-1,2,3,4,5,12-hexahydro-1,4-methano-5,12-methano-tetracene (**DMN[4]**), 1,4-dihydro-5,12-dimethoxy-1,4-ethano-tetracene (**1,4-DMA[2]**), 9,10-dimethoxyanthracene (**9,10-DMA**); and tetrathiafulvalene (**TTF**) derivatives: bis(ethylenedithiolene)-tetrathiafulvalene (**BED-TTF**), tetrakis(methylthio)-tetrathiafulvalene (**TTC<sub>1</sub>-TTF**), tetrakis(benzylthio)-tetrathiafulvalene (**TBT-TTF**). The molecular structures of these molecules together with their half-wave oxidation potentials ( $E_{1/2}^{ox}$  (V) vs Ag/AgCl, CH<sub>3</sub>CN) are shown in Scheme 6.1. Formation of the radical cations of these molecules in the (Al)-MCM-41 hosts were monitored by means of EPR and DR-UV-Vis spectroscopy.



**Scheme 6.1:** The electron donors used as electron transfer probe molecules in this work, together with their oxidation potentials, in parentheses. Oxidation potentials are with respect to the Ag/AgCl reference electrode in CH<sub>3</sub>CN.

The three loading methods described in Section 2.4 of Chapter 2 were adopted to assemble the donor molecules into the (Al)-MCM-41 hosts: (1) method A1, where solvent coexists with the solid (Al)-MCM-41; (2) method A2, where solvent is

evaporated off naturally in the dry box; and (3) method B2, where the entire assembling procedures are carried out in a vacuum condition (free of oxygen).

The standards and the methods used for spin concentration estimation have already been described in Section 2.5.9 in Chapter 2.

## 6.2. 1,4-DMB in (Al)-MCM-41

### 6.2.1. DR-UV-Vis Spectra of 1,4-DMB in (Al)-MCM-41

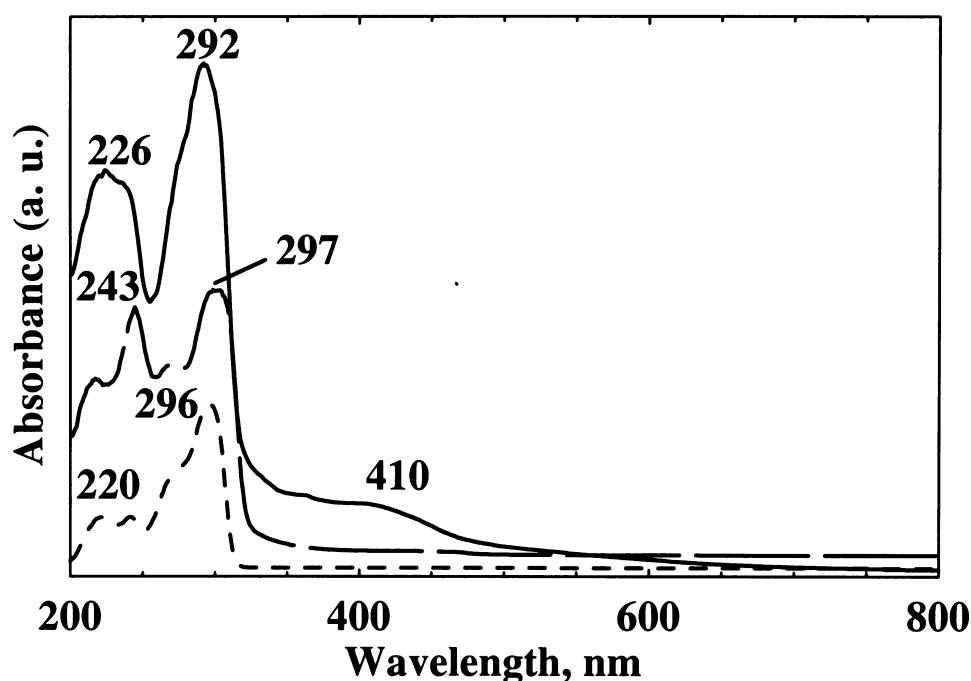


**Figure 6.1:** DR-UV-Vis spectra of 1,4-DMB in MCM-41 (dotted line), Al-MCM(15) (dashed line), and Al-MCM(15) after irradiation for ca. 20 min (solid line). 1,4-DMB was assembled into these hosts with  $\text{CH}_2\text{Cl}_2$  as solvent, using method A2.

As a typical example, Figure 6.1 shows the DR-UV-Vis spectra of 1,4-DMB assembled into the (Al)-MCM-41 with  $\text{CH}_2\text{Cl}_2$  as solvent, using method A2. In Si-MCM-41 (dotted line in Figure 6.1), the absorption bands with  $\lambda_{\text{max}}$  at 220, 243 and 296 nm are the characteristic absorption bands of the neutral 1,4-DMB.<sup>1,2</sup> When 1,4-DMB

was assembled into Al-MCM(15) (dashed line in Figure 6.1), the relative intensity of the absorption band at 243 nm was enhanced while the  $\lambda_{\max}$  of the other two bands shifted to 217 and 297 nm, respectively, indicating that 1,4-DMB has different interactions with the framework of Al-MCM-41 and Si-MCM-41. Due to the incorporated Al, Al-MCM-41 may have stronger interactions with the occluded 1,4-DMB molecules, influencing the electronic structure of 1,4-DMB as seen in the DR-UV-Vis spectra. After irradiation for ca. 20 min (solid line in Figure 6.1), the absorption bands presented at 217 and 297 nm before irradiation shifted to 226 and 292 nm, respectively. Furthermore, a new broad absorption band appeared in the visible region at ca. 350-600 nm with maximum at 410 nm. This new broad band is due to the characteristic absorption of the radical cation  $[1,4\text{-DMB}]^{\bullet+}$  which was reported to have absorption maxima at  $\lambda_{\max} = \text{ca. } 430\text{-}440 \text{ nm}$  and 460 nm.<sup>1-5</sup> The DR-UV-Vis study clearly shows that 1,4-DMB doesn't form a radical cation in the Si-MCM-41 and the Al-MCM-41 without irradiation. However, irradiation generates a 1,4-DMB radical cation in Al-MCM-41.

### 6.2.2. EPR Study of 1,4-DMB in (Al)-MCM-41

When 1,4-DMB was assembled into the Si-MCM-41 and the Al-MCM-41 hosts with THF as solvent, using assembling method A1 or A2, no EPR radical signal was observed before and after irradiation. Changing the solvent to  $\text{CH}_2\text{Cl}_2$ , still no EPR radical signal was detected without irradiation. Irradiation of the sample of 1,4-DMB that was assembled into the Si-MCM-41 with  $\text{CH}_2\text{Cl}_2$  as solvent, using method A1 gave no radical signal, either. However, irradiation of the sample of 1,4-DMB that was assembled into the Al-MCM-41 hosts with  $\text{CH}_2\text{Cl}_2$  as solvent, using method A1

evolved into a dark green color immediately. Typically, Figure 6.2 (A-a) and Figure 6.2 (B-a) show the first and second derivative EPR spectra recorded for the sample of 1,4-DMB that was assembled into the Al-MCM(15) with  $\text{CH}_2\text{Cl}_2$  as solvent, using assembling method A1.

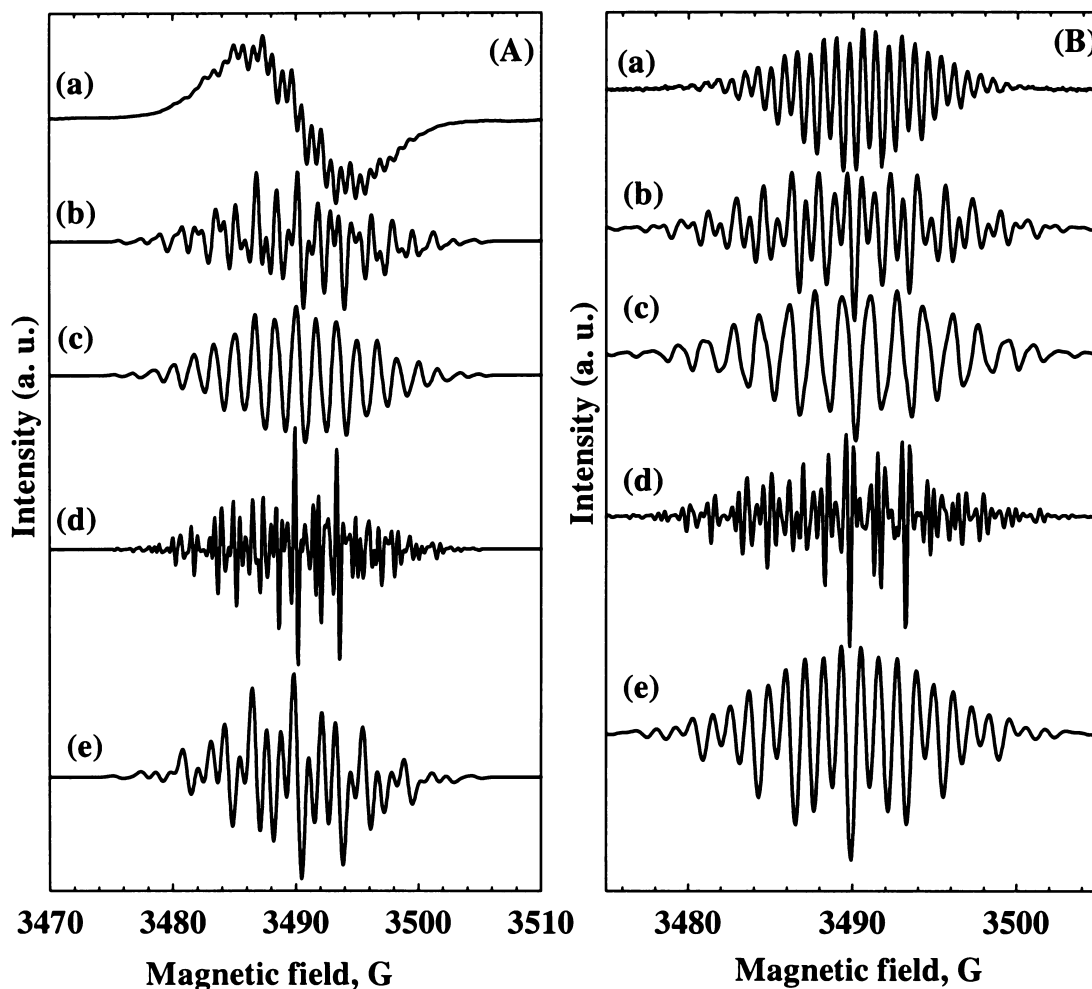
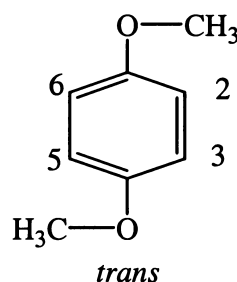
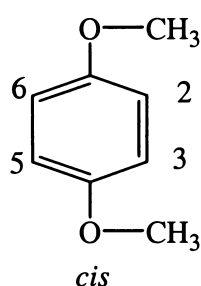


**Figure 6.2.** First (A) and second (B) derivative EPR spectra (room temperature) of: (a) 1,4-DMB assembled into Al-MCM(15) with  $\text{CH}_2\text{Cl}_2$  as solvent, using method A (experimental spectra); (b) *cis*-1,4-DMB radical cation (simulated spectra); (c) *trans*-1,4-DMB radical cation (simulated spectra); (d) *cis* and *trans* 1,4-DMB radical cation in 1:1 ratio. (e) 1,4-DMB radical cation (simulated using the average splitting constants of *cis* and *trans* 1,4-DMB radical cation).



**Table 6.1: The proton splitting constants of the 1,4-DMB radical cation**

	$a^H(\text{OCH}_3)$ (G)	$a^H(\text{aromatic ring})$ (G)	Reference
<i>Cis</i>	3.47		6
<i>Trans</i>	3.45		
<i>Cis</i>	+3.33	$a^H(2,3) = -2.68$ $a^H(5,6) = -1.81$	1,7
<i>Trans</i>	+3.45	$a^H(2,5) = 2.99$ $a^H(3,6) = 1.49$	
Average values	3.36	2.26	8



The proton hyperfine splitting constants of 1,4-DMB are summarized in Table 6.1. The computer simulation results using only the splitting constants of the DMB radical cations reported in the literature (see Table 6.1) were unsatisfactory. The simulated first and second derivative EPR spectra for these different models are shown in Figure 6.2. The EPR parameters of these simulated spectra are as follows:

Spectra (b) (*cis*-DMB radical cation): proton splitting constants  $a(6\text{H}, \text{OCH}_3) = 3.33$  G,  $a(2\text{H}, 2,3) = 2.68$  G,  $a(2\text{H}, 5,6) = 1.81$  G; linewidth = 0.60 G; and *g value* = 2.00505.

Spectra (c) (*trans*-DMB radical cation):  $a(6\text{H}, \text{OCH}_3) = 3.45$  G,  $a(2\text{H}, 2,5) = 2.99$  G,  $a(2\text{H}, 3,6) = 1.49$  G; linewidth = 0.60 G; *g value* = 2.00505.

Spectra (d) are the results of the addition of spectra (b) and spectra (c) in 1:1 ratio.

Spectra (e) are the simulated spectra using the average proton hyperfine splitting constants:  $a(6\text{H}, \text{OCH}_3) = 3.36$  G,  $a(4\text{H}, 2,3,5,6) = 2.26$  G; linewidth = 0.60 G; *g value* = 2.00505.

In the simulated spectra using proton splitting constants of the *cis*-1,4-DMB radical cation (Figures (b)) and the average splitting constants of the 1,4-DMB radical cation

(Figures (e)), the line positions in the second derivative approximately match with those in the experimental one, but the shape of the first derivative is completely different. The simulated *trans* (Figures 6.2 (c)) and the addition spectra (Figure 6.2 (d)) show more deviation from the experimental ones. Attempts to simulate the observed spectra by adjusting the ratios of the *cis* and the *trans* 1,4-DMB radical cation also failed. The computer simulation results strongly suggest that the observed spectra are due not only to the simple 1,4-DMB radical cations.

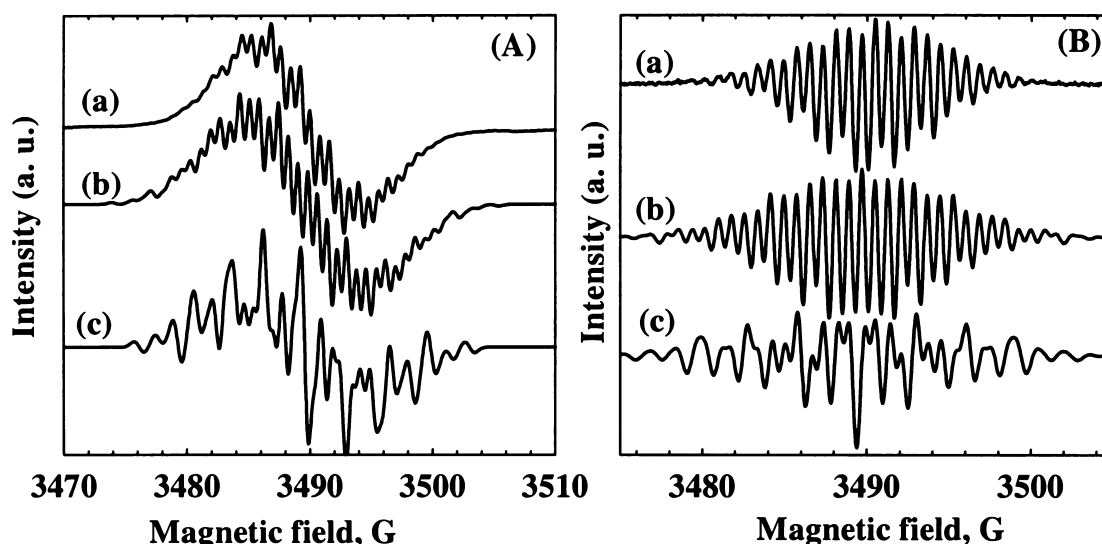


**Figure 6.3:** First derivative (A) and second derivative (B) EPR spectra (room temperature) of: (a) 1,4-DMB radical cation in Al-MCM(15) generated by irradiation (experimental spectra); (b) computer simulation results considering the Al hyperfine coupling contribution to the Hamiltonian parameters; and (c) computer simulation results without considering the Al hyperfine coupling contribution to the Hamiltonian parameters.

However, including the Al splitting constant in the Hamiltonian parameter settings during simulation, the experimental spectra can be approximately simulated using the following EPR parameters: **splitting constants of  $a(^{27}\text{Al}) = 0.78$  G,  $a(^6\text{H}) = 3.13$  G,  $a(^2\text{H}) = 2.40$  G and  $a(^2\text{H}) = 1.65$  G;  $g$  value = 2.0052; and linewidth = 0.82 G.** The

simulated first and second derivative spectra are shown in Figure 6.3 as Figure 6.3 A-b and Figure 6.3 B-b, respectively. It can be seen that the line positions match well between the simulated spectra and the experimental ones. The slight difference in the relative line intensities may be explained by the existence of *cis* and *trans* isomers of the 1,4-DMB radical cations, which results in difficulties in obtaining perfect simulation of the observed spectra. The spectra that were simulated using the above EPR parameters but without the  $^{27}\text{Al}$  hyperfine splitting constant, are shown in Figures 6.3 (c), which apparently do not match with the observed spectra. The computer simulation results indicate that 1,4-DMB radical cations are complexed with certain Al species in the Al-MCM-41 hosts.

Complexes of quinone radical cations with Al on the HY zeolite were also reported by Samoilova et al.<sup>9-11</sup> The ENDOR experiments, as well as the formation of paramagnetic complexes of quinones with  $\text{Al}^{3+}$  Lewis acid sites, support the mechanism that the formation of radical cations on the HY zeolite is *via* electron transfer to the Lewis acid sites.<sup>9-11</sup> The origin of the  $\text{Al}^{3+}$  ions was assigned to the extra-framework  $\text{Al}^{3+}$  ions formed by thermal treatment. The EPR study of 1,4-DMB in the Al-MCM-41 hosts in this work also demonstrates that the observed EPR spectra are due to the hyperfine coupling contributions from both the 1,4-DMB radical cation and the  $^{27}\text{Al}$ . Analogous of the radical cations of the quinone compounds in the zeolites, formation of the donor-acceptor complex of DMB with Lewis acid sites (extra-framework  $\text{Al}^{3+}$ ), may explain the observed EPR spectra, i.e., DMB forms a donor-acceptor complex with Lewis acid sites, which undergoes further electron transfer to the host upon photoirradiation, leaving stabilized  $\text{DMB}^{\bullet+}/\text{Al}$  form. The  $^{27}\text{Al}$  isotropic hyperfine splitting constants largely depend on the complexing ability of the electron donor molecules. When quinone compounds complexed with the Al in the zeolites, the  $^{27}\text{Al}$  hyperfine splitting

constants were estimated to be 5 MHz (1.79 G) for 1,4-benzoquinone, 3.8 MHz (1.36 G) for fluoranil and 6 MHz (2.15G) for chloranil.<sup>10</sup> In Al-MCM-41, the estimated hyperfine splitting constants (0.78 G) of  $^{27}\text{Al}$  in the 1,4-DMB/ $\text{Al}^{3+}$  complex is much smaller than these reported values, indicating that the 1,4-DMB/ $\text{Al}^{3+}$  complex is loosely complexed.

It should note that the signal intensity of the observed EPR spectrum (Figure 6.3 A-a) did not change significantly after several days, indicating that the 1,4-DMB radical cations generated in the Al-MCM-41 hosts by irradiation are quite stable and long-lived.

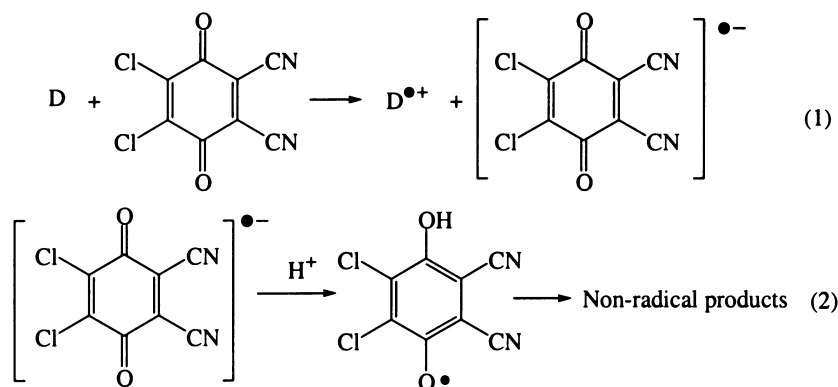
The spin concentration calculated from the observed EPR spectrum of 1,4-BDMB radical cation (as described in Chapter 5) was ca.  $2.8 \times 10^{-6}$  mol/g, which is far less than the total Al content ( $1.0 \times 10^{-3}$  mol/g) and the extra-framework Al content ( $1.8 \times 10^{-4}$  mol/g) in the Al-MCM(15) sample. No quantitative relationship between the probed electron acceptor sites and the Al content has been established using 1,4-DMB as electron transfer probe molecules.

### 6.3. 1,4-DMN in (Al)-MCM-41

#### 6.3.1. 1,4-DMN Radical Cation in Solution

The 1,4-DMN radical cation was generated using the  $\text{CF}_3\text{COOH}/\text{CH}_2\text{Cl}_2/\text{DDQ}$  method as described in Section 2.3.2 in Chapter 2. The radical cations ( $\text{D}^{*+}$ ) generated using this method *via* electron transfer to DDQ (Equation (1) in Scheme 6.3) are usually long-lived and relatively easy to observe by routine EPR technique, since the protonation of the DDQ radical anion to give the neutral radical overcomes the reversibility of the electron transfer (Scheme 6.3).<sup>12-15</sup> In this method, the DDQ radical anions are usually

not observed in the EPR spectra because the neutral DDQ radicals quickly form non-radical products (Equation (2) in Scheme 6.3).



**Scheme 6.2:** Formation and stabilization of radical cations of the electron donor molecule (D) using  $\text{CF}_3\text{COOH}/\text{CH}_2\text{Cl}_2/\text{DDQ}$  method.<sup>13</sup>

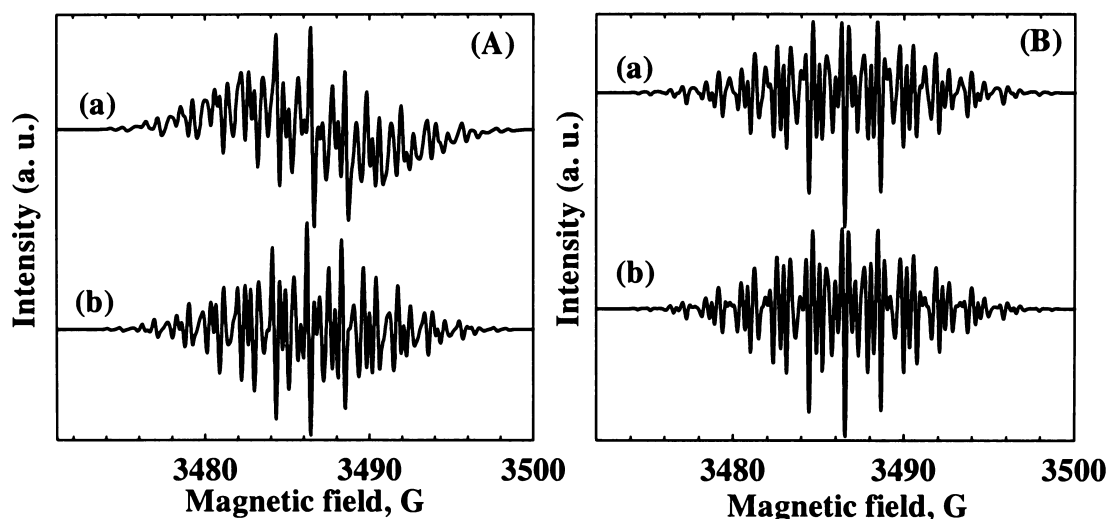
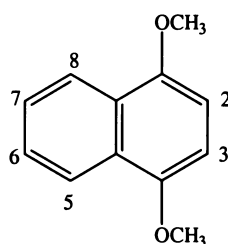


**Figure 6.4:** First (A) and second (B) derivative EPR spectra (room temperature) of:  
 (a) 1,4-DMN radical cation generated using  $\text{CF}_3\text{COOH} / \text{CH}_2\text{Cl}_2 / \text{DDQ}$  method and  
 (b) computer simulation results.

The first and the second derivative EPR spectra of the 1,4-DMN radical cation generated using  $\text{CF}_3\text{COOH}/\text{CH}_2\text{Cl}_2/\text{DDQ}$  method are shown in Figures 6.4 (a). The spectra can be approximately simulated using the following EPR parameters: **splitting**

constants of  $a(6H, OCH_3) = 2.104$  G,  $a(2H) = 3.43$  G,  $a(2H) = 1.642$  G,  $a(2H) = 0.734$  G;  $g$  value = 2.00512; and linewidth = 0.23 G. The splitting constants used for simulation are comparable with the values reported in the literature (lit.:  $a^H(OCH_3, 6H) = 2.194 \pm 0.006$ ;  $a^H(CH, 2,3) = 3.354 \pm 0.006$ ;  $a^H(CH, 5,8) = 1.456 \pm 0.006$ ;  $a^H(CH, 6,7) = 0.699 \pm 0.006$ ). The simulated spectra (first and second derivative) are shown in Figures 6.4-(b). It can be seen that the simulated spectra match with the experimental ones.



### 6.3.2. EPR spectra of 1,4-DMN in (Al)-MCM-41

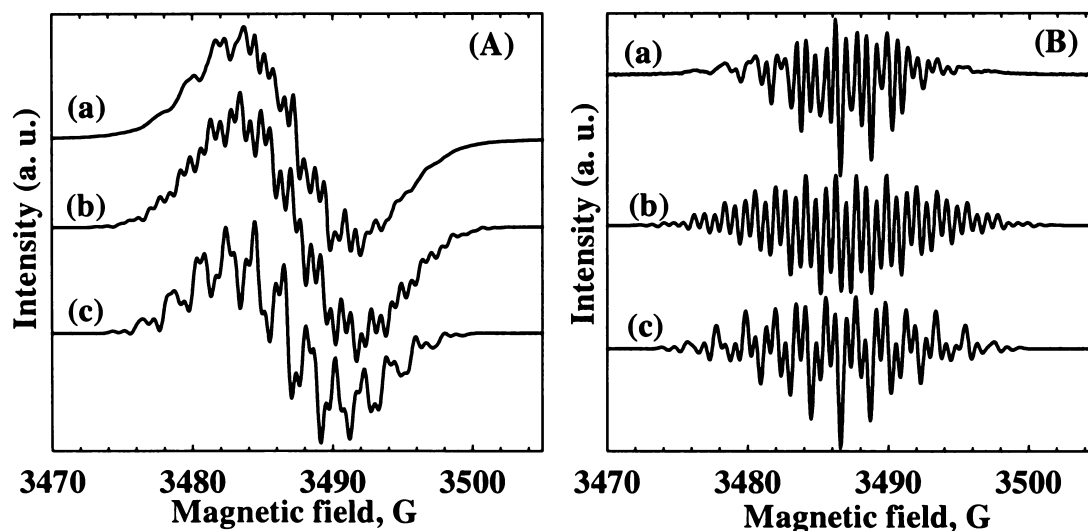


Figure 6.5: First (A) and second (B) derivative EPR spectra (room temperature) of: (a) 1,4-DMN assembled into the Al-MCM(15) with  $CH_2Cl_2$  as solvent, using method A1; (b) computer simulation results including the Al hyperfine coupling contribution to the Hamiltonian parameters; (c) computer simulation results without inclusion of the Al hyperfine coupling contribution to the Hamiltonian parameters.

No EPR radical signal was observed when 1,4-DMN was assembled into the Si-MCM-41 with  $\text{CH}_2\text{Cl}_2$  as solvent, using method A1. However, when 1,4-DMN was assembled into the Al-MCM(15) with the same method, the color of the sample gradually turned into blue. The first and the second derivative EPR spectra record for this sample are shown in Figure 6.5 (a) and Figure 6.5 (b), respectively.

Unlike 1,4-DMB, the radical cations of 1,4-DMN are formed spontaneously in the Al-MCM(15). Computer simulation shows that the spectra cannot be interpreted using only the splitting constants of the 1,4-DMN radical cation. However, adding an  $^{27}\text{Al}$  splitting constant of 0.78 G into the Hamiltonian parameter settings during simulation, the experimental spectra can be approximately simulated using the following EPR parameters: **splitting constants of  $a(^{27}\text{Al}) = 0.78$  G,  $a(6\text{H}) = 2.104$  G,  $a(2\text{H}) = 3.430$  G,  $a(2\text{H}) = 1.642$  G,  $a(2\text{H}) = 0.734$  G;  $g$  value = 2.00515; and linewidth = 0.63 G.** The simulated spectra are shown in Figures 6.5 (b). The simulation results indicate that the 1,4-DMN radical cation also complexed with the Lewis acid sites (extra-framework  $\text{Al}^{3+}$ ) as 1,4-DMB does in the Al-MCM-41 hosts. The  $^{27}\text{Al}$  hyperfine splitting constant involved in the Hamiltonian parameters is also ca. 0.78 G for 1,4-DMN, which is consistent with that for 1,4-DMB. This demonstrates that 1,4-DMN is only loosely complexed with the Lewis acid sites. The spectra that were simulated using the above EPR parameters but without the  $^{27}\text{Al}$  hyperfine splitting constant are shown in Figures 6.5 (c). Apparently, these spectra do not match with the experimental ones, confirming that  $^{27}\text{Al}$  is involved in hyperfine coupling with the 1,4-DMN radical cation. The higher intensities of some lines in the experimental spectra than those in the simulated spectra may be explained by the coexistence of some free 1,4-DMN radical cations in the Al-MCM-41 hosts.

## 6.4. DMN[2] and DMN[4] in (Al)-MCM-41

DMN[2] and DMN[4] have similar molecular structures and show similar behaviors in the (Al)-MCM-41 hosts. These two molecules will be discussed together in this section.

### 6.4.1. DR-UV-Vis Spectra of DMN[2] and DMN[4] in (Al)-MCM-41

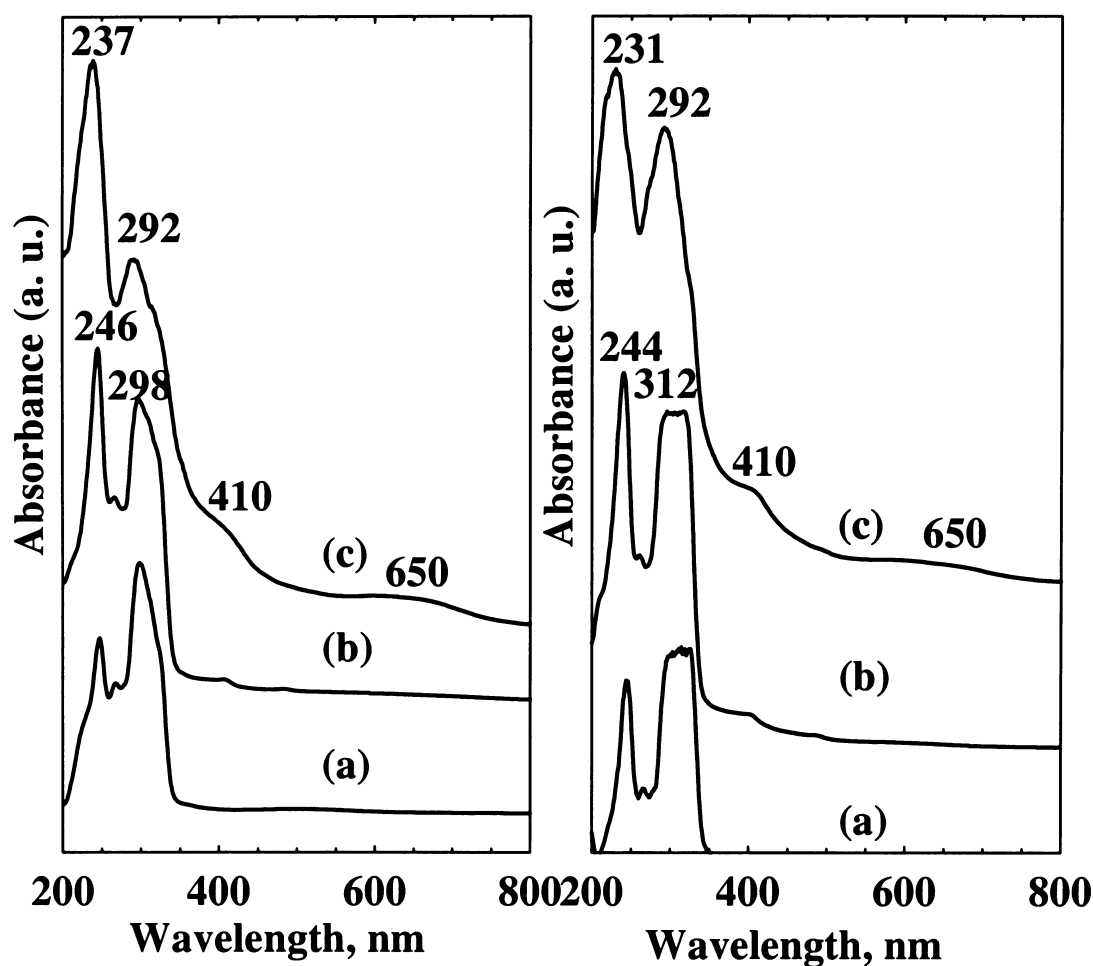


Figure 6.6: DR-UV-Vis spectra of DMN[2] (A) and DMN[4] (B) in: (a) Si-MCM-41; (b) Al-MCM(15) before irradiation; and (c) Al-MCM(15) after irradiation.

Figure 6.6 shows the DR-UV-Vis spectra of DMN[2] and DMN[4] in the (Al)-MCM-41 hosts. DMN[2] was assembled into these hosts with  $\text{CH}_2\text{Cl}_2$  as solvent, using method A2. In Si-MCM-41 (Figure 6.6 (A-a)), DMN[2] displays absorption with maxima at



246 and 298 nm. DMN[4] also displays absorption bands in the same region ( $\lambda_{\text{max}} = 244$  and 312 nm). It is noted that the absorption band with maximum at 312 nm was shifted to the longer wavelengths compared to that in cyclohexane ( $\lambda_{\text{max}} = 290$  nm) or in acetonitrile ( $\lambda_{\text{max}} = 292$  nm).<sup>16</sup> These absorption bands at low wavelength are characteristic absorption due to the neutral DMN[2] and DMN[4].

In Al-MCM-41 (Figures 6.6 (b)), the maxima of the absorption bands of these two molecules are identical to those in the Si-MCM-41 before irradiation. However, after irradiation, these samples show additional absorption bands with maxima at ca. 410 nm and 650 nm (broad), respectively (Figures 6.6 (c)). The absorption with maximum at 410 nm is assigned to the [DMN[2]]<sup>•+</sup> and [DMN[4]]<sup>•+</sup> according to the previous report for the DMN[4] radical cation generated by pulse irradiation in cyclohexane solution.<sup>16-19</sup> The characteristic absorption band of the radical cation [1,4-DMN]<sup>•+</sup> is at  $\lambda_{\text{max}} = 710$  nm with a shoulder at ca. 650 nm according the reports in the literature<sup>20-22</sup> whereas the (1,4-DMN)<sub>2</sub><sup>•+</sup> are in a broad absorption region of 550-750 nm with maxima at 660, 690 and 720 nm, respectively.<sup>3,22,23</sup> So, the extremely broad absorption centered at 650 nm is also assigned to the radical cations [DMN[2]]<sup>•+</sup> and [DMN[4]]<sup>•+</sup>. No observation of the [DMN[2]]<sup>•+</sup> and [DMN[4]]<sup>•+</sup> radical cations in the Al-MCM-41 without irradiation in the DR-UV-Vis spectra (Figures 6.6 (b)) is in contrast with the EPR result that these two kinds of radical cations can form spontaneously in the Al-MCM-41. This may be due to the concentration of the radical cations before irradiation was too low to detect by the DR-UV-Vis spectroscopy.

### 6.4.2. EPR Study of DMN[2] and DMN[4] in (Al)-MCM-41

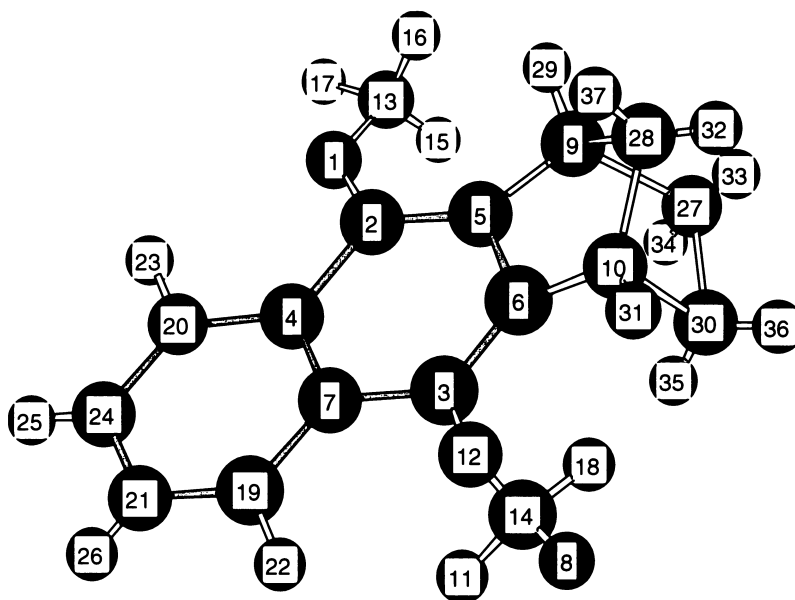
#### 6.4.2.1. Determination of the Splitting Constants of DMN[2] and DMN[4] Radical Cations

To facilitate the identification and interpretation of the radical species in the EPR study, the splitting constants of the radical cations of DMN[2] and [DMN[4] were determined by the computer calculation for the DMN[2] and the simulation of the EPR spectrum of DMN[4] radical cation generated directly in solution.

**Table 6.2: B3LYP DFT calculation results for the hyperfine splitting constants of DMN[2] radical cation in gas phase**

Atom	Spin density	Atom	Spin density	Atom	Isotropic Fermi Contact couplings (G)	Atom	Isotropic Fermi Contact couplings (G)
1 O	0.119752	20 C	0.075138	1 O (17)	-5.22770	20 C (13)	1.28601
2 C	0.163056	21 C	0.019927	2 C (13)	4.09361	21 C (13)	-0.35438
3 C	0.163056	22 H	-0.003401	3 C (13)	4.09361	22 H	-1.73712
4 C	0.007418	23 H	-0.003401	4 C (13)	-2.98012	23 H	-1.73712
5 C	0.085426	24 C	0.019927	5 C (13)	-1.06602	24 C (13)	-0.35438
6 C	0.085426	25 H	-0.001577	6 C (13)	-1.06602	25 H	-0.61512
7 C	0.007418	26 H	-0.001577	7 C (13)	-2.98012	26 H	-0.61512
8 H	0.005942	27 C	0.006798	8 H	3.27119	27 C (13)	1.99746
9 C	0.013404	28 C	0.008339	9 C (13)	-0.97291	28 C (13)	-0.70300
10 C	0.013404	29 H	0.000334	10 C (13)	-0.97291	29 H	-0.01459
11 H	0.000264	30 C	0.006798	11 H	0.06443	30 C (13)	1.99746
12 O	0.119752	31 H	0.000334	12 O (17)	-5.22770	31 H	-0.01459
13 C	-0.004986	32 H	-0.001081	13 C (13)	-1.02182	32 H	-0.83453
14 C	-0.004986	33 H	0.002863	14 C (13)	-1.02182	33 H	2.09206
15 H	0.005942	34 H	0.00020	15 H	3.27119	34 H	-0.16815
16 H	0.006219	35 H	0.000020	16 H	4.78200	35 H	-0.16815
17 H	0.000264	36 H	0.002863	17 H	0.06443	36 H	2.09206
18 H	0.006219	37 H	-0.000451	18 H	4.78200	37 H	-0.21818
19 C	0.075138			19 C (13)	1.28601		

The gas phase hyperfine splitting constants for the radical cation of DMN[2] were calculated by Professor Michael N. Paddon-Row, UNSW, by Density Functional Theory (DFT), using the B3LYP functional and the EPRiii basis set. The geometry of the radical cation of DMN[2] was optimized at the B3LYP/6-31G(d) level of theory. The calculated results are shown in Table 6.2. The assignment of the numbers of the atomic positions of DMN[2] is shown in Scheme 6.4.



Scheme 6.4: The assignment of the atomic positions of DMN[2].

In summary, the calculation results show the pronounced hyperfine splitting constants for the DMN[2] as follows:  $a(2H, 25,26) = 0.62$  G,  $a(2H, 22, 23) = 1.74$  G,  $a(1H, 32) = 0.83$  G,  $a(1H, 37) = 0.22$  G,  $a(2H, 33,36) = 2.09$  G,  $a(2H, 34, 35) = 0.17$  G,  $a(2H, 8, 15) = 3.3$  G,  $a(2H, 16, 18) = 4.78$  G,  $a(2H, 11, 17) = 0.064$ ,  $a(2H, 29, 31) = 0.01$  G.

The average splitting constants of DMN[2] radical cation (see below for the assignments of the numbers of the atomic positions ) may be assigned as follows:  $a(6H, OCH_3) = 2.72$  G,  $a(2H, 7,8) = 0.62$  G,  $a(2H, 6,9) = 1.74$  G,  $a(2H, 11,11) = 0.525$  G,  $a(4H, 2,3) = 1.13$  G.

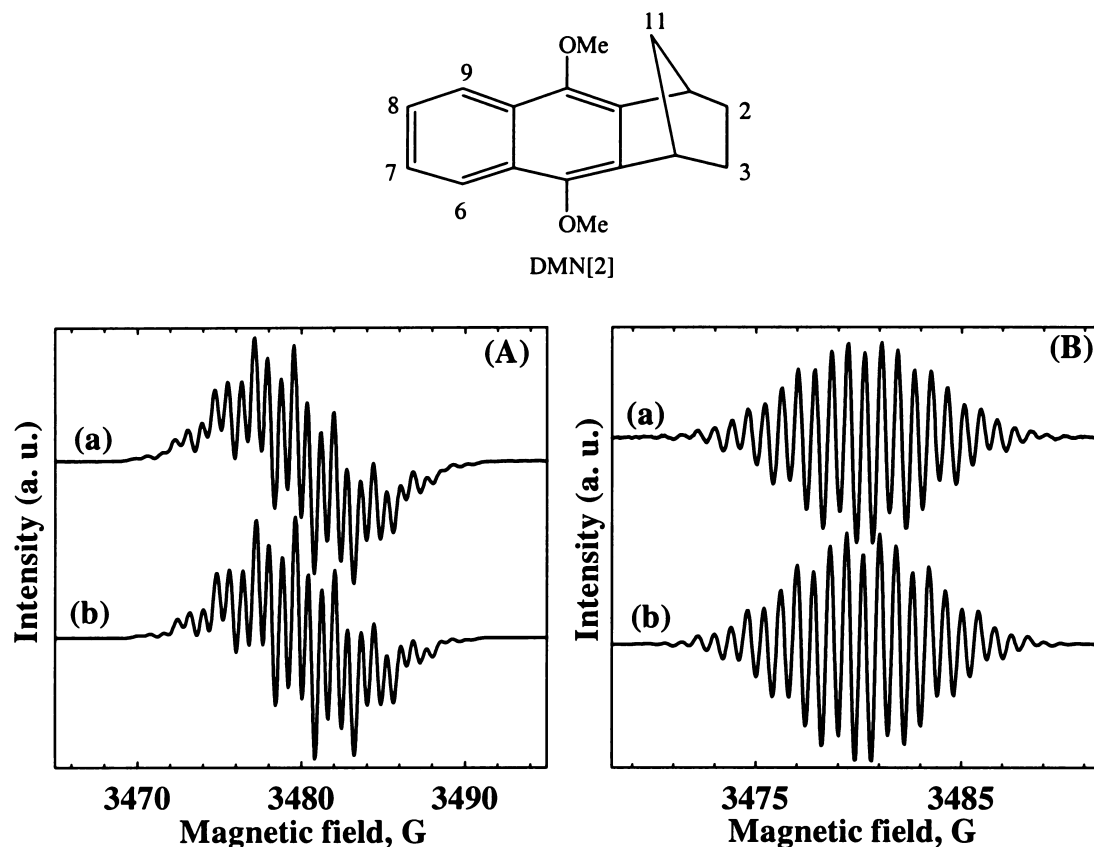
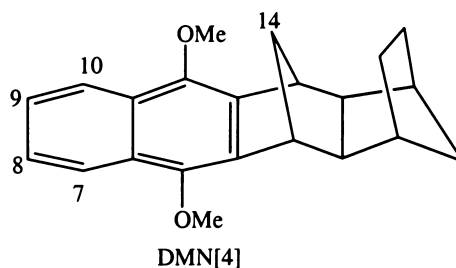


**Figure 6.7: First (A) and second (B) derivative EPR spectra (room temperature) of DMN[4] radical cation. Curves (a) are the experimental spectra of the DMN[4] radical cation generated using  $\text{CF}_3\text{COOH}/\text{CH}_2\text{Cl}_2/\text{DDQ}$  method; and curves (b) are the computer simulated spectra.**

Figure 6.7 shows the first derivative (A-a) and the second derivative (B-a) EPR spectra (room temperature) of the DMN[4] radical cation generated using the  $\text{CF}_3\text{COOH}/\text{CH}_2\text{Cl}_2/\text{DDQ}$  method. Curves (b) in each figure are computer simulated spectra, which perfectly match with the experimental spectra (a). The EPR parameters used for simulation are as follows:  $a(1\text{H}, 14) = 0.60\text{G}$ ,  $a(6\text{H}, \text{OCH}_3) = 2.40\text{ G}$ ,  $a(2\text{H}, 8,9) = 0.80\text{ G}$ ,  $a(2\text{H}, 7,10) = 1.60\text{ G}$ ;  $g\text{ value} = 2.00502$ ; and linewidth =  $0.64\text{ G}$ . These values are comparable with the computer calculation results for the DMN[2] radical cation.



#### 6.4.2.2. EPR Spectra of DMN[2] and DMN[4] in (Al)-MCM-41

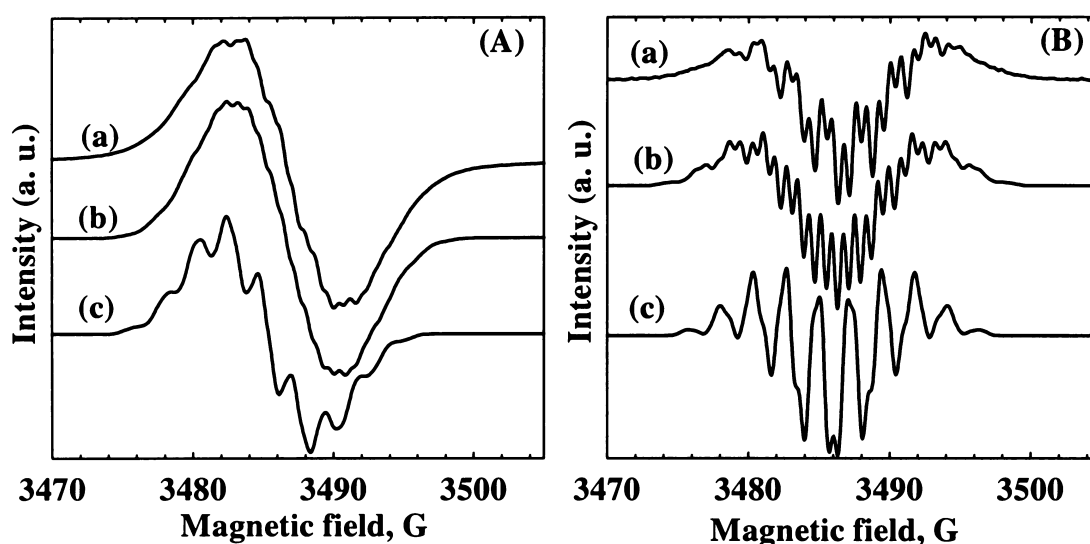


**Figure 6.8: First (A) and second (B) derivative EPR spectra (room temperature) of:**  
**(a) DMN[2] assembled into the Al-MCM(15) with CH<sub>2</sub>Cl<sub>2</sub> as solvent, using method A1; (b) computer simulation results including the Al hyperfine coupling contribution to the Hamiltonian parameters; (c) computer simulation results without inclusion of the Al hyperfine coupling contribution to the Hamiltonian parameters.**

No EPR signal was detected when DMN[2] and DMN[4] were loaded into the Si-MCM-41 (dehydrated at 473 K) with CH<sub>2</sub>Cl<sub>2</sub> as solvent, using method A1 and A2. However, a light blue color evolved gradually when DMN[2] and DMN[4] were loaded into the Al-MCM-41 (dehydrated at 473 K) hosts in the same experimental conditions. The corresponding first and second derivative EPR of DMN[2] and DMN[4] assembled

into the Al-MCM(15) are shown in Figures 6.8 (a) and Figure 6.9 (a), respectively. The spectra can be approximately simulated using the following EPR parameters:

DMN[2]: splitting constants of  $a(^{27}\text{Al}) = 0.78 \text{ G}$ ,  $a(6\text{H}, \text{OCH}_3) = 2.4 \text{ G}$ ,  $a(2\text{H}, 6,9) = 1.50 \text{ G}$ ,  $a(2\text{H}, 7,8) = 0.7 \text{ G}$ ,  $a(1\text{H}, 11) = 0.80 \text{ G}$ ;  $g \text{ value} = 2.0053$ ; and linewidth =  $1.0 \text{ G}$ .

DMN[4]:  $a(^{27}\text{Al}) = 0.30 \text{ G}$ ,  $a(6\text{H}, \text{OCH}_3) = 2.38 \text{ G}$ ,  $a(2\text{H}, 7,10) = 1.56 \text{ G}$ ,  $a(2\text{H}, 8,9) = 0.73 \text{ G}$ ,  $a(1\text{H}, 14) = 0.75 \text{ G}$ ;  $g \text{ value} = 2.00525$ ; and linewidth =  $0.7 \text{ G}$ .

As above, simulation without inclusion of  $^{27}\text{Al}$  hyperfine splitting failed to reproduce the observed spectra. The simulated spectra are shown in Figures 6.8 (b) (first derivative) and Figures 6.9 (b) (second derivative). It can be seen that the simulated spectra match with the experimental ones quite well. It is noteworthy that the  $^{27}\text{Al}$  hyperfine splitting constant for DMN[4] ( $0.3 \text{ G}$ ) is smaller than that for DMN[2] ( $0.78 \text{ G}$ ), indicating that DMN[4] molecules have weaker interaction with the Lewis acid sites. This is probably due to the steric effect of DMN[4], i.e., steric hindrance is more pronounced in DMN[4] molecules due to the additional rigid bridge, which prevents the approach of DMN[4] molecules to the Lewis acid sites.

Though DMN[2] and DMN[4] radical cations can be spontaneously generated in Al-MCM-41, irradiation of the sample can dramatically accelerate the rate of the reactions. For example, in a typical experiment of DMN[2] in Al-MCM(15), the spin concentration of the DMN[2] radical cations was  $3.2 \times 10^{-6} \text{ mol/g}$  before irradiation. Irradiation of the sample with UV lamp for 100 min increased the spin concentration nearly 4 times to  $1.2 \times 10^{-5} \text{ mol/g}$ . The spin concentration further increased up to  $2.4 \times 10^{-5} \text{ mol/g}$  and kept constant at this value in the next 3 months. This indicates DMN[2] radical cations are quite stable once formed in the Al-MCM-41 hosts.

To test whether the trace amounts of oxygen present in the dry box in any way influence the electron transfer processes, DMN[4] was also assembled into the (Al)-MCM(15) using loading method B2 which is rigorously oxygen free. Spontaneous formation of the DMN[4] radical cations was observed. The recorded spectra are not shown since they are like those presented in Figure 6.9. Irradiation also dramatically increased the spin concentrations of the DMN[4] radical cation. In a typical experiment, irradiation of 10 min increased the spin concentration 3 times from  $1.6 \times 10^{-6}$  mol/g to  $4.8 \times 10^{-6}$  mol/g.

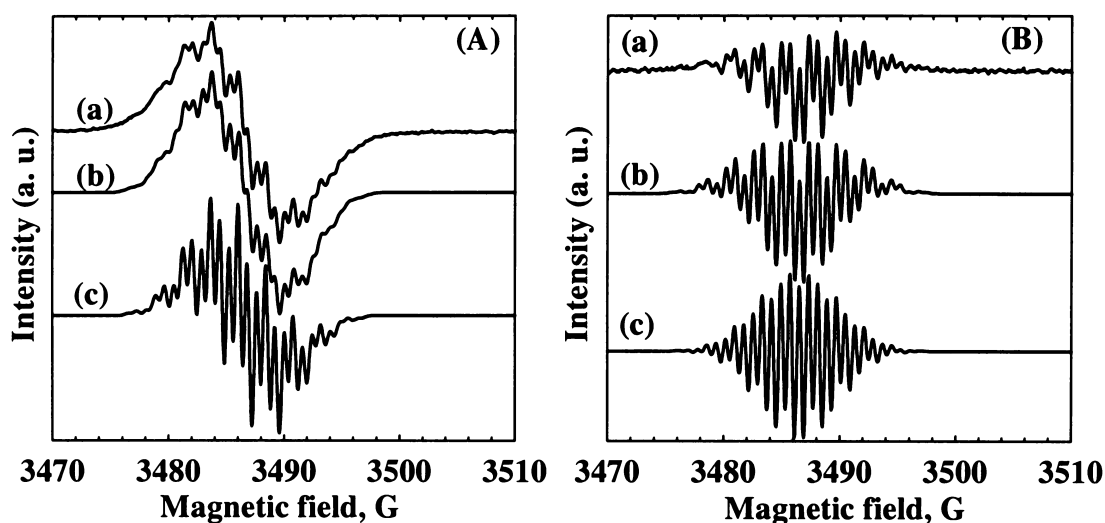


**Figure 6.9: First (A) and second (B) derivative EPR spectra (room temperature) of:**  
**(a) DMN[4] assembled into the Al-MCM(15) with CH<sub>2</sub>Cl<sub>2</sub> as solvent, using method A1; (b) computer simulation results including the Al hyperfine coupling contribution to the Hamiltonian parameters; (c) computer simulation results without inclusion of the Al hyperfine coupling contribution to the Hamiltonian parameters.**

However, these spin concentrations of the DMN[2] (or DMN[4]) radical cations generated using both methods A2 and B2 are far less than the total Al content ( $1.0 \times 10^{-3}$  mol/g) and the extra-framework Al content ( $1.8 \times 10^{-4}$  mol/g) in the Al-MCM(15)

sample. No direct connection with the Al content in Al-MCM-41 can be established using present data.

## **6.5. 9,10-DMA in (Al)-MCM-41**

### **6.5.1. DR-UV-Vis Spectra of 9,10-DMA in (Al)-MCM-41**

The UV-Vis spectrum of 9,10-DMA in  $\text{CH}_2\text{Cl}_2$  solution (dotted line in Figure 6.10) displays absorption bands at 330, 346, 365, 383, and 405 nm. In Si-MCM-41, 9,10-DMA shows absorption bands with maxima at 289, 339, 356, 377 and 397 nm (Figure 6.11 A, dashed line), which are assigned to the characteristic absorption bands of the neutral 9,10-DMA by comparison with the above solution spectrum. These absorption bands can also be observed after 9,10-DMA was assembled into the AlMCM(15) with  $\text{CH}_2\text{Cl}_2$  as solvent, using method A2 (solid line in Figure 6.10). Besides, a relatively weak absorption band is present at 525 nm (with a shoulder at ca. 673 nm). These new absorption bands are assigned to the 9,10-DMA radical cation according to the observation of the 9,10-DMA radical signals in the EPR study.

### **6.5.2. EPR Study of 9,10-DMA in (Al)-MCM-41**

#### **6.5.2.1. 9,10-DMA in Si-MCM-41 and Post-synthesized Al-MCM-41**

When 9,10-DMA was assembled into the Si-MCM-41 and the post-synthesized Al-MCM-41 (Si/Al = 14) with  $\text{CH}_2\text{Cl}_2$  as solvent, using method A1 and A2, no corresponding EPR paramagnetic signals were detected, indicating no radicals were spontaneously formed in Si-MCM-41 and the post-synthesized Al-MCM-41. It is known that Si-MCM-41 has no Al, thus no extra-framework Al; the post-synthesized



Al-MCM-41 has only small amounts of extra-framework Al. No observation of the EPR radical signals in these two MCM-41 hosts supports that the electron acceptor sites are associated with the extra-framework Al.

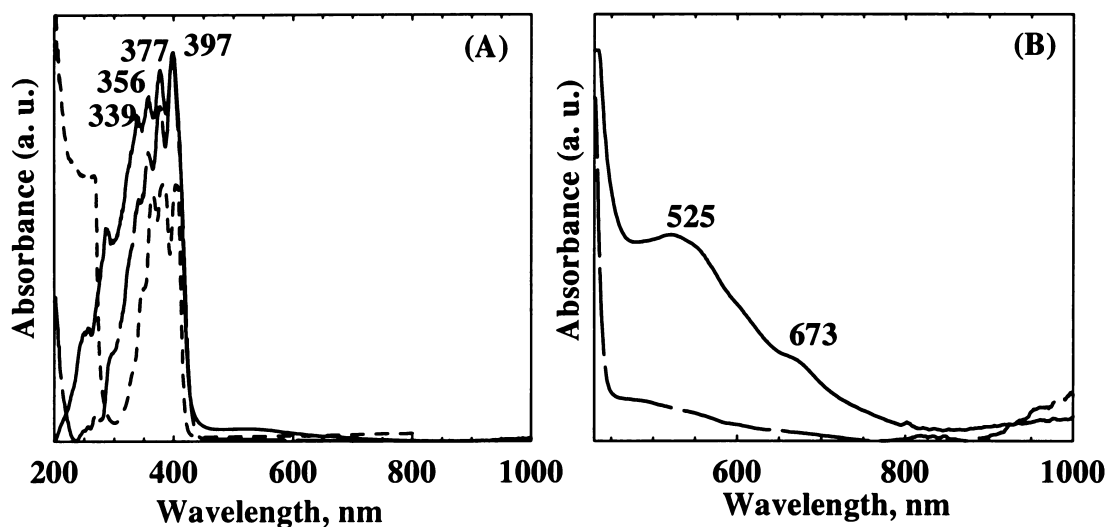
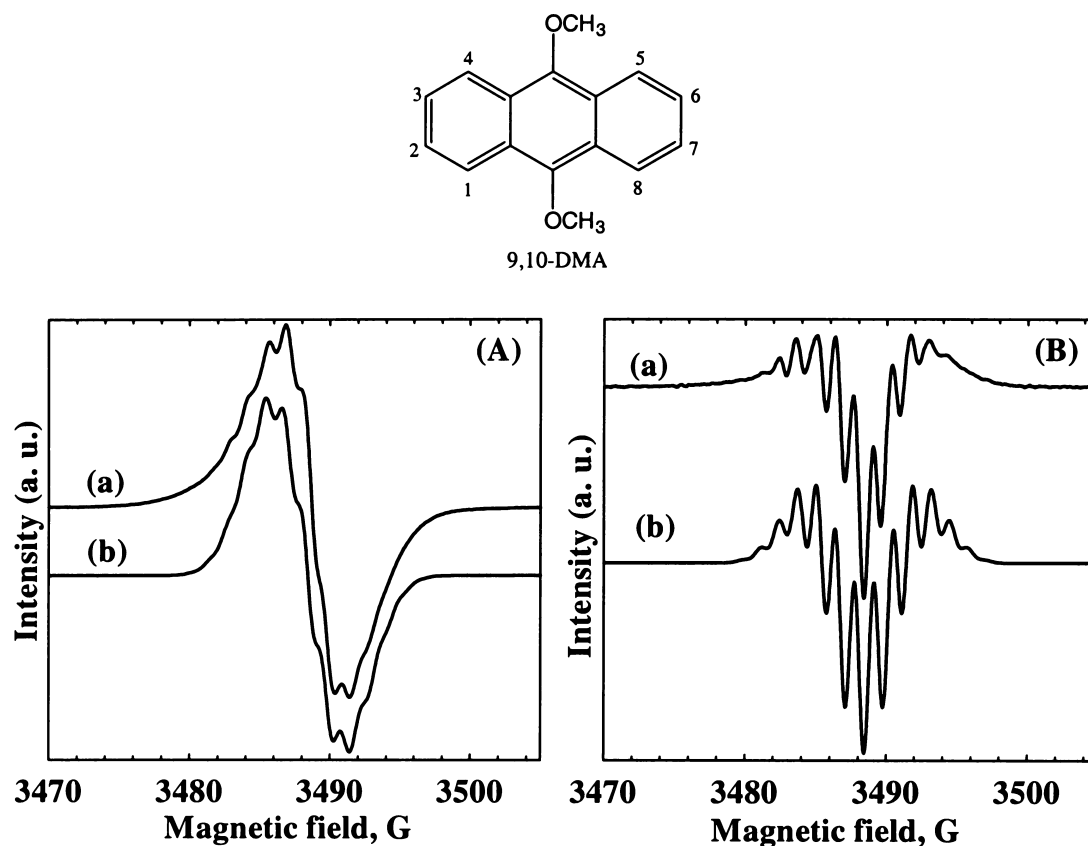


Figure 6.10: UV-Vis spectrum of 9,10-DMA in  $\text{CH}_2\text{Cl}_2$  solution (dotted line). DR-UV-Vis spectra of 9,10-DMA in Si-MCM-41 (dashed line) and that in Al-MCM(15) (solid line). Figure (B) shows the hyperfine structures in the region between 420 to 1000 nm.

#### 6.5.2.2. 9,10-DMA in Directly Synthesized Al-MCM-41

9,10-DMA radical cations were formed spontaneously in the directly synthesized Al-MCM-41 samples with  $\text{CH}_2\text{Cl}_2$  as solvent, using method A1 and A2. The color of the sample was grey-yellow. Figure 6.11 (A-a) and (B-a) show the first and second derivative EPR spectra of the 9,10-DMA radical cations generated in Al-MCM(15), respectively. The spectra can be well simulated using the following parameters:  $a(6\text{H}, \text{OCH}_3) = 1.186 \text{ G}$ ,  $a(4\text{H}, 1,4,5,8) = 1.600 \text{ G}$ ,  $a(4\text{H}, 2,3,6,7) = 1.080 \text{ G}$ ;  $g \text{ value} = 2.00550$ ; and  $\text{linewidth} = 1.14 \text{ G}$ . The splitting constants shown in the computer simulation are comparable to the values reported in the literature:<sup>8,24</sup>  $a(6\text{H}, \text{OCH}_3) = 1.186 \text{ G}$ ,  $a(\text{H}, 2,3,4,7) = 1.084 \text{ G}$ ,  $a(\text{H}, 1,4,5,8) = 1.752 \text{ G}$ . It is noteworthy in this case

that  $^{27}\text{Al}$  hyperfine splitting is not resolved in the observed spectra, and agreement between observed and simulated spectra could be achieved without including  $^{27}\text{Al}$  hyperfine coupling.



**Figure 6.11:** First derivative (A) and second derivative (B) EPR spectra (room temperature) of 9,10-DMA in Al-MCM(15). Curves (a) are the experimental spectra; and curves (b) are the computer simulated spectra.

**Table 6.3:** Spin concentration results from the EPR spectra of 9,10-DMA radical cation in the (Al)-MCM-41 hosts ( $\text{CH}_2\text{Cl}_2$  as solvent, using method A2).

	Si-MCM-41	Al-MCM(39)	Al-MCM(15)	Al-MCM(7)
Spin concentration of 9,10-DMA radical cation (mol in the cavity)	0	$3.6 \times 10^{-8}$	$1.3 \times 10^{-7}$	$4.3 \times 10^{-9}$
Spin concentration of 9,10-DMA radical cation (mol/g)	0	$1.2 \times 10^{-6}$	$4.3 \times 10^{-6}$	$1.4 \times 10^{-7}$
Total Al content (mol /g)	0	$4.2 \times 10^{-4}$	$1 \times 10^{-3}$	$2.1 \times 10^{-3}$
Extra-framework Al (mol/g)	0	$9.2 \times 10^{-5}$	$1.8 \times 10^{-4}$	$5.0 \times 10^{-4}$

Several important results can be derived from the spin concentration results tabulated in Table 6.3: (1) the electron acceptor sites responsible for the oxidation of the 9,10-DMA are associated with the incorporated Al, since no 9,10-DMA radical cations were observed in pure Si-MCM-41; (2) the spin concentration of the 9,10-DMA radical cation increases with increase of the Al content in the Al-MCM-41, but direct quantitative relation between them hasn't been found yet. Though the spin concentration of the DMA radical cation generated in the Al-MCM-41 hosts is closer to the extra-framework Al content than to the total Al content in the Al-MCM-41 samples, the amount of the extra-framework Al is still one order of the magnitude higher than that of the 9,10-DMA radical cations; (3) 9,10-DMA shows relatively low spin concentration in high Al content sample (Si/Al = 7). This may be due to the low surface area and less structure order of the Al-MCM(7) sample as shown in Chapter 3.

It was indicated before that 9,10-DMA doesn't give the corresponding radical cation in the post-synthesized Al-MCM-41 sample. No observation of the 9,10-DMA radical signal in the Si-MCM-41 was expected since it has no Al in the framework and thus no Lewis acid sites can be created. In the post-synthesized Al-MCM-41 sample, most of the Al atoms are incorporated into the MCM-41 framework as tetrahedral Al, evidenced by the  $^{27}\text{Al}$ -MAS-NMR (See Chapter 3). No observation of an EPR signal due to the 9,10-DMA radical cation in the post-synthesized Al-MCM-41 parallels to the smaller amount of the extra-framework Al in this material. This seems to support the notion that **the Lewis acid sites (extra-framework Al) are responsible for the electron acceptor sites in the Al-MCM-41 hosts.**

### 6.5.2.3. Loading Level Study of 9,10-DMA

Figure 6.12 shows the plots of the spin concentration of the 9,10-DMA radical cation generated in Al-MCM(39) with  $\text{CH}_2\text{Cl}_2$  as solvent, using method A2 *versus* the moles of 9,10-DMA/moles of Al in the Al-MCM(39) sample. The spin concentration of the 9,10-DMA radical cation increases steeply with increased loading of 9,10-DMA when the moles of 9,10-DMA/moles of Al  $\leq 2$ . Further increasing the loading level of the 9,10-DMA doesn't increase the spin concentration further. At the inflection point of moles of 9,10-DMA/moles of Al = 2, the spin concentration is ca.  $1.0 \times 10^{-6}$  mol/g, which is much less than the total Al content (ca.  $4.2 \times 10^{-4}$  mol/g) and the extra-framework Al content ( $9.2 \times 10^{-5}$  mol/g, about 22 % Al atoms are in the extra-framework position, see Section 3.3.2.1.1 in Chapter 3). The loading level study also indicates that the low spin concentration of the 9,10-DMA radical cation generated in the Al-MCM-41 is not due to an insufficient amount of the 9,10-DMA assembled into the Al-MCM-41.

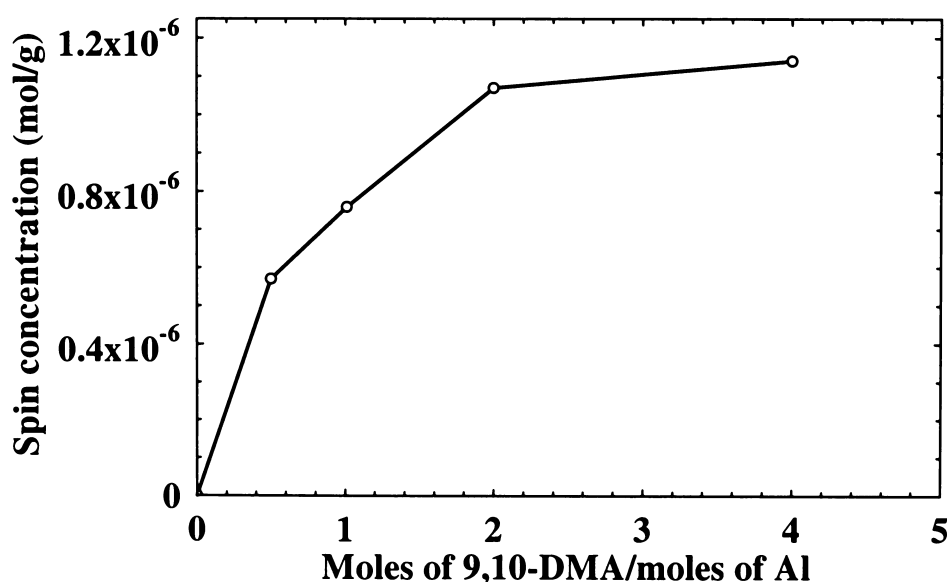


Figure 6.12: Relationship between the spin concentration and the loading level of the 9,10-DMA in Al-MCM(39).

## 6.6. DMA[2] in (Al)-MCM-41

### 6.6.1. DR-UV-Vis Spectra of DMA[2] in (Al)-MCM-41

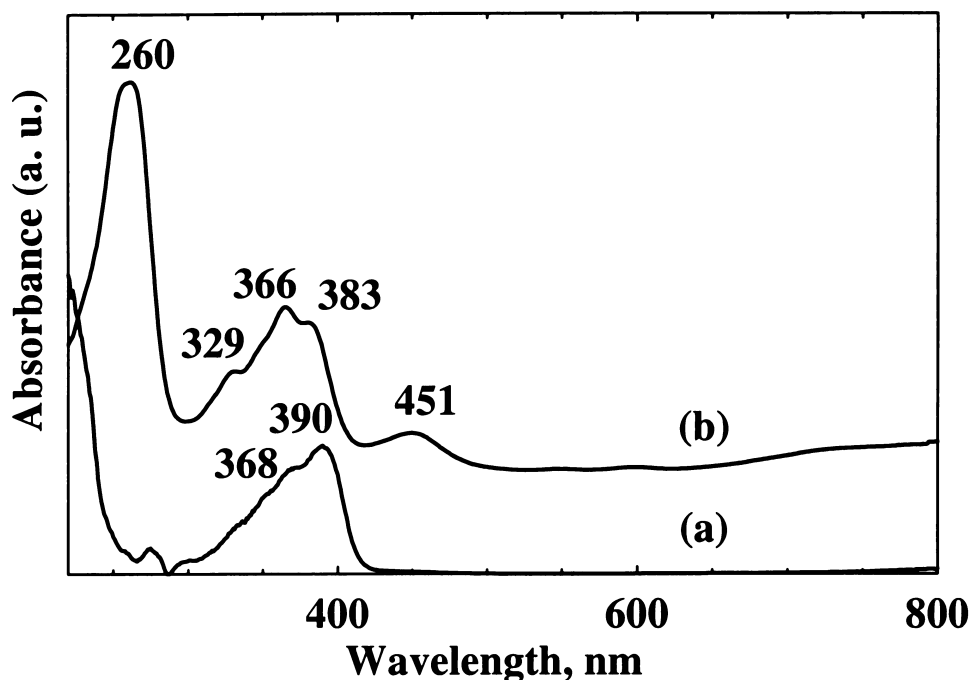
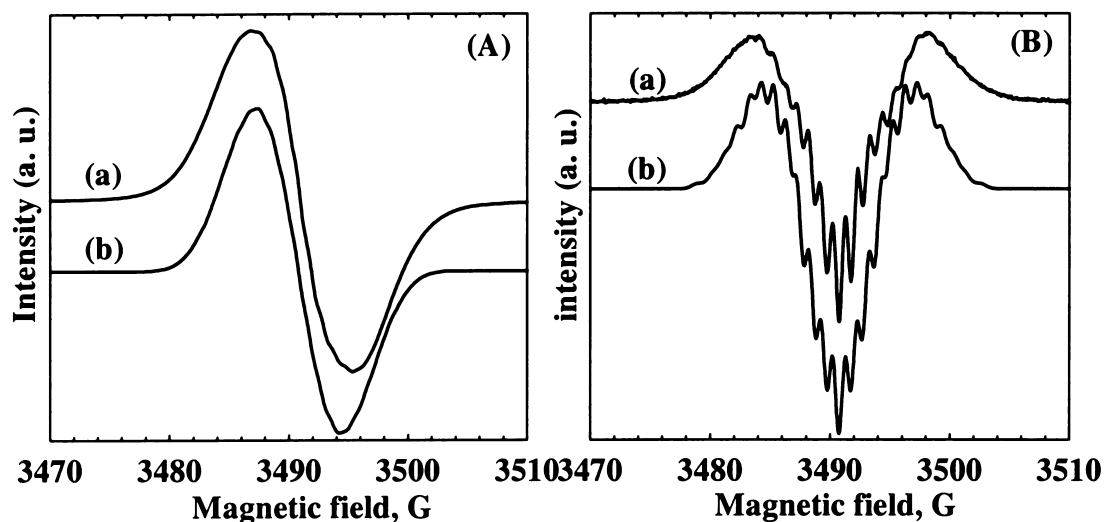


Figure 6.13: DR-UV-Vis spectra of DMA[2] in (a) Si-MCM-41 and (b) Al-MCM(39).

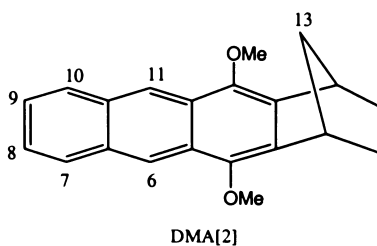
Figure 6.13 shows the DR-UV-Vis spectra of DMA[2] loaded into the Si-MCM-41 and the Al-MCM(39) with  $\text{CH}_2\text{Cl}_2$  as solvent, using method A2. In Si-MCM-41 (Figure 6.13 (a)), the DMA[2] exhibits absorption with maximum at 390 nm and a shoulder at ca. 368 nm, which are assigned to the neutral DMA[2] according to the reports for the analogous molecules. In Al-MCM(39) (Figure 6.13 (b)), these two absorption bands are shifted to 383 and 366 nm, respectively, accompanied by the changes of the relative peak intensities. The peak at 329 nm may also be due to the absorption of the neutral DMA[2] which is overlapped with the shoulder peak at 368 nm presented in Figure 6.13 (a). Two new pronounced absorption bands with maxima at 260 and 451 nm are assigned to the characteristic absorption bands of the DMA[2] radical cation according to the observation of the DMA[2] radical cation signals in the EPR study.

### 6.6.2. EPR Spectra of DMA[2] in (Al)-MCM-41



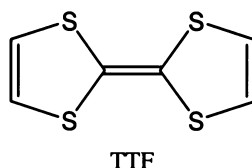
**Figure 6.14:** First derivative (A) and second derivative (B) EPR spectra (room temperature) of DMA[2] in Al-MCM(15). In each figure, curves (a) are the experimental spectra; and curves (b) are the computer simulated spectra.

No EPR radical signal was detected when DMA[2] was assembled into the MCM-41 with  $\text{CH}_2\text{Cl}_2$  as solvent, using method A1 and A2. However, the DMA[2] radical cation was generated spontaneously with the same loading methods in the Al-MCM-41 host. Generally, the color of the sample was pale yellow. The first and second derivative EPR spectra of the DMA radical cation formed in the Al-MCM(15) are shown in Figure 6.14 (A-a) and Figure 6.14 (B-a), respectively. The observed EPR spectra can be simulated using the following EPR parameters:  $a(6\text{H}, \text{OCH}_3) = 2.0 \text{ G}$ ,  $a(2\text{H}, 6,11) = 2.75 \text{ G}$ ,  $a(2\text{H}, 8,9) = 1.0 \text{ G}$ ,  $a(2\text{H}, 7,10) = 1.15 \text{ G}$ ;  $g \text{ value} = 2.00503$ ,  $\text{linewidth} = 1.22 \text{ G}$ . The simulated first and second derivative spectra are shown in Figure 6.14 as curve (A-b) and curve (B-b). Note that in this case also no  $^{27}\text{Al}$  hyperfine splitting is present.



## 6.7. TTF derivatives in (Al)-MCM-41

TTF ( $E^1_{1/2} = 0.37$  V;  $E^2_{1/2} = 0.67$  V) was first synthesized by Wudl et al. in 1970.<sup>25</sup> The first “organic metal” TTF-TCNQ<sup>26,27</sup> and the first molecular based superconductor  $[\text{TMTSF}]_2\text{X}$  ( $\text{X} = \text{PF}_6^-$ ,  $\text{AsF}_6^-$ )<sup>28,29</sup> were successively discovered. In the last three decades, various kinds of TTF derivatives have been synthesized in order to improve the electron donating power of the TTF analogues.<sup>30</sup> Since MCM-41 materials can act as electron acceptors as well as provide a polar and electrostatic microconfinement, it is interesting to know the properties of the TTF derivatives assembled inside the MCM-41, aiming at developing the nanoscale electronic conductors. In this respect, Hoekstra et. al.<sup>31</sup> reported that TTF could be encapsulated into the Si-MCM-41. The encapsulated TTF was influenced by the acidity of the host surface. In this work, three TTF derivatives, i.e., BEDT-TTF,  $\text{TTC}_1$ -TTF and TBT-TTF were assembled into the (Al)-MCM-41 hosts. The behaviours of these molecules in the (Al)-MCM-41 hosts were monitored by means of DR-UV-Vis and EPR spectroscopy.



### 6.7.1. DR-UV-Vis spectra of $\text{TTC}_1$ -TTF in (Al)-MCM-41

The UV-Vis spectrum of the  $\text{TTC}_1$ -TTF (Figure 6.15 (a)) displays absorption with maxima at 314 and 333nm, respectively, which are the characteristic absorption bands for the TTF derivatives.<sup>32-35</sup> The absorption at ca. 380 nm with a long tail to ca. 500 nm is due to the formation of the  $\text{TTC}_1$ -TTF radical cation.<sup>36</sup> The DR-UV-Vis spectrum of  $\text{TTC}_1$ -TTF in Si-MCM-41 (Figure 6.15 (b)) is basically identical to the UV-Vis

spectrum in  $\text{CH}_2\text{Cl}_2$  solution. When  $\text{TTC}_1\text{-TTF}$  was loaded into the Al-MCM(39) with  $\text{CH}_2\text{Cl}_2$  as solvent, using method A2 (Figure 6.15 (c)) and B2 (Figure 6.15 (d)), the spectra show a sharp band at 557 nm and 900 nm. The latter band is extremely broad in the range of 750-1100 nm which can be assigned to the charge transfer (CT) band of the  $\text{TTC}_1\text{-TTF/Al-MCM(39)}$ .<sup>34</sup> The absorption at 557 nm is assigned to the  $\text{TTC}_1\text{-TTF}$  dication.<sup>33,36</sup> These assignments are confirmed by the DR-UV-Vis spectra of the organic conducting thiophene oligomers in ZSM-5 which showed absorption peaks due to the cation radicals (polarons) in the region near 530 nm with a systematic bathochromic shift with increasing methyl substitution and a sharp slightly structured band between 800-900 nm due to the formation of the dications (bipolarons).<sup>37</sup>

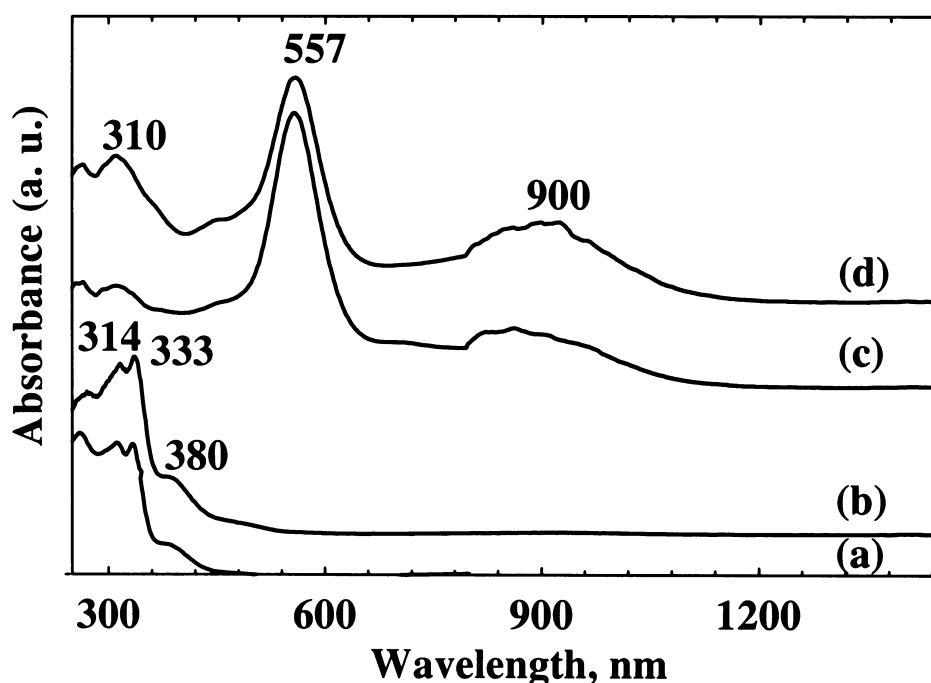


**Figure 6.15:** UV-Vis spectra of  $\text{TTC}_1\text{-TTF}$  in DM solution ( $\sim 10^{-6}$  M) (a) and DR-UV-Vis spectra of  $\text{TTC}_1\text{-TTF}$  loaded into (a) the Si-MCM-41 with  $\text{CH}_2\text{Cl}_2$  as solvent, using method A2, (c) the Al-MCM(39) with  $\text{CH}_2\text{Cl}_2$  as solvent, using method A2, and (d) the Al-MCM(39) with  $\text{CH}_2\text{Cl}_2$  as solvent, using method B2.



### 6.7.2. EPR Study of TTC<sub>1</sub>-TTF in (Al)-MCM-41

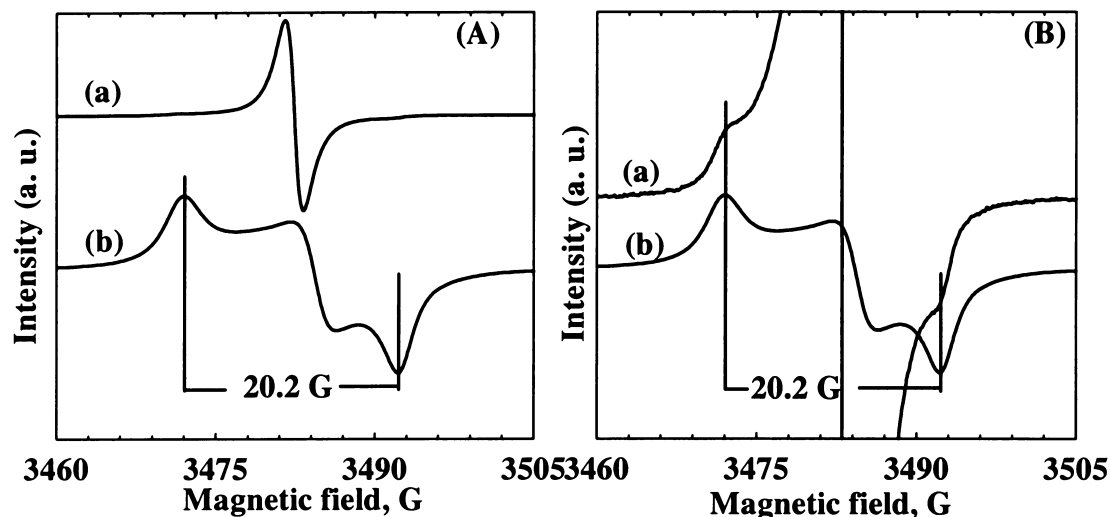


**Figure 6.16:** First-derivative EPR spectra (room temperature) of TTC<sub>1</sub>-TTF in Al-MCM(39) (A). TTC<sub>1</sub>-TTF was loaded with CH<sub>2</sub>Cl<sub>2</sub> as solvent, using method A2. Curve (a) is the initial spectrum and curve (b) is the spectrum after 1 week. In figure (B), the spectrum (a) was magnified to show the hyperfine structure of the species II.

Unlike 9,10-DMA, relatively weak EPR paramagnetic signals were detected when TTC<sub>1</sub>-TTF was loaded into the Si-MCM-41 and the post-synthesized Al-MCM-41 with CH<sub>2</sub>Cl<sub>2</sub> as solvent, using method A1 and A2 in the dry box. This is due to the formation of the TTC<sub>1</sub>-TTF radical cation, evidenced by the DR-UV-Vis spectrum. When TTC<sub>1</sub>-TTF was loaded into the Al-MCM-41 using method A1 and A2, strong EPR signals were detected. Figure 6.16 shows the EPR spectra of the TTC<sub>1</sub>-TTF in Al-MCM(39) as a typical example. Two paramagnetic species were observed. One (species I) possesses a narrow line with  $g$  value = 2.01 and linewidth ca. 1.2 G. The other one (species II) displays a broad peak-to-peak distance of ca. 20.2 G. The intensity ratio between these two species is 100: 3. After 1 week, the EPR intensity of the species I decreased dramatically and the species II was enhanced. Species II is quite similar to the previous

report for the EPR spectrum of the transformation state of the  $\kappa$ -(BEDT-TTF)<sub>2</sub>Cu[N(CN)<sub>2</sub>]<sub>2</sub>Br salt after annealing and quenching cycles at low temperature (4.2 K)<sup>38</sup>

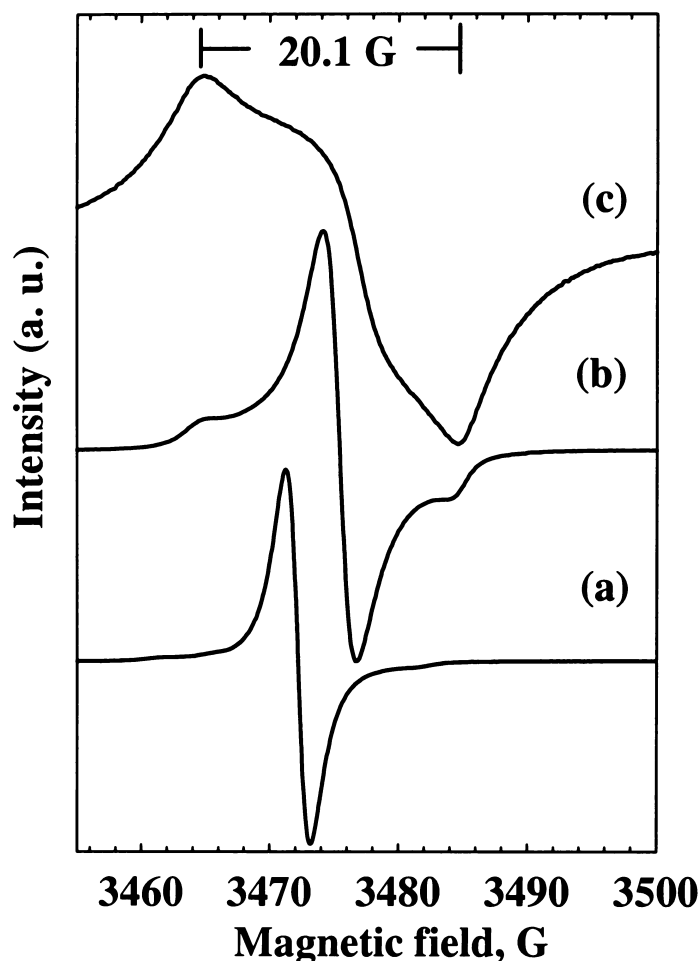


**Figure 6.17:** First-derivative EPR spectra (room temperature) of TTC<sub>1</sub>-TTF assembled into the Al-MCM(39) with CH<sub>2</sub>Cl<sub>2</sub> as solvent, using method B2: (a) initial EPR spectrum; (b) after evacuation for 10 min; (c) after evacuation for 18 hr.

The possible assignment of the species II to the superoxide ion was ruled out by an experiment in the complete absence of oxygen where the TTC<sub>1</sub>-TTF was loaded into the Al-MCM(39) using method B2. The initial EPR spectrum (Figure 6.17 (a)) (*g* value = 2.01) is identical to that when TTC<sub>1</sub>-TTF was loaded in a dry box (Figure 6.16 (a)). The intensity ratio between species I and species II is ca. 50:1. Evacuation of the sample

for 10 min gave the spectrum (b) whose central line shifted to higher field. Analysis of this spectrum shows that the intensity ratio between species I and species II is ca. 9:1. The increase of the intensity of the species II cannot be accounted by the decay of the intensity of the species I only, since the intensity of the species I decreased ca. 3 times while the intensity of the species II increased ca. 3 times. Apparently, transformation of the species I to species II does occur during evacuation. Further evacuation of the sample for 18 hr gave the spectrum (c) with peak to peak width of ca. 20.2 G, which is the characteristic EPR spectrum of species II. Transformation between these two species may be due to stronger interaction of the  $\text{TTC}_1\text{-TTF}$  with the electron acceptor sites in Al-MCM-41 after removal of the solvent by evacuation.

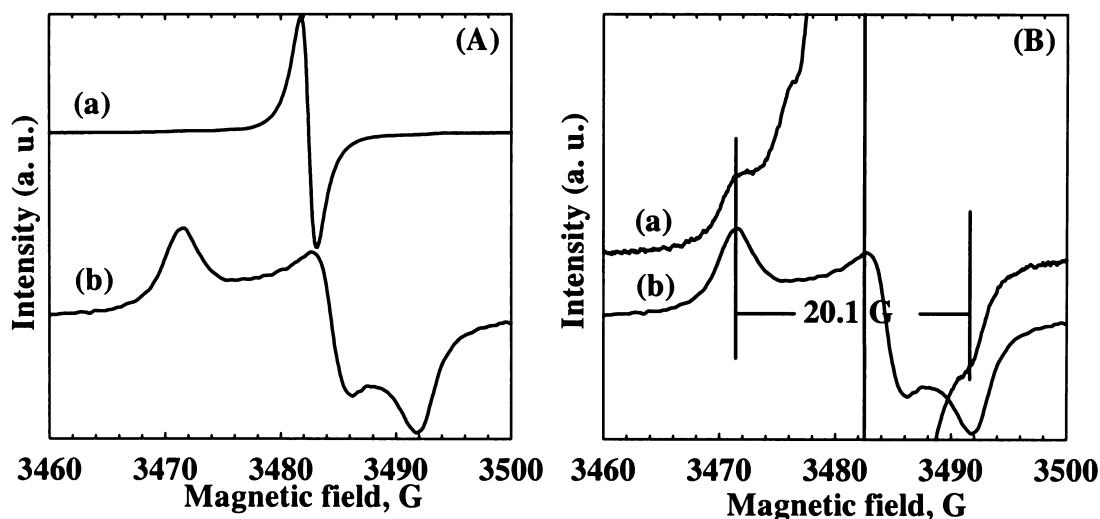


**Figure 6.18:** EPR spectra (room temperature) of TBT-TTF in Al-MCM(39) (A). TBT-TTF was loaded with  $\text{CH}_2\text{Cl}_2$  as solvent, using method A2. Curve (a) is the spectrum initial spectrum and curve (b) is the spectrum after 1 week. In figure (B), the spectrum (a) was magnified to show the hyperfine structure of the species II.

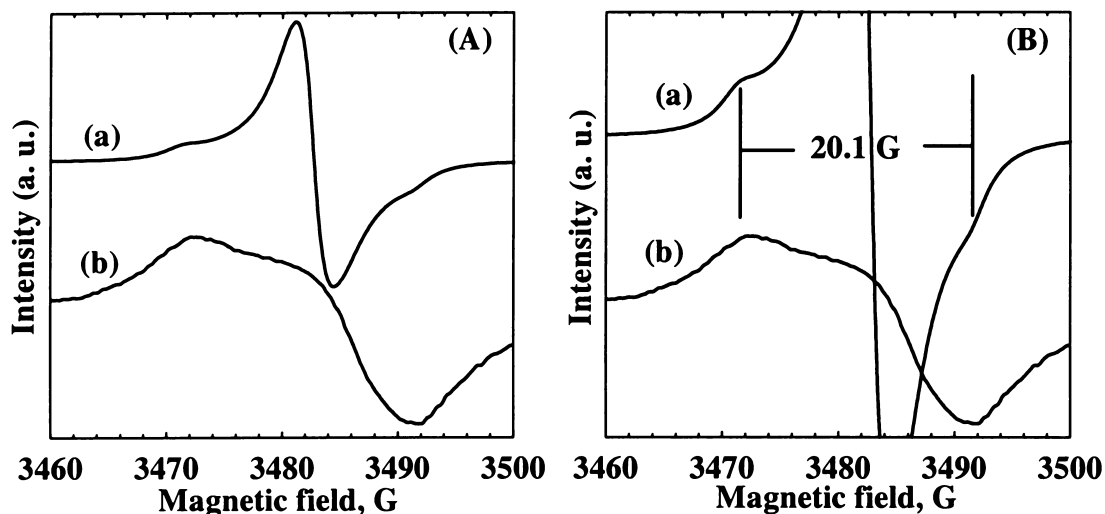


**Figure 6.19:** EPR spectra (room temperature) of BEDT-TTF in Al-MCM(39) (A). BEDT-TTF was loaded with  $\text{CH}_2\text{Cl}_2$  as solvent, using method A2. Curve (a) is the spectrum initial spectrum and curve (b) is the spectrum after 1 week. In figure (B), the spectrum (a) was magnified to show the hyperfine structure of the species II.

The EPR spectra of the other two molecules, BEDT-TTF and  $\text{TTC}_1\text{-TTF}$ , are also shown in Figure 6.19 and Figure 6.20. Two different species were also detected when these two molecules were assembled into the (Al)-MCM-41 hosts.

## 6.8. Other Molecules

Naphthalene and anthracene were also assembled into the (Al)-MCM-41. These two molecules do not spontaneously give the corresponding radical cations in the EPR study. No detection of the naphthalene radical cation may be due to its high oxidation potential. However, anthracene has lower oxidation potential than the DMN and DMA compounds which form the corresponding radical cations. The different behavior of anthracene may be due to its lack of the functional groups, which causes it to weakly

interact with the electron acceptor sites (Lewis acid sites) or be loosely adsorbed on the surface of the Al-MCM-41.

**Table 6.4: Oxidation potentials of the electron donors used as electron probes in this work**

Compound	Literature	Refere nce	This work	No IR <sup>a</sup>	IR <sup>b</sup>
	E <sub>1/2</sub> <sup>ox</sup> (V) (solvent, ref. electrode)		E <sub>1/2</sub> <sup>ox</sup> (V) (CH <sub>3</sub> CN, Ag/AgCl)		
TBT-TTF	—	—	0.47 (E <sub>1/2</sub> <sup>1</sup> ) 0.74 (E <sub>1/2</sub> <sup>2</sup> )	Yes	—
TTC1-TTF	0.47 (E <sub>1/2</sub> <sup>1</sup> , CH <sub>3</sub> CN, SCE <sup>f</sup> ), 0.71 (E <sub>1/2</sub> <sup>2</sup> , CH <sub>3</sub> CN, SCE)	<sup>44</sup>	0.48 (E <sub>1/2</sub> <sup>1</sup> ) 0.75 (E <sub>1/2</sub> <sup>2</sup> )	Yes	—
BED-TTF	0.524 (E <sub>1/2</sub> <sup>1</sup> ); 0.906 (E <sub>1/2</sub> <sup>2</sup> ) (CH <sub>2</sub> Cl <sub>2</sub> , SCE)	<sup>45</sup>	0.53 (E <sub>1/2</sub> <sup>1</sup> ) 0.83 (E <sub>1/2</sub> <sup>2</sup> )	Yes	—
	0.60 (E <sub>1/2</sub> <sup>1</sup> ); 1.0 (E <sub>1/2</sub> <sup>2</sup> ) (CH <sub>3</sub> CN, SCE)	<sup>46</sup>			
	0.567±0.027 (E <sub>1/2</sub> <sup>1</sup> ); 0.829 ± 0.50 (E <sub>1/2</sub> <sup>2</sup> ) (CH <sub>3</sub> CN, Ag/AgCl)	<sup>47</sup>			
Anthracene	1.09 (CH <sub>3</sub> CN, SCE)	<sup>48</sup>	1.06	No	—
DMA[2]	—	—	1.07	Yes	—
1,4-DMN	1.10 (CH <sub>3</sub> CN, Pt)	<sup>44</sup>	1.11	Yes	— <sup>d</sup>
	1.10 (CH <sub>3</sub> CN, SCE)				
1,4-DMN[2]	1.10 (CH <sub>3</sub> CN, Ag/AgCl)	<sup>17</sup>	1.11	Yes	Yes
1,4-DMN[4]	1.10 ± 0.03 (CH <sub>3</sub> CN, SCE)	<sup>16</sup>	1.11	Yes	Yes
9,10-DMA	1.18 (CH <sub>3</sub> CN, Pt)	<sup>44</sup>	1.18	Yes	—
	0.90 (CH <sub>3</sub> CN, SCE)	<sup>49</sup>			
1,4-DMB	1.34 (CH <sub>3</sub> CN, Pt)	<sup>44</sup>	1.34	No <sup>c</sup>	Yes <sup>e</sup>
	1.34 (CH <sub>3</sub> CN, SCE)	<sup>48,50</sup>			
Naphthalene	1.54 (CH <sub>3</sub> CN, SCE)	<sup>48</sup>	1.69	No	—
	1.70 (CH <sub>3</sub> CN, SCE)				
	1.18 (CH <sub>3</sub> CN, SCE)	<sup>49</sup>			

Notes: (a) The sample was not irradiated. (b) The sample was irradiated. (c) Radical cation was formed. (d) Not available. (e) No radical cation was formed. (f) SCE = Saturated calomel electrode.

## 6.9. Electron Accepting Ability of Al-MCM-41

The half wave oxidation potentials of the electron donor molecules were determined experimentally, because the reported values under different experimental conditions

showed discrepancies. The experimental and the literature oxidation potential values of the electron donor molecules studied in this work are tabulated in Table 5.9.

The reduction potential of the Al-MCM-41 is determined as described in Section 5.9 using the following well-known equation in solution:

$$\Delta G = E_{1/2}^{\text{Ox}} - E_{1/2}^{\text{Red}} - \Delta E_{00}^*$$

where  $\Delta G$  is the Gibbs energy change;  $E_{1/2}^{\text{Ox}}$  is the oxidation potential of the electron donor molecules;  $E_{1/2}^{\text{Red}}$  is the reduction potential of the Al-MCM-41; and the  $\Delta E_{00}^*$  is the energy level of the excited states (singlet and triplet excited states). The value of  $\Delta E_{00}^*$  is taken as zero since the used oxidation potentials of the electron donor molecules for calculation are those spontaneously formed radical cations.

Since the Al-MCM-41 can oxidize the 9,10-DMA but cannot oxidize the 1,4-DMB spontaneously, the reduction potential of the Al-MCM-41 can be estimated to be in the following range:

$$1.34 \text{ V} \geq E^{\text{Red}}(\text{Al-MCM-41}) \geq 1.18 \text{ V}$$

The reduction potential of Na ZSM-5 was estimated to be close to 1.6 eV (vs SCE) from the fact that trans-carbomethoxystilbene ( $E_0^{\text{Ox}} = 1.65 \text{ V vs SCE}$ ) was not oxidized, while the related trans-4-substituted-stilbenes with methoxy, dimethylamino, methyl, and chloro as the substituents ( $E_0^{\text{Ox}} < 1.6 \text{ V}$ ) were all readily oxidized under the same conditions.<sup>39-43</sup> The calculated reduction potential for the Al-MCM-41 is much smaller than the estimated value for the Na-ZSM-5, indicating that Al-MCM-41 has less electron accepting power than the Na-ZSM-5 does.

## 6.10. Summary

In summary, Various kinds of electron donor molecules were used as electron probe molecules to explore the electron acceptor sites in Al-MCM-41 by means of EPR, DR-UV-Vis and FTIR spectroscopy. The following are the summaries of the results and findings in this chapter:

- (1) Several methods (A1, A2 and B2) for assembling the organic molecules into the Al-MCM-41 have been explored.
- (2) Pure MCM-41 has no electron accepting ability at room temperature, indicating that it has no (or rather weak) electron acceptor sites at room temperature.
- (3) Extra-framework Al plays an important role in generating electron acceptor sites in the Al-MCM-41 samples.
- (4) The electron acceptor sites are assigned to the Lewis acid sites (extra-framework  $\text{Al}^{3+}$ ) generated by the dealumination during template removal by thermal calcination. However, no quantitative correlation between the probed electron acceptor sites and the extra-framework Al has been established based on the present data. Formation of the long-lived radical cations of the donors may be explained as follows: the donor molecules formed charge transfer complex with the Lewis acid sites. Further electron transfer to the Al-MCM-41 host may leave stable  $\text{D}^{•+}/\text{Al}$  form.
- (5) TTF derivatives exist in two phases in Al-MCM-41.
- (6) The reduction potential of the Al-MCM-41 is determined to be in the range  $1.18 \text{ V} \leq E^{\text{Red}}(\text{Al-MCM-41}) \leq 1.34 \text{ V}$ .

## 6.11. References for Chapter 6

- (1) Forbes, W. F.; Sullivan, P. D. *Can. J. Chem.* **1966**, *44*, 1501.
- (2) Tajima, S.; Tobita, S.; Shizuka, H. *J. Phys. Chem. A* **1999**, *103*, 6097.
- (3) O'Neill, P.; Steenken, S.; Schulte-Frohlinde, D. *J. Phys. Chem.* **1975**, *79*, 2773.
- (4) Grabner, G.; Monti, S.; Marconi, G.; Mayer, B.; Klein, C.; Köhler, G. *J. Phys. Chem.* **1996**, *100*, 20068.
- (5) Grabner, G.; Rauscher, W.; Zechner, J.; Getoff, N. *J. Chem. Soc., Chem. Commun.* **1980**, 222.
- (6) Zweig, A.; Hodgson, W. G.; Jura, W. H. *J. Am. Chem. Soc.* **1964**, *86*, 4124.
- (7) Forbes, W. F.; Sullivan, P. D.; Wang, H. M. *J. Am. Chem. Soc.* **1967**, *89*, 2705.
- (8) Sullivan, P. D. *J. Phys. Chem.* **1970**, *74*, 2563.
- (9) Samoilova, R. I.; Astashkin, A. V.; Dikanov, S. A.; Goldfarb, D.; Lunina, E. V. *Colloids Surf. A: Physicochem. Eng. Aspects* **1993**, *72*, 29.
- (10) Astashkin, A. V.; Samoilova, R. I. *Zeolites* **1991**, *11*, 282.
- (11) Samoilova, R. I.; Shubin, A. A.; Bowman, M. K.; Hüttermann, J.; Dikanov, S. *A. Chem. Phys. Lett.* **2000**, *316*, 404.
- (12) Davies, A. G.; Courtneidge, J. *Acc. Chem. Res.* **1987**, *20*, 90.
- (13) Davies, A. G.; Ng, K.-M. *Aust. J. Chem.* **1995**, *48*, 167.
- (14) Davies, A. G. *Chem. Soc. Rev.* **1993**, *22*, 299.
- (15) Handoo, K. L.; Gadru, K. *Curr. Sci.* **1986**, *55*, 920.
- (16) Oevering, H.; Paddon-Row, M. N.; Heppener, M.; Oliver, A. M.; Cotsaris, E.; Verhoeven, J. W.; Hush, N. S. *J. Am. Chem. Soc.* **1987**, *109*, 3258.
- (17) Warman, J. M.; Hom, M.; Paddon-Row, M. N.; Oliver, A. M.; Kroon, J. *Chem. Phys. Lett.* **1990**, *172*, 114.
- (18) Roest, M. R.; Verhoeven, J. W.; Schuddeboom, W.; Warman, J. M.; Lawson, J. M.; Paddon-Row, M. N. *J. Am. Chem. Soc.* **1996**, *118*, 1762.
- (19) Roest, M. R.; Lawson, J. M.; Paddon-Row, M. N.; Verhoeven, J. W. *Chem. Phys. Lett.* **1994**, *230*, 536.
- (20) Takahashi, Y.; Sankararaman, S.; Kochi, J. K. *J. Am. Chem. Soc.* **1989**, *111*, 2954.
- (21) Wallis, J. M.; Kochi, J. K. *J. Am. Chem. Soc.* **1988**, *110*, 8207.
- (22) Sankararaman, S.; Kochi, J. K. *J. Chem. Soc., Perkin Trans. 2* **1991**, 165.



- (23) Sehestad, K.; Holcman, J. *J. Phys. Chem.* **1978**, *82*, 651.
- (24) Sullivan, P. D. *J. Phys. Chem.* **1969**, *73*, 2790.
- (25) Wudl, F.; Smith, G. M.; Hufnagel, J. *J. Chem. Soc., Chem. Commun.* **1970**, 1453.
- (26) Ferraris, J.; Cowan, D. O.; Walatka, V. V.; Perlstein, J. H. *J. Am. Chem. Soc.* **1973**, *95*, 948.
- (27) Coleman, L. B.; Cohen, M. J.; Sandman, D. J.; Yamagishi, F. G.; Garito, A. F.; Heeger, A. J. *Solid State Commun.* **1973**, *12*, 1125.
- (28) Andrieux, A.; Duroure, C.; Jérôme, D.; Bechgaard, K. *J. Phys. Lett.* **1979**, *40*, 381.
- (29) Jérôme, D.; mazaud, A.; Ribault, M.; Bechgaard, K. *J. Phys. Lett.* **1980**, *41*, L195.
- (30) Segura, J. L.; Martín, N. *Angew. Chem. Int. Ed.* **2001**, *40*, 1372.
- (31) Hoekstra, K.; Bein, T. In *Book of Abstracts, 213th ACS National Meeting*; ACS, Washington, D. C.: San Francisco, **April 13-17, 1997**.
- (32) Bock, H.; Roth, B.; Schumaker, R. *Phosphorus and Sulfur* **1984**, *21*, 79.
- (33) Miguel, P. d.; Bryce, M. R.; Goldenberg, L. M.; Beeby, A.; Khodorkovsky, V.; Shapiro, L.; Niemz, A.; Cuello, A. O.; Rotello, V. *J. Mater. Chem.* **1998**, *8*, 71.
- (34) Bryce, M. R. *Adv. Mater.* **1999**, *11*, 11. And references therein.
- (35) Baetz, C.; Ehrenberg, H.; Fuess, H. *Phys. Chem. Chem. Phys.* **2000**, *2*, 5764.
- (36) Torrance, J. B.; Scott, B. A.; Welber, B.; Kaufman, F. B.; Seiden, P. E. *Phys. Rev. B* **1979**, *19*, 730.
- (37) Caspar, J. V.; Ramamurthy, V.; Corbin, D. R. *J. Am. Chem. Soc.* **1991**, *113*, 600.
- (38) Tanata, M. A.; Ishiguro, T. *Phys. Rev. B* **2000**, *61*, 3278.
- (39) Almgreen, M.; Thomas, J. K. *Photochem. Photobiol.* **1980**, *31*, 329.
- (40) Ebbeson, T. *J. Phys. Chem.* **1988**, *92*, 4581.
- (41) Goodman, J. L.; Peters, K. *J. Am. Chem. Soc.* **1985**, *107*, 6459.
- (42) Lewis, F. L.; Dykstra, R. E.; Gould, I. R.; Faird, S. *J. Phys. Chem.* **1988**, *92*, 7042.
- (43) Oelkrug, D.; Krabichler, G.; Honnen, W.; Wilkinson, F.; Willsher, C. J. *J. Phys. Chem.* **1988**, *92*, 3589.
- (44) Bard, A. J.; Lund, H. *Encyclopedia of Electrochemistry of the Elements (Organic Section)*; Marcel Dekker, Inc.: New York and Basel, **1984**.

- 
- (45) González, M.; Illescas, B.; Martín, N.; Segura, J. L.; Seoane, C.; Hanack, M. *Tetrahedron* **1998**, *54*, 2853.
- (46) Lichtenberger, D. L.; Johnston, R. L.; Hinkelmann, K.; Suzuki, T.; Wudl, F. J. *Am. Chem. Soc.* **1990**, *112*, 3302.
- (47) Papavassiliou, G. C. *Syn. Metal.* **1991**, *41-43*, 2535.
- (48) Murov, S. L.; Carmichael, I.; Hug, G. L. *Handbook of Photochemistry*; Marcel Dekker, Inc.: New York, Basel and Hong Kong, **1993**. p261.
- (49) Stevani, C. V.; Silva, S. M.; Badder, W. J. *Eur. J. Org. Chem.* **2000**, 4037.
- (50) Meites, L.; Zuman, P.; Scott, W. J.; Campbell, B. H.; Kardos, A. M.; Dubinsky, A.; Lampugnani, L.; Zuman, R. *Electrochemical Data (Part 1, Organic, Organometallic, and Biochemical Substances)*; John Wiley & Sons: New York, London, Sydney and Toronto, **1974**; Vol. A.

## Chapter 7

# Chemistry of Donor-Bridge-Acceptor Dyad Molecules in (Al)-MCM-41 Hosts

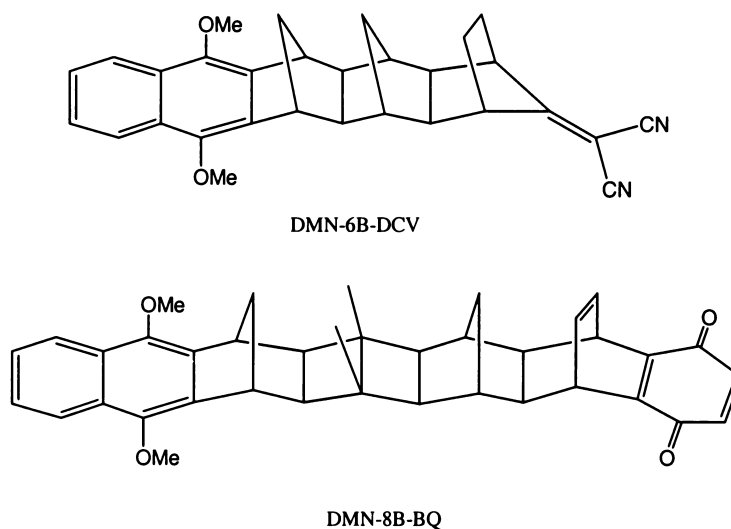
### 7.1. Introduction

Photoinduced charge separation in covalently linked rigid donor-bridge-acceptor (D-B-A) dyad occurs extremely rapidly, a result of electronic coupling mediated by a through-bond (TB) mechanism.<sup>1,2</sup> However, the lifetimes of the resulting charge-separated state are usually short in homogeneous solution (usually nanosecond or picosecond scales), which is also the consequence of the back electron transfer due to strong TB electronic coupling.<sup>1-12</sup>

Zeolites have proven to be highly amenable hosts for the heterogeneous photoinduced electron transfer reactions between redox pairs co-assembled within the zeolite channels, and/or at the zeolite surfaces.<sup>13</sup> Long-lived charge separated states of charge transfer complexes<sup>14-23</sup> or D-A molecules<sup>24-26</sup> in zeolites have been well documented. MCM-41 materials are zeotype one-dimensional hexagonal mesoporous molecular sieves with uniform pore size (30 Å). MCM-41 materials provide an intriguing prospect in host-guest chemistry due to their high surface area, large pore volume, and ordered mesoporous structures. Recent research shows that MCM-41 materials are promising host systems for photoredox reactions<sup>24,27-36</sup> to achieve long-lived photoinduced charge separation.

For the first time, Kuchi et al.<sup>37</sup> found that irradiation of the DMN-6B-DCV [donor = dimethoxynaphthalene (DMN); bridge = covalently linked 6 bond norbornylogous bridge (6B); acceptor = dicyanovinyl (DCV)] (structure is shown in Scheme 7.1) occluded inside

the channels of the Al-MCM-41 host (Si/Al 15, directly hydrothermally synthesized) led to the formation of a stable radical species with a lifetime of days. The observed radical species was tentatively attributed to the DCV radical anion of the dyad. It was found that the incorporated Al in the Al-MCM-41 host plays an important role in generating such a long-lived charge separated state. The many variations possible in this system, such as varying the Al content of the host, the pore size, the length of the hydrocarbon spacer and the redox properties of the dyad, provide intriguing opportunities to understand more fully and to control electron transfer processes in heterogeneous systems.



**Scheme 7.1:** Donor-bridge-acceptor dyads assembled into the (Al)-MCM-41 hosts.

In this chapter, the electron transfer processes of the DMN-6B-DCV dyad in the (Al)-MCM-41 hosts have been carefully examined. Furthermore, a new dyad DMN-8B-BQ [donor = dimethoxynaphthalene (DMN); bridge = 8 bond bridge (8B); acceptor = benzoquinone (BQ)] (see Scheme 7.1) was also assembled into the (Al)-MCM-41 hosts. The chemistry of these two dyads in the (Al)-MCM-41 hosts was studied using FTIR, DR-

UV-Vis and EPR spectroscopy. The electron transfer mechanism of the D-B-A molecules in (Al)-MCM-41 has been postulated.

## 7.2. DMN-6B-DCV in (Al)-MCM-41

### 7.2.1. FTIR spectra of DMN-6B-DCV in (Al)-MCM-41

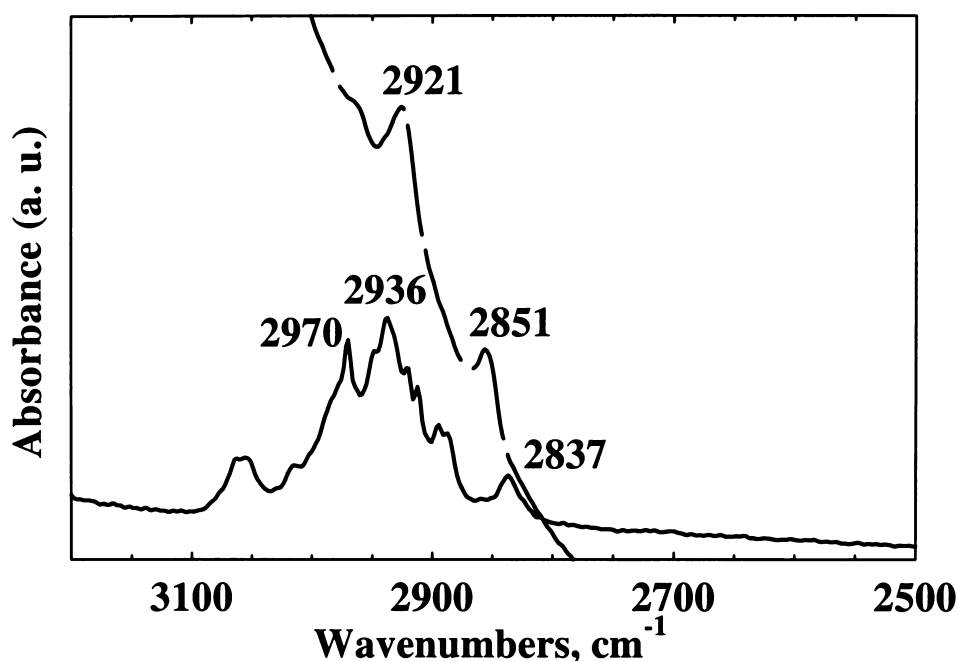
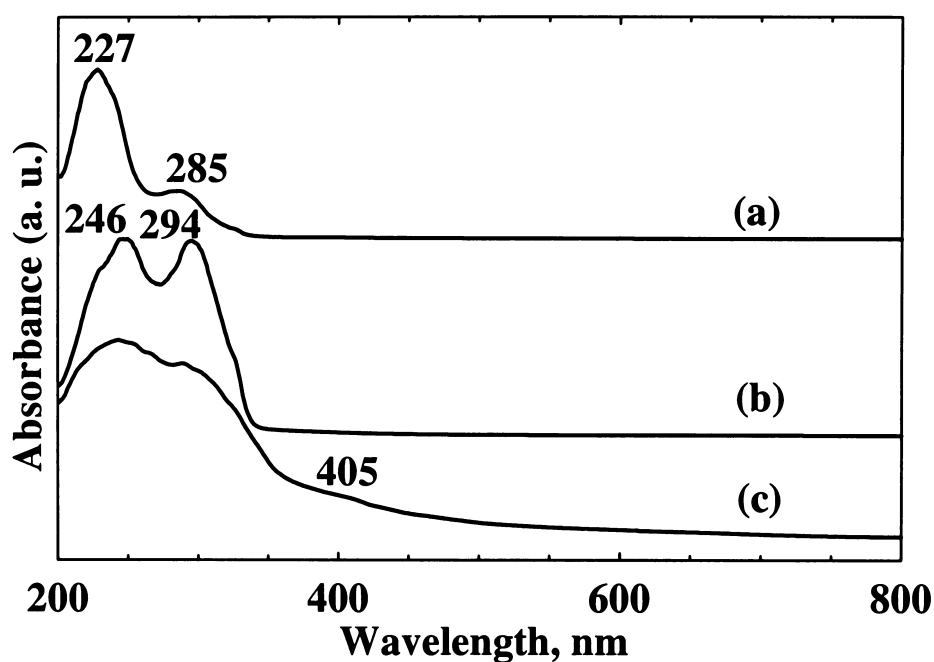


Figure 7.1. FTIR spectra of DMN-6B-DCV (solid line) and DMN-6B-DCV in Al-MCM(15).

The preliminary evidence that DMN-6B-DCV was assembled inside the channels of the (Al)-MCM-41 was obtained from the FTIR spectra shown in Figure 7.1. Pure DMN-6B-DCV (Figure 7.1 (a)) displays absorption bands at 2970, 2936 and 2837 cm<sup>-1</sup> respectively. The band at 2970 cm<sup>-1</sup> may be assigned to the CH stretching modes of the CH<sub>3</sub>O groups, and those at 2936 and 2837 cm<sup>-1</sup> to the symmetric and the asymmetric CH stretching modes of the CH<sub>2</sub> groups of the bridgeheads. In Al-MCM(15), these absorption bands are shifted

to 2963, 2921 and 2851  $\text{cm}^{-1}$ , respectively (Figure 7.1 (b)). The dramatic shifts of these bands demonstrate that both methoxy groups and the polynorbornane bridge DMN-6B-DCV molecules were strongly perturbed by the surface of the (Al)-MCM-41 (probably by the hydroxyl groups), indicating that the DMN-6B-DCV molecules were occluded inside the channels of the MCM-41. Apart from the CH stretching modes, other characteristic IR bands of DMN-6B-DCV were not discernible in the (Al)-MCM-41.

### 7.2.2. DR-UV-Vis Spectra of DMN-6B-DCV in (Al)-MCM-41



**Figure 7.2:** DR-UV-Vis spectra of DMN-6B-DCV in (a) Si-MCM-41, (b) Al-MCM(15), and (c) Al-MCM(15) after irradiation.

The DR-UV-Vis spectra of the DMN-6B-DCV assembled into the (Al)-MCM-41 (with  $\text{CH}_2\text{Cl}_2$  as solvent, using assembly method A2) are shown in Figure 7.2. In Si-MCM-41 (Figure 7.2 (a)), the neutral DMN-6B-DCV displays absorption bands with maxima at 227

and 285 nm. In Al-MCM(15) (Figure 7.2 (b)), these two bands are further shifted to the higher wavelength of 246 and 294 nm, respectively. Moreover, significant changes of the relative intensities of these two bands are also observed. Irradiation of the Al-MCM(15) sample assembled with DMN-6B-DCV gives a new broad band with maximum at ca. 405 nm with relatively weak intensity. This new band is assigned to the radical cation of the DMN group, the characteristic absorption of which was reported to be at ca. 400-410 nm.<sup>3-7,11</sup> The absorption due to the radical anion of the DCV group, which was reported to be at ca. 350 nm,<sup>7</sup> was not observed. The DR-UV-Vis spectroscopic study indicates that radical cation of DMN group was formed in the Al-MCM-41 hosts after irradiation.

### 7.2.3. EPR Study of DMN-6B-DCV in (Al)-MCM-41

#### 7.2.3.1. EPR Spectra of DMN<sup>•+</sup>-6B-DCV Radical Cation in Solution

In order to facilitate the identification and the interpretation of the EPR spectra of the DMN-6B-DCV radical species, DMN<sup>•+</sup>-6B-DCV radical cations were generated using the CF<sub>3</sub>COOH/CH<sub>2</sub>Cl<sub>2</sub>/DDQ method.<sup>38-41</sup> The spectrum (Figure 7.3 (a)) can be well simulated using the following EPR parameters: **a(6H, OCH<sub>3</sub>) = 2.434 G, a(2H, 2,5) = 1.642 G, a(2H, 3,4) = 0.784 G; g value = 2.0055; and linewidth = 0.40 G.** The simulated spectrum is shown in Figure 7.3 (b). It can be seen that the hydrogens on the hydrocarbon bridge are not involved in the hyperfine coupling with the DMN group in solution.

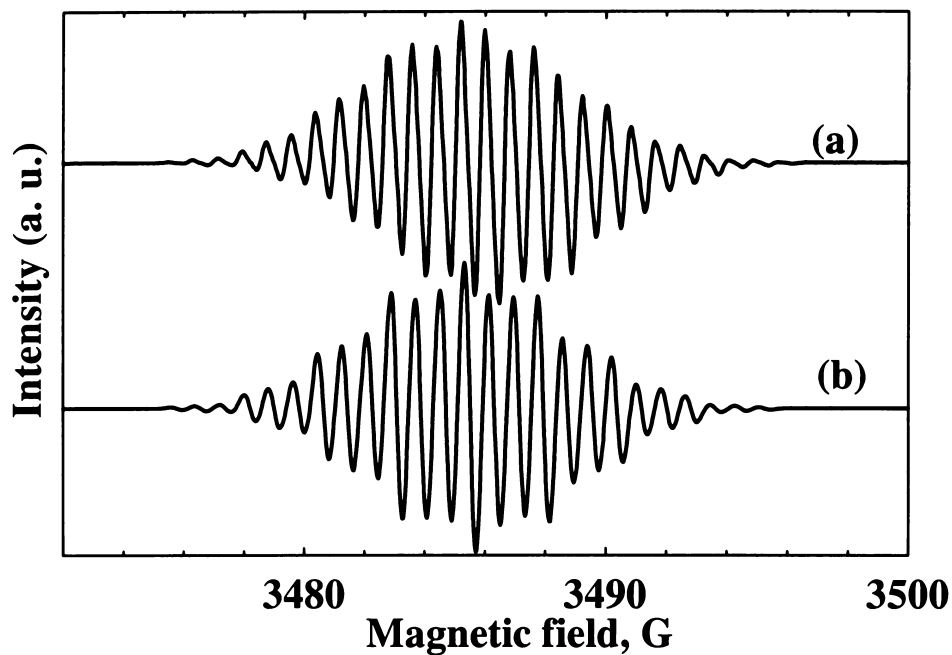
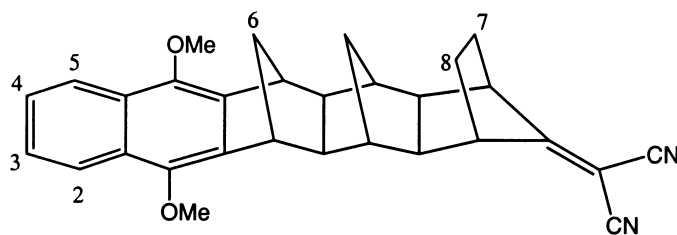


Figure 7.3. First derivative EPR spectra (room temperature) of (a)  $\text{DMN}^{+}\text{-6B-DCV}$  radical cation generated using the  $\text{CF}_3\text{COOH}/\text{CH}_2\text{Cl}_2/\text{DDQ}$  method and (b) computer simulation result.



Scheme 7.2: Number of atomic positions of DMN-6B-DCV (randomly assigned).

### 7.2.3.2. EPR Study of DMN-6B-DCV in Al-MCM-41

No EPR radical signal was observed when DMN-6B-DCV was assembled into the Si-MCM-41 or Al-MCM-41 with THF or  $\text{CH}_2\text{Cl}_2$  as solvent, using method A1 and A2. However, irradiation of the Al-MCM-41 samples assembled with DMN-6B-DCV ( $\text{CH}_2\text{Cl}_2$ ) gave radical signals. The color of the samples was green. As a typical example, the first and



the second derivative EPR spectra recorded for the DMN-6B-DCV assembled into the Al-MCM(15) with  $\text{CH}_2\text{Cl}_2$  as solvent, using method A1 are shown in Figure 7.4 (A-a) and (Figure 7.4 (B-a), respectively.

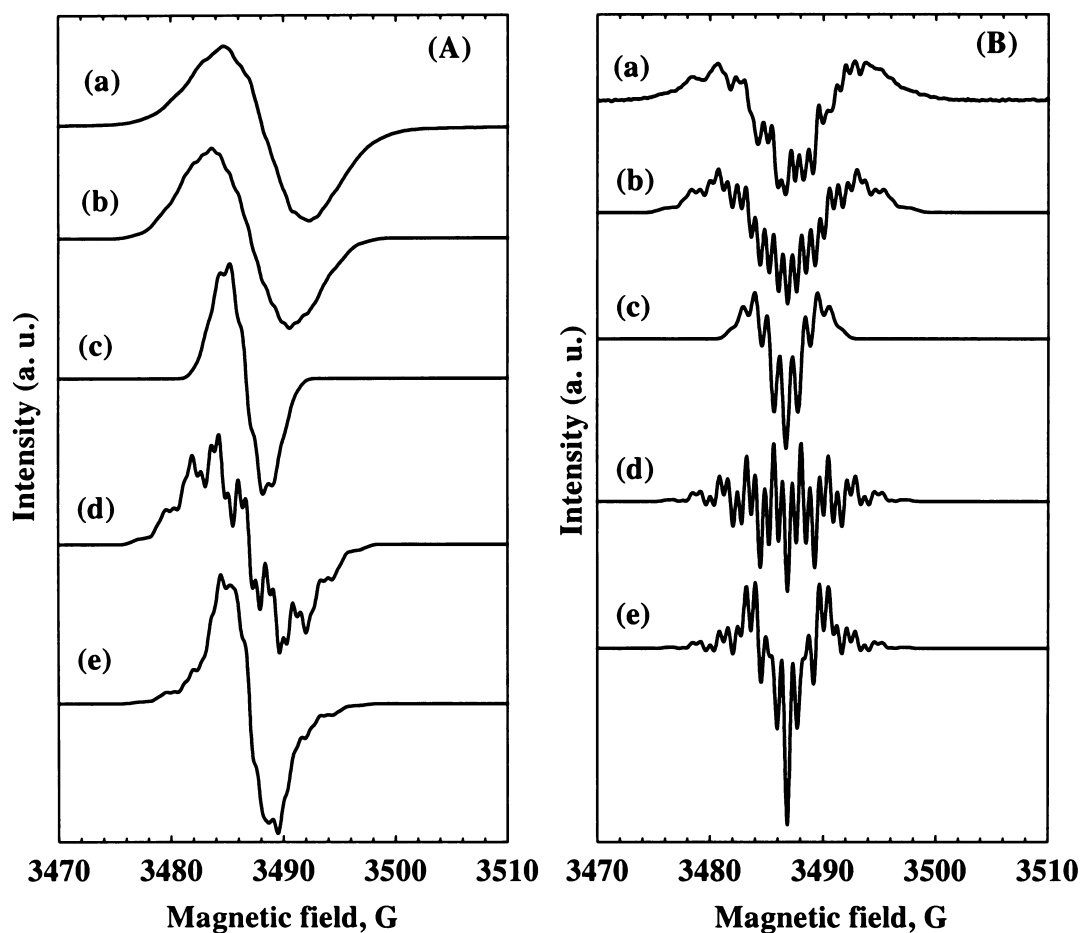
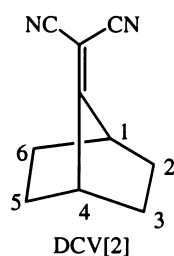


**Figure 7.4:** First (A) and second (B) derivative EPR spectra (room temperature) of DMN-6B-DCV in Al-MCM(15). DMN-6B-DCV was assembled into the Al-MCM(15) with  $\text{CH}_2\text{Cl}_2$  as solvent, using method A1. In each set: (a) experimental spectra; (b) simulated spectra for the radical cation of the DMN group which is complexed with the Al in the Al-MCM-41; (c) simulated spectra for the DCV radical anion; (d) simulated EPR spectra of the radical cation of the DMN group without including Al; (e) superimposed spectra of spectra (c) and (d).

To interpret the spectra, several models were considered and verified by computer simulation.

(1) Radical anion of the DCV group model. To determine the splitting constants of the radical anion of the DCV group, the gas phase hyperfine splitting constants of an analogous radical anion, dicyanovinylbornane (DCV[2]) radical anion, was kindly calculated and provided by Professor Michael N. Paddon-Row, UNSW, Australia. The detailed calculation method is the same as described in Section 6.4.2 in Chapter 6. Calculation results give the following hyperfine splitting constants:  $a(2^{14}\text{N}) = 1.0$  G,  $a(2\text{H}) = 1.06$  G,  $a(2\text{H}) = 2.38$  G,  $a(2\text{H}) = 1.2$  G,  $a(2\text{H}) = 0.87$  G,  $a(2\text{H}) = 0.15$  G. Based on these data, the EPR spectrum of the radical anion of the DCV group was simulated using the following EPR parameters: splitting constants of  $a(2^{14}\text{N}) = 1.0$  G,  $a(2\text{H}) = 1.2$  G,  $a(2\text{H}) = 0.87$  G;  $g$  value = 2.0052; and linewidth = 1.08 G. The simulated first and second derivative EPR spectra are shown in Figure 7.4 (A-c) and Figure 7.4 (B-c), respectively. Apparently, the experimental spectra are completely different from the simulated EPR spectra of the radical anion of the DCV group.



(2) Radical cation of the DMN group alone model. The EPR spectrum of the radical cation of the pure DMN group was simulated using the following EPR parameters: **splitting constants of (6H, OCH<sub>3</sub>) = 2.43 G,  $a(2\text{H}, 2,5) = 1.54$  G,  $a(2\text{H}, 3,4) = 0.784$  G,  $a(2\text{H}, 6,6) = 0.58$  G;  $g$  value = 2.0052; and linewidth = 0.80 G.** The simulated first and second derivative EPR spectra are shown in Figure 7.4 (A-d) and Figure 7.4 (B-d),

respectively. It can be seen that though some of the line positions match in the second derivative, the shape of the first and second derivative are different. Simulation also ruled out the DMN radical cation alone model.

(3)  $\text{DMN}^{\bullet+}$ -6B- $\text{DCV}^{\bullet-}$  charge separated state model. In this model, the radical signal of the  $\text{DMN}^{\bullet+}$  group and the  $\text{DCV}^{\bullet-}$  may be superimposed. Figure 7.4 (A-e) and Figure 7.4 (B-e) show the superimposed first and second derivative EPR spectra of the DMN radical cation (Figures 7.4 (c)) and the DCV radical anion (Figures 7.4 (d)) (1:1 ratio). Apparently, the experimental spectra cannot be interpreted with this mode.

(4) Complex of the radical cation of the DMN group with the Lewis acid sites of the Al-MCM-41 model. The EPR parameters used for simulation of this model are the same as those for the DMN radical cation (Figures 7.4 (d)), except that the Al hyperfine splitting constant (0.37 G) was added to the Hamiltonian EPR parameters. The simulated spectra are shown in Figure (7.4 (A-b)) and Figure (7.4 (B-b)), respectively. It can be seen that both the first and the second derivative EPR spectra approximately match the experimental ones, especially the shape of the first derivative and the line positions in the second derivative EPR spectrum. Computer simulation supports that the experimental spectra are due to the radical cation of the DMN group which was complexed with the Al species in the Al-MCM-41.

The above EPR signal persisted for several days if the sample was stored in the dry box. No quantitative relationship has been established between the Al content in the Al-MCM-41 hosts and the amount of the radical cations of the DMN group. The spin concentration results indicate that only ca. 4.5 % of the DMN-6B-DCV molecules are in the form of the long-lived  $\text{DMN}^{\bullet+}$ -6B-DCV radical cation species.

### 7.3. DMN-8B-BQ in (Al)-MCM-41

#### 7.3.1. DR-UV-Vis Spectrum of DMN-8B-BQ in Al-MCM-41

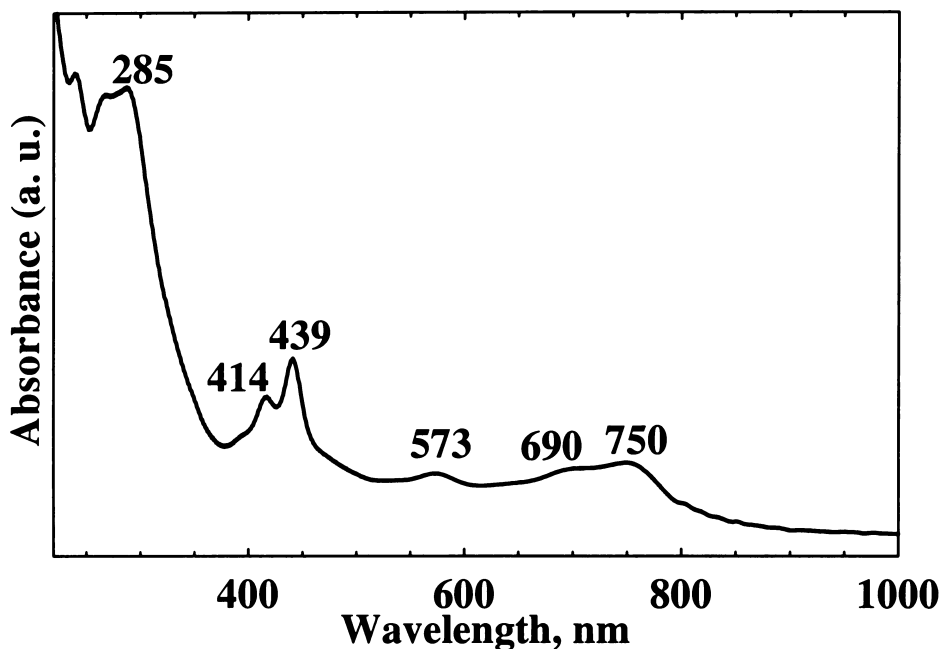


Figure 7.5: DR-UV-Vis spectra of DMN-8B-BQ in Al-MCM(15).

As a typical example, Figure 7.5 shows the DR-UV-Vis spectrum of the DMN-8B-BQ assembled into the Al-MCM(15) with  $\text{CH}_2\text{Cl}_2$  as solvent, using method A1. The characteristic absorption band of the neutral BQ in the MCM-41 host is in the range between 260–240 nm (see Section 5.4.2. in Chapter 5) and that of the neutral DMN[2] and DMN[4] is in the 290 nm region (see Section 6.4.2 in Chapter 6). Thus, the intense absorption band at ca. 285 nm in Figure 7.5 is tentatively assigned to the absorption band of the DMN group of the neutral DMN-8B-BQ. It is known that the DMN[2] and the DMN[4] radical cations display an absorption band at ca. 410 nm (See Section 6.4.2 in Chapter 6), <sup>3-</sup>

<sup>7,11</sup> whereas the 1,4-BQ radical anion has characteristic absorption bands at ca. 400 and 430 nm (see Table 5 in Chapter 5). In this case, the absorption bands with  $\lambda_{\max}$  at 414 and 439 nm are assigned to the radical anion of the BQ group. It is unlikely that the absorption band at 414 nm is due to the radical cation of the DMN group, though this assignment cannot be completely ruled out (wavelength matches). The broad absorption bands at 573, 690 and 750 nm are most probably the charge transfer bands of the BQ radical anion/Al-MCM-41 framework.<sup>42</sup>

### 7.3.2. EPR Study of DMN-8B-BQ in (Al)-MCM-41

No EPR radical signal was observed when DMN-8B-BQ was assembled into the Si-MCM-41 with THF as solvent, using method A1 and A2. Irradiation of the sample also gives no EPR radical signal. However, the sample assembled the DMN-8B-BQ into the Al-MCM-41 using the same method gives an EPR radical signal spontaneously. The color of the sample was green. As a typical example, Figure 7.5 (A-a) and Figure 7.5 (B-a) show the first and the second derivative EPR spectra recorded for the sample assembled the DMN-8B-BQ into the Al-MCM(15), respectively. Following models are considered for interpreting the spectra:

(1) BQ radical anion alone model. Based on the proton splitting constants of the BSQ radical anion (see Table 5.6 in Chapter 5), the EPR spectrum of the BQ radical anion was simulated using the following EPR parameters:  $a(4H) = 2.2$  G;  $g$  value = 2.0057; and linewidth = 1.10 G. The simulated spectra (first and second derivative) are shown in Figure 7.6 (A-d) (first derivative) and Figure 7.6 (B-d) (second derivative). Apparently, the experimental spectra cannot be explained using the BQ radical anion alone model.

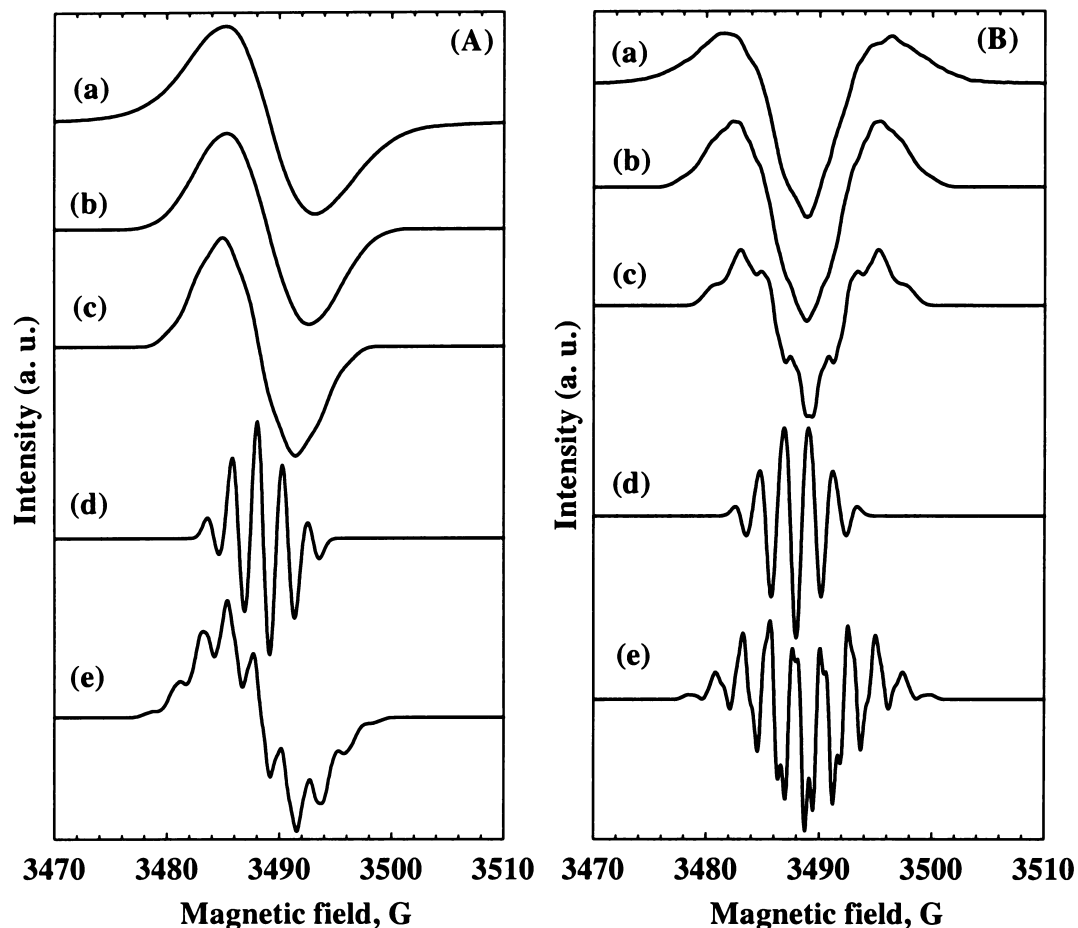
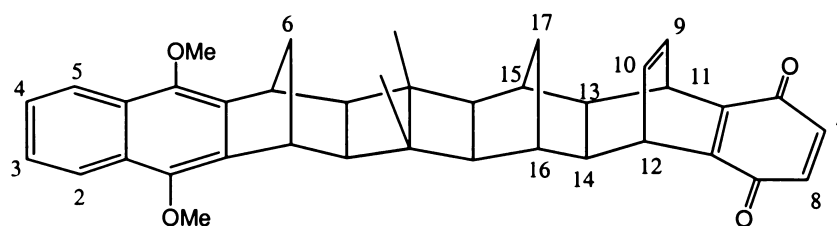


**Figure 7.6:** First (A) and second (B) derivative EPR spectra (room temperature) of DMN-8B-BQ in Al-MCM(15). In each set: (a) experimental spectra; (b) simulated spectra for the radical anion of the BQ group which is tightly bound with the Al in the Al-MCM-41; (c) simulated spectra for the BQ radical anion alone; (d) simulated EPR spectra of the radical cation of the DMN group without including Al; (e) superimposed spectra of spectra (c) and (d).



**Scheme 7.3:** Number of atomic positions (randomly assigned).

(2) Radical anion of the BQ group (bridged hydrogens involved in hyperfine coupling) without including Al model. Based on this model, the simulated first and second EPR spectra are shown in Figure 7.6 (A-c) and Figure (B-c), respectively. The simulation was carried out using the following EPR parameters: **splitting constants of  $a(6H, OCH_3) = 2.55$  G,  $a(2H, 2,5) = 1.6$  G,  $a(2H, 3,4) = 0.8$  G,  $a(1H, 6) = 1.0$  G,  $a(2H, 7,8) = 0.70$  G;  $g$  value = 2.0057; and linewidth = 1.15 G.** In this model, the simulated first derivative EPR spectrum looks similar to the experimental one, but the second derivative doesn't. In this case, complex of the radical cation of DMN group with the Lewis acid sites is ruled out.

(3)  $DMN^{\bullet+}8B-BQ^{\bullet-}$  charge separated state model. In this model, the radical signal of the  $DMN^{\bullet+}$  group and the  $BQ^{\bullet-}$  may be superimposed. Figure 7.6 (A-e) and Figure 7.4 (B-e) show the superimposed first and second derivative EPR spectra of the DMN radical cation (Figures 7.6 (c)) and the BQ radical anion (Figures 7.6 (d)) (1:1 ratio). Apparently, the experimental spectra cannot be interpreted with this mode.

(4) Tightly bound radical anion of the "BQ group / extra-framework Al of the Al-MCM-41" model. In this model, Al will be involved in the hyperfine coupling and affect the entire EPR spectra of the radical anion of the BQ group. It is also assumed that the unpaired electron can reach the other bridged hydrogens, instead of residing only on the BQ group. The EPR parameters used for simulation of this model are as follows: **splitting constants of  $a(Al) = 1.0$  G,  $a(4H,7,8,9,10) = 2.55$  G,  $a(2H, 11,12) = 1.6$  G,  $a(2H, 13,14) = 0.8$  G,  $a(1H, 17) = 1.0$  G,  $a(2H, 15,16) = 0.7$  G;  $g$  value = 2.0057; and linewidth = 1.15 G.** The simulated spectra are shown in Figure 7.6 (A-b) (first derivative) and Figure 7.6 (B-b) (second derivative). Both first and second derivative spectra match well, indicating that the

experimental spectra are due to the BQ radical anion, which is tightly bound to the extra-framework Al sites.

It is noteworthy that the above EPR signal was stable for several weeks if the sample was stored in the dry box. No quantitative relationship has been established between the Al content in the Al-MCM-41 hosts and the amounts of the radical anion of the BQ group. The spin concentration results indicate that only ca. 9.8 % of the DMN-8B-BQ molecules are in the form of the long-lived DMN-8B-BQ<sup>•-</sup> radical anion species.

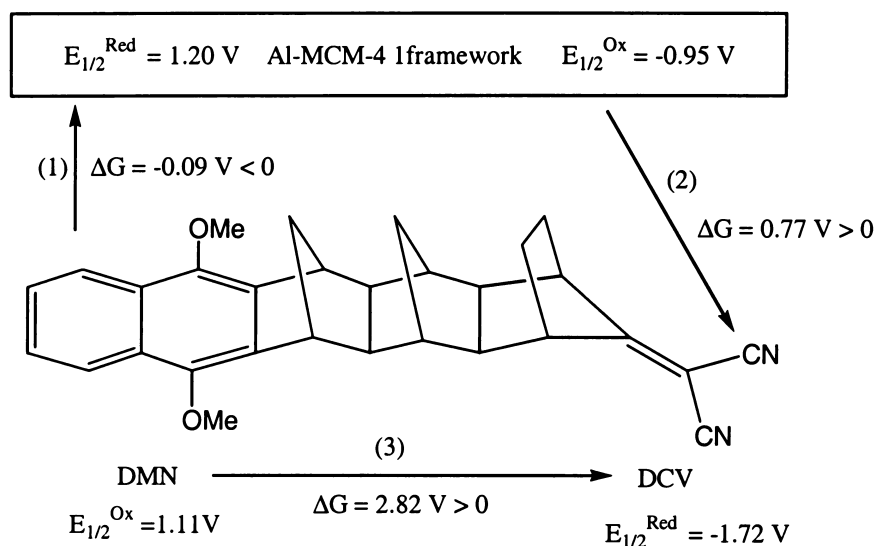
#### 7.4. Electron Transfer Mechanism of D-B-A Molecules in Al-MCM-41

To understand better the electron transfer processes of the D-B-A dyads (DMN-6B-DCV and DMN-8B-BQ) in the Al-MCM-41, the Gibbs free energy changes ( $\Delta G$ ) of each possible pathway have been shown in Scheme 7.4. To facilitate the explanation, the oxidation potential ( $E_{1/2}^{\text{Red}}$  (V) *versus*. Ag/AgCl, CH<sub>3</sub>CN) of the Al-MCM-41 host is given a value of -0.95 V, which is in the range determined in chapter 5; and the reduction potential of the Al-MCM-41 is given a value of 1.2 V, which is in the range determined in Chapter 6.

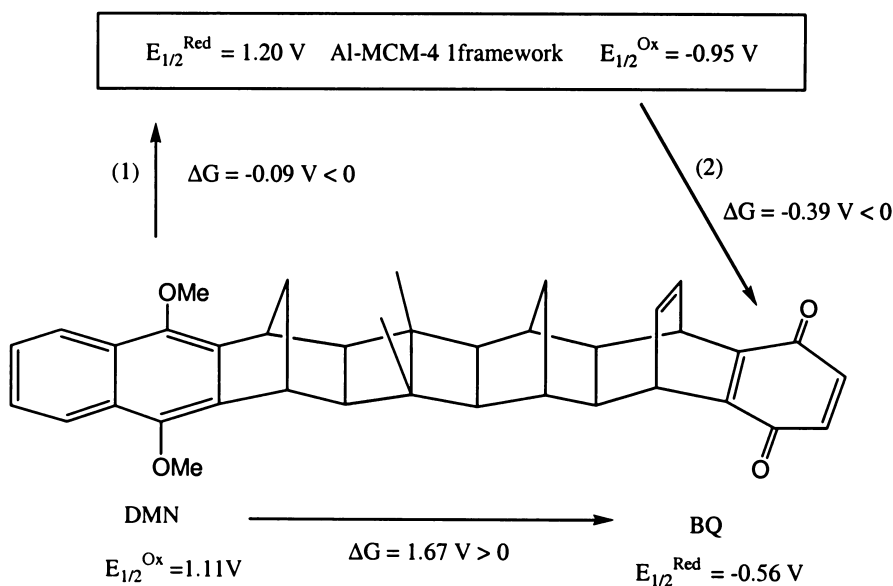
For DMN-6B-DCV, the driving force ( $\Delta G$ ) of the pathway (2), i.e., electron transfer from Al-MCM-41 framework to the DCV group to form the DCV radical anion, is positive. The driving force of the pathway (3), i.e., electron transfer from DMN group to the DCV group *via* the polynorbornane bridge, is more positive. These two pathways all need additional energy to initiate the electron transfer processes. Pathway (1), i.e., electron transfer from



the DMN group to the Al-MCM-41 framework, is the favourite mechanism, since the Gibbs free energy of this process is negative (-0.09 V).



**Scheme 7.4:** Possible electron transfer pathways for DMN-6B-DCV dyad in Al-MCM-41.



**Scheme 7.5:** Possible electron transfer pathways for DMN-6B-BQ dyad in Al-MCM-41.

For DMN-8B-BQ, the driving force of the pathway (3), i.e., electron transfer from DMN group to the BQ group *via* the polynorbornane bridge, is positive. The driving forces of the

pathway (1) and pathway (2) are all negative. However, pathway (2) is the favourite mechanism, since the difference of the Gibbs free energy (driving force) of this process is the most negative one.

DMN-8B-BQ can spontaneously form long-lived radical species while DMN-6B-DCV must be assisted by photoirradiation. The differences between these two dyads are the bridge length and the electron acceptor components. Since DMN-6B-DCV has shorter bridges (6 bond) than the DMN-8B-BQ, the electron transfer rate in the former should be faster than in the latter. The difference of the bond length cannot explain why DMN-6B-DCV needs photo-assistance. Apparently, the reason for the different behaviour of these two dyads in Al-MCM-41 must lie in the difference of the electron acceptor components. It is known that the reduction potential of BQ (-0.56 V) is much higher than that of the DCV (-1.72 V). More negative reduction potential of the DCV component in DMN-6B-DCV requires additional energy, which may be provided by the photoirradiation. As discussed in Chapter 6, spontaneous formation of the radical cations of DMN and its adducts, DMN[2] and DMN[4] takes place *via* electron transfer to the Lewis acid electron acceptor sites in Al-MCM-41. However, DMN-6B-DCV doesn't give any radical signals in the Al-MCM-41 without irradiation while DMN-8B-BQ does even without irradiation. Based on the above DR-UV-Vis, EPR and driving force studies, the EPR radical signal observed for DMN-6B-DCV in Al-MCM-41 after photoirradiation, is assigned to the radical cation of the DMN group, which formed a charge transfer complex with the Lewis acid sites of the Al-MCM-41 (extra-framework Al); while the EPR signal observed for the DMN-8B-BQ in Al-MCM-41 is assigned to the tightly bound "radical anion of the BQ group / extra-framework Al<sup>3+</sup>" ion pairs. In other words, DMN-6B-DCV takes pathway (1) after photoirradiation; while DMN-8B-BQ takes pathway (2), which can form BQ radical anions spontaneously. In both

processes, the Al, most probably the extra-framework Al in the Al-MCM-41, plays an important role.

It is noteworthy that photoinduced electron transfer processes through the hydrocarbon bridges of the dyads or the Al-MCM-41 framework cannot be completely ruled out only based on the above experimental results. Also, formation of long-lived charge separated state  $D^{\bullet+}-B-A^{\bullet-}$  via photoinduced electron transfer, where either the radical cation of the donor group (D) forms a charge transfer complex with the Lewis acid sites (extra-framework Al) or the radical anion of the acceptor group (A) forms an ion pair with the extra-framework  $Al^{3+}$ , cannot be completely ruled out, though computer simulation of the experimental EPR spectra using these two models failed.

## 7.5. Summary

In summary, the electron transfer processes of two dyads in the Al-MCM-41 hosts have been studied by means of EPR and DR-UV-Vis spectroscopy. It was suggested that the extra-framework Al either formed a charge transfer complex with the radical cation of the DMN group after photoirradiation in the case of the DMN-6B-DCV dyad; or formed a tightly bound “ion pair” with the radical anion of the BQ group in the case of the DMN-8B-BQ dyad. Extra-framework Al plays an important role in the electron transfer processes of these two dyads in the Al-MCM-41 hosts.

## 7.6. References for Chapter 7

- (1) Paddon-Row, M. N.; Oliver, A. M.; Warman, J. M.; Smit, K. J.; deHass, M. P.; Oevering, H.; Verhoeven, J. W. *J. Phys. Chem.* **1988**, 92, 6958.
- (2) Paddon-Row, M. N. *Acc. Chem. Res.* **1994**, 27, 18.
- (3) Oevering, H.; Paddon-Row, M. N.; Heppener, H.; Oliver, A. M.; Cotsaris, E.; Verhoeven, J. W.; Hush, N. S. *J. Am. Chem. Soc.* **1987**, 1987, 3258.
- (4) Warman, J. M.; Hom, M.; Paddon-Row, M. N.; Oliver, A. M.; Kroon, J. *Chem. Phys. Lett.* **1990**, 172, 114.
- (5) Roest, M. R.; Verhoeven, J. W.; Schuddeboom, W.; Warman, J. M.; Lawson, J. M.; Paddon-Row, M. N. *J. Am. Chem. Soc.* **1996**, 118, 1762.
- (6) Lawson, J. M.; Paddon-Row, M. N.; Schuddeboom, W.; warman, J. M.; Clayton, A. H. A.; Ghiggino, K. P. *J. Phys. Chem.* **1993**, 97, 13099.
- (7) Roest, M. R.; Lawson, J. M.; Paddon-Row, M. N.; Verhoeven, J. W. *Chem. Phys. Lett.* **1994**, 230, 536.
- (8) Penfield, K. W.; Miller, J. R.; Paddon-Row, M. N.; Cotsaris, E.; Oliver, A. M.; Hush, N. S. *J. Am. Chem. Soc.* **1987**, 109, 5061.
- (9) Lawson, J. M.; Craig, D. C.; Oliver, A. M.; Paddon-Row, M. N. *Tetrahedron* **1995**, 51, 3841.
- (10) Paquette, L. A.; Bellamy, F.; Böhm, M. C.; Gleiter, R. *J. Org. Chem.* **1980**, 45, 4913.
- (11) Verhoeven, J. W.; Koeberg, M.; Roest, M. R.; Paddon-Row, M. N.; Lawson, J. M. In *Biological Electron Transfer Chains: Genetics, Composition and Model of Operation*; Canters, G. W., Vijgenboom, E., Eds.; Kluwer Academic Publisher: Netherlands, **1988**, pp 51.
- (12) Verhoeven, J. W.; Kroon, J.; Paddon-Row, M. N.; Lawson, J. M. In *Supramolecular Chemistry*; Balzani, V., Cola, L. D., Eds.; Kluwer Academic Publishers: Netherlands, **1992**.
- (13) O'Neill, M. A.; Cozens, F. L.; Schepp, N. P. *J. Phys. Chem. B* **2001**, 105, 12746. And references therein.

- 
- (14) Vitale, M.; Castagnola, N. B.; Ortins, N. J.; Brooke, J. A.; Vaidyalingam, A.; Dutta, P. K. *J. Phys. Chem. B* **1999**, *103*, 2408.
- (15) Sankararaman, S.; Yoon, K. B.; Yabe, T.; Kochi, J. K. *J. Am. Chem. Soc.* **1991**, *113*, 1419.
- (16) Álvaro, M.; Chretien, M. N.; Ferrer, B.; Fornés, V.; García, H.; Scaiano, J. C. *Chem. Commun.* **2001**, 2106.
- (17) Yoon, K. B.; Park, Y. S.; Kochi, J. K. *J. Am. Chem. Soc.* **1996**, *118*, 12710.
- (18) Fukuzumi, S.; Yoshida, Y.; Urano, T.; Suenobu, T.; Imahori, H. *J. Am. Chem. Soc.* **2001**, *123*, 11331.
- (19) Park, Y. S.; Lee, E. J.; Chun, Y. S.; Yoon, Y. D.; Yoon, K. B. *J. Am. Chem. Soc.* **2002**, *124*, 7123.
- (20) Cano, M. L.; Cozens, F. L.; Fornes, V.; García, H.; Scaiano, J. C. *J. Phys. Chem.* **1996**, *100*, 18145.
- (21) Ramamurthy, V. *J. Photochem. Photobiol. C: Photochem. Rev.* **2000**, *1*, 145.
- (22) Sykora, M.; Kincaid, J. R. *Nature* **1997**, *387*, 162.
- (23) Yoon, K. B.; Hubig, S. M.; Kochi, J. K. *J. Phys. Chem.* **1994**, *98*, 3865.
- (24) Corma, A.; Fornés, V.; García, H.; Miranda, M. A.; Sabater, M. J. *J. Am. Chem. Soc.* **1994**, *116*, 9767.
- (25) Krueger, J. S.; Mayer, J. E.; Mallouk, T. E. *J. Am. Chem. Soc.* **1988**, *110*, 8232.
- (26) Yonemoto, E. H.; Kim, Y. I.; Schmehl, R. H.; Wallin, J. O.; Shoulders, B. A.; Richardson, B. R.; Haw, J. F.; Mallouk, T. E. *J. Am. Chem. Soc.* **1994**, *116*, 10557.
- (27) Konovalova, T. A.; Gao, Y.; Schad, R.; Kispert, L. D. *J. Phys. Chem. B* **2001**, *105*, 7459.
- (28) Krishna, R. M.; Prakash, A. M.; Kevan, L. *J. Phys. Chem. B* **2000**, *104*, 1796.
- (29) Sung-Suh, H. M.; Luan, Z.; Kevan, L. *J. Phys. Chem. B* **1997**, *101*, 10455.
- (30) Yamashita, H.; Tanaka, A.; Nishimura, M.; Koyano, K.; Tatsumi, T.; Anpo, M. *Stud. Surf. Sci. Catal.* **1998**, *117*, 551.
- (31) Moller, K.; Bein, T. *Chem. Mater.* **1998**, *10*, 2950. And references therein.
- (32) Krishna, R. M.; Kevan, L. *Phys. Chem. Chem. Phys.* **2001**, *3*, 5348.
- (33) Sinlapadech, S.; Koodali, R.; Krishna, R. M.; Kevan, L. *J. Phys. Chem. B* **2002**, *106*, 6251.

- 
- (34) Park, S. E.; Sung-Suh, H. M.; Kim, D. S.; Ko, J. *Stud. Surf. Sci. Catal.* **2000**, *129*, 807. reference therein.
- (35) Sinlapadech, S.; Krishna, R. M.; Luan, Z.; Kevan, L. *J. Phys. Chem. B* **2001**, *105*, 4350.
- (36) Choi, J. R.; Yoon, M.; Yim, Y.-H.; Jeoung, S. C. *Chem. Phys. Lett.* **2002**, *351*, 391.
- (37) Kuchi, V.; Oliver, A. M.; Paddon-Row, M. N.; Howe, R. F. *Chem. Commun.* **1999**, 1149.
- (38) Davies, A. G. *Chem. Soc. Rev.* **1993**, *22*, 299.
- (39) Davies, A. G.; Courtneidge, J. *Acc. Chem. Res.* **1987**, *20*, 90.
- (40) Davies, A. G.; Ng, K.-M. *Aust. J. Chem.* **1995**, *48*, 167.
- (41) Handoo, K. L.; Gadru, K. *Curr. Sci.* **1986**, *55*, 920.
- (42) Yoon, K. B. *Chem. Rev.* **1993**, *93*, 321. And reference therein.

## Chapter 8

### Summary and Future Work

#### 8.1. Summary

In summary, five different mesoporous (A)-MCM-41, including Si-MCM-41, three directly synthesized Al-MCM-41 (Si/Al = 39, 15 and 7, respectively), and a post-synthesized Al-MCM-41 (Si/Al = 14) were used as hosts to assemble various kinds of electron donors, acceptors and D-B-A dyads. To solve the structure collapse problem during thermal calcination, template removal by ozone treatment at low temperature (room temperature and 473 K) was studied. At room temperature, ozone treatment can largely cleave the long hydrocarbon chain of the CTAC molecule, but it cannot remove some organic residues formed inside the channels of the Al-MCM-41. At 423 K, ozone treatment can completely remove CTAC template molecules from as-synthesized Si-MCM-41 and low Al content Al-MCM-41 (Si/Al = 39), but still leave some organic residues in higher Al content samples (Si/Al = 15, 7).

Four methods (A1, A2, B1 and B2) for assembling the organic molecules into the (Al)-MCM-41 hosts have been examined. It was found that a proper assembling method is critical for exploring the redox nature and the redox sites in (Al)-MCM-41. This result may also extended to the other porous materials.

Pure MCM-41 has no (or rather weak) electron donor and acceptor sites at room temperature. However, Al-MCM-41 materials have been proved to be useful mesoporous hosts for the purpose of generating and stabilizing radical species. Hyperfine spin coupling of  $^{27}\text{Al}$  with some assembled electron donor and acceptor molecules has been found. The electron donor sites in Al-MCM-41 are attributed to the

negatively charged oxygen on the extra-framework aluminum (oxide ions). The electron acceptor sites are attributed to the Lewis acid sites (extra-framework  $\text{Al}^{3+}$ ) generated by dealumination during thermal calcination. The oxidation potential of the Al-MCM-41 is determined to be in the range of  $-0.92 \text{ V} \geq E^{\text{Ox}}(\text{Al-MCM-41}) \geq -1.0 \text{ V}$ ; while the reduction potential of the Al-MCM-41 is determined to be in the range of  $1.34 \text{ V} \geq E^{\text{Red}}(\text{Al-MCM-41}) \geq 1.18 \text{ V}$ .

The electron transfer processes of two dyads in the Al-MCM-41 hosts have been studied by means of EPR and DR-UV-Vis spectroscopy. It is suggested that the extra-framework Al either forms a charge-transfer complex with the radical cation of the DMN group in the case of the DMN-6B-DCV dyad, or forms a tightly bound ion pair with the radical anion of the BQ group in the case of the DMN-8B-BQ dyad. Al plays an important role in the electron transfer processes of these two dyads in the Al-MCM-41 hosts.

## 8.2. Future Work

- (1) Explore the influence of the surface hydroxyl groups on the electron transfer processes using high silanol-containing Al-MCM-41 hosts whose templates are removed by ozone treatments.
- (2) Improve the electron donating and accepting ability of the MCM-41 hosts by incorporating other metal ions, such as titanium and  $\text{MV}^{2+}$ .
- (3) Explore the possibility of constructing photoredox systems in the as-synthesized MCM-41 materials. This heterogeneous system combines the micelle and the mesoporous inorganic aluminosilicate framework features, and may provide intriguing prospects for achieving long-lived charge separation.



- 
- (4) Do ENDOR (electron nuclear double resonance) experiment to determine the  $^{27}\text{Al}$  hyperfine splitting constant in the systems studied in this work, to provide stronger evidences of the involvement of the Al in the electron transfer processes with the occluded redox species.
  - (5) Synthesis and assembly of some new D-B-A molecules, to improve understanding of the electron transfer processes of D-B-A molecules in the heterogeneous media.
  - (6) Synthesis of two new Al-MCM-41 samples, one contains only framework Al and the other one contains only extra-framework Al, check the spin concentration of radical cations and anions by assembling the electron donors and acceptors studied in this work, which may provide further evidence to the hypothesis of the electron donor and acceptor sites in Al-MCM-41 put forward in this work.
  - (7) Since this work hints that the extra-framework Al plays an important role in the electron transfer processes within the Al-MCM-41 hosts, it is interesting to emphasize the further work in pursuing novel hosts or substrates other than siliceous materials, such as metal oxides (e.g.  $\text{TiO}_2$ ,  $\text{Al}_2\text{O}_3$ ) and nanoparticles (e.g. carbon, silicon and other nanohybrid materials).